Physics of the Solid State, Vol. 44, No. 7, 2002, pp. 1203–1204. From Fizika Tverdogo Tela, Vol. 44, No. 7, 2002, pp. 1153–1154.
Original English Text Copyright © 2002 by Sho-ichi Iwamatsu, Vijayalakshmi, Yukihiro Kitamura, Masanori Hamajima, Inami Koike, Shizuaki Murata.

Photochemical and Thermal Rearrangement of Cyclohexadiene Derivatives of C_{60}: Formation and Characterization of Novel Compounds Relating to bis(fulleroid)[1]

Sho-ichi Iwamatsu*, K. P. Vijayalakshmi, Yukihiro Kitamura**, Masanori Hamajima**,**
Inami Koike, and Shizuaki Murata*, ****
** CREST, Japan Science and Technology Corporation (JST), Japan*
*** Graduate School of Environmental Studies, Nagoya University, Nagoya, 464-8601 Japan*
e-mail: murata@urban.env.nagoya-u.ac.jp

Among exohedral fullerene derivatives [1], fulleroid (a C_1 homologue with the [6,5] open structure on C_{60}) has been collecting much attention since its early discovery by Wudl, because it remains an original 60π-electron system [2]. In addition, its mechanically unique rearrangement toward methanofullerene (the [6,6] close structure with a cyclopropane ring) has been studied by both experimental and theoretical methods [3]. A novel fulleroid derivative, bis(fulleroid) containing two [6,5] open units connected by an ethylene (–CH=CH–) linker, was synthesized by Rubin using photoinduced isomerization of the cyclohexadiene derivative of C_{60} (an exohedral –CH=CH–CH=CH– adduct) via sequential [4 + 4] and [2 + 2 + 2] reactions

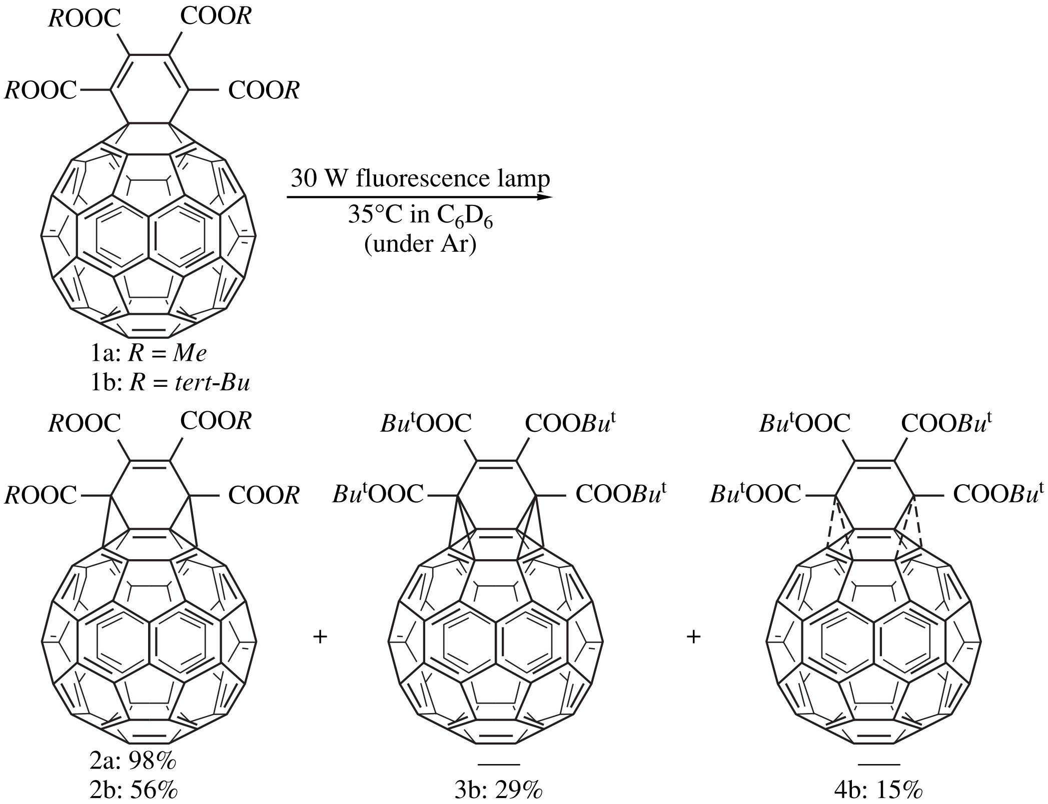

Products of the reaction.

---

[1] This article was submitted by the authors in English at the V International workshop "Fullerenes and Atomic Clusters." The proceedings of this workshop can be found in Phys. Solid State, Vol. 44, nos. 3–4 (2002).

1063-7834/02/4407-1203$22.00 © 2002 MAIK "Nauka/Interperiodica"

[4,5]. However, the occurrence of the related rearrangement of bis(fulleroid) toward bis(methano)fullerene was not known; however, the existence of bis(methano)fullerene could be found by using a multistep synthesis. Herein, we describe the first example of direct formation on bis(methano)fullerene by photoinduced rearrangement of the cyclohexadiene derivatives of C_{60}, which is a key precursor of bis(fulleroid).

Recently, we reported that the reactions of C_{60} with alkoxycarbonyl substituted palladacyclopentadiene derivatives gave the cyclohexadiene derivative 1a and irradiation of the toluene solution by visible light afforded bis(fulleroid) 2a [6]. On the other hand, similar rearrangement of 1b bearing *tert*-butyl ester afforded a mixture of the following three compounds: bis(fulleroid) (2b), bis(methano)fullerene (3b), and fulleroid-methanofulle-rene (4b) [see figure]. When the reaction mixture was obtained after 12 h of irradiation in C_6D_6 at 35°C, products 2b, 3b, and 4b were observed in a 56 : 29 : 15 ratio (87% conversion). The products (2b and 3b) were easily separated by silica-gel chromatography.

In the C_s symmetric ^{13}C NMR spectra of 2b, 32 signals assignable to sp^2 carbons were observed together with one sp^3 signal at 57.72 ppm. Compound 3b also showed 30 C_s symmetric signals in the sp^2 carbon region and 3 kinds of sp^3 carbons, the chemical shifts of which (44.93, 53.47, and 66.87 ppm, respectively) resembled those of the previously reported bis(methano)fullerene. The four kinds of singlet signals assignable to the *t*-butyl groups in the ^{1}H NMR spectrum of 4b indicated that the structure was C_1 symmetric.

Although Rubin and Cheng did not describe the possibilities of thermal isomerization of their cyclohexadiene derivatives toward bis(fulleroid), 1a and 1b converted into 2a and a mixture with 2b and 3b upon heating at 150 and 110°C, respectively. However, unlike the related fulleroid-methanofullerene (C_{60}–CR_2) system, neither photochemical nor thermal isomerization of bis(fulleroid) (2) to bis(methano)fullerene (3) nor the reverse reaction (3 to 2) proceeded even under forcing conditions resulting in decomposition of the *tert*-butylester. The production of fulleroid under kinetic conditions was discussed, and methanofullerene was considered to be a thermodynamically controlled product. The speculations were supported by semiempirical MO calculations, and fulleroid is 6 kcal/mol less stable than methanofullerene. On the contrary, in our AMI calculations, bis(fulleroid) (2b) is 27.6 and 14.0 kcal/mol more stable than bis(methano)fullerene (3b) and 1b, respectively.

REFERENCES

1. A. Hirsch, *The Chemistry of Fullerenes* (Thieme Verlag, Stuttgart, 1994), Chap. 4; M. S. Meier, *The Chemistry of Fullerenes*, Ed. by R. Taylor (World Scientific, Singapore, 1995), Chaps. 9, 10.
2. T. Suzuki, Q. Li, K. C. Khemani, *et al.*, Science **254**, 1186 (1991); A. B. Smith, III, R. M. Strongin, L. Brard, *et al.*, J. Am. Chem. Soc. **115**, 5829 (1993); F. Diederich, L. Issacs, and D. Philp, Chem. Soc. Rev. **23**, 243 (1994) and references therein.
3. M. Eiermann, F. Wudl, M. Prato, and M. Maggini, J. Am. Chem. Soc. **116**, 8364 (1994); R. A. J. Janssen, J. C. Hummelen, and F. Wudl, J. Am. Chem. Soc. **117**, 544 (1995); R. Gonzales, J. C. Hummelen, and F. Wudl, J. Org. Chem. **60**, 2618 (1995); M. H. Hall, H. Lu, and P. B. Shevlin, J. Am. Chem. Soc. **123**, 1349 (2001) and references therein.
4. M. J. Arce, A. L. Viado, S. I. Khan An, and Y. Rubin, J. Am. Chem. Soc. **118**, 3775 (1996); W. Qia, M. D. Bartberger, S. J. Pastor, *et al.*, J. Am. Chem. Soc. **122**, 8333 (2000).
5. T.-Y. Hsiao, K. C. Santhosh, K. F. Liou, and C.-H. Cheng, J. Am. Chem. Soc. **120**, 12232 (1998); T.-Y. Hsiao, S. K. Chidambareswaran, and C.-H. Cheng, J. Org. Chem. **63**, 8617 (1998).
6. H. Inoue, H. Yamaguchi, T. Suzuki, *et al.*, Synlett 1178 (2000).

Physics of the Solid State, Vol. 44, No. 7, 2002, pp. 1205–1207. Translated from Fizika Tverdogo Tela, Vol. 44, No. 7, 2002, pp. 1155–1157.
Original Russian Text Copyright © 2002 by V. Zubov, I. Zubov.

On the Thermodynamic Properties of Higher and Smaller Fullerites*

V. I. Zubov[1, 2] **and I. V. Zubov**[1, 2]
[1] *Peoples Friendship University, ul. Miklukho-Maklaya 6, Moscow, 117198 Russia*
[2] *Institute of Physics, Federal University of Goiás, Goiânia, GO, Brazil*
e-mail: zubov@fis.ufg.br

Abstract—The temperature dependences of the saturation vapor pressure of C_{96} and C_{36} fullerites and their properties along the sublimation curves are calculated using a correlation method of unsymmetrized self-consistent field that allows for strong anharmonicity of the lattice vibrations. The calculation is performed in terms of the Girifalco intermolecular potential with parameters recently determined for these fullerenes. Since experimental data on C_{96} and C_{36} fullerites are unavailable, the results of our calculations are compared with our results obtained earlier for the most commonly encountered fullerite C_{60}. The specific features in the dependences of the properties of C_{96} and C_{36} fullerites on the number of atoms per molecule are revealed. *© 2002 MAIK “Nauka/Interperiodica”.*

1. INTRODUCTION

This work continues calculations of the thermodynamic properties of the high-temperature modifications of fullerites. At present, the most commonly encountered fullerite C_{60} and the next fullerite C_{70} have been adequately studied experimentally and theoretically. Particularly, it is known that the fullerite molecules are orientationally ordered in the crystal lattice at low temperatures and rotate almost freely in the face-centered cubic lattice (with a small admixture of the face-centered close-packed phase in C_{70}) at high temperatures. It is assumed that other fullerites should behave similarly.

Girifalco [1] was the first to investigate theoretically the properties of the high-temperature modifications of fullerites. Taking into account the fact that the C_{60} molecule has a nearly spherical form, he derived the intermolecular potential for orientationally disordered (solid, gaseous, and hypothetical liquid) phases:

$$\Phi_G(r) = -\alpha\left(\frac{1}{s(s-1)^3} + \frac{1}{s(s+1)^3} - \frac{2}{s^4}\right) + \beta\left(\frac{1}{s(s-1)^9} + \frac{1}{s(s+1)^9} - \frac{1}{s^{10}}\right), \quad (1)$$

where $s = r/2a$, r is the distance between the centers of molecules, and a is the radius of their rigid core. Verheijen *et al.* [2] accomplished a generalization of the Girifalco potential (1) for C_{70}. Kniaz’, Girifalco, and Fischer [3] and, independently, Abramo and Caccamo [4] applied the Girifalco potential (1) to the orientationally disordered solid phase of C_{70}. This corresponds to the approximation of the C_{70} cage by a sphere whose radius is determined by fitting the lattice constant calculated with this potential to the experimental lattice constant. Saito *et al.* [5] and Molchanov *et al.* [6] earlier used a spherical approximation for higher fullerenes with the radius depending on the number of atoms per molecule.

The intermolecular potentials proposed by Girifalco and Verheijen were used in the calculations of the equilibrium thermodynamic properties of the high-temperature phases of C_{60} [7–9] and C_{70} [10, 11] fullerites with due regard for the intramolecular vibrations (which make the major contribution to the heat capacities) over extended regions of their phase diagrams, including the sublimation curves [8, 10]. The agreement between theory and experiment was quite reasonable.

In recent years, considerable interest has been expressed by scientists both in higher fullerites, such as C_{76}, C_{84} [12–14], and C_{96} [15], and in smaller fullerites, especially in C_{36} [16, 17]. A method of calculating the coefficients of the Girifalco potential (1) from the known coefficients for C_{60} [1] was proposed earlier in [18]. This approach was based on the spherical approximation of the form of the fullerene molecules; i.e., it did not require additional fitting parameters. The coefficients of the potential were calculated for a series of smaller and higher fullerenes (from C_{28} to C_{96}). It is of interest that the coefficients α and β decrease with an increase in the number of atoms per molecule, even though the minimum of the potential and the depth of the potential well increase. Potential (1) with coefficients taken from [18] was used for analyzing the saturation vapor pressure and the thermodynamic proper-

---

[*] This paper was presented at the V International Workshop “Fullerenes and Atomic Clusters,” St. Petersburg, Russia, July 2–6, 2001. See Proceedings of the V International Workshop in *Fizika Tverdogo Tela* (Physics of the Solid State), 2002, nos. 3–4.

1063-7834/02/4407-1205$22.00 © 2002 MAIK “Nauka/Interperiodica”

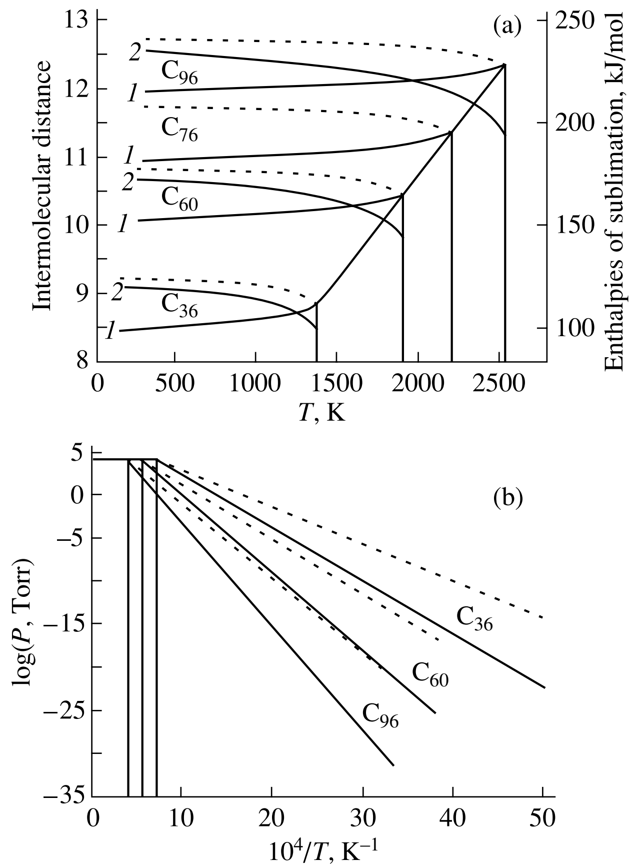

Fig. 1. Properties of fullerites along the sublimation curves: (a) (*1*) the mean intermolecular distance and (*2*) the enthalpy of sublimation and (b) logarithms of the saturation vapor pressures. Dashed lines represent the thermodynamically unstable branches of the sublimation curves.

ties of two higher fullerites, namely, C_{76} and C_{84} [19, 20]. Good agreement between the calculated and available experimental data was observed in [12–14].

In the present work, the properties of the higher C_{96} and smaller C_{36} fullerites were calculated using a correlation method of unsymmetrized self-consistent field (see, for example, [7–9]).

2. CALCULATION TECHNIQUE

The zeroth-order approximation of the method used includes strong anharmonicity of the lattice vibrations up to the fourth order, and the perturbation theory takes into account the fifth and sixth anharmonic terms. First, we solve a system of equations describing the temperature dependences of the saturation vapor pressure and the mean intermolecular distance of the crystal along the phase equilibrium curve. A virial expansion with inclusion of the second terms was used for the gaseous phase. The appropriate equations were obtained in our earlier works [8, 11]. At temperatures below the limiting temperature T_S ($T < T_S$), the equations have two pairs of roots, namely, $P_{1\mathrm{sat}}(T) < P_{2\mathrm{sat}}(T)$ and $a_1(T) < a_2(T)$ [P_{sat} is the saturation vapor pressure], which become identical when $T = T_S$. At $T > T_S$, real solutions to these equations are absent. The isothermal modulus B_T of the crystal is positive along the lower branch and negative along the upper branch; therefore, it corresponds to the absolutely unstable thermodynamic states. The limiting temperature T_S [$P_{\mathrm{sat}}(T_S)$] is the point of loss of thermodynamic stability (the spinodal point) of the two-phase crystal–vapor system. Along the lower branches, we calculated the thermodynamic properties associated with the lattice vibrations.

Coefficients of relationship (2)

Fullerite	*A*	*B*, K	10^4 *C*, K^{-1}
C_{36}	9.2868	6279.5	3.6434
C_{60}	9.4253	9032.3	2.6268
C_{96}	9.5337	12241.73	1.9619

3. RESULTS AND DISCUSSION

The figure represents the temperature dependences of the mean intermolecular distance and the enthalpy of sublimation for C_{36} and C_{96} fullerites and the dependence of the logarithm of the saturation vapor pressure on the inverse temperature. The unstable branches are depicted by the dashed lines. As far as we know, experimental data on these fullerites are unavailable. For this reason, we compared the results of our calculations with our data obtained earlier for the most commonly encountered fullerite C_{60} [8]. The curve $a(T)$ for C_{76} [19] is also shown in Fig. 1a for comparison. It is evident that the intermolecular distance and the spinodal temperature increase with an increase in the number of atoms per molecule. As can be seen from the figure, the points $a(T_S)$ lie along a nearly straight line.

The dependence $\log P_{\mathrm{sat}}(1/T)$ for both branches exhibits a nearly linear behavior. For the lower branch, this behavior agrees well with the available experimental data for C_{60}, C_{70}, C_{76}, and C_{84}. The dependence $\log P_{\mathrm{sat}}(1/T)$ can be more precisely described by the following relationship over the entire range of temperatures:

$$\log P_{\mathrm{sat}} = A - \frac{B}{T} - CT. \tag{2}$$

The coefficients involved in relationship (2) are presented in the table. Note that the last term accounts for the anharmonicity of the lattice vibrations. Despite the relatively small value, the coefficient C contributes appreciably to the saturation vapor pressure P_{sat} at high temperatures. It is seen from the table that the constant term in relationship (2) is virtually independent of the number of atoms per molecule. Consequently, the saturation vapor pressures at the spinodal points of different fullerites differ insignificantly. The coefficient B increases and the coefficient C decreases as the number of atoms per molecule increases.

It should be noted that the isothermal modulus B_T of the crystal and the shear coefficient C_{44} vanish at the spinodal points.

The good agreement observed between the results of our calculations and the experimental data obtained earlier for C_{60} [7–9], C_{70} [10, 11], C_{76}, and C_{84} [19, 20] fullerites suggests that experimental data obtained in the future will also agree with our calculations for C_{36} and C_{96}.

REFERENCES

1. L. F. Girifalco, J. Phys. Chem. **96**, 858 (1992).
2. M. A. Verheijen, H. Meekes, P. Bennema, *et al.*, Chem. Phys. **166**, 287 (1992).
3. K. Kniaz’, L. F. Girifalco, and J. E. Fischer, J. Phys. Chem. **99**, 16804 (1995).
4. M. C. Abramo and C. Caccamo, J. Phys. Chem. Solids **57**, 1751 (1996).
5. Y. Saito, T. Yoshikawa, N. Fujimoto, and H. Shinihara, Phys. Rev. B **48** (12), 9182 (1993).
6. S. P. Molchanov, A. M. Popov, and A. V. Sukhorukov, Poverkhnost, Nos. 8–9, 42 (1994).
7. V. I. Zubov, N. P. Tretiakov, J. F. Sanchez, and A. A. Caparica, Phys. Rev. B **53** (18), 12080 (1996).
8. V. I. Zubov, J. F. Sanchez-Ortiz, J. N. Teixeira Rabelo, and I. V. Zubov, Phys. Rev. B **55** (11), 6747 (1997).
9. V. I. Zubov, J. F. Sanchez, N. P. Tretiakov, *et al.*, Carbon **35** (6), 729 (1997).
10. V. I. Zubov, N. P. Tretiakov, I. V. Zubov, *et al.*, J. Phys. Chem. Solids **58** (12), 2039 (1997).
11. V. I. Zubov, N. P. Tretiakov, I. V. Zubov, and J. B. Marques Barrio, J. Phys. Chem. Solids **60**, 547 (1999).
12. H. Kawada, Y. Fujii, H. Nakao, *et al.*, Phys. Rev. B **51**, 8723 (1995).
13. B. Brunetti, G. Gigli, E. Siglio, *et al.*, J. Phys. Chem. B **101**, 10 715 (1997).
14. V. Piacente, C. Patchette, G. Gigli, and P. Scardala, J. Phys. Chem. A **101**, 4303 (1997).
15. M. C. Abramo, C. Caccamo, D. Costa, and G. Pellicane, Europhys. Lett. **54** (4), 468 (2001).
16. Z. Slanina, X. Zhao, and E. Osawa, Chem. Phys. Lett. **290**, 311 (1998).
17. C. Piscotti, J. Yarger, and A. Zettl, Nature **393**, 771 (1998).
18. V. I. Zubov, Mol. Mater. **13**, 385 (2000).
19. V. I. Zubov, N. P. Tretiakov, and I. V. Zubov, Eur. Phys. J. B **17**, 629 (2000).
20. V. I. Zubov, N. P. Tretiakov, and J. N. Teixeira Rabelo, Mol. Mater. **13**, 349 (2000).

Translated by O. Moskalev

Physics of the Solid State, Vol. 44, No. 7, 2002, pp. 1208–1211. Translated from Fizika Tverdogo Tela, Vol. 44, No. 7, 2002, pp. 1158–1161.
Original Russian Text Copyright © 2002 by Gerasimenko, Belogolovskiĭ, Revenko, Chernyak, Svistunov, Shaternik, Rudenko, Hatta, Sasaki.

METALS AND SUPERCONDUCTORS

Electron–Boson Interaction in Nonsuperconducting Magnetic Metals

A. Yu. Gerasimenko*, M. A. Belogolovskiĭ*, Yu. F. Revenko*, O. I. Chernyak*, V. M. Svistunov*, V. E. Shaternik, É. M. Rudenko**, E. Hatta***, and T. Sasaki*****
** Donetsk Physicotechnical Institute, National Academy of Sciences of Ukraine, Donetsk, 83114 Ukraine*
e-mail: vlamis@hsts.fti.ac.donetsk.ua
*** Institute of Metal Physics, National Academy of Sciences of Ukraine, Kiev, 03680 Ukraine*
**** Nanoelectronics Laboratory, Graduate School of Engineering, Hokkaido University, Sapporo 060-0813, Japan*
Received September 26, 2001

Abstract—Gadolinium- and chromium-based normal metal–insulator–metal tunnel junctions were studied. Spectral functions of the Gd and Cr electron–boson interaction were reconstructed, from which it follows that the magnetic subsystem plays a noticeable role in the electron transport in magnetic metals. *© 2002 MAIK “Nauka/Interperiodica”.*

Interaction of electrons with low-energy boson excitations results in renormalization of the carrier effective mass m^* in metals ($m^* > m_e$, where m_e is the electron mass), which, in turn, affects the kinetic and thermodynamic properties of the metals [1]. A wealth of information on the structure of quasiparticle spectra of conductors can be obtained from tunneling spectroscopy, which is based on measuring $I(V)$ curves and their derivatives with respect to voltage V for structures of the metal–insulator–metal type. The presently available spectral information is, however, confined in most cases to superconductors, in which the amplitude of the effect is comparatively large. Moreover, except for a small number of papers [2], tunneling spectroscopy studies have been limited to investigation of the electron–phonon coupling. Such an analysis can be applied only to simple materials, because in most cases a system has additional boson-type excitations, interaction with which is also reflected in the $I(V)$ curves. It would be of use to identify and estimate their contribution.

For illustration, we consider magnetic transition metals whose carriers interact not only with phonons but also with magnetic excitations, so that the effective-mass renormalization $\lambda = m^*/m_e - 1$ contains electron–phonon ($\lambda_{e\text{–ph}}$) and electron–magnon ($\lambda_{e\text{–}m}$) contributions: $\lambda = \lambda_{e\text{–ph}} + \lambda_{e\text{–}m}$. Theoretical calculations for magnetic metals, which were made with inclusion of lattice vibrations alone, could not account for the experimental values of λ obtained [3]. The calculated $\lambda_{e\text{–ph}}$ were systematically underevaluated; for instance, the theoretical value for gadolinium is $\lambda_{e\text{–ph}} = 0.4$, whereas heat capacity measurements yield $\lambda = 1.1$ and de Haas–van Alfven experiments suggest $\lambda = 1.2$–2.1. A conjecture was put forward [3] that the reason for these discrepancies lies in the interaction of electrons with the magnetic excitations of gadolinium. We present here the first experimental data on electron tunneling into ferromagnetic gadolinium (the Curie temperature T_C = 297 K, total magnetic moment 7.55 μ_B), which provide support for this conjecture and unambiguously indicate the existence of strong electron–magnon coupling in this material. We note that the conclusion that the effect of magnons on electron transport in this material is of importance was drawn earlier by Akimenko *et al.* [4] from microcontact spectroscopy data; however, because of the local heating generated at high voltages, the spectral resolution was not good enough to elucidate all the details of electron interaction with the magnetic excitations. The tunneling method employed by us in studies of nonsuperconducting metals is devoid of this shortcoming.

Another object studied by us is antiferromagnetic chromium (Néel temperature T_N = 311 K), whose tunneling characteristics were measured earlier [5], but the shape of the electron–boson interaction function was not determined. We note that theory likewise disagrees here with experiment concerning the electronic-mass renormalization, namely, $\lambda^{\text{theor}} = 0.25$ [6], whereas electronic heat capacity measurements yield $\lambda = 0.5$ [7].

Our analysis of electron-tunneling data for normal metal–insulator–metal junctions is based on the concepts discussed in [8, 9]. We shall discriminate the voltage-even contribution $\sigma_+(V) = [dI(+V)/dV + dI(-V)/dV]/2$ to the differential junction conductivity from the voltage-odd contribution $\sigma_-(V) = [dI(+V)/dV - dI(-V)/dV]/2$. As shown in [9], $\sigma_-(V)$ is proportional to the real part of the self-energy $\Sigma(\omega)$ of electrons in the

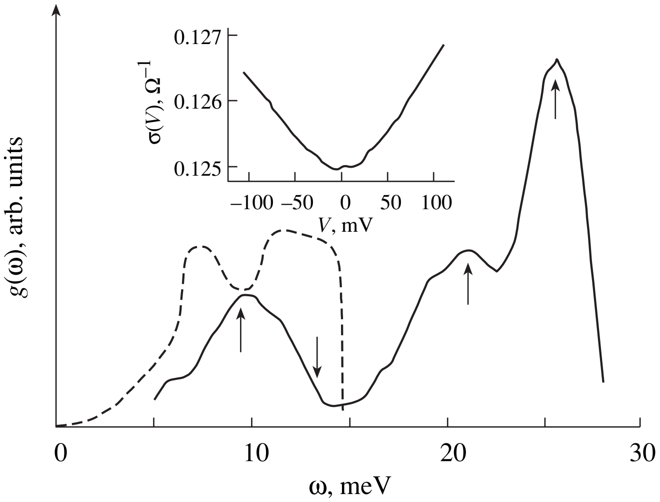

Fig. 1. Spectral function of the electron–boson coupling in gadolinium (solid line) and phonon density of states calculated in [11] (dashed line). Arrows specify the position of the singularities ($\partial\omega/\partial\mathbf{k} = 0$) in the magnon dispersion curves from [12]. Inset shows the electrical conductivity of the Gd–Gd-oxide–Al tunnel junction at 4.2 K.

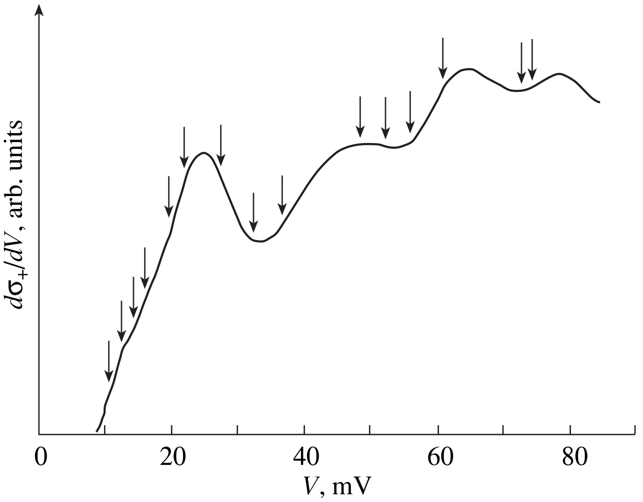

Fig. 2. Derivative $d\sigma_+(V)/dV$ for the Gd–Gd-oxide–Al junction. Arrows specify the position of the singularities in the Raman spectrum of single-crystal Gd_2O_3 [15].

metallic plates. If the renormalization effects are significant only for one of the plates, then

$$\sigma_-(V) = -C\sigma(0)\mathrm{Re}\,\Sigma(eV). \qquad (1)$$

While there is currently no common opinion on the nature of the effect and on the magnitude of the corresponding coefficient C (see [9]), the proportionality of $\sigma_-(V)$ to $\mathrm{Re}\Sigma(eV)$ has been established experimentally for a number of metals [8–10] and will be demonstrated below for magnetic materials. The latter means that we can presently determine the shape of the energy dependence of $\Sigma(\omega)$ rather than that of the amplitude. This information in itself is significant, because it permits one to establish the energies of the characteristic boson excitations in a system and estimate their relative effect. Moreover, by measuring the $\sigma_-(V)$ dependence, one can reconstruct the shape of the spectral function $g(\omega)$ of the electron–boson interaction in a normal metal [9]:

$$g(\omega) = \frac{2\omega}{Ce\sigma(0)\pi^2}\int_0^\infty \frac{d\sigma_-(V)/dV}{V^2 - (\omega/e)^2}dV. \qquad (2)$$

In magnetic metals, there are two main types of boson excitations with which the conduction electrons interact, namely, phonons and magnons. The former are usually below the latter in energy, thus permitting one to separate their relative contributions to $g(\omega)$ and, thus, compare the efficiency of electron scattering from these two types of quasiparticle excitations.

While the odd part of the conductivity contains information on the spectra of the plates, $\sigma_+(V)$ is related to the processes occurring in the barrier [2]. As a first approximation, one can assume the derivative $d\sigma_+(V)/dV$ to be proportional to the spectral density of boson excitations $F_B(\omega)$ in the insulator separating the two metallic layers [2, 8]. We compare here these data for the oxides forming potential barriers in heterostructures based on gadolinium and chromium.

The gadolinium junctions were prepared from high-purity single-crystal Gd from which 2- to 3-mm thick ribbon-shaped samples about 10 mm^2 in area were cut; the samples were polished mechanically and oxidized in air to obtain a thin insulating film of gadolinium oxide, after which an aluminum film serving as a second electrode was evaporated on the oxidized surface. The chromium-based tunnel structures were produced by oxidizing Cr films about 100 nm thick in air at normal pressure and a film temperature of 470–500 K. After the thickness of the chromium oxide serving as an insulator reached about 5 nm, a thin silver overlayer was deposited.

In both cases, the measurements were carried out at 4.2 K and the sample resistance at zero voltage varied from a few units to a few tens of ohms. The differential conductivity $dI(V)/dV$ was measured by the standard low-frequency technique of harmonic detection [10], with a modulating signal amplitude of 1 mV. The second derivatives were obtained by numerical differentiation of the conductivity curves for the two types of heterostructures studied.

The reconstructed curves of some samples exhibited weak features which, in our opinion, have no relation to electron–boson interactions in the plates and the barrier. In particular, the reconstructed function $g(\omega)$ of gadolinium had a small peak in the zero-energy region. This peak originates from the asymmetry in the zero anomaly (which was observed to exist in nearly all $dI(V)/dV$ relations for gadolinium junctions) and is due

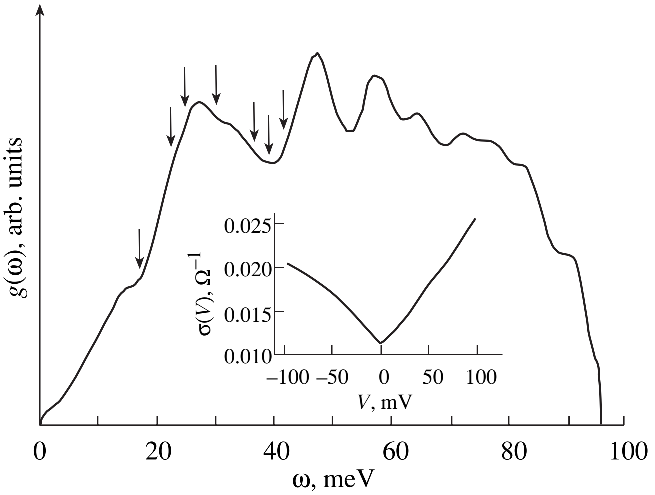

Fig. 3. Spectral function of the electron–boson coupling in chromium. Arrows specify the position of the singularities ($\partial\omega/\partial\mathbf{k} = 0$) in the phonon dispersion curves taken from [16]. Inset shows the electrical conductivity of the Cr–Cr-oxide–Ag tunnel junction at 4.2 K.

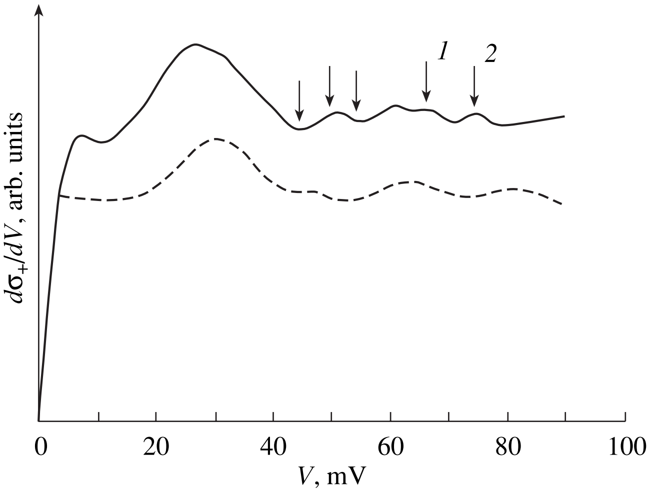

Fig. 4. Derivative $d\sigma_+(V)/dV$ for the Cr–Cr-oxide–Ag junction. The solid line is calculated in this work, and the dashed line is the data from [5]. Arrows specify the position of the singularities ($\partial\omega/\partial\mathbf{k} = 0$) in the dispersion curves of magnons [17] and of optical phonons (arrows *1*, *2*) [18] for the Cr_2O_3 single crystal.

apparently to the tunneling electrons interacting with the magnetic moments localized in the barrier. We do not show these features in the net curves presented below.

Figure 1 displays an electron–boson interaction spectrum $g(\omega)$ reconstructed for Gd. As follows from [11, 13], the gadolinium phonon density of states is cut off at 14–15 meV; as a result, the part of $g(\omega)$ that corresponds to higher energies may be due to interaction with other excitations, for instance, with magnons. The important role of magnetic excitations in gadolinium is indicated by measurements of the temperature dependence of the electrical resistivity [14], which imply that within a broad temperature interval the electrons scatter primarily from magnons rather than from phonons. To check this conjecture, we start from the well-known fact that the $g(\omega)$ features directly reflect the van Hove singularities at the critical points in the $\omega(\mathbf{k})$ dispersion curves where the derivatives of $\omega(\mathbf{k})$ vanish [2]. As follows from Fig. 1, the data on magnons in gadolinium obtained by inelastic neutron scattering at 78 K [12] correlate well with our results. Let us turn now to the even part $\sigma_+(V)$ of the conductivity (Fig. 2), which, according to the theory, should reflect the boson excitation spectra in the insulating layer of the tunnel junction. Indeed, the derivative $d\sigma_+(V)/dV$ reveals nonlinearities up to 80–100 mV, which agree satisfactorily with the data extracted from Raman spectra of Cd_2O_3 single crystals [15].

Similar conclusions also apply to the reconstructed $g(\omega)$ for the Cr–Cr-oxide–Ag film structures illustrated in Fig. 3. According to the phonon dispersion curves for chromium [16], its lattice vibration spectrum is cut off at 40–41 meV. Therefore, all the features observed in the reconstructed spectral function of electron–boson interaction above 40 meV (Fig. 3) can be assigned to the electron–magnon interaction. We are not aware of any published data on the magnon spectra of chromium. The barrier characteristic $d\sigma_+(V)/dV$ obtained by us (Fig. 4) is in good agreement with the analogous electron-tunneling data from [5] and specific features of the magnon spectrum of Cr_2O_3 [17], whereas information on phonons in this compound is lacking.

The above results suggest that interaction of electrons with a magnetic subsystem plays as important a role in electron transport as electron scattering from lattice vibrations. This conclusion may be considered, in particular, as supportive evidence that the disagreement between the calculated renormalized electronic mass [3] and its experimental values is due to the contribution of the electron–magnon coupling. The approach developed in this work can be readily applied to studies of the nature of electron transport in cuprates and manganites, where the magnetic subsystem, as well as the phonon subsystem, is known to play a substantial role.

REFERENCES

1. G. Grimvall, *The Electron–Proton Interaction in Metals* (North-Holland, Amsterdam, 1981).
2. E. L. Wolf, *Principles of Electron Tunneling Spectroscopy* (Oxford Univ. Press, New York, 1985; Naukova Dumka, Kiev, 1990).
3. H. L. Skriver and I. Mertig, Phys. Rev. B **41** (10), 6553 (1990).
4. A. I. Akimenko, A. B. Verkin, N. M. Ponomarenko, and I. K. Yanson, Fiz. Nizk. Temp. **8** (10), 1084 (1982) [Sov. J. Low Temp. Phys. **8**, 547 (1982)].

5. G. I. Rochlin and P. K. Hansma, Phys. Rev. B **2** (6), 1460 (1970).
6. A. S. Barker, Jr., B. I. Halperin, and T. M. Rice, Phys. Rev. Lett. **20** (8), 384 (1968).
7. A. W. Overhauser, Phys. Rev. **128** (3), 1437 (1962).
8. J. M. Rowell, W. L. McMillan, and W. L. Feldmann, Phys. Rev. **180** (3), 658 (1969).
9. V. M. Svistunov and M. A. Belogolovskiĭ, *Tunneling Spectroscopy of Quasiparticle Excitations in Metals* (Naukova Dumka, Kiev, 1986).
10. V. M. Svistunov, M. A. Belogolovskiĭ, O. I. Chernyak, *et al.*, Zh. Éksp. Teor. Fiz. **84** (5), 1781 (1983) [Sov. Phys. JETP **57**, 1038 (1983)].
11. R. Ramji Rao and C. S. Menon, J. Phys. Chem. Solids **35** (3), 425 (1974).
12. W. C. Koehler, H. R. Child, R. M. Nicklow, *et al.*, Phys. Rev. Lett. **24** (1), 16 (1970).
13. S. S. Kushwaha and A. Kumar, J. Phys. C **4** (13), 1674 (1971).
14. N. V. Volkenshtein, V. P. Dyakina, and V. E. Startsev, Phys. Status Solidi B **57** (1), 9 (1973).
15. J. Gouteron, D. Michel, A. M. Lejus, and J. Zarembowich, J. Solid State Chem. **38**, 288 (1981).
16. G. Simonelli, R. Pasianot, and E. J. Savino, Phys. Rev. B **55** (9), 5570 (1997).
17. E. J. Samuelsen, M. T. Hutchings, and G. Shirane, Solid State Commun. **7** (15), 1043 (1969).
18. D. R. Renneke and D. W. Lynch, Phys. Rev. **138** (2A), A530 (1965).

Translated by G. Skrebtsov

Physics of the Solid State, Vol. 44, No. 7, 2002, pp. 1212–1217. Translated from Fizika Tverdogo Tela, Vol. 44, No. 7, 2002, pp. 1162–1167.
Original Russian Text Copyright © 2002 by Parfen'eva, Smirnov, Misiorek, Mucha, Jezowski, Ritter, Assmus.

**METALS
AND SUPERCONDUCTORS**

Unusual Behavior of the Lattice Thermal Conductivity and of the Lorenz Number in the $YbIn_{1-x}Cu_{4+x}$ System

L. S. Parfen'eva*, I. A. Smirnov*, H. Misiorek, J. Mucha**, A. Jezowski**,
F. Ritter***, and W. Assmus*****

** Ioffe Physicotechnical Institute, Russian Academy of Sciences, Politekhnicheskaya ul. 26, St. Petersburg, 194021 Russia*
e-mail: Igor.Smirnov@pop.ioffe.rssi.ru
*** Institute of Low-Temperature and Structural Research, Polish Academy of Sciences, Wroclaw 50-950, Poland*
**** Goethe University, Frankfurt-am-Main, 60-054 Germany*

Received October 3, 2001

Abstract—Samples of various compositions were obtained in the homogeneity range of the Yb–In–Cu system ($YbIn_{1-x}Cu_{4+x}$), from stoichiometric ($YbInCu_4$) to $YbIn_{0.905}Cu_{4.095}$. Their lattice constant (at 300 K and in the range 20–100 K), total thermal conductivity, and electrical resistivity (from 4 to 300 K) were measured. All the compositions studied exhibited an isostructural phase transition at $T_v \simeq$ 40–80 K driven by a change in the Yb ion valence state. It was shown that within the $YbIn_{1-x}Cu_{4+x}$ homogeneity range, the lattice thermal conductivity κ_{ph} decreases with increasing x; at $T > T_v$, κ_{ph} grows with temperature and the Lorenz number (which enters the Wiedemann–Franz law for the electronic component of thermal conductivity) of the light heavy-fermion system, to which $YbIn_{1-x}Cu_{4+x}$ belongs for $T < T_v$, behaves as it does in classical heavy-fermion systems. Thermal cycling performed through T_v generates stresses in the $YbIn_{1-x}Cu_{4+x}$ lattice, which entails an increase in the electrical resistivity and a decrease in the thermal conductivity. "Soft anneal" (prolonged room-temperature aging of samples) makes the effect disappear. A conclusion is drawn as to the nature of the effects observed. *© 2002 MAIK "Nauka/Interperiodica".*

1. INTRODUCTION

$YbInCu_4$ is an interesting subject for research. This compound has an $AuBe_5$-type cubic lattice and undergoes (at atmospheric pressure and T_v ~ 40–80 K) an isostructural phase transition which is accompanied by a change in the Yb valence from 3 (in the high-temperature phase, $T > T_v$) to 2.9 (in the low-temperature phase, $T < T_v$). The high-temperature phase is a semimetal, and the low-temperature phase belongs to light heavy-fermion systems. The parameter γ (the coefficient of the linear-in-temperature term in the electronic heat capacity) of $YbInCu_4$ at $T < T_v$ is ~50 mJ/mol K^2. For more details on the properties of this interesting material, see [1, 2].

The phase transition temperature T_v ~ 40–80 K is frequently assigned to the $YbInCu_4$ composition. However, the Yb–In–Cu system in the homogeneity range ($YbIn_{1-x}Cu_{4+x}$) exhibits a deviation from stoichiometry. The stoichiometric $YbInCu_4$ has T_v ~ 40 K. As the composition shifts to $YbIn_{0.8}Cu_{4.2}$, T_v increases to 70–80 K [3–6].

The Yb–In–Cu phase diagram was studied in [5, 6] in the most interesting compositional region (Fig. 1a). The homogeneity range of the Yb–In–Cu phase extends from the nominal $YbInCu_4$ to a composition with a higher Cu content, with Cu beginning to occupy the In sites [$Yb(In_{1-x}Cu_x)Cu_4$] and T_v shifting from 40 to 70–80 K. At the same time, the phase transition changes character from abrupt to gradual.

Earlier [7, 8], we studied the thermal conductivity of two samples of $YbIn_{0.83}Cu_{4.17}$ composition,[1] which, according to the phase diagram of Fig. 1a, lies close to $YbIn_{0.8}Cu_{4.2}$, exhibiting the maximum melting temperature.

It was found [8] that (i) the Lorenz number L entering the Wiedemann–Franz law for the electronic component of the thermal conductivity κ_e behaves in a light heavy-fermion system (to which $YbIn_{0.83}Cu_{4.17}$ can be assigned at $T < T_v$) like a classical heavy-fermion system and that (ii) the lattice thermal conductivity κ_{ph} of $YbIn_{0.83}Cu_{4.17}$ increases with temperature, following a law close to $T^{0.3}$ for $T > T_v$.

This behavior of $\kappa_{ph}(T)$, characteristic of amorphous or heavily defected materials, was associated in [8] with the substitution of copper for indium in $YbInCu_4$

---

[1] The samples studied in [8] were prepared in two different laboratories, namely, at the Physicotechnical Institute, RAS, St. Petersburg, Russia (sample 1*P*), and at the Frankfurt-am-Main University, Germany (sample 2*F*). The thermal conductivity of the stoichiometric $YbInCu_4$ sample (T ~ 40 K) was measured at the Technical University (Vienna, Austria) [9]. The experimental data reported in [9] were not analyzed in detail.

and the attendant formation of a large number of defects which could serve as phonon scatterers.

Accordingly, the purpose of this work was the following.

(1) To prepare a set of samples within the homogeneity range, including the stoichiometric composition corresponding to T_v ~ 40 K.

(2) To measure $\kappa_{ph}(T)$ and $L(T)$ within the homogeneity range of $YbIn_{1-x}Cu_{4+x}$ and study the variation of κ_{ph} as a function of x and the behavior of $\kappa_{ph}(T)$ for $T > T_v$ and of $L(T)$ for $T < T_v$ in a stoichiometric sample. It was also of interest to determine whether this composition would exhibit an increase in κ_{ph} for $T > T_v$, because, as follows from the phase diagram (Fig. 1a), no copper substitution for indium should take place in the stoichiometric composition.

2. SAMPLE PREPARATION AND EXPERIMENTAL TECHNIQUE

The composition of the crystal was shown to depend on the method by which it was prepared [5, 6]. The cast polycrystalline samples for this work were produced by directional vertical-Bridgman crystallization from a melt with an original Cu concentration only slightly below the stoichiometric valve. The melt started to solidify with the formation of crystals having a phase-transition temperature T_v ~ 70 K. The material that crystallized in later stages had a T_v near 40 K.

The material was melted in tantalum crucibles sealed in an argon atmosphere [6]. Electron-beam heating was chosen to ensure a steep enough temperature gradient at the interface between the liquid and solid phases in the crucible during the crystal growth. The ingot thus obtained was cut into five samples (samples *1*–*5*, Fig. 1b). Their lattice constant a was measured at 300 K (Table 1) and in the temperature interval 20–100 K (Fig. 2). The $a(T)$ relation obtained for sample *5* was found to correlate well with the data reported in [10] for $YbInCu_4$ with T_v ~ 40 K. All the samples were single-phase and had an $AuBe_5$-type cubic lattice.

The total thermal conductivity κ_{tot} and the electrical resistivity ρ were measured in the 4- to 300-K region on a setup similar to the one described in [11].

3. EXPERIMENTAL RESULTS AND DISCUSSION

Figure 3 presents temperature dependences of κ_{tot} and ρ obtained on samples *1* and *4* in measurement runs from 300 to 4 K.[2] We note that $\kappa_{tot}(T)$ of sample *4* was found to coincide well with that of the stoichiometric $YbInCu_4$ sample with T_v ~ 40 K reported in [9].

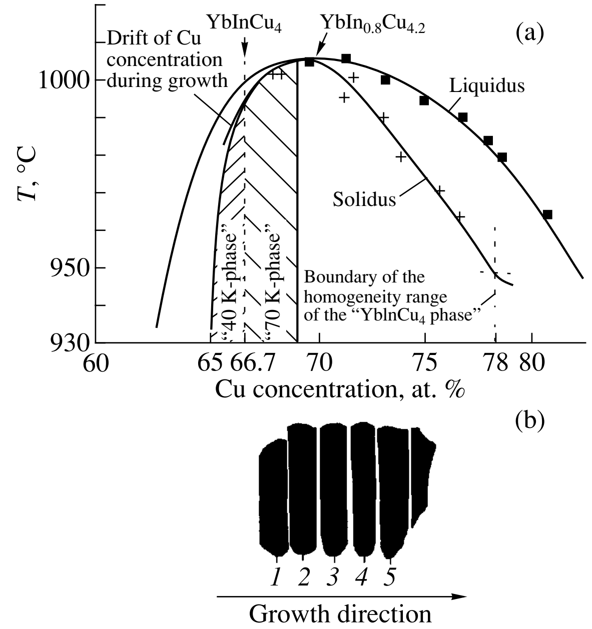

Fig. 1. (a) Phase diagram of the Yb–In–Cu system ($YbIn_{1-x}Cu_{4+x}$) and (b) schematic image of the samples cut from the ingot. Labels *1*–*5* are the sample numbers.

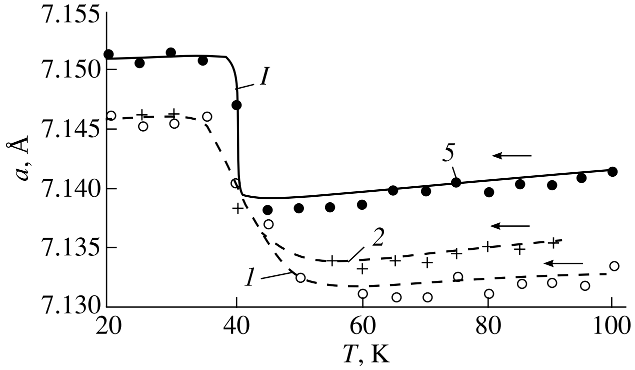

Fig. 2. Temperature dependence of the lattice constant a in the $YbIn_{1-x}Cu_{4+x}$ system. Solid curve *I* is the data from [10]. Labels *1*, *2*, and *5* are the sample numbers.

Prior to turning to an analysis of the experimental data obtained, we first determined the composition of our $YbIn_{1-x}Cu_{4+x}$ samples. To do this, we estimated (although not with sufficient precision) the values of T_v from the $a(T)$, $\rho(T)$, and $\kappa_{tot}(T)$ relations for all five samples studied, after which we used the $T_v(x)$ graph obtained in [12] for the $YbIn_{1-x}Cu_{4+x}$ system to find x

Table 1. Lattice constant a at 300 K for samples *1*–*4* of the $YbIn_{1-x}Cu_{4+x}$ system

Sample no.	a, Å
1	7.152(2)
2	7.154(5)
3	7.161(3)
4	7.164(4)

---

[2] We also measured the $\rho(T)$ relation for sample *3*.

Table 2. Values of T_V derived from measurements of $a(T)$, $\rho(T)$, and $\kappa_{tot}(T)$ on samples *1–5*, and the corresponding values of x for the $YbIn_{1-x}Cu_{4+x}$ system obtained from the $T_V(x)$ relation obtained in [12]

Sample no.	T_V, K			Average value of T_V, K	x	Sample composition
	$a(T)$	$\rho(T)$	$\kappa_{tot}(T)$			
1	60	60	60	60	0.095	$YbIn_{0.905}Cu_{4.095}$
2	55	–	–	55	0.060	$YbIn_{0.94}Cu_{4.06}$
3	–	48	–	48	0.038	$YbIn_{0.962}Cu_{4.038}$
4	–	44	42	43	0.015	$YbIn_{0.985}Cu_{4.015}$
5	40	–	–	40	0	$YbInCu_4$

and the approximate composition of the samples (Table 2).

We chose two samples with extreme compositions, *1* and *4*, to measure $\kappa_{tot}(T)$ and $\rho(T)$. Unfortunately, because of the mechanical defects introduced in the course of ingot cutting, the stoichiometric sample *5* was found to be unsuitable for the measurement of $\rho(T)$ and $\kappa_{tot}(T)$.

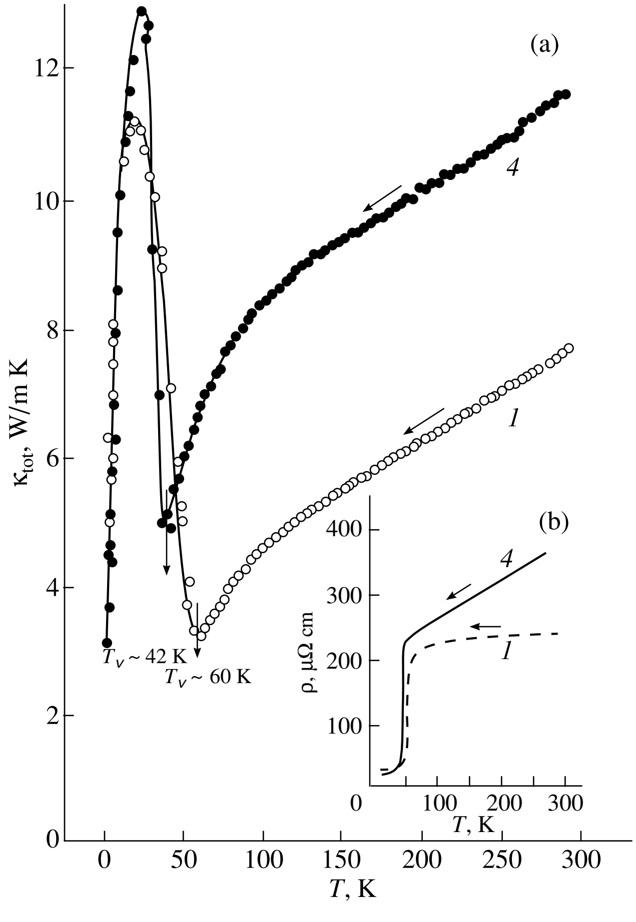

Fig. 3. Temperature dependences of (a) κ_{tot} and (b) ρ for samples *1* and *4*.

According to the data available in the literature, in the homogeneity range of $YbIn_{1-x}Cu_{4+x}$, all compositions in the $T < T_V$ and $T > T_V$ temperature intervals are metals and semimetals, respectively; therefore, κ_{tot} should include both electronic and lattice components:

$$\kappa_{tot} = \kappa_e + \kappa_{ph}, \quad (1)$$

where κ_e can be calculated using the Wiedemann–Franz relation,

$$\kappa_e = LT/\rho. \quad (2)$$

The samples studied cannot be classed among "pure" metals and semimetals; therefore, according to the classical theory of thermal conductivity, $L = L_0$ for these samples ($L_0 = 2.45 \times 10^{-8}$ W Ω/K^2 is the Sommerfeld value of the Lorenz number). We isolated $\kappa_{ph}(T)$ from $\kappa_{tot}(T)$ and calculated $L_x/L_0(T)$ for the $T < T_V$ temperature interval by the technique described by us in detail in [8].

3.1. Behavior of the Lattice Thermal Conductivity

For $T > T_V$, where all the samples studied are dirty semimetals, the validity of using $L = L_0$ in Eq. (2) is unquestionable. Within this temperature region, the $\kappa_{ph}(T)$ relations for samples *1* and *4* calculated from Eqs. (1) and (2) with $L = L_0$, as well as the ones for the $YbIn_{0.83}Cu_{4.17}$ samples 1*P* and 2*F* [8], grow with increasing temperature, following a power law $\kappa_{ph} \sim T^n$, where n ~ 0.3–0.38, which is close to the values of n found for samples 1*P* and 2*F* [8] (Fig. 4a).

Thus, we obtained an answer to one of the questions in our study, namely, as to the behavior of the $\kappa_{ph}(T)$ relation of the close-to-stoichiometric sample *4* (T_V ~ 43 K) at high temperatures being exactly like that for $YbIn_{0.83}Cu_{4.17}$. This casts doubt on the conjecture that the growth of $\kappa_{ph}(T)$ in samples of the $YbIn_{1-x}Cu_{4+x}$ system originates from their being strongly defected by Cu substituting for In. It is possible, however, that stoichiometric $YbInCu_4$ also has defects associated with the presence of some lattice disorder. The nature and origin of such disorder have not thus far been established; this would require additional studies. One can-

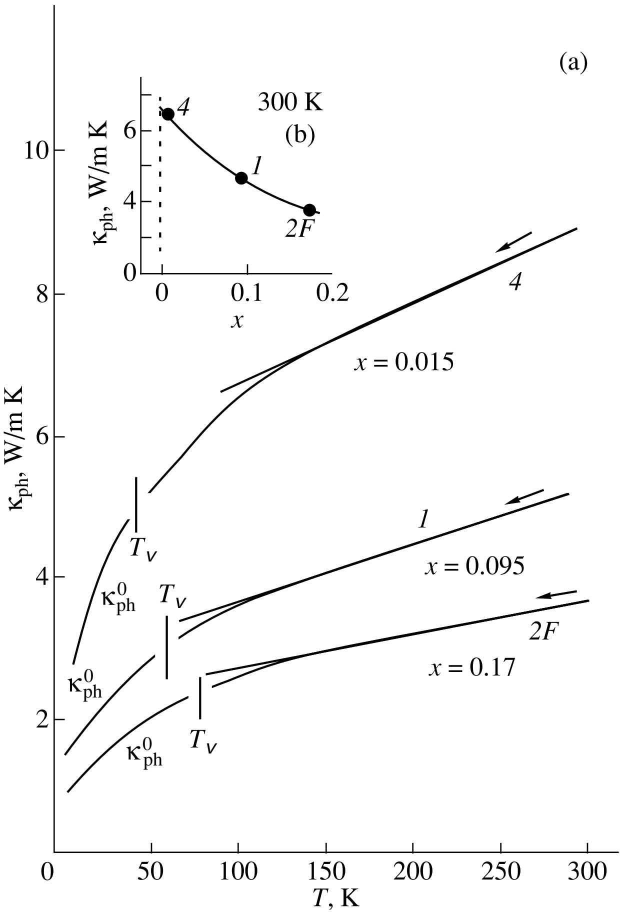

Fig. 4. Dependences of κ_{ph} on (a) temperature and (b) x at 300 K for samples *1*, *4*, and 2*F* [8] of the $YbIn_{1-x}Cu_{4+x}$ system. See the text and [8] for the explanation of κ_{ph}^0.

not exclude the possibility that this behavior of $\kappa_{ph}(T)$ is inherent (for some other reasons) in a certain group of heavy-fermion materials [8].

Figure 4b presents the values of κ_{ph} (300 K) for three compositions in the homogeneity range of the $YbIn_{1-x}Cu_{4+x}$ system. As expected, κ_{ph} decreases with increasing x.

3.2. Behavior of the Lorenz Number

We now consider the behavior of the $L_x/L_0(T)$ ratio for $T < T_v$ in the close-to-stoichiometric sample *4*. We used the technique developed in [8] [extrapolation of the values of κ_{ph} from the high-temperature domain by a power law to the region of $T < T_v$ (κ_{ph}^0 in Fig. 4) and determination of $L_x/L_0(T)$ from the relation $\kappa_e = L_xT/\rho = \kappa_{tot} - \kappa_{ph}^0$] to calculate $L_x/L_0(T)$ for sample *4* in the temperature range 10–35 K ($T < T_v$) and compared the values thus obtained with the $L_x/L_0(T)$ relation for sample 2*F* [8], which had the $YbIn_{0.83}Cu_{4.17}$ composition. It was found that they practically coincide and behave as they should in classical heavy-fermion systems [8, 13] (Fig. 5).

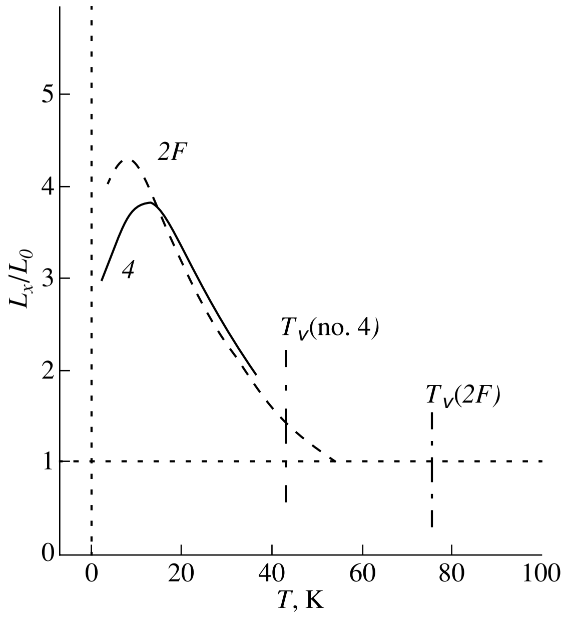

Fig. 5. Temperature dependence of L_x/L_0 for samples *4* ($YbIn_{0.985}Cu_{4.015}$) and 2*F* ($YbIn_{0.83}Cu_{4.17}$) [8].

This provided an answer to the second question; namely, the behavior of the $L_x/L_0(T)$ relation in the homogeneity range is the same for classical and light heavy-fermion systems.

4. THE EFFECT OF PHASE-TRANSITION-INDUCED DEFECTS ON κ_{ph}

Measurements of the temperature dependence of electrical resistivity in $YbInCu_4$ revealed an interesting phenomenon [14]. In the course of thermal cycling made through T_v, ρ was observed to increase in the $T > T_v$ and $T < T_v$ regions (Fig. 6a). We note that the growth of ρ in the $T > T_v$ region was considerably stronger (by a factor greater than two). Repeated cycling resulted in a stronger growth of ρ (particularly for $T > T_v$). No microcracks formed in the course of the cycling, and the lattice constant did not change [10]. The effect described above was assigned [4] to the generation of stresses in the $YbInCu_4$ lattice, because the phase transition entails a change in the Yb valence from 3 to 2.9 (when crossing T_v from the higher temperature region) and from 2.9 to 3 (in the reverse run).

Thermal conductivity is sensitive to the formation of various defects in a material [14]. Therefore, it appeared only natural to study how defects that form under thermal cycling in the $YbIn_{1-x}Cu_{4+x}$ system would influence the thermal conductivity.

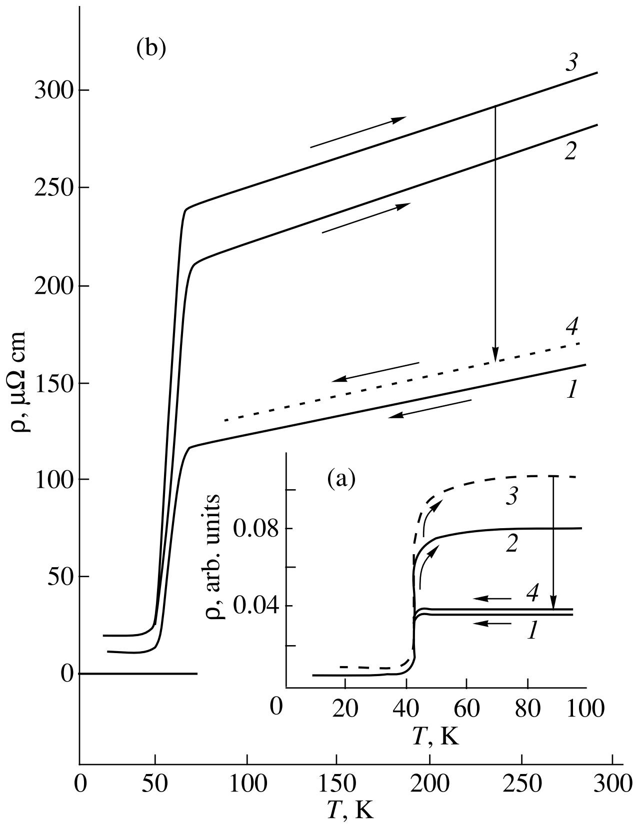

Fig. 6. (a) Temperature dependence of ρ obtained under thermal cycling of $YbInCu_4$ [4]: (*1*) cooling from 100 to 4 K (direct run), (*2*) first warming-up cycle (reverse run from 4 to 100 K), (*3*) second warming-up cycle (reverse run from 4 to 100 K) of the sample cooled again to 4 K after the first warming-up cycle, and (*4*) after the anneal of the sample that passed the second warming-up cycle (annealing for several hours at 300°C). (b) Temperature dependence of ρ for sample *3*: (*1*) measurement under cooling from 300 to 4 K (direct run), (*2*) first warming-up cycle (reverse run from 4 to 300 K), (*3*) second warming-up cycle (reverse run from 4 to 300 K) of the sample cooled again to 4 K after the first heating cycle, and (*4*) measurements from 300 to 4 K after the sample passed cycle *3* after month-long storage at room temperature.

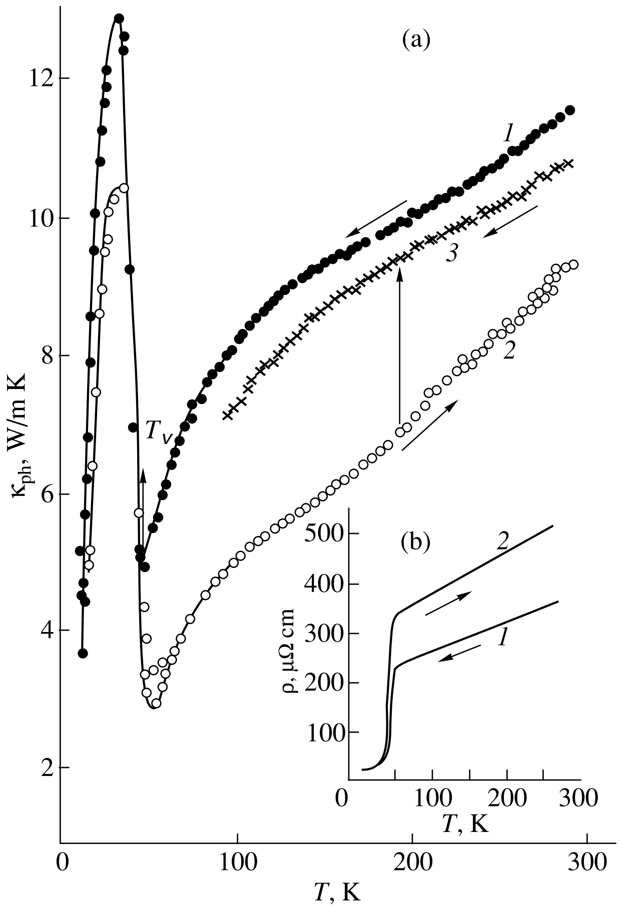

Fig. 7. Temperature dependences of (a) κ_{tot} and (b) ρ for sample *4*; (a) (*1*) direct run (300 ⟶ 5 K), (*2*) reverse run (5 ⟶ 300 K), and (*3*) direct run (300 ⟶ 80 K), measurement after the sample was stored for 30 days at room temperature (after having been measured in cycle *2*); and (b) (*1*) direct run (300 ⟶ 5 K), measurement on the sample corresponding to curve *3* in Fig. 7a, and (*2*) reverse run (5 ⟶ 300 K), measurement on the sample corresponding to curve *2* in Fig. 7a. Part of the ρ(T) data obtained on sample *4* are omitted.

Figures 6b and 7 plot the temperature dependences of ρ and κ_{tot} obtained by us under thermal cycling of samples *3* and *4*.[3] The data on ρ(T) were found to reproduce the results quoted in [4] (compare Figs. 6a, 6b).

Samples *4* (Fig. 7a) and *1* exhibited a noticeable decrease in κ_{tot} both for $T < T_v$ and for $T > T_v$. As in the case of thermal cycling for ρ(T), the effect is the strongest in the $T > T_v$ region.

Most of the measurements were made on sample *4* (Fig. 7). After the thermal cycling, κ_{tot} is observed to decrease substantially (curve *2*, Fig. 7a).[4] We made an interesting observation. The defects that had formed in the sample after the thermal cycling disappeared almost completely after the soft anneal, i.e., after the sample was kept at room temperature for a month (curve *3*, Fig. 7a). It is of interest to estimate the influence of the defects created during the cycling on κ_{ph}.

We consider the $T > T_v$ region, where, as already mentioned, one can assume with confidence that $L = L_0$ when calculating κ_e. Figure 8 presents data on $\kappa_{ph}(T)$ for samples *1* and *4*, which were calculated assuming $L = L_0$ in Eqs. (1) and (2). Straight lines *1* and *4* in Fig. 8 relate to samples *1* and *4* not subjected to thermal cycling, and lines *1a* and *4a* correspond to samples *1* and *4* subjected to thermal cycling. We see that $\Delta\kappa_{ph}$ (Fig. 8) of sample *4*, which is close in composition to stoichiometry ($YbIn_{0.985}Cu_{4.015}$), is larger than that of

---

[3] Similar measurements were also performed on sample *1*.

[4] We measured the lattice constant of sample *4* both before and after the cycling. As in [10], we did not observe any change in it.

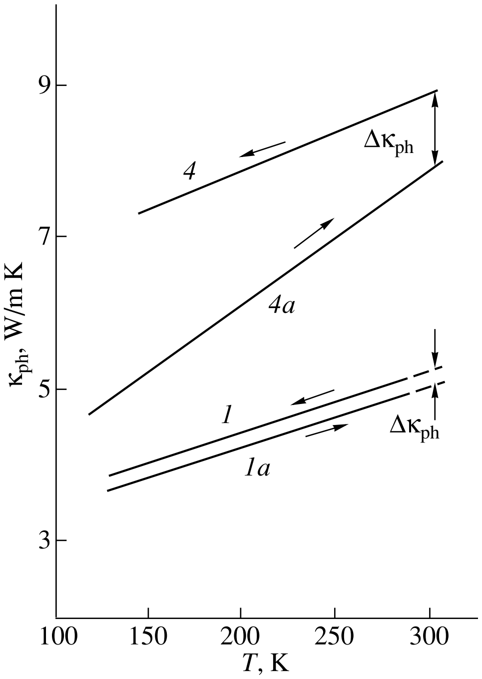

Fig. 8. Temperature dependence of κ_{ph} obtained for samples *1* and *4* in the temperature region $T > T_V$; lines *4* and *1* are measurements from 300 to 5 K (direct run), and lines *4a* and *1a* are measurements from 5 to 300 K (reverse run). $\Delta\kappa_{ph}$ is the change in the lattice thermal conductivity under cycling.

sample *1* ($YbIn_{0.905}Cu_{4.095}$) throughout the temperature range studied.

Thus, one can conclude that the defects that were formed in $YbIn_{1-x}Cu_{4+x}$ by thermal cycling decrease κ_{ph}. The electrical conductivity $\sigma = 1/\rho$ decreases to a greater extent under thermal cycling than κ_{ph} does. Prolonged soft annealing of samples at room temperature suppresses this effect in $\rho(T)$, $\kappa_{tot}(T)$, and $\kappa_{ph}(T)$.

Unfortunately, an analysis of the behavior of $\kappa_{ph}(T)$ before and after thermal cycling does not permit one to determine the nature of these defects. It is possible that the phase transition does indeed generate stresses associated with the change in the Yb valence state, as is suggested in [14]. One cannot, however, exclude the possibility that thermal cycling induces only small displacements of Cu from the equilibrium sites.

ACKNOWLEDGMENTS

The authors express gratitude to N.F. Kartenko and N.V. Sharenkova for the lattice constant measurements made at 300 K.

This work was conducted within bilateral agreements between the Russian Academy of Sciences, Deutsche Forschungsgesellschaft (Germany), and the Polish Academy of Sciences and was supported by the Russian Foundation for Basic Research (project no. 99-02-18078) and the Polish Committee for Scientific Research (grant no. 2PO3B 129-19).

REFERENCES

1. J. L. Sarrao, C. D. Immer, Z. Fisk, *et al.*, Phys. Rev. B **59** (10), 6855 (1999).
2. A. V. Goltsev and G. Bruls, Phys. Rev. B **63** (15), 155109 (2001).
3. B. Kindler, D. Finsterbusch, R. Graf, *et al.*, Phys. Rev. B **50** (2), 704 (1994).
4. J. L. Sarrao, C. D. Immer, C. L. Benton, *et al.*, Phys. Rev. B **54** (17), 12207 (1996).
5. A. Löffert, M. L. Aigner, F. Ritter, and W. Assmus, Cryst. Res. Technol. **34** (2), 267 (1999).
6. A. Löffert, S. Hautsch, F. Ritter, and W. Assmus, Physica B (Amsterdam) **259**, 134 (1999).
7. I. A. Smirnov, L. S. Parfen’eva, A. Jezowski, *et al.*, Fiz. Tverd. Tela (St. Petersburg) **41** (9), 1548 (1999) [Phys. Solid State **41**, 1418 (1999)].
8. A. V. Golubkov, L. S. Parfen’eva, I. A. Smirnov, *et al.*, Fiz. Tverd. Tela (St. Petersburg) **44** (6), 973 (2002) [Phys. Solid State **44** (6), 1016 (2002)].
9. T. Bauer, E. Gratz, G. Hutflesz, *et al.*, Physica B (Amsterdam) **186/188**, 494 (1993).
10. J. M. Lawrence, S. M. Shapiro, J. L. Sarrao, and Z. Fisk, Phys. Rev. B **55** (21), 14467 (1997).
11. A. Jezowski, J. Mucha, and G. Pompe, J. Phys. D **20**, 1500 (1987).
12. K. Yoshimura, N. Tsujii, K. Sorada, *et al.*, Physica B (Amsterdam) **281/282**, 141 (2000).
13. V. I. Belitsky and A. V. Goltsev, Physica B (Amsterdam) **172**, 459 (1991).
14. V. S. Oskotskiĭ and I. A. Smirnov, *Defects in Crystals and Thermal Conductivity* (Nauka, Leningrad, 1972).

Translated by G. Skrebtsov

Physics of the Solid State, Vol. 44, No. 7, 2002, pp. 1218–1223. Translated from Fizika Tverdogo Tela, Vol. 44, No. 7, 2002, pp. 1168–1173.
Original Russian Text Copyright © 2002 by Panova, Khlopkin, Chernoplekov, Shikov.

METALS AND SUPERCONDUCTORS

Effect of Amorphization on the Electronic and Lattice Specific Heat of an Ni_2B Alloy

G. Kh. Panova, M. N. Khlopkin, N. A. Chernoplekov, and A. A. Shikov
Russian Research Centre Kurchatov Institute, pl. Kurchatova 1, Moscow, 123182 Russia
e-mail: khlopkin@isssph.kiae.ru

Received August 1, 2001; in final form, November 19, 2001

Abstract—The specific heats of the Ni_2B amorphous system and of its crystal analog were studied in the temperature range 3–270 K. The data obtained permitted us to isolate the contribution due to atomic vibrations from the experimentally measured specific heat, determine the electronic density of states at the Fermi level and the temperature dependence of the characteristic Debye parameter Θ, and to calculate some average frequencies (moments) of the vibrational spectrum. The electronic density of states at the Fermi level increases under amorphization. An analysis of the temperature dependence of the lattice specific heat showed that amorphization brings about a substantial growth in the density of vibrational states at low frequencies, whereas the spectrum-averaged and rms frequencies change very little, which is in good agreement with neutron diffraction measurements. *© 2002 MAIK “Nauka/Interperiodica”.*

1. INTRODUCTION

Studies of lattice dynamics and of the thermodynamic, kinetic, and other properties of systems which can exist in both the crystalline and amorphous phases contribute noticeably to our understanding of many physical properties characterizing the amorphous state [1]. The most convenient objects for such studies are metal–metal and metal–metalloid metallic glasses, which have been shown to be capable of transfer to metastable or stable crystalline states under annealing [2, 3]. Among the latter, the systems consisting of atoms differing strongly in mass are of considerable interest, because they exhibit different dynamics on the microscopic level. For instance, the atomic-vibration energy spectrum of a diatomic system with strongly differing atomic masses reveals, as a rule, two maxima which differ substantially in the position of their energy.

The most complete and reliable information on the structure and dynamics of such systems can be gained from elastic and inelastic neutron scattering experiments and, to a certain extent, from specific-heat measurements.

Measurements of the specific heat carried out over a broad temperature range permit one to judge the amorphization-induced changes in the vibrational and electronic excitations occurring at low and high energies. It should be pointed out that experimental data on the low-temperature specific heat make it possible to analyze the low-frequency part of the vibrational spectrum ($\hbar\omega < 2$ meV), which is difficult to access when employing the inelastic cold-neutron scattering method.

The purpose of this work was to study the effect of amorphization on the vibrational and electronic spectra of the Ni_2B system and to compare the data with inelastic neutron scattering measurements performed on the same samples.

The choice of the Ni_2B system was motivated by its amorphous phase having an appropriate crystalline analog and by the large difference between the masses of its constituent atoms ($M_{Ni}/M_B \sim 5.4$). In addition, neutron studies of the vibration excitation spectra of this system in the amorphous and crystalline states have been performed [4], as well as investigations into its structure in the amorphous state.

2. EXPERIMENTAL TECHNIQUES

The specific-heat measurements were carried out on the same samples as the neutron studies [4]. The samples in the amorphous state were obtained by rapid quenching on the surface of a rotating copper disk in an inert atmosphere. The sample composition was checked by chemical analysis; the exact content of the constituents (in atomic percent) corresponded to $Ni_{66.0}{}^{11}B_{34.0}$ for the crystalline sample and to $Ni_{63.9}{}^{11}B_{36.1}$ for the amorphous sample. The structure of the systems under study was revealed by x-ray and neutron diffraction. The x-ray diffraction curves follow a general pattern characteristic of amorphous systems and demonstrate no long-range order.

We present here the temperature dependences of the specific heats of the Ni_2B amorphous system and of its crystalline analog measured over a broad temperature range (3–270 K).

The specific heat of a sample was measured on two experimental setups by the adiabatic method with pulsed heating. The experimental error was about 2% in the temperature interval of 3–5 K, 1% in the region 5–10 K, and 0.2–0.5% in the range from 10 to 270 K. The specific-heat data are tabulated in units of J/g-atom K, with 1 g-atom being 42.48 g for the crystalline sample and 41.48 g for the amorphous sample.

3. EXPERIMENTAL RESULTS

The results of the specific-heat measurements carried out at constant pressure on the Ni_2B amorphous system and its crystalline analog are summed up in Figs. 1–5 and Tables 1 and 2. As seen from Fig. 1 and Table 1, at low temperatures, the specific heat of the amorphous system C_{am} is larger than that of its crystalline analog, C_{cr}. The specific-heat difference $C_{am} - C_{cr}$ increases with temperature to reach a maximum at 60 K. As the temperature increases still further, $C_{am} - C_{cr}$ decreases and passes through zero at 190 K, and at temperatures above 190 K, we have $C_{am} < C_{cr}$.

We note that the relative change in the specific heat at the transition from the crystalline to the amorphous system is large at low temperatures; indeed, the relative specific-heat difference $(C_{am} - C_{cr})/C_{cr}$ is greater than 100% at 18 K, whereas at temperatures above 200 K, the change in the specific heat does not exceed 0.6%.

Figure 2 plots the temperature dependences of the specific heats at low temperatures (in the range 3–13 K) in the C/T vs. T^2 coordinates. As seen from Fig. 2, at low temperatures, the experimental data on the specific heat are well fitted by the $C = \gamma T + \beta T^3$ relation, which makes straight lines in the C/T vs. T^2 coordinates. In the interval from 4 to 8 K for the amorphous phase, and from 3 to 10 K for the crystalline phase, the rms deviation of experimental data from a relation of the type $C = \gamma T + \beta T^3$ is of the order of 1.5%.

The temperature interval within which this relation holds for the amorphous system is substantially smaller than that for the crystalline one. At temperatures above 8 K for the amorphous sample, and above 10 K for the crystalline sample, the specific heat deviates systematically from the $C = \gamma T + \beta T^3$ relation; indeed, the experimentally measured specific heat grows with temperature faster than that given by extrapolation of this relation from the low-temperature domain. At temperatures from 10 to 20 K, the C/T vs. T^2 plot has a convex-down curvature.

Least-squares estimates of the coefficients γ and β and the limiting low-temperature value of the characteristic Debye temperature Θ_L related to β through $\beta = 12\pi^4 R/(5\Theta_L^3)$ are presented in Table 2. Here and subsequently, R is the universal gas constant.

As seen from Fig. 2 and Table 2, amorphization resulted in an increase in the coefficients of both the linear- and cubic-in-temperature terms, with the former increasing insignificantly and that of the cubic term growing by 40%.

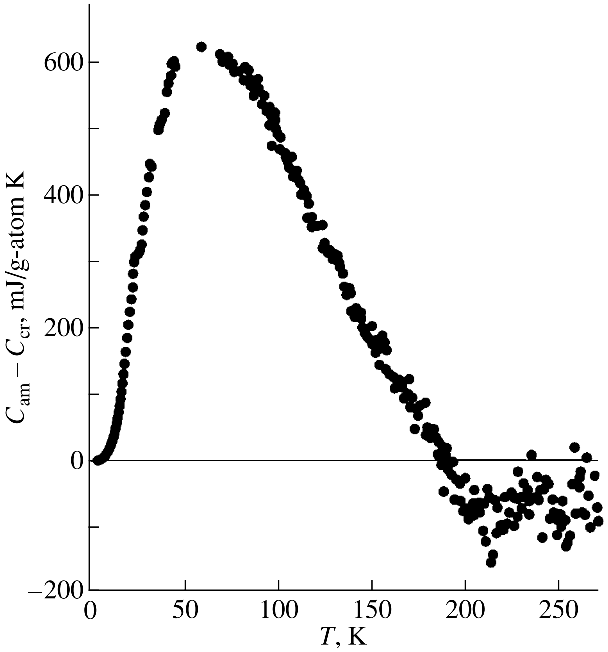

Fig. 1. Specific-heat difference between the amorphous and crystalline Ni_2B in the region 3–270 K.

4. ANALYSIS AND DISCUSSION OF THE RESULTS

The lattice (vibrational) specific heat C_{vib} was isolated from the experimentally measured C_p by subtracting the correction C_A, which combines all the other contributions to the specific heat from the anharmonic effects and thermal expansion of the substance, as well as from the conduction electrons:

$$C_{vib} = C_p - C_A = C_p - [\gamma + (A - \gamma)(C_{vib}/3R)^2]T, \quad (1)$$

where C_p is the molar heat capacity at constant pressure, C_{vib} is the vibrational contribution to the specific heat in the harmonic approximation, γ is the electronic specific heat coefficient at low temperatures, and A is the coefficient of the linear-in-temperature term of the specific heat at constant pressure at high temperatures.

The interpolation relation for C_A yields the corresponding linear asymptotic behavior at both low and high temperatures and provides a smooth transition between the low- and high-temperature asymptotic lines through a relation similar to the Nernst–Lindemann expression [5].

The value of γ was determined in the standard manner, namely, from the low-temperature asymptotic

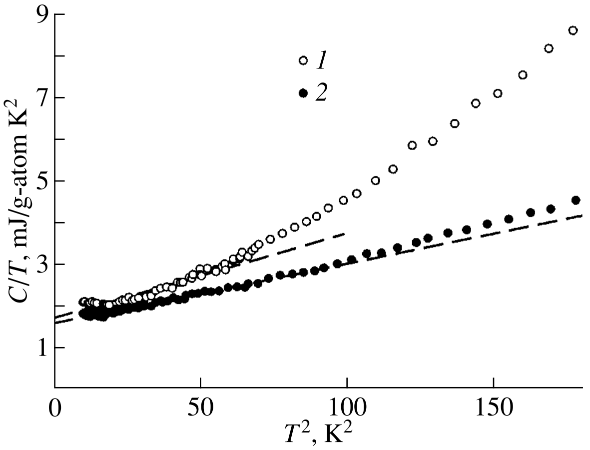

Fig. 2. Temperature dependence of the low-temperature specific heat of Ni_2B in (*1*) the amorphous and (*2*) crystalline states.

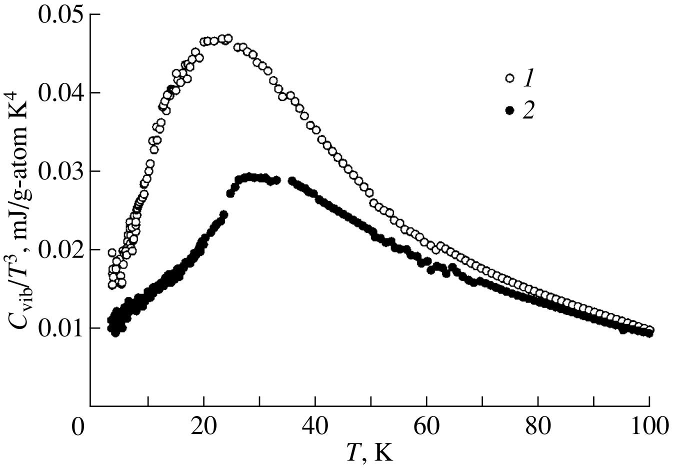

Fig. 3. Temperature dependence of the lattice specific heat of Ni_2B in (*1*) the amorphous and (*2*) crystalline states.

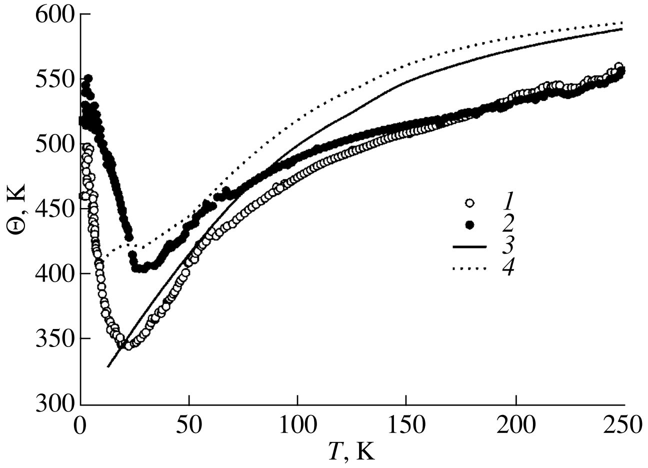

Fig. 4. Debye parameter Θ plotted as a function of temperature for Ni_2B in (*1, 3*) the amorphous and (*2, 4*) crystalline states; (*1, 2*) are derived from the specific heat and (*3, 4*) are calculated from the vibrational spectrum obtained in an inelastic neutron scattering measurement [4].

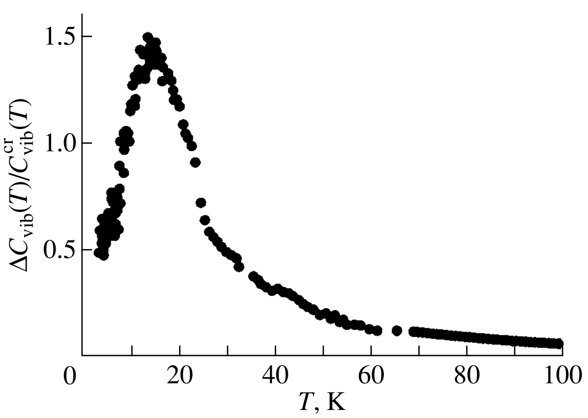

Fig. 5. Temperature dependence of the relative change in the lattice specific heat of the Ni_2B system at amorphization in the region 3–30 K [see Eq. (5)].

behavior of the temperature dependence of the specific heat described by the relation $C = \gamma T + \beta T^3$. The value of A, together with the parameters Ω_2, Ω_4, and Ω_* which characterize the vibrational spectrum, was derived from the high-temperature asymptotic behavior of the specific heat by approximating its temperature dependence with a relation of the type

$$C_p = 3R\left[1-\frac{1}{12}\left(\frac{\Omega_2}{T}\right)^2+\frac{1}{240}\left(\frac{\Omega_4}{T}\right)^4+\varphi\left(\frac{\Omega_*}{T}\right)\right] + T\left[\gamma+(A-\gamma)\left(\frac{C_p}{3R}\right)^2\right], \qquad (2)$$

where

$$\varphi(z) = \frac{z^2\exp z}{[1-(\exp z)^2]} - \left(1-\frac{z^2}{12}+\frac{z^4}{240}\right). \qquad (3)$$

This relation for the asymptotic decomposition of the lattice specific heat at high temperatures was proposed in [6] and used in [7]. The quantities Ω_2 and Ω_4 are expressed in units of temperature and are related to the moments of the vibrational spectrum through

$$(\Omega_n)^n = \langle\omega^n\rangle = \left(\int_0^\infty g(\omega)\omega^n d\omega\right)\Big/\left(\int_0^\infty g(\omega)d\omega\right). \qquad (4)$$

Table 1. Specific heat at constant pressure C_p of the amorphous Ni_2B system and of its crystalline analog as functions of temperature T

T, K	C_p, J/g-atom K	
	amorphous	crystalline
3	0.00630	0.00530
4	0.00800	0.00731
5	0.01066	0.00971
6	0.01437	0.01254
7	0.01918	0.01591
8	0.0256	0.0199
9	0.0344	0.0248
10	0.0463	0.0307
12	0.0814	0.0465
14	0.1323	0.0685
16	0.1995	0.0984
18	0.287	0.1402
20	0.400	0.2001
22	0.535	0.279
25	0.773	0.458
30	1.236	0.850
35	1.767	1.296
40	2.346	1.793
45	2.921	2.339
50	3.468	2.910
55	4.035	3.498
60	4.706	4.134
65	5.494	4.865
70	6.298	5.669
75	7.019	6.424
80	7.726	7.150
90	9.128	8.578
100	10.44	9.953
110	11.68	11.26
120	12.87	12.51
130	14.00	13.70
140	15.05	14.81
150	16.01	15.83
160	16.91	16.77
170	17.74	17.65
180	18.50	18.46
190	19.20	19.20
200	19.82	19.88
210	20.44	20.52
220	21.07	21.15
230	21.70	21.75
240	22.23	22.30
250	22.68	22.76
260	23.04	23.09
270	23.22	23.30

Table 2. Parameters characterizing the samples of an amorphous Ni_2B alloy and of its crystalline analog

Parameter	Amorphous	Crystalline	Change in parameter upon amorphization, %
γ, mJ/g-atom K^2	1.71	1.61	6
β, mJ/g-atom K^4	0.0200	0.0141	42
Θ_L, K	459	516	–11
Θ_H, K	613	605	–1
$\Omega_{\ln}$, K	236	269	–12
Ω_{-2}, K	230	261	–11
Ω_{-1}, K	285	308	–8
Ω_1, K	379	383	–1
Ω_2, K	474	469	1(–2)
Ω_4, K	582	578	0.7(1)
Ω_*, K	620	620	0(2)
A, mJ/g-atom K^2	14	14	0

Note: The coefficients γ and β approximate the low-temperature specific heat by the relation $C = \gamma T + \beta T^3$. Θ_L and Θ_H are the low- and high-temperature values of the characteristic Debye parameter, respectively. The quantities Ω_{-2}, Ω_{-1}, Ω_1, Ω_2, Ω_4, and $\Omega_{\ln}$ relate to the average frequencies (moments) of the vibrational spectrum in accordance with Eqs. (4) and (6). Given in parentheses are estimates of the amorphization-induced change in the quantities Ω_2, Ω_4, and $\Omega_{\ln}$ obtained by approximation of the specific-heat difference in the 100- to 270-K temperature interval (see Fig. 1).

Here, $g(\omega)$ is the vibrational density-of-states function. The quantity Ω_* in Eq. (2) is close in magnitude to Ω_n in Eq. (4) for $n = 6$.

By properly varying the four fitting parameters A, Ω_2, Ω_4, and Ω_*, we succeeded in approximating the experimental results by Eqs. (1)–(3) within the temperature interval 150–270 K with an rms deviation of the order of 0.3%. We note that, because of the narrowness of the temperature interval within which the experimental data were fitted, the errors in determination of the quantities Ω_2, Ω_4, and Ω_* are strongly correlated and comparable in magnitude to the variations that the quantities indicated above undergo under amorphization. Extending the fitting region toward low temperatures is impeded by the poor convergence of the approximating series in the low-temperature domain.

If, however, one directly describes the specific-heat difference, the convergence becomes much better, thus making it possible to broaden the approximation region toward lower temperatures and to improve the accuracy of determination of the change in the corresponding parameters in the approximating relation, because both the systematic experimental error in specific-heat measurements and the divergences in the approximating relation cancel out to a considerable extent when one analyzes difference effects. Within the 100- to 270-K region, the specific-heat difference is described by the corresponding difference between the relations of the type of Eqs. (1) and (2) with an rms error of less than 0.2% of the total specific heat. The estimates of the changes in Ω_2, Ω_4, and Ω_* under amorphization obtained in this approximation are given in parentheses in Table 2.

Table 2 lists the values of the parameters A, Ω_2, Ω_4, and Ω_* obtained by least-squares fitting. Also presented is the limiting high-temperature value of the Debye temperature Θ_H related to the second moment of the phonon spectrum through $\Omega_2 = \Theta_H\sqrt{3/5}$.

Because the lattice specific heat at a temperature T is contributed substantially by lattice vibrations with energies $E < 5kT$ (k is the Boltzmann constant), the low-temperature specific heat contains information on the low-frequency part of the vibrational spectrum. It was shown in [8] that at low temperatures and low energies, the quantity C_{vib}/T^3 is a good approximation to the function $g(\omega)/\omega^2$ for $\omega = 4.93T$ (the frequency is expressed in units of temperature). Therefore, the lattice specific heat in the low-temperature domain can be conveniently analyzed by plotting the temperature dependence of the specific heat in the C_{vib}/T^3 vs. T coordinates; these coordinates are traditionally used to analyze the deviation of the temperature behavior of specific heat from the Debye law $C \sim T^3$.

As seen from Fig. 3, the temperature dependence of $C_{\text{vib}}(T)/T^3$ for the amorphous Ni_2B system passes through a broad maximum at $T \approx 20$ K which corresponds to the presence in the vibrational spectrum of a strong low-frequency mode at an energy $E \approx 10$ meV. Crystalline Ni_2B exhibits a similar, although weaker, maximum at $T \approx 30$ K which corresponds to a low-frequency mode at $E \approx 15$ meV. The change in amplitude of the maximum in the $C_{\text{vib}}(T)/T^3$ relation and its shift toward lower temperatures in going over from the amorphous to crystalline state suggest that the amorphization increases the density of vibrational states at energies of the order of 10–15 meV.

The information that can be extracted from the relation under study becomes less significant with increasing temperature because of the fast decrease in the quantity C_{vib}/T^3. For this reason, the temperature dependence of the specific heat over a broad temperature range is more conveniently analyzed using the temperature dependence of the characteristic Debye parameter Θ; it is a finer characteristic which governs, in particular, the rate with which $C_{\text{vib}}(T)$ reaches the high-temperature asymptotic behavior. Figure 4 presents temperature dependences of Θ derived for both systems from specific-heat data, as well as those calculated from experimental inelastic neutron scattering spectra [4]. At temperatures of 20–70 K, there is good agreement between the data derived from the specific heat and that obtained in the neutron experiment for both the absolute value of the characteristic parameter Θ and for the change in this parameter induced by amorphization. Outside this temperature interval, good agreement is observed to occur only in the difference effect, i.e., in the change in Θ under amorphization, while the absolute values of Θ inferred from the specific heat and neutron scattering reveal a noticeable disagreement. We note that the characteristic Debye parameter Θ derives, in this temperature region, from the low-energy part of the vibrational spectrum, where the neutron experiment is not expected to yield high accuracy. Therefore, we believe that at temperatures below 15 K (and in the corresponding energy interval below 7 meV), the data inferred from the specific heat are more reliable and that the difference is due to the errors inherent in neutron experiments at low energies.

The temperature dependence of the Debye parameter passes through a broad minimum in the 20- to 30-K region, which corresponds to the maximum in the temperature dependence of the quantity C_{vib}/T^3. As the temperature increases, the difference between the values of the parameter Θ characterizing the amorphous and crystalline states decreases.

The distortion of the vibrational spectrum at low energies occurring upon amorphization can be conveniently described by the relative change in the lattice specific heat of an amorphous system compared with that of its crystalline analog, i.e., by a dimensionless quantity of the kind

$$\Delta C_{\text{vib}}(T)/C^{\text{cr}}_{\text{vib}}(T) = [C^{\text{am}}_{\text{vib}}(T) - C^{\text{cr}}_{\text{vib}}(T)]/C^{\text{cr}}_{\text{vib}}(T). \quad (5)$$

The temperature dependence of this relative change in the lattice specific heat of the alloys under study caused by amorphization is presented graphically in Fig. 5. In this system, amorphization results in the appearance of a maximum in the temperature dependence of the relative change in the lattice specific heat $\Delta C_{\text{vib}}(T)/C^{\text{cr}}_{\text{vib}}(T)$ at $T = 15$ K, which indicates that an increase in the energy density of vibrational states at low energies occurs in going over from an amorphous system to the crystalline system.

Model-free quantitative estimates of such parameters of the vibrational spectrum as the spectrum-averaged vibration frequency can be obtained by calculating the moments of the vibrational spectrum, some of which are directly expressed through integrals of the lattice specific heat [9].

We calculated these moments using experimental specific-heat data; within the range 10–270 K, the integration was performed by experimental points, and outside this range, the specific heat was extrapolated using either the low-temperature asymptotic behavior of the type $C = \beta T^3$ or the high-temperature dependence given by the model of the Debye spectrum, as was done in [10]. The results of the calculations are given in Table 2, which presents, for convenience of comparison, not the spectral moments $\langle\omega^n\rangle$ but rather the corresponding average frequencies Ω_n determined in accordance with Eq. (4) and expressed in units of temperature, with the logarithmically averaged frequency $\Omega_{\ln}$ determined by the relation

$$\log(\Omega_{\ln}) = \frac{\langle\omega^{-1}\ln\omega\rangle}{\langle\omega^{-1}\rangle} = \left(\int_0^\infty \frac{g(\omega)\ln\omega}{\omega}d\omega\right) \Big/ \left(\int_0^\infty \frac{g(\omega)}{\omega}d\omega\right). \tag{6}$$

As seen from Table 2, amorphization brings about a noticeable decrease in the frequencies Ω_{-2}, Ω_{-1}, and $\Omega_{\ln}$ characterizing the low-energy part of the spectrum, which corresponds to a growth in the density of vibrational states at low energies. As the order of the corresponding moment increases, the amorphization effect decreases and even reverses sign; indeed, the frequencies characterizing the high-energy part of the spectrum (Ω_2, Ω_4, Ω_*) increase under amorphization.

The higher the order of the vibrational-spectrum moment, the closer the corresponding frequency approaches the vibration frequency cutoff; therefore, the behavior of the moments described above can be treated as an indication that the spectral density of vibrational states at high energies and the cutoff frequency of atomic vibrations increase at amorphization. It should be pointed out that the effect of an increase in the cutoff vibration frequency under amorphization was observed in this system directly in the neutron experiment [4]; therefore, the data on the character of distortion of the vibrational spectrum at high energies obtained by two completely independent methods (neutron scattering and specific-heat measurements) are in good agreement.

ACKNOWLEDGMENTS

The authors are indebted to G.F. Syrykh for providing the samples and to M.G. Zemlyanov for discussions of the results.

This study was supported by the Russian Foundation for Basic Research, project no. 00-02-16181.

REFERENCES

1. *Glassy Metals*, Vol. II: *Atomic Structure and Dynamics, Electronic Structure, Magnetic Properties*, Ed. by H. Beck and H.-J. Guntherodt (Springer, Berlin, 1983; Mir, Moscow, 1986), Topics in Applied Physics, Vol. 53.
2. G. Kh. Panova, N. A. Chernoplekov, A. A. Shikov, *et al.*, Zh. Éksp. Teor. Fiz. **88** (3), 1012 (1985) [Sov. Phys. JETP **61**, 595 (1985)].
3. G. Kh. Panova, N. A. Chernoplekov, A. A. Shikov, *et al.*, Zh. Éksp. Teor. Fiz. **90** (4), 1351 (1986) [Sov. Phys. JETP **63**, 791 (1986)].
4. M. G. Zemlyanov, G. F. Syrykh, N. A. Chernoplekov, and E. Schwab, Zh. Éksp. Teor. Fiz. **94** (11), 365 (1988) [Sov. Phys. JETP **67**, 2381 (1988)].
5. L. A. Reznitskiĭ, *Calorimetry of Solids (Structural, Magnetic, Electronic Transformations)* (Mosk. Gos. Univ., Moscow, 1981).
6. V. N. Naumov, Phys. Rev. B **49** (18), 13247 (1994).
7. M. I. Katsnelson, I. I. Naumov, A. V. Trefilov, *et al.*, Philos. Mag. B **75** (3), 389 (1997).
8. A. Junod, T. Jarlborg, and J. Muller, Phys. Rev. B **27** (3), 1568 (1983).
9. A. Junod, Solid State Commun. **33** (1), 55 (1980).
10. A. V. Mirmel'shteĭn, A. E. Kar'kin, V. E. Arkhipov, and V. I. Voronin, Fiz. Met. Metalloved. **58** (5), 1008 (1984).

Translated by G. Skrebtsov

Physics of the Solid State, Vol. 44, No. 7, 2002, pp. 1224–1228. Translated from Fizika Tverdogo Tela, Vol. 44, No. 7, 2002, pp. 1174–1178.
Original Russian Text Copyright © 2002 by Knot'ko, Putlyaev, Morozov.

METALS AND SUPERCONDUCTORS

Phonon Spectra of La-Containing $Bi_2Sr_2CaCu_2O_8$-Based Solid Solutions Measured by Inelastic Neutron Scattering

A. V. Knot'ko*, V. I. Putlyaev*, and S. I. Morozov**
** Moscow State University, Vorob'evy gory, Moscow, 119899 Russia*
e-mail: knotko@inorg.chem.msu.ru
*** Institute of Physics and Power Engineering, All-Russia Research Center,*
pl. Bondarenko 1, Obninsk, Kaluzhskaya oblast, 249020 Russia

Received June 14, 2001; in final form, September 13, 2001

Abstract—Phonon spectra of $Bi_2Sr_{2-y}Ca_{1-x}La_{x+y}Cu_2O_{8+\delta}$ solid solutions ($x = y = 0$; $x = 0$, $y = 0.25$; $x = 0.25$, $y = 0$; $x = 0$, $y = 0.5$) were measured by inelastic neutron scattering on a DIN-2PI direct-geometry spectrometer. A full-profile analysis of the x-ray diffraction data yielded an estimate of the distribution of alkaline-earth (AE) and La atoms over the Ca and Sr positions in the $Bi_2Sr_2CaCu_2O_8$ structure. An assignment of the main features in the phonon spectrum to dominant vibrations of certain atoms was made. In particular, the correlation of the x-ray structural data with spectroscopic data implies that the feature due to cation vibrations in the Sr crystallographic positions of the basic 2212 structure (near 11 meV) is single-mode in behavior. Substitution of La for an AE atom modifies the high-frequency part (>40 meV) of the phonon spectrum (which corresponds to vibrations of oxygen in the SrO and CuO_2 layers of the $Bi_2Sr_2CaCu_2O_8$ structure) and affects the cut-off frequencies in the spectra of solid solutions of various compositions. A comparison of the results obtained in this study with earlier spectra of the 2212 compound, in which Ca was substituted for by Nd, indicates that the shape and intensity of the high-frequency vibration spectra of the samples studied are related to the average cation charge in the SrO layer of the $Bi_2Sr_2CaCu_2O_8$ structure. *© 2002 MAIK "Nauka/Interperiodica".*

1. INTRODUCTION

Heterovalent cation substitution in various crystallographic positions plays an important part in modification of the functional properties (T_c, J_c, room-temperature electrical conductivity, etc.) of high-temperature superconductors. Superconducting compounds based on $Bi_2Sr_2CaCu_2O_8$ (Bi2212) can be used as potential materials for cables and ribbons. Of particular interest are solid solutions obtained in the substitution of rare-earths for alkaline-earth elements in the Bi2212 structure. This substitution can be effected over a broad concentration range and, at a certain substitution level, brings about a metal–semiconductor transition driven by a decrease in the carrier (hole) concentration in the CuO_2 layers under heterovalent substitution [1, 2]. In view of the significant role played by electron–phonon coupling in the mechanism of superconductivity, investigation of the effect of heterovalent substitution on the superconductor lattice dynamics is of particular interest. This issue is dealt with in a number of publications [3, 4]. In [4], the combined effect of two factors on the lattice dynamics is considered, namely, of the carrier concentration variation and of the built-in stress in the crystal (the so-called "built-in pressure"), which is generated by the difference in the ionic radii of Ca^{2+} and Y^{3+} (1.26 and 1.10 Å [5]).

To separate these effects, in our earlier study [6], we chose solid solutions with Cd substituted for by Nd, whose ionic radii are larger than that of Y and almost identical to that of a substituted alkaline-earth (AE) ion (1.25 Å for Nd^{3+}). A comparison of the spectra obtained with those presented in [3] suggests that the built-in pressure affects the vibrations of oxygen in the CuO_2 layers only insignificantly. At the same time, the magnetic moment of the Nd^{3+} ion can produce an additional contribution to the inelastic neutron scattering (INS) spectrum, which introduces a certain ambiguity into interpreting the experimental results. In this study, a similar problem of separating the effects of the built-in pressure and cation charge state on the oxygen atom dynamics was solved by replacing the AE metal ion by a nonmagnetic ion La^{3+}, which is close to Nd in mass and radius and is isostructural in the outer shell configuration.

It was also of interest to investigate the effect of the crystallographic position occupied by the cation to be substituted for on the high-frequency vibration spectrum of the crystal. Therefore, we studied 2212 solid solutions with substitution of both La^{3+} for Ca^{2+} and La^{3+} for Sr^{2+} (the ionic radii of Ca^{2+}, Sr^{2+}, and La^{3+} are 1.26, 1.40, and 1.30 Å, respectively).

2. EXPERIMENT AND DATA TREATMENT

The $Bi_2Sr_{2-y}Ca_{1-x}La_{x+y}Cu_2O_{8+\delta}$ samples ($x = 0$, $y = 0$; $x = 0.25$, $y = 0$; $x = 0$, $y = 0.25$; $x = 0$, $y = 0.5$) were prepared from nitrate–oxynitrate mixtures obtained by dissolution of ChDA-grade Bi_2O_3, $SrCO_3$, and CuO and of OSCh-grade $CaCO_3$ and La_2O_3 in 20% nitric acid, with subsequent evaporation of the solution thus prepared. The samples were synthesized by the technique that was used in [6] to prepare Nd-containing Bi2212-based solid solutions and included decomposition of the salt mixture at 750°C and several subsequent 24-h stages of annealing at 860°C alternated with grinding. All the anneals were performed in air.

X-ray phase analysis of the samples performed with a DRON-3M diffractometer ($CuK_{\alpha,\,\mathrm{ave}}$ radiation; silicon used as the internal standard for determination of the unit-cell parameters) showed their composition to agree with that of $Bi_2Sr_2CaCu_2O_8$-based solid solutions. The least-squares refined unit-cell parameters are listed in Table 1. The data indicate that a monotonic parameter variation bears out the formation of solid solutions.

The inelastic neutron scattering (INS) experiments were performed on a DIN-2PI direct-geometry spectrometer installed on an IBR-2 reactor (JINR, Dubna) [7]. The spectra were recorded at room temperature in the time-of-flight mode for neutrons of initial energy E_0 = 8.15 meV and increased energy E within the scattering angle interval of 42°–134° (the detectors mounted at smaller angles revealed a considerable neutron flux with energies above 100 meV which constituted a thermal background). The spectrometer resolution was $\Delta E/E \approx$ 5–8% for energy transfer $\varepsilon = E - E_0$ = 0–100 meV, with the momentum transferred to the neutron lying in the ranges Q = 1.8–4.2 $Å^{-1}$ for ε = 6 meV and Q = 5.9–8.7 $Å^{-1}$ for ε = 100 meV. The spectra were normalized by the vanadium elastic peak.

The spectra were treated in the incoherent approximation [8], with multiphonon scattering included [9]. After the usual corrections to the detector efficiency and neutron flux attenuation by the sample were made, the INS spectra were treated to obtain the $G(\varepsilon)$ function; i.e., the lattice frequency spectrum was weighted by the factor $\sum \exp(-2W_i)\, c_i\sigma_i\langle|\xi_i(\varepsilon)|^2\rangle/m_i$, where c_i, σ_i, m_i, and $\langle|\xi_i(\varepsilon)|^2\rangle$ are the concentration, scattering cross section, mass, and mean square of the polarization vectors of the ith atom, respectively, and $\exp(-2W_i)$ is the Debye–Waller factor (the so-called neutron-weighted spectral density of vibrational states).

Figure 1 displays neutron-weighted frequency spectra for our samples averaged over measurements on all detectors within the scattering angle range of 42° to 134°. To facilitate numerical evaluations of the differences in the phonon density-of-states spectra between samples with different La contents, the low-frequency part (ε < 50 meV) of these spectra was fitted by a superposition of Gaussians:

$$I = [A/w(\pi/2)^{1/2}]\exp[-2(\varepsilon - \varepsilon_c)/w]^2, \qquad (1)$$

where I is the intensity, ε is the energy, and A, w, and ε_c are parameters. By subtracting the sum of the Gaussians describing the low-frequency part from the $G(\varepsilon)$ spectrum, we isolated the part of the spectrum that is due, according to literature data, to vibrations of oxygen in the CuO_2 and SrO layers (Fig. 2) and that can likewise be approximated by the functions of Eq. (1). The parameters of the Gaussians for all samples are listed in Table 2, and the functions describing the $G(\varepsilon)$ spectrum of the $Bi_2Sr_2CaCu_2O_8$ sample are plotted in Fig. 1.

Table 1. Parameters of the orthorhombic unit cell of the $Bi_2Sr_{2-y}Ca_{1-x}La_{x+y}Cu_2O_{8+\delta}$ solid solutions (in Å)

Composition	$x = 0$, $y = 0$	$x = 0.25$, $y = 0$	$x = 0$, $y = 0.25$	$x = 0$, $y = 0.5$
a	5.426(3)	5.432(3)	5.437(4)	5.441(3)
b	5.426(3)	5.432(3)	5.437(4)	5.441(3)
c	30.91(3)	30.76(3)	30.73(4)	30.53(2)

3. DISCUSSION OF RESULTS

The assignment of the various parts of the spectra obtained to specific atomic vibrations was made, as in [6], by comparing the experimental data with the results quoted in [3, 10–12] for the solid solutions $Bi_2Sr_2Ca_{1-x}Y_xCu_2O_{8+\delta}$ and unsubstituted $Bi_2Sr_2CaCu_2O_8$. This assignment yielded the same conclusions as in [6], namely, that peak *1* relates to vibrations of Bi; peak *2*, to those of Sr; peaks *3* and *4*, to vibrations of Cu and the cations in the Ca layer; peak *5*, to the superposition of vibrations of Cu and of several types of oxygen vibrations; peak *6*, to vibrations of oxygen in the SrO layer; and peak *7*, to those of oxygen in the CuO_2 layer.

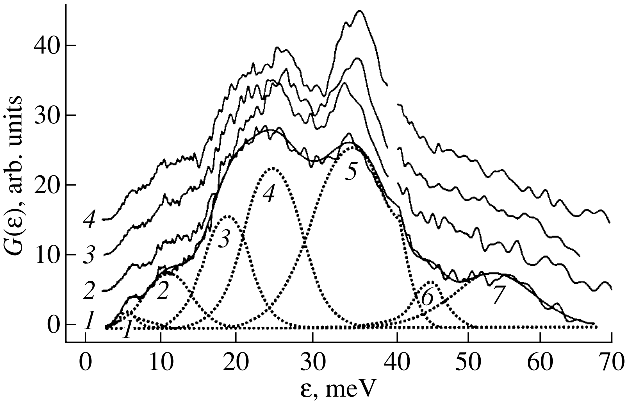

Fig. 1. Spectra $G(\varepsilon)$ of $Bi_2Sr_{2-y}Ca_{1-x}La_{x+y}Cu_2O_{8+\delta}$ solid solutions with (*1*) $x = 0$, $y = 0$; (*2*) $x = 0.25$, $y = 0$; (*3*) $x = 0$, $y = 0.25$; and (*4*) $x = 0$, $y = 0.5$. Dashed lines (*1*–*7*) refer to Gaussians approximating the $G(\varepsilon)$ spectrum and corresponding to specific atom group vibrations.

Table 2. Parameters of the Gaussians in Eq. (1) used to fit the experimentally obtained $G(\varepsilon)$ spectra of $Bi_2Sr_{2-y}Ca_{1-x}La_{x+y}Cu_2O_{8+\delta}$ solid solutions

Gaussian no.		1	2	3	4	5	6	7
$x = 0, y = 0$	ε_c (meV)	5.7	11	19	25	35	48	67
	w (meV)	2.0	6.0	6.0	7.4	10	8.9	23
	A (a.u.)	5.8	57	120	210	330	70	220
$x = 0, y = 0.25$	ε_c (meV)	5.9	11	21	27	35	48	64
	w (meV)	2.1	6.2	8.3	4.9	8.4	8.8	23
	A (a.u.)	5.0	53	220	82	290	88	240
$x = 0, y = 0.5$	ε_c (meV)	6.4	11	21	27	36	47	63
	w (meV)	2.7	4.3	8.5	4.7	8.0	8.3	23
	A (a.u.)	13	39	220	86	300	86	240
$x = 0.25, y = 0$	ε_c (meV)	6.2	11	19	25	35	50	67
	w (meV)	2.5	4.9	6.0	6.0	10	11	25
	A (a.u.)	8.5	42	120	170	350	100	220

Figures 1 and 2 demonstrate a slight shift of the oxygen vibration spectrum toward higher frequencies induced by the La substitution for Ca. By contrast, substitution of La for Sr virtually does not produce this effect.

The shift of peak *2* induced by variation of the Nd content was earlier shown [6] to correlate well with the (estimated in [13]) distributions of the rare-earth (RE) and AE atoms over the crystallographic positions. A similar estimate was made in this study for Bi2212-based La-containing solid solutions. The calculation was performed by a full-profile analysis of x-ray diffractograms (Rietveld refinement). The calculation made use of the RIETAN code [14]. The results obtained are given in Table 3.

Because of the closeness of the atomic scattering factors for Sr and the 0.49La + 0.51Ca system, which places a constraint on the applicability of x-ray diffraction to analysis of the cation distribution in the system under study, the inclusion of second-order parameters (incommensurate modulation) appeared unreasonable and the calculations were performed taking into account the substructural reflections only. Thus, the peak with $d = 2.44$ Å corresponding to an incommensurately modulated superstructure was disregarded in the calculations, which increased the value of the R_{wp} factor. The effect of modulation on the substructural peaks was included by accepting 2 Å for the rms atomic displacement in the Bi_2O_2 layer, which corresponds [15] to the modulation amplitude. The rms displacement for the other atoms was assumed to be 0.02 Å.

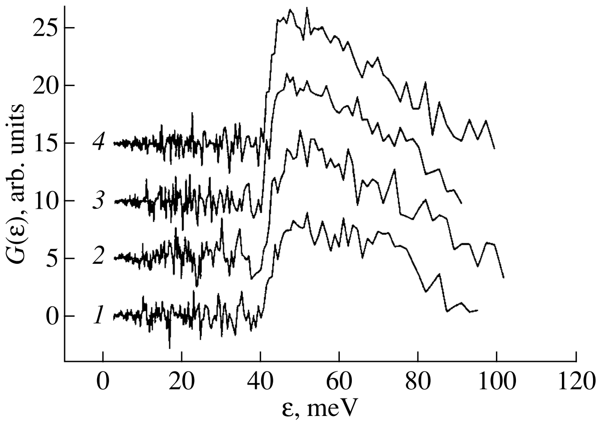

Fig. 2. High-frequency parts of the spectra of Fig. 1.

The calculations made with different values of the rms atomic displacement in a specific layer showed that this quantity only weakly affects the cation distributions obtained. The data obtained in repeated experiments and calculations with different sets of initial conditions were found to be reproducible. It was thus concluded that the Rietveld refinement technique can be used in x-ray diffraction calculations to analyze the cation distribution in the solid solutions under study. Because the x-ray diffraction methods have only limited applicability to our problem, it appears reasonable to employ them only to identify the crystallographic position most favorable for a given cation.

The atomic vibration frequency ratio in the SrO layer for various La concentrations was estimated using the data in Table 3, as was done in [6], from the relation

$$\omega_1/\omega_2 = ((Z_1\mu_2)/(Z_2\mu_1))^{1/2}, \tag{2}$$

where ω is the vibration frequency; $Z = Z(\mathrm{La})\alpha + Z(\mathrm{Sr})(1-\alpha)$; $Z(\mathrm{La})$ and $Z(\mathrm{Sr})$ are the charges of the La^{3+} and Sr^{2+} ions, respectively; $\mu = \alpha m(\mathrm{La}) + \beta m(\mathrm{Ca}) + (1 - \alpha - \beta)m(\mathrm{Sr})$; α is the fraction of the Sr crystallographic positions occupied by La and β is that occupied by Ca; and $m(\mathrm{La})$, $m(\mathrm{Sr})$, and $m(\mathrm{Ca})$ are the atomic masses of

La, Sr, and Ca, respectively. Indices 1 and 2 relate to solid solutions with different La concentrations being compared. Equation (2) was derived within a model of atomic vibrations in a field of a rigid crystal under the assumption of the interatomic interaction force (in a predominantly ionic crystal) being proportional to the average cation charge ($(1 - \alpha - \beta)Sr^{2+} + \beta Ca^{2+} + \alpha La^{3+}$) for a constant anion charge (O^{2-}). This model satisfactorily describes, as a rule, the so-called single-mode behavior of the vibrational spectrum of a substitutional solid solution (see, e.g., [16]).

The results obtained are given in Table 4. In this case, while the approximate calculations are in poorer agreement with the observed atomic-vibration frequencies in the SrO layer than for the Nd-containing solid solutions [6] (which may stem from the ionic radii of Nd^{3+} and La^{3+} being different), the shift of these frequencies is in the right direction.

In addition to the vibration frequency shift of the cations in the SrO layer (the low-frequency part of the spectrum), one observes a certain modification of the high-frequency part of $G(\varepsilon)$ which depends on the type and extent of La substitution for the AE metals (Fig. 2). It is in this part of the spectrum that the effects associated with both the carrier concentration variation in the CuO_2 sheet and the built-in pressure should become manifest. Figure 2 shows the growth of $G(\varepsilon)$ in the 40–60-meV interval (peak *6*) for all the La-containing samples compared with unsubstituted Bi2212. We note that substitution of La for Ca somewhat increases, as already mentioned, the cut-off frequency. A similar effect of the increase in the cut-off frequency was observed [6] when Nd was substituted for Ca in a $Bi_2Sr_2Ca_{0.25}Nd_{0.75}Cu_2O_{8+\delta}$ sample (see Fig. 3).

The observed differences in the shape of the oxygen vibration spectra in Bi2212-based Nd- and La-containing solid solutions can apparently be related to either the difference in the ionic radii of Nd^{3+} and La^{3+} (1.25 and 1.30 Å [5]) or the charge differences between the crystallographic layers containing oxygen (most probably, the SrO and Bi_2O_2 layers). As follows from our spectra obtained for different scattering angles, the presence of a magnetic moment on the Nd^{3+} ion, unlike La^{3+}, whose magnetic moment is zero, does not contribute noticeably to the phonon spectrum in the low-frequency domain. This is much less likely to occur in the high-frequency part of the spectrum for the momentum transfers used in this study.

Table 5 lists the average ionic radii and cation charges in the Ca and Sr positions for the compositions of interest (based on this work and [13]). We readily see that the differences between these radii are quite small, which suggests that the size factor (the built-in pressure effect) cannot be the main reason for the observed differences in the high-frequency part of the Bi2212-based RE-containing solid solutions.

Table 3. Distributions of atoms *X* (La, Ca, Sr) on the sublattice of alkaline-earth elements *Y* (Ca, Sr) calculated for the following solid solutions: (1) $Bi_2Sr_{1.75}La_{0.25}CaCu_2O_{8+\delta}$, (2) $Bi_2Sr_{1.5}La_{0.5}CaCu_2O_{8+\delta}$, and (3) $Bi_2Sr_2Ca_{0.75}La_{0.25}Cu_2O_{8+\delta}$; *X*(*Y*) is the occupation of the *Y* atom positions by *X* atoms

X(*Y*)	1—$Sr_{1.75}La_{0.25}$	2—$Sr_{1.5}La_{0.5}$	3—$Ca_{0.75}La_{0.25}$
Sr(Sr)	1.54	1.46	1.68
Ca(Sr)	0.24	0.34	0.08
La(Sr)	0.22	0.20	0.24
Sr(Ca)	0.21	0.04	0.32
Ca(Ca)	0.76	0.66	0.67
La(Ca)	0.03	0.30	0.01
R_{wp}, %	8.35	7.59	8.26

Table 4. Ratios ω_1/ω_2 for $Bi_2Sr_{2-y}Ca_{1-x}La_{x+y}Cu_2O_{8+\delta}$ solid solutions; experimental and calculated from Eq. (2) ($x_1 = y_1 = 0$)

Solid-solution composition	$Bi_2Sr_{2-y}Ca_{1-x}La_{x+y}Cu_2O_{8+\delta}$		
	$x_2 = 0$, $y_2 = 0.25$	$x_2 = 0$, $y_2 = 0.5$	$x_2 = 0.25$, $y_2 = 0$
Calculation	0.960	0.974	0.995
Experiment	0.997	0.995	0.976

A comparison of the spectra of the Nd-containing solid solutions presented in [6] with our spectra of the La-containing Bi2212 suggests that the intensity redistribution between the oxygen vibrational modes observed to occur in the substitution of La for the AE metals is related primarily to the increase in the average cation charge in the SrO layer.

The other effect, namely, the increase in the cut-off frequency ω_{cut} induced by La or Nd substitution for Ca,

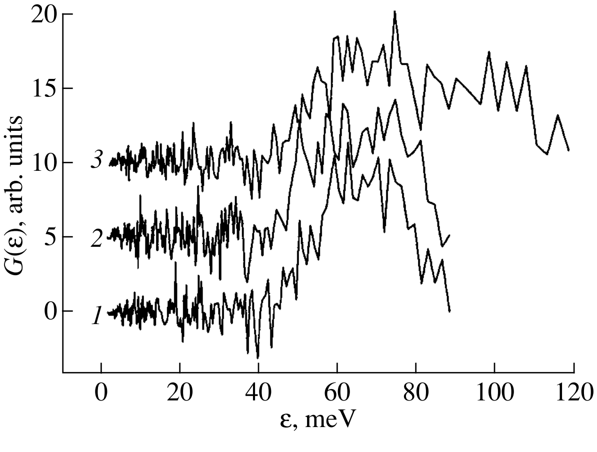

Fig. 3. High-frequency parts of the $G(\varepsilon)$ spectra for $Bi_2Sr_2Ca_{1-x}Nd_xCu_2O_{8+\delta}$ samples with *x* equal to (*1*) 0.1, (*2*) 0.25, and (*3*) 0.75.

Table 5. Average ionic radii (R, Å) and charges (Z) of cations in the Sr(1) and Ca(2) positions calculated for $Bi_2Sr_{2-x}La_xCa_{1-y-z}Nd_yLa_zCu_2O_{8+\delta}$ solid solutions

Composition	$x = y = z = 0$	$x = z = 0$, $y = 0.1$	$x = z = 0$, $y = 0.25$	$x = z = 0$, $y = 0.75$	$y = z = 0$, $x = 0.25$	$y = z = 0$, $x = 0.5$	$y = x = 0$, $z = 0.25$
(1) R	1.40	1.38	1.39	1.37	1.37	1.37	1.38
Z	2.00	2.04	2.00	2.19	2.11	2.10	2.12
(2) R	1.27	1.31	1.29	1.30	1.29	1.28	1.31
Z	2.00	2.02	2.25	2.37	2.03	2.30	2.01

is also apparently connected with a change in the ionic charge state and, possibly, with the small difference between the Ca and La cation radii ($R_{Ca} < R_{La}$). Some of the differences in the shape of the high-frequency part of the spectra produced by the substitution of La and Nd for Ca probably originate from the different contrasts that the partial spectra of these atoms exhibit in the net neutron-weighted spectrum, as well as from different occupation of the alternative positions (in this case, of the positions of Sr). Substitution of La for Sr produces the same change in the shape of the high-frequency spectrum. As in the first case, this is associated with the change in the cation charge state. This is not accompanied, however, by an increase in ω_{cut}. In our opinion, the latter is due to the size effect, because the radius of La is noticeably smaller than that of Sr.

4. CONCLUSION

Thus, we have measured phonon spectra of the $Bi_2Sr_{2-y}Ca_{1-x}La_{x+y}Cu_2O_{8+\delta}$ solid solutions by inelastic neutron scattering.

The La distribution over the Ca and Sr crystallographic positions in these solid solutions was estimated from a full-profile analysis of the diffraction patterns, and it was shown not to be at variance with the results obtained in neutron dynamic measurements.

It was shown that substitution of La for AE metals in the $Bi_2Sr_2CaCu_2O_8$ structure produces noticeable changes in the high-frequency part ($\varepsilon > 40$ meV) of the neutron-weighted frequency spectrum compared to unsubstituted $Bi_2Sr_2CaCu_2O_8$. These changes are probably associated with the increase in the average cation charge in the SrO layer of the $Bi_2Sr_2CaCu_2O_8$ structure.

REFERENCES

1. A. Manthiram and J. B. Goodenough, Appl. Phys. Lett. **53**, 420 (1988).
2. N. A. Babushkina, M. V. Dobrotvorskaya, N. A. Kasatkina, *et al.*, Physica C (Amsterdam) **197**, 299 (1992).
3. B. Renker, F. Gompf, D. Ewert, *et al.*, Z. Phys. B **77**, 65 (1989).
4. M. Kakihana, M. Osada, M. Kall, *et al.*, Phys. Rev. B **53**, 11796 (1996).
5. R. D. Shannon and C. T. Prewitt, Acta Crystallogr. B **25**, 935 (1969).
6. A. V. Knot'ko, A. V. Garshev, V. I. Putlyaev, and S. I. Morozov, Fiz. Tverd. Tela (St. Petersburg) **42**, 1537 (2000) [Phys. Solid State **42**, 1579 (2000)].
7. V. A. Parfenov, P. S. Klemyshev, I. G. Morozov, and A. F. Pavlov, in *Proceedings of a Symposium on Neutron Inelastic Scattering, Vienna, 1977* (IAEA, Vienna, 1978), Vol. 1, p. 81.
8. V. F. Turchin, *Slow Neutrons* (Gosatomizdat, Moscow, 1963; Israel Program for Scientific Translations, Jerusalem, 1965).
9. A. Sjolandar, Ark. Fys. **14**, 315 (1958).
10. D. Shimada, N. Tsuda, U. Paltzer, and F. W. de Wette, Physica C (Amsterdam) **298**, 195 (1998).
11. P. P. Parshin, M. G. Zemlyakov, and A. V. Irodova, Fiz. Nizk. Temp. **22** (5), 564 (1996) [Low Temp. Phys. **22**, 435 (1996)].
12. P. P. Parshin, M. G. Zemlyakov, A. V. Irodova, *et al.*, Fiz. Tverd. Tela (St. Petersburg) **38**, 1665 (1996) [Phys. Solid State **38**, 919 (1996)].
13. A. V. Knot'ko, A. V. Garshev, A. G. Veresov, *et al.*, Materialovedenie, No. 1, 42 (2000).
14. F. Izumi, *The Rietveld Method*, Ed. by R. A. Young (Oxford Univ. Press, Oxford, 1993), Chap. 13.
15. P. A. Miles, S. J. Kennedy, G. J. McIntyre, *et al.*, Physica C (Amsterdam) **294**, 275 (1998).
16. H. Böttger, *Principles of the Theory of Lattice Dynamics* (Physik, Weinheim, 1983; Mir, Moscow, 1986).

Translated by G. Skrebtsov

Physics of the Solid State, Vol. 44, No. 7, 2002, pp. 1229–1234. Translated from Fizika Tverdogo Tela, Vol. 44, No. 7, 2002, pp. 1179–1184.
Original Russian Text Copyright © 2002 by Petrov, Balaev, Gokhfel'd, Shaĭkhutdinov, Aleksandrov.

METALS
AND SUPERCONDUCTORS

Temperature Evolution of the Hysteresis in the Current–Voltage Characteristic of a Polycrystalline High-Temperature Superconductor with 1-2-3 Structure

M. I. Petrov[1], D. A. Balaev[1], D. M. Gokhfel'd[1, 2], K. A. Shaĭkhutdinov[1], and K. S. Aleksandrov[1]

[1] *Kirensky Institute of Physics, Siberian Division, Russian Academy of Sciences, Akademgorodok, Krasnoyarsk, 660036 Russia*

[2] *Reshetnev Siberian State Aerospace University, Krasnoyarsk, 660014 Russia*

e-mail: smp@iph.krasnoyarsk.su

Received July 20, 2001; in final form, November 1, 2001

Abstract—The temperature evolution of the current–voltage (*I*–*U*) characteristic of a contact of the break-junction type with direct conduction is investigated on a polycrystalline HTSC of the Y–Ba–Cu–O system. The experimental *I*–*U* characteristics possessing a hysteresis are correctly described in the framework of the Kümmel–Nicolsky theory for an *S*–*N*–*S* contact (*S* stands for a superconductor; *N*, for a normal metal) in which the Andreev reflection of quasiparticles from the *N*–*S* interface is considered. It is shown that the shape of the *I*–*U* curve, as well as the existence of a hysteresis, is determined by the ratio of the number of "long" and "short" intergranular boundaries in the polycrystal under investigation. The coincidence of the calculated and experimental *I*–*U* curves made it possible to estimate the effective length of "natural" intergranular boundaries in polycrystalline HTSC materials. The estimate is obtained from the experimental temperature dependence of the critical current in the sample under investigation. *© 2002 MAIK "Nauka/Interperiodica".*

1. INTRODUCTION

Bulk HTSC polycrystals possess much lower current-carrying capacity than single crystals and thin films. It is well known that the main limiting factor is the intergranular boundaries, whose presence results in the formation of a random network of weak links *S*–*N*–*S* (*S* is a superconductor and *N* is a normal metal) in a polycrystal. The distribution of geometrical parameters of individual weak links in such a network is described by a certain distribution function determined by the technology of the synthesis of polycrystals.

Junctions at microcracks (break junctions) were actively studied during the first years following the discovery of HTSC materials. However, break junctions continue to be attractive objects of investigation [1], since they make it possible to study both tunnel junctions and contacts with direct (metallic-type) conduction. The formation of a microcrack in a bulk HTSC sample in the case of a direct-conduction contact leads to a decrease in the effective cross-sectional area. The current density in the breaking region is much higher than the current density in the sample volume; consequently, weak links in the breaking region are the first to pass to the resistive state and determine the critical current and the current–voltage (*I*–*U*) characteristic of the sample until degradation of the superconductivity begins in the bulk of the sample. Consequently, the resistive state of a contact of the break-junction type is determined by the superposition of a finite number of weak links. It becomes possible to measure the *I*–*U* characteristics of junctions at natural intergranular boundaries over a wide temperature range in the region of current densities much higher than the critical value; this almost entirely eliminates the effect of self-heating, which is difficult to achieve in bulk HTSC samples.

In order to describe the experimentally observed *I*–*U* curves for *S*–*N*–*S* junctions of the Josephson type, the resistive shunted junction (RSJ) model [2] or its modifications [3, 4] are often used. However, this model is only an equivalent electric circuit and does not reflect the quantum physical processes of charge carrier transport in an *S*–*N*–*S* junction [2, 5, 6].

The charge carrier transport in an *S*–*N*–*S* junction is determined by physical processes such as tunneling, the proximity effect, and Andreev reflection [7]. Starting from the publications by Artemenko, Volkov, and Zaĭtsev [8, 9], several models have been developed in which the major role in the formation of *I*–*U* characteristics is assigned to Andreev reflection. In the pioneering works [8, 9], the *I*–*U* curves for microbridges were calculated only for the limiting cases, namely, near T_c and at voltages across a junction much larger than the energy gap in the superconductor. Blonder *et al.* [10] described the *I*–*U* curves of an *S*–*N* point contact and of a microconstriction; in this case, the shape of the *I*–*U* curve is determined by the barrier transparency. The theory describes the excess current and arc-shaped features in *I*–*U* curves (subharmonic gap structure) but fails to describe the negative differential resistance (NDR). In experiments, the NDR is manifested in the fixed stable current mode as a hysteresis loop on the *I*–*U* curves [11]. Some authors analyze the *I*–*U* curves of *S*–*N*–*S* junctions in various approximations (see, for example, [12–14]); however, *I*–*U* curves calculated on the basis of these models do not contain segments corresponding to NDR.

In our opinion, the most attractive theory capable of describing *I*–*U* curves of *S*–*N*–*S* structures in wide ranges of the mean free paths (l) of carriers in the *N* layer and geometrical thicknesses of the *N* layer ($2a$) is the Kümmel–Nicolsky theory [15]. This theory takes into account the contribution from Andreev reflections in the *S*–*N*–*S* to the current junction and predicts the existence of NDR in pure ($l > 2a$ [11]) *S*–*N*–*S* structures. This theory also describes the excess current and gap singularities at voltages that are multiples of the energy gap Δ. The theory developed in [15] was successfully used to describe some results obtained on *S*–*N*–*S* contacts with low-temperature superconductors [6]. The authors of [15–17] pointed out that the hysteresis observed on *I*–*U* curves of a weakly linked HTSC can be interpreted in the framework of this theory.

It has been proved [18] that a simplified version of the Kümmel–Nicolsky theory [5] satisfactorily describes the experimental *I*–*U* curves for composites $Y_{0.75}Lu_{0.25}Ba_2Cu_3O_7 + BaPb_{1-x}Sn_xO_3$ ($x = 0, 0.1$) measured at 4.2 K. In these composites, the normal metal $BaPb_{1-x}Sn_xO_3$ forms artificial metal boundaries between HTSC crystallites. For $x = 0$, the "clean" limit is realized in composites, while for $x = 0.1$, an effectively dirty limit ($l < 2a$ [11]) exists.

The aim of the present work is to demonstrate the applicability of the theory [15] not only to a network of weak links with artificially created metallic intergranular boundaries [18] but also to *I*–*U* characteristics of polycrystallites with natural intergranular boundaries in HTSC materials.

We measured *I*–*U* curves with a hysteresis loop of break-junction-type contacts with direct conduction in the temperature range 4.2–95 K. The results obtained are described satisfactorily in the framework of the theory [15] under the assumption that junctions of various geometric length are connected in series.

2. EXPERIMENT

We used the standard ceramic technology of fabrication of HTSC $Y_{0.75}Lu_{0.25}Ba_2Cu_3O_7$. The time of final firing was 40 h at 910°C. The Debye powder pattern displays only reflections corresponding to the 1-2-3 structure. The superconducting-transition temperature T_c as determined from magnetic measurements coincides with the temperature corresponding to the beginning of the resistive transition and amounts to 93.5 K.

Samples with a typical size of $2 \times 2 \times 10$ mm were sawed out from synthesized pellets. The sample was glued to a sapphire substrate. The central part of the sample was polished down to obtain a cross-sectional area $S \sim 0.2 \times 1$ mm. For such a value of S, the critical current at 4.2 K was ~2 A (current density 1000 A/cm^2). Further controllable decrease in the area S under inevitable mechanical stresses at current and potential contacts is very difficult. In order to obtain a contact of the break-junction type, the sample with the above value of S was bent together with the substrate with the help of screws of spring-loaded current contacts, which led to the emergence of a microcrack in the part of the sample between the potential contacts. As a result, either a tunneling contact (with resistance $R > 10\ \Omega$) or a direct-conduction contact ($R < 10\ \Omega$) was formed. For $R \sim 1$–$2\ \Omega$, the samples possess a critical current $J_c \sim 1$–10 mA at 4.2 K, which corresponds to a decrease in the value of S by a factor of ~10^2–10^3. It should be noted that the shape of the *I*–*U* curves for the samples was completely preserved after thermocycling from 4.2 to 100 K, but thermocycling to room temperature increased the value of R and the contact was converted into a tunneling contact.

During measurements, the samples were held in a helium heat-exchange atmosphere. The *I*–*U*-curve measurements were made under steady-state conditions in the fixed current mode. Relatively low values of the transport current (up to 150 mA) and of the voltage drop across the sample (up to ~100 mV) made it possible to eliminate the effect of self-heating [19]. The critical current was determined from the *I*–*U* curve using the 1-μV criterion [20].

3. RESULTS AND DISCUSSION

Figures 1 and 2a show typical examples of experimental *I*–*U* curves recorded at 4.2 K. The curves display the presence of a critical current and a segment with a nonlinear $U(I)$ dependence followed by a jumpwise (repeated in some cases) increase in the value of U accompanied by a hysteresis. In the region of large values of I and U, the $U(I)$ dependence is close to linear, and its extrapolation to the value $U = 0$ gives an excess current I_{ex} whose existence confirms the metallic type of conduction of the junctions formed [10].

The current due to Andreev reflections in an *S*–*N*–*S* contact, according to theory [15], has the form (in the notation used in [15])

$$j = C\sum_k \sum_{n=1}^{\infty} P_N(E_k)\{[f(E_k)k_e - (1-f(E_k))k_h] \times \exp(-(2na - a + b)/l)(|A_n^-|^2 - |A_n^+|^2)\}. \tag{1}$$

Here, $f(E_k)$ is the Fermi energy distribution function for quasiparticles, P_N is the probability of finding a quasiparticle in the N region, $A_n^+(E)$ and $A_n^-(E)$ are the probabilities of the nth Andreev reflection for holes (+) and electrons (–), b is the starting position from which quasiparticles begin their motion when an electric field

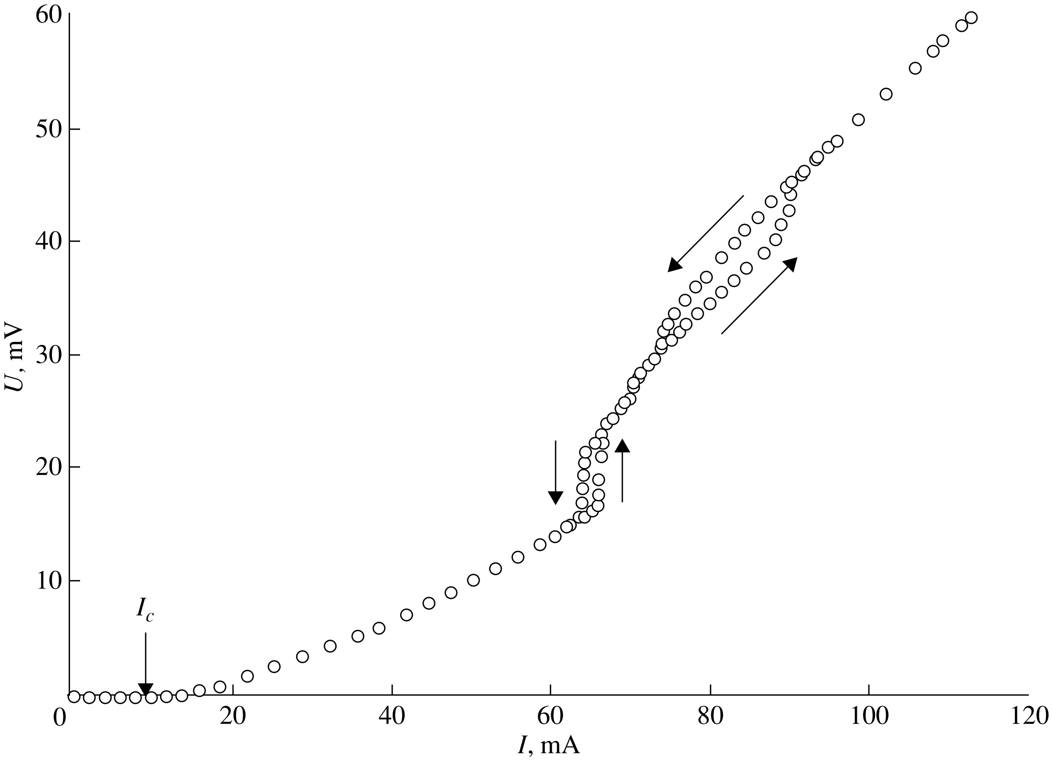

Fig. 1. Experimental *I–U* curve recorded for a sample at $T = 4.2$ K.

starts acting in the *N* layer, *n* is the number of Andreev reflections, and *C* is the constant defined in [15]. In our calculations, we used the density of states for charge carriers in an HTSC material [21].

The theory describes the *I–U* curves for *S–N–S* contacts with the above characteristic features excluding the region near $U \approx 0$, since the calculation of the critical current is a separate problem [7].

An example of a theoretical *I–U* curve is given in Fig. 2b. It can be seen that such a theoretical dependence cannot describe the experimental *I–U* curves shown in Figs. 1 and 2a, in which the hysteresis is observed for larger values of *U*. On the other hand, the multiple hysteresis loops observed on some *I–U* curves (Fig. 1) indicate that the *U*(*I*) dependence is formed by a superposition of *I–U* curves for several contacts with different parameters. A similar conclusion was drawn for a point HTSC contact from an analysis of the effect of radiation on the shape of *I–U* curves [22].

We processed the experimental curve shown in Fig. 2a by using the formula

$$U(I) = \sum_i V_i U_i(I, 2a_i), \qquad (2)$$

where $U_i(I, 2a_i)$ are the *I–U* characteristics of *S–N–S* junctions with various values of $2a$ defined by Eq. (1) and V_i are the weight factors indicating the effect of a contact with a given value of $2a$ on the resultant (superposition) *I–U* curve (with the obvious normalization $\sum_i V_i = 1$).

It was found that Eq. (2) correctly describes the experimental data even when the sum in this formula contains only two terms. The best agreement was attained for values of $2a_1/l = 0.15$, $V_1 = 0.34$, $2a_2/l = 0.5$, and $V_2 = 0.66$. Figure 2b shows the theoretical *I–U* curves for each of these two junctions, while Fig. 2a shows their superposition. It can be seen that the theoretical dependence obtained as a result of superposition coincides with the experimental *I–U* curve, including in the region with hysteresis, but the segment of the experimental *U*(*I*) dependence corresponding to values of *U* close to zero cannot be described by the theory from [15] (see above).

Figure 3a shows the experimental *I–U* curves for one of the samples (the same as in Fig. 2a) in the coordinates (*T*, *I*, *U*). Figure 3b presents the temperature evolution of the superposition *I–U* curve shown in Fig. 2b in the same coordinates. The only variable parameter was the temperature-dependent energy gap given by the BCS theory. The theory [15] correctly describes the decreases in the area of the hysteresis loop and its vanishing upon an increase in temperature. At temperatures above 4.2 K, the discrepancy between the theoretical and experimental *U*(*I*) dependences becomes more pronounced, but the difference between these dependences does not exceed 9%. It is important

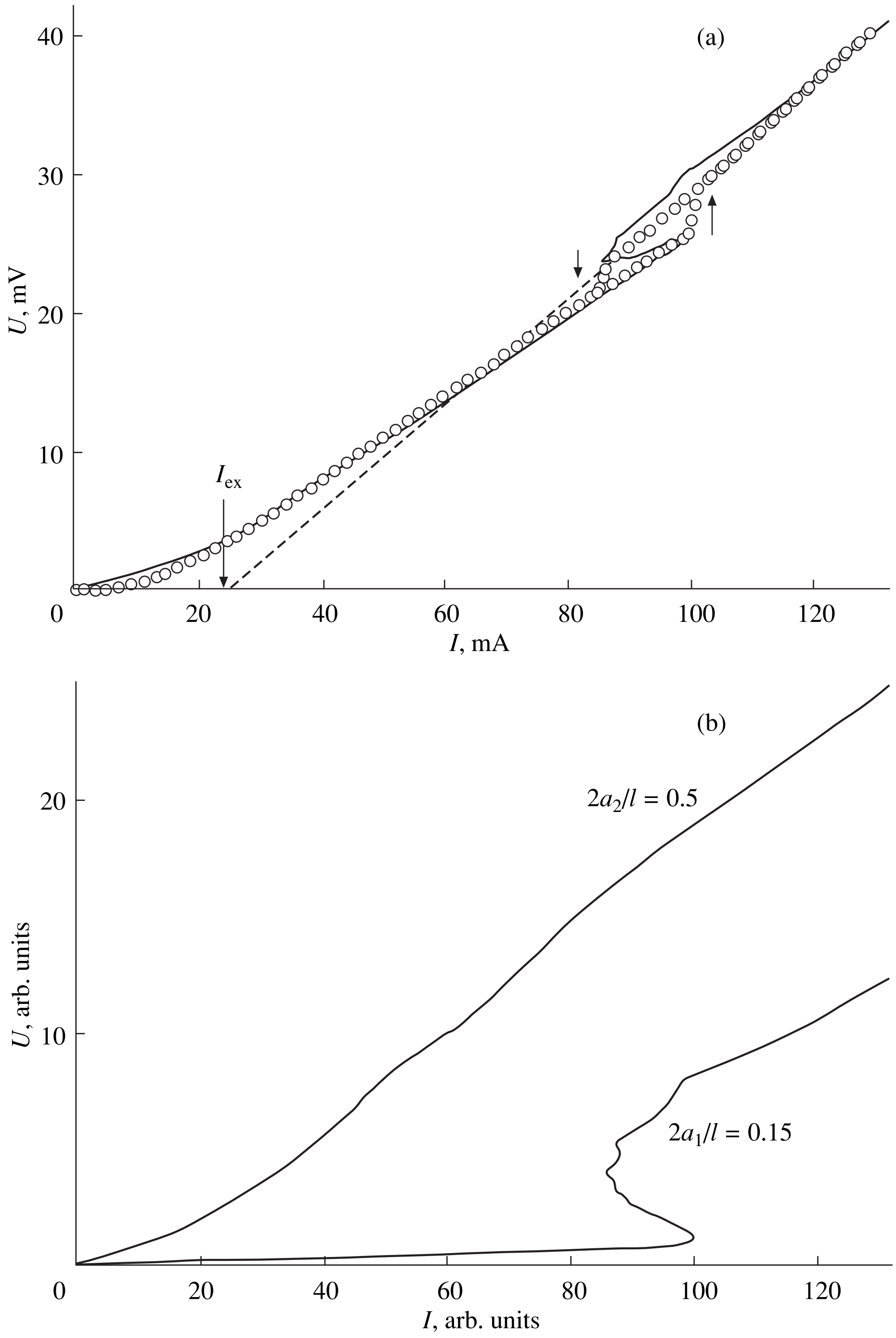

Fig. 2. Experimental *I*–*U* curve recorded for a sample at $T = 4.2$ K (circles). Solid curves are (a) the resultant superposition curve calculated on the basis of Eq. (2) for $V_1 = 0.34$ and $V_2 = 0.66$ and (b) the theoretical *I*–*U* curves for *S*–*N*–*S* junctions with parameters $2a_1/l = 0.15$ and $2a_2/l = 0.5$ calculated using Eq. (1).

to note that the experimental points corresponding to the jumpwise change in voltage are described by the theory quite successfully. A similar satisfactory agreement was also attained for other samples under investigation over a wide temperature range.

Knowing the mean free path of charge carriers, the lengths of intergranular boundaries in the HTSC material under investigation can be estimated by fitting to the experimental *I*–*U* curves. If we take for *l* the value ~20 Å given in [23] for a Y–Ba–Cu–O system, we obtain $2a_1 = 3$ Å and $2a_2 = 10$ Å. These values agree with the results obtained for natural intergranular boundaries in polycrystalline Y–Ba–Cu–O [24] and in a bicrystal [25]. The obtained values of coefficients

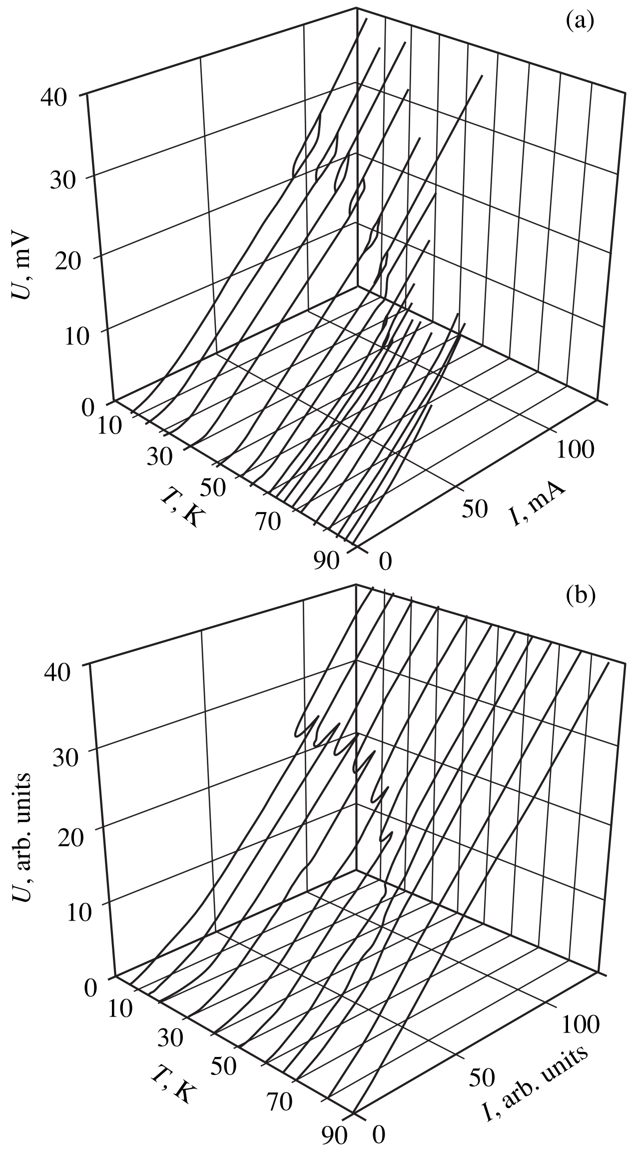

Fig. 3. Temperature evolution of *I*–*U* curves presented in Fig. 2: (a) experiment and (b) theory.

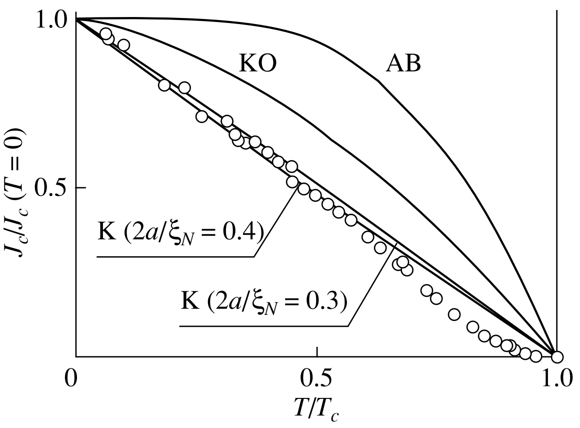

Fig. 4. Temperature dependence of normalized critical current $J_c(T)/J_c(0)$. Circles correspond to experimental data, and solid curves are theoretical calculations: the Ambegaokar–Baratoff (AB) dependence [31], the Kulik–Omel'yanchuk (KO) dependence [30], and the Kupriyanov (K) dependence [28].

$V_1 = 0.34$ and $V_2 = 0.66$ can be interpreted as follows: the *I*–*U* characteristic is defined by at least three series-connected contacts, one of which is 3 Å long and the other is 10 Å.

The length of intergranular boundaries can also be estimated from the experimental temperature dependence of critical current [24–27]. The experimental $J_c(T)$ dependence of the sample under investigation is shown in Fig. 4. In some theoretical works [7, 28, 29], the dependence of the critical current of a weak link with direct conduction on the temperature and thickness of the metallic layer was investigated. The theoretical curves from [7, 28], which describe similar results, are in good agreement with our experimental data. In the present work, we describe $J_c(T)$ on the basis of an earlier and simpler theory [28]. Figure 4 shows the theoretical curves from [28]. In a wide temperature range, good agreement is observed between the experimental $J_c(T)$ curve and the theoretical dependences for a weak link having a thickness of the *N* layer of $2a = (0.3$–$0.4\xi_N)$, where ξ_N is the coherence length in the normal metal for $T = T_c$ [28]. Figure 4 also shows the $J_c(T)$ dependence predicted by the theory [28] for $2a = 0$, which coincides with the Kulik–Omel'yanchuk (KO) temperature dependence for clean short microbridges [30] and with the dependence obtained in [7] for clean short *S*–*N*–*S* junctions, as well as the Ambegaokar–Baratoff (AB) $J_c(T)$ dependence for tunneling contacts [31]. The cardinal difference (even in the sign of curvature) of the experimental $J_c(T)$ dependence from the AB dependence is an extra argument confirming that a direct-conduction contact is formed in the sample under investigation. In [32], the value $\xi_N \sim 50$ Å is given for intergranular boundaries in Y–Ba–Cu–O. Using this value, we estimate the length of the intergranular boundary to be ~15–20 Å. This estimate is close to the value $2a_2 = 10$ Å obtained from the processing of the *I*–*U* curve (clearly, the critical current in series-connected junctions is determined by the worst of these junctions, i.e., by the longer one, since $J_c \sim \exp(-2a)$ in most of the theories from [7, 11, 20, 28, 29]). It should be noted that near T_c, the experimental and theoretical results differ noticeably; the experimental temperature dependence of the critical current becomes quadratic: $J_c \sim (1 - T/T_c)^2$. Such a behavior of the critical current near T_c has been observed by many authors for HTSC film structures [25, 27, 32], HTSC point contacts [33], and in bulk HTSC polycrystals [24, 26] and has been discussed more than once. We can indicate at least two reasons for such a behavior. A small coherence length in HTSC materials reduces the pair potential at the *S*–*N* interface; as a result, the function $J_c(T)$ becomes quadratic and not linear, proportional to $(1 - T/T_c)$ [34]. Thermal fluctuations near T_c also affect the $J_c(T)$ dependence [35, 36].

4. CONCLUSION

Thus, we have proved that the theory [15] based on Andreev reflections can be used to obtain a satisfactory description of the temperature evolution of *I–U* curves with a hysteretic behavior at junctions formed by natural boundaries in HTSC polycrystals. Such a description is found to be possible in the framework of a model with metal-type series-connected contacts with different effective lengths. The existence of a hysteresis loop and its shape are determined by the ratio of long and short intergranular boundaries in the HTSC polycrystals under investigation.

It should be noted that materials characterized by *I–U* curves with a sharp transition from a low to a high differential resistance (i.e., possessing a clearly manifested broad hysteresis loop) can be used in short-circuit current limiters [37, 38].

ACKNOWLEDGMENTS

This work was supported by the Sixth Competition of Evaluation of Youth Projects, Russian Academy of Sciences, 1999 (grant no. 55), and was partly supported by the Krasnoyarsk Regional Science Foundation (grant no. 10F162M).

REFERENCES

1. V. M. Svistunov, V. Yu. Tarenkov, A. I. D’yachenko, and E. Hatta, Pis’ma Zh. Éksp. Teor. Fiz. **71** (7), 418 (2000) [JETP Lett. **71**, 289 (2000)].
2. D. E. McCumber, J. Appl. Phys. **39** (7), 3113 (1968).
3. R. G. Seed, C. Vittoria, and A. Widom, J. Appl. Phys. **75** (12), 8195 (1994).
4. K. Saitoh, I. Ishimaru, H. Fuke, and Y. Enomoto, Jpn. J. Appl. Phys. **36** (3A), L272 (1997).
5. L. A. A. Pereira and R. Nicolsky, Physica C (Amsterdam) **282–287**, 2411 (1997).
6. L. A. A. Pereira, A. M. Luiz, and R. Nicolsky, Physica C (Amsterdam) **282–287**, 1529 (1997).
7. U. Gunsenheimer, U. Schüssler, and R. Kümmel, Phys. Rev. B **49** (9), 6111 (1994).
8. S. N. Artemenko, A. F. Volkov, and A. V. Zaĭtsev, Zh. Éksp. Teor. Fiz. **76** (5), 1816 (1979) [Sov. Phys. JETP **49**, 924 (1979)].
9. A. V. Zaĭtsev, Zh. Éksp. Teor. Fiz. **78** (1), 221 (1980) [Sov. Phys. JETP **51**, 111 (1980)].
10. G. E. Blonder, M. Tinkham, and T. M. K. Klapwijk, Phys. Rev. B **25** (7), 4515 (1982).
11. K. K. Likharev, Rev. Mod. Phys. **51** (1), 101 (1979).
12. A. F. Volkov and T. M. Klapwijk, Phys. Lett. A **168**, 217 (1992).
13. U. Gunsenheimer and A. D. Zaikin, Phys. Rev. B **50** (9), 6317 (1994).
14. E. V. Bezuglyi, E. N. Bratus’, V. S. Shumeiko, *et al.*, Phys. Rev. B **62** (21), 14439 (2000).
15. R. Kümmel, U. Gunsenheimer, and R. Nicolsky, Phys. Rev. B **42** (7), 3992 (1990).
16. R. Nicolsky, Cryogenics **29** (3), 388 (1989).
17. T. P. Devereaux and P. Fulde, Phys. Rev. B **47** (21), 14638 (1993).
18. M. I. Petrov, D. A. Balaev, D. M. Gohfeld, *et al.*, Physica C (Amsterdam) **314**, 51 (1999).
19. W. Scocpol, M. R. Beasley, and M. Tinkham, J. Appl. Phys. **45** (9), 4054 (1974).
20. A. Barone and G. Paterno, *Physics and Applications of the Josephson Effect* (Wiley, New York, 1982; Mir, Moscow, 1984).
21. H. Plehn, Q.-J. Wacker, and R. Kümmel, Phys. Rev. B **49** (17), 12140 (1994).
22. A. A. Verevkin, V. A. Il’in, and V. S. Étkin, Sverkhprovodimost: Fiz., Khim., Tekh. **2** (7), 128 (1989).
23. L. P. Gor’kov and N. B. Kopnin, Usp. Fiz. Nauk **156** (1), 117 (1988) [Sov. Phys. Usp. **31**, 850 (1988)].
24. M. I. Petrov, D. A. Balaev, B. P. Khrustalev, and K. S. Aleksandrov, Physica C (Amsterdam) **235–240**, 3043 (1994).
25. J. Manhart, P. Chaudhary, D. Dimos, *et al.*, Phys. Rev. Lett. **61** (21), 2476 (1988).
26. M. I. Petrov, D. A. Balaev, S. V. Ospishchev, *et al.*, Phys. Lett. A **237**, 85 (1997).
27. S. Benacka, V. Strbik, S. Chromik, *et al.*, Fiz. Nizk. Temp. **24** (7), 621 (1998) [Low Temp. Phys. **24**, 468 (1998)].
28. M. Yu. Kupriyanov, Fiz. Nizk. Temp. **7** (6), 700 (1981) [Sov. J. Low Temp. Phys. **7**, 342 (1981)].
29. A. Furusaki and M. Tsukada, Phys. Rev. B **43** (13), 10164 (1991).
30. I. O. Kulik and A. N. Omel’yanuk, Fiz. Nizk. Temp. **3** (7), 945 (1977) [Sov. J. Low Temp. Phys. **3**, 459 (1977)].
31. V. Ambegaokar and A. Baratoff, Phys. Rev. Lett. **10** (11), 486 (1963).
32. J. W. C. De Vries, G. M. Stolmann, and M. A. M. Gijs, Physica C (Amsterdam) **157**, 406 (1989).
33. B. A. Aminov, N. B. Brandt, N. M. Tkhu, *et al.*, Sverkhprovodimost: Fiz., Khim., Tekh. **2** (1), 93 (1989).
34. D. Deutscher and K. A. Müller, Phys. Rev. Lett. **59** (15), 1745 (1987).
35. V. Ambegaokar and B. J. Galperin, Phys. Rev. Lett. **22** (25), 1364 (1969).
36. M. I. Petrov, D. A. Balaev, K. A. Shaĭkhutdinov, and K. S. Aleksandrov, Fiz. Tverd. Tela (St. Petersburg) **41** (6), 969 (1999) [Phys. Solid State **41**, 881 (1999)].
37. M. I. Petrov, D. A. Balaev, V. I. Kirko, and S. G. Ovchinnikov, Zh. Tekh. Fiz. **68** (10), 129 (1998) [Tech. Phys. **43**, 1255 (1998)].
38. M. I. Petrov, S. N. Krivomazov, B. P. Khrustalev, and K. S. Aleksandrov, Solid State Commun. **82** (6), 453 (1992).

Translated by N. Wadhwa

Physics of the Solid State, Vol. 44, No. 7, 2002, pp. 1235–1240. Translated from Fizika Tverdogo Tela, Vol. 44, No. 7, 2002, pp. 1185–1189.
Original Russian Text Copyright © 2002 by Poklonski, Vyrko.

SEMICONDUCTORS AND DIELECTRICS

Nonlinear Screening of the Field of a Dopant Ion on the Metal Side of the Mott Phase Transition in Semiconductors

N. A. Poklonski and S. A. Vyrko
Belarussian State University, ul. F. Skariny 4, Minsk, 220050 Belarus
e-mail: poklonski@bsu.by

Received July 30, 2001

Abstract—The nonlinear screening of an ionized donor by the degenerate gas of conduction electrons in a crystalline semiconductor is analyzed. For nonlinear screening, the charge density of the electron cloud screening the ion is not proportional to the total electrostatic potential produced by the ion and cloud. As a result, the potential decreases with the distance from the ion more weakly than it does within the linear approximation and the energy of the electrostatic correlation between the ion and screening cloud is smaller. *© 2002 MAIK “Nauka/Interperiodica”.*

The phenomenon of screening implies that an ion creates a nonuniformly charged and, on the average, spherically symmetric cloud of free charges of opposite sign around itself [1, 2]. The charge of the cloud is equal in magnitude and opposite in sign to the charge of the ion. In combination, these charges produce an electrostatic (time-averaged) potential $\varphi(\mathbf{r})$, where $\mathbf{r}$ is the radius vector directed from the center of the ion to the screening cloud.

In order to describe the screening of the electric field of ions in the degenerate electron gas of a semiconductor, the Thomas–Fermi model is used [3–8]. Within this model, the dependence of the electron energy E on the quasi-wave vector $\mathbf{k}$ at the distance r from the ion is given by the formula $E = (\hbar k)^2/2m - e\varphi(\mathbf{r})$, where e and m are the modulus of the charge and the effective mass of an electron, respectively.[1] Within the linear-screening approximation, it is assumed that the modulus of the potential energy of an “average” electron $|e\varphi(\mathbf{r})|$ is smaller than the Fermi energy E_F and the charge density of the screening cloud is proportional to $\varphi(r)$. In this case, the total electrostatic potential produced by an ion with charge Ze and by the conduction band electrons screening it is described by the equation [1–8]

$$\varphi(r) = \frac{Ze}{4\pi\varepsilon r}\exp\left(\frac{-r}{\lambda}\right). \qquad (1)$$

Here, $\varepsilon = \varepsilon_r\varepsilon_0$ is the dielectric permittivity of the semiconductor due to the electrons in the valence band, ε_0 is the electric constant, and λ is the screening length for the Coulomb potential.

The aim of this paper is to describe the nonlinear screening of an ion with charge $Ze > 0$ in an n-type semiconductor, that is, to describe the case when the energy of an electron $|e\varphi(\mathbf{r})|$ in the field of the ion is not small in comparison with the Fermi energy E_F and the charge density of the screening cloud is not proportional to $\varphi(\mathbf{r})$. In addition, the correlation interaction energies between the ion and the screening electron cloud calculated within the linear- and nonlinear-screening approximations are compared.

1. Let us consider the nonlinear screening of an ionized donor by the degenerate gas of conduction electrons in an electrically neutral crystalline semiconductor. We start from the Poisson equation [5–8]

$$\Delta\varphi = -\frac{1}{\varepsilon_0}\left[\frac{\rho_s(\mathbf{r})}{\varepsilon_r} + Ze\delta(\mathbf{r})\right] = \frac{e}{\varepsilon_0}\left[\frac{n(\mathbf{r})-n}{\varepsilon_r} - Z\delta(\mathbf{r})\right], \qquad (2)$$

where $\delta(\mathbf{r})$ is the three-dimensional Dirac delta function, $\rho_s(\mathbf{r})$ is the screening charge density, and $n(\mathbf{r}) - n$ is the deviation of the concentration of the conduction band electrons from its average value n at a distance r from the ion.

In the vicinity of the ion, the conduction electron concentration corresponding to the electrostatic potential $\varphi(\mathbf{r})$, which varies only slightly on the scale of the wavelength of an “average” electron, can be written in the form [9]

$$\begin{aligned} n(\mathbf{r}) &= \int_0^{+\infty} g(E_{\text{kin}})f(E_{\text{kin}} - e\varphi(\mathbf{r}) - E_F)dE_{\text{kin}} \\ &= \int_0^{+\infty} g(E + e\varphi(\mathbf{r}))f(E - E_F)dE, \end{aligned} \qquad (3)$$

---

[1] In [4], the change in the quadratic dependence of $E(\mathbf{k})$ on the quasi-momentum $\hbar\mathbf{k}$ due to holes in the valence band was taken into account.

1063-7834/02/4407-1235$22.00 © 2002 MAIK “Nauka/Interperiodica”

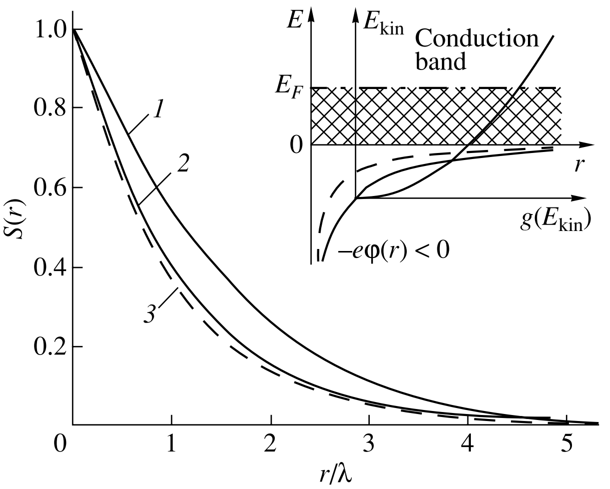

Fig. 1. The screening function $S(r)$ of an ionized donor in (*1*) *n*-Si and (*2*) *n*-GaAs at $n = 10^{19}$ cm^{-3} and $T \longrightarrow 0$ K. Curve *3* corresponds to $S(r) = \exp(-r/\lambda)$. Inset: the filling of the conduction band by electrons (shaded region) near a screened ion; $-e\varphi(r) < 0$ is the potential energy of an electron at a distance r from the ion, the dashed line corresponds to the linear screening, and $g(E_{\text{kin}}) \propto \sqrt{E_{\text{kin}}}$ is the dependence of the electron density of states in the conduction band on the kinetic energy.

where $E = E_{\text{kin}} - e\varphi(\mathbf{r})$ is the total energy of an electron, which is equal to the sum of its kinetic E_{kin} and potential energy $-e\varphi(\mathbf{r})$; $g(E_{\text{kin}})$ is the electron density of states in the conduction band; $f(E - E_F) = [1 + \exp((E - E_F)/k_BT)]^{-1}$ is the Fermi–Dirac distribution; E_F is the Fermi energy; and k_BT is the thermal energy.

In Eq. (3), the energy is measured from the bottom of the conduction band ($E = 0$) and it is taken into account that the energy of a conduction electron not captured on the bonding orbital by the ion cannot be negative (Fig. 1). If the electrons can occupy the states below the bottom of the conduction band (this takes place for the screening of the nucleus of a superatom, which is a selectively doped nanosize region in an intrinsic semiconductor [10]), the lower limit of integration in Eq. (3) should be replaced by $-e\varphi(\mathbf{r}) < 0$.

We suppose that the electron density of states in the conduction band is equal to the density of states in the undoped semiconductor [3, 7]:

$$g(E_{\text{kin}}) = \frac{2^{1/2} m^{3/2} \nu}{\pi^2 \hbar^3} \sqrt{E_{\text{kin}}}, \tag{4}$$

where m is the effective mass of the electron density of states in one valley, ν is the number of equivalent energy valleys (minimums of the kinetic energy) in the conduction band, and $\hbar$ is Planck's constant.

Thus, Eq. (2) in combination with Eqs. (3) and (4) gives a self-consistent description of the nonlinear screening of the impurity ion with charge $Ze > 0$ ignoring fluctuations of the potential energy of the conduction band electrons in the crystalline semiconductor.

It should be noted that, according to [11], the relative dielectric permittivity of a crystalline semiconductor ε_r depends on the distance from the screened impurity ion situated at a site (or interstitial space) of the crystal lattice. According to calculations for silicon [12] and germanium crystals [13], the permittivity ε_r due to the electrons of the valence band changes from $\varepsilon_r = 1$ in the vicinity of the ion to $\varepsilon_r = 11.47$ (Si) and 15.40 (Ge) at distances of order of the lattice constant a. For this reason, Eq. (2) is applicable at distances $r > a$ from the ion, where the dielectric permittivity of the crystalline lattice is equal to $\varepsilon_r\varepsilon_0$.

In works [14, 15], the substitution of the exact expression (3) into Eq. (2) provokes objections. The reason for this is that if $\varphi(\mathbf{r})$ in Eq. (2) is assumed to be the time-average of the potential at the point $\mathbf{r}$, then, after substituting Eq. (3), the average value of the function ρ_s in the right-hand part of Eq. (2) is replaced by the function of the average value. This is acceptable for linear functions of $\varphi(\mathbf{r})$ only. For this reason, if fluctuations of the potential energy of the electrons are significant, only the linearized Poisson equation $\Delta\varphi = \lambda^{-2}\varphi$ and its solution given by Eq. (1) have meaning.

The one-electron density of states in Eq. (4) can be used to describe the screening of an impurity ion in a crystalline metal when the degenerate electron gas is on a background of regularly situated ion cores and fluctuations of the potential energy of the conduction electrons do not occur. In an *n*-type semiconductor, the large electron concentration is due to the large concentration of dopant ions (donors). Since the arrangement of the impurity ions in the crystal lattice is random, spatial fluctuations of the electron potential energy occur (we denote the variance of these fluctuations by W^2). However, if the energy levels of impurity atoms lie in an allowed energy band of the crystalline semiconductor, the electron gas can be degenerate ($E_F \gg k_BT$) and, at the same time, the inequality $E_F > W$ can hold. For example, this occurs (at least, for $T \longrightarrow 0$) in PbTe:Tl [16] and HgSe:Fe [17] crystals. In particular, Fe atoms in HgSe are donors whose energy levels lie in the conduction band at a distance of approximately 220 meV from its bottom. At concentrations of Fe atoms $N < 5 \times 10^{18}$ cm^{-3}, all Fe^{2+} ions autoionize, transforming into Fe^{3+} ions. The concentration of conduction electrons n is equal to the concentration of the ionized donors N in this case. As the concentration of Fe atoms (donors) increases further, only a part of them becomes ionized. In this case, the Fermi level is stabilized in the vicinity of the donor level. The correlation in the arrangement of the Fe^{3+} donors occurs due to their Coulomb repulsion, which tends to arrange positive charges on Fe atoms that are as far apart as possible. It is obvious that if all randomly arranged donors are ionized, their ordering does not occur [18], because the positions of the donors are fixed in space, and, therefore, Eq. (4) is applicable at $E_F > W$ in this case.

Further, we consider the screening of the Coulomb potential of an impurity ion in a doped crystalline semiconductor in which the electron density of states is described by Eq. (4).

In the case of a linearly screened ion (at $e|\varphi| \ll E_F$ in a degenerate electron gas and at $e|\varphi| \ll k_B T$ in a nondegenerate gas), Eq. (2) in combination with Eqs. (3) and (4) is reduced to the linear equation [19]

$$\Delta\varphi = -\frac{\partial\rho_s}{\partial\varphi}\bigg|_{\varphi=0}\frac{\varphi}{\varepsilon} = \frac{\varphi}{\lambda^2}, \qquad (5)$$

whose solution is Eq. (1) with the screening length

$$\lambda^{-2} = \frac{e^2}{\varepsilon}\frac{\partial n}{\partial E_F}\bigg|_{\varphi=0} = \frac{e^2}{\varepsilon}\frac{2^{1/2}m^{3/2}\nu}{\pi^2\hbar^3 k_B T}\int_0^\infty \sqrt{E} f(1-f)dE. \qquad (6)$$

In a degenerate semiconductor, when $f(1-f) \longrightarrow k_B T\delta(E-E_F)$, where $\delta(E-E_F)$ is the Dirac delta function, Eq. (6) gives the Thomas–Fermi screening length

$$\lambda = \left(\frac{2\varepsilon E_F}{3e^2 n}\right)^{1/2}. \qquad (7)$$

For nonlinear screening, it is shown in [20, 21] that Eq. (2) with Eqs. (3) and (4) has a unique stable solution in the thermodynamic equilibrium at $\partial\rho_s/\partial\varphi < 0$. In three-dimensional space, this solution can be represented in the form [6]

$$\varphi(\mathbf{r}) = \frac{Ze}{4\pi\varepsilon r}S(r), \qquad (8)$$

where $S(r)$ is the screening function of the Coulomb potential satisfying the boundary conditions

$$\lim_{r\to 0} S(r) = 1, \quad \lim_{r\to\infty} S(r) = 0.$$

In the linear approximation, we have $S(r) = \exp(-r/\lambda)$.

In the spherical coordinates, the Laplacian of the potential in Eq. (8) is equal to

$$\Delta\varphi(\mathbf{r}) = \frac{Ze}{4\pi\varepsilon r}\frac{d^2S(r)}{dr^2}; \qquad (9)$$

therefore, the charge density of the electron cloud screening the ion is found from Eq. (2) to be

$$\rho_s = -\frac{Ze}{4\pi r}\frac{d^2S}{dr^2} = -e[n(\mathbf{r}) - n], \qquad (10)$$

where $n(\mathbf{r})$ is given by Eq. (3).

In using Eqs. (3)–(10), Eq. (2) can be reduced to the following equation for the screening function of the ion $S(r)$:

$$\frac{d^2S}{dr^2} = 4\pi r\frac{2^{1/2}m^{3/2}\nu}{\pi^2\hbar^3}\int_0^\infty\left(\sqrt{E + \frac{Ze^2S}{4\pi\varepsilon r}} - \sqrt{E}\right)f dE. \qquad (11)$$

If the impurity ion is screened by a degenerate electron gas ($E_F = \frac{\hbar^2}{2m}\left(\frac{3\pi^2 n}{\nu}\right)^{2/3} \gg k_B T$), then $f \longrightarrow \theta(E_F - E)$, where $\theta(E_F - E)$ is the Heaviside unit-step function, and Eq. (11) can be simplified to

$$\frac{d^2S}{dr^2} = \frac{2^{7/2}m^{3/2}\nu}{3\pi\hbar^3\sqrt{r}}\left(\left(\frac{Ze^2S}{4\pi\varepsilon} + E_F r\right)^{3/2} - \left(\frac{Ze^2S}{4\pi\varepsilon}\right)^{3/2} - (E_F r)^{3/2}\right). \qquad (12)$$

At $\nu = 1$ and $\varepsilon_r = 1$, Eq. (12) is reduced to the equation derived in [6].

Let us analyze the solution to Eq. (12) for $Z = +1$. We normalize the Fermi level E_F to $\nu^{2/3}E_B$, where $E_B = e^2/8\pi\varepsilon a_B$ and $a_B = 4\pi\varepsilon\hbar^2/e^2m$ are the Bohr energy and Bohr radius of an electron in a valley of the conduction band, respectively. (To find a solution for $Z > 1$, the following substitutions should be made in $S(r)$ obtained for $Z = 1$: $r \longrightarrow rZ$, $E_F \longrightarrow E_F/Z^2$, and $k_B T \longrightarrow k_B T/Z^2$.)

Figure 1 shows the $S(r)$ dependences numerically calculated from nonlinear equation (12) for *n*-Si and *n*-GaAs with the electron concentration $n = 10^{19}$ cm^{-3} at $T = 0$. At this conduction electron concentration, both *n*-Si and *n*-GaAs are on the metal side of the Mott metal–insulator transition. (The values of the concentration of hydrogen-like impurities corresponding to the Mott transition in weakly compensated semiconductors can be found in [22].) The calculations for *n*-Si (curve *1*) were carried out for the parameters $m \approx 0.33m_0$, $\nu = 6$, $\varepsilon_r \approx 11.5$, $E_B\nu^{2/3} \approx 112$ meV, $E_F \approx 16$ meV, and $\lambda = 0.8$ nm; for *n*-GaAs (curve *2*), the parameters were taken to be $m \approx 0.067m_0$, $\nu = 1$, $\varepsilon_r \approx 12.4$, $E_B \approx 5.9$ meV, $E_F \approx 260$ meV, and $\lambda = 3.45$ nm. It is obvious that the larger the Fermi energy E_F, the stronger the nonlinear screening and the closer $S(r)$ calculated by Eq. (12) to the linear approximation $S(r) = \exp(-r/\lambda)$ with the screening length given by Eq. (7).

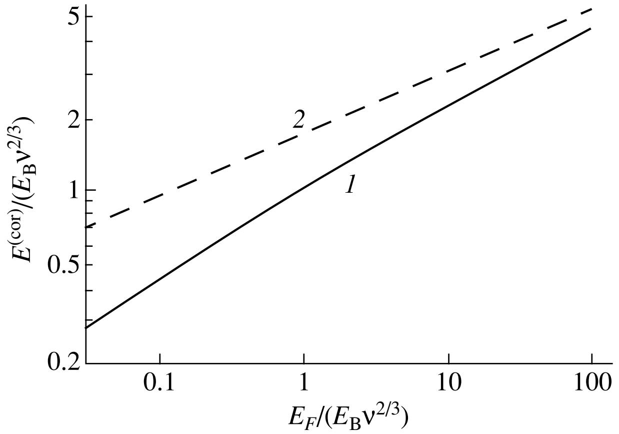

Fig. 2. The dependence of the correlation energy $E^{(\mathrm{cor})}$ on the Fermi level E_F at $T \longrightarrow 0$ (curve *1*) calculated by Eq. (19) with the use of Eq. (12); curve *2* corresponds to the linear approximation (13). The correlation energy is normalized to the Bohr energy E_{B} and the number of the valleys in the conduction band ν.

2. In order to describe the electrostatic correlations [1, 2] in an electron (hole) or electron–hole plasma, it is necessary to calculate the interaction energy between the screened charge and screening electron cloud $E_1 < 0$ and the interaction energy between the electrons of the cloud E_2. The correlation energy $E^{(\mathrm{cor})} = -(E_1 + E_2)$ in the case of the linear screening was calculated in [9, 23–27] to be

$$E^{(\mathrm{cor})} = -(E_1 + E_2) = -\frac{3}{4}E_1 = \frac{3e^2}{16\pi\varepsilon\lambda}, \qquad (13)$$

where the screening length λ for the ion screened by a degenerate electron gas is determined by Eq. (7).

For nonlinear screening, the energy of the Coulomb interaction between an ion with charge $+e$ and a screening electron cloud with density $\rho_s(\mathbf{r})$ given by Eq. (10) is

$$E_1 = \frac{e}{4\pi\varepsilon}\int\frac{\rho_s(\mathbf{r})}{r}d^3\mathbf{r} = -\frac{e}{4\pi\varepsilon}\int_0^{\infty}4\pi r^2\frac{e}{4\pi r^2}\frac{d^2S}{dr^2}dr$$
$$= -\frac{e^2}{4\pi\varepsilon}\left|\frac{dS}{dr}\right|_{r=0} < 0. \qquad (14)$$

Using Eq. (10), the interaction energy between the electrons of the spherically symmetric screening cloud can be represented as

$$E_2 = \frac{1}{2\varepsilon}\int\rho_s(\mathbf{r})d^3\mathbf{r}\frac{1}{4\pi}\int\frac{\rho_s(\mathbf{r}')}{|\mathbf{r}-\mathbf{r}'|}d^3\mathbf{r}' > 0. \qquad (15)$$

To perform the integration over $d^3\mathbf{r}' = -2\pi r'^2dr'd(\cos\theta)$ in this equation, we direct the polar axis along $\mathbf{r}$ such that $\cos\theta = \cos(\mathbf{r}, \mathbf{r}')$. In this case, we have

$$\frac{1}{4\pi}\int\frac{\rho_s(\mathbf{r}')}{|\mathbf{r}-\mathbf{r}'|}d^3\mathbf{r}' = \frac{1}{2}\left(\int_0^r\int_{-1}^1\frac{r'^2\rho_s(r')}{|\mathbf{r}-\mathbf{r}'|}dr'd(\cos\theta)\right.$$
$$\left.+\int_r^{+\infty}\int_{-1}^1\frac{r'^2\rho_s(r')}{|\mathbf{r}-\mathbf{r}'|}dr'd(\cos\theta)\right). \qquad (16)$$

By using the relationship [28, 29]

$$\frac{1}{|\mathbf{r}-\mathbf{r}'|} = \begin{cases}\dfrac{1}{r}\displaystyle\sum_{l=0}^{\infty}\left(\frac{r'}{r}\right)^l P_l(\cos\theta) & \text{for} \quad r' < r\\ \dfrac{1}{r'}\displaystyle\sum_{l=0}^{\infty}\left(\frac{r}{r'}\right)^l P_l(\cos\theta) & \text{for} \quad r' > r,\end{cases}$$

where $P_l(\cos\theta)$ are the Legendre functions, and integrating Eq. (16) over $\cos\theta$, we obtain

$$\frac{1}{4\pi}\int\frac{\rho_s(\mathbf{r}')}{|\mathbf{r}-\mathbf{r}'|}d^3\mathbf{r}' = \int_0^r\frac{r'^2}{r}\rho_s(r')dr' + \int_r^{+\infty}r'\rho_s(r')dr'. \qquad (17)$$

By substituting Eq. (10) into Eq. (17), we obtain

$$\frac{1}{4\pi}\int\frac{\rho_s(\mathbf{r}')}{|\mathbf{r}-\mathbf{r}'|}d^3\mathbf{r}' = \frac{e}{4\pi}\left(\int_0^r\frac{r'}{r}\frac{d^2S(r')}{dr'^2}dr'\right.$$
$$\left.+\int_r^{+\infty}\frac{d^2S(r')}{dr'^2}dr'\right) = \frac{e}{4\pi r}(1-S(r)).$$

Thus, integration over $\mathbf{r}$ in Eq. (15) gives

$$E_2 = \frac{1}{2\varepsilon}\int_0^{+\infty}4\pi r^2\left(\frac{e}{4\pi r}\right)^2\frac{d^2S}{dr^2}(1-S(r))dr$$
$$= \frac{e^2}{8\pi\varepsilon}\int_0^{+\infty}\left(\frac{dS}{dr}\right)^2dr. \qquad (18)$$

According to Eqs. (14) and (18), the total correlation energy due to the nonlinear screening of the impurity ion by the conduction electrons is

$$E^{(\mathrm{cor})} = -(E_1 + E_2)$$
$$= \frac{e^2}{8\pi\varepsilon}\left(\left|\frac{dS}{dr}\right|_{r=0} - \frac{1}{2}\int_0^{+\infty}\left(\frac{dS}{dr}\right)^2dr\right). \qquad (19)$$

Within the linear-screening approximation, $S(r) = \exp(-r/\lambda)$ and Eq. (19) reduces to Eq. (13).

For the ion screening, the dependences of the energies $E^{(\mathrm{cor})}$ on E_F at $T \longrightarrow 0$ calculated by Eqs. (19) and

(13) are shown in Fig. 2, where the energies are normalized to $\nu^{2/3}E_B$ and the electron concentration in a valley of the conduction band is n/ν. It is seen that as the Fermi energy increases, the correlation energy $E^{(\text{cor})}$ numerically calculated by Eq. (19) using the exact screening function $S(r)$ from Eq. (12) tends to the value of $E^{(\text{cor})}$ calculated from Eq. (13) within the linear approximation.

It should be noted that the thermal ionization energy of hydrogen-like impurity atoms decreases by $E^{(\text{cor})}$ in comparison with that for isolated impurities [24]. The energy $E^{(\text{cor})}$ also makes the main contribution to the energy gap narrowing in crystalline semiconductors for strong doping [9].

According to [9, 27, 30], the energy-gap narrowing in a crystalline semiconductor, which is determined by photoluminescence, is equal to the sum of the decrease in the energy of a nonequilibrium hole[2] due to its screening by electrons of the conduction band and the decrease in the energy of the electrons due to their exchange interaction:

$$\Delta E_g \equiv E_{g0} - E_g = \Delta E_g^{(\text{cor})} + \Delta E_g^{(\text{exc})} > 0, \tag{20}$$

where E_{g0} and E_g are the energy gaps in the undoped and doped crystals, respectively; $\Delta E_g^{(\text{cor})} = E^{(\text{cor})} > 0$ is the electrostatic correlation energy of the hole and the screening electron cloud; and $\Delta E_g^{(\text{exc})} = E^{(\text{exc})} > 0$ is the decrease in the energy of an electron due to the exchange interaction with other electrons of the conduction band.

According to the Wigner–Seitz theory [31], the exchange energy $E_{WS}^{(\text{exc})}$ per electron is two times smaller than the one-particle exchange energy $E_S^{(\text{exc})}$ calculated according to Slater [32]. According to [9, 27, 30], the exchange energy per electron at $T \longrightarrow 0$ is

$$E^{(\text{exc})} = E_{WS}^{(\text{exc})} = \frac{1}{2}E_S^{(\text{exc})} = \frac{3e^2}{16\pi^2\varepsilon}k_F, \tag{21}$$

where $\hbar k_F = \sqrt{2mE_F}$ is the Fermi quasi-momentum and $n = \nu(2mE_F)^{3/2}/3\pi^2\hbar^3$ is the total electron concentration in ν valleys of the conduction band.

Thus, we have described the nonlinear screening of a positively charged impurity ion by degenerate electron gas within the Thomas–Fermi model and calculated the correlation energy of the ion and screening electrons for the case when they do not form bound states.

ACKNOWLEDGMENTS

This work was supported by a grant for the Belarusian State University.

REFERENCES

1. L. D. Landau and E. M. Lifshitz, *Course of Theoretical Physics*, Vol. 5: *Statistical Physics* (Nauka, Moscow, 1976; Pergamon, Oxford, 1980), Part 1.
2. E. M. Lifshitz and L. P. Pitaevskiĭ, *Course of Theoretical Physics*, Vol. 5: *Statistical Physics* (Nauka, Moscow, 1978; Pergamon, New York, 1980), Part 2.
3. B. I. Shklovskiĭ and A. L. Efros, *Electronic Properties of Doped Semiconductors* (Nauka, Moscow, 1979; Springer, New York, 1984).
4. L. R. Logan and J. L. Egley, Phys. Rev. B **47** (19), 12532 (1993).
5. N. H. March, in *Theory of the Inhomogeneous Electron Gas*, Ed. by S. Lundqvist and N. H. March (Plenum, New York, 1983; Mir, Moscow, 1987).
6. M. I. Chibisov, Fiz. Plazmy **14** (2), 181 (1988) [Sov. J. Plasma Phys. **14**, 101 (1988)].
7. N. B. Brandt and S. M. Chudinov, *Electrons and Phonons in Metals* (Mosk. Gos. Univ., Moscow, 1990).
8. A. V. Nikiforov, V. G. Novikov, and V. B. Uvarov, *Quantum-Statistical Models of High Temperature Plasma and Computing Methods of Rosseland Lengths and Equations of State* (Fizmatlit, Moscow, 2000).
9. N. A. Poklonski and A. I. Syaglo, Zh. Prikl. Spektrosk. **64** (3), 367 (1997).
10. E. A. Andryushin and A. P. Silin, Fiz. Tverd. Tela (Leningrad) **33** (1), 211 (1991) [Sov. Phys. Solid State **33**, 123 (1991)].
11. K. R. Brownstein, Phys. Rev. B **48** (3), 1984 (1993).
12. P. Csavinszky, Phys. Rev. B **28** (10), 6076 (1983).
13. A. Fleszar, Phys. Rev. B **36** (11), 5925 (1987).
14. D. A. Frank-Kamenetskiĭ, *Course on Plasma Physics* (Atomizdat, Moscow, 1968).
15. L. P. Kudrin, *Statistical Plasma Physics* (Atomizdat, Moscow, 1974).
16. S. A. Nemov and Yu. I. Ravich, Usp. Fiz. Nauk **168** (8), 817 (1998) [Phys. Usp. **41**, 735 (1998)].
17. I. M. Tsidil'kovskiĭ, Usp. Fiz. Nauk **162** (2), 63 (1992) [Sov. Phys. Usp. **35**, 85 (1992)].
18. J. Mycielski, Solid State Commun. **60** (2), 165 (1986).
19. V. L. Bonch-Bruevich and S. G. Kalashnikov, *Physics of Semiconductors* (Nauka, Moscow, 1990).
20. A. V. Efanov and M. V. Éntin, Fiz. Tekh. Poluprovodn. (Leningrad) **20** (10), 1932 (1986) [Sov. Phys. Semicond. **20**, 1213 (1986)].
21. J. Wermer, *Potential Theory* (Springer, Berlin, 1974; Mir, Moscow, 1980).
22. N. A. Poklonski and A. I. Syaglo, Fiz. Tverd. Tela (St. Petersburg) **40** (1), 147 (1998) [Phys. Solid State **40**, 132 (1998)].
23. D. ter Haar, in *Problems in Thermodynamics and Statistical Physics*, Ed. by P. T. Landsberg (Macmillan, London, 1971; Mir, Moscow, 1974).

---

[2] Before recombination, the hole in the degenerate electron gas of the conduction band has an opportunity to form a screening cloud around itself and transform into an electrically neutral quasiparticle, a so-called plasma exciton [9].

24. N. A. Poklonski, A. I. Syaglo, and G. Biskupski, Fiz. Tekh. Poluprovodn. (St. Petersburg) **33** (4), 415 (1999) [Semiconductors **33**, 402 (1999)].
25. H. P. D. Lanyon and R. A. Tuft, IEEE Trans. Electron Devices **ED-26** (7), 1014 (1979).
26. P. T. Landsberg, A. Neugroschel, F. A. Lindholm, and C. T. Sah, Phys. Status Solidi B **130** (1), 255 (1985).
27. D. N. Bychkovskiĭ, O. V. Konstantinov, and B. V. Tsarenkov, Fiz. Tekh. Poluprovodn. (St. Petersburg) **29** (1), 152 (1995) [Semiconductors **29**, 80 (1995)].
28. G. B. Arfken, *Mathematical Methods for Physicists* (Academic, New York, 1966; Atomizdat, Moscow, 1970).
29. T. D. Lee, *Mathematical Methods of Physics* (Mir, Moscow, 1965).
30. O. V. Konstantinov, O. I. Obolenskiĭ, and B. V. Tsarenkov, Fiz. Tekh. Poluprovodn. (St. Petersburg) **31** (5), 571 (1997) [Semiconductors **31**, 484 (1997)].
31. F. Seitz, *Modern Theory of Solids* (McGraw-Hill, New York, 1940; Gostekhizdat, Moscow, 1949).
32. J. C. Slater, *Insulators, Semiconductors, and Metals* (McGraw-Hill, New York, 1967; Mir, Moscow, 1969).

Translated by A. Poushnov

Physics of the Solid State, Vol. 44, No. 7, 2002, pp. 1241–1248. Translated from Fizika Tverdogo Tela, Vol. 44, No. 7, 2002, pp. 1190–1197.
Original Russian Text Copyright © 2002 by Parfen'ev, Farbshteĭn, Shul'pina, Yakimov, Shalimov, Turchaninov.

SEMICONDUCTORS AND DIELECTRICS

Defect Formation in Tellurium in Various Gravity Conditions

R. V. Parfen'ev*, I. I. Farbshteĭn*, I. L. Shul'pina*, S. V. Yakimov*,
V. P. Shalimov, and A. M. Turchaninov*****

** Ioffe Physicotechnical Institute, Russian Academy of Sciences, Politekhnicheskaya ul. 26, St. Petersburg, 194021 Russia*
e-mail: r.parfeniev@mail.ioffe.ru
*** Baĭkov Institute of Metallurgy and Materials Sciences, Russian Academy of Sciences,*
Leninskiĭ pr. 49, Moscow, 117911 Russia
**** Kompozit R & D Company, Korolev, Moscow oblast, Russia*

Received July 30, 2001

Abstract—The effect of gravity (from micro- to a rather high gravity, $5g_0$) acting during tellurium crystallization on the concentration of neutral (N_D) and electrically active (N_{AD}) acceptor-type structural defects in samples grown both under complete remelting of the starting ingot and under directed seed recrystallization of an ingot was studied. The concentrations N_{AD} and N_D and their distribution over the sample length were derived from the electrical characteristics (conductivity and the Hall effect) measured along the ingots in the temperature range 1.6–300 K. The contributions of various mechanisms to hole scattering were found from an analysis of the temperature behavior of the mobility. The results obtained were compared with the characteristics of samples grown following a similar program under normal conditions. The presence of N_{AD} defects is characteristic of the initial crystallization stage of all samples. N_{AD} is substantially lower ($N_{AD} \sim 10^{15}$ cm^{-3}) than $N_D \sim 10^{18}$ cm^{-3} and decreases exponentially in the course of sample crystallization. Complete remelting under microgravity revealed indications of strong supercooling and spontaneous crystallization, as well as spatial oscillations of the electrical resistivity over the sample length caused by N_D modulation. These observations are related to the specific features of the melting and crystallization in zero gravity, namely, the melt breaking away from the wall of the ampoule and the increasing role of Marangoni convection. *© 2002 MAIK "Nauka/Interperiodica".*

1. INTRODUCTION

This study is a part of the program dealing with investigation of the effect of gravity on the solidification and electrical properties of anisotropic semiconductors, namely, of tellurium and its alloys with selenium and silicon [1]. Te and Se stand out among the widely known elemental semiconductors (Si, Ge, Te, Se) because of the clearly pronounced anisotropy in their structural and physical properties; this is due to the complex structure of their crystal lattice (space group $D_3^{4(6)}$), which consists of helical trigonal chains stacked in a hexagon, with the in-chain coupling being substantially stronger than the interchain coupling [2, 3].

The low-temperature concentration and mobility of holes in pure Te are extremely sensitive to the presence of structural and point defects, mechanical stresses, and dislocations. At the same time, the electrophysical properties of Te are known well enough [2, 3] for Te to serve as a model material in studying new phenomena. These circumstances, as well as the low melting temperature (T_m = 452°C), make Te and Te-based alloys convenient subjects for experimental investigation of the specific features accompanying crystallization in various gravities.

Our preceding publications reported on investigations of the electrophysical properties of Te samples obtained both in a rather high gravity (up to $10g_0$) [1, 4] and in microgravity (μg) [5, 6]. Our interest was focused there primarily on studying the effect of the gravity level on the dopant redistribution in the course of directed crystallization and on the possibility of obtaining more uniform samples with the lowest possible hole concentration. Sample 1 in [5], called here SC-μg, had the highest mobility and, hence, the lowest defect concentration. This sample is a Czochralski-grown single crystal that underwent partial recrystallization in space conditions.

We show here that by measuring the galvanomagnetic properties of pure Te over a broad temperature range, 1.6–300 K, one can determine the concentration profile along the length of the ingot not only for the electrically active impurities but also for the intrinsic charged defects N_{AD}, as well as estimate the concentration N_D and distribution over the ingot length of neutral defects which govern the carrier mobility. This method of mobility analysis, used to compare the content and distribution of N_D in polycrystalline Te samples prepared in various gravity levels and initial crystallization conditions, revealed specific features originating from detached solidification, an effect characteristic of melting under zero-gravity conditions.

2. EXPERIMENT

This communication presents the results of a comparative study of Te samples prepared in various gravities by directed crystallization in a sealed volume and a moving temperature gradient, more specifically, in weightlessness (μg) in a tubular ChSK-1 Cristallizator furnace on the MIR spacecraft and at a rather high gravity on a CF-18 centrifuge ($5g_0$) in a Meudon furnace, as well as in normal conditions ($1g_0$) in the same furnaces following a technique described elsewhere [1, 4, 5]. Samples of two series were studied, namely, seed-remelted (series S) and remelted without seed (series W). The seeds were cleaved from a pure Te single crystal ($p_{77\,\mathrm{K}} = 10^{14}$ cm^{-3}) along the threefold symmetry axis C_3, which was the preferential growth direction of the Te crystal. In all cases, the seed was preliminarily attached by melting to a polycrystalline Te ingot with a hole concentration $p_{77\,\mathrm{K}} \sim 10^{14}$ cm^{-3}. Samples S-$1g_0$, S-$5g_0$, and W-$5g_0$ were remelted in a Meudon furnace; S-μg, W-μg, and W-$1g_0$, in a Crystallizator furnace.

The ingots grown in microgravity could be easily taken out of the ampoules because of their only slightly touching the walls, unlike those prepared at an elevated gravity and in Earth conditions. Photographs of the samples are presented in Fig. 1 (top). To facilitate visualization of the crystal structure, the ingots were treated with a selective etchant (30 vol % HNO$_3$).

The series-S samples had a mosaic structure. The blocks in the samples were oriented predominantly along the growth axis C_3, except sample S-$5g_0$, which is seen to have variously oriented blocks, including some directed perpendicular to the growth axis. While samples of series W also consisted of blocks, they were much smaller in size and randomly oriented.

The real structure of the S-μg and W-μg samples was studied by x-ray back-reflection topography on a single- and double-crystal setup [5].

X-ray topographic investigation of the S-μg sample showed its surface to have a fine-grained mosaic structure. The grains on the sample surface coincide in crystallographic orientation, on the average, with the seed; the grain size is 5–10 μm. Some of the grains are strongly stressed.

X-ray topographic analysis of the cross sections of the W-μg sample showed the blocks in two parts of the sample to differ considerably in size. At the start of the sample, the distribution of the blocks measuring 0.6–1.0 mm is not centrosymmetric relative to the longitudinal axis of the sample. The large blocks have a fragmentary structure and are strongly stressed. The end of the ingot exhibits a uniform fine-grained structure. The grains vary in size from 5 to 50 μm and are randomly

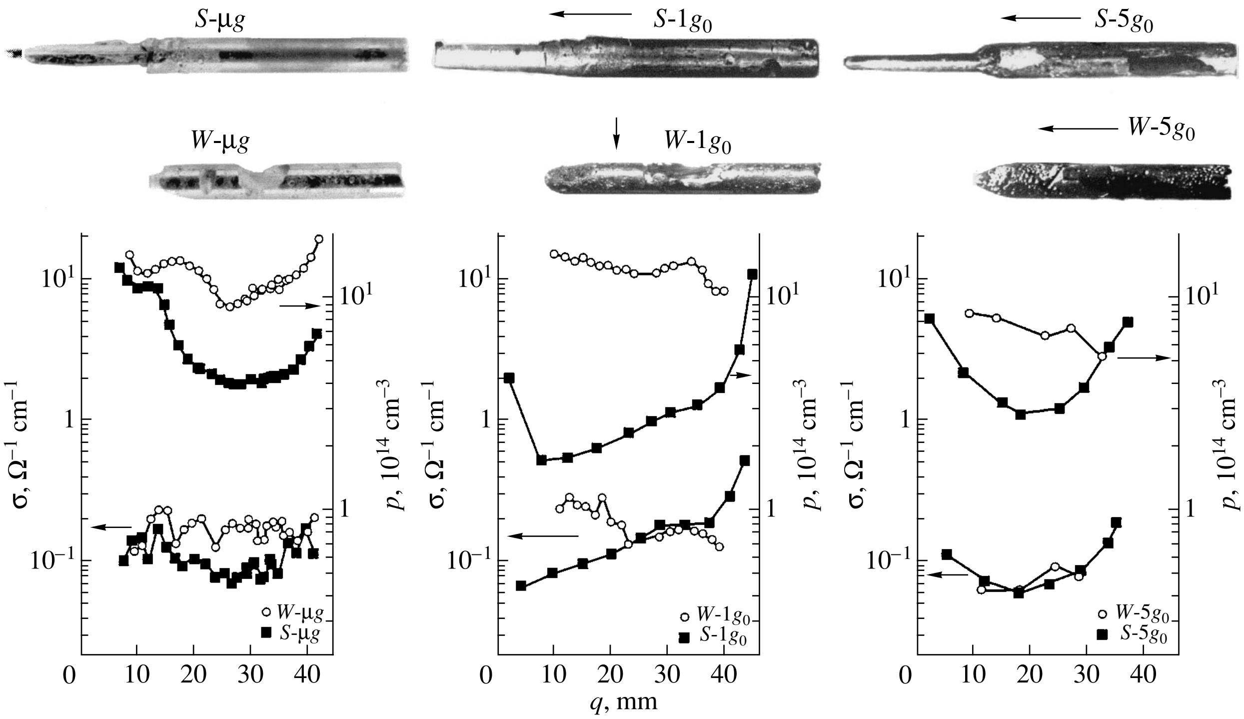

Fig. 1. Photographs of the samples grown in a sealed volume at various gravity levels with a seed (S) and without it (W), and the profiles of their electrical conductivity and hole concentration at 77 K. The arrows indicate the direction of gravity in the course of directed ingot solidification; μg, $1g_0$, and $5g_0$ relate to the gravity levels. The remelted sample size is identified by the length q on the horizontal axis.

oriented. This suggests that before solidification the melt was actually supercooled and that the second half of the ingot apparently solidified through homogeneous spontaneous crystallization.

3. ELECTRICAL PROPERTIES

The electrical conductivity and the Hall effect in a magnetic field of 0.5 T were measured at a number of points along all samples. Possible surface defects and contamination were removed by treating the samples with a polishing etchant, and their electrical characteristics were subsequently remeasured. The electrical properties of the samples were found to remain virtually unaffected [5].

The measurements at 77–200 K were made by means of spring contacts spaced at about 1.5 mm. For measurements at lower temperatures, two pairs of Bi–Sb potential contacts spaced at ~5 mm were soldered in the middle of each of two equal parts of the sample on both sides of the sample. The part lying closer to the beginning of crystallization was called part I; the other, part II. Figure 1 shows the profiles of the electrical conductivity $\sigma_{77\,\mathrm{K}}$ obtained in the polycrystalline ingots. As the gravity increases, the samples are seen to become more homogeneous. Also shown are the profiles of the hole concentration p derived from the Hall coefficient $R_{77\,\mathrm{K}} = 1.18/ecp$. In all the samples, the sign of the Hall coefficient at 77 K corresponded to p-type conduction.

The profiles of the Hall mobility $u_H = R\sigma$ of the samples measured at 77 K are displayed in Fig. 2. The Hall mobility $R\sigma$ was found to be the highest and nearly constant in the main part of the S-1g_0 sample. In the S-μg and S-5g_0 samples, $R\sigma$ is smaller in magnitude, but it increases monotonically away from the starting point of crystallization and is accompanied by a simultaneous increase in the hole concentration p (Fig. 1). In series-W samples, the hole concentration remains, on the average, virtually unchanged along the length of the ingot, whereas $R\sigma$ varies nonmonotonically.

Figure 3 illustrates the measurements made on parts I and II of the samples. The sharp rise in $\sigma(T)$ and the drop in $R(T)$ at temperatures above 200 K signal the transition to intrinsic conduction and are characteristic of Te with an acceptor impurity concentration below 10^{15} cm^{-3}. In this region, $\sigma(T)$ approaches an exponential relation,

$$\sigma(T) = Ae^{-\frac{\Delta E}{2kT}}, \qquad (1)$$

where $\Delta E = 0.334$ eV, which conforms to the available data on the band gap in Te [2, 3].

The carrier mobility in polycrystalline samples with a block structure in the region of extrinsic conduction is only weakly temperature-dependent. This implies that carrier scattering from neutral structural defects dominates in polycrystalline samples. The higher hole mobility in parts II compared with that in parts I of the samples indicates that the crystal structure improves and the hole scattering intensity from defects reduces in the direction of solidification, a point already made in the analysis of Fig. 1. Such variations in structural per-

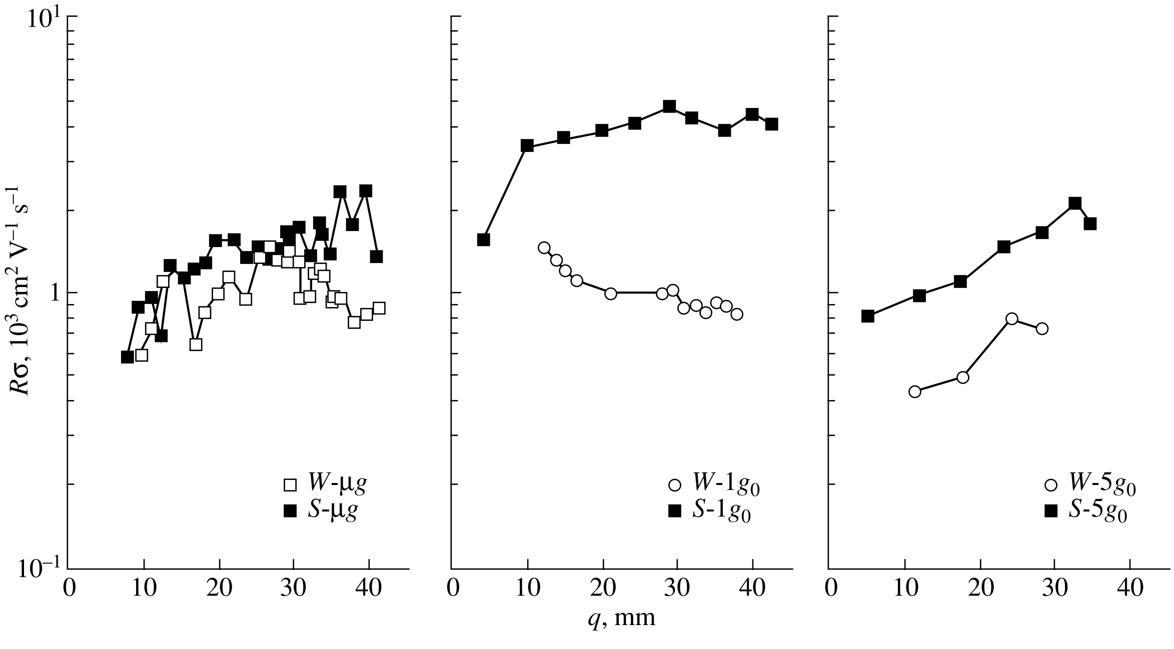

Fig. 2. Variation of the hole mobility $R\sigma$ at 77 K along the sample as shown in Fig. 1; q is the distance from the starting point of crystallization.

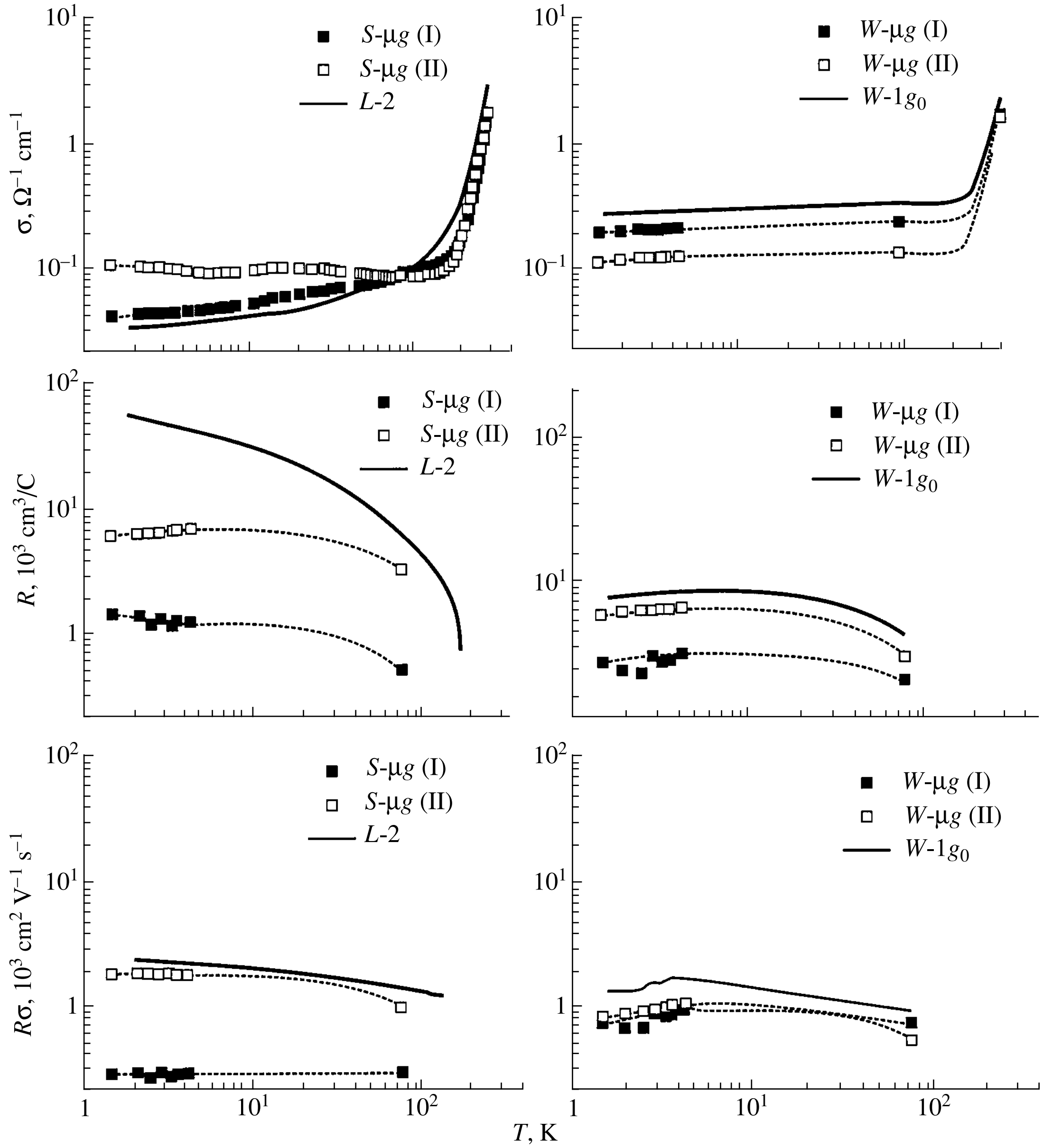

Fig. 3. Temperature dependences of the electrical conductivity σ, Hall coefficient R, and mobility Rσ of the space-grown samples shown in comparison with the parameters of the samples that were crystallized on the Earth on identical equipment and in the same technological regime. S are seed-grown samples, and W are samples grown without seed. Sample L-2 was cleaved from the ingot obtained by zone melting [7].

fection have been observed to occur in experiments on directed solidification of PbTe⟨Ag⟩ performed on a centrifuge in various gravity conditions [8].

The improvement of structure along the length of the samples is also supported by the temperature dependences of conductivity obtained on different parts of the samples (Figs. 2, 3). Figure 4 compares the σ(T) dependence of our samples with data from a study [7] on the effect of stepped anneal on the electrical characteristics of Te crystal samples cleaved from ingots grown by zone melting.

Comparison of the results suggests that the difference between parts I and II of the S-μg sample is due to the different anneal times.

4. ANALYSIS AND DISCUSSION

As already discussed in [5], the concentration profiles shown in Fig. 1 for series-S samples can be described by a relation that takes into account both impurity segregation under directed crystallization occurring at a finite rate under conditions of complete melt mixing and exponential decay of the native, electrically active acceptor-type structural defects (of concentration N_{AD}) in the initial solidification stage:

$$p(q) = k_{\mathrm{eff}} C_0 (1 - q/l)^{k_{\mathrm{eff}} - 1} + N_{AD}^0 \exp(-q/q_0), \quad (2)$$

where k_{eff} is the effective distribution coefficient (assumed to be a constant), C_0 is the initial impurity concentration in the melt, l is the total ingot length, q/l is the reduced distance along the ingot, N_{AD}^0 is the initial defect concentration, and q_0 is the characteristic N_{AD} decay length.

Figure 5 compares the experimental hole concentration distribution at 77 K (Fig. 2) with the curves calculated using Eq. (2). Table 1 lists the parameters of the calculated relations.

Considered within this model, the hole concentration profile $p(q)$ depends on the relative magnitude of the acceptor impurity and lattice defect concentrations, N_i and N_{AD}, respectively, varying along the ingot length. For $N_{AD} > N_i$, the observed hole concentration profile does not permit sufficiently accurate determination of the parameters of Eq. (2). In this case, the minimum in the $p(q/l)$ dependence shifts along the ingot away from the starting point of solidification. This situation was observed in polycrystalline samples of the W series.

The data of Table 1 show that gravity does affect the crystallization process. The segregation coefficient k_{eff} decreases with increasing gravity. This is paralleled by an increase in the parameter q_0 characterizing the distance in which the concentration of electrically active defects that formed in the initial crystallization stage decreases.

The fit of the experimental data to Eq. (2) means that in all the experiments of series S the melt underwent fairly intense mixing. In weightlessness, where there is practically no gravitational convection, the mixing is driven by a weaker, thermocapillary mechanism (Marangoni convection) and k_{eff} increases. The structure of the Marangoni flow under directed crystallization in an ampoule was treated in [9]. In contrast to the conventional hydrodynamic flow, the velocity in the surface layer in this case is the highest. Therefore, convection under microgravity conditions turns out to be very sensitive to the character of contact between the melt and the ampoule walls.

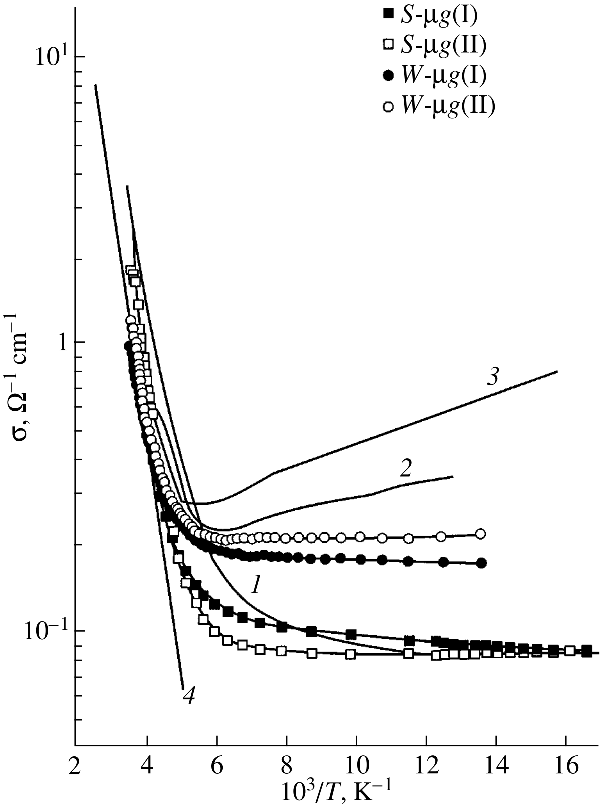

Fig. 4. Temperature dependence of the electrical conductivity of the samples grown in weightlessness (S-μg, W-μg) and of sample L-1 prepared on the Earth (*1*) before annealing and (*2*, *3*) after two-stage annealing of 5 h each, respectively, performed at 370°C; (*4*) is the calculation using Eq. (1).

The S-1g_0 and S-5g_0 samples crystallized in the downward-heating regime. In these conditions, there is no gravitational mixing in a standard melt. However, the density of the Te melt reaches a minimum near the solidification point [10]. This anomaly can be explained by the fact that as the melt temperature decreases to approach T_m, tellurium atoms join in chains to form a molecular-type liquid; this is what reduces the density while simultaneously leading to an anomalous increase in the viscosity of the melt. This initiates convection flows of gravitational origin near

Table 1. The parameters entering Eq. (2) for the ingots under study

Gravity level	C_0, 10^{14} cm^{-3}		k_{eff}		N_{AD}^0, 10^{15} cm^{-3}		q_0/l	
	S	W	S	W	S	W	S	W
μg	4	~11	0.8	~0.55	6	~8.0	0.09	~0.09
1g_0	3.55	~8.5	0.42	~0.95	0.6	~1.2	0.05	~25
5g_0	5.48	~3	0.27	~0.99	0.85	~0.85	0.17	~25

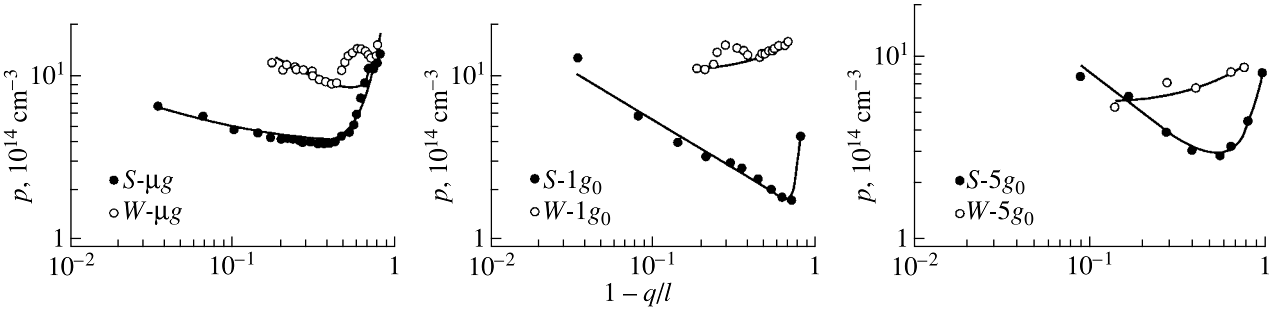

Fig. 5. Hole concentration vs. fraction of solidified melt, *q*/*l*, in Te polycrystals grown with a seed (*S*) and without it (*W*) at various gravity levels. The points relate to experimental data, and the solid lines are plots of Eq. (2) with the parameters given in Table 1.

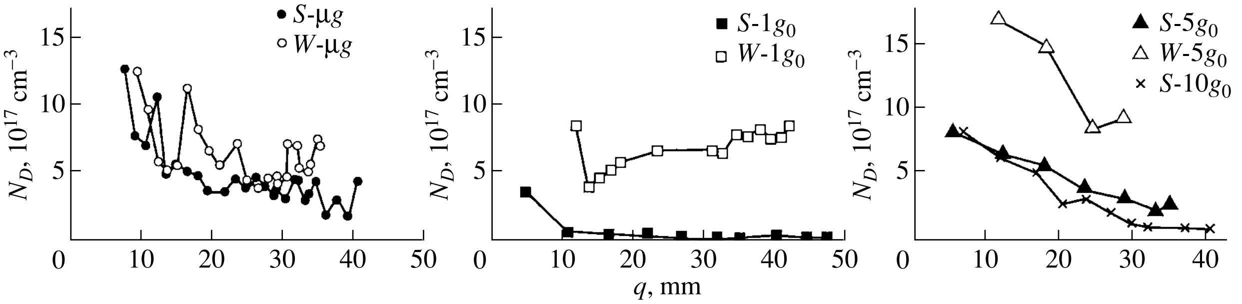

Fig. 6. Comparison of defect concentrations N_D for samples grown with a seed (*S*) and without it (*W*) at various gravity levels. The values of N_D for the *S*-5g_0 and *S*-10g_0 samples were calculated using the data published in [1].

the crystallization front. This situation was discussed in [4]. As a sample is centrifuged with the ampoule axis aligned with the vector of acceleration, another factor that substantially amplifies convective mixing comes into play, namely, the Coriolis force directed perpendicular to the ampoule axis [11]. As a result, $k_{\rm eff}$ becomes considerably reduced (Table 1).

A quantitative analysis of the temperature dependences of the hole mobility displayed in Fig. 3 permits one to estimate the contribution of neutral defects to hole scattering. The temperature dependence of the reciprocal Ohmic hole mobility $1/u_0 = f(1/T)$ of samples obtained in weightlessness was described in [12] as resulting from three factors: (i) scattering from phonons ($1/u_L \sim T^{3/2}$) dominating above 30 K; (ii) scattering from charged centers ($1/u_i \sim T^{-3/2}/N_i$), which is dominant at low temperatures; and (iii) temperature-independent scattering, which imposes a constraint on the maximum hole mobility. An experimental study of the effect of annealing on the temperature behavior of $1/u_0$ performed at $1g_0$ revealed that this temperature-independent scattering occurs from neutral defects, where the quantity $1/u_D$ is proportional to the neutral-defect concentration N_D [13, 14]. The character of the $1/u_0(T)$ dependence observed in the *S* and *W* series samples conforms to this interpretation.

The resulting reciprocal mobility can be described in the first approximation by the relation (the Matthiessen rule) [13]

$$\frac{1}{u_0} = \frac{1}{u_L} + \frac{1}{u_i} + \frac{1}{u_D} = AT^{3/2} + BN_iT^{-3/2} + CN_D. \quad (3)$$

The $1/u_0(T)$ relation found for the *SC*-μ*g* sample in [12] was used to determine the quantities *A* and *B*, which were subsequently employed to determine $1/u_D$ and, hence, N_D in more defected samples. The experimental temperature dependences of $1/u_0$ obtained for samples grown in microgravity were compared in [12] with calculations made using Eq. (3). The parameters used and the calculated concentrations N_D for parts II of samples *SC*-μ*g*, *S*-μ*g*, and *W*-μ*g* are given in Table 2. The concentration N_i for each sample was assumed to be temperature-independent and equal to the hole Hall concentration at 77 K; thus, only one parameter (CN_D) was varied.

Using the relation given in [14], one can calculate the N_D distribution for all samples from the experimental data presented in Fig. 2. The results are displayed in

Table 2. The parameters in Eq. (3) for the hole mobility in samples obtained in microgravity

Sample	A, 10^{-7} $\frac{\mathrm{V\,s}}{\mathrm{cm^2\,K^{3/2}}}$	B, 10^{-19} V s cm $\mathrm{K}^{3/2}$	N_i, 10^{14} cm^{-3}	CN_D, $\frac{\mathrm{V\,s}}{\mathrm{cm}^2}$	N_D, cm^{-3}
SC-μg (II)	3	4.9	4.1	9.3×10^{-6}	7.7×10^{15}
S-μg (II)	3	4.9	5.6	7.6×10^{-4}	6.3×10^{17}
W-μg (II)	3	4.9	18	1.0×10^{-3}	8.3×10^{17}

Fig. 6. N_D is seen to decrease with moving away from the starting point of crystallization. Comparative calculations of N_D yield the following values: 4×10^{14} cm^{-3} for the Czochralski-grown single crystal (after annealing at 320°C for 120 h), 6×10^{17} cm^{-3} for the sample cleaved from the zone-melted ingot (L-1), 1×10^{17} cm^{-3} after the first 5-h annealing stage at 370°C, and 4×10^{16} cm^{-3} after the second 5-h long annealing.

However, the W-μg sample reveals a nonmonotonic decrease in N_D along the ingot, which can be associated with a transition to crystallization from a supercooled state under conditions favoring detached solidification. This is also supported by the x-ray topography data on micrograin size presented above. According to the model from [15], detached solidification occurs in the region of the meniscus adjacent to the crystallization front. In this region, detached solidification changes the Marangoni convection conditions and the impurity segregation and grain orientation become different from those in the regions where the melt contacts the ampoule walls. At points of contact, the C_3 axis of the micrograins is directed predominantly perpendicular to the inner ampoule walls (as in the case of tellurium whiskers growing from the vapor phase). Thus, the spatial variation of the resistivity along such an ingot can be assigned to the increase in the role of the grain boundaries perpendicular to the current in the region of contact with the ampoule and to the anisotropy of Te conductivity ($\sigma_{33} \cong 2\sigma_{\perp}$ [2, 3]). This is corroborated by a correlation between the profile of N_D calculated for 77 K and the profile of ρ(300 K), in which carrier scattering from phonons dominates over that from point defects (Fig. 7). Such features were not observed in ingots grown at $g \geq 1g_0$, where the melt is always in contact with the ampoule walls in the region of the crystallization front.

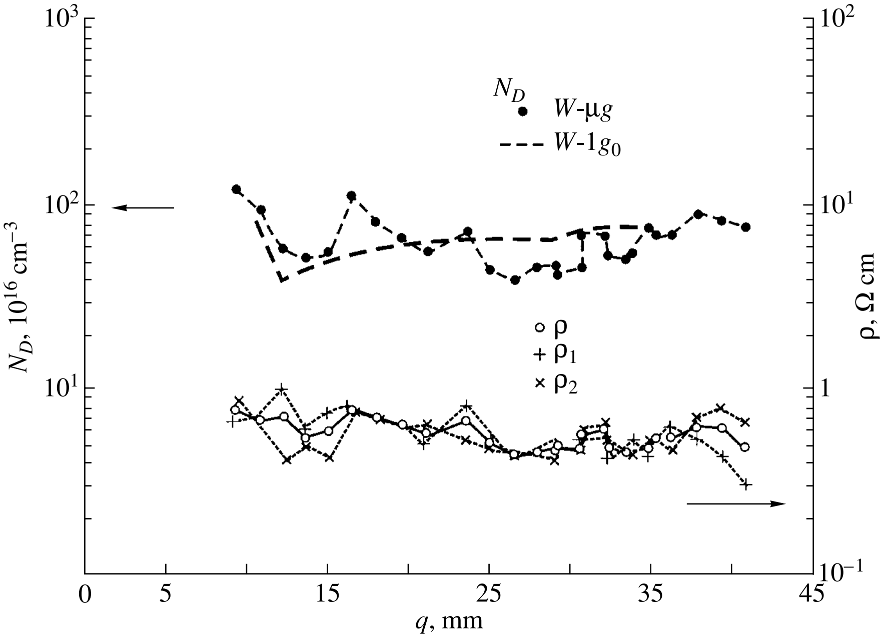

Fig. 7. Modulation of defect concentration N_D along the W-μg and W-$1g_0$ samples derived from the hole mobility at 77 K, and the profile of 300-K electrical resistivity ρ of the W-μg sample obtained by averaging the measurements made on opposite sides of the sample, ρ_1 and ρ_2.

Thus, microgravity offers a possibility of obtaining microcrystalline structures consisting of anisotropic grains.

5. CONCLUSIONS

The results of our investigation of tellurium samples obtained by directed crystallization in microgravity on the MIR spacecraft, as well as in normal conditions at $1g_0$ and on a TsF-18 centrifuge at $5g_0$, can be summed up as follows.

(1) The extremely high sensitivity of the Te electrical properties at low temperatures to the presence of neutral and electrically active native defects and impurities makes it possible to map the impurity and defect profiles along an ingot at a level of 10^{-5} at. %, a figure that cannot be reached by other methods.

(2) The hole concentration in the initial part of all Te ingots studied decreases, which contrasts with the case of normal crystallization and is associated with the decrease in the concentration of native, electrically active defects N_{AD} as the ingot undergoes crystallization. We succeeded in quantitatively fitting the acceptor distribution profile observed in all samples with one relation that takes into account the initial exponential decay of the native defect concentration and the redistribution of the acceptor impurity in the course of directed crystallization in the case of partial mixing with an effective segregation coefficient k_{eff}.

(3) The low-temperature hole mobility in polycrystalline samples obtained in microgravity was found to be an order of magnitude smaller than that in a single crystal partially remelted in space with no contact with the ampoule walls. This indicates that neutral defects play a major role in hole scattering in polycrystalline samples. The defect concentration in polycrystals was estimated as $N_D \approx 10^{18}$ cm^{-3}. We succeeded in quantitatively describing the data on the temperature dependence of mobility for all samples by taking into account the temperature-dependent hole scattering from ions and acoustic phonons, as well as the temperature-independent scattering from neutral impurities.

(4) Complete remelting of Te without a seed in microgravity is accompanied by supercooling of the melt and spontaneous nucleation, which brings about the formation of a homogeneous microcrystalline structure with differently oriented grains (~5 μm) at the end of the ingot.

Point contacts of the melt with the ampoule walls (detached solidification) affect the orientation of the crystallites forming at these points and, hence, result in modulation of the resistivity and carrier mobility along the ingot because of the Te electrical resistivity being different in different crystallographic directions.

REFERENCES

1. L. L. Regel', I. V. Vidensky, A. V. Mikhailov, *et al.*, in *Proceedings of the International Astronautical Congress, Innsbruck, Austria* (Pergamon, New York, 1986).
2. P. Grosse, *Die Festkörpereigenschaften von Tellur* (Springer, Berlin, 1969), Springer Tracts in Modern Physics, p. 48.
3. *Landolt-Börnstein: Numerical Data and Functional Relationships in Science and Technology, New Series* (Springer, Berlin, 1983), Group III, Vol. 17.
4. L. L. Regel', A. M. Turchaninov, R. V. Parfeniev, *et al.*, J. Phys. III **2** (3), 373 (1992).
5. R. V. Parfen'ev, I. I. Farbshteĭn, I. L. Shul'pina, *et al.*, Fiz. Tverd. Tela (St. Petersburg) **42** (2), 238 (2000) [Phys. Solid State **42**, 244 (2000)].
6. R. V. Parfeniev, I. I. Farbstein, S. V. Yakimov, *et al.*, in *Proceedings of Joint 10th European and 5th Russian Symposium on Physical Sciences in Microgravity, St. Petersburg, Russia, 1997*, Vol. 2, p. 56.
7. I. I. Farbshteĭn, Author's Abstracts of Candidate's Dissertation (Inst. Poluprovodnikov Akad. Nauk SSSR, Leningrad, 1965).
8. H. Rodot, L. L. Regel', and A. M. Turchaninov, J. Cryst. Growth **104**, 280 (1990).
9. V. S. Avduevskiĭ, S. D. Grishin, and L. V. Leskov, *Scientific Reading on Aviation and Cosmonautics, Year 1980* (Nauka, Moscow, 1981), pp. 15–24.
10. A. R. Regel' and V. M. Glazov, *Physical Properties of Electronic Melts* (Nauka, Moscow, 1980).
11. W. A. Arnold, PhD Thesis (Clarkson University, Potsdam, 1994).
12. R. V. Parfeniev, I. I. Farbshtein, S. V. Yakimov, *et al.*, Acta Astronaut. **48** (2–3), 87 (2001).
13. I. I. Farbshteĭn, A. M. Pogarskiĭ, and S. S. Shalyt, Fiz. Tverd. Tela (Leningrad) **7** (8), 2383 (1965) [Sov. Phys. Solid State **7**, 1925 (1965)].
14. C. Erginsoy, Phys. Rev. **79**, 1013 (1950).
15. L. L. Regel' and W. R. Wilcox, Microgravity Sci. Technol. **14**, 152 (1999).

Translated by G. Skrebtsov

Physics of the Solid State, Vol. 44, No. 7, 2002, pp. 1249–1253. Translated from Fizika Tverdogo Tela, Vol. 44, No. 7, 2002, pp. 1198–1202.
Original Russian Text Copyright © 2002 by Olikh, Ostrovskiĭ.

SEMICONDUCTORS AND DIELECTRICS

Ultrasound-Stimulated Increase in the Electron Diffusion Length in *p*-Si Crystals

O. Ya. Olikh and I. V. Ostrovskiĭ
Shevchenko National University, Vladimirskaya ul. 64, Kiev, 03127 Ukraine
e-mail: olikh@mail.univ.kiev.ua

Received May 30, 2001; in final form, October 18, 2001

Abstract—The effect of ultrasound on the diffusion length of minority charge carriers in dislocation-free *p*-Si is investigated in the frequency range 0.8–5.5 MHz. The diffusion length is measured by the surface photovoltage method. It is found that the diffusion length reversibly increases (by a factor of two at a sound intensity of 3 W/cm^2) in response to ultrasound. The dependences of the diffusion length on the ultrasound amplitude and the kinetic characteristics upon switching on and switching off the ultrasound are analyzed. The phenomena observed are explained within the proposed model of transformation of recombination centers under the effect of ultrasound. *© 2002 MAIK "Nauka/Interperiodica".*

1. INTRODUCTION

It is known that intense ultrasonic waves propagating in solids substantially affect the state of structural defects [1–6]. For example, the ultrasound effect brings about the formation of a surface layer in silicon [1] and the dissociation of complex aggregates consisting of several point defects [2], enhances gettering of point defects by dislocations and precipitates [3], and decreases the energy barrier to defect diffusion [4–6]. Considerable progress toward physical understanding of the ultrasound effect has been achieved by elucidating the dislocation mechanism of the acoustodefect interaction [4, 6, 7]. However, dislocation-free solids remain poorly investigated.

In the present work, we analyzed how the ultrasound affects silicon single crystals prepared from *Cz*–*p*-Si (solar-cell grade). The results obtained are essential to the understanding of the mechanism of the physical processes associated with the interaction of ultrasonic waves and a subsystem of point defects in dislocation-free semiconductor crystals.

2. SAMPLES AND EXPERIMENTAL TECHNIQUE

The effect of ultrasound on the diffusion length L of minority charge carriers in *Cz*–*p*-Si was investigated using boron-doped *p*-Si(100) wafers 340 μm thick (ρ = 0.5–2 Ω cm) with an oxygen concentration $N_\mathrm{O} \leq 10^{18}$ cm^{-3} and a carbon concentration $N_\mathrm{C} \leq 10^{17}$ cm^{-3}. According to x-ray diffraction analysis, the dislocation density was less than 10 cm^{-2}; i.e., the samples were virtually free of dislocations.

The diffusion length was measured by the surface photovoltage method [8, 9]. This method is based on analyzing the dependence of the surface photovoltage V_{sp} on the monochromatic light wavelength. The advantage of the surface photovoltage method is its applicability under the conditions of variations in the carrier concentration in the sample [10]. Figure 1 depicts a schematic drawing of the experimental cell. The surface photovoltage V_{sp} was measured by the capacitor method with the use of an electrode applied on the sample surface opposite to the illuminated surface. The experiments were performed at room temperature.

In semiconductor wafers, ultrasonic vibrations were excited by ceramic (TsTS-19) piezoelectric transducers cemented to the sample. An ac voltage with a frequency f = 0.8–5.5 MHz and an amplitude V_{us} up to 40 V was applied to one of the piezoelectric transducers to generate acoustic vibrations in the silicon sample. The generation of acoustic vibrations was controlled by another

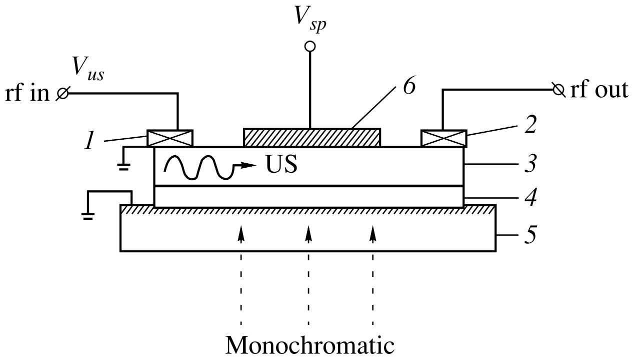

Fig. 1. A schematic drawing of the experimental cell for measuring the diffusion length of minority charge carriers in a semiconductor wafer in an ultrasound field: (*1*, *2*) piezoelectric transducers, (*3*) silicon sample, (*4*) mica, (*5*) glass with an applied transparent electrode, and (*6*) metal electrode for recording the photovoltage.

1063-7834/02/4407-1249$22.00 © 2002 MAIK "Nauka/Interperiodica"

piezoelectric transducer mounted at the opposite end of the silicon sample. The ultrasonic waves induced in the sample were identified as Lamb waves (the a_0 and s_0 modes) on the basis of the measured wave velocities.

The intensity W_{us} of ultrasound generated in the sample was approximately equal to 0.5 W/cm^2 at V_{us} = 10 V and f = 0.8 MHz.

3. EXPERIMENTAL RESULTS AND DISCUSSION

The diffusion length of minority charge carriers (electrons) was measured in the absence of ultrasound and after its generation. In the absence of ultrasound, the initial diffusion length L_0 in the p-Si samples under investigation is equal to 15–25 µm. The ultrasound effect leads to an increase in the diffusion length L by 100% at maximum sound intensities. It should be noted that all ultrasound-stimulated changes are reversible; i.e., after switching off the ultrasound, the parameters of the material regain their original values for some time.

The characteristic dependences of the relative change in the diffusion length L on the time of ultrasonic treatment are displayed in Fig. 2. The observed behavior of the time dependence of the diffusion length L—an increase after the ultrasound is switched on (portion *ab*) and a decrease after it is switched off (portion *bc*)—is typical of all the frequencies and amplitudes of the ultrasound used. The maximum diffusion length L_{us} is reached for an ultrasonic treatment time of 5×10^3 s and depends on the ultrasound intensity. Figure 3 shows typical dependences of the diffusion length L_{us} on the ultrasound intensity W_{us}. It can be seen that the sound-stimulated increase in the diffusion length L is characterized by a threshold at $W_{us} \approx 0.5$ W/cm^2 and saturation at higher ultrasound intensities (>2 W/cm^2). Moreover, there is a pronounced hysteresis. It is seen that the dependence $L_{us}(W_{us})$ follows the curve *ABCD* in the course of the initial ultrasonic treatment and the curve *AFED* in subsequent cycling. The initial dependence (*ABCD*) can be regained if the samples are allowed to stand for two or three weeks at room temperature.

During ultrasonic treatment, the temperature of the silicon wafer was monitored using a copper–constantan thermocouple. It was found that, at a maximum ultrasound intensity, the sample temperature increased by 15–18 K. After check heating of the silicon sample by 18 K in the absence of ultrasound, the diffusion length L increased by less than 10%. Note that the measured temperature dependence of the diffusion length L agrees with the data obtained in [11] to within the experimental error in the measurement of the length L (5–7%).

As is known, the charge carrier recombination in silicon at moderate degrees of doping (<10^{18} cm^{-3}) and at room temperature predominantly proceeds through deep levels [12, 13]. Under the assumption that the above mechanism of charge carrier recombination remains dominant in a crystal subjected to ultrasonic treatment, we can write the following relationship in the framework of the Shockley–Read–Hall model:

$$L^{-2} = D^{-1}\nu_T \sum_k S_k N_k, \qquad (1)$$

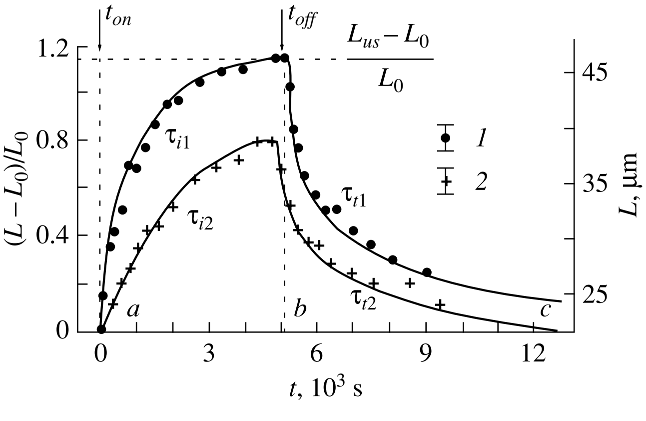

Fig. 2. Time dependences of the diffusion length: increase (portion *ab*) after switching on the ultrasound ($t = t_{on}$) and decrease (portion *bc*) after switching off the ultrasound ($t = t_{off}$). f = 0.78 MHz. V_{us} = (*1*) 35 and (*2*) 25 V. The diffusion length L_0 in the absence of ultrasound is equal to 22 µm. $\tau_{i1} < \tau_{i2}$ and $\tau_{t1} = \tau_{t2}$.

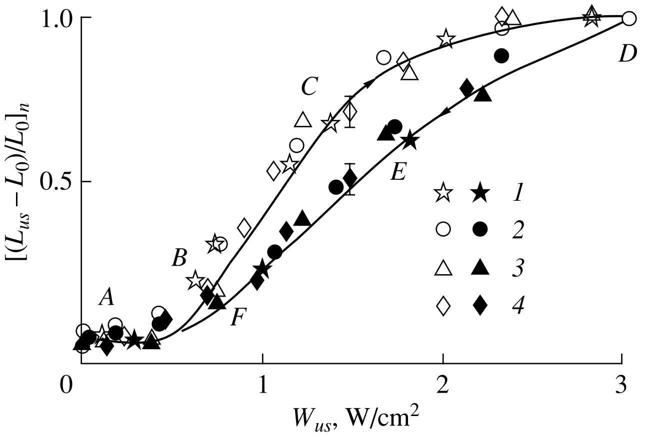

Fig. 3. Dependence of the diffusion length on the ultrasound intensity. The data obtained in the initial and subsequent ultrasonic treatment cycles are represented by open and closed symbols, respectively. Different types of symbols indicate the results obtained at different ultrasonic frequencies for different samples. f = (*1–3*) 0.78 and (*4*) 1.8 MHz. The ratio $[(L_{us} - L_0)/L_0]_n = 1$ corresponds to $(L_{us} - L_0)/L_0$ = (*1*) 1.2, (*2*) 1.15, (*3*) 0.95, and (*4*) 0.48.

where D is the diffusion coefficient of electrons, ν_T is the thermal velocity of electrons, and S_k and N_k are the capture cross section and the concentration of the kth recombination centers, respectively. From relationship (1), it follows that the reciprocal of the diffusion length squared is directly determined by the parameters of the deep levels involved and that the change in the length $\Delta L^{-2} \equiv L_0^{-2} - L^{-2}$ is proportional to the change in (S_kN_k), because, under the experimental conditions, the product $(D^{-1}\nu_T)$ remains virtually constant. On this basis, the ascending and descending portions of the curve $L(t)$ (portions ab and bc in Fig. 2) can be described by the expressions

$$\Delta L_i^{-2} = \Delta L_{us}^{-2}[1 - \exp(-t/\tau_i)], \qquad (2)$$

$$\Delta L_t^{-2} = \Delta L_{us}^{-2}\exp(-t/\tau_t), \qquad (3)$$

where $\Delta L_{us}^{-2} \equiv L_0^{-2} - L_{us}^{-2}$ and τ_i and τ_t are the characteristic times of changes in the system of recombination centers in the cases of an increase (ΔL_i) and decrease (ΔL_t) in the diffusion length of minority charge carriers, respectively. It should be noted that expressions (2) and (3) are standard equations used for first-order kinetic processes. According to expressions (2) and (3), we can write the following relationships:

$$F_i \equiv \ln\left(\frac{L_0^2}{L^2}\frac{L_{us}^2 - L^2}{L_{us}^2 - L_0^2}\right) = -\frac{t}{\tau_i}, \qquad (4)$$

$$F_t \equiv \ln\left(\frac{L_{us}^2}{L^2}\frac{L^2 - L_0^2}{L_{us}^2 - L_0^2}\right) = -\frac{t}{\tau_t}. \qquad (5)$$

The time dependences of F_i and F_t at different amplitudes V_{us} are shown in Figs. 4a and 4b, respectively. As is seen from these figures, the dependences $F_i(t)$ and $F_t(t)$ are well approximated by straight lines whose slopes can be used to determine the characteristic times τ_i and τ_t. The calculations demonstrate that the characteristic time τ_i depends on the ultrasound amplitude, whereas the time τ_t is independent of this parameter. In subsequent ultrasound switching-on and switching-off cycles, the characteristic times τ_i and τ_t remain unchanged.

Let us analyze the observed dependence of the characteristic time τ_i on the ultrasound amplitude within the diffusion theory of transformation of recombination centers. In the general form, the characteristic relaxation time τ for a system of recombination centers can be represented as

$$\tau = \tau_0\exp(E_a^0/kT), \qquad (6)$$

where E_a^0 is the activation energy of the process which results in a change in the diffusion length L (for example, diffusion of atoms or ions involved in defects) and τ_0 is a constant which is the reciprocal of the thermal relaxation frequency. Under the conditions of mechanical loading of the crystal, the change in the activation energy E_a^0 can be approximated by a linear dependence [4, 6, 14]: $E_a = E_a^0 - \gamma\sigma$, where σ is the mechanical stress and γ is a certain activation volume. In our case of ultrasonic treatment of the crystal, we have $\sigma_{us} = (2\rho_s\nu_{us}W_{us})^{1/2}$ (where ρ_s is the silicon density and ν_{us} is the ultrasonic wave velocity) and the parameter γ has the meaning of the effective coefficient of interaction between ultrasonic waves and crystal defects.

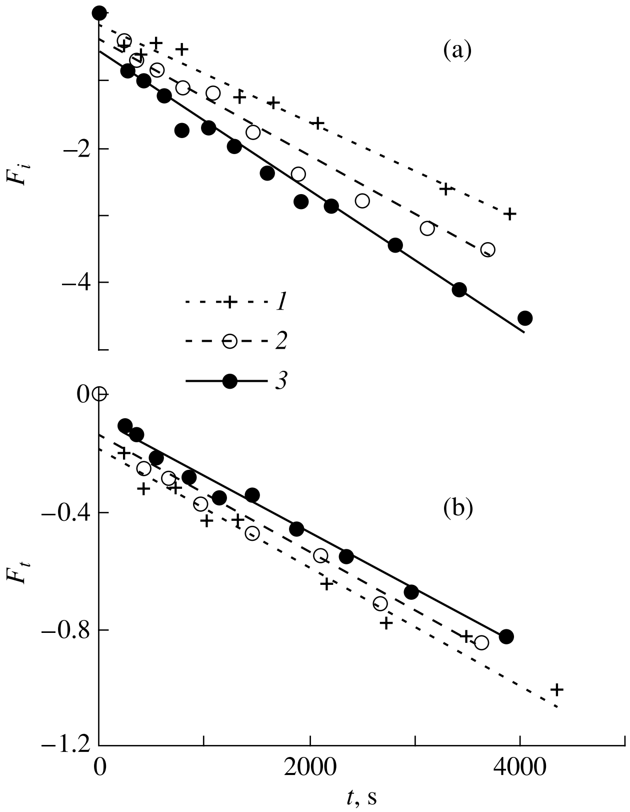

Fig. 4. Time dependences of (a) F_i and (b) F_t [see relationships (4) and (5)] at different amplitudes V_{us}: (*1*) 25, (*2*) 30, and (*3*) 35 V. $f = 0.78$ MHz. The characteristic relaxation times τ_i and τ_t calculated from the slopes of the dependences $F_i(t)$ and $F_t(t)$ are as follows: τ_i = (*1*) 21, (*2*) 16, and (*3*) 15 min and $\tau_t \approx$ (*1–3*) 80 min.

As a consequence, under the conditions of ultrasonic treatment, we obtain the following expression for the characteristic relaxation time:

$$\tau = \tau_0\exp((E_a^0 - \gamma\sigma_{us})/kT). \qquad (7)$$

Expression (7) permits us to evaluate the parameter γ. The experimental dependence of the characteristic relaxation time τ on σ_{us} is depicted in Fig. 5. The parameter γ was determined from the slope of the

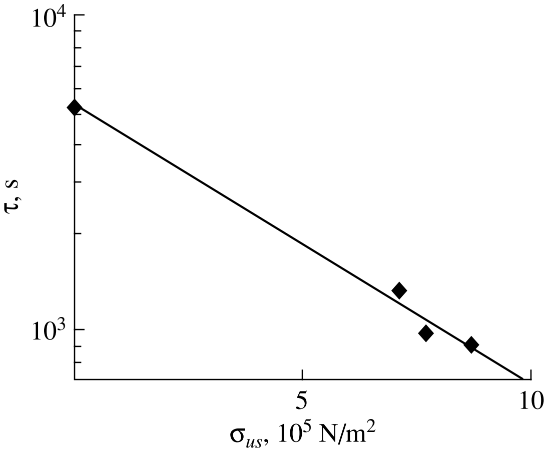

Fig. 5. Dependence of the relaxation time on the mechanical stress in an ultrasound field.

straight line in this figure: $\gamma = (8 \pm 2) \times 10^{-27}$ m^3. The obtained value of γ corresponds to an effective acousto-defect interaction range of 12 Å, which is comparable to the lattice parameter. This can be associated only with point defects (including their complexes). The physical meaning of the parameter γ can be defined as the effective volume of interaction between the elastic field of a complex defect and ultrasonic vibrations.

4. A POSSIBLE MECHANISM OF THE ULTRASOUND EFFECT

When analyzing the possible mechanisms of the ultrasound effect on the diffusion length in silicon of solar-cell grade, proper allowance must be made for the following factors: (i) the relatively small initial diffusion lengths L_0 (of the order of tens of microns), which suggests a high concentration of recombination centers (of the order of 10^{13}–10^{14} cm^{-3}); (ii) the long-term (of the order of tens of minutes) transient processes after switching on and switching off the ultrasound, which is characteristic of the diffusion mechanism of transformation of defect structures [4]; and (iii) the reversibility of the amplitude and time changes.

The experimental data obtained can be interpreted in the framework of the model of a bistable acoustoactive recombination center. Within this model, it is assumed that a defect can exist in two stable states (*A* and *B*) with different carrier capture cross sections (for example, $S_A > S_B$). In the absence of ultrasound, the probability of finding the defect in the *A* state is higher than that in the *B* state. After switching on the ultrasound, a number of defects transform into the *B* state. Consequently, the recombination rate decreases as the result of a decrease in the capture cross section. After switching off the ultrasound, the system of defects reverts to the original state. In silicon, the system of defects can consist of pairs, each formed by a dopant atom and an interstitial metal atom, for example, Cr–B, Fe–B, and Fe–Al pairs whose bistability has long been known [15–17]. It should be emphasized that it is these heavy metal impurities which are responsible for the considerable decrease in the diffusion length of minority charge carriers [11, 12].

As an example, we consider an iron–boron pair. The presence of iron at a concentration of 10^{13}–10^{14} cm^{-3} in silicon leads to a decrease in the diffusion length L_0 to 20 μm [11, 12]. At room temperature, iron atoms in Si : B are almost completely bound in Fe_i–B_s complexes [18]. The bistability of these complexes stems from the fact that the iron ion can occupy either the *T* interstice nearest to the B atom (configuration *A*) or the next-nearest interstice (configuration *B*) [16]. In a pair with configuration *B*, the spacing between the two energy levels that correspond to the two charge states Fe^{2+} and Fe^+ is smaller by 0.14 eV [16]. Within the model under consideration, the sound-stimulated transition of a complex from the *A* state to the *B* state can be treated as diffusion of the interstitial iron ion from one interstice to another interstice in an ultrasound field, followed by the recharging $Fe^{2+} \longrightarrow Fe^+$ in a number of defects until thermodynamic equilibrium between different charge states is attained. A decrease in the fraction of Fe^{2+} ions should lead to a decrease in the electron capture cross section and a subsequent increase in the diffusion length *L*. In the ultrasound field, the diffusion of impurity atoms is stimulated by their interaction with nonequilibrium phonons excited by ultrasonic waves [19]. The recharging of ions with a change in their spatial position was described in [20].

In order to verify the validity of the model described above, we performed experiments with illumination of the samples under investigation. According to Lagowski *et al.* [10], sufficiently intense illumination (~10 W/cm^2) of silicon crystals with white light at room temperature brings about the decomposition of pairs of the Fe–B type. In turn, this leads to a decrease in the diffusion length of minority charge carriers, because the electron capture cross section of interstitial iron ions is larger that of the Fe_i–B_s pair. Illumination of the studied samples in the absence of ultrasound causes the diffusion length *L* to decrease by approximately 15%. In the case when the samples are illuminated in the course of ultrasonic treatment, the diffusion length decreases to a considerably larger extent and the ultrasound-stimulated increase in the diffusion length is virtually suppressed under exposure to light. In the framework of the proposed model, this fact is explained by the photoinduced decomposition of the pairs.

Furthermore, silicon contains other defects that can participate in the acoustodefect interaction, namely, complexes involving vacancies. In particular, a vacancy–boron pair can be considered a bistable defect [21]. In this case, different configurations of the vacancy complex with a dopant atom exhibit significantly different recombination properties due to partial internal charge redistribution [22]. Therefore, the ultrasound-induced transition in this defect should result in a change in the diffusion length *L*.

5. CONCLUSIONS

Thus, the results obtained in the present work can be summarized as follows.

(1) The reversible increase in the diffusion length of electrons in dislocation-free *p*-Si crystals under the effect of ultrasound is observed for the first time.

(2) The effective volume of the acoustodefect interaction is estimated as $\gamma = (8 \pm 2) \times 10^{-27}$ m^3. This indicates that the ultrasonic waves interact with point defects.

(3) A model of ultrasound-induced transformation of recombination centers in a silicon crystal is proposed. Consideration is given to the possible ultrasound-induced transformations in different defects, namely, pairs containing impurity atoms located at sites and interstices and complexes involving vacancies.

ACKNOWLEDGMENTS

This work was supported in part by the Institut für Halbleiterphysik Frankfurt (Oder).

REFERENCES

1. I. V. Ostrovskiĭ, L. P. Steblenko, and A. B. Nadtochiĭ, Fiz. Tverd. Tela (St. Petersburg) **42** (3), 478 (2000) [Phys. Solid State **42**, 488 (2000)].
2. S. Ostapenko and R. Bell, J. Appl. Phys. **77** (10), 5458 (1995).
3. I. B. Ermolovich, V. V. Milenin, R. V. Konakova, *et al.*, Fiz. Tekh. Poluprovodn. (St. Petersburg) **31** (4), 503 (1997) [Semiconductors **31**, 427 (1997)].
4. V. S. Arakelyan, A. A. Avakyan, and L. K. Kapanaktsyan, Fiz. Tverd. Tela (Leningrad) **27** (8), 2536 (1985) [Sov. Phys. Solid State **27**, 1521 (1985)].
5. M. K. Sheinkman, L. V. Borkovskaya, B. R. Dzhumaev, *et al.*, Mater. Sci. Forum **196–201**, 1467 (1995).
6. A. I. Vlasenko, Ya. M. Olikh, and R. K. Savkina, Fiz. Tekh. Poluprovodn. (St. Petersburg) **33** (4), 410 (1999) [Semiconductors **33**, 398 (1999)].
7. Ju. M. Khalack, V. M. Loktev, A. B. Nadtochii, *et al.*, Condens. Matter Phys. **11**, 61 (1997).
8. A. M. Goodman, J. Appl. Phys. **32** (12), 2550 (1961).
9. J. Lagowski, P. Edelman, M. Dexter, and W. Henley, Semicond. Sci. Technol. **7** (2), A185 (1992).
10. J. Lagowski, P. Edelman, A. M. Kontkiewicz, *et al.*, Appl. Phys. Lett. **63** (22), 3043 (1993).
11. F. Shimura, T. Okui, and T. Kusama, J. Appl. Phys. **67** (11), 7168 (1990).
12. D. K. Schroder, IEEE Trans. Electron Devises **44** (1), 160 (1997).
13. A. Hanglaiter, Phys. Rev. B **35** (17), 9149 (1987).
14. J. P. Hirth and J. Lothe, *Theory of Dislocations* (McGraw-Hill, New York, 1967; Atomizdat, Moscow, 1972).
15. A. Chantre and D. Bois, Phys. Rev. B **31** (12), 7979 (1985).
16. H. Nakashima, T. Sadoh, and T. Tsurushima, Phys. Rev. B **49** (24), 16983 (1994).
17. H. Overhof and H. Weihrich, Phys. Rev. B **55** (16), 10508 (1997).
18. G. Zoth and W. Berholz, J. Appl. Phys. **67** (11), 6764 (1990).
19. V. N. Pavlovich, Phys. Status Solidi B **180** (1), 97 (1993).
20. V. L. Vinetskiĭ and G. E. Chaĭka, Fiz. Tverd. Tela (Leningrad) **28** (11), 3389 (1986) [Sov. Phys. Solid State **28**, 1908 (1986)].
21. A. Chantre, Phys. Rev. B **32** (6), 3687 (1985).
22. O. O. Awadelkarim and B. Monemar, Phys. Rev. B **38** (14), 10116 (1988).

Translated by O. Borovik-Romanova

Physics of the Solid State, Vol. 44, No. 7, 2002, pp. 1254–1256. Translated from Fizika Tverdogo Tela, Vol. 44, No. 7, 2002, pp. 1203–1205.
Original Russian Text Copyright © 2002 by Bryushinin, Dubrovskiĭ, Petrov, Sokolov, Vainos, Kalpouzos.

SEMICONDUCTORS AND DIELECTRICS

Nonstationary Photovoltage Induced in Tin Disulfide Crystals under Strong Surface Excitation

M. A. Bryushinin[1, 2], G. B. Dubrovskiĭ[1], A. A. Petrov[1], I. A. Sokolov[1, 2],
N. A. Vainos[3], and C. Kalpouzos[3]

[1] *Ioffe Physicotechnical Institute, Russian Academy of Sciences, Politekhnicheskaya ul. 26, St. Petersburg, 194021 Russia*
[2] *Institute of Problems of Mechanical Engineering, Russian Academy of Sciences,*
Bol'shoĭ pr. 61, Vasil'evskiĭ Ostrov, St. Petersburg, 199178 Russia
[3] *Institute of Electronic Structure and Laser, FORTH, Heraklion, Greece*

Received October 26, 2001

Abstract—The specific features of nonstationary photovoltage excitation in molecular crystals of tin disulfide are investigated. A substantial change in the dependence of the photocurrent amplitude on the spatial frequency of the interference pattern is revealed. The observed behavior is explained in terms of the model of a photoconductor with different-type charge carriers of the same sign. © *2002 MAIK "Nauka/Interperiodica".*

1. INTRODUCTION

Crystals of tin disulfide (SnS_2) are characterized by strong anisotropy of their properties and polytypism due to the layered structure of this material. The crystal structure of SnS_2 exhibits a molecular close packing [1]. The smallest structural unit of SnS_2 crystals is a monomolecular layer that consists of three atomic layers, namely, S–Sn–S. The adjacent molecular layers are linked through van der Waals forces. Superstructural perturbations of the simplest structures of the crystal, which are associated with regular rotations of the molecular layers, bring about the formation of different polytypic modifications.

The optical properties of SnS_2 have been investigated in many works [2–5]. It is found that SnS_2 crystals possess an appreciable photoconductivity in the visible range [6–8] and a short response time [9, 10]. However, the properties of SnS_2 crystals over a wide range of incident frequencies are still not clearly understood.

The main objective of the present work was to investigate experimentally the nonstationary photovoltage [11] in SnS_2 crystals at different wavelengths of the writing light and to reveal the specific features of the surface excitation of electric current under short-wave radiation.

2. SAMPLES AND EXPERIMENTAL SETUP

A schematic drawing of the experimental setup for measuring the nonstationary photovoltage is shown in Fig. 1. The coherent radiation was excited by an LGN-215 helium–neon laser ($\lambda = 633$ nm, $P_{out} \approx 40$ mW) and LPM-11 helium–cadmium ($\lambda = 442$ nm, $P_{out} \approx 1$ mW) and Liconix-4240NB helium–cadmium ($\lambda = 325$ nm, $P_{out} \approx 6$ mW) lasers. The laser light was separated into two beams to form an interference pattern on the surface of the studied crystals. One of the beams was modulated in phase with the frequency ω and amplitude Δ to induce spatial oscillations in an interference pattern. The measurements of the unsteady photocurrent were carried out using Unipan-233-7 and EG&G-7260 lock-in nanovoltmeters. Crystals of SnS_2 were grown by the gas-transport reaction technique and had a characteristic size of $5 \times 5 \times 0.04$ mm. The electrodes were applied on the front surface of the crystal at a distance of ~1 mm from each other with the use of a fine-dispersed silver paste.

3. EXPERIMENTAL RESULTS

No characteristic indications of bipolar photoconductivity, namely, changes in the sign of the photocur-

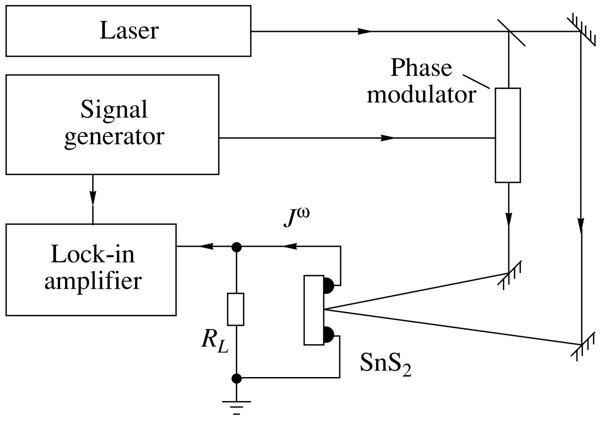

Fig. 1. A schematic drawing of the experimental setup for measuring nonstationary photovoltage in SnS_2 crystals.

1063-7834/02/4407-1254$22.00 © 2002 MAIK "Nauka/Interperiodica"

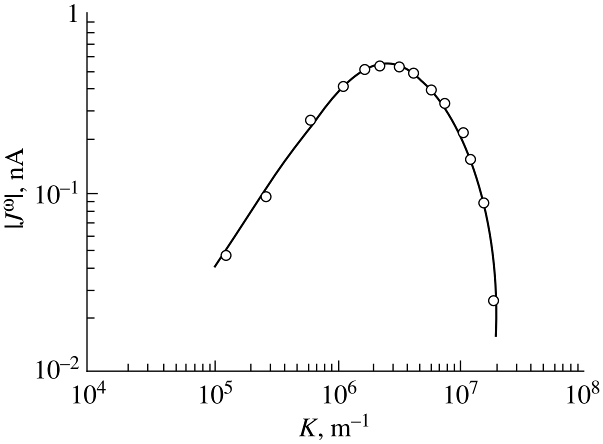

Fig. 2. Dependence of the amplitude of unsteady photocurrent on the spatial frequency of the interference pattern at the wavelength $\lambda = 633$ nm ($P_0 = 33$ mW, $\omega/2\pi = 100$ kHz). Points are the experimental data. The solid line represents the theoretical dependence calculated from the standard relationship (1).

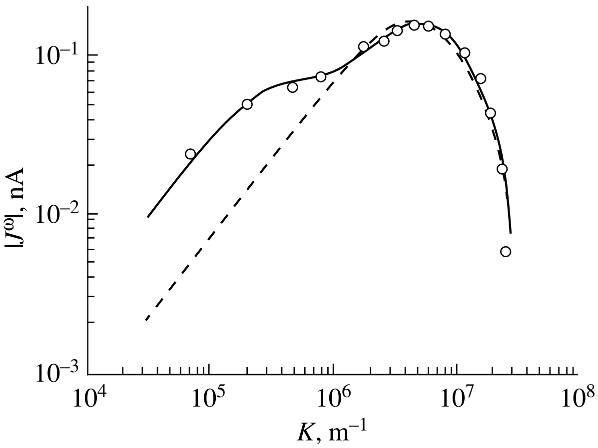

Fig. 3. Dependence of the amplitude of unsteady photocurrent on the spatial frequency K at the wavelength $\lambda = 442$ nm ($P_0 = 0.29$ mW, $\omega/2\pi = 140$ kHz). Points are the experimental data. The dashed line represents the theoretical dependence calculated from the standard relationship (1). The solid line indicates the theoretical curve described by relationship (2).

rent with variations in the frequency of phase modulation [12] or the spatial frequency [13], were observed for any of the wavelengths used (633, 442, and 325 nm). For all these wavelengths, the photocurrent sign corresponded to the electronic component.

The dependence of the nonstationary photovoltage on the spatial frequency at the wavelength $\lambda = 633$ nm is shown in Fig. 2. The experimental curve is well approximated by the standard relationship

$$J^{\omega} \propto \frac{\sigma_0 K}{1 + K^2 L_d^2}. \quad (1)$$

Here, σ_0 is the photoconductivity of the crystal, K is the spatial frequency, and L_d is the diffusion length of carrier transfer. The linear increase in the nonstationary photovoltage in the initial portion is associated with an increase in the diffusion field: $E_D = (k_B T/e)K$. The decrease observed in the nonstationary photovoltage at high spatial frequencies is inversely proportional to the spatial frequency K and can be explained by the decrease in the amplitude of the lattice photocurrent [11]. Since the photocurrent reaches a maximum at $KL_d = 1$, the diffusion length of electrons can be estimated from the position of the photocurrent peak. For the SnS_2 crystal under investigation, the electron diffusion length L_d is equal to 0.38 μm.

Figure 3 depicts the dependence of the nonstationary photovoltage on the spatial frequency at the wavelength $\lambda = 442$ nm. It can be seen that the experimental curve approximated by the standard relationship (1) is characterized by considerable errors at low spatial frequencies (dashed line in Fig. 3). This discrepancy vanishes under the assumption that charge transfer in the crystal occurs through two channels, namely, with the participation of light and heavy charge carriers of the same sign [14]. In this case, the relationship between the photocurrent and the spatial frequency takes the following form:

$$J^{\omega} \propto \frac{\sigma_1 K}{1 + K^2 L_{d1}^2} + \frac{\sigma_2 K}{1 + K^2 L_{d2}^2}. \quad (2)$$

Here, L_{d1} and L_{d2} are the diffusion lengths of the light and heavy electrons, respectively, and σ_1 and σ_2 are the contributions of the corresponding channels of charge transfer to the total photoconductivity of the material. The experimental dependence is best approximated by expression (2) at $L_{d1} = 0.15$ μm, $L_{d2} = 2.0$ μm, and $\sigma_2/\sigma_1 = 4.3$.

The dependence of the amplitude of unsteady photocurrent on the spatial frequency at $\lambda = 325$ nm (Fig. 4) deviates from the standard behavior to a considerably larger extent compared to the curve recorded at $\lambda = 442$ nm. The approximation of the experimental dependence by expression (2), which was derived for two types of carriers, is not fully adequate for all the spatial frequencies. By comparing relationships (1) and (2), we can modify the expression describing the photocurrent amplitude for the case of three types of carriers of the same sign as follows:

$$J^{\omega} \propto \sum_{m=1}^{3} \frac{\sigma_m K}{1 + K^2 L_{dm}^2}. \quad (3)$$

The experimental data are most closely approximated by this expression with the following parameters: $L_{d1} = 0.16$ μm, $L_{d2} = 0.85$ μm, $L_{d3} = 0.11$ μm, $\sigma_2/\sigma_1 = 2.1$, and $\sigma_3/\sigma_1 = 20$.

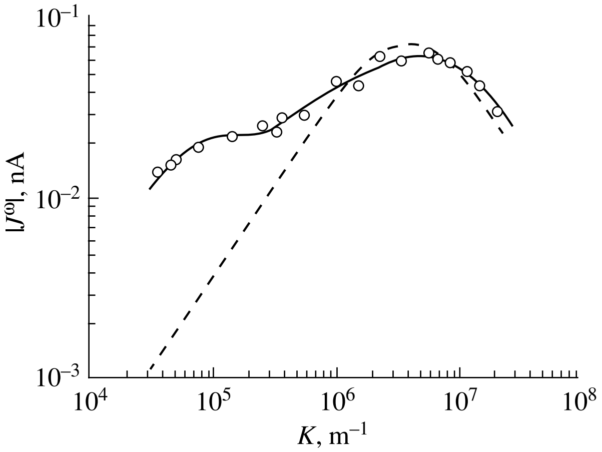

Fig. 4. Dependence of the amplitude of unsteady photocurrent on the spatial frequency K at the wavelength λ = 325 nm (P_0 = 3.8 mW, $\omega/2\pi$ = 94 kHz). Points are the experimental data. The dashed line represents the theoretical dependence calculated from the standard relationship (1). The solid line indicates the theoretical curve described by relationship (3).

Different-type charge carriers that are characterized by different diffusion lengths of their transfer can be excited with incident light owing to two specific features of the band structure of the SnS_2 crystal. First, the conduction band of the crystal exhibits two minima with an energy gap of ~0.8 eV [3, 15]. Consequently, illumination of the crystal with red light (λ = 633 nm, $h\nu$ = 1.96 eV) leads primarily to the generation of carriers from impurity levels into a valley with a lower energy, whereas the illumination with blue light (λ = 442 nm, $h\nu$ = 2.81 eV) and, especially, ultraviolet radiation (λ = 325 nm, $h\nu$ = 3.82 eV) result in the band-to-band and impurity generation of electrons into two valleys and, possibly, into a third, even higher energy band. Second, actual samples of tin disulfide crystals have a layered structure with alternating layers of different polytype structures. The band gap E_g for the most commonly encountered polytypic modification of SnS_2 crystals (1H) is equal to 2.18 eV [1, 16]. A larger band gap is observed only in the 9R structure: E_g = 3.38 eV [16]. Therefore, the total photocurrent can be determined by the generation of carriers with different transport parameters in alternating layers of the crystal with different polytype structures. It is evident that carriers generated in high-energy bands can have larger diffusion lengths due to a decrease in the van der Waals gap.

ACKNOWLEDGMENTS

This work was supported by the Russian Foundation for Basic Research (project no. 00-02-16890) and NATO (grant nos. HTEH.LG 970314 and CNS 972 900).

REFERENCES

1. G. B. Dubrovskiĭ, Fiz. Tverd. Tela (St. Petersburg) **40** (9), 1712 (1998) [Phys. Solid State **40**, 1557 (1998)].
2. P. Greenaway and R. Nitsche, J. Phys. Chem. Solids **26**, 1445 (1965).
3. G. Domingo, R. Itoga, and C. Kannewurf, Phys. Rev. **143**, 536 (1966).
4. P. Lee and G. Said, J. Phys. D **1**, 837 (1968).
5. M. Au. Yang and M. Cohen, Phys. Rev. **178**, 1279 (1969).
6. S. Patil and R. Tredgold, J. Phys. D **4**, 718 (1971).
7. R. Nakata, M. Yamaguchi, S. Zembutsu, and M. Sumita, J. Phys. Soc. Jpn. **32**, 1153 (1972).
8. T. Shibata, Y. Makanushi, T. Miura, and T. Kishi, J. Phys. Chem. Solids **51**, 1297 (1990).
9. J. M. Lanzafame, R. J. D. Miller, A. A. Muenter, and B. A. Parkinson, J. Phys. Chem. **96**, 2820 (1992).
10. S. Xu, C. C. Miller, S. J. Diol, *et al.*, Chem. Phys. Lett. **272**, 209 (1997).
11. M. P. Petrov, I. A. Sokolov, S. I. Stepanov, and G. S. Trofimov, J. Appl. Phys. **68** (5), 2216 (1990).
12. N. Korneev, S. Mansurova, P. Rodriguez, and S. Stepanov, J. Opt. Soc. Am. B **14** (2), 396 (1997).
13. S. I. Stepanov and G. S. Trofimov, Fiz. Tverd. Tela (Leningrad) **31** (1), 89 (1989) [Sov. Phys. Solid State **31**, 49 (1989)].
14. M. A. Bryushinin, G. B. Dubrovsky, and I. A. Sokolov, Appl. Phys. B **B68** (5), 871 (1999).
15. *Landolt-Börnstein: Numerical Data and Functional Relationships in Science and Technology, New Series*, Ed. by O. Madelung (Springer-Verlag, Berlin, 1983), Vol. 17.
16. S. Acharya and O. N. Srivastava, Phys. Status Solidi A **65** (2), 717 (1981).

Translated by N. Korovin

Physics of the Solid State, Vol. 44, No. 7, 2002, pp. 1257–1262. Translated from Fizika Tverdogo Tela, Vol. 44, No. 7, 2002, pp. 1206–1210.
Original Russian Text Copyright © 2002 by Aleĭnikova, Kozlov, Kozlova, Sobolev.

SEMICONDUCTORS AND DIELECTRICS

Electronic and Crystal Structures of Isomorphic ZnP_2 and CdP_2

K. B. Aleĭnikova*, A. I. Kozlov, S. G. Kozlova**, and V. V. Sobolev*****
** Voronezh State University, Universitetskaya pl. 1, Voronezh, 394693 Russia*
*** International Laboratory of High-Temperature Superconductivity and Solid-State Electronics, Academy of Sciences of Moldova, Akademiei 5, Chisinau, MD2028 Moldova*
**** Udmurt State University, Universitetskaya ul. 1, Izhevsk, 426034 Russia*
e-mail: kozlov@lises.asm.md

Received October 1, 2001

Abstract—This paper reports on the results of precision investigations into the crystal structure of zinc diphosphide and cadmium diphosphide single crystals. The complete sets of fundamental optical functions are calculated for both crystals in the range 2.2–5.3 eV. The dielectric function is resolved into components for the first time. Three basic parameters of the oscillators are determined, and the electronic structures of ZnP_2 and CdP_2 are compared. © *2002 MAIK “Nauka/Interperiodica”.*

1. INTRODUCTION

Anisotropic crystals of ZnP_2 and CdP_2 have been attracting the particular attention of researchers for a long time owing to their unique properties and possible practical applications [1–3]. These crystals are characterized by a considerable band gap E_g, mechanical stability, chemical durability, and high optical activity [2, 3]. Single-crystal ZnP_2 and CdP_2 crystallize in a tetragonal lattice with space group $P4_12_12 = D_4^4$. Moreover, ZnP_2 crystals can exist in an enantiomorphic form with space group $P4_32_12 = D_4^8$. The unit cell contains eight formula units. The unit cell parameters (a and c) are reported in [4–6]. As was shown earlier in [7], the main structural fragments of zinc and cadmium diphosphides are composed of phosphorus spiral chains oriented along the [100] and [010] directions.

In ZnP_2 and CdP_2 tetragonal crystals, the Brillouin zone has the form of a rectangular parallelepiped. The specific features of the band symmetry, the dispersion laws, and the selection rules are considered in [8]. Calculations of the band structure of ZnP_2 and CdP_2 crystals in the framework of the pseudopotential formalism are described in [9–12]. In these works, the spin-orbit interaction is ignored in the band-structure calculations due to its small magnitude: $\Delta E_{\text{s.o.}} < 0.05$ eV. It has been found that the band topology in the vicinity of the band gap E_g is virtually independent of the pseudopotential type. The optimum values of E_g prove to be equal to 1.58 eV for ZnP_2 and 0.81 eV for CdP_2. For ZnP_2 crystals, the valence band top is located at the Γ point and the absorption edge is determined by direct forbidden transitions. For CdP_2 crystals, the valence band top is shifted to the Z point; as a consequence, the absorption edge is determined by indirect transitions. Leznyak [13] calculated the band structure of CdP_2 crystals in the framework of the augmented plane wave method. In this case, the Γ and Z points are found to be energetically similar to each other.

Sobolev and Syrbu [14] proved that the edge absorption in zinc and cadmium diphosphides is determined by indirect transitions in the vicinity of the direct transitions: $E_{gi} = 1.97$ eV and $E_{gd} = 2.30$ eV for ZnP_2 and $E_{gi} = 1.70$ eV and $E_{gd} = 2.11$ eV for CdP_2. Moreover, Sobolev *et al.* [15] investigated the polarized reflectance spectra of zinc diphosphide at temperatures of 77 and 300 K. However, the reflectance spectra of cadmium diphosphide were measured only for the polarization $\mathbf{E} \perp \mathbf{c}$ [8]. In these spectra, the reflectance drastically decreased in the near-ultraviolet range due to imperfection of the samples and the measurement procedure used in the experiments. Ambrazeavicius *et al.* [16] studied the reflection and thermoreflection spectra of cadmium diphosphide for both polarizations. Evstigneev *et al.* [17] measured and analyzed the electroreflection spectra of zinc diphosphide only at room temperature. More reliable data on the reflectance spectra of zinc and cadmium diphosphides were obtained in [12, 18]. The precision method used in these works made it possible to measure the reflection coefficient R with an accuracy of 0.5% and a reproducibility of ≈0.03%. The measurements were carried out in the energy range 2–5 eV at temperatures of 80 and 293 K for two polarizations of light ($\mathbf{E} \perp \mathbf{c}$ and $\mathbf{E} \parallel \mathbf{c}$). The samples were measured under vacuum. Nitrogen traps were used to prevent deposition of water and oil vapors. When analyzing the experimental data, Sobolev *et al.* [12] considered the maxima of the integrated reflectance spectra $R(E)$ rather than the absorption or permit-

Table 1. Bond lengths (Å) in ZnP$_2$ and CdP$_2$ crystals

ZnP$_2$		CdP$_2$	
Zn–P$_1$	2.3878	Cd–P$_1$	2.579
Zn–P$_1$	2.3899	Cd–P$_1$	2.583
Zn–P$_2$	2.4063	Cd–P$_2$	2.581
Zn–P$_2$	2.3555	Cd–P$_2$	2.529
P$_1$–P$_2$	2.1658	P$_1$–P$_2$	2.171
P$_1$–P$_2$	2.206	P$_1$–P$_2$	2.203

Table 2. Bond angles (deg) in ZnP$_2$ and CdP$_2$ crystals

ZnP$_2$		CdP$_2$	
P$_1$–P$_2$–Zn	109.07	P$_1$–P$_2$–Cd	110.10
P$_1$–P$_2$–Zn	104.48	P$_1$–P$_2$–Cd	103.35
P$_1$–P$_2$–P$_1$	106.89	P$_1$–P$_2$–P$_1$	109.82
Zn–P$_2$–Zn	115.8	Cd–P$_2$–Cd	110.18
Zn–P$_2$–P$_1$	113.85	Cd–P$_2$–P$_1$	115.66
Zn–P$_2$–P$_1$	106.01	Cd–P$_2$–P$_1$	106.97
P$_2$–Zn–P$_2$	124.17	P$_2$–Cd–P$_2$	125.06
P$_2$–Zn–P$_1$	112.54	P$_2$–Cd–P$_1$	114.8
P$_2$–Zn–P$_1$	109.24	P$_2$–Cd–P$_1$	110.5
P$_2$–Zn–P$_1$	105.06	P$_2$–Cd–P$_1$	104.26
P$_2$–Zn–P$_1$	103.35	P$_2$–Cd–P$_1$	100.21
P$_1$–Zn–P$_1$	99.39	P$_1$–Cd–P$_1$	97.83
Zn–P$_1$–Zn	108.35	Cd–P$_1$–Cd	107.26
Zn–P$_1$–P$_2$	112.21	Cd–P$_1$–P$_2$	114.11
Zn–P$_1$–P$_2$	111.55	Cd–P$_1$–P$_2$	110.68
Zn–P$_1$–P$_2$	110.27	Cd–P$_1$–P$_2$	110.47
Zn–P$_1$–P$_2$	105.06	Cd–P$_1$–P$_2$	103.00
P$_2$–P$_1$–P$_2$	109.17	P$_2$–P$_1$–P$_2$	110.68

tivity spectra; i.e., the true energies and intensities of the complete set of optical transitions were disregarded. This can lead to an ambiguous interpretation of the origin of the peaks observed in the reflectance spectra $R(E)$. In order to solve the complicated problem of constructing an adequate model of the band structure of any crystal, it is expedient to analyze the complete set of optical fundamental functions rather than only one of them (reflection) [19, 20].

In the present work, we performed precision investigations into the optical spectra and the atomic structure of zinc and cadmium diphosphides with the aim of obtaining more reliable data on the geometry of chemical bonds and the electronic structure of ZnP$_2$ and CdP$_2$ isomorphic crystals.

2. X-RAY STRUCTURAL INVESTIGATIONS

The experimental x-ray diffraction data used in calculations of the crystal structures of zinc and cadmium diphosphides were collected on a Hilger–Watts automated four-circle diffractometer ($\lambda \mathrm{Mo}K\alpha$, graphite monochromator, $\theta/2\theta$ scan mode).

The unit cell parameters of ZnP$_2$ and CdP$_2$ single crystals with space group $P4_12_12$ at room temperature (293 K) are as follows: $a = b = 5.2768(7)$ Å and $c = 19.753(3)$ Å for CdP$_2$ and $a = b = 5.0586(7)$ Å and $c = 18.506(4)$ Å for ZnP$_2$. The crystal structure of ZnP$_2$ was refined in two enantiomorphic space groups. For the space group $P4_12_12$, the discrepancy factor was approximately equal to 3% (the number of reflections used in the structure refinement was ≈2000). For ZnP$_2$ crystals with space group $P4_32_12$, the unit cell parameters proved to be somewhat different. These two structures can be distinguished by the optical rotation along the c axis. The crystal structure of CdP$_2$ was refined in the space group $P4_12_12$; in this case, the discrepancy factor was approximately equal to 3.4% (the number of reflections used in the structure refinement was ≈1000). For this reason, the results of x-ray structure determination are given only for the space group $P4_12_12$ (Tables 1, 2).

For both crystals, the structure is characterized by three independent atoms, namely, P(1), P(2), and Zn (Cd). These atoms occupy three equivalent eightfold positions. The zinc atom is surrounded by four phosphorus atoms (for each sort there are two phosphorus atoms); in turn, each of the phosphorus atoms is bonded to two zinc atoms and two phosphorus atoms. After refinement of the crystal structures of zinc and cadmium diphosphides, the P–P bond lengths in phosphorus atomic chains are found to be virtually identical to the P–P bond lengths in black crystalline phosphorus. The Zn–P and Cd–P interatomic distances are slightly less than the sum of their tetrahedral radii [21]. Most likely, this is associated with ionic bonding in the crystals. The smallest bond angles in ZnP$_2$ and CdP$_2$ crystals are equal to 99.39° and 97.83°, respectively. At the same time, the largest bond angles in ZnP$_2$ and CdP$_2$ are equal to 124.17° and 125.06°, respectively. A similar correlation is also observed for the other bond angles. For both crystals, the P–P bond lengths are very close to each other (the difference amounts to only 0.003–0.005 Å). It should be noted that, prior to precision measurements, the P–P bond lengths in CdP$_2$ were assumed to be equal to 2.157 and 2.227 Å, respectively; i.e., after the refinement, their values changed significantly.

3. CALCULATIONS OF OPTICAL FUNCTIONS

The spectra of the optical functions for both crystals were calculated in the range 2.2–5.3 eV in polarized light. The calculations were carried out using the data obtained earlier in [12, 18] and Kramers–Kronig inte-

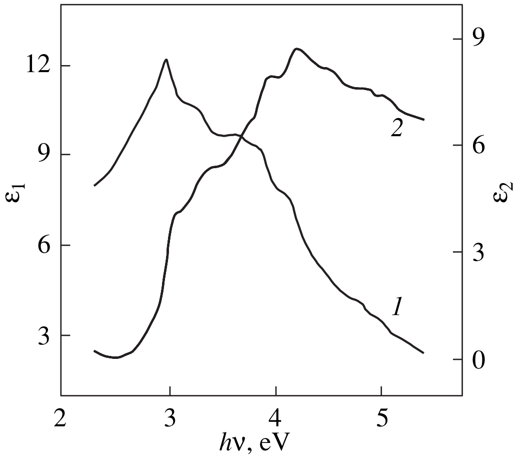

Fig. 1. Optical functions (*1*) ε_1 and (*2*) ε_2 of the ZnP_2 crystal for **E** || **c** at a temperature of 80 K.

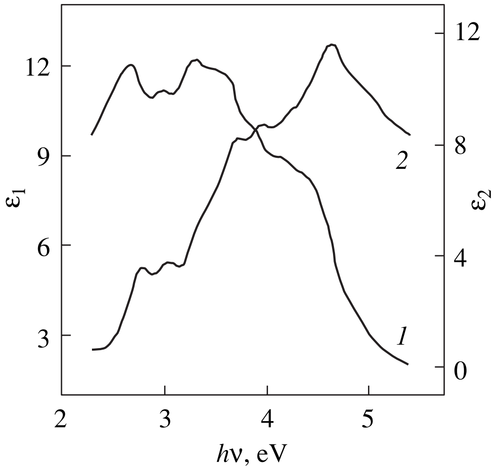

Fig. 2. Optical functions (*1*) ε_1 and (*2*) ε_2 of the ZnP_2 crystal for **E** ⊥ **c** at a temperature of 80 K.

gral relationships. The data in the range 5–12 eV and in the transparency range (required for correct calculations) were taken from other authors. It was found that the main features in the optical spectra at temperatures of 80 and 293 K coincide with each other. However, all the features revealed at room temperature are less pronounced and certain of them almost disappear.

In this work, we compared the spectra of the following functions: the reflection coefficient R; the imaginary (ε_2) and real (ε_1) parts of the permittivity ε; the absorption coefficient μ; the refractive index n; the index of absorption k; the integral function of the coupled density of states multiplied by the probability of transitions, which is equal to $\varepsilon_2 E^2$ within a constant factor; the effective number n_{eff} of valence electrons involved in optical transitions at a given energy; the effective permittivity ε_{eff}; the differential (electrooptical) functions α and β; the phase angle of reflected light θ; and the functions of the bulk $(-\mathrm{Im}(\varepsilon)^{-1})$ and surface $[-\mathrm{Im}(\varepsilon + 1)^{-1}]$ plasmons. All these functions are interrelated; however, each function has a specific meaning.

The specific features of the spectra $R(E)$ were described in detail in [12, 18]. The spectra of the functions n and ε_1 are similar to those of R in the long-wavelength range. At shorter wavelengths, the functions n and ε_1 decrease drastically and the reflectance spectra exhibit only the most intense peaks. The spectra of the functions k, ε_2, and, to a lesser extent, $\varepsilon_2 E^2$ and μ are very similar to the reflectance spectrum, especially for the polarization **E** ⊥ **c**; however, the intensity distribution in this case is slightly different. The absorption coefficient at an energy of 5 eV reaches 0.9×10^6 cm^{-1} for ZnP_2 and 1.1×10^6 cm^{-1} for CdP_2. The functions of the bulk and surface plasmons have similar spectra but differ in magnitude. The spectra of these functions contain all the peaks revealed in the reflectance spectrum, except for those observed at the longest wavelengths. The functions n_{eff} and ε_{eff} increase monotonically but do not attain saturation in the energy range under investigation. The differential function $\alpha(E)$ decreases monotonically and resembles, to some extent, the curve $n(E)$. The differential function β exhibits a more complex behavior: the dependence $\beta(E)$ is similar to the curve $R(E)$ near the band gap E_g and follows an asymmetric curve at $h\nu > 3.5$ eV.

Figures 1–4 depict the spectral dependences of the optical functions ε_1 and ε_2 for ZnP_2 and CdP_2 crystals at a temperature 80 K for two polarizations (**E** ⊥ **c** and **E** || **c**). It is seen that the studied crystals possess a clearly pronounced optical anisotropy. The curves of the real (ε_1) and imaginary (ε_2) parts of the permittivity of zinc and cadmium diphosphides at different polarizations exhibit quite a different behavior. The absolute values of ε_1 and ε_2 for ZnP_2 crystals are less than those for CdP_2 crystals, because the latter crystals are characterized by a stronger reflection over virtually the entire range of energies.

However, a comparison of the dependences of the functions ε_1 and ε_2 on the incident radiation energy for ZnP_2 and CdP_2 crystals at the same polarizations (Figs. 1, 3 and 2, 4) has revealed many common features, especially at the polarization **E** ⊥ **c**.

4. PARAMETERS OF OPTICAL TRANSITIONS IN ZnP_2 AND CdP_2 CRYSTALS

As a rule, the spectral bands associated with optical transitions in solids overlap significantly; certain of these transitions do not manifest themselves in the integrated curve. For this reason, we used the Argand diagram technique [20] to resolve the spectra $\varepsilon_2(E)$ into partial components attributed to the particular groups of optical transitions with close energies. To accomplish this resolution, the integrated curves $\varepsilon_2 = f(\varepsilon_1)$ were

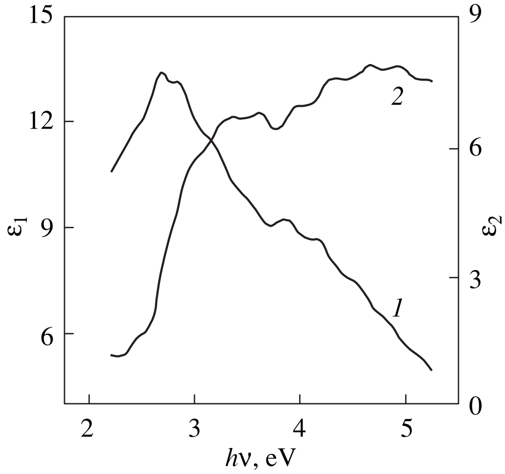

Fig. 3. Optical functions (*1*) ε_1 and (*2*) ε_2 of the CdP_2 crystal for **E** || **c** at a temperature of 80 K.

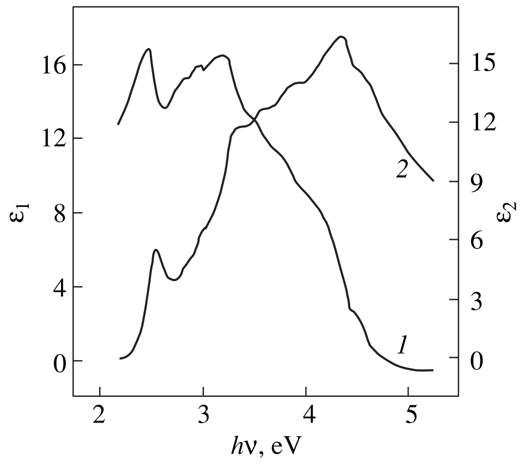

Fig. 4. Optical functions (*1*) ε_1 and (*2*) ε_2 of the CdP_2 crystal for **E** ⊥ **c** at a temperature of 80 K.

divided into portions that could be adequately described by semicircumferences. The portions thus obtained were used to construct the partial functions and to determine the residues of the functions ε_1 and ε_2. This process was simulated on a computer and repeated for the time the residues of Argand curves contained portions that could be represented by circumferential parts. As a result, we determined the following basic parameters of elementary oscillators: (1) the energy position of the maximum of the band associated with the optical transition E_i (2) the half-width of this band H_i, and (3) the oscillator strength f_i which is responsible for the transition probability. The results obtained are presented in Tables 3 and 4.

According to our calculations, the integrated spectra $\varepsilon_2(E)$ for ZnP_2 and CdP_2 crystals in the range 2.2–5.3 eV can be reproduced using 12 Lorentz oscillators (for each polarization), whereas the spectra $R(E)$ at low temperatures exhibit only nine or ten features. It is worth noting that, in this case, intensive transitions with oscillator strengths $f_i > 1$ are not revealed, the f_i values for the polarization **E || c** are considerably less than those for the polarization **E** ⊥ **c**, and the half-widths H_i of the bands attributed to the oscillators change insignificantly.

All the bands observed can be separated into two groups. The first group contains completely polarized bands (transitions are allowed only for one polarization). The second group involves bands observed at different polarizations with close energies E_i but with different oscillator strengths f_i. These groups of effective oscillators are associated with interband transitions (or

Table 3. Parameters E_i (eV), H_i (eV), and f_i for O_i oscillators of zinc diphosphide

O_i	**E** || **c**, 80 K			**E** ⊥ **c**, 80 K		
	E_i	H_i	f_i	E_i	H_i	f_i
O_1	2.81	0.15	0.006	2.76	0.26	0.071
O_2	3.06	0.15	0.048	3.02	0.27	0.064
O_3	3.20	0.18	0.038	3.27	0.27	0.049
O_4	3.36	0.24	0.097	3.41	0.29	0.089
O_5	3.54	0.30	0.086	3.61	0.31	0.100
O_6	3.74	0.34	0.133	3.72	0.31	0.160
O_7	3.95	0.33	0.217	3.95	0.32	0.232
O_8	4.21	0.36	0.273	4.20	0.33	0.238
O_9	4.38	0.33	0.129	4.44	0.34	0.209
O_{10}	4.59	0.37	0.260	4.66	0.41	0.497
O_{11}	4.87	0.39	0.249	4.95	0.42	0.342
O_{12}	5.09	0.40	0.141	5.10	0.43	0.288

Table 4. Parameters E_i (eV), H_i (eV), and f_i for O_i oscillators of cadmium diphosphide

O_i	**E** ∥ **c**, 80 K			**E** ⊥ **c**, 80 K		
	E_i	H_i	f_i	E_i	H_i	f_i
O_1	2.47	0.24	0.018	2.57	0.14	0.071
O_2	2.75	0.23	0.045	2.79	0.19	0.025
O_3	2.91	0.23	0.081	2.89	0.22	0.056
O_4	3.05	0.24	0.064	3.06	0.26	0.105
O_5	3.28	0.34	0.206	3.33	0.32	0.307
O_6	3.44	0.31	0.048	3.41	0.26	0.076
O_7	3.59	0.35	0.224	3.62	0.38	0.453
O_8	3.92	0.34	0.218	3.90	0.36	0.473
O_9	4.12	0.29	0.092	4.13	0.29	0.249
O_{10}	4.28	0.39	0.289	4.35	0.42	0.942
O_{11}	4.59	0.37	0.351	4.62	0.34	0.481
O_{12}	4.89	0.36	0.342	4.92	0.40	0.572

with metastable excitons) characterized by close energies and oscillator strengths.

5. DISCUSSION

Earlier [8, 15], the specific features of the electronic structure of ZnP_2 and CdP_2 crystals were analyzed using only six peaks observed in the reflectance spectra at **E** ⊥ **c**. In [12], a similar analysis was performed with inclusion of 19 features revealed in the reflectance spectra for both polarizations. Figure 5 illustrates the correspondence between the energies of the ε_2 peaks of hypothetically identical nature, which were obtained in the present work. We analyzed the energies and intensities of 48 spectral features attributed to optical transitions in both crystals. Transitions whose energies in Fig. 5 are connected by straight lines have the same (or nearly the same) origin. For ZnP_2 crystals, virtually all spectral features are shifted toward the high-energy range by approximately 0.3 eV. However, certain pairs of oscillators are characterized by either smaller shifts (for example, by a shift of approximately 0.2 eV for O_1 and O_2 oscillators at (**E** ⊥ **c**) and for O_{12} at (**E** ∥ **c**) or even larger shifts (0.38 eV for O_3 at **E** ⊥ **c**). The absence of the spectral features associated with excitons suggests that the band gap is determined by indirect transitions. It can be seen that alternation of the ε_2 peaks is violated in the vicinity of E_g. Therefore, judging from the similarity of the optical functions of ZnP_2 and CdP_2 crystals, the structural similarity of their crystal lattices, and the similarity of the nature of the chemical bonds, we can assume that the energy bands of these crystals have a similar structure. This inference is confirmed by the band-structure calculations performed earlier in [9–12]. However, the electronic spectrum of each compound exhibits its own specific features that have defied simplified band calculation. Since the above anomalies are observed near E_g, it can be assumed that the upper valence bands or lower conduction bands at specific points (directions) of the Brillouin zone in both crystals possess quite a different topology. It is universally

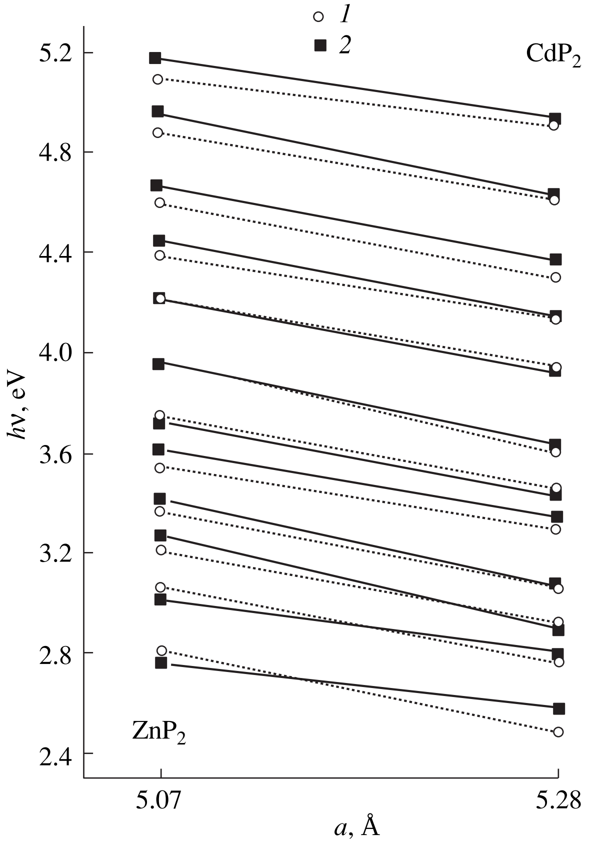

Fig. 5. Correspondence of the maxima of the components obtained upon resolution of the imaginary part of the dielectric function ε_2 for ZnP_2 and CdP_2 crystals at a temperature of 80 K. Polarization: (*1*) **E** ∥ **c** and (*2*) **E** ⊥ **c**.

accepted that a more correct calculation of the band structure of the crystals must include the results of analyzing the optical spectra. We believe that the results obtained in the present work for the first time can be used to determine the electronic structure of ZnP_2 and CdP_2 anisotropic crystals more precisely.

REFERENCES

1. V. B. Lazarev, V. Ya. Shevchenko, L. Kh. Grinberg, and V. V. Sobolev, *Semiconductor Compounds II–V* (Nauka, Moscow, 1976).
2. *Chemistry and Technology of Phosphides and Phosphorus-Containing Alloys: Collected Papers* (IPM Akad. Nauk Ukr. SSR, Kiev, 1979).
3. *Physics of Non-Tetrahedrally Bonded Elements and Binary Compounds*, Ed. by O. Madelung (Springer-Verlag, Berlin, 1983).
4. J. C. White, Acta Crystallogr. **18**, 217 (1965).
5. J. Horn, Bull. Acad. Pol. Sci., Ser. Sci. Chim. **17** (2), 69 (1969).
6. A. U. Sheleg, A. A. Kutas, and N. P. Tekhanovich, Phys. Status Solidi A **58**, K179 (1980).
7. K. B. Aleinikova, N. S. Rabotkina, A. V. Arsenov, and E. I. Zavalishin, in *Proceedings of the 1st International Symposium on the Physics and Chemistry of II–V Compounds, Mogilany, 1980*, p. 39.
8. V. V. Sobolev, N. N. Syrbu, and T. N. Sushkevich, Phys. Status Solidi B **43** (1), 73 (1971).
9. Yu. I. Polygalov, A. S. Poplavnoĭ, and V. E. Tupitsyn, Izv. Vyssh. Uchebn. Zaved., Fiz., No. 3, 123 (1981).
10. M. A. Bunin, A. I. Gusatinskiĭ, V. I. Minin, *et al.*, Fiz. Tekh. Poluprovodn. (Leningrad) **15** (8), 1617 (1981) [Sov. Phys. Semicond. **15**, 937 (1981)].
11. V. E. Tupitsyn, Yu. I. Polygalov, and A. S. Poplavnoĭ, Fiz. Tekh. Poluprovodn. (Leningrad) **15** (12), 2414 (1981) [Sov. Phys. Semicond. **15**, 1402 (1981)].
12. V. V. Sobolev, A. I. Kozlov, Iu. I. Polygalov, *et al.*, Phys. Status Solidi B **154**, 377 (1989).
13. L. A. Leznyak, Vestsi Akad. Navuk BSSR, No. 4, 91 (1985).
14. V. V. Sobolev and N. N. Syrbu, Phys. Status Solidi B **43** (1), K87 (1971).
15. V. V. Sobolev, N. N. Syrbu, and Ya. A. Ugai, Phys. Status Solidi **31**, K51 (1969).
16. G. Ambrazeavicius, G. Babonas, N. S. Korets, and S. Marcinkevicius, Litov. Fiz. Sb. **23** (3), 59 (1983).
17. A. I. Evstigneev, O. V. Snitko, V. G. Fedotov, *et al.*, Ukr. Fiz. Zh. **30** (3), 471 (1985).
18. V. V. Sobolev, A. I. Kozlov, I. I. Tychina, *et al.*, Zh. Prikl. Spektrosk. **38** (3), 504 (1983).
19. V. V. Sobolev, *Intrinsic Energy Levels of IV Solid Compounds* (Shtiintsa, Kishinev, 1978).
20. V. V. Sobolev and V. V. Nemoshkalenko, *Methods of Computational Physics in the Theory of Solids: The Electronic Structure of Semiconductors* (Naukova Dumka, Kiev, 1988).
21. B. F. Ormont, *Introduction to Physical Chemistry and Crystal Chemistry of Semiconductors* (Vysshaya Shkola, Moscow, 1982).

Translated by O. Borovik-Romanova

Physics of the Solid State, Vol. 44, No. 7, 2002, pp. 1263–1267. Translated from Fizika Tverdogo Tela, Vol. 44, No. 7, 2002, pp. 1211–1214.
Original Russian Text Copyright © 2002 by Kompan, Baĭkov, Melekh, Yakubovich.

Luminescence Spectra of Nominally Pure $BaCeO_3$ Perovskite Crystals

M. E. Kompan, Yu. M. Baĭkov, B. A.-T. Melekh, and A. V. Yakubovich

Ioffe Physicotechnical Institute, Russian Academy of Sciences,
Politekhnicheskaya ul. 26, St. Petersburg, 194021 Russia
e-mail: kompan@solid.ioffe.rssi.ru

Received October 16, 2001

Abstract—Luminescence spectra of barium cerate $BaCeO_3$, a starting material in the family of mixed conductors with protonic and oxygen conduction, are studied for the first time. The photoluminescence of this material is shown to be due to transitions involving cerium ions. A model of the recombination process is proposed. The luminescence of samples subjected to various post-growth treatments is measured, and the connection between the type of the treatment and the specific changes in the luminescence spectra is interpreted. *© 2002 MAIK "Nauka/Interperiodica".*

1. INTRODUCTION

Materials with ionic, including protonic, conduction exhibit properties that are unusual for most solids, which makes them interesting subjects for basic research and suggests promising applications. It is believed, in particular, that protonic conductors and mixed conductors with protonic conduction could play a key role in water vapor conversion systems, fuel elements, etc.

Progress along these lines depends substantially, however, on the extent to which the technological characteristics of these materials are known and on the possibility of preparing materials with required properties. The inherent ability of the compounds in this group to fairly easily lose or incorporate some species of atoms can both facilitate and hinder control of the properties of a given material. This applies particularly to materials whose constituent ions (atoms) have a considerable mobility and can also be present in gaseous form. In this case, spontaneous or properly controlled variation of the stoichiometry can also be effected in the post-growth period at comparatively low temperatures.

Barium cerate ($BaCeO_3$) is a starting material for the family of compounds with protonic conduction which can combine with electronic or hole conduction and with noticeable oxygen transport. The actual transport numbers depend on the temperature and material stoichiometry, the latter being dependent, in turn, on external conditions.

Since the discovery of protonic conduction in yttrium-doped barium cerate [1], hydrogen has been incorporated by bringing a material into contact with water vapor at an elevated temperature (~900 K). The fraction of vacancies on the oxygen sublattice plays a substantial role in this process; these vacancies are produced by deliberate doping of the material by rare-earth elements or yttrium in the course of synthesis. The incorporation of hydrogen proceeds in this case by the reaction

$$H_2O_{(gas)} + V_O^{++} + O_O \rightleftarrows 2(OH)_O^{+}. \qquad (1)$$

The charges in Eq. (1) are relative to the main charge of the corresponding lattice site [2]; V_O^{++} denotes the oxygen vacancy, which imparts an effective 2^+ charge to the now empty lattice site, and $(OH)_O^{+}$ is the OH^- group at the oxygen site; this group has a real negative unit charge and, thus, is positively singly charged with respect to the site it occupies, which actually belongs to the negatively doubly charged oxygen anion. According to this equation, two protons are incorporated together with one oxygen anion, thus ensuring overall charge neutrality. The OH^- anions sitting at the oxygen sites have a comparatively weakly bound proton, which provides a basis for the onset of hopping protonic conduction in the oxygen ion network.

High-melting barium cerate (>2500 K) has been available in the past only in the form of a ceramic. Recently, however, samples containing sufficiently large (a few millimeters in size) single crystals have been obtained by rf melting [3], which permits one to make reproducible measurements and, thus, to draw conclusions concerning the inherent bulk properties of this material.

The high hydrogen content revealed in nominally pure (undoped) crystals of this material came as a surprise, because this is at odds with the present-day ideas on the proton incorporation mechanism [4]. To begin with, this disagreed with the universally accepted mechanism of hydrogen incorporation into barium cerate.

We studied luminescence spectra of $BaCeO_3$ subjected to various thermochemical treatments, including saturation with hydrogen from water vapor. We isolated and identified the native luminescence of the material and traced the changes in the spectra to the specific features of the crystal state.

2. SAMPLES FOR THE STUDIES AND EXPERIMENTAL TECHNIQUE

Samples of crystalline barium cerate were obtained by direct cold-crucible rf melting [3] of a stoichiometric mixture of OSCh-grade cerium oxide and barium carbonate. The main part of the ingot thus obtained was a conglomerate of intergrown needle-shaped single crystals measuring about 1 mm in cross section. The central part of the ingot was, as a rule, straw-yellow in color; in some cases, however, the color of some regions of the ingot could be as dark as nearly black for the same compositions and conditions of synthesis. Annealing the material thus obtained in air at T = 1000 K for 4 h changed the color to yellow-orange. X-ray diffraction analysis showed the starting material to be pseudocubic with a lattice parameter a = 0.4396 nm, with the symmetry becoming orthorhombic after annealing in air.

The material was optically studied by photoluminescence spectroscopy. The luminescence was excited by a pulsed nitrogen laser (λ = 337 nm, pulse duration 6 ns). The studies were carried out in the temperature interval 78–300 K. The photoluminescence signal was detected with a FÉU-79 PM tube and isolated with a pulsed lock-in detector. The spectral data presented in this communication were not corrected for the spectral response of the instrument.

The technique of hydrogen incorporation was developed earlier in our studies of thermodesorption. Desorbed hydrogen and water were measured to monitor the course of incorporation. The incorporation techniques employed are described in [4, 5].

3. IDENTIFICATION OF THE LUMINESCENCE BAND

As far as we know, no studies of the barium cerate luminescence have been carried out before. The energy band gap of this material, as derived from optical absorption spectra presented in [6], is 4.1 eV at room temperature, with a temperature-induced shift of about 0.39 meV/K. This value provides an estimate for the possible spectral position of the edge luminescence.

A cerium ion that occupies a lattice site possesses, however, characteristic features which quite frequently determine some of the optical properties of cerium-containing materials. In particular, materials doped with trivalent cerium are mostly good luminophores [7, 8]. According to the $BaCeO_3$ formula, the valency (charge state) of cerium is four. However, ions of this element are capable of changing valency and exist in the Ce^{3+} state. When hydrogen is incorporated as a proton, the formation of the Ce^{3+} ion can ensure charge compensation without the attendant incorporation of the oxygen anion by the mechanism described by Eq. (1). Simultaneous detection of Ce^{3+} would prove the existence of a proton incorporation mechanism other than that in Eq. (1).

Experimentally, no room-temperature luminescence was revealed. At low temperatures (78 K), crystalline $BaCeO_3$ excited by light with wavelength 337 nm emits luminescence in the blue spectral region (curve *1* in Fig. 1). The luminescence band is a poorly resolved

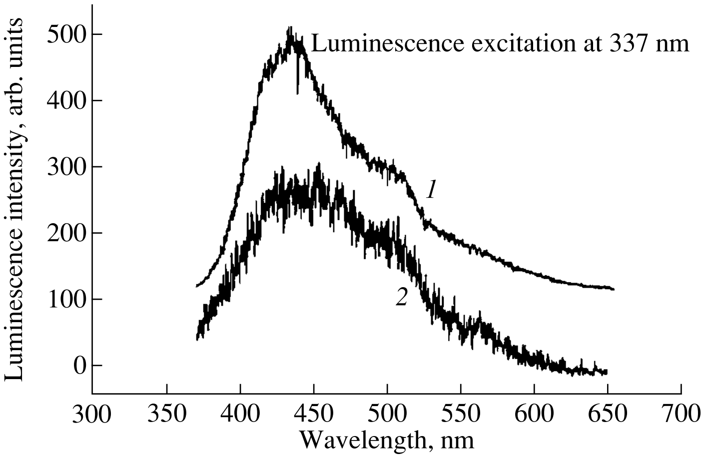

Fig. 1. Luminescence spectra of (*1*) crystalline barium cerate and (*2*) $ZrO_2/CaO : Ce^{3+}$ fianite measured at 78 K. The bands are seen to be almost the same.

doublet with the maxima peaking near 425 and 500 nm, the shorter wavelength component being more intense. The band is similar in shape and position to those observed in [7, 8] for the trivalent cerium ion. This gives us grounds to assign the short- and long-wavelength components of the band to the $^2D \longrightarrow 4F_{5/2}$ and $^2D \longrightarrow 4F_{7/2}$ transitions, respectively [7, 8]. To check the preliminary assignment of the band to the Ce^{3+} ion, we measured (in the same conditions) the luminescence of $ZrO_2/CaO : Ce^{3+}$ fianite doped with trivalent cerium. The spectrum of this sample is shown for comparison in Fig. 1 (curve *2*). Except for some fine-structure details, the spectra are seen to be essentially identical, thus validating the assignment of the observed barium cerate band to the recombination luminescence of the Ce^{3+} ions.

This interpretation permits one to consider the energy diagram of the levels involved in the optical transitions in more detail. We shall base our analysis on a scheme similar to the Born–Haber cycle [9, 10]. Let us consider a variant of this scheme presented in Fig. 2 as applied to this case.

According to this scheme, the level of the Ce^{3+} ion falls into the crystal band gap. Basically, Ce^{3+} ions should not be present in a stoichiometric composition; however, the Ce^{3+} state may come to life as a result of doping or of thermal or optical excitation. For instance, when barium cerate is doped by tantalum, one of the outer shell electrons does not form valence bonds and can be localized on a cerium ion with the attendant charge exchange,

$$Ce^{4+} + e^- \rightleftharpoons Ce^{3+}. \qquad (2)$$

In our case, the Ce^{3+} level is not strictly localized in these conditions, because cerium ions make up the crystal lattice. The presence of an electron in this level (and, thus, the formation of the Ce^{3+} ion in the crystal) indicates only local occupation of the corresponding level in the crystal.

The Ce^{3+} ion, in turn, can donate an electron to the conduction band. The ion involved, which was initially Ce^{3+}, becomes Ce^{4+}, and it becomes possible for the electron to move in the conduction band. The reverse process is a possible recombination mechanism. Considering that the Ce^{4+} density in the crystal is very high, of the order of 10^{22} cm^{-3}, the probability of this process may be expected to be high enough to make the corresponding recombination radiation experimentally observable.

Moreover, it may be conjectured that such a transition should dominate over interband recombination even in the case of direct band-to-band excitation, because electron encounter with a photoexcited hole should compete with the recombination process by the scheme of Eq. (2), which can take place at any point of the lattice. If the material is initially doped and Ce^{3+} ions are present with the valence band filled, this channel will be all the more dominant.

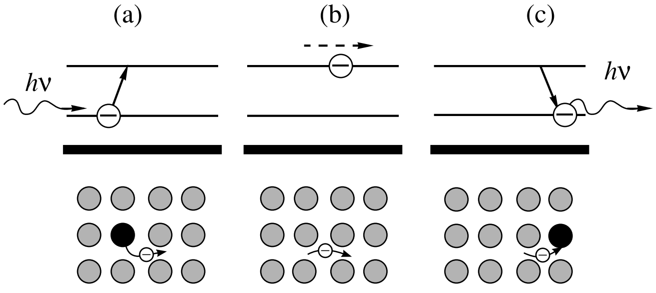

Fig. 2. Energy diagram illustrating the electronic transitions involved in the excitation and emission of the luminescence in barium cerate (the Born–Haber cycle). Bottom: charge exchange of the Ce^{3+} ion and its movement over the crystal accompanying the excitation and recombination in the electron subsystem; grey circles are Ce^{4+}, and black circles are Ce^{3+}. (a) An electron is excited from Ce^{3+}, which becomes Ce^{4+}; (b) an electron is in the conduction band, with no Ce^{3+} ions present in the local region; and (c) an electron recombines to form Ce^{3+}.

Let us compare the proposed model with the available numerical data on the energy parameters of $BaCeO_3$. As already mentioned, the optical band gap was found to be 4.1 eV [6]. The energy level of an electron localized with the Ce^{3+} formation (relative to the valence-band top) can be identified with the activation energy of hole conduction in $BaCeO_3$, $E_{a,h} = 0.7$ eV. Then, the energies of the optical photons accompanying the process described by Eq. (2) should be related through

$$E_{\mathrm{exc}} = 3.7 \geq E_g - E_{a,h} = 3.4 \geq 2.9 \text{ eV} = E_{\mathrm{lum}}. \qquad (3)$$

This relation states that the excitation energy of this transition cannot be less than the gap between the acceptor level and the conduction-band bottom and the luminescence photon cannot have a higher energy than this quantity. The relation is seen to be indeed satisfied, which is an argument for the proposed model of the transition.

4. LUMINESCENCE OF NOMINALLY PURE CRYSTALS

By determining the origin of the luminescence band, one can study the influence of technological prehistory on the crystal states. We may recall that one of our aims is to study the reasons for the irreproducibility of the characteristics of the crystals obtained by crucibleless high-temperature melting. As we will show below, the ambiguity is introduced in the last stage of the technological procedure, where a few hours of contact with the atmosphere in the laboratory at an elevated sample

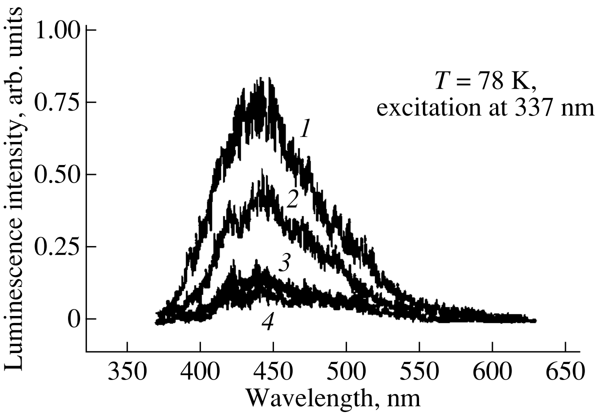

Fig. 3. Luminescence spectra of barium cerate crystals subjected to additional treatments are shown on the same scale. Spectra *1*, *2*, and *4* relate to a nominally undoped material, and spectrum *3* corresponds to a material doped originally with yttrium (10 at. %). Spectra *2* and *3* show the luminescence of reference samples not treated after their preparation. Spectrum *1* corresponds to the undoped sample annealed in water vapor, and *4* is the spectrum from part of the same sample annealed in dry oxygen.

temperature was enough to change various, including optical, characteristics of the materials.

To substantiate this statement, we compared the luminescence intensities in the Ce^{3+} band of different parts of two starting samples, namely, a nominally pure and an yttrium-doped barium cerate crystal undergoing different additional treatments. Six samples were used in a series of experiments, among which were three pieces of the undoped and three of the yttrium-doped $BaCeO_3$ (10 mol %) samples. Of each material, one sample was subjected to annealing in water vapor (during which the protons were introduced), one sample was annealed in dry oxygen, and one sample was used as a reference.

The experiment revealed a strong dependence of the luminescence intensity in the band corresponding to recombination through Ce^{3+} on the type of material and its technological prehistory. The undoped crystal initially exhibited a noticeable luminescence intensity in the range 400–500 nm. Annealing with proton incorporation (at 700 K and a water pressure of 2.7 kPa for 40 h) resulted in a twofold increase in the intensity of the band in question (curve *1* in Fig. 3). Annealing a similar sample in dry oxygen, which corresponds to achieving the maximum-valence states of the metals involved, reduced the intensity of the band by a factor of four to five. The spectrum of the yttrium-doped sample (curve *3*) contains weak components near 420 and 440 nm, but this spectrum changed only insignificantly under additional treatment.

5. DISCUSSION OF RESULTS

The results of our experiments fit into a common model which qualitatively describes the connection of the luminescence spectra with the technological prehistory of $BaCeO_3$ samples.

The starting samples obtained by high-temperature synthesis in air contain an uncontrollable amount of protons, because the water vapor pressure in laboratory air can be as high as 1.5–2.5 kPa. In the originally undoped samples, this incorporation of protons is due to the cerium being an intermediate-valence metal and proceeds through the formation of the Ce^{3+} ions. The reverse treatment, i.e., the oxidation, which removes protons from the sample, brings about luminescence quenching in the band under study.

The intensity of the band assigned to Ce^{3+} in the yttrium-doped sample is weak. This is only natural, because the incorporation of protons into samples of this type does not require a change in the valence state of the cerium ions [see [1] and Eq. (1)]. Moreover, the incorporation of trivalent yttrium ions into the material should hinder the introduction of other trivalent ions (cerium) simply by the Le Chatelier principle. A more rigorous analysis of the equilibrium made with due account of the Ce^{3+} concentration in the doped compound and based on the material balance and charge neutrality equations supports the above qualitative conclusion.

6. CONCLUSION

Thus, we studied the luminescence of the $BaCeO_3$ perovskite, which is a starting material for the family of proton-conducting perovskites. A luminescence band was found in the range 420–480 nm; this band was shown to originate from recombination through the cerium ion in another valence state, Ce^{3+}. It was established that incorporation of hydrogen into a barium cerate sample not deliberately doped entails charge exchange of the tetravalent cerium to Ce^{3+}, a process providing charge compensation when protons are incorporated into the lattice. It was also shown that the nominally pure material obtained in high-temperature synthesis can contain an uncontrollable amount of introduced protons. To obtain more accurate results, the material should be additionally normalized to remove this ambiguity, for instance, by annealing it in dry oxygen, the procedure used by us.

ACKNOWLEDGMENTS

The authors are indebted to V.P. Gorelov for valuable discussions.

This study was supported by the Russian Foundation for Basic Research (project no. 00-03-32476) and, partially, by INTAS (grant no. 99-0636).

REFERENCES

1. A. V. Strelkov, A. R. Kaul’, and E. K. Shalkova, in *Proceedings of the IX All-Union Conference on Physical Chemistry and Electrochemistry of Melts and Solid Electrolytes, 1986*, Vol. III, Part I.
2. F. A. Kröger and H. J. Vink, Solid State Phys. **3**, 307 (1957).
3. E. K. Shalkova, Yu. M. Baĭkov, B. A.-T. Melekh, *et al.*, Zh. Neorg. Khim. **35**, 262 (1990).
4. Yu. M. Baĭkov, V. M. Egorov, N. F. Kartenko, *et al.*, Pis’ma Zh. Tekh. Fiz. **22** (11), 91 (1996) [Tech. Phys. Lett. **22**, 476 (1996)].
5. Yu. M. Baikov and E. K. Shalkova, J. Solid State Chem. **97**, 224 (1992).
6. T. He, P. Ehrhart, and P. Meuffeis, J. Appl. Phys. **79**, 3219 (1996).
7. S. Okamoto, K. Tanaka, and Y. Inoue, Appl. Phys. Lett. **76**, 946 (2002).
8. M. Raukas, S. A. Basun, W. van Schaik, *et al.*, Appl. Phys. Lett. **69**, 3300 (1996).
9. M. Born, Verh. Dtsch. Phys. Ges. **21**, 679 (1919).
10. F. Haber, Verh. Dtsch. Phys. Ges. **21**, 650 (1919).

Translated by G. Skrebtsov

Physics of the Solid State, Vol. 44, No. 7, 2002, pp. 1268–1277. Translated from Fizika Tverdogo Tela, Vol. 44, No. 7, 2002, pp. 1215–1223.
Original Russian Text Copyright © 2002 by Antsygina, Poltavskaya, Chishko.

DEFECTS, DISLOCATIONS, AND PHYSICS OF STRENGTH

Interaction of Translational and Rotational Modes of a Molecular Impurity in Two-Dimensional Atomic Crystals

T. N. Antsygina, M. I. Poltavskaya, and K. A. Chishko
Verkin Institute of Low-Temperature Physics and Engineering, National Academy of Sciences of Ukraine, Kharkov, 61103 Ukraine
e-mail: chishko@ilt.kharkov.ua

Received October 3, 2001

Abstract—The interaction between the translational and rotational degrees of freedom of a diatomic homonuclear molecule that executes a motion at the site of a two-dimensional close-packed atomic matrix located on a close-packed atomic substrate (a molecular substitutional impurity in the crystal field of the two-dimensional lattice of a solidified rare gas) is investigated theoretically. The relationships describing the effective dynamic properties of an impurity rotator in the presence of translational excitations of its center of inertia are derived in the framework of consistent procedures on the basis of the Lagrangian (the functional-integral method) and Hamiltonian (the canonical-transformation method) formalisms. The inclusion of the translational–rotational interaction leads to a radical change in the inertial properties of the molecule. This manifests itself in a change in the form of the operator for the rotational kinetic energy as compared to the corresponding expression for a free rotator. The inertia tensor components for the molecule become functions of molecular orientation, and the molecule, in terms of rotational motion, transforms into a "parametric rotator" whose effective kinetic energy is represented as a generalized quadratic form of the angular momentum (or the angular velocity) components with a symmetry corresponding to the symmetry of the external crystal field. The translational–rotational interaction also results in the renormalization of the parameters of the crystal potential without a change in its initial form. *© 2002 MAIK "Nauka/Interperiodica".*

1. INTRODUCTION

The effects associated with the interaction between translational and rotational degrees of freedom in molecular crystals and solid solutions containing molecular components manifest themselves in many physical properties of these solids [1]. Examples are provided by the low-frequency anomalies of the transverse phonon modes in molecular and ionic–molecular lattices, the specific features in the temperature dependences of the elastic moduli for a number of molecular crystals, structural distortion of the orientationally ordered phases due to phonon–libron interaction, etc. (see [1] and references therein). The aforementioned effects are best understood in classical solids. However, there are a number of works devoted to the investigation of these phenomena in molecular cryocrystals [2, 3]. Apart from the results regarding the thermodynamics of cryosystems in the presence of phonon–libron interaction, the problems of inelastic phonon scattering by rotational degrees of freedom of individual molecules [4–7] and molecular complexes [8, 9] have been solved for these objects. It should be emphasized that it is these cryocrystals that appear to be the most appropriate objects for the investigation of the effects under consideration. This can be explained by the fact that, in these systems, phonons and librons are the sole possible types of collective excitations. Moreover, the conditions favorable for observing specific quantum effects that have no analogs in classical solids can be achieved at low temperatures.

Solid solutions of homonuclear and heteronuclear molecules in atomic matrices composed of solidified rare gases form a particular group of objects whose properties can be substantially affected by translational–rotational interaction.

As was shown earlier in [10–15], the rotational constant B of an impurity and the crystal field constant $\mathcal{K}$ in three-dimensional solutions prove to be extremely sensitive to the presence of translational modes in the lattice. In particular, the interaction between a molecule rotator and short-wavelength phonons leads to the fact that the values of B and $\mathcal{K}$ for an impurity in the atomic cryomatrix differ significantly from those for a free molecule [13–15]. Consideration of this circumstance made it possible to interpret successfully the experimental data on the heat capacity of Ar(Kr)–$N_2(O_2)$ solutions [12, 14, 15].

Two-dimensional cryosolutions involving molecular impurities are substantially more complicated systems. These systems are prepared by applying atomic–molecular mixtures on substrates (most frequently represented by graphite and some metals) [16–28]. In this case, the two-dimensional sample under investigation, as a rule, is produced not on a crystalline substrate but is applied on a sublayer consisting of atoms of the same inert element that forms the matrix of the two-dimensional solution. In the two-dimensional system, the impurity motion in the direction perpendicular to the layer is less hindered than that in a bulk crystal and the translational oscillations are characterized by low frequencies. Moreover, since the potential in which the impurity moves has no inversion center, any rotation of the rotator is accompanied by the displacement of its center of inertia and, vice versa, the displacement of the center of inertia of the molecule leads to its simultaneous rotation. Therefore, oscillations of the center of inertia of the impurity molecule are related directly to the molecular rotational degrees of freedom and the rotation of the impurity cannot be considered by disregarding the interaction with displacements of the molecule as a whole.

As a consequence, the dynamics of the impurity molecule in the two-dimensional solution appears to be substantially more complex than that in the three-dimensional system. This can appreciably affect the behavior of all physical characteristics. At present, the above problem has not been adequately studied. The purpose of the present work is to fill this gap.

2. FORMULATION OF THE PROBLEM

Let us consider the problem of motion of a diatomic homonuclear molecule in a two-dimensional close-packed monoatomic matrix (a solidified rare gas) located on a substrate composed of atoms of the same compound. The interaction between the impurity and the environment will be included in the atom–atom potential approximation [29]. In the system under consideration, the interactions of the impurity with the matrix and the substrate can be described by potentials of the same type (for example, the Lenard-Jones potential). Note that, in the general case, the parameters of the potentials corresponding to the impurity–matrix and impurity–substrate interactions should be treated as being different.

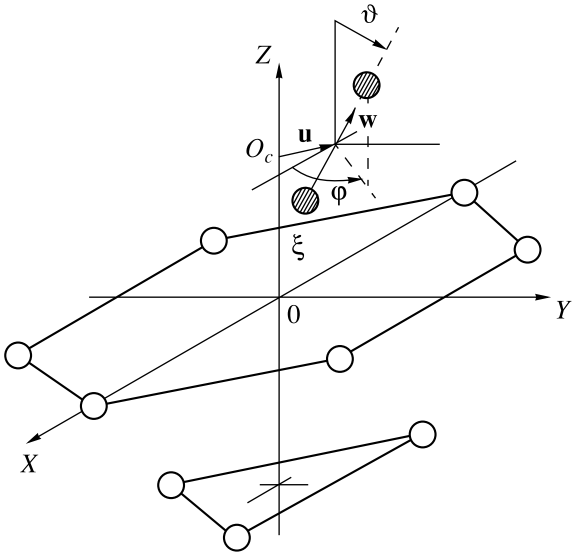

A geometry of the problem (the meaning of all the designations is given in the text).

It is assumed that the origin of the coordinates is located at a lattice site in which a matrix atom is replaced by a diatomic homonuclear impurity molecule with mass M and internuclear distance $2d$. The configuration of the system is displayed in the figure. The matrix and the substrate represent two-dimensional atomic layers with a triangular lattice. The $0Z$ axis of the Cartesian coordinate system is perpendicular to the atomic layers, and the $0X$ and $0Y$ axes are oriented along the matrix plane. The interatomic distances in both the matrix and the substrate are equal to R_1, and the distance between the layer and substrate is defined as $c = \gamma R_1$ (for a perfect close packing of hard spheres, $\gamma = \sqrt{2/3}$). Since the parameters of the interaction of matrix atoms with each other and with the impurity molecule are different, the equilibrium position O_c of the center of inertia of the impurity does not coincide with the layer plane $z = 0$. From simple symmetrical considerations, the point O_c lies on the $0Z$ axis at a certain distance z_0 from the origin of the coordinates.

The complete Hamiltonian of the impurity–matrix–substrate system has the form

$$H = \frac{\hat{\mathbf{P}}^2}{2M} + B\hat{\mathbf{L}}^2 + U. \qquad (1)$$

Hereafter, we will use a system of units in which the Planck and Boltzmann constants are equal to unity. The first term in formula (1) is the translational kinetic energy for the center of inertia of the molecule. The quantity $\hat{\mathbf{P}} = -i\partial/\partial\mathbf{u}$ is the momentum of the impurity, and $\mathbf{u}$ is the displacement of the center of inertia of the impurity from the equilibrium position O_c. The second term in Hamiltonian (1) is the rotational kinetic energy for the impurity molecule. In this case, $B = 1/(2J)$ is the rotational constant, $J = Md^2$ is the moment of inertia of the impurity, and $\hat{\mathbf{L}}^2$ is the square of the angular momentum of the impurity, which can be represented in the form

$$\hat{\mathbf{L}}^2 = -\left[\frac{1}{\sin\vartheta}\frac{\partial}{\partial\vartheta}\left(\sin\vartheta\frac{\partial}{\partial\vartheta}\right) + \frac{1}{\sin^2\vartheta}\frac{\partial^2}{\partial\varphi^2}\right]. \qquad (2)$$

Here, the angles ϑ and φ, which specify the orientation of the rotator, are determined as follows: the ϑ angle is measured from the $0Z$ axis and the φ angle is reckoned from the $0X$ axis.

The last term in relationship (1) describes the interaction of the impurity with the matrix and substrate atoms and can be written as

$$U = \sum_{\boldsymbol{\delta}} \{ V_1(|R_1\boldsymbol{\delta} - \mathbf{R}_a|) + V_1(R_1\boldsymbol{\delta} - \mathbf{R}_b) \} + \sum_{\boldsymbol{\Delta}} \{ V_2(|R_2\boldsymbol{\Delta} - \mathbf{R}_a|) + V_2(R_2\boldsymbol{\Delta} - \mathbf{R}_b) \}, \tag{3}$$

where V_1 is the potential of the interaction between the impurity and matrix atoms, V_2 is the potential of the interaction between the impurity and substrate atoms, R_2 is the distance from the origin of the coordinates to the nearest neighbors in the substrate, and $\boldsymbol{\delta}$ and $\boldsymbol{\Delta}$ are the unit vectors specifying the direction to the nearest neighbors in the layer and the substrate, that is,

$$\delta_{1,2} = (\pm 1, 0, 0), \quad \delta_{3,4,5,6} = \left(\pm\frac{1}{2}, \pm\frac{\sqrt{3}}{2}, 0\right),$$
$$\Delta_{1,2} = b\left(\pm\frac{\sqrt{3}}{2}, \frac{1}{2}, -\gamma\sqrt{3}\right), \tag{4}$$
$$\Delta_3 = b(0, -1, -\gamma\sqrt{3}), \quad b = (1 + 3\gamma^2)^{-1/2}.$$

The atomic coordinates in the molecule are written in the form

$$\mathbf{R}_{a,b} = \mathbf{R}_0 + \mathbf{u} \pm \mathbf{w}d, \tag{5}$$

where $\mathbf{w} = (\sin\vartheta\cos\varphi, \sin\vartheta\sin\varphi, \cos\vartheta)$ is the unit vector specifying the spatial orientation of the impurity molecule and $\mathbf{R}_0 = (0, 0, z_0)$ is the coordinate of the equilibrium position of the center of inertia of the molecule.

Since the potentials $V_1(R)$ and $V_2(R)$ are short-range potentials, it is sufficient to include only the nearest neighbors in Hamiltonian (1). In the system under consideration, the impurity molecule has six neighbors in the matrix (in the layer, the coordination number $z_1 = 6$) and three neighbors in the substrate (the coordination number $z_2 = 3$). Note also that the theory proposed below, in principle, is valid for short-range potentials $V_1(R)$ and $V_2(R)$ of an arbitrary type. Hence, all further calculations will be carried out without specifying the form of these potentials. The explicit form of an interatomic interaction potential is necessary only for performing numerical calculations for particular systems.

In relationship (3), the interaction of the impurity molecule with the neighbors is included in the quasi-static approximation, i.e., under the assumption that atoms of the crystalline environment are immobile. This implies that we ignore features of the interaction between the impurity and phonons of the matrix and restrict our consideration to the case of atom–atom potentials in the self-consistent field approximation by assuming that phonon excitations of the matrix lead only to the renormalization of the rotational constant B and the crystal field amplitude [15, 30]. For the problem under investigation, this approach appears to be quite justified, because the effect of oscillations of the center of inertia of the impurity is maximum at sufficiently low frequencies, whereas the interaction with phonons significantly affects the impurity motion due to the contribution of high-frequency excitations of the matrix [15, 30].

The relationships presented in this section in the general form represent the problem of the motion of a diatomic homonuclear impurity in a two-dimensional crystal on the substrate. However, this statement of the problem does not allow us to obtain its analytical solution, because the interaction between the orientational and translational degrees of freedom substantially complicates the dynamics of motion of the impurity molecule.

The dynamics of the system under investigation can be analytically described only with due regard for additional physical considerations to simplify the problem.

3. POTENTIAL ENERGY FOR THE IMPURITY–MATRIX–SUBSTRATE SYSTEM

The low-temperature range $T \leq B$ is of prime (both theoretical and experimental) interest, because it is in this range that the dependences of many physical characteristics of the system exhibit the most pronounced nontrivial behavior; in particular, anomalies are observed in the impurity heat capacity, etc. [31, 32]. In the studied system at given temperatures, the center of inertia of the oscillating impurity molecule is displaced from the equilibrium position by the distances u, which are small compared to the lattice parameter R_1; i.e., $u/R_1 \ll 1$. The ratio d/R_1 should be regarded as the second inherent small parameter of the problem.

By using relationship (5), potential (3) can be represented in the form

$$U = \sum_{\mathbf{n}} \{ V_1(|\rho_1\mathbf{n} + \mathbf{w}d - \mathbf{u}|) + V_1(|\rho_1\mathbf{n} - \mathbf{w}d - \mathbf{u}|) \} + \sum_{\mathbf{N}} \{ V_2(|\rho_2\mathbf{N} + \mathbf{w}d - \mathbf{u}|) + V_2(|\rho_2\mathbf{N} - \mathbf{w}d - \mathbf{u}|) \}, \tag{6}$$

where

$$\rho_1\mathbf{n} = R_1\boldsymbol{\delta} - \mathbf{R}_0, \quad \rho_2\mathbf{N} = R_2\boldsymbol{\Delta} - \mathbf{R}_0.$$

Here, $\mathbf{n}$ and $\mathbf{N}$ are the unit vectors that specify the directions from the equilibrium position O_c of the center of inertia of the impurity to the sites corresponding to the nearest neighbors in the layer and the substrate, respectively; that is,

$$\mathbf{n}_{1,2} = b_1(\pm 1, 0, -\zeta), \quad \mathbf{n}_{3,4,5,6} = b_1\left(\pm\frac{1}{2}, \pm\frac{\sqrt{3}}{2}, -\zeta\right),$$
$$\mathbf{N}_{1,2} = b_2\left(\pm\frac{\sqrt{3}}{2}, \frac{1}{2}, -\sqrt{3}(\gamma+\zeta)\right), \tag{7}$$
$$\mathbf{N}_3 = b_2(0, -1, -\sqrt{3}(\gamma+\zeta)),$$

where

$$\zeta = \frac{z_0}{R_1}, \quad b_1 = (1+\zeta^2)^{-1/2}, \quad b_2 = [1+3(\gamma+\zeta)^2]^{-1/2}.$$

Now, we expand potential (6) into a series in terms of small additions $|\mathbf{u} \pm \mathbf{w}d| \ll \rho_{1,2}$. In the fourth order, we have

$$U = \sum_{a=0}^{4} V^{(a)}(\mathbf{u}, \mathbf{w}), \tag{8}$$

where the subscript a indicates the order of smallness of the corresponding term in relationship (6). The potential should be expanded up to the fourth-order terms, because it is these terms which account for a nontrivial angular dependence of the crystal field for the impurity that essentially affects the rotational spectrum of the impurity molecule [15]. The zeroth-order term in expression (8) is an insignificant constant and can be omitted. The first-order term, which is independent of the molecular orientation, can be written as

$$V^{(1)}(\mathbf{u}) = -2\left[D_1^{(1)}\sum_{\mathbf{n}}(\mathbf{nu}) + D_2^{(1)}\sum_{\mathbf{N}}(\mathbf{Nu})\right]. \tag{9}$$

In what follows, we will use the designation

$$D_\alpha^{(m)} = \frac{\partial^m V_\alpha(\rho_\alpha)}{\partial \rho_\alpha^m}, \tag{10}$$

where the subscript α is equal to 1 for quantities referring to the matrix and 2 for quantities relating to the substrate. The superscript m = 1, 2, 3, and 4 indicates the order of the derivative. For subsequent consideration, it is expedient to note the following facts. As is seen from definition (7), the Z components of all the vectors $\mathbf{n}_i$ (i = 1, …, 6) are equal to each other. The same holds for the vectors $\mathbf{N}_i$ (i = 1, 2, and 3). In order to simplify the representation, these components are conveniently designated as follows:

$$p_1 = -b_1\zeta, \quad p_2 = -\sqrt{3}b_2(\gamma+\zeta). \tag{11}$$

The condition for equilibrium of the center of inertia of the molecule is that relationship (9) be equal to zero. This leads to the equation

$$\sum_{\alpha=1,2} z_\alpha p_\alpha D_\alpha^{(1)} = 0, \tag{12}$$

which determines the parameter ζ. The magnitude and sign of the ζ parameter considerably depend on the matrix and the substrate material. The estimates made for real systems of the Ar(Kr, Xe)–N_2(O_2) type demonstrate that the heavier the matrix atoms, the closer the equilibrium position of the impurity to the layer plane. In the case of very heavy atoms, for example, Xe, the center of inertia of the molecule is located between the layer and substrate; i.e., the ζ parameter has a negative sign.

After a number of transformations, the second-order term takes the form

$$V^{(2)}(\mathbf{u}, \mathbf{w}) = \frac{G_z + G_0}{2}(u_x^2 + u_y^2) + \frac{G_z}{2}u_z^2 - \frac{G_0 d^2}{2}w_z^2. \tag{13}$$

Here,

$$G_0 = \sum_{\alpha=1,2} z_\alpha A_\alpha(3b_\alpha^2 - 2),$$
$$G_z = 2\sum_{\alpha=1,2} z_\alpha(D_\alpha^{(2)} - b_\alpha^2 A_\alpha), \tag{14}$$

where

$$A_\alpha = D_\alpha^{(2)} - D_\alpha^{(1)}/\rho_\alpha.$$

Note that the coefficients G_0 and G_z in formula (13) have a positive sign. It follows from expression (13) that, to the second order in the parameters d/R_1 and u/R_1, the translational and rotational motions of the impurity molecule are independent. In this case, the center of inertia of the molecule moves like an anisotropic spatial oscillator.

The interaction between the translational and rotational degrees of freedom of the molecule arises beginning with the third-order terms. We will restrict our consideration of this interaction to the main approximation (linear in $\mathbf{u}$). By ignoring the terms cubic in $\mathbf{u}$, which describe the anharmonicity of oscillatory motion of the center of inertia of the impurity and are of no interest in our problem, the third-order term can be represented by the expression

$$V^{(3)}(\mathbf{u}, \mathbf{w}) \equiv H_{\text{int}} = -d^2 \sum_\nu f_\nu u_\nu, \quad \nu = x, y, z. \tag{15}$$

Here,

$$f_\nu = \left(K_0 + \frac{K_1}{3}\right)\Delta_{\nu z} + \sum_{ij} \Gamma_\nu^{ij} Q_{ij}(\mathbf{w}), \qquad (16)$$

where Q_{ij} is the dimensionless quadrupole molecule moment written as

$$Q_{ij} = w_i w_j - \Delta_{ij}/3, \qquad (17)$$

Δ_{ij} is the Kronecker symbol (i, $j = x$, y, and z), and the matrices Γ_ν^{ij} have the form

$$\Gamma_x = \begin{pmatrix} 0 & K_2 & K_0 \\ K_2 & 0 & 0 \\ K_0 & 0 & 0 \end{pmatrix}, \quad \Gamma_y = \begin{pmatrix} K_2 & 0 & 0 \\ 0 & -K_2 & K_0 \\ 0 & K_0 & 0 \end{pmatrix}, \qquad (18)$$

$$\Gamma_z = \begin{pmatrix} 0 & 0 & 0 \\ 0 & 0 & 0 \\ 0 & 0 & K_1 \end{pmatrix}.$$

The quantities K_0, K_1, and K_2 are defined by the relationships

$$K_0 = \frac{1}{2}\sum_{\alpha = 1, 2} z_\alpha p_\alpha \left[D_\alpha^{(3)} b_\alpha^2 + \frac{A_\alpha}{\rho_\alpha}(2 - 3b_\alpha^2)\right],$$

$$K_1 = \sum_{\alpha = 1, 2} z_\alpha p_\alpha \left(D_\alpha^{(3)} + 2\frac{A_\alpha}{\rho_\alpha}\right) - 3K_0$$

$$= \frac{1}{2}\sum_{\alpha = 1, 2} z_\alpha p_\alpha \left[D_\alpha^{(3)}(2 - 3b_\alpha^2) + \frac{A_\alpha}{\rho_\alpha}(2 - 9b_\alpha^2)\right], \qquad (19)$$

$$K_2 = \frac{b_2^3}{4} z_2 \left(D_2^{(3)} - 3\frac{A_2}{\rho_2}\right).$$

The first term in expression (16) is independent of the molecular orientation and can be taken into account by two methods. On the one hand, this term can be introduced into the equilibrium condition (12), which results in a small correction $\sim(d/\rho_\alpha)^2$ to the parameter ζ. Since the parameter ζ enters into the coefficients G_0 and G_z, the corresponding correction also arises in these coefficients. On the other hand, for the unchanged equilibrium condition (12), the first term in expression (16) can be retained and taken into consideration interchangeably with the other terms that are dependent on **w**. In this case, we also obtain the correction $\sim(d/\rho_\alpha)^2$ to the coefficients G_0 and G_z. This correction precisely coincides with that derived in the first case. Therefore, both methods of including the contribution of the first term in expression (16) lead to the same result. In what follows, we will use the second method, which seems to be more reasonable.

The fourth-order terms in the potential energy of the impurity–matrix–substrate system can be represented by the expression

$$V^{(4)}(\mathbf{w}) = \frac{d^4}{12}[G_1 w_z^4 + G_s w_y w_z (3w_x^2 - w_y^2) + G_2 w_z^2]. \qquad (20)$$

Here,

$$G_1 = \frac{1}{8}\sum_{\alpha = 1, 2} z_\alpha \mathcal{P}_\alpha (35 b_\alpha^4 - 40 b_\alpha^2 + 8),$$

$$\mathcal{P}_\alpha = D_\alpha^{(4)} - \frac{6D_\alpha^{(3)}}{\rho_\alpha} + \frac{15A_\alpha}{\rho_\alpha^2}, \qquad (21)$$

$$G_s = b_2^3 z_2 p_2 \mathcal{P}_2,$$

$$G_2 = 3\sum_{\alpha = 1, 2} \frac{z_\alpha}{\rho_\alpha}(2 - 3b_\alpha^2)\left(D_\alpha^{(3)} - \frac{3A_\alpha}{\rho_\alpha}\right).$$

When writing expression (20), we retained only the terms that refer to the crystal field and determine the nontrivial angular dependence of the potential energy for the rotator. Particularly, in formula (20), the second term associated with the substrate leads to lowering of the symmetry of the system (to the symmetry group S_6) and to removal of the degeneracy of the z component of the impurity angular momentum. The term applying the correction $\sim(d/\rho_\alpha)^2$ to the coefficient G_0 was also retained in expression (20). We disregarded the terms ($\sim u_\nu^4$) that correspond to the fourth-order anharmonicities and the terms that describe the translational–rotational interaction and have orders higher than those in relationship (15). The corrections associated with these terms, if required, can be allowed for in terms of the perturbation theory.

Hence, with allowance made for the foregoing, Hamiltonian (1) of the system takes the following form:

$$H = B\hat{\mathbf{L}}^2 + H_{\text{tr}} + H_{\text{int}} + H_c. \qquad (22)$$

Here,

$$H_{\text{tr}} = \frac{1}{2}\sum_\nu \left(\frac{\hat{P}_\nu^2}{M} + M\Omega_\nu^2 u_\nu^2\right), \qquad (23)$$

where

$$\Omega_x^2 = \Omega_y^2 = \frac{G_z + G_0}{M} = \Omega_\perp^2, \quad \Omega_z^2 = \frac{G_z}{M}. \qquad (24)$$

The term H_c is given by

$$H_c = -\frac{\tilde{G}_0 d^2}{2} w_z^2 + \frac{d^4}{12}[G_1 w_z^4 + G_s w_y w_z (3w_x^2 - w_y^2)], \qquad (25)$$

$$\tilde{G}_0 = G_0 - \frac{d^2 G_2}{6},$$

and the term H_{int} is defined by relationship (15). The coefficients $\tilde{G}_0$ and G_1 in expression (25) are of positive sign, and the coefficient G_s is of negative sign. From relationships (14) and (21), it is seen that the first two terms in expression (25) are determined by the matrix and the substrate, whereas the last term with a lower symmetry (the symmetry group S_6) is associated only with the crystal field of the substrate. The coefficient of the last term is one order of magnitude less than the coefficients of the first two terms.

In the case when the center of inertia of the impurity molecule is fixed and located at the origin of the coordinates, the rotational part of Hamiltonian (22) transforms to the corresponding relationship obtained in [31].

As follows from expression (24), the translational frequency Ω_z is always lower than the frequency $\Omega_\perp$. Physically, this result is quite obvious, because the motion in the direction perpendicular to the layer is less hindered compared to that in the layer plane. It is of interest that, as the mass of atoms forming the matrix and substrate increases, the frequency Ω_z increases monotonically, whereas the frequency $\Omega_\perp$ decreases monotonically.

In order to analyze how the oscillatory motion of the center of inertia of the molecule affects its rotation, we will use two methods, namely, the functional-integral and canonical-transformation approaches.

4. THE FUNCTIONAL-INTEGRAL METHOD

In this section, we will formally separate the translational and rotational degrees of freedom in the framework of the functional-integral method. In this method, the partition function Z of the system under consideration has the following form within an insignificant normalizing factor [30]:

$$Z = \int \mathcal{D}[\mathbf{u}(\tau)]\mathcal{D}[\mathbf{w}(\tau)]\exp(S), \qquad (26)$$

where the total action for the impurity

$$S = \int_0^\beta d\tau \mathcal{L}(\tau), \quad \beta = 1/T$$

is expressed through the Lagrangian $\mathcal{L}(\tau)$, which depends on the imaginary time τ and has the form

$$\mathcal{L} = \mathcal{L}_{\text{tr}} + \mathcal{L}_{\text{rot}} + \mathcal{L}_{\text{int}} + \mathcal{L}_c. \qquad (27)$$

Here,

$$\mathcal{L}_{\text{tr}} = -\frac{M}{2}\sum_\nu (\dot{u}_\nu^2 + \Omega_\nu^2 u_\nu^2),$$
$$\mathcal{L}_{\text{int}} = -H_{\text{int}}, \quad \mathcal{L}_c = -H_c, \qquad (28)$$

$$\mathcal{L}_{\text{rot}} = -\frac{J}{2}\left(\frac{\partial \mathbf{w}}{\partial \tau}\right)^2 = -\frac{J}{2}(\dot{\vartheta}^2 + \dot{\varphi}^2 \sin^2\vartheta), \qquad (29)$$

and the dot means differentiation with respect to τ.

With the aim of eliminating the translational degrees of freedom, we represent the total action S as the sum of two terms. The first term S_0 depends only on the rotational degrees of freedom and the second term S_1 includes both rotational and translational degrees of freedom, that is,

$$S_0 = \int_0^\beta d\tau(\mathcal{L}_{\text{rot}} + \mathcal{L}_c), \quad S_1 = \int_0^\beta d\tau(\mathcal{L}_{\text{tr}} + \mathcal{L}_{\text{int}}).$$

Let now us expand $u_\nu(\tau)$ (entering into S_1) into a series in terms of the Matsubara frequencies $\omega_n = 2\pi n T$ ($n = 0, \pm1, \ldots$), that is,

$$u_\nu(\tau) = T\sum_n \xi_\nu(\omega_n)\exp(-i\omega_n\tau),$$

$$\xi_\nu(\omega_n) = \int_0^\beta d\tau u_\nu(\tau)\exp(i\omega_n\tau).$$

Next, in integral (26), we change the variables

$$\tilde{\xi}_\nu(\omega_n) = \xi_\nu(\omega_n) - \frac{d^2}{M}\frac{\mathcal{F}_\nu(\omega_n)}{\omega_n^2 + \Omega_\nu^2}, \qquad (30)$$

where $\mathcal{F}_\nu(\omega_n)$ are the transforms of components (16) of the vector $f_\nu(\tau)$. After integration over the translational variables, the partition function (26) takes the form of the product $Z = Z_{\text{tr}} Z_1$, where the first multiplier accounts for the oscillatory motion of the center of inertia of the molecule and represents the partition function of an oscillator [33]. The second multiplier is defined by the expression

$$Z_1 = \int \mathcal{D}[\mathbf{w}(\tau)]\exp(S_0 + \Delta S), \qquad (31)$$

where the term

$$\Delta S = \frac{Td^4}{2M}\sum_\nu\sum_n \frac{\mathcal{F}_\nu(\omega_n)\mathcal{F}_\nu(-\omega_n)}{\omega_n^2 + \Omega_\nu^2} \qquad (32)$$

describes the rotation of the molecule with allowance made for the influence of oscillations of the center of inertia on the rotation. In our problem, the translational frequencies Ω_ν are the largest energy parameters. On the other hand, as was noted above, our interest here is in the temperature range $T \leq B$; hence, the temperature in the given problem is the smallest energy parameter. On this basis, by analogy with the rearrangement performed in [30], after the inverse transformation with respect to time, we obtain the following relationship for the additional term:

$$\Delta S = \frac{d^4}{2M}\sum_{\nu}\frac{1}{\Omega_{\nu}^2}\int_0^{\beta} d\tau\, f_{\nu}(\tau)^2 - \frac{d^4}{2M}\sum_{\nu}\frac{1}{\Omega_{\nu}^4}\int_0^{\beta} d\tau\, \dot{f}_{\nu}(\tau)^2. \quad (33)$$

The terms in relationship (33) describe essentially different effects. The first term contains the additive constant that shifts the energy origin and also the components that renormalize the coefficients $\tilde{G}_0$, G_1, and G_s in expression (25) for the crystal field. After a number of manipulations with the use of formulas (16) and (18), the corresponding corrections can be represented in the form

$$\Delta\tilde{G}_0 = \frac{2d^2}{M}\left(\frac{2K_0^2 - K_2^2}{\Omega_{\perp}^2} + \frac{K_0K_1}{\Omega_z^2}\right),$$
$$\Delta G_1 = \frac{6}{M}\left(\frac{4K_0^2 - K_2^2}{\Omega_{\perp}^2} - \frac{K_1^2}{\Omega_z^2}\right), \quad \Delta G_s = -\frac{24K_0K_2}{M\Omega_{\perp}^2}. \quad (34)$$

From expressions (14), (21), and (34), it follows that the correction $\Delta\tilde{G}_0$ to the term proportional to w_z^2 is of the order of $(d/\rho_1)^2$, whereas the corrections ΔG_1 and ΔG_s do not depend on d. For real systems, all these corrections turn out to be considerable in magnitude. Note that the signs of the corrections $\Delta\tilde{G}_0$ and ΔG_1 depend on a particular system, whereas the correction ΔG_s is universally positive and, thus, decreases the rotational barrier in the low-symmetry term in expression (25). Therefore, the translational–rotational interaction leads to an efficient isotropization of the crystal field.

The second term in relationship (33) is the quadratic form of the components of the angular velocity $\dot{\mathbf{w}}$ of the rotator and, hence, is the addition to the rotational kinetic energy for the impurity molecule. The corresponding additional term in the rotational part of the Lagrangian $\mathscr{L}_{\text{rot}}$ has the form

$$\Delta\mathscr{L}_{\text{rot}} = -\frac{d^4}{2M}\sum_{\nu}\frac{\dot{f}_{\nu}^2}{\Omega_{\nu}^4}$$
$$= -\frac{1}{2}\{\Delta J_{\perp}\dot{w}_{\perp}^2 + \Delta J_z\dot{w}_z^2 + \Delta J_{ij}(\mathbf{w})\dot{w}_i\dot{w}_j\}, \quad (35)$$

where

$$\Delta J_{\perp} = \frac{4d^4}{M\Omega_{\perp}^4}K_2^2, \quad \Delta J_z = \frac{4d^4}{M\Omega_{\perp}^4}K_0^2, \quad (36)$$

$$\Delta J_{ij}(\mathbf{w}) = \sqrt{\Delta J_{\perp}\Delta J_z}$$
$$\times\begin{pmatrix} \lambda_1 w_z^2 + 2w_yw_z & 2w_xw_z & 2w_xw_y \\ 2w_xw_z & \lambda_1 w_z^2 - 2w_yw_z & w_x^2 - w_y^2 \\ 2w_xw_y & w_x^2 - w_y^2 & \lambda_2 w_z^2 \end{pmatrix}, \quad (37)$$

$$\lambda_1 = \frac{K_0}{K_2} - \frac{K_2}{K_0}, \quad \lambda_2 = \frac{K_0}{K_2}\left[\left(\frac{K_1\Omega_{\perp}^2}{K_0\Omega_z^2}\right)^2 - 3\right]. \quad (38)$$

Unlike the potential energy, in which only constants are renormalized, allowance made for the effects of the translational–rotational interaction leads to a change in the type of rotational kinetic energy of the system, which takes the symmetric quadratic form of the angular velocity components $\dot{w}_{\nu}$. It is also easy to demonstrate that Lagrangian (35) is invariant with respect to transformations of the group S_6.

The corrections to the moment of inertia of the free rotator $J = Md^2$ are conveniently represented as terms of two types. Terms of the first type are the relatively small positive additions (36), which are independent of the molecular orientation and differ for rotator rotations about the 0Z axis and the axes lying in the plane $z = 0$. By virtue of these terms, the rotator proves to be “heavier” and becomes anisotropic at any rotation angle. Terms of the second type are described by expression (37) and depend on the molecular orientation. Specifically, this group of terms involves the off-diagonal elements, which appear owing to the presence of the anisotropic field of the substrate with a threefold axis in the system. As a result, the inertial properties of the impurity turn out to be very complex functions of the rotation angles. Thus, the interaction between the translational and rotational degrees of freedom of the impurity molecule in the crystal field leads to the fact that the molecule becomes a “parametric” rotator whose dynamics significantly differs from the behavior of a simple isotropic rotator. Physically, this effect stems from the fact that the impurity molecule rotates in the noninertial coordinate system related to its center of inertia, which oscillates in the anisotropic potential produced by the neighbors in the layer and the substrate.

The approach proposed in this section enables us to analyze how the translational degrees of freedom affect the rotational dynamics of the molecule and to provide a clear physical interpretation of the observed effects. At the same time, when constructing the thermodynamics, we face the necessity of performing the functional integration in relationship (31). This integration cannot be accomplished using an analytical method, because the Lagrangian in relationship (31) has a complex form. Consequently, thermodynamic functions of the system should be calculated by numerical techniques. As regards the numerical procedure, it is conveniently constructed reasoning from the eigenvalue problem, i.e., by solving the appropriate Schrödinger equation. One of the most delicate moments in the realization of the above technique is correct representation of the Hamiltonian, which should be a Hermitian conjugate operator analog of the quadratic form (35). In principle, this procedure is realizable; however, the approach outlined in the next section seems to be more reasonable for deriving the Hamiltonian of the system under investigation.

5. THE CANONICAL-TRANSFORMATION METHOD

The translational and rotational degrees of freedom can be efficiently separated in terms of the canonical-transformation method as directly applied to Hamiltonian (22). As was noted in the preceding section, the rotational constant B of the impurity molecule in the studied system is small compared to the frequencies of translational oscillations of its center of inertia. This circumstance is essential to the procedure described below. First, we transform such components in Hamiltonian (22) that involve the translational variables; i.e., we take the unitary transformation of the Hamiltonian $H_0 = H_{\mathrm{tr}} + H_{\mathrm{int}}$, that is,

$$\tilde{H}_0 = \exp(-i\hat{s}_1)(H_{\mathrm{tr}} + H_{\mathrm{int}})\exp(i\hat{s}_1), \tag{39}$$

where

$$\hat{s}_1 = \sum_{\nu}\sigma_\nu P_\nu, \quad \sigma_\nu = -\frac{d^2 f_\nu}{M\Omega_\nu^2}. \tag{40}$$

The quantities σ_ν are chosen such that the coefficients of the terms linear in u_ν are equal to zero. As a result, we have

$$\tilde{H}_0 = H_{\mathrm{tr}} - \Delta H_0, \quad \Delta H_0 = \frac{d^4}{2M}\sum_{\nu}\frac{f_\nu^2}{\Omega_\nu^2}. \tag{41}$$

The addition obtained in expression (41) leads to the same effects as the first term in formula (33); i.e., it renormalizes all the coefficients in Hamiltonian (25). In this case, the form of the crystal field remains unchanged and the corrections $\Delta\tilde{G}_0$, ΔG_1, and ΔG_s exactly coincide with the corrections defined by relationships (34).

After transformation similar to that given by expressions (39) and (40), the rotational kinetic energy takes the form

$$\exp(-i\hat{s}_1)B\hat{\mathbf{L}}^2\exp(i\hat{s}_1) = B\hat{\mathbf{L}}^2 + \Delta H_1 + \Delta H_2. \tag{42}$$

Here,

$$\Delta H_1 = -d^2 B(\hat{\mathbf{L}}\hat{\mathbf{T}} + \hat{\mathbf{T}}\hat{\mathbf{L}}), \quad \Delta H_2 = d^4 B\hat{\mathbf{T}}^2. \tag{43}$$

$$\hat{\mathbf{T}} = \mathbf{w}\times\hat{\mathbf{\Pi}}, \quad \hat{\mathbf{\Pi}} = \frac{2}{M}\sum_{\nu}\hat{P}_\nu\frac{\mathbf{\Lambda}_\nu}{\Omega_\nu^2}, \quad \Lambda_\nu^i = \Gamma_\nu^{ij}w_j. \tag{44}$$

From relationships (43) and (44), it follows that the addition ΔH_2 is quadratic in $\hat{P}_\nu$. In the limit of low temperatures, after averaging over the oscillatory variables, the term ΔH_2 leads to the same effects as the term ΔH_0. However, the arising corrections have higher orders in B/Ω_ν.

The operator ΔH_1 is linear in translational angular momenta of the center of inertia of the impurity and depends on the translational and rotational variables. In order to eliminate the terms linear in $\hat{P}_\nu$, we take the second canonical transformation

$$\tilde{H}_1 = \exp(-i\hat{s}_2)(H_{\mathrm{tr}} + \Delta H_1)\exp(i\hat{s}_2), \tag{45}$$

where

$$\hat{s}_2 = \sum_{\nu}\kappa_\nu u_\nu, \quad \kappa_\nu = 2d^2 B\frac{F_\nu}{\Omega_\nu}. \tag{46}$$

As a result, we obtain

$$\tilde{H}_1 = H_{\mathrm{tr}} - \Delta H_3, \quad \Delta H_3 = \frac{2d^4B^2}{M}\sum_{\nu}\frac{F_\nu^2}{\Omega_\nu^4}, \tag{47}$$

where

$$F_\nu = \hat{\mathbf{L}}(\mathbf{w}\times\hat{\mathbf{\Lambda}}_\nu) + (\mathbf{w}\times\hat{\mathbf{\Lambda}}_\nu)\hat{\mathbf{L}}. \tag{48}$$

It is evident that the second canonical transformation should result in the appearance of additions of higher orders in B/Ω_ν in Hamiltonian (15).

Our interest is only in the operator part (with respect to the angular variables) of ΔH_3, because the nonoperator part leads to renormalization of the crystal field amplitude with corrections of higher orders $\sim(B/\Omega_\nu)^2$ as compared to ΔH_2. For the same reason, we disregard the corrections arising from the unitary transformation of H_c. By using relationships (18) and (48), for the operator part of ΔH_3, we obtain

$$\begin{aligned}\Delta H_3 = 2B^2\{&\Delta J_\perp\Phi_\perp^2 + \Delta J_z\Phi_z^2 \\ &+ \Delta J_{ij}(\mathbf{w})\Phi_i\Phi_j - 4i\sqrt{\Delta J_\perp\Delta J_z}\hat{\Upsilon}\},\end{aligned} \tag{49}$$

where

$$\mathbf{\Phi} = \mathbf{w}\times\hat{\mathbf{L}}, \quad \Phi_\perp^2 = \Phi_x^2 + \Phi_y^2,$$

$$\begin{aligned}\hat{\Upsilon} = \frac{\lambda_1 - \lambda_2}{2}&w_z(1-2w_z^2)\Phi_z + 6w_xw_yw_z\Phi_x \\ &+ 3w_z(w_x^2 - w_y^2)\Phi_y + w_y(3w_x^2 - w_y^2)\Phi_z,\end{aligned}$$

and the quantities $\Delta J_\perp$, ΔJ_z, and $\Delta J_{ij}(\mathbf{w})$ are defined by expressions (36) and (37). Thus, relationship (49) represents the correction ΔH_{rot} to the operator for the rotational kinetic energy.

The change-over from Hamiltonian (49) to the classical Lagrangian is accomplished through the transformation

$$\mathbf{\Phi} \longrightarrow -J\dot{\mathbf{w}} = J\frac{d\mathbf{w}}{dt}, \qquad (50)$$

where t is the real time. As a result of this change-over, the first three terms in formula (49) exactly coincide with the analogous terms in Lagrangian (35). The classical analog of the last term [in formula (49)] providing a Hermitian character of the complete Hamiltonian of the system is reduced to the total derivative of the function

$$\Psi(\mathbf{w}) = \frac{\lambda_1 - \lambda_2}{4} w_z^2(1 - w_z^2) + w_y w_z(3w_x^2 - w_y^2)$$

with respect to the imaginary time and, hence, does not contribute to the classical action of the system.

6. DISCUSSION

Undeniably, the most pronounced effect resulting from the interaction between the translational and rotational degrees of freedom of the molecule rotator resides in the radical change in the inertial properties of the molecule. This manifests itself in the change in the form of the operator for the rotational kinetic energy as compared to the corresponding expression for the free rotator. The inertia tensor components for the molecule become functions of molecular orientation. Physically, this is explained by the fact that the coordinate system related to the center of inertia of the rotator is noninertial due to the complex translational motion executed by the center of inertia in the external (crystal) field. The discussed phenomena are of special importance in such two-dimensional atomic–molecular systems and three-dimensional lattices (for, example, face-centered close-packed structures) in which the rotator moves in the crystal potential without an inversion center and, hence, any rotator rotation is attended by the displacement of the center of inertia and vice versa. Therefore, the translational–rotational interaction is the crucial factor controlling the dynamics of the molecule at the lattice site. As a result, the molecule, in terms of rotational motion, transforms into a parametric rotator whose dynamic response radically differs from the behavior of a free rotator. In particular, the effective kinetic energy can be represented in the generalized quadratic form of the angular momentum (angular velocity) components with a symmetry identical to that of the external crystal field.

Certainly, the translational–rotational interaction also results in renormalization of the parameters of the crystal potential. However, although the corresponding corrections are sufficiently large (25–30% for a typical cryosystem), the potential form determined by the symmetry of the system remains unchanged.

The key point in our problem is the adequate separation of the translational and rotational degrees of freedom of the quantum rotator in the external field with the specified symmetry. In the present work, this procedure was performed in the framework of two approaches, namely, the Lagrangian and Hamiltonian formalisms. Needless to say, both approaches eventually lead to completely coinciding results; however, each of them is of quite independent significance in the analysis of so complex a problem as the investigation of the influence of translations on the effective properties of a rotational subsystem. The results obtained with the use of the Lagrangian formalism enable us to analyze qualitatively the complex behavior of the parametric rotator in the framework of classical mechanics. On the other hand, the Hamiltonian formalism, which is based on the canonical transformation, immediately gives the Hermitian conjugate operator for the rotational kinetic energy. The combined use of the results derived within both approaches makes it possible to change over from classical mechanics to quantum mechanics and vice versa and, thus, to check the reliability of the rather complex computational technique as a whole.

In this work, the aforementioned scheme is realized for an impurity molecule moving in a field generated by a system of fixed surrounding atoms. However, it is amply clear that the results obtained will be qualitatively correct in the case of vibrations of the surrounding monoatomic lattice (i.e., in the case of phonon interaction) and also in the case when the adjacent sites are occupied by similar molecules and when librons arising in the system of the aforementioned parametric rotators occur in addition to phonons in the lattice. The results of the present work can also be rather easily modified for the problem of the effective substrate potential acting on a molecule adsorbed on the crystal surface. The above consideration allows us to make the inference that the simplest potentials usually used for solving such problems [34], as a rule, cannot be considered to be adequate for a real situation, particularly where the rotational excitation spectra of adsorbates are involved [35–37]. These problems and the effects of the translational–rotational interaction in the thermodynamics and kinetics of cryocrystals (specifically, two-dimensional cryocrystals) will be investigated in separate works.

REFERENCES

1. R. M. Lynden-Bell and K. H. Michel, Rev. Mod. Phys. **66** (3), 721 (1994).
2. A. F. Prikhot'ko, V. G. Manzhelii, I. Ya. Fugol', *et al.*, in *Cryocrystals,* Ed. by B. I. Verkin and A. F. Prikhot'ko (Naukova Dumka, Kiev, 1983).
3. *Physics of Cryocrystals,* Ed. by V. G. Manzhelii and Yu. A. Freiman (American Inst. of Physics Press, New York, 1996).

4. C. Ebner and C. C. Sung, Phys. Rev. B **2** (6), 2115 (1970).
5. R. G. Bohn and C. F. Mate, Phys. Rev. B **2** (6), 2121 (1970).
6. J. E. Huebler and R. G. Bohn, Phys. Rev. B **17** (4), 1991 (1978).
7. C. L. Reynolds, Jr. and A. C. Anderson, Phys. Rev. B **22** (11), 5547 (1980).
8. T. N. Antsygina, K. A. Chishko, and V. A. Slusarev, J. Low Temp. Phys. **111** (3/4), 503 (1998).
9. T. N. Antsygina, V. A. Slusarev, and K. A. Chishko, Zh. Éksp. Teor. Fiz. **114** (2), 555 (1998) [JETP **87**, 303 (1998)].
10. J. Manz, J. Am. Chem. Soc. **102** (6), 1801 (1980).
11. J. Manz and K. Mirsky, Chem. Phys. **46** (6), 457 (1980).
12. V. G. Manzheliĭ, E. A. Kosobutskaya, V. V. Sumarokov, *et al.*, Fiz. Nizk. Temp. **12** (2), 151 (1986) [Sov. J. Low Temp. Phys. **12**, 86 (1986)].
13. T. N. Antsygina and V. A. Slusarev, Fiz. Nizk. Temp. **19** (1), 67 (1993) [Low Temp. Phys. **19**, 48 (1993)].
14. T. N. Antsygina and V. A. Slusarev, Fiz. Nizk. Temp. **20** (3), 255 (1994) [Low Temp. Phys. **20**, 202 (1994)].
15. T. N. Antsygina, K. A. Chishko, and V. A. Slusarev, Phys. Rev. B **55** (6), 3548 (1997).
16. J. G. Dash, Fiz. Nizk. Temp. **1** (7), 839 (1975) [Sov. J. Low Temp. Phys. **1**, 401 (1975)].
17. M. H. W. Chan, A. D. Migone, K. D. Miner, and Z. R. Li, Phys. Rev. B **30**, 2681 (1984).
18. A. D. Migone, Zhong-Rong Li, M. H. W. Chan, and M. R. Giri, Phys. Rev. B **28** (11), 6525 (1983).
19. H. You and S. C. Fain, Phys. Rev. Lett. **56** (3), 244 (1986).
20. R. D. Etters and B. Kuchta, J. Low Temp. Phys. **111** (3/4), 272 (1998).
21. J. Stoltenberg and O. E. Vilches, Phys. Rev. B **22** (6), 2920 (1980).
22. R. Marx and R. Braun, Solid State Commun. **33** (2), 229 (1980).
23. O. E. Vilches, R. C. Ramos, Jr., and D. A. Ritter, Czech. J. Phys. **46** (S1), 397 (1996).
24. N. S. Sullivan and K. Kim, J. Low Temp. Phys. **113** (5/6), 705 (1998).
25. N. S. Sullivan and K. Kim, J. Low Temp. Phys. **110** (1/2), 597 (1998).
26. N. S. Sullivan and K. Kim, J. Low Temp. Phys. **111** (3/4), 533 (1998).
27. M. Bienfait, G. M. Gay, P. Zeppenfeld, *et al.*, J. Low Temp. Phys. **111** (3/4), 555 (1998).
28. H. Wiechert and K.-D. Kortmann, J. Low Temp. Phys. **111** (3/4), 561 (1998).
29. A. I. Kitaĭgorodsky, *Molecular Crystals* (Nauka, Moscow, 1972).
30. T. N. Antsygina and V. A. Slusarev, Teor. Mat. Fiz. **77**, 234 (1988).
31. M. I. Poltavskaya and K. A. Chishko, Fiz. Nizk. Temp. **26** (4), 333 (2000) [Low Temp. Phys. **26**, 289 (2000)].
32. M. I. Poltavskaya and K. A. Chishko, Fiz. Nizk. Temp. **26** (8), 837 (2000) [Low Temp. Phys. **26**, 615 (2000)].
33. L. D. Landau and E. M. Lifshitz, *Course of Theoretical Physics*, Vol. 5: *Statistical Physics* (Nauka, Moscow, 1964; Pergamon, Oxford, 1980).
34. D. W. Brown, P. L. Sokol, and S. A. FitzGerald, Phys. Rev. B **59** (20), 13258 (1999).
35. T. B. McRury and J. R. Sams, Mol. Phys. **19** (3), 337 (1970).
36. T. B. McRury and J. R. Sams, Mol. Phys. **19** (3), 353 (1970).
37. T. B. McRury and J. R. Sams, Mol. Phys. **20** (1), 49 (1971).

Translated by O. Borovik-Romanova

Physics of the Solid State, Vol. 44, No. 7, 2002, pp. 1278–1283. Translated from Fizika Tverdogo Tela, Vol. 44, No. 7, 2002, pp. 1224–1229.
Original Russian Text Copyright © 2002 by Mezhennyĭ, Mil'vidskiĭ, Reznik.

DEFECTS, DISLOCATIONS, AND PHYSICS OF STRENGTH

Specific Features in the Generation and Motion of Dislocations in Silicon Single Crystals Doped with Nitrogen

M. V. Mezhennyĭ*, M. G. Mil'vidskiĭ, and V. Ya. Reznik****
** Giredmet Federal State Unitary Enterprise, Moscow, 109017 Russia*
*** Institute for Chemical Problems of Microelectronics, Bol'shoĭ Tolmachevskiĭ per. 5, Moscow, 109017 Russia*
e-mail: icpm@mail.girmet.ru

Received September 21, 2001

Abstract—The specific features in the generation and motion of dislocations are investigated in Si : N single crystals grown by the Czochralski method. The motion of dislocation loops is analyzed by the four-point bending technique in the temperature range 500–800°C. The dislocation loops are preliminarily introduced into the samples with the use of a Knoopp indenter at room temperature. It is found that doping with nitrogen leads to a considerable increase in the critical stress of the onset of dislocation motion from surface sources (indentations) and in the stress of the generation of dislocations from internal sources. The velocity of dislocation motion in Si : N crystals is less than that in undoped crystals (under comparable loads). The hardening effect of nitrogen is explained by the fact that nitrogen promotes the decomposition of a solid solution of oxygen in silicon during postcrystallization cooling. *© 2002 MAIK "Nauka/Interperiodica".*

1. INTRODUCTION

Silicon wafers of large diameters are widely used in microelectronics. In this respect, investigation into their mechanical strength is a topical problem. An increase in the wafer diameter considerably increases the probability of generating dislocations in the wafers in the course of heat treatment and epitaxial growth processes extensively used in producing ultralarge-scale integrated circuits. Hence, analysis of the factors responsible for the specific features in the generation and motion of dislocations in initially dislocation-free wafers have acquired particular importance. It is well known (see, for example, [1]) that the dynamics of dislocations in semiconductor single crystals is substantially affected by impurities. In silicon single crystals, first and foremost, these are dopants of Group III and V elements of the periodic table and oxygen. The effect of these impurities on the mechanical properties of silicon has received sufficient attention in the literature.

The effect of nitrogen as an impurity has been examined to a considerably lesser extent, even though, in recent years, this element has found wide use as a dopant for the Czochralski growth of large-sized dislocation-free silicon single crystals containing no vacancy micropores [2]. Abe *et al.* [3] and Sumino *et al.* [4] studied single crystals grown by crucibleless melting and showed that doping with nitrogen leads to their hardening, specifically to an increase in the upper yield stress. Yonenaga and Sumino [5] investigated the dislocation mobility in Czochralski-grown Si : N single crystals at temperatures of 600–800°C. These authors did not reveal a noticeable effect of nitrogen on the dislocation dynamics in the studied samples. Unfortunately, no data on structural features of the studied crystals and, primarily, on their type (whether they were vacancy-type or interstitial-type crystals [6]) were reported in [5].

The purpose of the present work was to investigate the specific features in the generation and motion of dislocations in vacancy-type dislocation-free Si : N single crystals grown by the Czochralski method.

2. SAMPLE PREPARATION AND EXPERIMENTAL TECHNIQUE

The samples used in the measurements were cut from Si : (B, N) single-crystal wafers 150 mm in diameter (resistivity, ~5 Ω cm). The crystals were grown by the Czochralski method in a "vacancy" mode in the ⟨001⟩ direction. The nitrogen content was equal to 1.6×10^{14} cm^{-3} for samples of series *1* and 1.6×10^{15} cm^{-3} for samples of series *2*. The oxygen content was ~(7–8) × 10^{17} cm^{-3}. A nitrogen-free wafer cut from the vacancy-type crystal with approximately the same resistivity and oxygen content (sample series *3*) was used as a reference wafer. All the above samples were examined in the postgrowth state.

The samples for mechanical testing were prepared in the form of parallelepipeds 25 × 4 × 0.6 mm in size with {100} large faces. The long side of the sample was oriented along the ⟨110⟩ direction. The samples were chemically polished in an acid mixture HF : HNO_3 = 1 : 6 for 5 min. In the process, a layer ~40 μm thick was removed from the surface. Then, several indentations were made on the sample surface with the use of a Knoopp indenter (the indenter load was 0.25 N, and the loading time was 15 s). After indentation, the sample was subjected to four-point bending in a special setup described in [7]. The mechanical testing was performed at temperatures from 500 to 800°C. In order to decrease the effect of transient processes associated with heating and cooling, the sample was placed in a furnace preheated to a given temperature and held under load; then, the sample was removed from the setup and quenched in air. The time of heating the sample to a testing temperature did not exceed 5 min. The loading time was 20 min. The sample side containing indentations was subjected to tensile deformation. The indentation of the sample surface and the subsequent loading at a testing temperature gave rise to dislocation half-loops in the surface layer. These half-loops consisted of two 60° segments and one fragment of a screw dislocation aligned parallel to the sample surface. In our case, the sample bending with the bending axis perpendicular to the long side of the sample resulted in the activation of four systems of glide dislocations: $(111)[\bar{1}01]$, $(111)[0\bar{1}1]$, $(\bar{1}\bar{1}1)[0\bar{1}\bar{1}]$, and $(\bar{1}\bar{1}1)[101]$. In the experiments performed, we examined the mobility of 60° dislocation-loop segments.

The stresses responsible for the generation of dislocations by internal sources in the wafer bulk were determined from the onset of the multiple generation of dislocations that were not induced by indentations. After selective chemical etching, numerous slip bands were observed on the surface of these samples and the samples themselves underwent macrobending.

The structural transformations in the studied samples were controlled by optical microscopy after selective etching in a mixture of hydrofluoric and chromic acids (HF : 0.15M CrO_3 = 1 : 1, 10 min). The density of growth microdefects in all the samples under investigation was 10^5–10^6 cm^{-3}.

3. RESULTS

Figure 1 displays the dependences of the velocity of dislocation motion on the applied shear stress at temperatures of 500 and 600°C. It is seen that doping with nitrogen leads to a noticeable decrease in the velocity of dislocation motion under comparable stresses. This effect is most pronounced at a temperature of 500°C.

Dislocations begin to move from indentations when stresses exceed the critical stress τ_{cr}. This term is used in reference to a stress corresponding to the onset of motion of a dislocation loop with the minimum size visible with an optical microscope (for example, we reliably distinguished 2- to 3-μm dislocation loops under the Polyvar microscope used in our investigations).

In the studied ranges of stresses and temperatures, the results obtained are adequately described by the standard relationship [8]

$$V = V_0(\tau/\tau_0)^n \exp[-E/kT], \qquad (1)$$

where V is the dislocation velocity, V_0 is the constant characterizing the crystal matrix, τ is the applied stress, τ_0 = 1 MPa, k is the Boltzmann constant, T is the temperature, and E is the activation energy of dislocation motion.

An increase in the applied stress is accompanied by the generation and motion of dislocations from internal sources in addition to the motion of dislocations from indentations. The generation of dislocation by internal sources in the sample bulk brings about an appreciable plastic deformation and the formation of numerous slip bands. In what follows, the stress of the onset of these processes will be referred to as the stress of plastic deformation τ_{pl} due to internal sources.

At testing temperatures of 700 and 800°C, our attempts to construct the dependence of the dislocation

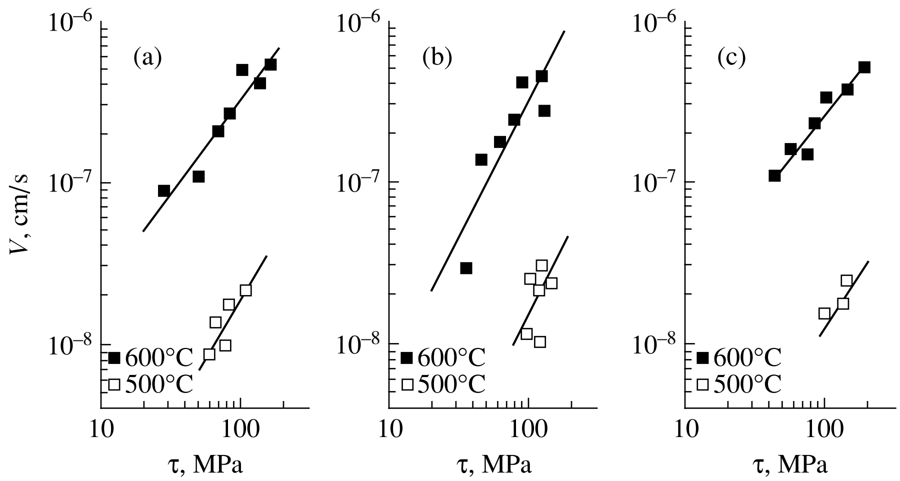

Fig. 1. Dependences of the velocity of dislocation motion on the applied shear stress for samples of series (a) *3*, (b) *1*, and (c) *2*.

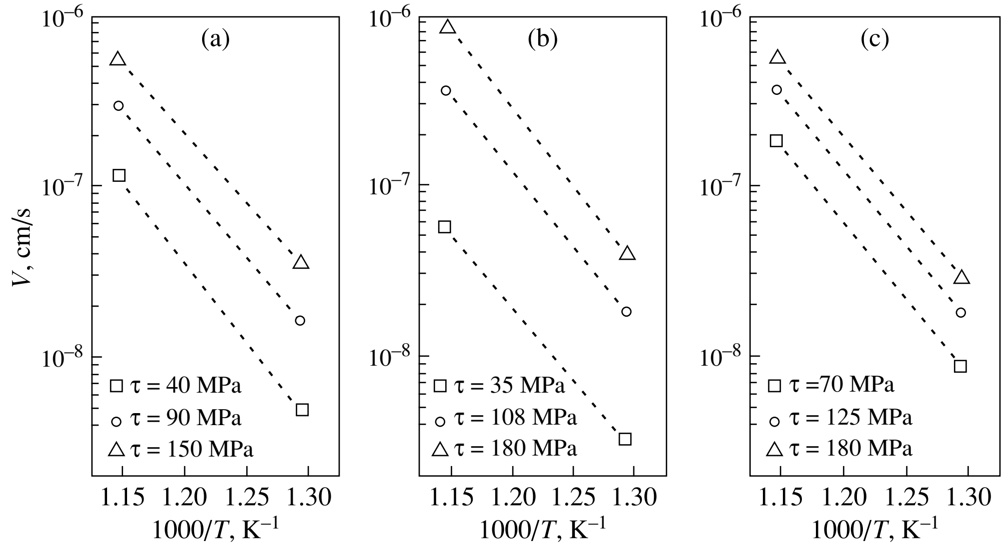

Fig. 2. Temperature dependences of the velocity of dislocation motion in samples of series (a) *3*, (b) *1*, and (c) *2*.

velocity on the applied stress were unsuccessful. This is explained by the fact that the stresses τ_{cr} at these temperatures are close to the values of τ_{pl}, which complicates control over the motion of dislocations generated by indentations. As a result, the range of used stresses at which it was possible to obtain reliable data on the velocity of individual dislocations moving from indentations appeared to be very narrow.

Figure 2 shows the temperature dependences of the velocity of dislocation motion in the studied samples under different applied stresses, which were constructed using the results of measurements at temperatures of 500 and 600°C. The experimental points are connected by straight dashed lines. The results obtained allow us to roughly estimate the activation energy E of dislocation motion. The calculated energies E for sample series *1*, *2*, and *3* are equal to 1.75, 1.80, and 1.70 eV, respectively.

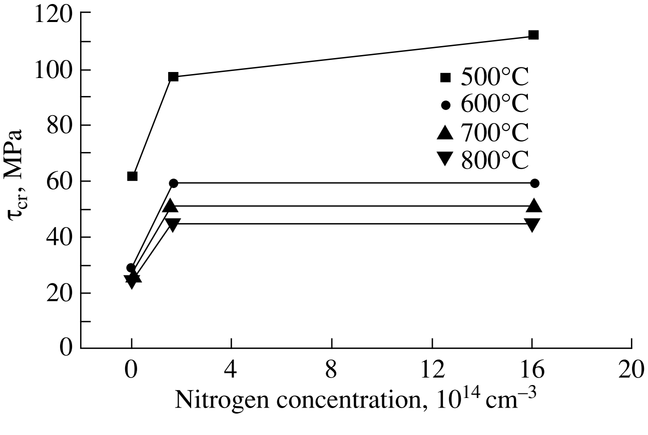

Fig. 3. Dependences of the critical stress of the onset of dislocation motion on the nitrogen concentration in the studied samples.

The dependences of the critical stress τ_{cr} on the nitrogen concentration in silicon wafers over the entire range of temperatures are plotted in Fig. 3. As can be seen from Fig. 3, doping with nitrogen results in a substantial (almost twofold) increase in the critical stress τ_{cr} as compared to that in the reference samples. Note that the maximum changes are observed at a nitrogen concentration of 1.6×10^{14} cm^{-3}. An increase in the nitrogen concentration to 1.6×10^{15} cm^{-3} does not lead to a further noticeable increase in the critical stress τ_{cr}.

The temperature dependences of the stresses τ_{cr} and τ_{pl} for the studied samples are displayed in Fig. 4. It is seen from this figure that doping with nitrogen not only increases the critical stress τ_{cr} but also substantially affects the processes associated with the generation and motion of dislocations from internal sources, thus increasing the stress τ_{pl}. It is worth noting that the increase in τ_{pl} is more pronounced at temperatures above 600°C.

The influence of nitrogen doping on the stresses τ_{cr} (the lower bound of each bar) and τ_{pl} (the upper bound of each bar) is illustrated by the histograms depicted in Fig. 5. Changes in the stresses τ_{cr} and τ_{pl} with an increase in the testing temperature at the same nitrogen concentration in the samples under investigation are shown in Fig. 5a. Changes in the stresses τ_{cr} and τ_{pl} with an increase in the nitrogen concentration at the same temperature of the samples are displayed in Fig. 5b. As can be seen from these figures, an increase in the testing temperature is accompanied by a considerable activation of internal sources of dislocation generation, which results in a drastic decrease (by a factor of five or eight)

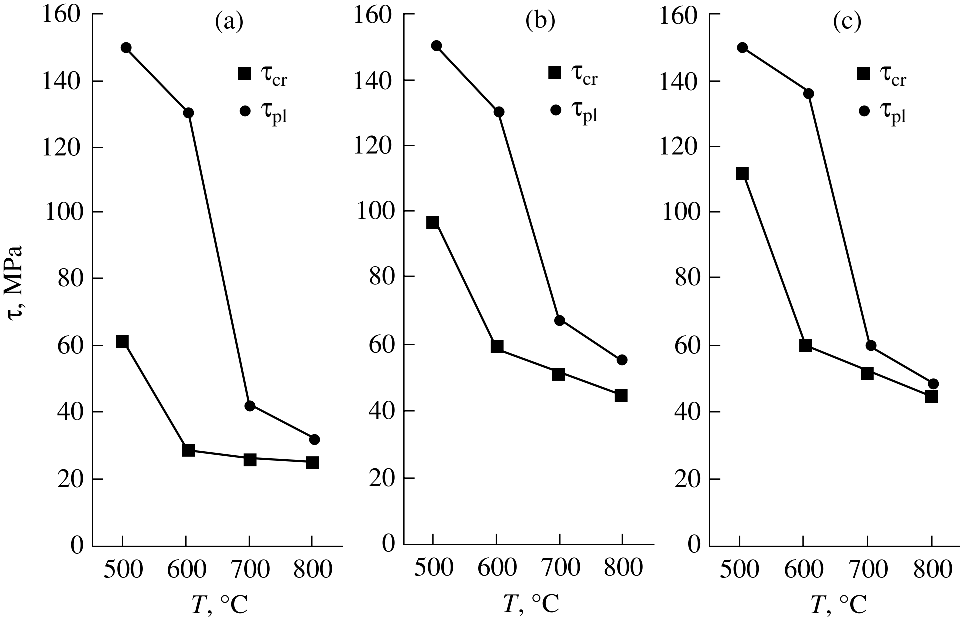

Fig. 4. Temperature dependences of the critical stress τ_{cr} of the onset of dislocation motion from indentations and the critical stress τ_{pl} of the onset of the multiple generation and motion of dislocations from internal sources for samples of series (a) *3*, (b) *1*, and (c) *2*.

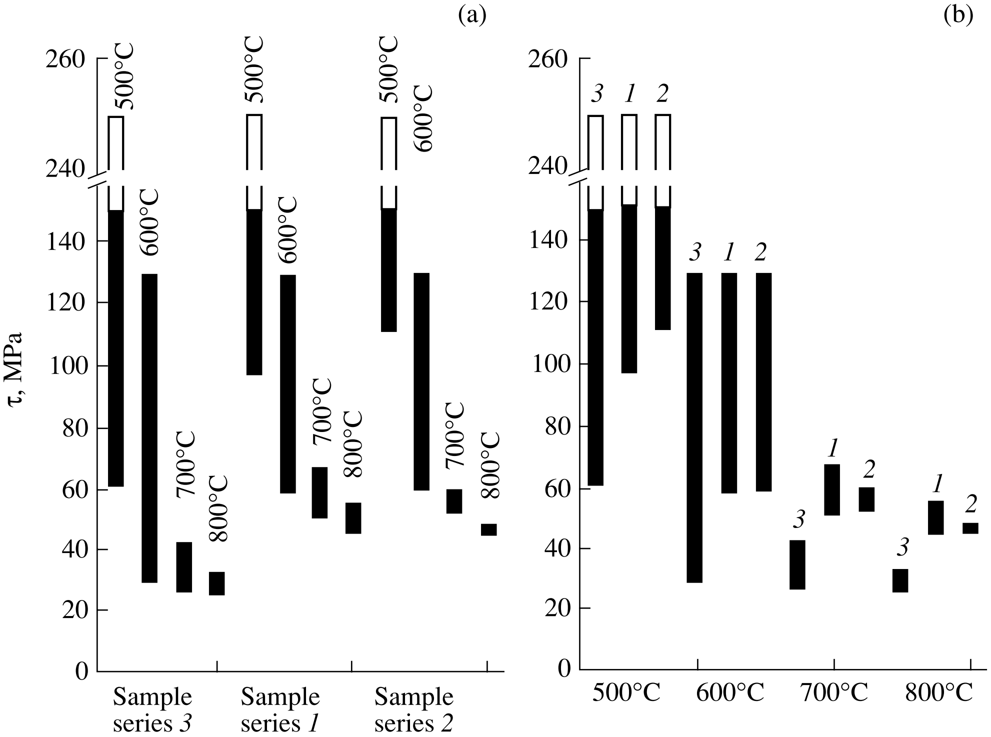

Fig. 5. Histograms of the critical stress τ_{cr} (the lower bound of each bar) of the onset of dislocation motion from indentations and the critical stress τ_{pl} (the upper bound of each bar) of the onset of multiple generation and motion of dislocations from internal sources: (a) identical nitrogen concentrations and different temperatures and (b) different nitrogen concentrations and identical temperatures. Numerals indicate the numbers of sample series. For samples deformed at a temperature of 500°C, the boundaries separating differently colored regions correspond to stresses above which the samples undergo brittle fracture.

in the stress τ_{pl}. At a temperature of 800°C, the stresses τ_{cr} and τ_{pl} are virtually identical in all the studied samples.

In the samples deformed at a temperature of 500°C, the brittle fracture is observed at stresses higher than a certain applied stress. For this reason, the histogram bars for a testing temperature of 500°C are separated into black and white regions. The boundary separating these regions corresponds to the stress above which the samples undergo brittle fracture, and the upper bound of the white region corresponds to the upper yield stress of silicon at 500°C [9].

4. DISCUSSION

The experimental data obtained indicate that, in the temperature range 500–800°C, deformation processes in the studied samples are substantially affected by the applied stresses. The generation and motion of dislocations from surface concentrators of stresses can be reliably observed only at temperatures of 500 and 600°C in the shear stress range 30–130 MPa. With a further increase in the stress, the samples undergo brittle fracture in the course of deformation at 500°C and plastic bending at 600°C. However, in the latter case, the samples also exhibit indications of brittle fracture.

An increase in the temperature to 700°C and, especially, to 800°C brings about an appreciable increase in the silicon plasticity. In turn, this leads to a considerable activation of internal sources of dislocation generation in the bulk of the sample under investigation. At these temperatures, the stress τ_{pl} decreases drastically and becomes comparable to the critical stress τ_{cr}, the density of dislocations in the deformed samples increases significantly, well-defined slip bands are observed on the surface of these samples, and the samples themselves undergo purely plastic bending without any indications of brittle fracture even at shear stresses larger than 50 MPa. All these factors substantially complicate the reliable determination of the dynamic characteristics of dislocations at the given temperatures. Thus, we can state that a pronounced crossover from brittle fracture to plastic bending occurs in the studied samples in the temperature and stress ranges covered. This crossover is observed at a temperature slightly exceeding 600°C.

The doping with nitrogen leads to hardening of the single-crystal wafers. This manifests itself in a considerable increase in the stresses τ_{cr} and τ_{pl}, a noticeable decrease in the dislocation velocities, and an increase in the activation energy of dislocation motion. The most appreciable changes are observed already at a nitrogen concentration of 1.6×10^{14} cm^{-3}. At this level of doping, the critical stress τ_{cr} is nearly doubled (at a temperature of 600°C) and the activation energy of dislocation motion increases by a factor of 1.15 as compared to those for the reference sample not doped with nitrogen. Note that the stress τ_{pl} in the studied samples with this concentration of nitrogen also substantially increases in the temperature range 700–800°C. A further increase in the nitrogen concentration to 1.6×10^{15} cm^{-3} is not attended by appreciable hardening. Furthermore, at temperatures of 700 and 800°C, the stress τ_{pl} in the samples at this level of nitrogen doping becomes even smaller than that in the samples with a nitrogen concentration of $\sim 1.6 \times 10^{14}$ cm^{-3}.

The experimental data obtained are insufficient to make unambiguous inferences about the nature of the hardening effect of nitrogen. It is worth noting that doping with nitrogen even at concentrations of the order of 10^{14} cm^{-3} substantially affects the dynamic properties of dislocations, whereas a similar effect for traditional donor and acceptor dopants in silicon is observed at concentrations higher by three or four orders of magnitude [10]. Therefore, we can assume that the hardening effect of nitrogen stems not from the direct interaction of nitrogen atoms with generated dislocations but from the influence of nitrogen on the state of an ensemble of intrinsic point defects in a growing single crystal. This influence results in changes in the formation of growth microdefects during postcrystallization cooling of an ingot. Specifically, the hardening effect of nitrogen can be associated with a more rapid decomposition of an oxygen supersaturated solid solution in silicon at temperatures below 800°C and a considerable increase in the content of disperse oxygen-containing precipitates (clusters) acting as efficient stoppers against dislocation motion in the crystal. This is confirmed by the results of the electron microscopic investigation performed by Nakai *et al.* [11], according to which, in Czochralski-grown crystals doped with nitrogen, an increase in the nitrogen concentration leads to a decrease in the size of oxygen-containing precipitates and an increase in their density.

At the same time, the fact that an increase in the nitrogen concentration to 1.6×10^{15} cm^{-3} in the samples leads to a slight decrease in the stress τ_{pl} (as compared to that in the samples with a nitrogen concentration of 1.6×10^{14} cm^{-3}) does not exclude the possible direct effect of nitrogen on the generation and motion of dislocations. Since the solubility of nitrogen in silicon is very limited, the formation of a nitrogen supersaturated solid solution in silicon and its partial decomposition with the formation of disperse nitrogen-containing precipitates cannot be ruled out at nitrogen concentrations of the order of $\sim 10^{15}$ cm^{-3}. The decomposition can proceed both directly during cooling of the grown crystal and upon subsequent heat treatment.

5. CONCLUSION

Thus, it was established that doping with nitrogen results in a considerable increase in the critical stress of the onset of dislocation motion from indentations and in the stress of the dislocation generation by internal sources. Under comparable loads, the velocities of dislocation motion in crystals doped with nitrogen are less than those in undoped crystals. The assumption was made that the hardening effect of nitrogen is associated with the fact that nitrogen promotes the decomposition of an oxygen supersaturated solid solution in a crystal during postcrystallization cooling. This leads to a substantial increase in the concentration of disperse oxygen-containing precipitates hindering the generation and motion of dislocations in the ingot bulk.

REFERENCES

1. M. G. Mil'vidskiĭ and V. B. Osvenskiĭ, *Structural Defects in Semiconductor Single Crystals* (Metallurgiya, Moscow, 1984).
2. W. Ohashi, A. Ikari, Y. Ohta, *et al.*, in *Proceedings of Kazusa Academia Park Forum on the Silicon and Technology of Silicon Materials, 1999*, p. 80.
3. T. Abe, K. Kikuchi, S. Shirai, and S. Muraoke, in *Semiconductor Silicon 81*, Ed. by H. R. Huff, R. J. Kriegler, and Y. Takeishi (Electrochemical Society, Pennington, 1981), p. 54.
4. K. Sumino, I. Yonenaga, M. Imai, and T. Abe, J. Appl. Phys. **54**, 5016 (1983).
5. I. Yonenaga and K. Sumino, Jpn. J. Appl. Phys. **21**, 47 (1982).
6. M. G. Mil'vidskiĭ, Izv. Vyssh. Uchebn. Zaved., Mater. Élektron. Tekh. **3**, 4 (1999).
7. B. Ya. Farber and V. I. Nikitenko, Phys. Status Solidi A **73**, K141 (1982).
8. K. Sumino, in *Proceedings of the 1st International Autumn School on Gettering and Defect Engineering in the Semiconductor Technology, Garzau, 1985*, Ed. by H. Richter, p. 41.
9. I. Yonenaga and K. Sumino, Phys. Status Solidi A **50**, 685 (1978).
10. M. Imai and K. Sumino, Philos. Mag. A **4**, 599 (1983).
11. K. Nakai, Y. Inoue, H. Yokota, *et al.*, in *Proceedings of the 3rd International Symposium on Advance Science and Technology of Silicon Materials, 2000*, p. 88.

Translated by O. Borovik-Romanova

Physics of the Solid State, Vol. 44, No. 7, 2002, pp. 1284–1290. Translated from Fizika Tverdogo Tela, Vol. 44, No. 7, 2002, pp. 1230–1235.

DEFECTS, DISLOCATIONS, AND PHYSICS OF STRENGTH

Specific Features in the Generation and Motion of Dislocations in Heat-Treated Silicon Wafers

M. V. Mezhennyĭ*, M. G. Mil'vidskiĭ, V. F. Pavlov*, and V. Ya. Reznik****

** Giredmet Federal State Unitary Enterprise, Moscow, 109017 Russia*

*** Institute for Chemical Problems of Microelectronics, Bol'shoĭ Tolmachevskiĭ per. 5, Moscow, 109017 Russia*

e-mail: icpm@mail.girmet.ru

Received July 16, 2001; in final form, September 27, 2001

Abstract—The specific features in the generation and motion of dislocations in silicon single-crystal wafers after different heat treatments are investigated by the four-point bending technique. It is demonstrated that annealing of silicon single-crystal wafers at a temperature of 450°C leads to their substantial hardening as compared to the postgrowth state. The oxygen-containing precipitates and precipitate dislocation pileups formed in the silicon wafer bulk during multistage heat treatment are efficient heterogeneous nucleation sites of dislocations under the action of thermal or mechanical stresses. It is found that the multistage heat treatment of the silicon wafers under conditions providing the formation of an internal getter within their bulk results in considerable disordering of the wafer structure. The inference is made that the formation of the defect state in the crystal lattice of silicon and the strength characteristics of silicon wafers substantially depend on the temperature–time schedules of the low-temperature stage of multistage heat treatment. © *2002 MAIK "Nauka/Interperiodica".*

1. INTRODUCTION

The problem of the mechanical strength of dislocation-free silicon single-crystal wafers and, especially, the problems concerning the nature of heterogeneous nucleation of dislocations in these wafers and the factors responsible for the dynamic properties of dislocations have been the center of attention of many researchers [1–5]. This is associated with at least two reasons. On the one hand, the existing tendency of the diameter of grown single crystals to increase leads to a considerable increase in the probability of generating dislocations in silicon wafers during high-temperature treatments used to produce instrumental compositions due to an increase in both the thermal stress in silicon wafers and their own weight. On the other hand, silicon wafers with an internal getter are used in manufacturing modern ultralarge-scale integrated circuits. This getter in silicon wafers is produced through the controlled decomposition of an oxygen supersaturated solid solution in silicon. Depending on their nature and size, the oxygen-containing precipitates formed in this case in the wafer bulk can play the role of heterogeneous nucleation sites of dislocations and act as stoppers against dislocation motion, thus hindering the dislocation generation and propagation [6, 7]. In the present work, we elucidated how multistage heat treatments used to form the internal getter in silicon wafers affect the dynamic properties of dislocations in these wafers.

2. SAMPLE PREPARATION AND EXPERIMENTAL TECHNIQUE

The samples used in the measurements were cut from vacancy-type dislocation-free silicon single-crystal wafers 150 mm in diameter. The crystals were grown by the Czochralski method in the $\langle 100 \rangle$ direction. The concentration of oxygen dissolved in the samples was equal to $(7–8) \times 10^{17}$ cm^{-3}. The resistivity varied from 1 to 5 Ω cm. The silicon wafers were examined both in the postgrowth state and after different multistage heat treatments, including treatment under conditions providing the formation of an internal getter in the silicon wafers (the heat treatment conditions for the wafers under investigation are given in Table 1).

Table 1. Conditions of multistage heat treatment of silicon wafers

Sample series no.	Heat treatment conditions
1	Postgrowth state
2	1000°C/15 min + 450°C/16 h
3	1000°C/15 min + 650°C/16 h
4	1000°C/15 min + 450°C/16 h + 800°C/4 h + 1000°C/4 h
5	1000°C/15 min + 650°C/16 h + 800°C/4 h + 1000°C/4 h

Table 2. Structural characteristics of the initial samples

Sample series no.*	Half-width of the rocking curve	Number of interference maxima in sectional topograms	Microdefect concentration, cm^{-3}		
			X-ray sectional topography	optical microscopy	electron microscopy
1	2.9″	The initial portion of the fourth maximum	–	$\sim 8 \times 10^5$	–
2	2.9″	3	–	$\sim 5 \times 10^5$	–
3	3.1″	3	–	$\sim 5 \times 10^5$	–
4	4.7″	Not found	$\sim 1 \times 10^9$	$\sim 3 \times 10^9$	$\sim 4 \times 10^{11}$
5	4.0″	The initial portion of the first maximum	$\sim 1 \times 10^{10}$	$\sim 2 \times 10^{10}$	$\sim 1 \times 10^{11}$

* Numbering of the sample series corresponds to that in Table 1.

For mechanical testing, the samples were prepared in the form of parallelepipeds 25 × 4 × 0.6 mm in size with {100} large faces. The long side of the sample was oriented along the ⟨110⟩ direction. The samples were chemically polished in an acid mixture $HF : HNO_3 = 1 : 6$ for 5 min. In the process, a layer ~40 μm thick was removed from the surface. Then, several indentations were made on the sample surface with the use of a Knoopp indenter (the indenter load was 0.25 N, and the loading time was 15 s). After indentation, the sample was subjected to four-point bending in a special setup described in [8]. The mechanical testing was performed at temperatures from 600 to 800°C. In order to decrease the effect of transient processes associated with heating and cooling, the sample was placed in a furnace preheated to a given temperature and held under load; then, the sample was removed from the setup and quenched in air. The time of heating the sample to a testing temperature did not exceed 5 min. The loading time was 20 min. The sample side containing indentations was subjected to tensile deformation. The indentation of the sample surface and the subsequent loading at a testing temperature gave rise to dislocation half-loops in the surface layer. These half-loops consisted of two 60° segments and one fragment of a screw dislocation aligned parallel to the sample surface. In our case, the application of bending stresses along the [110] direction with respect to the $[1\bar{1}0]$ bending axis led to the activation of four systems of glide dislocations: $(111)[\bar{1}01]$, $(111)[0\bar{1}1]$, $(\bar{1}\bar{1}1)[0\bar{1}\bar{1}]$, and $(\bar{1}\bar{1}1)[101]$. In these experiments, we examined the mobility of 60° dislocation-loop segments.

The stresses responsible for the generation of dislocations by internal sources in the wafer bulk were determined from the onset of the multiple generation of dislocations that were not induced by indentations. After selective chemical etching, numerous slip bands were observed on the surface of these samples and the samples themselves underwent macrobending.

The regularities in the generation and motion of dislocations in the silicon samples were investigated by optical microscopy, x-ray diffractometry, x-ray topography, and transmission electron microscopy. For optical microscopy, the samples were subjected to selective etching in a mixture of the composition $HF : 0.15M\ CrO_3 = 1 : 1$.

3. RESULTS

The results of investigations into the structural perfection of the initial samples in the postgrowth state and after different heat treatments are presented in Table 2. All the samples under investigation contain microdefects. The microdefect density in the as-grown samples is of the order of $\sim 8 \times 10^5$ cm^{-3}. The heat treatments at temperatures of 450 and 650°C (sample series *2* and *3*) do not lead to considerable changes in the density of the defects observed. The multistage heat treatment under conditions providing the formation of the internal getter (sample series *4* and *5*) results in a drastic increase in the microdefect density to 10^9–10^{10} cm^{-3} according to optical microscopy and x-ray topography and to 10^{11} cm^{-3} according to transmission electron microscopy. Since the capabilities of revealing high microdefect densities by optical microscopy and x-ray topography are rather limited, the results of electron microscopic investigations should be treated as more reliable data. An increase in the microdefect density in the samples is accompanied by a substantial broadening of the rocking curves and a decrease in the number of interference maxima (pendellösung) observed in the sectional topograms (Fig. 1). These data indicate that the formation of the internal getter in the silicon wafers is

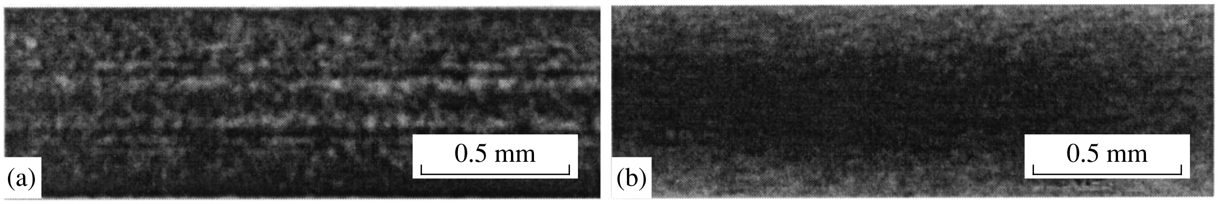

Fig. 1. Sectional topograms for samples of series (a) *1* and (b) *4* [(220) refection, MoK_α radiation].

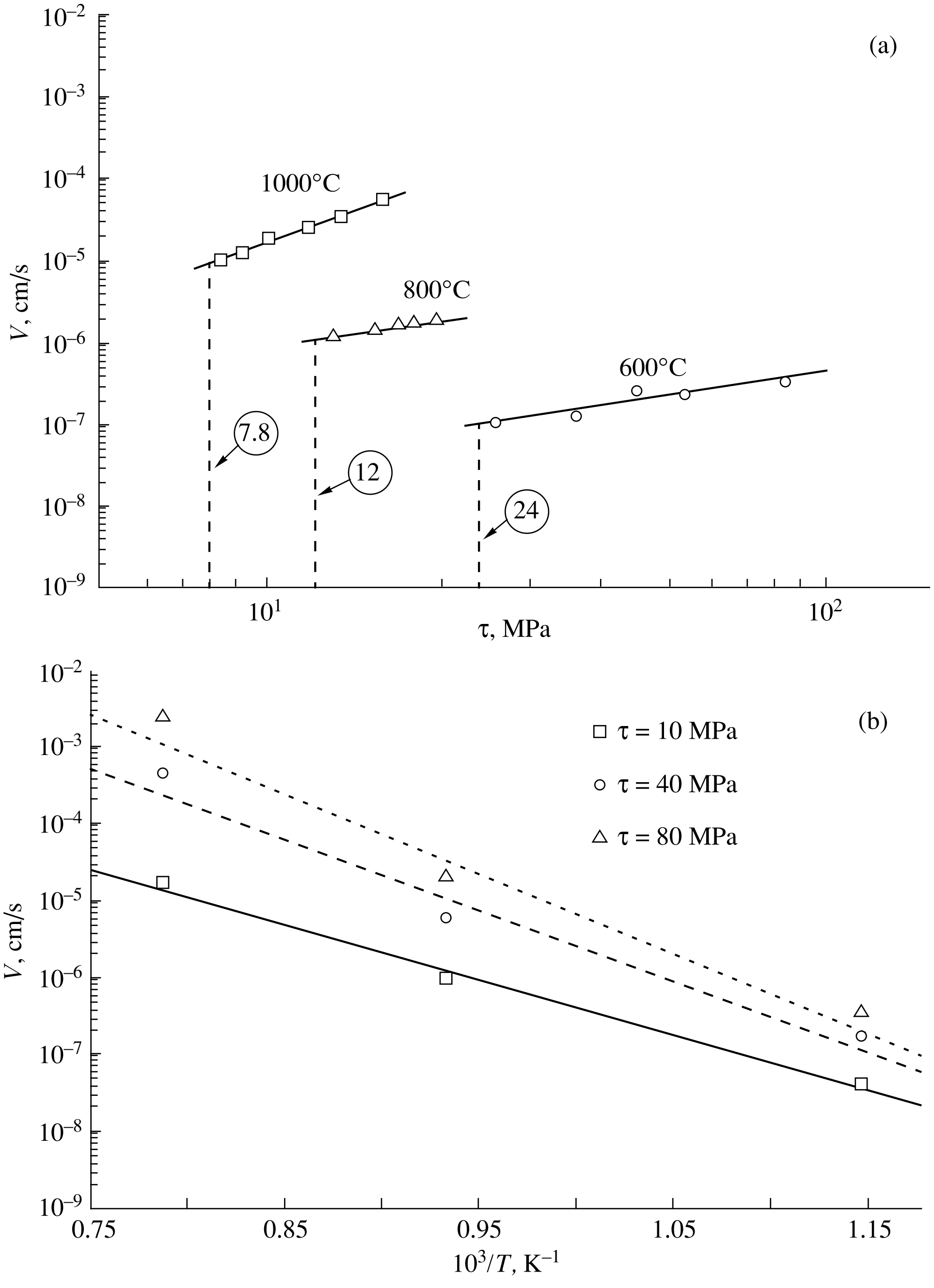

Fig. 2. Dependences of the velocity of dislocation motion in samples of series *1* on (a) the shear stress and (b) temperature. Dashed lines in panel (a) indicate the critical stresses τ_{cr} (the corresponding values in terms of MPa are given in circles).

attended by an appreciable deterioration of their integrated structural perfection.

The dependences of the velocity of dislocation motion on the shear stress and temperature for samples in the postgrowth state (sample series *1*) are depicted in Fig. 2. In the studied ranges of stresses and temperatures, the results obtained are satisfactorily described by the standard relationship [1]

$$V = V_0(\tau/\tau_0)^n \exp[-E/kT], \qquad (1)$$

where V is the dislocation velocity, V_0 is the constant characterizing the crystal matrix, τ is the applied stress, $\tau_0 = 1$ MPa, k is the Boltzmann constant, T is the temperature, and E is the activation energy of dislocation motion. The activation energy calculated from the data obtained is equal to 1.8 eV.

It should be noted that dislocations begin to move from indentations when stresses exceed the critical stress τ_{cr}. In what follows, this quantity will be referred to as the critical stress of the onset of dislocation motion. In our case, the critical stress τ_{cr} is considered to mean a stress corresponding to the onset of motion of a dislocation loop with the minimum size visible with an optical microscope. In actual fact, dislocation loops ~3 μm in size could be reliably distinguished with the Polyvar optical microscope used in our investigations. As can be seen from Fig. 2, the critical stress τ_{cr} considerably decreases with an increase in the temperature.

Figure 3 shows the dependences of the velocity of dislocation motion from indentations on the shear stress at a temperature of 600°C and the critical stress τ_{cr} for samples of series *2*, *3*, and *5*. It is worth noting that the critical stress τ_{cr} for the samples after multistage heat treatment under the conditions of the formation of the internal getter (sample series *5*) is substantially less than those for the samples after low-temperature heat treatment (sample series *2* and *3*). The dislocation mobility in samples of series *5* is sufficiently high at considerably smaller shear stresses. In these samples, the multiple generation of dislocations by internal sources is observed at stresses above 40 MPa, which appreciably complicates control over the motion of dislocations generated by indentations. The same situation occurs in samples of series *2* and *3* at stresses higher than 95 and 80 MPa, respectively.

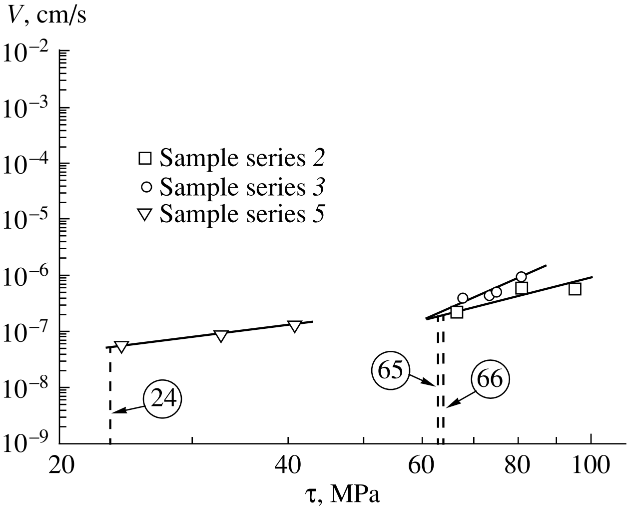

Fig. 3. Dependences of the velocity of dislocation motion on the shear stress at 600°C for samples of series *2*, *3*, and *5*. Dashed lines indicate the critical stresses τ_{cr} (the corresponding values in terms of MPa are given in circles).

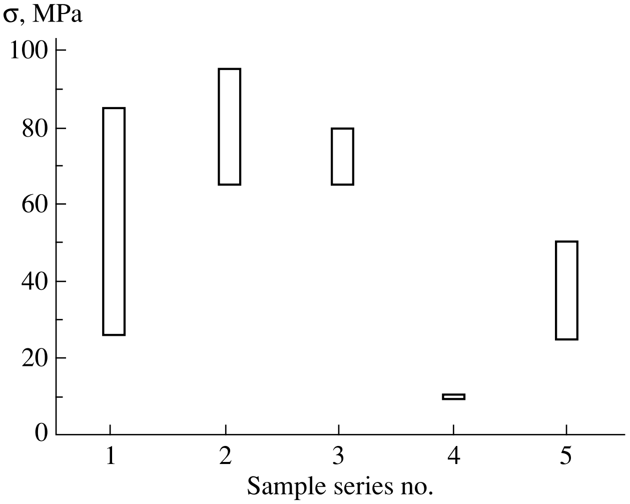

Fig. 4. Histogram of the critical stress of the onset of dislocation motion from indentations (the lower bound of each bar) and the critical stress of the onset of multiple dislocation glide from internal sources (the upper bound of each bar) in the studied samples at 600°C.

In samples of series *4*, the multiple generation of dislocations by internal stresses is observed at shear stresses less than 10 MPa when dislocations generated by indentations remain immobile. For this reason, we failed to examine the dependences of the velocity of dislocation motion on the applied stress for samples of this series. With an increase in the testing temperature to 800°C, this effect was already observed in samples of series *3* and *5*, which made the determination of the dislocation velocities at this temperature impossible. It should be noted that the shear stress of the onset of dislocation generation by internal sources in the as-grown crystals (sample series *1*) is considerably larger than that in the heat-treated samples. This circumstance allows examination of the dislocation mobility in these samples at temperatures as high as 1000°C (Fig. 2). The sole exception is provided by samples of series *2* in which the critical stress τ_{cr} and the stress of dislocation generation by internal sources at testing temperatures of 600 and 800°C are substantially larger than those in

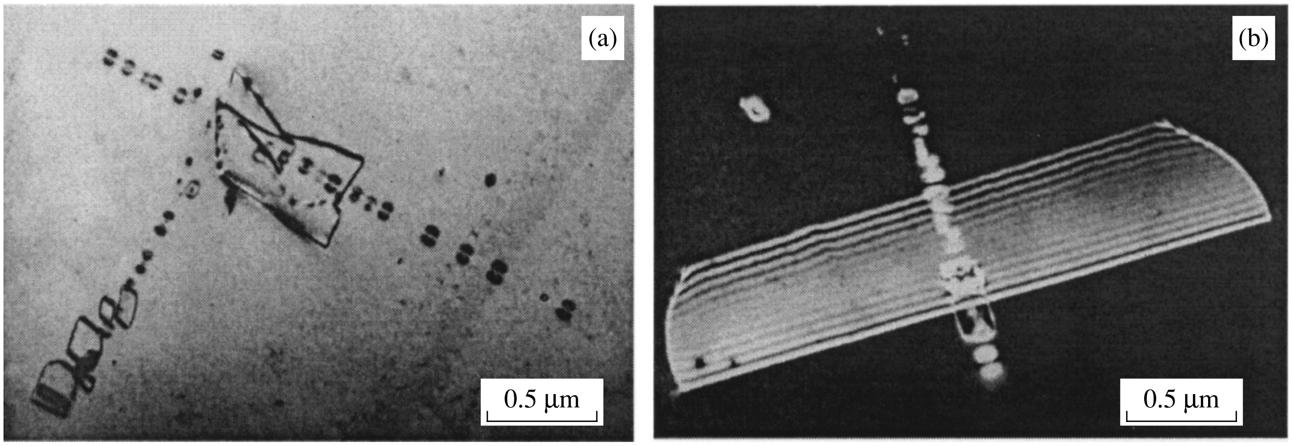

Fig. 5. (a) Bright-field (**g** = 220, $s < 0$) and (b) dark-field (**g** = 220, $s > 0$) transmission electron microscope images illustrating the prismatic slip of dislocation loops by the action of oxygen-containing precipitates under mechanical loading of samples of series *4* and *5*.

the as-grown samples. In samples of series *3*, these stresses are comparable at a testing temperature of 800°C.

Figure 4 depicts the histogram characterizing the behavior of the studied samples in the course of mechanical testing at 600°C. In this histogram, the lower bound of each bar corresponds to the critical stress τ_{cr} and the upper bound of each bar corresponds to the stress of the onset of multiple dislocation generation by internal sources in the samples. The low-temperature heat treatment at 450 and 650°C for 16 h (sample series *2* and *3*) leads to a considerable increase in the critical stress τ_{cr} as compared to that in the as-grown samples. Moreover, the stress of the onset of multiple dislocation generation by internal sources also increases in the samples heat treated at 450°C. The multistage heat treatment under conditions providing the formation of the internal getter in the silicon wafers (sample series *4* and *5*) is accompanied by a noticeable loss of their strength. From this viewpoint, the four-stage heat treatment involving the low-temperature stage at 450°C (sample series *4*) is the most dangerous. The critical stress τ_{cr} for samples of series *5* is virtually comparable to those characteristic of the samples in the postgrowth state. However, the multiple dislocation generation by internal sources in samples of series *5* occurs under considerably smaller stresses.

The electron microscopic investigation of the samples after mechanical testing demonstrated that oxygen-containing precipitates formed through the decomposition of an oxygen supersaturated solution upon heat treatment providing the formation of the internal getter play the role of heterogeneous nucleation sites of dislocations in the wafer bulk. The dislocation loops arising around precipitates propagate in the wafer bulk through the prismatic slip mechanism (Fig. 5).

4. DISCUSSION

The results obtained indicate that low-temperature heat treatment at 450°C (for 16 h) results in substantial hardening of the silicon wafers as compared to their postgrowth state. This is confirmed both by an increase in the critical stress τ_{cr} and the stress of the onset of multiple dislocation generation by internal sources and by a decrease in the velocity of dislocation motion under external stresses. As the temperature of low-temperature annealing increases to 650°C, the critical stress τ_{cr} in the silicon wafers, as before, remains larger than that in the as-grown samples, whereas the stress of the onset of multiple dislocation generation by internal sources somewhat decreases.

The multistage heat treatment under conditions providing the formation of the efficient internal getter in the bulk of the silicon wafers lead to a loss of their strength. This loss of strength is especially large (compared to the postgrowth state) in the case when the low-temperature (nucleation) stage of multistage annealing is performed at 450°C (sample series *4*). The critical stress τ_{cr} and the stress of the onset of multiple dislocation generation by internal sources in these wafers almost coincide with each other and are several times less than those in the postgrowth wafers. Silicon wafers of this series are also characterized by the worst structural perfection among all the studied wafers (Table 2). When the low-temperature stage of annealing is performed at 650°C, the aftereffects of the multistage heat treatment are not so drastic. In actual fact, the critical stresses τ_{cr} in these wafers are, though smaller, virtually

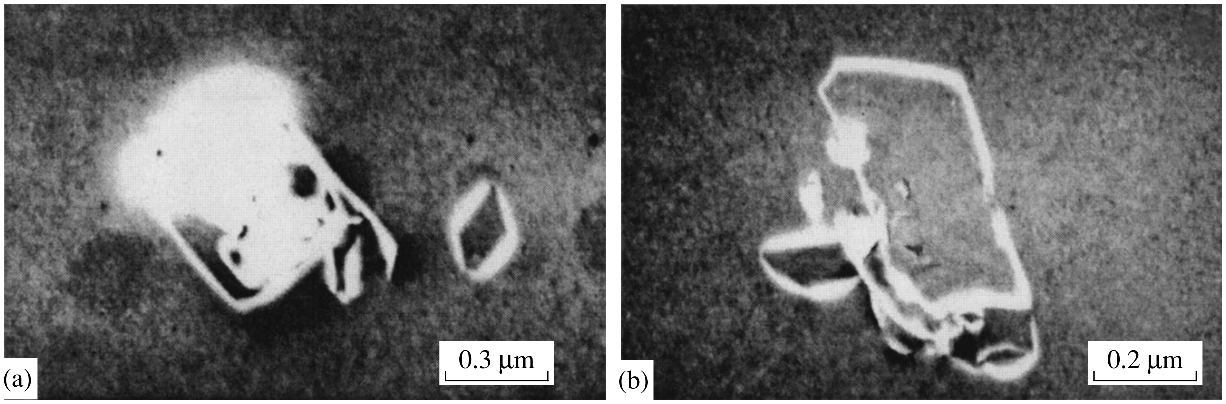

Fig. 6. Dark-field (**g** = 220, $x < 0$) transmission electron microscope images illustrating different mechanisms of dislocation loop generation during mechanical testing of silicon wafers. The images correspond to the initial stage of prismatic slip of dislocation loops. Sample series: (a) *4* (dislocation loops generated in the habit plane of the oxygen-containing precipitate nonconservatively climb to the glide plane) and (b) *5* (generation of a tangle of dislocation loops and their retardation at small-sized precipitates).

comparable to those in the as-grown wafers, whereas the stresses of the onset of multiple dislocation generation by internal sources decrease from ~85 to ~50 MPa (sample series *5*).

It seems likely that the observed effects are caused primarily by structural transformations in the silicon crystal lattice due to the decomposition of the oxygen supersaturated solution during heat treatment of the silicon wafers. It is well known that heat treatment of silicon wafers at a temperature of 450°C brings about the generation of thermodonors, i.e., clusters consisting of several oxygen atoms. The concentration of these clusters in silicon wafers can be as high as 10^{16} cm^{-3}. Apparently, it is these clusters that play the role of efficient stoppers hindering the generation of dislocation loops and their propagation in the crystal matrix under external loads. An increase in the annealing temperature to 650°C (sample series *3*) results in a certain increase in the size of the formed oxygen-containing clusters. In this case, in addition to small-sized clusters acting as stoppers, the crystal lattice involves a number of larger sized oxygen-containing formations which play the role of heterogeneous nucleation sites of dislocations. After this annealing, the critical stress τ_{cr} in the silicon wafers remains sufficiently large, whereas the stress of the onset of multiple dislocation generation by internal sources somewhat decreases compared to that in the silicon wafers in the postgrowth state.

In the course of multistage (in our case, four-stage) heat treatment, a great number of sufficiently large-sized oxygen-containing precipitates and precipitate dislocation pileups are formed in the wafer bulk. These formations play the role of an efficient getter for rapidly diffusing contaminations. Electron microscopic observations revealed that the concentration of gettering centers in the silicon wafers can be as large as (1–4) × 10^{11} cm^{-3}. It is found that layered precipitates ~150 nm in size are formed in silicon wafers for which the low-temperature (nucleation) stage of the heat treatment is carried out at 450°C. In the case when the low-temperature stage of the heat treatment is performed at 650°C, the oxygen-containing precipitates increase in size to ~220 nm and in thickness to ~100 nm. Note that the crystal lattice also contains precipitates with considerably smaller sizes. The sufficiently large-sized oxygen-containing precipitates formed in the wafer bulk are efficient heterogeneous nucleation sites of dislocations under the action of thermal or mechanical stresses.

During mechanical testing of silicon wafers with an internal getter, the generation of dislocation loops can occur through two different mechanisms. In the first case, dislocation loops are initially generated around precipitates in the precipitate habit plane. Then, these loops nonconservatively climb to the glide plane and propagate in the crystal lattice through the prismatic slip mechanism (Fig. 6a). In the second case, tangles of dislocation loops (a number of which are located in the corresponding glide planes) are formed around large-sized precipitates; in the process, small-sized precipitates contained in the crystal matrix act as stoppers against dislocation motion (Fig. 6b). The difference in the defect states formed in the crystal lattice upon multistage heat treatment of sample series *4* and *5* is most likely the main reason for the considerable difference in their strength properties.

5. CONCLUSION

The above results demonstrated that the correct choice of temperature–time schedules for the low-temperature (nucleation) stage of annealing is of crucial importance. In particular, we established that multistage heat treatment involving the low-temperature stage at 650°C offers undeniable advantages.

REFERENCES

1. H. Alexander, in *Dislocation in Solids*, Ed. by F. R. N. Nabarro (Elsevier, Amsterdam, 1986), Vol. 7, Chap. 35, pp. 113–235.
2. K. Sumino, in *Proceedings of the 1st International Autumn School on Gettering and Defect Engineering in the Semiconductor Technology, Garzau, 1985*, Ed. by H. Richter, p. 41.
3. S. Senkader, K. Jurkschat, D. Gambaro, *et al.*, Philos. Mag. A **81** (3), 759 (2001).
4. I. V. Peidous and K. V. Loiko, Proc.—Electrochem. Soc. **17**, 145 (2000).
5. I. V. Peidous, K. V. Loiko, N. Balasubramaniam, and T. Schuelke, Proc.—Electrochem. Soc. **17**, 180 (2000).
6. K. L. Enisherlova, M. G. Mil'vidskiĭ, V. Ya. Reznik, and T. F. Rusak, Kristallografiya **36** (5), 1259 (1991) [Sov. Phys. Crystallogr. **36**, 711 (1991)].
7. M. V. Mezhennyĭ, M. G. Mil'vidskiĭ, V. F. Pavlov, and V. Ya. Reznik, Fiz. Tverd. Tela (St. Petersburg) **43** (1), 47 (2001) [Phys. Solid State **43**, 47 (2001)].
8. B. Ya. Farber and V. I. Nikitenko, Phys. Status Solidi A **73**, K141 (1982).

Translated by O. Borovik-Romanova

Physics of the Solid State, Vol. 44, No. 7, 2002, pp. 1291–1297. Translated from Fizika Tverdogo Tela, Vol. 44, No. 7, 2002, pp. 1236–1242.
Original Russian Text Copyright © 2002 by Skvortsov, Litvinenko.

DEFECTS, DISLOCATIONS, AND PHYSICS OF STRENGTH

Acoustic Emission Caused by an Edge Dislocation Breaking Away and Coming to Rest in an Isotropic Medium

A. A. Skvortsov and O. V. Litvinenko
Ul'yanovsk State University, ul. L'va Tolstogo 42, Ul'yanovsk, 432700 Russia
e-mail: scvor@sv.uven.ru

Received July 16, 2001; in final form, October 15, 2001

Abstract—Acoustic emission produced by a moving edge dislocation in an isotropic crystal is investigated theoretically. It is shown that the acoustic-emission spectrum associated with a dislocation breaking away and coming to rest is similar to that associated with the annihilation of two dislocations. In the case where a linear defect breaks away and comes to rest periodically, additional extrema appear in the acoustic-emission spectrum and the frequencies corresponding to the maxima in the spectrum are multiples of the dislocation hopping frequency between minima of the potential-energy profile. Both cases of large and small distances of the acoustic-emission detection point from a dislocation array are considered. The latter case is exemplified by experimentally observed acoustic emission associated with electric-field-stimulated motion of edge dislocations in silicon.

1. INTRODUCTION

Dislocations in crystals can move under the action of mechanical stresses [1], electric [2] and magnetic fields [3], etc. Break-away and motion of dislocations, as well as other plastic effects [4], are accompanied by the emission of acoustic waves differing in type and spectrum.

There is a great body of experimental data on acoustic emission (AE), but their interpretation presents severe problems. In addition, the acoustic pulses produced by individual dislocations can be detected only in exceptional cases [5]. Therefore, in order to make a direct comparison between experimental spectra and predicted dependences, it is convenient to construct acoustic images of the elementary acts of plastic deformation associated with an ensemble of linear defects. On the other hand, when all dislocations move in a similar manner and their AE spectra are roughly the same, the experimentally observed total AE spectra can be qualitatively analyzed using the calculated spectrum for a single dislocation.

In this paper, we consider the case where AE is produced by parallel straight edge dislocations which either once or periodically break away and come to rest in an isotropic medium.

2. THE ELASTIC RADIATION FIELD OF PARALLEL STRAIGHT EDGE DISLOCATIONS

Acoustic radiation generated by a set of arbitrarily moving dislocations is described in crystal acoustics [6] by a dynamic wave equation and a modified Hooke law with allowance for time-dependent lattice distortions due to dislocations:

$$\rho\frac{\partial^2 v_i(\mathbf{r},t)}{\partial t^2}-\lambda_{iklm}\nabla_k\nabla_l v_m(\mathbf{r},t)=\lambda_{iklm}\nabla_k j_{lm}(\mathbf{r},t), \quad (1)$$

$$\sigma_{ik}(\mathbf{r},t)=\lambda_{iklm}\int[\nabla_l v_m(\mathbf{r},t')+j_{lm}(\mathbf{r},t')]dt', \quad (2)$$

where ρ is the density of the medium, $v_i(\mathbf{r}, t)$ is the vibrational velocity of elements of the medium, $\sigma_{ik}(\mathbf{r}, t)$ is the stress tensor, λ_{iklm} is the elastic moduli tensor, and j_{lm} is the dislocation flux density tensor.

Let us consider an array of parallel straight edge dislocations occupying a finite volume and moving in one of their slip planes, which is dictated by external forces. The rectangular coordinate frame is set with the z axis along the dislocation lines and the x axis lying in the slip plane in which the dislocations move. Therefore, the slip direction and the Burgers vectors of the edge dislocations are parallel to the x axis. In the case of an infinite isotropic medium, Eqs. (1) and (2) were solved by the Green's function method in [4]. The solution for the time Fourier transform of the vibrational velocity has the form

$$v_i^{\omega}(\mathbf{R})=\frac{ic_t^2}{2}\nabla_m\int_{-\infty}^{\infty}\frac{dx'dy'}{|\mathbf{R}-\mathbf{R}'|^2}j_{km}^{s\omega}(\mathbf{R}')$$

$$\times\left\{\left[(2N_iN_k-\delta_{ik})\frac{\partial^2}{\partial\omega^2}H_0^{(2)}\left(\frac{\omega|\mathbf{R}-\mathbf{R}'|}{c_l}\right)\right.\right.$$

$$\left.+\frac{|\mathbf{R}-\mathbf{R}'|^2}{c_l^2}(N_iN_k-\delta_{ik})H_0^{(2)}\left(\frac{\omega|\mathbf{R}-\mathbf{R}'|}{c_l}\right)\right] \quad (3)$$

1063-7834/02/4407-1291$22.00 © 2002 MAIK "Nauka/Interperiodica"

$$+\left[(\delta_{ik}-2N_iN_k)\frac{\partial^2}{\partial\omega^2}H_0^{(2)}\left(\frac{\omega|\mathbf{R}-\mathbf{R}'|}{c_t}\right)\right.$$

$$\left.\left.-\frac{|\mathbf{R}-\mathbf{R}'|^2}{c_t^2}N_iN_kH_0^{(2)}\left(\frac{\omega|\mathbf{R}-\mathbf{R}'|}{c_t}\right)\right]\right\}.$$

Here, **R** is the projection of the radius vector onto the *xy* plane; $N_i = (\mathbf{R}-\mathbf{R}')_i/|\mathbf{R}-\mathbf{R}'|$; $H_0^{(2)}$ is the zero-order Hankel function of the second kind; c_l and c_t are the velocities of longitudinal and transverse acoustic waves in the medium, respectively; and

$$v_i^{\omega}(\mathbf{R}) = \int_{-\infty}^{\infty} v_i(\mathbf{R},t)e^{-i\omega t}d\omega,$$
$$j_{ik}^{s\omega}(\mathbf{R}) = \int_{-\infty}^{\infty} j_{ik}^{s}(\mathbf{R},t)e^{-i\omega t}d\omega, \tag{4}$$

where the superscript *s* denotes the symmetrical part of a tensor. The primed coordinates are restricted to the localization region of the dislocation array, and the unprimed coordinates specify the AE detection point.

Let us consider the case of large distances from the dislocation ensemble. In the wave zone, where $\omega|\mathbf{R}-\mathbf{R}'|/c_\alpha \gg 1$ ($\alpha = t, l$), the Hankel function in Eq. (3) can be approximated by its asymptotic expression for large values of the argument and $|\mathbf{R}-\mathbf{R}'|$ can be replaced by $|\mathbf{R}| = R$. In accordance with [4], we obtain

$$v_i^{\omega}(\mathbf{R}) = c_t^2\left(\frac{|\omega|}{2\pi\mathbf{R}}\right)^{1/2}\sum_{\alpha=l,t}\frac{\Phi_{ikm}^{(\alpha)}(\mathbf{n})}{c_\alpha^{5/2}}$$
$$\times\exp\left[-i\left(\frac{\omega R}{c_\alpha}-\frac{\pi}{4}\operatorname{sgn}\omega\right)\right]\int_{-\infty}^{\infty} j_{km}^{s\omega}(\mathbf{R}')dx'dy', \tag{5}$$

where **n** is a unit vector along **R**, $\Phi_{ikm}^{(l)}(\mathbf{n}) = n_in_kn_m$, and $\Phi_{ikm}^{(t)}(\mathbf{n}) = (\delta_{ik}-n_in_k)n_m$.

An asymptotic expression for the Fourier transform of the stress tensor can be found by substituting Eq. (5) into Eq. (2) and taking into account that the tensor $j_{ik}(\mathbf{R}, t)$ vanishes outside the dislocation array and, therefore, the second term in Eq. (2) is equal to zero. Integration with respect to time is reduced to division by $i\omega$ in accordance with the properties of the integral transformations [7]. The elastic moduli tensor for an isotropic medium is [4]

$$\lambda_{iklm} = \rho(c_l^2-2c_t^2)\delta_{ik}\delta_{lm}+\rho c_t^2(\delta_{il}\delta_{km}+\delta_{im}\delta_{kl}).$$

As a result, we obtain

$$\sigma_{il}^{\omega}(\mathbf{R}) = -\rho c_t^2\left(\frac{|\omega|}{2\pi R}\right)^{1/2}\sum_{\alpha=l,t}\frac{\Psi_{iklm}^{(\alpha)}(\mathbf{n})}{c_\alpha^{7/2}}$$
$$\times\exp\left[-i\left(\frac{\omega R}{c_\alpha}-\frac{\pi}{4}\operatorname{sgn}\omega\right)\right]\int_{-\infty}^{\infty} j_{km}^{s\omega}(\mathbf{R}')dx'dy', \tag{6}$$

where

$$\Psi_{iklm}^{(l)}(\mathbf{n}) = [c_l^2\delta_{ik}+2c_t^2(n_in_k-\delta_{ik})]n_ln_m,$$
$$\Psi_{iklm}^{(t)}(\mathbf{n}) = c_t^2n_l(\delta_{im}n_k+\delta_{km}n_i-2n_in_kn_m).$$

This solution is valid for all frequencies ω satisfying the condition $\omega R/c_\alpha \gg 1$. Since the distance from the dislocation array to the acoustic-radiation measurement point is assumed to be large but finite, the wave zone approximation becomes invalid for frequencies close to zero.

Now, we consider the case where $\omega|\mathbf{R}-\mathbf{R}'|/c_\alpha$ is small. The Hankel function can be replaced by its small-argument expansion, in which the dominant contribution for $\omega \longrightarrow 0$ comes from the terms involving the logarithm of the argument

$$H_0^{(2)}(z) = -\frac{2i}{\pi}\ln\frac{z}{2}+\frac{iz^2}{2\pi}\ln\frac{z}{2}-\dots.$$

We will keep only the first two terms when calculating the second derivative of $H_0^{(2)}$ in Eq. (3) and only the first term in calculating the Hankel function itself. In the derivative, we neglect the constant terms, retaining only the terms that involve the frequency logarithm. The vibrational velocity of elements of the medium is obtained to be

$$v_i^{\omega}(\mathbf{R}) = -\frac{(\gamma^2+1)}{2\pi}\int_{-\infty}^{\infty}\frac{N_m}{|\mathbf{R}-\mathbf{R}'|}j_{im}^{s\omega}(\mathbf{R}')dx'dy', \tag{7}$$

where $\gamma = c_t/c_l$.

The stress tensor is found, as in the preceding case, by substituting Eq. (7) into Eq. (2). Taking into account that $j_{ii}(\mathbf{R}) = 0$ for dislocations moving in their slip plane, we obtain

$$\sigma_{ik}^{\omega}(\mathbf{R}) = \frac{i\rho c_l^2}{\pi\omega}(1-\gamma^4)$$
$$\times\int_{-\infty}^{\infty}\frac{1}{|\mathbf{R}-\mathbf{R}'|^2}\{(1-2\gamma^2)\delta_{ik}j_{lm}^{s\omega}(\mathbf{R}')N_lN_m-j_{ik}^{s\omega}(\mathbf{R}') \tag{8}$$
$$+N_m[j_{km}^{s\omega}(\mathbf{R}')N_i+j_{im}^{s\omega}(\mathbf{R}')N_k]\}dx'dy'.$$

With $\mathbf{R}-\mathbf{R}'$ replaced by **R**, Eqs. (7) and (8) become large-distance approximations. We note that, for an arbitrary dislocation flux tensor, the elastic fields in Eqs. (7) and (8) are not wave fields. Indeed, a function describes a wave if its argument has the form $t - R/c_\alpha$. According to the retardation theorem [7], the Fourier transform of such a function contains the factor $\exp(-i\omega R/c_\alpha)$. Equations (7) and (8) do not contain this factor, in contrast to Eqs. (5) and (6), which represent a superposition of longitudinal and transverse waves. The reason for this difference is that the condition $\omega|\mathbf{R}-\mathbf{R}'|/c_\alpha \ll 1$ implies not only that the frequency is low, but also that the characteristic distance from the dislocation array (the origin of perturbations) to the detection point of the elastic fields is small in comparison with the wavelength of the acoustic radiation. Therefore, the elastic fields exhibit no wave properties in this approximation.

3. ACOUSTIC EMISSION CAUSED BY AN EDGE DISLOCATION BREAKING AWAY AND SLOWING DOWN

3.1. The Wave Approximation

Let us investigate the acoustic radiation field (at large distances from the dislocation cluster, $\omega R/c_\alpha \gg 1$) produced by a dislocation which is originally at rest and then breaks away.

As shown in [4], AE occurs only if dislocations are in a nonsteady state of motion. Acoustic emission caused by a dislocation breaking away has two components; one of them is due to the fact that the dislocation starts moving (and, therefore, the dislocation flux j_{ik} becomes nonzero), and the other is associated with further nonuniform motion of the dislocation. Under the usually realized plastic-deformation conditions, the dominant contribution to AE is due to the appearance and vanishing of the dislocation flux rather than to accelerated dislocation motion [8]. For this reason, we will consider only the former AE component and the velocity of a moving dislocation will be assumed to be constant in what follows.

Let time zero correspond to the instant at which the dislocation starts moving. In the coordinate frame chosen, the dislocation glides along the x axis in the xz plane. In this case, only two components of the flux density tensor are nonzero,

$$j_{xy}(\mathbf{R}, t) = j_{yx}(\mathbf{R}, t) = bv\theta(t)\delta(y)\delta(x - vt). \tag{9}$$

Here, b is the magnitude of the Burgers vector of the dislocation, v is the dislocation velocity after its breaking away, $\theta(t)$ is the Heaviside function, and $\delta(y)$ is the delta function. The Fourier transform of Eq. (9) is

$$j_{xy}^{\omega}(\mathbf{R}) = b\delta(y)\theta(x)e^{-i\omega x/v}. \tag{10}$$

Substituting Eq. (10) into Eqs. (5) and (6), we find the spectral components of the elastic fields. For the nonzero components, we introduce the notation $\Sigma_\mu(\mathbf{R}, t)$ with $\mu = 1, 2, \ldots, 5$, where $\Sigma_1 = \sigma_{xx}$, $\Sigma_2 = \sigma_{xy}$, $\Sigma_3 = \sigma_{yy}$, $\Sigma_4 = v_x$, and $\Sigma_5 = v_y$. When integrating over $\mathbf{R}'$, we take into account that the dislocation flux density vanishes at infinity. Since the problem has cylindrical symmetry, it is convenient to introduce cylindrical coordinates (polar radius R and polar angle φ) in the xy plane. In this case, $n_x = \cos\varphi$, $n_y = \sin\varphi$, and the elastic-field components are found to be

$$\Sigma_\mu^{\omega}(\varphi) = \operatorname{sgn}\omega \frac{\rho b c_t^2 v}{\sqrt{4\pi R|\omega|}} \times \sum_{\alpha = l, t} \frac{\Lambda_\mu^{(\alpha)}(\varphi)}{c_\alpha^{3/2}} \exp\left[-i\left(\frac{\omega R}{c_\alpha} + \frac{\pi}{4}\operatorname{sgn}\omega\right)\right], \tag{11}$$

where the $\Lambda_\mu^{(\omega)}(\varphi)$ functions describe the angular dependence of the elastic fields [4].

In the case where a uniformly moving dislocation comes to rest, the solution can be shown to be exactly the same. We note that Eq. (11) for the AE fields of a dislocation that starts moving becomes identical to the expressions derived in [4] for the AE fields that are produced in the process of annihilation of two edge dislocations moving toward each other if the velocity v in Eq. (11) is replaced by the difference between the dislocation velocities $v_2 - v_1$. Indeed, the problem of dislocation annihilation is reduced to our problem if we go over to a uniformly moving coordinate frame in which one of the two dislocations is at rest. In this coordinate frame, the velocity of the other dislocation is $v_2 - v_1$ and its AE is not affected by the dislocation at rest.

Knowing the spectral components of the elastic fields given by Eq. (11), we can find the Fourier transform of the acoustic energy flux density [6]:

$$P_i = -\sigma_{ik} v_k.$$

According to the multiplication theorem [7], the Fourier transform of the product of two functions is the convolution between their Fourier transforms:

$$P_i^{\omega} = -\sigma_{ik}^{\omega}(\mathbf{R}) v_k^{\omega}(\mathbf{R}) = -\frac{1}{2\pi}\int_{-\infty}^{\infty} \sigma_{ik}^{\omega}(\mathbf{R}, \beta) v_k^{\omega}(\mathbf{R}, \omega - \beta) d\beta. \tag{12}$$

The normalization factor in Eq. (12) corresponds to the normalization of the Fourier transforms in Eq. (4).

The AE energy density $\mathcal{E}$ is related to the energy flux density through the continuity equation

$$\frac{\partial}{\partial t}\mathcal{E} + \operatorname{div} P_i = 0. \tag{13}$$

In order to find the AE energy spectrum, we replace the differentiation with respect to time in Eq. (13) by the factor $i\omega$ and integrate over the volume. Using Gauss's theorem, the second term in Eq. (13) can be transformed into an integral over the lateral surface of a cylinder whose axis coincides with the z axis (the normal to the bases of this cylinder is perpendicular to the energy flux density vector P_k, which lies in the xy plane). As a result, we find the spectrum of the differential acoustic energy (per unit dislocation length) emitted into an elementary angle $d\varphi$:

$$dE^{\omega}(\varphi) = -P_i^{\omega} n_i R dz d\varphi.$$

Substituting Eqs. (11) and (12), we arrive at a final expression,

$$dE^{\omega}(\varphi) = \frac{\rho b^2 v^2}{8\pi\omega} \qquad (14)$$
$$\times (e^{-i\omega R/c_l}\gamma^4 \sin^2 2\varphi + e^{-i\omega R/c_t}\cos^2 2\varphi)d\varphi.$$

It is seen from Eq. (14) that the AE intensity decreases with increasing frequency, which is usually observed in experimental AE spectra of moving dislocations [3]. However, at frequencies ω close to zero, the AE energy in Eq. (14) tends to infinity, which is physically meaningless. This implies, as indicated above, that the wave approximation becomes invalid for low frequencies.

Let us consider the modification of this approximation for low frequencies. Substituting the Fourier transform of the dislocation flux density given by Eq. (10) into Eqs. (7) and (8) and replacing $\mathbf{R} - \mathbf{R}'$ by $\mathbf{R}$, we find that the Fourier transform of the vibrational-velocity vector of the medium is proportional to $1/\omega$ and the Fourier transform of the stress tensor is proportional to $1/\omega^2$. The convolution between these functions varies as $1/\omega^2$; therefore, the AE energy dE^{ω}, which is proportional to this convolution divided by $i\omega$, varies as $1/\omega^3$. In this approximation, the AE intensity tends to infinity at low frequencies. We do not present the corresponding calculations here, because they reinforce the statement that the linear theory of elasticity is inadequate for the description of elastic fields near the dislocation core.

3.2. *The Case of Small Distances from the Dislocation Array*

In the case of $(\omega|\mathbf{R} - \mathbf{R}'|/c_{\alpha}) \ll 1$, the Fourier transform of the vibrational velocity of elements of the medium can be found by substituting Eq. (10) into Eq. (7). Upon integrating with respect to the primed coordinates, we obtain an expression involving the integral sine and integral cosine of the argument $\pm(i\omega/v)(x \pm iy)$, which hamper further calculations. For this reason, we seek a solution in the form of a power series. Expanding the exponential in a Maclaurin series and taking the integrals, we obtain

$$v_x^{\omega}(\mathbf{R}) = \frac{i(\gamma^2+1)b}{4\pi}e^{-i\omega x/v}$$
$$\times\left(e^{-\omega y/v}\left[\ln\frac{i\omega R}{v}e^{-i\omega} + \sum_{k=1}^{\infty}\frac{\left(\frac{i\omega R}{v}\right)^k e^{-i\omega k}}{kk!}\right]\right. \qquad (15)$$
$$\left. - e^{\omega y/v}\left[\ln\frac{i\omega R}{v}e^{i\varphi} + \sum_{k=1}^{\infty}\frac{\left(\frac{i\omega R}{v}\right)^k e^{i\varphi k}}{kk!}\right]\right).$$

In what follows, the dislocation velocity is assumed to be small, such that $\omega R/v \gg 1$. Since a power-law function increases faster than does a logarithmic function, we neglect the first term in square brackets in Eq. (15) and keep only the largest of the remaining terms. For this purpose, we consider the function $q^k/kk!$, with q being large. For small values of k, this function increases with k; however, it goes to zero as $k \longrightarrow \infty$. Using the Stirling formula for large values of k, it can be shown that this function reaches its maximum at $k \approx q$, the maximum being $e^q/(\sqrt{2\pi}q^{3/2})$. In each of the two sums in Eq. (15), we retain only this maximum term and, after simple algebra, obtain the following asymptotic expression for the vibrational velocity of the medium in the case where the dislocation velocity is small:

$$v_x^{\omega}(\mathbf{R}) = \sqrt{i}b(\gamma^2+1)\left(\frac{v}{2\pi\omega R}\right)^{3/2}\sin\frac{3\varphi}{2}. \qquad (16)$$

In a similar manner, we find

$$v_y^{\omega}(\mathbf{R}) = \sqrt{i}b(\gamma^2+1)\left(\frac{v}{2\pi\omega R}\right)^{3/2}\cos\frac{3\varphi}{2}. \qquad (16a)$$

An asymptotic expression for the stress tensor can be derived by substituting Eq. (10) into Eq. (8), integrating the power series term by term, and determining the maximum term. As a result, the nonzero components of the stress tensor σ_{ik}^{ω} are found to be

$$\sigma_{xx}^{\omega}(\mathbf{R}) = \sigma_{yy}^{\omega}(\mathbf{R}) = \frac{2\rho c_l^2(1-\gamma^4)b}{\sqrt{i}(2\pi)^{3/2}}\left(\frac{v}{\omega R}\right)^{5/2}\sin\frac{5\varphi}{2}. \qquad (17)$$

In order to find the Fourier transform of the acoustic energy flux density, we first calculate the Fourier transform of its third time derivative,

$$\left(\frac{\partial^3}{\partial t^3}P\right)_i^{\omega} = (i\omega)^3\sigma_{ik}^{\omega} * v_k^{\omega} + 3(i\omega)^2\sigma_{ik}^{\omega} * (i\omega)v_k^{\omega}$$
$$+ 3(i\omega)\sigma_{ik}^{\omega} * (i\omega)^2 v_k^{\omega} + \sigma_{ik}^{\omega} * (i\omega)^3 v_k^{\omega},$$

because the Fourier transforms of the lower order derivatives and of the function itself have an indeterminate form of the $(\infty - \infty)$ type. The expression obtained should be divided by $(i\omega)^3$ and substituted into Eq. (13). Proceeding in the same manner as in the preceding case, the spectrum of the differential AE energy is found to be

$$dE^{\omega}(\varphi) = \frac{2\rho c_l^2(1+\gamma^2)(1-\gamma^2)b^2v^4}{\pi^2R^3\omega^4}\sin^2\frac{5\varphi}{2}d\varphi. \qquad (18)$$

4. ACOUSTIC EMISSION OF AN EDGE DISLOCATION PERIODICALLY TRAVELING FROM ONE EQUILIBRIUM POSITION TO ANOTHER

Now, we consider the AE of a dislocation breaking away and coming to rest periodically. It is assumed that an edge dislocation moves with a constant velocity v from one minimum of the Peierls energy profile to another (separated by a distance a, the spatial profile period), where the dislocation comes to rest, and, after some time, the process is repeated (with a period T) many times (Fig. 1; N is the number of repetitions). In this case, the dislocation flux density tensor has the form

$$j_{xy}(\mathbf{R}, t) = j_{yx}(\mathbf{R}, t) = bv\delta(y)\delta(x - vt) \times \sum_{k=0}^{N-1}\left\{\theta(t - kT) - \theta\left(t - \frac{a}{v} - kT\right)\right\} \tag{19}$$

and its Fourier transform is

$$j^{\omega}_{xy}(\mathbf{R}) = b\delta(y)e^{-i\omega x/v} \times \sum_{k=0}^{N-1}\left\{\theta\left(\frac{x}{v} - kT\right) - \theta\left(\frac{x}{v} - \frac{a}{v} - kT\right)\right\}. \tag{20}$$

4.1. The Wave Approximation

Substituting Eq. (20) into Eqs. (5) and (6), we find the spectral components of the elastic fields:

$$\Sigma^{\omega}_{\mu}(\varphi) = \operatorname{sgn}\omega\frac{\rho b c_t^2 v}{\sqrt{4\pi R|\omega|}}\sum_{\alpha = l, t}\frac{\Lambda^{(\alpha)}_{\mu}(\varphi)}{c_{\alpha}^{3/2}} \times \sum_{k=0}^{N-1}\left\{\exp\left[-i\left(\frac{\omega R}{c_{\alpha}} + \omega kT + \frac{\pi}{4}\operatorname{sgn}\omega\right)\right] - \exp\left[-i\left(\frac{\omega R}{c_{\alpha}} + \omega kT + \frac{\omega a}{v} + \frac{\pi}{4}\operatorname{sgn}\omega\right)\right]\right\}. \tag{21}$$

This expression differs from Eq. (11) only in the number of terms describing an elementary act of the dislocation breaking away or coming to rest with allowance for the delay time of each of these events.

In calculating the convolution between v_k and σ_{ik}, it is convenient to multiply the corresponding components in Eq. (21) together and, removing the square brackets, integrate each term separately. The final result differs from Eq. (14) only by an additional factor $\sum_{k=0}^{N-1} e^{-i\omega kT}(1 + e^{-i\omega a/v})$, which can be calculated using the familiar formula for the sum of the first N terms of a geometric progression. Thus, we obtain

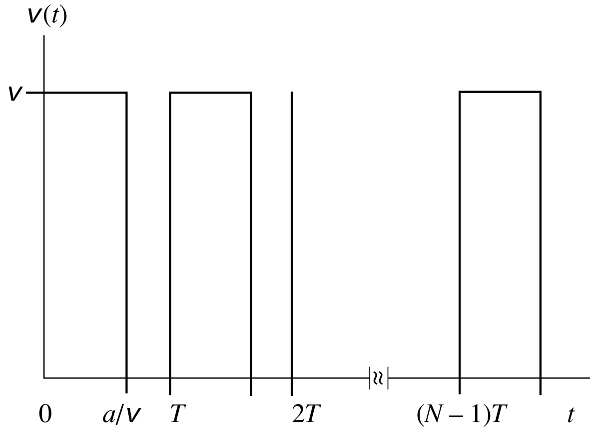

Fig. 1. Time dependence of the edge dislocation velocity (schematic).

$$\frac{dE^{\omega}(\varphi)}{d\varphi} = \frac{\rho b^2 v^2}{8\pi\omega}(e^{-i\omega R/c_l}\gamma^4\sin^2 2\varphi + e^{-i\omega R/c_t}\cos^2 2\varphi) \times \frac{1 - e^{-i\omega TN}}{1 - e^{-i\omega T}}(1 + e^{-i\omega a/v}). \tag{22}$$

One usually calculates the modulus of the spectral density when processing experimental data. This quantity is

$$\left|\frac{dE^{\omega}(\varphi)}{d\varphi}\right| = \frac{\rho b^2 v^2}{4\pi|\omega|} \times \sqrt{(\gamma^4 - 1)\sin^2 2\varphi + 1 + \frac{\gamma^4}{2}\sin^2 4\varphi\cos\left(\frac{\omega R}{c_t} - \frac{\omega R}{c_l}\right)} \times \frac{|\sin\omega TN/2||\cos\omega a/2v|}{|\sin\omega T/2|}. \tag{23}$$

Here, the radicand is the result of superposition of longitudinal and transverse waves that are emitted when the dislocation breaks away or comes to rest. Because of this factor, the spectral density $|dE^{\omega}(\varphi)/d\varphi|$ oscillates with a period of $\Delta\omega = 2\pi c_l c_t/R(c_l - c_t)$. This period is fairly small, because $\omega R/c_{\alpha} \ll 1$. However, the radicand in Eq. (23) is reduced to a constant at certain values of the observation angle ($\varphi = 0$ or $\pi/2$).

The factor $|\sin\omega TN/2|$ is a bounded, rapidly oscillatory function of ω at large values of N; therefore, we replace it by the period average of the sine modulus equal to $2/\pi$.

The AE energy is zero at $\omega = (\pi v/a) + (2\pi v/a)k$, when $|\cos\omega a/2v|$ vanishes. The positions of these minima in the energy spectrum could be used to determine the time (a/v) it takes for a dislocation to pass from one equilibrium position to the next. However, in an actual experiment, especially when the temperature and the

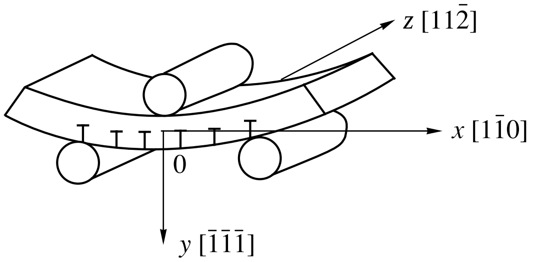

Fig. 2. Schematic illustration of silicon plate loading for the introduction of edge dislocations.

intensity of external perturbations experienced by a dislocation are not high, the transition time a/v is much shorter than the residence time in an equilibrium position $T - a/v$. In this case, the cosine in the numerator in Eq. (23) varies much faster than does the sine in the denominator and, therefore, can also be replaced by its period average.

However, $|\cos(\omega a/2v)|$ becomes a slowly varying function when the residence time is very short and the jumplike motion of the linear defect is rather continuous. Let us estimate the critical hopping frequency f_c above which the dislocation motion ceases to be periodic. The dislocation velocity averaged over a period T (Fig. 2) is $\langle v\rangle = a/T = af$. This value should be close to the hopping velocity v when the dislocation motion becomes unceasing. Since v cannot exceed the velocity of sound in the given material, the maximum average velocity is $\langle v\rangle = c_\alpha$ and, therefore, $f_c = c_\alpha/a$. The spatial period of the Peierls energy profile in a crystal is comparable to the lattice parameter, ~5 Å. The velocity of sound in solids is ~5 km/s. Therefore, $f_c \sim 10^{13}$ Hz and, in what follows, we will assume that the frequencies are far below this value.

Thus, the AE spectrum of a periodically hopping edge dislocation can be represented in the form

$$\left|\frac{dE^\omega(\varphi)}{d\varphi}\right| = \frac{\rho b^2 v^2}{\pi^3|\omega|}$$
$$\times\sqrt{(\gamma^4-1)\sin^2 2\varphi + 1 + \frac{\gamma^4}{2}\sin^2 4\varphi\cos\left(\frac{\omega R}{c_t}-\frac{\omega R}{c_l}\right)} \quad (24)$$
$$\times\frac{1}{\left|\sin\frac{\omega T}{2}\right|}.$$

This expression goes to infinity at frequencies $\omega = (2\pi/T)k$ (where k is an integer), i.e., in the case where the frequency is an integral multiple of the hopping cyclic frequency of the dislocation. In actuality, this only means that the AE intensity sharply increases at the frequencies indicated above, as is the case with resonances in dissipative media in comparison with nondissipative ones (the energy dissipation is not included in our model).

4.2. The Case of Small Distances from the Dislocation Array

It can be shown that, as in the wave-zone approximation (Subsection 4.1), the Fourier transform of the differential AE energy of a dislocation periodically hopping from one equilibrium position to another is identical to that of a dislocation once breaking away [Eq. (18)] and differs only in its having an additional harmonic factor (which is the same as that obtained in Subsection 4.1). The modulus of the AE spectral density in this case is

$$\left|\frac{dE^\omega(\varphi)}{d\varphi}\right| = \frac{\rho c_l^2(1+\gamma^2)\left|1-\gamma^2\right| b^2 v^4}{\pi^3 R^3\omega^4}\frac{\sin^2\frac{5\varphi}{2}}{\left|\sin\frac{\omega T}{2}\right|}. \quad (25)$$

Therefore, in both cases, one can determine the dislocation hopping frequency $2\pi/T$ from the positions of the maxima (especially of the first, most pronounced, maximum) in the experimental AE spectrum.

On the whole, as before, the AE spectral density falls off with increasing frequency.

If there is an array of parallel dislocations moving with the same velocity (Fig. 1), the total AE energy can be found as the sum of the AE energies produced by each of them. In this case, Eqs. (24) and (25) should be multiplied by the dislocation density and integrated with respect to the coordinates R and φ. This eliminates the coordinate dependence, but the frequency dependence remains the same. Therefore, the shape of the AE spectrum will not change; only the AE intensity will increase in this case.

If the hopping frequencies of dislocations are slightly different, then the peaks of the AE spectrum will be broadened and only a characteristic hopping frequency can be determined from them.

5. AN EXPERIMENTAL SPECTRUM OF ACOUSTIC EMISSION PRODUCED BY MOVING EDGE DISLOCATIONS IN SILICON

Below, we compare our calculations with an experimental AE spectrum in a dislocated silicon plate of (111) orientation. Dislocation motion was caused by passing a direct current of density 1.3×10^5 A/m^2 along the $[1\bar{1}0]$ direction (Fig. 2) at a temperature of 370 K. The sample preparation and experimental technique are described in detail in [9, 10]. Here, we discuss the applicability of the results obtained above to the experiment in question.

Our predictions are made for an isotropic medium. Silicon crystals are well known to be weakly anisotropic, and (111) plates of diamond-like semiconductors are elastically isotropic [11].

The criterion for the smallness of the distance of an AE detector from the array of dislocations was the

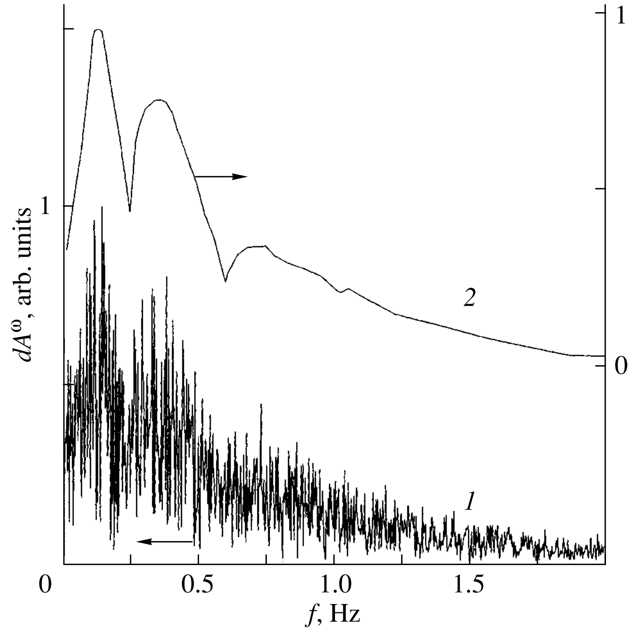

Fig. 3. (*1*) Fourier transform dA^{ω} of an AE signal taken during electric-current annealing of dislocated silicon plates (average dislocation density in the sample 5×10^6 cm^{-2}) for a current density $j = 5 \times 10^5$ A/m^2 at $T = 303$ K and (*2*) the envelope of the AE spectrum.

smallness of the quantity $\omega h/c_{\alpha}$ in comparison with unity, where h is the half-thickness of the plate (h = 200 μm). The highest AE intensity was observed in the frequency range 0–2 Hz, which is far below f_c; the velocity of transverse acoustic waves in silicon is roughly 5 km/s, and the velocity of longitudinal acoustic waves is ~9 km/s [12]. Thus, we have $\omega h/c_{\alpha} \sim 10^{-8} \ll 1$, which corresponds to the short-distance approximation described by Eq. (25).

The medium was assumed to be infinite in space. If a medium has a surface, then a transient AE appears when a dislocation reaches the surface. In the experiment in question, the electric current caused dislocations to slip in the (111) plane along the $[1\bar{1}0]$ direction; therefore, we can assume that dislocations did not glide to the upper and lower surfaces. At the electric-current strength used, the mean dislocation velocity did not exceed several micrometers per day [12], and, during the AE detection (~7 min), dislocations could not also reach the end faces of the plate, because there were no linear defects near the end faces (Fig. 2). Therefore, the transient AE can be neglected in the experiment under discussion.

Indeed, the experimental AE spectrum (Fig. 3) is consistent with the theoretical predictions, except for the absence of a sharp increase at low frequencies in it, which can be attributed to the imperfection of the mathematical model used. On the whole, the AE intensity falls off with increasing frequency and the envelope of rapid oscillations (curve *2* in Fig. 3) exhibits three clearly identifiable peaks whose positions correspond to frequencies that are multiples of the characteristic hopping frequency of dislocations.

6. CONCLUSION

Thus, we have investigated the spectral characteristics of acoustic emission produced by straight edge dislocations which once or periodically break away and come to rest. It was shown that, in both the wave zone and at small distances of the AE detection point from the dislocation cluster, the AE intensity sharply decreases with increasing frequency. In both cases, periodically interrupted motion of linear defects gives rise to additional peaks in the AE spectrum, whose frequencies are multiples of the characteristic hopping frequency of dislocations. The calculated AE spectra were shown to agree qualitatively with the experimental data obtained in single crystals of silicon; therefore, the frequency and time characteristics of the dislocation motion can be determined from the experimental AE spectra of the material.

REFERENCES

1. V. S. Boĭko and L. F. Krivenko, Zh. Éksp. Teor. Fiz. **80** (1) 255 (1981) [Sov. Phys. JETP **53**, 129 (1981)].
2. V. A. Kalitenko, I. Ya. Kucherov, and V. M. Perga, Fiz. Tekh. Poluprovodn. (Leningrad) **22** (4), 578 (1988) [Sov. Phys. Semicond. **22**, 361 (1988)].
3. V. I. Al'shits and E. V. Darinskaya, Pis'ma Zh. Éksp. Teor. Fiz. **70** (11–12), 749 (1999) [JETP Lett. **70**, 761 (1999)].
4. V. D. Natsik and K. A. Chishko, Fiz. Tverd. Tela (Leningrad) **14** (11), 3126 (1972) [Sov. Phys. Solid State **14**, 2678 (1972)].
5. S. Mil'shtein, Phys. Status Solidi A **171**, 371 (1999).
6. V. A. Krasil'nikov and V. V. Krylov, *Introduction to Physical Acoustics* (Nauka, Moscow, 1984).
7. M. A. Lavrent'ev and B. V. Shabat, *Methods of the Theory of Functions of a Complex Variable* (Nauka, Moscow, 1973).
8. K. A. Chishko, Fiz. Tverd. Tela (Leningrad) **31** (1), 223 (1989) [Sov. Phys. Solid State **31**, 122 (1989)].
9. A. A. Skvortsov, A. M. Orlov, K. E. Nikitin, and O. V. Litvinenko, Pis'ma Zh. Tekh. Fiz. **26** (21), 82 (2000) [Tech. Phys. Lett. **26**, 974 (2000)].
10. A. A. Skvortsov, A. M. Orlov, and A. A. Solov'ev, Fiz. Tverd. Tela (St. Petersburg) **43** (4), 616 (2001) [Phys. Solid State **43**, 640 (2001)].
11. Yu. A. Kontsevoĭ, Yu. M. Litvinov, and É. A. Fattakhov, *Plasticity and Strength of Semiconductor Materials and Structures* (Radio i Svyaz', Moscow, 1982).
12. *Handbook of Physical Quantities*, Ed. by I. S. Grigoriev and E. Z. Meilikhov (Énergoatomizdat, Moscow, 1991; CRC, Boca Raton, 1997).

Translated by Yu. Epifanov

Physics of the Solid State, Vol. 44, No. 7, 2002, pp. 1298–1304. Translated from Fizika Tverdogo Tela, Vol. 44, No. 7, 2002, pp. 1243–1248.
Original Russian Text Copyright © 2002 by Ovid'ko, Sheĭnerman.

DEFECTS, DISLOCATIONS, AND PHYSICS OF STRENGTH

Misfit Dislocations in Thin Films on Plastically Deformed Substrates

I. A. Ovid'ko and A. G. Sheĭnerman

Institute of Problems in Mechanical Engineering, Russian Academy of Sciences,
Vasil'evskiĭ ostrov, Bol'shoĭ pr. 61, St. Petersburg, 199178 Russia

e-mail: ovidko@def.ipme.ru

Received October 8, 2001; in final form, November 8, 2001

Abstract—A theoretical model describing the nucleation of misfit dislocations (MD) in interfaces between films and plastically deformed substrates with disclinations is proposed. The ranges of the parameters (disclination strength, density of the disclination ensemble, film thickness, and degree of misfit) within which MD nucleation is energetically favorable are found. It is shown that at certain strengths of disclinations and densities of their ensemble the critical thickness of the film on a plastically deformed substrate with disclinations can exceed that on an undeformed defect-free substrate by a few times. *© 2002 MAIK "Nauka/Interperiodica".*

1. INTRODUCTION

Thin-film heterostructures enjoy broad application in present-day micro- and nanoelectronics. The stability of the properties of heterostructures, which is of prime importance for their successful use in technology, depends substantially on the presence of defects and stress fields in the films (see, e.g., reviews [1–5] and monographs [6, 7]). For instance, the difference in the crystal lattice parameters between the substrate and film materials gives rise to the formation of internal stresses in the films, more specifically, of misfit stresses which considerably affect the evolution of the structure and functional properties of the films. In particular, if the film thickness is in excess of a certain critical value, the misfit stresses become partially accommodated through the formation of misfit dislocations (MDs) in the interface separating the substrate and the film [1–16]. Such MDs disrupt the interface coherence, which can quite frequently degrade the functional properties of heterostructures. Recently, methods for increasing the critical film thickness on substrates were proposed based on the concept of formation of thin buffer layers of a given structure between films and substrates (see, e.g., [17–20]). An alternative method of increasing the critical thickness of films on substrates is proposed and studied theoretically in this paper. This method consists essentially in a preliminary plastic deformation of the substrate with the formation of edge dislocation walls and stress fields which suppress MD nucleation and, accordingly, increase the critical thickness of a film.

2. DISCLINATIONS IN PLASTICALLY DEFORMED SUBSTRATES

Plastic deformation of a crystal is frequently accompanied by the formation of edge dislocation walls in them (small-angle grain boundaries) [21, 22]. For instance, dislocation walls of one type form when the substrate is bent. Such walls actually represent small-angle grain boundaries, each of them crossing the substrate to terminate at the opposite free surface of the latter. Dislocation walls (small-angle boundaries) in substrates can substantially affect the misfit stress relaxation processes in epitaxial layers deposited on them. In particular, the formation of dislocation walls of one type in a plastically deformed substrate is capable of narrowing the ranges of the parameters (the film thickness and the degree of misfit) within which MD formation in the interface separating the film and the substrate is energetically favorable. To calculate the critical parameters for MD nucleation at the boundary between a plastically deformed substrate (containing dislocation walls) and a film, one has to determine the stress fields generated by the dislocation walls in the film. At distances in excess of the separation between neighboring dislocations in dislocation walls, the disclination component provides a major contribution to the stress fields of such dislocation walls. Therefore, to simplify the calculation of the stress fields created in a film by edge dislocation walls, we will approximate each such wall by a wedge disclination (which bounds the wall) near the film–substrate interface (Fig. 1). Generally speaking, each finite dislocation wall is bounded by two disclinations. The second disclination bounds the dislocation wall near the free substrate surface opposite to that on which a film is deposited. The stress fields of the second disclination are screened efficiently by the (nearest) free surface and, therefore, do not affect, in any way, dislocation nucleation in the film.

3. A FILM ON A SUBSTRATE WITH DISCLINATIONS: MODEL

Let us consider a system consisting of a semi-infinite substrate with disclinations and a film of thickness h (Fig. 1). The film and the substrate are assumed to be elastically isotropic solids with equal shear moduli G and equal Poisson ratios ν. We assume that the disclinations in the substrate are of the wedge type, have the same strength ω, and are the same distance p apart, forming two infinite orthogonal rows at a distance d from the substrate surface (Fig. 1). We shall also assume that the substrate and film lattices are of the same type, the two basis vectors of each lattice lie in the interface plane and are pairwise parallel, and that the parameters of each lattice corresponding to these basis vectors are equal. (For instance, the crystal lattices of the Ge_xSi_{1-x}/Si system are mutually oriented as (001)[110] || (001)[110].) In this case, the boundary separating the substrate and film lattices is characterized by a two-dimensional dilatation misfit f determined from the relation $f = 2(a_1 - a_2)/(a_1 + a_2)$, where a_1 and a_2 are the lattice parameters of the substrate and the film, respectively.

When a film grows coherently on a substrate, the lattice misfit between the different phases and the disclinations in the substrate give rise to the formation of elastic strains in the film. For certain values of the parameters of the system (misfit f, film thickness h, distance d from the disclinations to the film–substrate interface, separation p between the disclinations, and disclination strength ω), the interface can transform to a semicoherent state characterized by MD nucleation (Fig. 2). To find the conditions favoring MD nucleation, we compare the energy of the system in the coherent state (without MDs) with that after a first single MD has formed in the system. In doing this, we assume that the positions of the disclinations in the substrate are fixed and are not affected by the MD nucleation. Within this model, the MD is an edge dislocation with the Burgers vector $\mathbf{b} = (b_l \mathbf{e}_l)$, where $\mathbf{e}_l$ is a unit vector parallel to the x_2x_3 plane and forms an angle φ with the x_2 axis. This MD line lies on an m axis related to the coordinates x_2 and x_3 through the expressions $x_2 = x_2^0 - m\sin\varphi$ and $x_3 = x_3^0 + m\cos\varphi$, where x_2^0 and x_3^0 are constants (Fig. 2).

In the case of a film growing coherently on the substrate, the energy W_0 of the system is a sum of the energy W^f of proper film strains associated with the presence of a misfit, proper energy W^{ar} of two orthogonal rows of disclinations, and the energy W^{ar-f} with which the disclination rows interact with the misfit stresses:

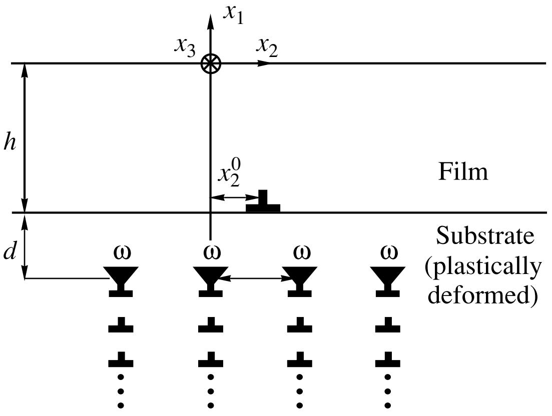

Fig. 1. Misfit dislocation in the interface between the film and a plastically deformed substrate. Wedge disclinations (triangles) bound dislocation walls of deformation origin. The disclination row along the x_3 axis is not shown.

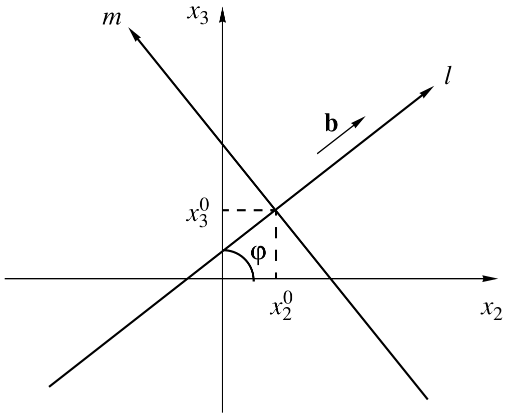

Fig. 2. Two coordinate frames on the plane. The Burgers vector of a dislocation is directed along the l axis, and the dislocation line coincides with the m axis.

$$W_0 = W^f + W^{af} + W^{ar-f}. \quad (1)$$

The energy W of a system with a single MD can be written as

$$W = W^f + W^{ar} + W^{ar-f} + W^d + W^{f-d} + W^{ar-d} + W^c, \quad (2)$$

where W^d is the proper MD elastic energy, W^{f-d} is the interaction energy between the MD and the misfit stresses, W^{ar-d} is the interaction energy between the MD and the disclination rows, and W^c is the MD core energy. (All the energies are reduced to a unit MD length.) For an MD to nucleate at the film–substrate interface, the energy W of the system with the MD must be less than the energy W_0 of the system without the MD:

$$W - W_0 = W^d + W^{f-d} + W^{ar-d} + W^c < 0. \tag{3}$$

To determine the ranges of parameters within which an MD can nucleate, we calculate (in the next section) the quantities W^d, W^{f-d}, W^{ar-d}, and W^c entering into Eq. (3). As already pointed out, these quantities are the corresponding average linear energy densities per unit MD length. We note that the linear densities of the proper energy of an MD, its interaction energy with the elastic misfit stress field, and the MD core energy are the same at any point of the MD line. At the same time, the linear interaction energy density between the MD and a disclination row is different at different points of the MD line. Therefore, in our subsequent calculation of W^{ar-d}, we average this energy density over the MD line.

4. THE ENERGY OF A DISLOCATION IN A THIN-FILM SYSTEM WITH DISCLINATIONS

The proper energy W^d (per unit MD length) of an MD lying in the film–substrate interface is given by [23]

$$W^d = \frac{Db^2}{2}\left(\ln\frac{2h-b}{b} - \frac{1}{2}\right), \tag{4}$$

where b is the magnitude of the MD Burgers vector **b** and $D = G/[2\pi(1-\nu)]$.

The elastic interaction energy W^{f-d} (per unit MD length) between the MD and the misfit stress fields is [23]

$$W^{f-d} = -4\pi(1+\nu)db_lhf. \tag{5}$$

The average interaction energy W^{ar-d} (per unit MD length) between the MD and two disclination rows is given by [24]

$$W^{ar-d} = -b_l\left\langle \int_{-h}^{0} \sigma_{ll}^{ar}(x_1, x_2 = x_2^0 - m\sin\varphi, \; x_3 = x_3^0 + m\cos\varphi)\,dx_1 \right\rangle_m, \tag{6}$$

where

$$\sigma_{ll}^{ar}(x_1, x_2, x_3) = \sigma_{22}^{ar}(x_1, x_2)\cos^2\varphi + \sigma_{33}^{ar}(x_1, x_3)\sin^2\varphi$$

is the component of the stress tensor generated by the two disclination rows; $\sigma_{22}^{ar}(x_1, x_2)$ and $\sigma_{33}^{ar}(x_1, x_3)$ are the stresses generated by disclination rows parallel to the x_2 and x_3 axes, respectively; and $\langle\ldots\rangle_m$ denotes averaging over the coordinate m along the MD line. To calculate the energy W^{ar-d}, we present the stresses $\sigma_{22}^{ar}(x_1, x_2)$ and $\sigma_{33}^{ar}(x_1, x_3)$ in the form

$$\sigma_{kk}^{ar}(x_1, x_k) = \sum_{n=-\infty}^{\infty}\sigma_{kk}^{\Delta}(x_1, x_k - np), \quad k = 2, 3, \tag{7}$$

where $\sigma_{kk}(x_1, x_k)$ is the component of the stress tensor generated by a disclination of strength ω with a line $(x_1 = -h - d,\ x_k = 0)$. The stress $\sigma_{kk}^{\Delta}(x_1, x_k)$ can be expressed through the stress function $\chi(x_1, x_k)$ of this disclination as [25]

$$\sigma_{kk}^{\Delta}(x_1, x_k) = \frac{\partial^2\chi(x_1, x_k)}{\partial x_1^2}, \quad k = 2, 3. \tag{8}$$

Using Eqs. (6)–(8) and the expression [22]

$$\chi(x_1, x_k) = \frac{D\omega}{4}[(x_1 + h + d)^2 + x_k^2]\ln\frac{(x_1 + h + d)^2 + x_k^2}{(x_1 - h - d)^2 + x_k^2} \quad (k = 2, 3) \tag{9}$$

for the stress functions $\chi(x_1, x_2)$ and $\chi(x_1, x_3)$, we obtain

$$W^{ar-d} = -\frac{D\omega b_l d}{2}[\langle g((x_2^0 - m\sin\varphi)/p)\rangle_m\cos^2\varphi + \langle g((x_3^0 + m\cos\varphi)/p)\rangle_m\sin^2\varphi], \tag{10}$$

where

$$g(t) = \sum_{n=-\infty}^{\infty}\left[\ln\frac{d^2 + p^2(t-n)^2}{(2h+d)^2 + p^2(t-n)^2} - \frac{4h(h+d)(2h+d)/d}{(2h+d)^2 + p^2(t-n)^2}\right]. \tag{11}$$

Summation of the series in Eq. (11) yields

$$g(t) = \ln\frac{\cosh(2\pi d/p) - \cos(2\pi t)}{\cosh(2\pi(2h+d)/p) - \cos(2\pi t)} - \frac{4\pi h(h+d)}{pd}\frac{\sinh(2\pi(2h+d)/p)}{\cosh(2\pi(2h+d)/p) - \cos(2\pi t)}. \tag{12}$$

The energy W^c of the dislocation core is approximately equal to $Db^2/2$ [21].

Equations (3)–(5) and (10) yield the following necessary condition for MD nucleation:

$$\frac{b}{h}\left\{\ln\frac{2h-b}{b}+\frac{1}{2}-\frac{\omega d}{b}\operatorname{sgn}(b_l)\right.$$
$$\times\left[\langle g((x_2^0-m\sin\varphi)/p)\rangle_m\cos^2\varphi\right.$$
$$\left.\left.+\langle g((x_3^0+m\cos\varphi)/p)\rangle_m\sin^2\varphi\right]\right\} \tag{13}$$
$$<8\pi(1+\nu)\operatorname{sgn}(b_1)f.$$

5. THE CRITICAL PARAMETERS OF FILMS ON SUBSTRATES WITH DISCLINATIONS

To determine the ranges of parameters within which MD nucleation in the film–substrate interface is energetically favorable, we consider first the situation in which the projection of the MD line on the plane containing the disclination network is parallel to one of the disclination rows; i.e., φ = *s*π/2, where *s* = –1, 0, 1, 2. In this case, we have

$$\langle g((x_2^0-m\sin\varphi)/p)\rangle_m\cos^2\varphi = 0,$$
$$\langle g((x_3^0+m\cos\varphi)/p)\rangle_m\sin^2\varphi = g(x_3^0/p)$$

for φ = ±π/2 and

$$\langle g((x_2^0-m\sin\varphi)/p)\rangle_m\cos^2\varphi = g(x_2^0/p),$$
$$\langle g((x_3^0+m\cos\varphi)/p)\rangle_m\sin^2\varphi = 0$$

for φ = 0 or π. Hence, in the case under study, the ranges of the *f* and *h* parameters in which an MD can nucleate at the film–substrate boundary depend on the x_2^0 (or x_3^0) coordinate of the MD line relative to the disclination network. The values of x_2^0 and x_3^0 will be calculated below from the condition of the minimum of the energy W^{ar-d}.

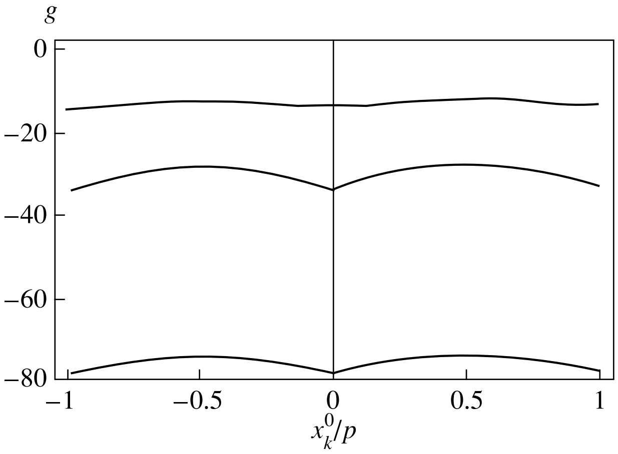

Fig. 3. Functions $g(x_k^0/p)$ plotted for the cases (top to bottom) $d/p = 0.2$, $h/p = 0.3$; $d/p = 0.05$, $h/p = 0.3$; and $d/p = 0.05$, $h/p = 0.5$.

Figure 3 plots the $g(x_k^0/p)$ relations ($k = 2, 3$) for various values of d/p and h/p. As seen from Fig. 3, for any values of d/p and h/p, the maxima of the $g(x_k^0/p)$ functions lie at points $x_k^0 = (j + 1/2)p$ and their minima are at $x_k^0 = \tilde{j}p$, where *j* and $\tilde{j}$ are integers, $k = 2$ if φ = 0 or π, and $k = 3$ for φ = ±π/2.[1] Hence, the energy W^{ar-d} passes through a minimum at $x_k^0 = (j + 1/2)p$ for $b_l = +b$ and at $x_k^0 = \tilde{j}p$ for $b_l = -b$. Substituting into Eq. (13) two different pairs of equalities [($x_k^0 = p/2$, $b_l = +b$) and ($x_i^0 = 0$, $b_l = -b$), with $k = 2$ if φ = 0, π and $k = 3$ for φ = ±π/2], we obtain the following relations for the critical values of the misfit:

$$8\pi(1+\nu)f^{+} = \frac{b}{h}\left\{\ln\frac{2h-b}{b}+\frac{1}{2}+\frac{2\omega d}{b}\right.$$
$$\times\left[\ln\frac{\cosh\pi(2h+d)/p}{\cosh\pi d/p}\right. \tag{14}$$
$$\left.\left.+\frac{2\pi h(h+d)}{pd}\tanh\pi(2h+d)/p\right]\right\},$$

$$8\pi(1+\nu)f^{-} = \frac{b}{h}\left\{-\ln\frac{2h-b}{b}-\frac{1}{2}+\frac{2\omega d}{b}\right.$$
$$\times\left[\ln\frac{\sinh\pi(2h+d)/p}{\sinh\pi d/p}\right. \tag{15}$$
$$\left.\left.+\frac{2\pi h(h+d)}{pd}\cosh\pi(2h+d)/p\right]\right\}.$$

In Eqs. (14) and (15), f^{+} and f^{-} are the maximum and minimum values of the misfit *f* at which an MD with φ being a multiple of π/2 and b_l equal to $+b$ and $-b$, respectively, can nucleate in the film–substrate interface.

Figure 4 displays plots of $f^{+}(h/b)$ and $f^{-}(h/b)$ in the h/b vs. *f* coordinate frame for different values of ω. Nucleation of MDs with $b_l = b$ is energetically favorable for $f > f^{+}(h/b)$ (region I in Fig. 4). MDs with $b_l = -b$ can form for $f < f^{-}(h/b)$ (region III). Nucleation of

---

[1] Differentiation of Eq. (12) yields the same result.

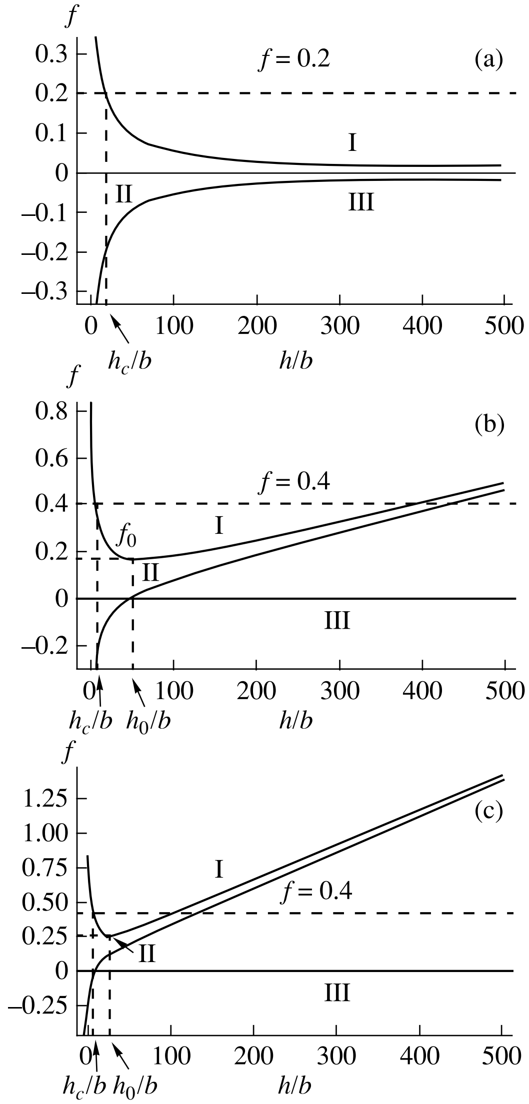

Fig. 4. Phase diagram of the system plotted in the (h/b, f) coordinate frame for the case of the MD Burgers vector parallel to the disclination network lines with parameters $d = 20b$, $p = 250b$, and (a) $\omega = 0°$, (b) $\omega = 1°$, and (c) $\omega = 3°$. The lower and upper curves of f^- and f^+, respectively, separate region I, where MDs with $b_l = +b$ can nucleate, region II, where MDs do not nucleate, and region III of possible nucleation of MDs with $b_l = -b$. The values of f^+ and f^- are normalized against $1/[8\pi(1 + \nu)]$.

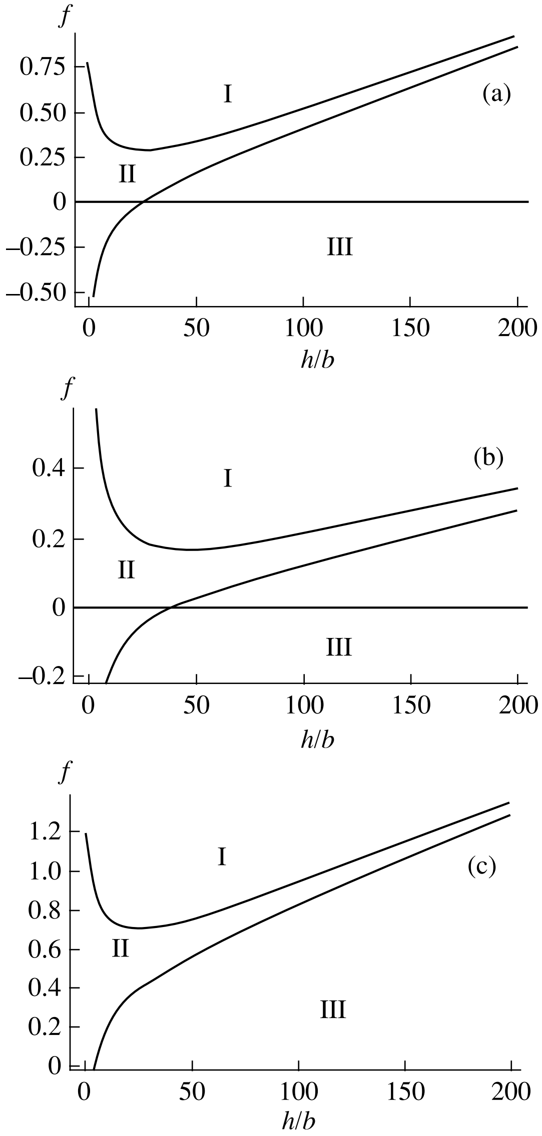

Fig. 5. Phase diagram of the system plotted in the (h/b, f) coordinate frame for the case of the MD Burgers vector parallel to the disclination network lines with parameters $\omega = 2°$ and (a) $d = 5b$, $p = 100b$, (b) $d = 5b$, $p = 300b$, and (c) $d = 50b$, $p = 100b$. The notation is the same as in Fig. 4.

MDs of both signs is energetically unfavorable for $f^-(h/b) < f < f^+(h/b)$ (region II). If the substrate has no disclinations ($\omega = 0$) (Fig. 4a), MDs can nucleate in a film of thickness h larger than the certain critical value h_c given by the intercept of the $f^+(h/b)$ (for $f > 0$) or $f^-(h/b)$ (for $f < 0$) curve with a horizontal line $f = \text{const}$. For $\omega > 0$, the $f^+(h/b)$ curve passes through a minimum (f_0), and for $f < f_0$, the critical film thickness is given by the intercept of a horizontal line $f = \text{const}$ with the $f^-(h/b)$ curve. As a result, for $f < f_0$ and $f \approx f_0$, the presence of disclinations in the substrate brings about a substantial increase (by a few times) in the critical thickness h_c compared with that for a film on a defect-free undeformed substrate. The critical thickness of a film reaches its maximum value h_0 for $f \longrightarrow f_0$, $f < f_0$. A comparison of Figs. 4b and 4c indicates that the value of h_0 for $\omega = 1°$ is larger than that for $\omega = 3°$.

Figure 5 presents the phase diagram of the system in the (h/b, $8\pi(1 + \nu)f$) coordinates for different distances d from the disclinations to the interface and different distances p between the disclinations. As seen from Fig. 5, an increase in d or a decrease in p shifts region

II, where MDs do not nucleate, toward larger misfits, while, at the same time, bringing about a decrease in h_0.

Now, we consider the case where the projection of the MD line onto the plane containing a disclination network is not parallel to any of the disclination rows ($\varphi \neq n\pi/2$, where n is an integer). To analyze this case, one has to calculate the quantities $\langle g(x_2^0 - m\sin\varphi)\rangle_m$ and $\langle g(x_3^0 + m\cos\varphi)\rangle_m$ entering into Eq. (14). In view of the periodicity of the function $g(t)$, as well as accepting the conditions $\sin\varphi \neq 0$ and $\cos\varphi \neq 0$, we obtain

$$\langle g(x_2^0 - m\sin\varphi)\rangle_m = \langle g(x_3^0 + m\sin\varphi)\rangle_m$$

$$= \frac{1}{2\pi}\int_{-\pi}^{\pi} g(t)dt = -\frac{4\pi h(h+2d)}{pd}. \qquad (16)$$

Substituting Eq. (16) into Eq. (13), we obtain the following two equations for the minimum (f'^+) and maximum (f'^-) values of the misfit f for which the nucleation of MDs with $\varphi \neq n\pi/2$ and b_l equal to $+b$ and $-b$, respectively, is possible in the film–substrate interface:

$$8\pi(1+\nu)f'^+$$

$$= \frac{b}{h}\left(\ln\frac{2h-b}{b} + \frac{1}{2} + \frac{4\pi\omega h(h+2d)}{bp}\right), \qquad (17)$$

$$8\pi(1+\nu)f'^-$$

$$= \frac{b}{h}\left(-\ln\frac{2h-b}{b} - \frac{1}{2} + \frac{4\pi\omega h(h+2d)}{bp}\right). \qquad (18)$$

As follows from Eqs. (17) and (18), an increase in ω or d or a decrease in p shifts the $f'^+(h/b)$ and $f'^-(h/b)$ curves toward larger values of f.

To find the ranges of parameters within which MDs with any Burgers vector (either parallel or not parallel to the disclination network rows) do not nucleate, the f^-, f^+, f'^-, and f'^+ were plotted vs. h/b in the same coordinate frame (not displayed here). It was found that the parameter region in which MDs with a Burgers vector oriented arbitrarily in the interface plane do not nucleate coincides with the region where nucleation of MDs with Burgers vectors parallel to one of the disclination rows is not possible (region II in Fig. 4b).

6. CONCLUSION

Thus, we carried out a theoretical study of the conditions favoring nucleation of misfit dislocations in thin films on plastically deformed substrates containing disclination ensembles. It was shown that disclinations present in the substrate affect the ranges of the parameters (film thickness h and misfit f) in which film growth without MD nucleation is energetically favorable. For certain values of f (depending on the disclination strength ω, distance p between the disclinations, and distance d from the disclinations to the interface), the critical thickness of a film on a substrate with disclinations substantially exceeds the critical thickness of a film grown on an undeformed defect-free substrate. Increasing the parameter d or ω or decreasing the parameter p shifts the (h, f) region in which MDs do not nucleate toward larger values of f. The results obtained indicate a possibility of effectively increasing the critical thickness of single-crystal films through preliminary plastic deformation of their substrates.

ACKNOWLEDGMENTS

The authors are indebted to A.L. Kolesnikova for valuable discussions.

This study was supported by the Russian Foundation for Basic Research (project no. 01-02-16853), INTAS program (grant no. 99-0216), the US Office of Naval Research (grant no. 00014-01-1-1020), and the Volkswagen Foundation (research project no. 05019225).

REFERENCES

1. E. A. Fitzgerald, Mater. Sci. Rep. **7** (1), 87 (1991).
2. J. H. van der Merve, Crit. Rev. Solid State Mater. Sci. **17** (3), 187 (1991).
3. S. C. Jain, A. H. Harker, and R. A. Cowley, Philos. Mag. A **75** (6), 1461 (1997).
4. I. A. Ovid'ko, in *Nanostructered Films and Coatings*, Ed. by G. M. Chow, I. A. Ovid'ko, and T. Tsakalakos (Dordrecht, Kluwer, 2000), p. 231.
5. I. A. Ovid'ko, Rev. Adv. Mater. Sci. **1** (2), 61 (2000).
6. Yu. A. Tkhorik and L. S. Khazan, *Plastic Deformation and Misfit Dislocations in Heteroepitaxial Structures* (Naukova Dumka, Kiev, 1983).
7. M. Yu. Gutkin and I. A. Ovid'ko, *Defects and Mechanisms of Plasticity in Nanostructural and Noncrystalline Materials* (Yanus, St. Petersburg, 2001).
8. S. C. Jain, T. J. Gosling, J. R. Willis, *et al.*, Philos. Mag. A **65** (5), 1151 (1992).
9. T. J. Gosling, R. Bullough, S. C. Jain, and J. R. Willis, J. Appl. Phys. **73** (12), 8267 (1993).
10. U. Jain, S. C. Jain, S. Nijs, *et al.*, Solid-State Electron. **36** (3), 331 (1993).
11. T. J. Gosling and J. R. Willis, Philos. Mag. A **69** (1), 65 (1994).
12. F. Bailly, M. Barbé, and G. Cohen-Solal, J. Cryst. Growth **153**, 115 (1995).
13. M. Yu. Gutkin, A. E. Romanov, and E. C. Aifantis, Phys. Status Solidi A **151** (2), 281 (1995).
14. M. Yu. Gutkin, K. N. Mikaelyan, and I. A. Ovid'ko, Fiz. Tverd. Tela (St. Petersburg) **40** (11), 2059 (1998) [Phys. Solid State **40**, 1864 (1998)]; Fiz. Tverd. Tela (St. Petersburg) **43** (1), 42 (2001) [Phys. Solid State **43**, 42 (2001)].
15. I. A. Ovid'ko, J. Phys.: Condens. Matter **11** (34), 6521 (1999); **13** (4), L97 (2001).

16. M. Yu. Gutkin, I. A. Ovid’ko, and A. G. Sheinerman, J. Phys.: Condens. Matter **12** (25), 5391 (2000).
17. D. Maroudas, L. Zepeda-Riiz, and W. H. Weinberg, Appl. Phys. Lett. **73** (6), 753 (1998).
18. G. Kästner, U. Gösele, and T. Y. Tan, Appl. Phys. A **66** (1), 13 (1998).
19. L. Zepeda-Ruiz, W. H. Weinberg, and D. Maroudas, J. Appl. Phys. **85** (7), 3677 (1999).
20. Y. Obayshi and K. Shintani, J. Appl. Phys. **88** (10), 105 (2000).
21. J. P. Hirth and J. Lothe, *Theory of Dislocations* (McGraw-Hill, New York, 1967; Atomizdat, Moscow, 1972).
22. V. I. Vladimirov and A. E. Romanov, *Disclinations in Crystals* (Nauka, Leningrad, 1986).
23. V. I. Vladimirov, M. Yu. Gutkin, and A. E. Romanov, Poverkhnost, No. 6, 46 (1988).
24. T. Mura, *Micromechanics of Defects in Solids* (Martinus Nijhoff Publ., Dordrecht, 1987), p. 1.
25. V. V. Novozhilov, *Theory of Elasticity* (Sudpromgiz, Leningrad, 1958).

Translated by G. Skrebtsov

Physics of the Solid State, Vol. 44, No. 7, 2002, pp. 1305–1309. Translated from Fizika Tverdogo Tela, Vol. 44, No. 7, 2002, pp. 1249–1253.
Original Russian Text Copyright © 2002 by Malygin.

DEFECTS, DISLOCATIONS,
AND PHYSICS OF STRENGTH

Dislocation Mechanism of Dynamic Polygonization of a Crystal Caused by Its Bending

G. A. Malygin
Ioffe Physicotechnical Institute, Russian Academy of Sciences, Politekhnicheskaya ul. 26, St. Petersburg, 194021 Russia
e-mail: malygin.ga@pop.ioffe.rssi.ru

Received November 9, 2001

Abstract—The mechanism of dynamic polygonization of a crystal is investigated in the case where only a single slip system is operative. The analysis is based on the evolution equation of the density of geometrically necessary dislocations (GNDs) generated by the crystal bending. The formation of vertical tilt walls of edge dislocations is treated as the synergetic process of GND self-organization. The spacing between these walls and the local crystal misorientation associated with them are determined. *© 2002 MAIK "Nauka/Interperiodica".*

1. INTRODUCTION

Plastic deformation of crystals is usually accompanied by the emergence of crystallographically misoriented domains (blocks, fragments). The misorientation can be both small (a few minutes of arc) and as large as tens of degrees. The mean size of fragments may also vary over a wide range, from hundreds of nanometers to several millimeters. On the whole, the fragment sizes decrease and their misorientation increases with increasing plastic deformation. The formation of misoriented domains in a deformed crystal is a result of local (or overall) elastic bending and twisting of the crystal during its plastic deformation. Dislocational relaxation of bends (their plastic accommodation) gives rise to plastic rotations of local crystal domains relative to one another. The geometrically necessary dislocations (GNDs) [1] involved in the accommodation are usually concentrated at the boundaries of crystal fragments. The higher the density of GNDs of one sign at the boundaries, the higher the crystallographic misorientation of the corresponding crystal fragments.

In this paper, we consider a mechanism of dynamic polygonization (DP) of a crystal during its bending at the initial stage of plastic deformation (easy-glide stage) when only one slip system is operative. The DP is the formation of vertical walls of dislocations perpendicular to the dislocation slip plane [2, 3]. Unlike the static polygonization (which is the formation of misoriented block dislocation structures in a crystal at elevated temperatures [4, 5]), the DP is observed at low and moderate temperatures. The DP is also called slip polygonization, because the formation of walls of dislocations in it does not involve diffusive dislocation climb, in contrast to the case of static polygonization. A dynamic polygon structure in the form of a periodic system of tilt walls of dislocations arises, for instance, in the crystal regions adjacent to the grips of the testing machine, because the crystal is bent in those regions [3]. First, we consider the formation of such dislocation structures in terms of energy and geometry. Then, we analyze the DP in terms of dislocation kinetics, which allows us to find the conditions of the formation of dynamic polygon structures and calculate the spacing between adjacent walls of dislocations in these structures as a function of the microscopic parameters that determine the evolution of the dislocation network in the deformed crystal. In terms of kinetics, the formation of dynamic polygon structures is the synergetic process of self-organization of GNDs [6].

2. POLYGONIZATION OF BENT CRYSTALS

When a crystal is bent, GNDs can be distributed randomly (Fig. 1a) or form a system of dislocation walls with an average spacing Λ between them (Fig. 1b) or all GNDs can make up a single tilt wall (Fig. 1c). The dislocation distribution in the form of a single wall corresponds to a minimum energy of the dislocation array. Indeed, in an elastically bent crystal, the GND density is $\rho = 1/bR$ [7], where b is the Burgers vector and R is the bending radius of the crystal. The total number of dislocations in the crystal is equal to $N = 4\rho L l_0$, where $2l_0$ is the crystal height and $2L$ is its width. If the dislocations are distributed at random, then their total energy, equal to the sum of the self-energies of the dislocations and their interaction energy, is given by [8]

$$E_s = A\rho\ln\frac{1}{r_0\rho^{1/2}}, \quad A = \frac{\mu b^2}{2\pi(1-\nu)}. \tag{1}$$

Here, μ is the shear modulus, ν is the Poisson ratio, and r_0 is the effective radius of the dislocation core. If the

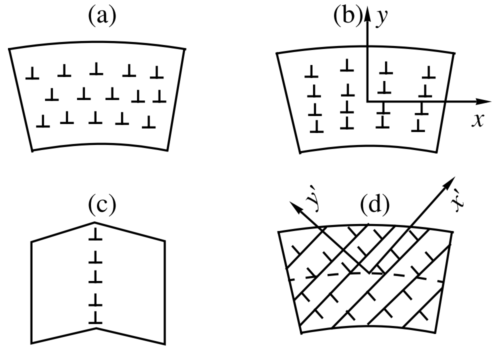

Fig. 1. Distribution of (a–c) virtual and (d) real dislocations in a bent crystal.

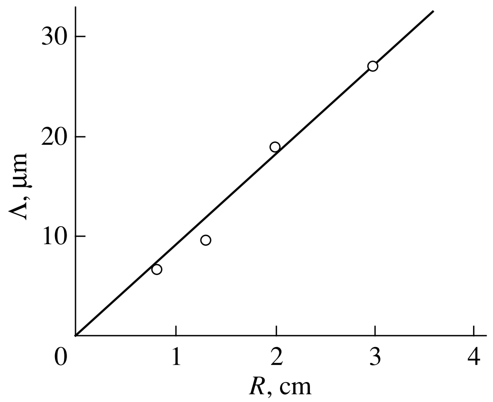

Fig. 2. Spacing between dislocation walls Λ plotted as a function of the bending radius *R* using the experimental data from [2] for a Zn crystal.

GNDs form a system of $n = 2L/\Lambda$ vertical walls (Fig. 1b) or a single tilt wall (Fig. 1c), their total energy is

$$E_n = A\rho\ln\frac{h_n}{r_0}, \quad E_1 = A\rho\ln\frac{h_1}{r_0}, \tag{2}$$

with h_n and h_1 being the spacings between dislocations in walls and in the single tilt wall, respectively. Using the relations $\rho = (h_n\Lambda)^{-1} = (2h_1L)^{-1}$, the differences in energy between the three states of the dislocation array are found to be

$$\begin{aligned} E_s - E_n &= \frac{1}{2}A\rho\ln\frac{\Lambda}{h_n} > 0, \\ E_n - E_1 &= \frac{1}{2}A\rho\ln\frac{2L}{\Lambda} > 0. \end{aligned} \tag{3}$$

From Eqs. (3), it follows that $E_s > E_n > E_1$; that is, the dislocation array in the form of a single wall has a minimum energy. As seen from Eqs. (1) and (2), this result is due to the fact that the dislocation interaction energy decreases with decreasing spacing between dislocations in the order $\rho^{-1/2} > h_n > h_1$. The misorientation of the corresponding crystal fragments increases in the reverse order: $\omega_s < \omega_n < \omega_1$, where $\omega_s = b\rho^{1/2}$, $\omega_n = b/h_n$, and $\omega_1 = b/h_1$. The elastic strain of a bent crystal is $\varepsilon = y/R = \omega$, where ω is the bending angle and y is the distance from the neutral axis (Fig. 1a). Substituting $R^{-1} = b\rho$ into this expression, we obtain a relation between the strain, bending angle, and GND density: $\varepsilon = \omega = b\rho y$. This relation corresponds to the case where the plastic deformation is proportional to the dislocation density characterized by the mean free path y. The real, rather than virtual, GNDs are in the slip planes (Fig. 1d). Therefore, in the case of plastic bend relaxation (Fig. 1d), the shear strain is equal to $\gamma_p = \varepsilon/m = b\rho x'$, where m is the orientation factor of the slip planes and x' is the mean free path of dislocations in them. Putting the mean free path of dislocations equal to $l = x' = l_0/2m$, we obtain the Ashby relation [1] $\rho = \gamma_p/bl$ between the GND density and plastic strain. Here, $l \sim l_0$ characterizes the size of the bending region. The mean magnitude of the plastic crystal misorientation is $\omega_p = \gamma_p = b\rho l = l/R$. When the plastic bending is localized in the form of a system of vertical dislocation walls with average spacing Λ between them (Figs. 1b, 1d), the mean free path of dislocations is Λ; therefore, the local crystal misorientation associated with each wall is $\omega_n = b/h_n = b\rho\Lambda = \Lambda/R$, because $\rho = 1/h_n\Lambda$. Figure 2 shows the dependence of Λ on the bending radius R based on the experimental data from [2] for a Zn crystal. This dependence is seen to be linear; therefore, the crystal misorientation ω_n associated with the formation of tilt walls, as well as the dislocation density in these walls, does not vary with Λ and R. It is obvious that the tilt angle ω_n and the spacing h_n between dislocations in a tilt wall are determined not only by the geometric and energetic factors. Furthermore, as we will see later, these parameters are mainly determined by kinetic factors.

3. THE EVOLUTION EQUATION OF GEOMETRICALLY NECESSARY DISLOCATIONS

From the energies and geometric parameters evaluated above, one can infer in which direction the GND array will evolve. However, the parameters of the resulting polygon structures remained undetermined. Furthermore, the estimations made above ignore the effect of the crystal structure on the dislocation mobility in the broad sense, i.e., not only on the velocities of dislocations but also on their immobilization at insurmountable obstacles, with the consequence that when immobilized, dislocations cease to take part in the redistribution of dislocations in the crystal. In terms of the kinetic mechanism, the spatial and temporal evolution of the GND density is described by the equation [9–12]

$$\frac{\partial\rho}{\partial t} + \left(\frac{\partial J_x}{\partial x} + \frac{\partial J_y}{\partial y}\right) = S(\rho), \tag{4}$$

where J_x and J_y are the dislocation fluxes in the dislocation slip plane and along the normal to it, respectively; $S(\rho)$ is a term describing the generation of dislocations and their immobilization and annihilation; and t is time. According to the Ashby relation, the GND generation rate is $\dot{\rho} = \dot{\gamma}/bl = (u/l)\rho$, because $\dot{\gamma} = b\rho u$, where u is the dislocation velocity. In the case of dynamic polygonization, we have $J_y = 0$ and, therefore, Eq. (4) can be written in the form

$$\frac{\partial\rho}{\partial t} + \frac{\partial J_x}{\partial x} = \frac{u}{l}\rho - h_d u \rho^2. \tag{5}$$

The second term on the right-hand side of Eq. (5) describes the process of dislocation immobilization due to the formation of dipoles from edge dislocations of the same sign; h_d is the spacing between parallel slip planes (trapping range) at which dislocations can trap one another. The flux $J_x(x)$ can be spatially inhomogeneous because GNDs can be nonuniformly distributed over the slip planes and produce long-range stresses [8, 9]:

$$\begin{aligned}\tau_d(x,t) &= A\int\frac{\rho(x',t)}{x'-x}dx' \\ &\approx A\left(2R_0\frac{\partial\rho}{\partial x} + \frac{1}{9}R_0^3\frac{\partial^3\rho}{\partial x^3} + \dots\right),\end{aligned} \tag{6}$$

where $R_0 \approx \rho^{-1/2}$ is a characteristic cutoff of the local dislocation interaction. In the case of thermally activated dislocation motion, the nonlocal dislocation diffusion flux is $J_x^{\mathrm{df}} = u\rho[(\partial \ln u/\partial\tau)_{\tau_d = 0}]\tau_d$, where $\partial \ln u/\partial\tau = V/kT$, V is the activation volume, and T is the temperature. It is assumed that $\tau_d \ll \tau$, where τ is the bending stress applied to the crystal. We also take into account the drift component of the dislocation flux $J_x^{\mathrm{dr}} = u\rho$. Substituting the total flux into Eq. (5), we arrive at the evolution equation for the GND density:

$$\begin{aligned}\frac{\partial\rho}{\partial t} + u\frac{\partial\rho}{\partial x} + \left(\frac{2VA}{kT}\right)u\frac{\partial}{\partial x}\left(\sqrt{\rho}\frac{\partial\rho}{\partial x} + \frac{1}{9\rho^{1/2}}\frac{\partial^3\rho}{\partial x^3}\right) \\ = \frac{u}{l}\rho - h_d u\rho^2.\end{aligned} \tag{7}$$

Linearizing Eq. (7), it can be shown that near the critical points $\rho_1 = 0$ and $\rho_2 = 1/h_d l$, the region of stability of the dislocation density against fluctuations of the form $\exp(\omega t + iqx)$ is determined by the equation $\omega(q) = \omega_1(q) + i\omega_2(q)$, where

$$\begin{aligned}\omega_1(q) &= u\left[\frac{1}{l} - 2h_d\rho_{1,2} + \frac{VA}{kT}\rho_{1,2}^{1/2}\left(2q^2 - \frac{1}{9\rho_{1,2}}q^4\right)\right], \\ \omega_2 &= uq.\end{aligned} \tag{8}$$

From the condition $\partial\omega_1/\partial q = 0$, we find the critical wave vectors $q_{1,2} = 3\rho_{1,2}^{1/2}$; the corresponding critical frequencies are

$$\begin{aligned}\omega_1(q_1) &= u/l > 0, \\ \omega_1(q_2) &= \frac{u}{l}\left[9\left(\frac{VA}{kT}\right)\frac{1}{h_d}\left(\frac{1}{h_d l}\right)^{1/2} - 1\right].\end{aligned} \tag{9}$$

From the above equations, it follows that the dislocation density is unstable against convective fluctuations. In addition, the initial, zero density of GNDs is unstable with respect to long-wavelength fluctuations with $\lambda_1 = 2\pi/q_1 \longrightarrow \infty$, whereas the equilibrium dislocation density ρ_2 is stable against fluctuations with $\lambda_2 = (2\pi/3)(h_d l)^{1/2}$ provided that $\omega_1(q_2) < 0$, i.e., in sufficiently thick ($l > l_c$) crystals. For example, for $\mu V/2\pi(1-\nu)kT = 5 \times 10^3$, $h_d/b = 5$, and $b = 0.3$ nm, we have $l_c \approx 0.3$ mm.

4. POLYGONIZATION KINETICS

Equation (5), which describes the GND density evolution, is a nonlinear integral differential equation. In the preceding section, we used the differential expansion of the integral in Eq. (6) and approximated the evolution equation by the pure differential equation (7). In this section, a solution to this equation is found by taking into account only the first gradient term in parentheses in Eq. (7). This solution will allow us to describe the dynamics (kinetics) of the formation of a polygon structure and calculate its parameters. We seek a solution to Eq. (7) in the form of $\rho = \rho(z, t)$, where $z = x - Ut$, with U being a constant velocity. Substituting the total derivative $\partial\rho/\partial t = \partial'\rho/\partial' t - U\partial\rho/\partial z$ into Eq. (7), we obtain

$$\begin{aligned}\frac{\partial'\rho}{\partial' t} + (u-U)\frac{\partial\rho}{\partial z} + \left(\frac{2VA}{kT}\right)u\frac{\partial}{\partial z}\left(\sqrt{\rho}\frac{\partial\rho}{\partial z}\right) \\ = \frac{u}{l}\rho - h_d u\rho^2.\end{aligned} \tag{10a}$$

In what follows, we assume that $U = u$. Using the relation $\partial'\rho/\partial' t = (\partial\rho/\partial\gamma)\dot{\gamma}$, where $\dot{\gamma} = b\rho u$, and introducing

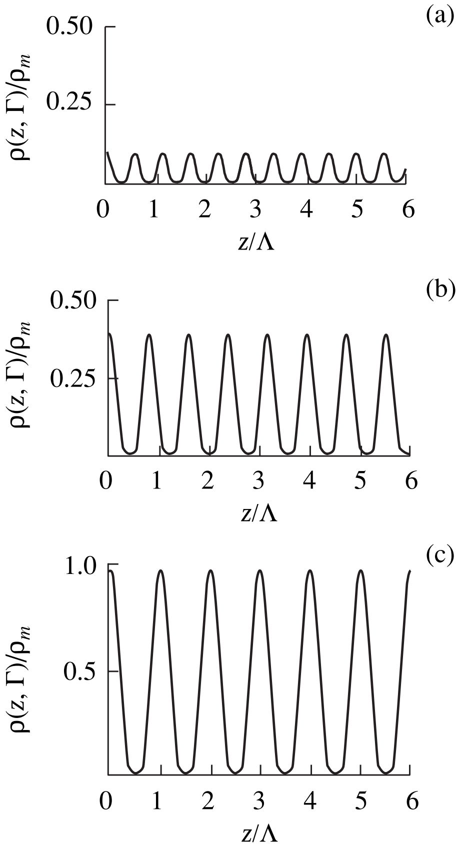

Fig. 3. Dislocation density distribution in a bent crystal for different values of the dimensionless deformation Γ: (a) 0.1, (b) 0.5, and (c) ∞.

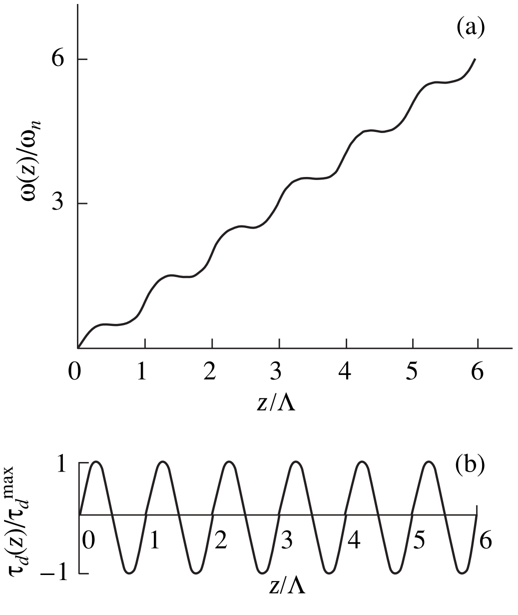

Fig. 4. Space variations of (a) the tilt angle and (b) internal stress in a polygon structure.

the dimensionless variables

$$\Psi = \frac{\rho}{\rho_2}, \quad \Gamma = \frac{h_d}{b}\gamma, \quad Z = \frac{z}{\Lambda_0}, \qquad \Lambda_0^2 = 2\left(\frac{VA}{kT}\right)\frac{1}{h_d\rho_2^{1/2}}, \tag{10b}$$

we represent Eq. (10a) in the dimensionless form

$$\Psi\frac{\partial\Psi}{\partial\Gamma} + \frac{\partial}{\partial Z}\left(\sqrt{\Psi}\frac{\partial\Psi}{\partial Z}\right) = \Psi(1-\Psi). \tag{11a}$$

In the case of a self-similar solution $\Psi(\Gamma, Z') = \phi(\Gamma)\varphi(Z')$, where $Z' = \phi^{-1/4}Z$, the variables $\phi(\Gamma)$ and $\varphi(Z')$ are separated and Eq. (11a) is reduced to two equations:

$$\frac{\partial\phi}{\partial\Gamma} = 1-\phi, \quad \frac{\partial}{\partial Z'}\left(\sqrt{\varphi}\frac{\partial\varphi}{\partial Z'}\right) = \varphi(1-\varphi). \tag{11b}$$

A solution to the first equation has the form $\phi(\Gamma) = 1 - \exp(-\Gamma)$. Substitution of $\varphi = \psi^{2/3}$ into the second equation and single integration gives

$$\left(\frac{\partial\psi}{\partial Z'}\right)^2 = \frac{9}{5}\psi^{5/3}\left(1-\frac{5}{7}\psi^{2/3}\right). \tag{12}$$

Integration of Eq. (12) using the substitution $\psi = (7/5)^{3/2}f^6$ leads to an elliptic integral of the first kind, $F(\theta, k) = Z'/2\sqrt{70}$, where $f = \cos\theta$ and $k = 2^{-1/2}$. In terms of the Jacobian elliptic function $\mathrm{cn}(x, k)$, a solution to Eqs. (10a) and (11a) can be written in the following compact form using the notation introduced above:

$$\rho(\Gamma, z) = \rho_m[1-\exp(-\Gamma)]\mathrm{cn}^4\left(\frac{z}{\Lambda'(\Gamma)}, k\right). \tag{13a}$$

Here, $\Gamma = (h_d/b)\gamma$, $\rho_m = (7/5)\rho_2$, $z = x - Ut$, $\Lambda'(\Gamma) = \Lambda'_m[1 - \exp(-\Gamma)]^{1/4}$, and $\Lambda'_m = 2\sqrt{70}F(\pi/2, k)\Lambda_0$.

This solution describes the evolution of the GND density (as a function of crystal deformation) in the form of a uniformly moving space-modulated dislocation structure of period Λ' depending on the amount of deformation. For the modulus equal to $k = 2^{-1/2}$, the Jacobian elliptic function can be approximated by a trigonometric cosine to within 10% and Eq. (13a) takes the form

$$\rho(\Gamma, z) \approx \rho_m[1-\exp(-\Gamma)]\cos^4\left(\pi\frac{z}{\Lambda(\Gamma)}\right), \tag{13b}$$

where $\Lambda(\Gamma) = \Lambda_m[1 - \exp(-\Gamma)]^{1/4}$, with $\Lambda_m = 2\pi\sqrt{70}\,\Lambda_0$. Figure 3 shows the dislocation structure as described by Eq. (13b) for different values of the dimensionless deformation Γ. It is notable that an increase in the deformation leads to an increase in the dislocation density in dislocation walls, and the spacing between walls also increases, from the fluctuation wavelength $\lambda_c = (2\pi/3)\rho_2^{-1/2} \approx 1$ μm to $\Lambda_m = 20$ μm ($l = 5$ mm, $h_d/b = 5$).

Using the relation $\rho = b^{-1}\partial\omega/\partial z$, the misorientation of the crystal associated with the formation of a polygon structure can be written as

$$\omega(\Gamma, z) = b\int_0^z \rho(\Gamma, z)dz. \tag{14}$$

Figure 4a shows the space variation of the tilt angle $\omega(z)$ in the crystal described by Eqs. (13b) and (14) for $\Gamma \longrightarrow \infty$. It is seen that the formation of each dislocation wall leads to crystal misorientation characterized by tilt angle $\omega_n = (3/8)b\rho_m\Lambda_m$. With increasing deformation, the tilt angle increases as $\omega(\Gamma) = \omega_n[1 - \exp(-\Gamma)]^{5/4}$. Since each dislocation wall is a pileup of dislocations of the same sign, its formation causes stresses which, according to Eqs. (6) and (13b), are equal to

$$\tau_d(z, \Gamma) = \frac{2A}{\sqrt{\rho}}\frac{\partial\rho}{\partial z}$$

$$= \tau_d^{\max}[1 - \exp(-\Gamma)]^{1/4}\sin\left(\frac{2\pi z}{\Lambda_m[1 - \exp(-\Gamma)]^{1/4}}\right), \tag{15}$$

$$\tau_d^{\max} = 2\pi\frac{A}{\Lambda_m}\rho_m^{1/2}.$$

Figure 4b shows the distribution of internal stresses in a polygon structure described by Eq. (15) for $\Gamma \longrightarrow \infty$. It is seen that the stress reaches a maximum value near dislocation walls and vanishes in the walls themselves.

In closing, we present qualitative estimates of the parameters of the polygon dislocation structure. The spacing Λ_m between dislocation walls was estimated above. Using the parameters indicated above, we obtain $\rho_m = 1.8 \times 10^7$ cm^{-2} and $\omega_n = 3 \times 10^{-4}$. These estimates are consistent, in order of magnitude, with the data presented in Fig. 2 and taken from [2] ($\omega_n = \Lambda/R = 9 \times 10^{-4}$). As for the internal stresses, Eq. (15) gives $\tau_d^{\max} \approx 10^{-8}\mu$. This value seems to be underestimated, which could be due to the approximation of the internal stresses by Eq. (6).

Thus, using the kinetic approach, we investigated the formation of dislocation polygon structures in bent crystals and calculated the parameters of these structures and their dependence on crystal deformation.

REFERENCES

1. M. F. Ashby, Philos. Mag. **21** (170), 399 (1970).
2. C. T. Wei and P. A. Beck, J. Appl. Phys. **27** (12), 1508 (1956).
3. K. Higashida, J. Takamura, and N. Narita, Mater. Sci. Eng. **81** (1/2), 239 (1986).
4. B. I. Smirnov, V. V. Shpeĭzman, and R. S. Chudnova, Fiz. Tverd. Tela (Leningrad) **23** (10), 2964 (1981) [Sov. Phys. Solid State **23**, 1729 (1981)].
5. S. V. Ray and G. M. Pharr, J. Am. Ceram. Soc. **75** (2), 347 (1992).
6. G. A. Malygin, Usp. Fiz. Nauk **169** (9), 979 (1999).
7. J. E. Nye, Acta Metall. **1** (2), 153 (1953).
8. J. P. Hirth and J. Lothe, *Theory of Dislocations* (McGraw-Hill, New York, 1967; Atomizdat, Moscow, 1972).
9. G. A. Malygin, Fiz. Tverd. Tela (St. Petersburg) **37** (1), 3 (1995) [Phys. Solid State **37**, 1 (1995)].
10. Sh. Kh. Khannanov, Fiz. Met. Metalloved. **84** (3), 12 (1997).
11. G. A. Malygin, Fiz. Tverd. Tela (Leningrad) **32** (4), 1102 (1990) [Sov. Phys. Solid State **32**, 646 (1990)].
12. G. A. Malygin, Fiz. Tverd. Tela (Leningrad) **31** (7), 43 (1989) [Sov. Phys. Solid State **31**, 1123 (1989)].

Translated by Yu. Epifanov

Physics of the Solid State, Vol. 44, No. 7, 2002, pp. 1310–1315. Translated from Fizika Tverdogo Tela, Vol. 44, No. 7, 2002, pp. 1254–1259.
Original Russian Text Copyright © 2002 by Golovin, Ivolgin, Lebedkin.

DEFECTS, DISLOCATIONS, AND PHYSICS OF STRENGTH

Unstable Plastic Flow in the Al–3% Mg Alloy in the Process of Continuous Nanoindentation

Yu. I. Golovin*, V. I. Ivolgin*, and M. A. Lebedkin**
** Derzhavin Tambov State University, Tambov, 392622 Russia*
e-mail: golovin@tsu.tmb.ru
*** Institute of Solid State Physics, Russian Academy of Sciences, Chernogolovka, Moscow oblast, 142432 Russia*

Received August 15, 2001; in final form, October 12, 2001

Abstract—Methods of dynamic nanoindentation were used to study unstable modes of plastic flow in micro- and submicrovolumes of the Al–3% Mg alloy. It was established that, depending on the rate of loading and dimensions of the deformed region, various regimes of unstable plastic deformation are realized. In the course of deformation, the irregular deformation curve (corresponding to a random process) reveals a quasi-periodic behavior with a characteristic amplitude of hardness oscillations. *© 2002 MAIK "Nauka/Interperiodica".*

1. INTRODUCTION

Unlike purely elastic deformation, plastic deformation in crystalline solids is always nonuniform in space and time because of the discrete nature at the atomic level. The character and magnitude of macroscopic effects caused by this fundamental discreteness are mainly determined by microscopic mechanisms of elementary acts of plasticity and by the degree of their cooperative character. The registered macroscopic manifestations of the instability of the mechanical behavior of a sample also substantially depend on its geometry and sensitivity and resolution of the apparatus used.

The effects that have been best studied to date are the regularities and the nature of instability of irreversible deformation in macroscopic samples upon uniaxial compression or tension, such as the Savart effect, which manifests itself in the form of deformation jumps in a soft testing machine (known from 1837) and the Portevin–Le Chatelier effect, which causes load jumps in a hard testing machine (studied from the beginning of the 20th century) [1–12]. Several main mechanisms of the irreversible microscopic mechanical instability have been revealed, such as (1) dynamic aging in the process of deformation, caused by the interaction of moving dislocations with mobile impurity atoms; (2) the formation and development of localized shear bands and slip bands, twins, kink bands, etc.; (3) phase transitions induced by deformation; and (4) the generation and growth of pores, cracks; etc.

When studying processes of deformation instability, two aspects are usually distinguished: (a) the dynamics of an individual isolated event and (b) statistical and correlational regularities of a large number of such events. In both cases, special methods and devices that would ensure high spatial and time resolution unattainable with standard testing devices are required to correctly analyze the dynamics of the process. In this work, we undertook special measures to enhance space–time resolution, data throughput, and the memory of the registering apparatus.

In the last decade, in view of the sharply increased interest in nonlinear dissipative systems and processes of self-organization in them, the processes of deformation instability have also been considered from the viewpoint of the theory of dynamic systems [2, 11, 12], which made it possible to substantially improve the understanding of the nature of the mechanical properties of materials. The interest in these problems is not only due to fundamental reasons, but also is caused by purely pragmatic ones, since the character of plastic flow (stable or unstable) and the degree of correlation between individual load jumps, their amplitudes, and frequencies substantially affect the applied deformation force, the microscopic geometry (degree of roughness) of the surface of the sample, and the susceptibility to failure upon forming pressure for many practically important materials.

Another group of factors that cause interest in collective phenomena in systems of defects is related to the involvement of a nanoscopic scale in physical materials science and in nanotechnologies, which requires allowance for the specific behavior of materials in submicron volumes. It is well known that the constancy of mechanical properties manifests itself in a limited range of specimen dimensions and deformation rates; as a result, the material behavior in nanovolumes cannot be derived, as a rule, from data obtained on macroscopic samples. In this connection, the main purpose of this work was to investigate the regularities of deformation in the Al–3 wt % Mg alloy (on local deformation with small loads of 10^{-3} to 10 N), whose behavior in macrovolumes (in particular, the transition from the uniform to discontinuous (jumplike) flow mode, as well as the nature and statistic characteristics of ensembles of jumps) has been well studied on macroscopic samples [2–12].

In order to localize the deformation zone to several nanometers and, simultaneously, to continuously register the load and the deformation, we chose the method of nanoindentation. This method makes it possible to study fine details of the deformation dynamics both on the level of isolated deformation jumps and for the entire statistic ensemble of a large number of jumps. However, commercial nanotesters, which usually possess a very high resolution in depth (to 0.1 nm in the best samples), have too low a time resolution, which is insufficient to correctly investigate fast processes in the deformation zone.

In a relatively narrow range of loads and strain rates, the investigation of the kinetics of the local deformation of aluminum alloys was performed in [13, 14], where a transition from the stable to an unstable regime was revealed after some critical value of the indenter-penetration depth h was achieved. However, it should be taken into account that as h grows, the relative rate of deformation $\dot{\varepsilon}$ decreases. This follows from the expression $\dot{\varepsilon} = dh/hdt$ that is usually employed for estimation of the average value of $\dot{\varepsilon}$ under an indenter [15, 16]. For this reason, it is necessary to understand what in reality affects the transition from one mode of deformation to another, i.e., whether this is the size factor, strain-rate factor, or a combination of both. The small time resolution of the apparatus used in [13, 14] prevented the authors from observing fine details in fast jumps and from classifying them. Finally, neither the shape nor the statistics of jumps were analyzed in those works; therefore, one cannot judge the mechanisms and the origin of jumps and the degree of their correlation at various stages of local deformation.

The aim of this work was to experimentally investigate and discuss these problems.

2. EXPERIMENTAL

The main principles and methods of investigation of materials during continuous local deformation (nanoindentation or depth-sensing testing) have repeatedly been described previously (see, e.g., [17–25]). However, to investigate fast dynamic processes, these methods had to be improved to enhance their time resolution.

One feature of our setup is a horizontal arrangement of the mobile rod, which permitted us to decrease the mass and, consequently, the inertia of the mobile parts of the setup. The rod was mounted on an elastic suspension, ensuring its translational motion without friction. The total rigidity of the suspension was 10^{-4} N/μm; this permitted us to realize a “soft” scheme of loading, which is more sensitive to deformation jumps than the “rigid” scheme. At one end of the rod, a standard Berkovich diamond indenter was attached; at the middle portion of the rod, a capacitance sensor of translation was mounted. The loading was made using a magnetoelectric drive in which a mobile coil interacted with an immobile dc ring magnet. By changing the amplitude, duration, and shape of current pulses in the coil, which were specified by a computer, we could vary the parameters of the loading pulse applied to the indenter.

The signal from the force and translation sensors were applied to a decade analog-to-digital converter and were subsequently processed on a personal computer. The above-described method and the setup ensured the measurement of the dynamics of the process of micro- and nanoindentation in a range of loads P from 1 to 300 mN, penetration depths h from 1–5 nm to 10 μm, and times from hundreds of microseconds to hundreds of seconds. The maximum resolution of the setup was 1 nm in depth, 0.1 mN in force, and 50 μs in time. To perform measurements at greater loads, a special attachment was used which permitted us to obtain forces to a maximum value $P_m = 15$ N with a depth resolution of 20 nm upon indentation.

All the experiments were carried out using indentation with force linearly increasing in time $P = \mu t$. The variation of the loading time t from 5 to 200 s and of the maximum force of the indenter penetration P_m between 10 mN and 15 N permitted us to change the rate of the force increase μ by a factor of more than four orders of magnitude in a range from 0.1 to 1500 mN/s.

The samples of the Al–3% Mg alloy were spark-cut from commercial sheet products in the form of parallelepipeds 3 × 5 × 40 mm in dimension. The side faces of the samples were polished using a paste with 5-μm grains to remove a layer 50–100 μm thick. Then, the samples were annealed at 450°C for 2 h and quenched in water, which gave a grain size of 200–250 μm. The final surface finish was performed using electropolishing.

3. RESULTS

In the process of the experimental investigation, more than 1000 files containing primary information on pair functions $P(t)$ and $h(t)$ were accumulated; using these data, other dependences, e.g., P–h diagrams (Fig. 1), were subsequently constructed. It follows from the entire body of the data obtained that three regimes of flow are typical; they are characterized by (1) a smooth (to an accuracy of the setup noise), (2) irregular discontinuous (jumplike), and (3) ordered steplike growth of h in time (see corresponding insets *a–c* in Fig. 1). In the limiting cases (at very low or very high loading rates), only one or two instead of three types of kinetic curves could be realized. Under conventional conditions, successive changes in the regime of flow from the first type to the second and then to the third type were observed, which could be related to the

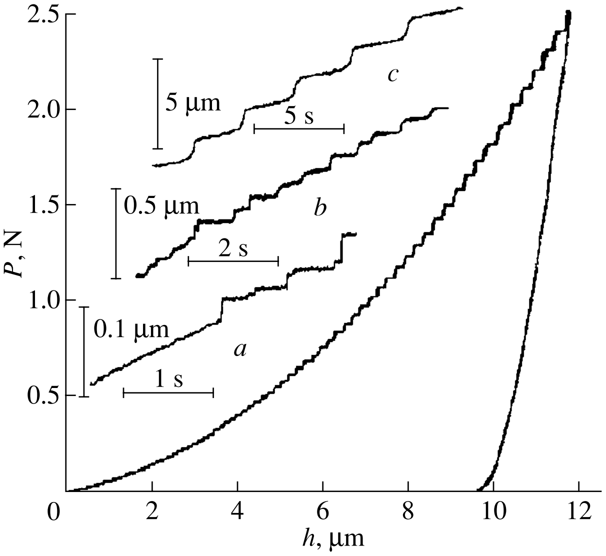

Fig. 1. Typical *P*–*h* diagram obtained upon indentation of the Al–3% Mg alloy under conditions of a linear increase in the force at a rate $\mu = 12.5$ mN/s. The maximum value of the force is $P_m = 2.5$ N. The insets show typical kinetic curves of indenter penetration in the depth–time coordinates: (a) the initial stage of penetration, when a change from a smooth to a jumplike regime of deformation occurs; (b) the intermediate stage, when the jumplike irregular mode of flow is replaced by a regular steplike mode; and (c) the final stage of the regular steplike growth of *h*.

interchange of the physically different stages of indenter penetration into the sample. These transitions could occur sharply or gradually, by means of a competitive replacement of one type of behavior by another (inset *b* in Fig. 1), which caused a change in the course of all the other dependences constructed on the basis of the primary data (Figs. 2–6).

Since the fast variations of the quantities h, $\dot{h}$, $\dot{\varepsilon}$, etc. took place against the background of their global variation in the course of the indenter penetration into the sample, in what follows we will distinguish their instantaneous values and values averaged over intervals involving several local variations. The latter are designated by characters in angular brackets. In contrast to the stage of irregular jumps, in all strain-rate regimes that lead to deformation in ordered steps, a linear growth of the depth of jumps Δh was observed with increasing $\langle h\rangle$ (Fig. 2), which means the constancy of the ratio $\Delta\sigma/\langle\sigma\rangle = \Delta H/\langle H\rangle$ at a fixed value of μ (here $\sigma = H = 0.0379P(t)/h^2(t)$ is the average contact stress at the surface of the indent equal to the Meyer hardness H). As μ changed by four orders of magnitude, $\Delta H/\langle H\rangle$ changed by a factor of less than two. The ordered regime appeared after the penetration depth achieved a certain critical value h_c, which also only weakly depended on the rate of growth of the load at the indenter μ (Fig. 3). The $\langle P\rangle = f\langle h\rangle$ dependence in this case became close to quadratic, for which reason the smoothed value of the hardness $\langle H\rangle$ became virtually independent of $\langle h\rangle$ (Fig. 4).

In contrast to uniaxial compression or tension in a rigid testing machine such as an Instron device, the rates $\langle\dot{h}\rangle \neq \text{const}$ and $\langle\dot{\varepsilon}\rangle \neq \text{const}$ are not constant upon nanoindentation. In the process of indenter penetration into the sample, they decrease ($\langle\dot{h}\rangle$ weakly and $\langle\dot{\varepsilon}\rangle$ strongly) and oscillate, similar to other variables, about the average (in each stage) values. It follows from Figs. 5 and 6 that again three regions can be distinguished in the $\dot{h}(t)$, $\dot{h}(\langle h\rangle)$, and $\dot{\varepsilon}(\langle h\rangle)$ dependences: one with a smooth variation (to an accuracy of the setup noise), one with irregular discontinuous (jumplike) variations, and one with ordered quasi-periodic variations. In this connection, it is necessary to clarify, apart from the obvious effect of the size factor, the effect of the rate factors. It is seen from Fig. 6 that for the transition into the regime of ordered jumps, two coupled conditions should be fulfilled: $\langle h\rangle > h_c$ and $\langle\dot{\varepsilon}\rangle < \dot{\varepsilon}_c$.

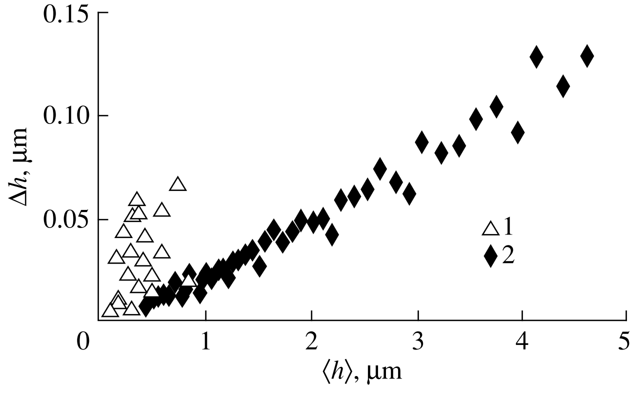

Fig. 2. Variation of the amplitude of jumps Δh as a function of depth $\langle h\rangle$ for (1) irregular and (2) regular jumps of unstable plastic deformation ($P_m = 250$ mN, $\mu = 1.25$ mN/s).

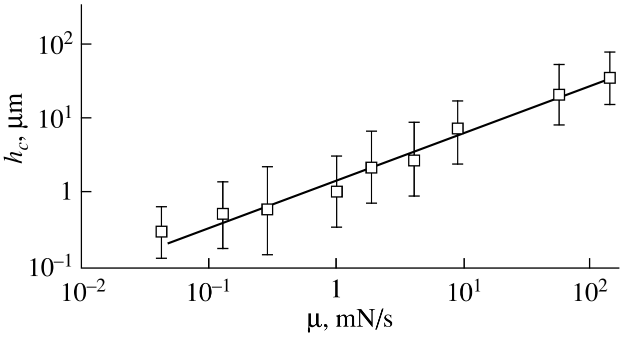

Fig. 3. Variation of the critical depth of indents h_c corresponding to the establishment of the regime of formation of regular jumps as a function of the rate of increase in the force μ.

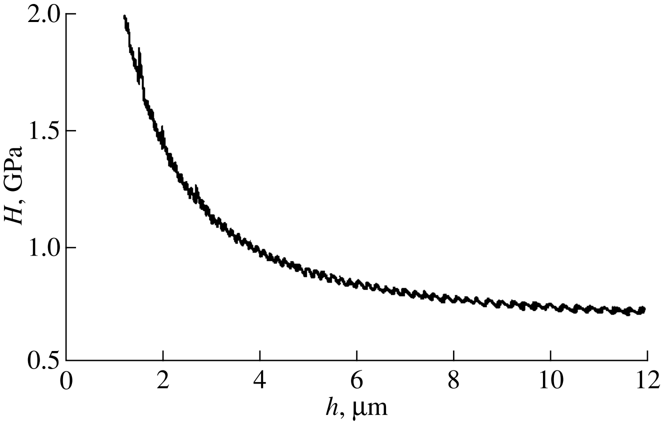

Fig. 4. Correlation between the hardness H and the penetration depth h (P_m = 2.5 N, μ = 12.5 mN/s).

4. DISCUSSION

The existence, in the general case, of three stages in the kinetics of the indenter penetration obviously entails a change in the conditions and mechanisms of plastic flow with an increase in $\langle h \rangle$ and simultaneous decrease in $\langle \dot{\varepsilon} \rangle$. In view of the absence of jumps with an amplitude reliably exceeding the level of noise in the channel of the depth measurement at small h, it is difficult to answer with certainty whether or not there are jumps in the very beginning of the process of indenter penetration into the sample. In setups with enhanced vibroprotection (as compared to this work), sharp changes in h were observed at $h \approx$ 5–10 nm and small loading rates even in plastic materials such as Al and Cu [26, 27]. In this case, the $P(h)$ dependence at the stage of retardation of the growth rate of h was close to purely elastic in accordance with the Hertz law $P \sim h^{3/2}$ [26, 27] and during the jump in h the magnitude of P remained virtually unaltered; i.e., the material suffered deformation without hardening, as does a Newtonian liquid. The authors of [26, 27] relate the generation of such jumps (with an amplitude $\Delta h \sim$ 10–20 nm) to the generation and evolution of small dislocation pileups or slip lines containing $\Delta h/b \approx 10^2$ dislocations (b is the Burgers vector), which seems to be quite reasonable. It cannot be ruled out that in our case as well, i.e., in the Al–3% Mg alloy, such jumps took place at small h but were masked or were too rare and refined by the setup vibrations to a level comparable with the noise level.

At $h >$ 50–200 nm (depending on the magnitude of μ), the amplitude of jumps became much higher than the noise level, which permitted us to reliably identify the jumps and analyze their parameters. Of course, this does not eliminate the fundamental problem of the role of noise in the dynamics of a potentially unstable system subject to a jumplike relaxation of metastable states. The operation speed of our setup permitted us to determine the real duration of the front edges of such jumps: at $h >$ 100 nm, it was $t_f = 10^{-4}$ to 10^{-3} s. In combination with the depth of the jump Δh = 10–100 nm, this gives an estimate for the average dislocation velocity in pileups of about $\Delta h/t_f \approx 10^{-4}$ m/s, which agrees with the conventional concepts of the mobility of dislocations near the yield strength. We emphasize that the magnitude of t_f found is a physical characteristic of the process of deformation of a given material rather than a reflection of transient processes in the mechanics or electronics of the nanoindentation device, whose duration was less than t_f. As was mentioned above, the transition to the stage of ordered jumps was accompanied by changes in various parameters of the deformation. In particular, each individual jump became more smooth, the deformation rate at the front decreased, and the deformation rate at the plateau increased (see inset *c* to Fig. 1). The amplitude of jumps normalized to the current values of $\langle h \rangle$ became close to constant in this case. These features indicate a change in the mechanism of instability.

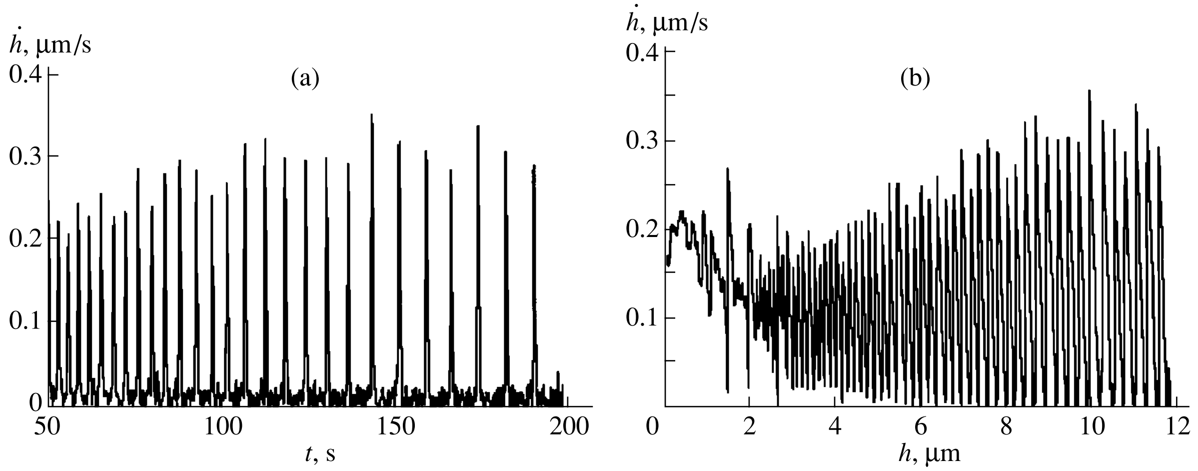

Fig. 5. Dependence of the linear rate of indenter penetration on (a) the time t and (b) current depth of the indenter penetration h.

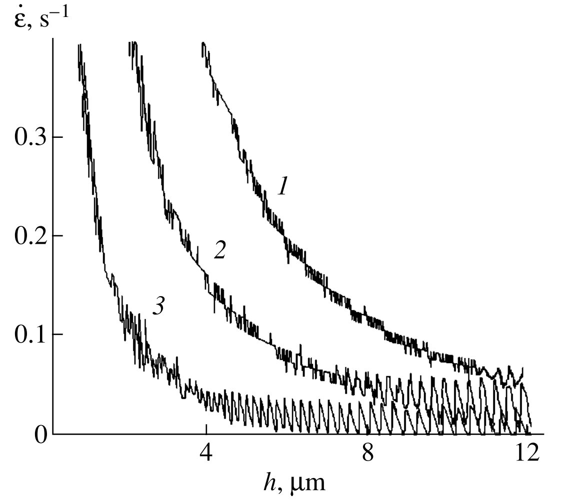

Fig. 6. Variation of the rate of relative deformation $\dot{\varepsilon}$ as a function of the current depth of the indenter penetration *h* in the region where the change in the regimes of plastic flow occurs at various rates of the force growth μ: (*1*) μ = 125, (*2*) 50, and (*3*) 12.5 mN/s. The maximum load was the same in all cases (P_m = 2.5 N).

Note that this by no means should be due to changes in the conditions of motion of individual dislocations. The change in the type of kinetic curves of the indenter penetration may be related to changes in the character of collective processes in their system. For example, upon uniaxial deformation, the manifestations of the Portevin–Le Chatelier effect are quite various and, in particular, as in this work, the irregular discontinuous (jumplike) curves are replaced by quasi-periodic ones as the deformation rate decreases. A dynamic analysis shows that upon uniaxial deformation, this tendency is related to the transition between the dynamic regimes of a deterministic chaos and self-organizing criticality [28].

As is known, in Al–Mg alloys there exists a range of strain rates $\dot{\varepsilon}$ in which the strain-rate dependence of the flow stresses has a negative slope [4, 8, 11], which provides conditions for the development of a self-oscillating process. The microscopic cause for such a behavior is the deformation aging, i.e., blocking of gliding dislocations by impurity atoms [1, 4–12] in a certain range of velocities of moving dislocations. The dynamic and statistic characteristics of steps carry information on the mobility of impurity atoms and dislocations and on the correlations between them; these problems will be the subject of another paper. As is seen from Fig. 7, the development of instabilities for the process of loading on the whole resembles a random process. However, at the stage of regular jumps, the phase trajectory acquires a form characteristic of nonlinear periodic oscillations (see inset to Fig. 7), which makes it possible to reconstruct the *N*-like curve of the strain-rate sensitivity of hardness (or average flow stresses under the indenter). Note that the amplitude of the loop in the phase diagram of these ordered oscillations upon nanoindentation is much smaller than that for irregular oscillations

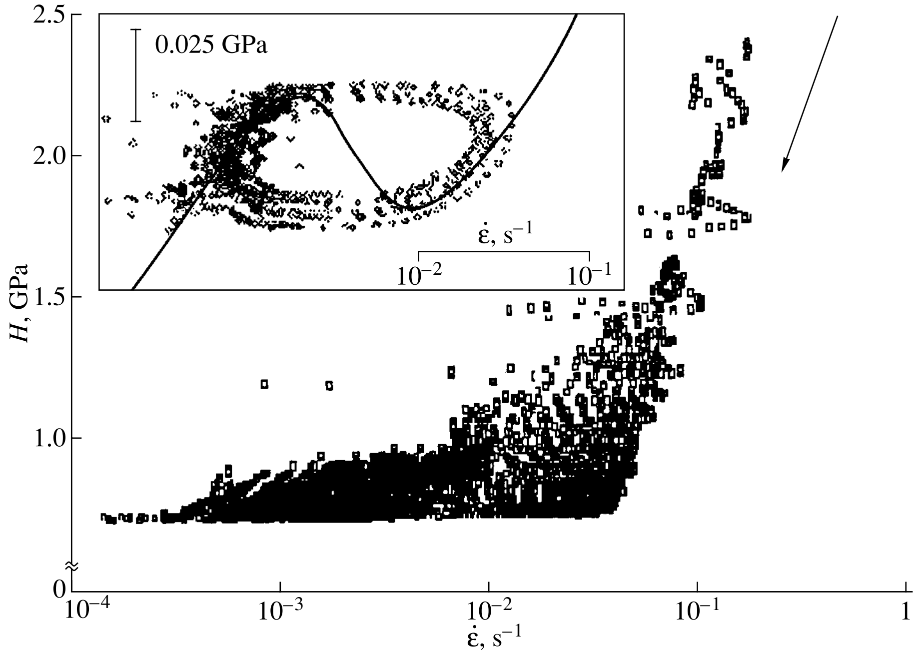

Fig. 7. Phase portrait of the process of the indenter penetration for the entire cycle of penetration (the arrow indicates the direction of the change in *H* with increasing current depth of the indenter penetration *h*). The inset displays a portion of the phase trajectory consisting of five successive pulsations at the stage of regular jumps; the solid line shows the reconstruction of the *N*-like dependence of the hardness *H* on the rate of relative deformation $\dot{\varepsilon}$.

and agrees in order of magnitude with the range of $\dot{\varepsilon}$ instability of flow given in [10] for macroscopic samples deformed by uniaxial compression. No better coincidence appears to be possible, since the concrete shape of the experimental loop depends not only on the properties of the material but also on the scheme of loading, the geometry of the sample, and the inertial properties of the testing machine. Indeed, the experimentally detected rates $\dot{\varepsilon}$ are underestimated in any case, since according to the testing scheme and calculation method, they refer to the entire loaded region (upon nanoindentation) or to the entire sample (upon uniaxial tests). It is obvious that the greater the locally deformed volume of the material (e.g., in the head of a dislocation pileup) differs from the sample volume, the greater the averaging of $\dot{\varepsilon}$ and the greater it differs from the local value $\dot{\varepsilon}_{\mathrm{loc}}$ that determines the position of the "working point" at the strain-rate dependence. From this viewpoint, a nanotester, without doubt, ensures a greater locality, i.e., a greater closeness of the measured magnitude of $\dot{\varepsilon}$ to $\dot{\varepsilon}_{\mathrm{loc}}$, than in the case of tests in a machine of the Instron type, as well as (in view of the smaller mass of moving parts) smaller distortions of the time characteristics of the jumps.

The above results and the discussion leave little doubt that the regular jumps are a result of deformation aging and can be considered a manifestation of the Portevin–Le Chatelier effect under conditions of continuous nanoindentation (or of the Savart effect, since the nanotester employed represents a soft testing machine).

5. CONCLUSION

Thus, it was shown in this paper that under the conditions of continuous nanoindentation (or microcontact interaction) in Al–3%, Mg can develop two types of instability of plastic deformation controlled by different mechanisms. Upon the transition from disordered discontinuous (jumplike) deformation to ordered deformation that develops when two interrelated conditions are fulfilled, i.e., $\langle h \rangle > h_c$ and $\langle \dot{\varepsilon} \rangle < \dot{\varepsilon}_c$, the normalized depths of the jumps $\Delta h/\langle h \rangle$ and the normalized hardness $\Delta h/\langle h \rangle$ acquire constant values only weakly depending on the rate of the indenter penetration into the sample, which corresponds to the appearance of repeated limiting cycles in the phase diagram.

ACKNOWLEDGMENTS

This work was supported in part by the Russian Foundation for Basic Research (project nos. 01-02-16573 and 01-02-16641) and by the Ministry of Education of the Russian Federation (project in the field of natural sciences, code no. E00-3.4-123).

REFERENCES

1. M. A. Shtremel', *Strength of Alloys*, Part II: *Deformation* (Mosk. Inst. Stali i Splavov, Moscow, 1997).
2. G. A. Malygin, Usp. Fiz. Nauk **169** (9), 979 (1999) [Phys. Usp. **42** (9), 887 (1999)].
3. B. J. Brindley and P. J. Worthington, Metall. Rev. **15**, 101 (1970).
4. P. Penning, Acta Metall. **20**, 1169 (1972).
5. L. P. Kubin and Y. Estrin, Acta Metall. **33**, 397 (1985).
6. Y. Estrin and P. L. Kubin, Acta Metall. **34** (12), 2455 (1986).
7. K. Chihab, Y. Estrin, L. P. Kubin, and J. Vergnol, Scr. Metall. **21**, 203 (1987).
8. L. P. Kubin, K. Chihab, and Y. Estrin, Acta Metall. **36** (10), 2707 (1988).
9. L. P. Kubin and Y. Estrin, Acta Metall. Mater. **38** (5), 697 (1990).
10. J. Balic and P. Lukac, Acta Metall. Mater. **41** (5), 1447 (1993).
11. M. A. Lebedkin and L. R. Dunin-Barkovskiĭ, Zh. Éksp. Teor. Fiz. **113** (5), 1816 (1998) [JETP **86**, 993 (1998)].
12. M. Lebyodkin, Y. Brechet, Y. Estrin, and L. Kubin, Acta Mater. **44** (11), 4531 (1996).
13. G. Berges, N. Q. Chinh, A. Juhash, and J. Lendvai, J. Mater. Res. **13** (6), 1411 (1998).
14. G. Berges, N. Q. Chinh, A. Juhash, and J. Lendvai, Acta Mater. **46** (6), 2029 (1998).
15. S. I. Bulychev and V. P. Alekhin, *Material Tests by Continuous Indentation* (Mashinostroenie, Moscow, 1990).
16. P. Grau, G. Berg, H. Meinhard, and S. Mosch, J. Am. Ceram. Soc. **81**, 1557 (1998).
17. J. B. Pethica, R. Hutchings, and W. C. Oliver, Philos. Mag. A **48** (4), 593 (1983).
18. M. F. Doerner and W. D. Nix, J. Mater. Res. **1** (4), 601 (1986).
19. D. L. Joslin and W. C. Oliver, J. Mater. Res. **5** (1), 123 (1990).
20. G. M. Pharr, W. C. Oliver, and F. R. Brotzen, J. Mater. Res. **7** (3), 613 (1992).
21. W. C. Oliver and G. M. Pharr, J. Mater. Res. **7** (6), 1564 (1992).
22. T. F. Page, W. C. Oliver, and C. J. McHargue, J. Mater. Res. **7**, 450 (1992).
23. B. N. Lucas and W. C. Oliver, Mater. Res. Soc. Symp. Proc. **358**, 645 (1995).
24. Yu. I. Golovin, V. I. Ivolgin, V. V. Korenkov, and A. I. Tyurin, Pis'ma Zh. Tekh. Fiz. **23** (16), 15 (1997) [Tech. Phys. Lett. **23**, 621 (1997)].
25. Yu. I. Golovin, A. I. Tyurin, V. I. Ivolgin, and V. V. Korenkov, Zh. Tekh. Fiz. **70** (5), 82 (2000) [Tech. Phys. **45**, 605 (2000)].
26. S. Suresh, T.-G. Nieh, and B. W. Choi, Scr. Mater. **41** (9), 951 (1999).
27. A. Gouldstone, H.-J. Koh, K.-Y. Zeng, *et al.*, Acta Mater. **48**, 2277 (2000).
28. M. S. Bharathi, M. Lebyodkin, G. Ananthakhrishna, *et al.*, submitted to Phys. Rev. Lett. **87**, 165508 (2001).

Translated by S. Gorin

Physics of the Solid State, Vol. 44, No. 7, 2002, pp. 1316–1322. Translated from Fizika Tverdogo Tela, Vol. 44, No. 7, 2002, pp. 1260–1265.

DEFECTS, DISLOCATIONS, AND PHYSICS OF STRENGTH

Hierarchy of Statistical Ensembles of Nanodefects on the Surface of Stressed Molybdenum

A. Ya. Bashkarev*, V. I. Vettegren', and V. N. Svetlov****
* St. Petersburg State Technical University, Politekhnicheskaya ul. 29, St. Petersburg, 195251 Russia
** Ioffe Physicotechnical Institute, Russian Academy of Sciences,
Politekhnicheskaya ul. 26, St. Petersburg, 194021 Russia
e-mail: Victor.Vettegren@pop.ioffe.rssi.ru
Received October 23, 2001

Abstract—The evolution of the distribution of nanodefects that are formed under the effect of tensile stresses existing at the surface of polished foils of molybdenum was studied. The nanodefects form four statistical ensembles in which the size distribution is determined by the maximum of the configurational entropy. The energy of formation and the average size of nanodefects in adjacent ensembles differ by a factor of three. When the concentration of nanodefects in one of the ensembles reaches a thermodynamically optimum value of ≈5%, part of the nanodefects annihilates and the other part becomes transformed into nanodefects of the next (higher) hierarchical level. The application of a load to the sample studied continuously generates nanodefects that form the first (lowest-level) ensemble, which leads to periodic oscillations in the concentrations of nanodefects in all four ensembles. *© 2002 MAIK "Nauka/Interperiodica".*

1. INTRODUCTION

Investigations using scanning tunneling microscopy (STM) show that, on the polished surface of metals such as Cu, Au, Mo, and Pd, defects that have the shape of a pyramid indent of nanometer size are formed under the effect of tensile stresses [1–8]. These defects are transformed and annihilate upon the motion of material bands in directions parallel to the dislocation slip planes [5, 8, 9].

In [8], the size distribution of nanodefects was considered on the basis of a model of reversible coalescence (aggregation) of atomic "steps" formed at sites where dislocations emerge onto the crystal surface. In this model, the energy of formation of a nanodefect is proportional to the dimensions y of its walls: $E = y\Delta U_0$, where ΔU_0 is the energy of aggregation of atomic steps. Therefore, the expression for the canonical distribution of the thermodynamic probability of fluctuations of energy at a constant volume [10, 11] is

$$f(E) = \beta\frac{(\beta E)^{m-1}}{\Gamma(m)}\exp(-\beta E), \qquad (1)$$

where m is the number of degrees of freedom and $\beta \equiv 1/k_BT$ was rewritten in the form [8, 12]

$$n(y) = n_0 y^2\exp(-\beta y\Delta U_0). \qquad (2)$$

Here, $n(y)$ is the concentration of nanodefects with wall lengths y, $n_0 \equiv C_a\beta(\Delta U_0)^2/2$, and C_a is a normalizing constant.

Expression (2) describes the experimental size distributions in objects such as nanodefects at the surfaces of loaded foils of metals (copper, gold, and molybdenum [8]), carbon-black particulates in compounded rubbers [12], or supramolecular formations at the surface of glassy polymethyl methacrylate [13]. This gave grounds to conclude that the above objects form statistical ensembles and that their size distributions are specified by the maximum of entropy [8, 12].

In [9], the nanodefect-size distribution was described by the Poisson distribution. In [11], it was shown that both descriptions are equivalent. The choice depends on what we are more interested in: energy fluctuations or fluctuations of the number of particles. In the first case, the distribution of fluctuations is described by the expression for the canonical distribution of the thermodynamic probability (Eq. (1)); in the second case, by the expression for the Poisson distribution.

Detailed investigations of the distribution of nanodefects on the surfaces of stressed copper foils [9] showed that, to more correctly describe the experimental distributions, one should use the sum of distributions (2)

$$n(y) = \sum_{i=1}^{n} n_{0i}y_i^2\exp(-\beta y_i\Delta U_{0i}), \qquad (3)$$

where n_{0i} and ΔU_{0i} are the normalization constant and the energy of aggregation for the ith distribution, respectively.

Such a description implies that the aggregate of nanodefects consists of a few statistical thermodynamic ensembles with different intrinsic energies ΔU_{0i}. The idea of the existence of several statistic ensembles was confirmed in [8]. The set of nanodefects on the surface of stressed copper samples proved to form a multilevel hierarchical system in which nanodefects of the $(i + 1)$th rank are formed at the expense of nanodefects of the ith level. This work continues that cycle of investigations. Its aim is to clarify to what extent the phenomenon of the existence of a hierarchy of statistical ensembles of nanodefects on the surface of stressed metals is common on the whole. As is known, copper refers to fcc metals; in this work, we investigate the distributions of nanodefects on the surface of a bcc metal, namely, molybdenum.

2. EXPERIMENTAL

We investigated the profiles of surfaces of rolled molybdenum (99.96%) foils approximately 60 μm thick. The samples were cut using special knives along the rolling direction, polished using a GOI paste, and washed in ethyl alcohol and acetone. Auger spectroscopy showed that the surface of the samples was covered by a carbon layer ≈2 nm thick.

The topograms of the surface of stressed samples were recorded in an atmosphere of dried nitrogen using an RTP-1 scanning tunnel microscope [1]. The observation window was 10 × 10 μm.

Because of the sample creep under a load, the observation window shifts relative to the measuring tip in the STM. As a result, the defect images become distorted. To minimize the distortions, the magnitude of the tensile stress was chosen such that, while recording a single topogram (≈40 min), the image of the surface region under study be displaced no more than 0.3% of the window size (10 × 10 μm). This condition was satisfied at a load of 800 MPa, at which the rate of creep was $\dot{\varepsilon} \approx 1 \times 10^{-6}$ s^{-1}. The uniaxial tensile stress was applied to the samples using a special spring device [1].

Figure 1 schematically displays a typical nanodefect formed on the surface of molybdenum. It has the form of an "indent" of a pyramid whose vertex is directed into the sample and whose opposite walls are parallel to dislocation slip planes in the bcc lattice, i.e., {110} and {112} [5]. The depths of such "indents" is ≈10 nm. The apical angles group near two values, ≈50° and 90°. No preferential orientation of the defect walls relative to the surface and the direction of tension was observed.

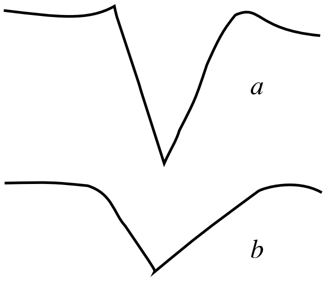

Fig. 1. Cross sections of nanodefects with depths of 7–10 nm on the surface of molybdenum. The apical angles are (*a*) ≈50° and (*b*) 90°.

The depth of nanodefects in each scan was measured manually. The distance between two sequential scans was 100 nm. Thus, only those nanodefects were detected whose size l in the direction perpendicular to the scanning direction exceeded 100 nm. "Coarse" nanodefects ($l > 200$ nm) crossed scans several times; their depth in successive scans was, as a rule, different. This was explained by the fact that the length of dislocations that emerged onto the surface was less than 100 nm. Therefore, the different sections of a coarse nanodefect were considered to be independent.

Since the average value of the apical angles of the nanodefects was ≈70°, the length of their walls was estimated as

$$y \approx \frac{2d}{\cos 35°} \approx 2.4d. \tag{4}$$

The magnification of the image in the direction perpendicular to the plane of the surface was 2.5×10^6 (25 nm/cm). This permitted us to investigate nanodefects with a depth from 5 nm. The number of nanodefects in the topograms was from 1000 to 5000, depending on the time passed after loading; this ensured our obtaining sufficiently reliable statistic distributions of nanodefect sizes.

3. NANODEFECT-SIZE DISTRIBUTION

The nanodefect-depth distribution was described by the expression

$$n(d) = \sum_{i=1}^{n} n_{0i} d_i^2 \exp(-2.4\beta d_i \Delta U_{0i}) \tag{5}$$

following from Eq. (3) with allowance for (4).

According to the model of aggregation [8], the magnitude of the parameter $\beta\Delta U_{01}$ for the first term in Eq. (5) is independent of time and the ratio $\Delta U_i/\Delta U_{i+1}$ for neighboring terms in (5) is equal to three. In the framework of this model, we sought the best coincidence between the calculated and experimental distributions by choosing a proper value of the parameter $\beta\Delta U_{01}$ and coefficients n_{0i}.

We analyzed 30 topograms obtained at various time moments (from 1 to 184 h; time to rupture was 186 h) after applying a tensile stress of 800 MPa. For example, Fig. 2 displays the nanodefect-depth distribution obtained 60 h after loading. It is seen that the distribution found using Eq. (5) (solid curve) satisfactorily

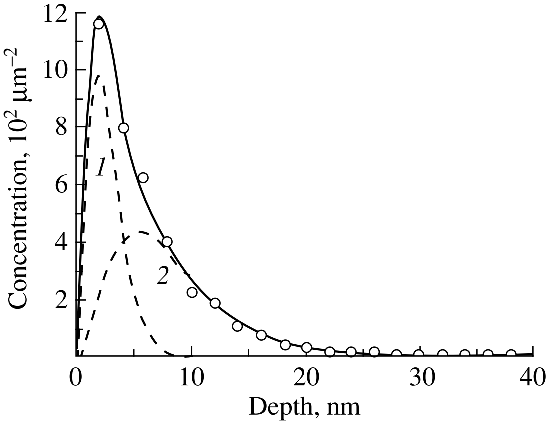

Fig. 2. Approximation (using Eq. (5)) of the depth distribution of nanodefects formed on the surface of a molybdenum sample after 60 h. Solid line, total distribution; dashed lines, first (*1*) and second (*2*) elementary distributions. The third and fourth distributions have a low intensity and cannot be seen in this figure. The distributions were found from the topogram obtained at a magnification of 2.5×10^6.

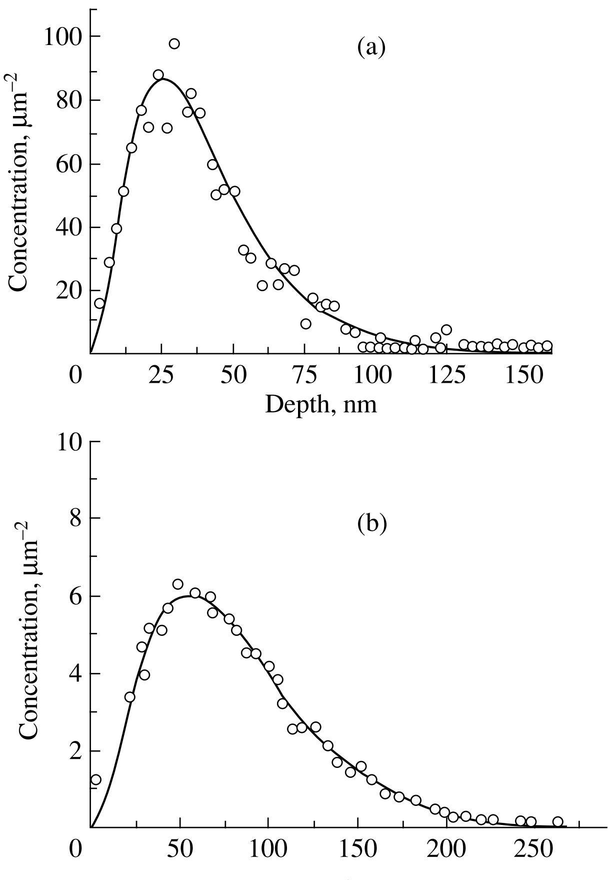

Fig. 3. Depth distributions of nanodefects found from the topograms obtained at magnifications of (a) 8.3×10^5 and (b) 2.8×10^5.

describes the experimental data. It turned out that the nanodefect-depth distributions on the surface of stressed molybdenum are also equally well described at other time moments. The number of terms in the sum (5) (i.e., the number of constituting elementary distributions), depending on the time after the application of the tensile stress, varied from two to four.

Since we were forced to use up to five adjustable parameters in those calculations (four n_{0i} and ΔU_{01}), we tried to make sure the four elementary distributions of nanodefects in an independent way. To this end, one and the same topogram was analyzed at magnifications of 2.5×10^6, 8.3×10^5, and 2.8×10^5 (25, 8.3, and 2.8 nm/cm, respectively).

It follows from Eq. (2) that the position of the distribution maximum d_{mi} is related to the energy of formation of nanodefects as

$$d_m = \frac{2}{\beta\Delta U_{0i}}.$$

The parameter $2.4\beta\Delta U_{01} \approx 0.038$ is approximately 0.038 per lattice parameter or ≈ 0.286 nm^{-1}; hence, the position of the maximum of the first elementary distribution should correspond to ≈7 nm. This distribution is the most intense, and the position of its maximum determines the position of the maximum of the total experimental distribution. The maximum of the total distribution obtained at a magnification of 2.5×10^6 turned out to be located at ≈8 nm (Fig. 2).

With decreasing magnification, the finest nanodefects cease to be visible. In accordance with the aggregate model, as the magnification decreases by a factor of three (to 8.3×10^5), the experimental distribution should represent a sum consisting of the second, third, and fourth distributions. The position of the second elementary distribution should be at $d_{m2} = 2 \times 3/(\beta\Delta U_{01}) = 3d_{m1} = 21$ nm. The maximum of the total distribution was found to be at ≈25 nm (Fig. 3a).

After processing the topogram obtained at the magnification of 2.8×10^5, the distribution shown in Fig. 3b was obtained. According to the aggregate model, it should consist of two elementary distributions: third and fourth ones. Its maximum is at ≈70 nm, whereas according to the aggregate model, the maximum of the third elementary distribution should be located at $d_{m3} = 2 \times 9/(\beta\Delta U_{01}) = 9d_{m1} = 63$ nm. The size distribution is described by expression (2) and is specified by the maximum value of the configurational entropy.

It is of interest to find the average depth of defects $\langle d_i \rangle$ that form the ensembles. It follows from (2) that this depth is related to $\beta\Delta U_{0i}$ as

$$\langle d_i \rangle \approx \frac{1.25}{\beta\Delta U_{0i}}. \tag{6}$$

For nanodefects that form the first ensemble, it was equal to ≈11 nm; for the defects of the second ensemble, to ≈32 nm; for the third ensemble, ≈95 nm; and for the fourth ensemble, ≈285 nm.

4. OSCILLATIONS OF THE CONCENTRATION OF NANODEFECTS

Figure 4 depicts fragments of the topograms recorded at time moments of 64, 87, 88, and 117 h after the application of tensile stresses. It is seen that the concentration of defects first grows (Figs. 4a, 4b), then decreases (Fig. 4c), and then again increases (Fig. 4d).

A detailed analysis shows that not only the total concentration of defects suffers oscillations with time, but their concentrations in each of the four ensembles also oscillate (Fig. 5). The oscillation period was ≈21 h. The concentration oscillations in successive ensembles occur in counterphase: an increase in the concentration of coarse nanodefects always occurs at the expense of a decrease in the concentration of finer defects.

Thus, the kinetics of defect formation has an hierarchical character: the nanodefects of the $(i + 1)$th rank are formed from the nanodefects of the ith rank. For example, it is seen from Fig. 5 that the nanodefects of the third rank begin to accumulate when the concentration of nanodefects of the second rank reaches a maximum value of C_2^{cr}. In turn, the nanodefects of the fourth rank begin to accumulate after the concentration of nanodefects of the third reaches its maximum value C_3^{cr}.

It was found in [8, 14, 15] that the processes of accumulation of nanodefects on the surface of copper foils and of cracks in granites under the effect of mechanical stresses also have an hierarchical character; i.e., the nanodefects and cracks form a number of hierarchical

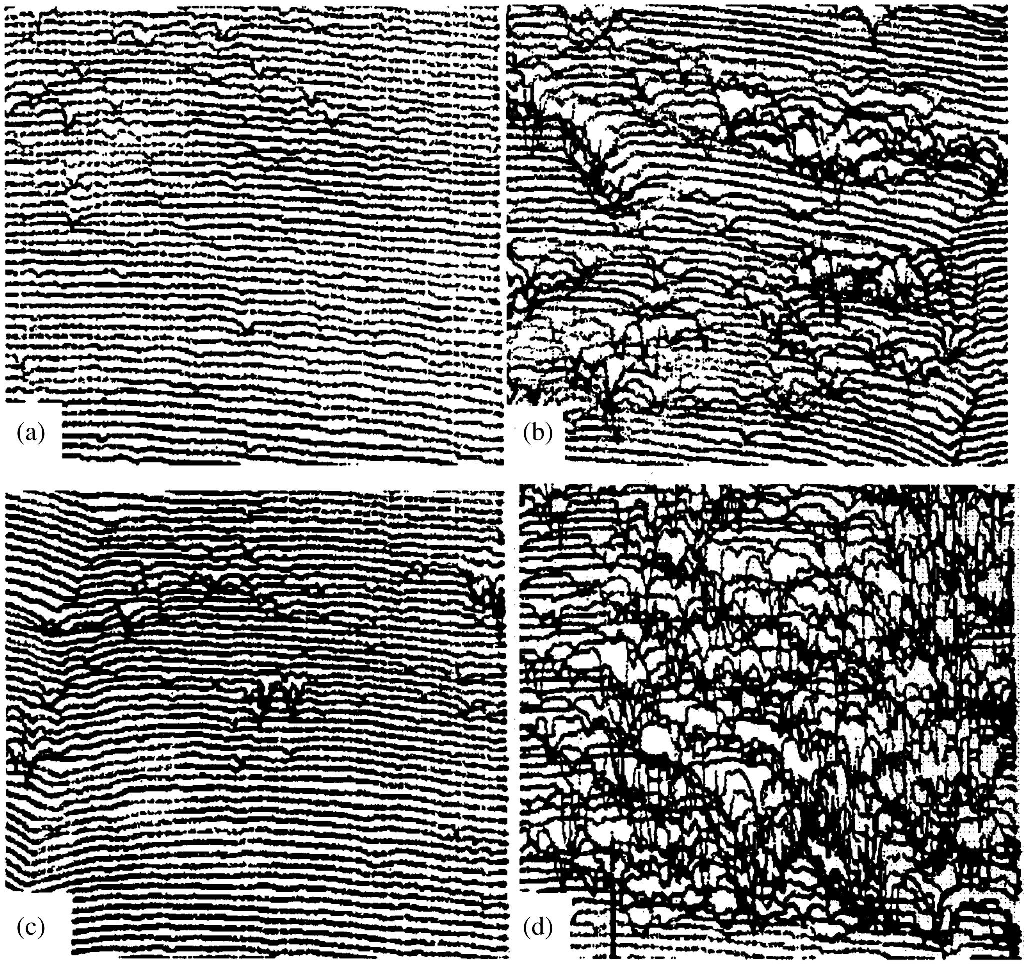

Fig. 4. Fragments of topograms of the surface of a molybdenum sample obtained at various time moments after loading: (a) 64, (b) 87, (c) 88, and (d) 117 h.

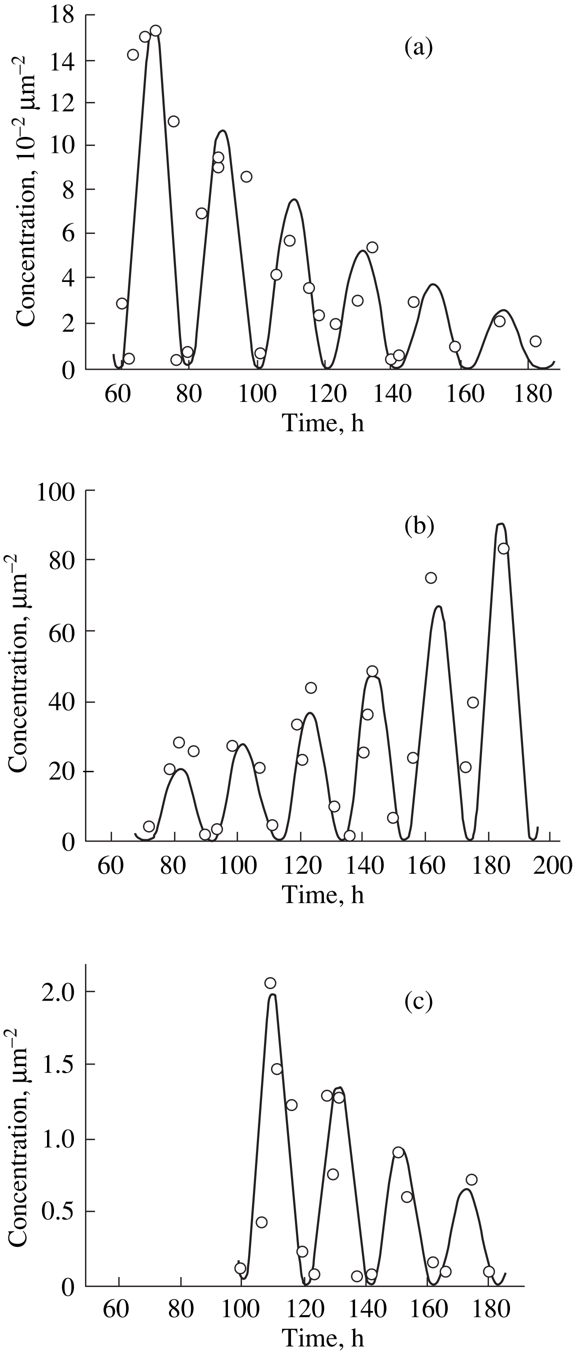

Fig. 5. Time dependences of the concentration of nanodefects that form (a) second, (b) third, and (c) fourth ensembles.

statistical ensembles. Thus, the hierarchy of defect formation in loaded materials exists not only in metals but also in other solids.

In order to clarify the origin of the appearance of oscillations, we calculated the fraction of the surface layer occupied by nanodefects when their concentration for a certain of the four hierarchical ensembles had the maximum value C_i^{cr}. In calculations, we assumed that in each ensemble the nanodefects have a depth $\langle d_i \rangle$. The width of the defects, i.e., the length of the segment along the sample surface in the direction of scanning, was estimated as $h \approx 2\langle d \rangle \tan 35° \approx 1.4d$ and their length was accepted to be equal to the distance between the scans $l_s \approx 100$ nm. The volume of a nanodefect was calculated as $V_d \approx l_s d^2$. The volume of the layer occupied by the nanodefects of the ith ensemble was estimated as $V_s \approx L^2\langle d_i \rangle - \sum_{j=1}^{3} L^2 \langle d_j \rangle$, where L is the dimension of the observation window (100 μm) and the index j labels the ensembles except for the ith one. The calculations show that the maximum value of the concentration of nanodefects in the surface layer of molybdenum was $C_i^{\text{cr}} = (5 \pm 1)\%$ for each of the four ensembles.

It was shown in [8] that the value of 5% corresponds to a thermodynamically optimum concentration of nanodefects in the surface layer at which the entropy reaches its maximum value $\Delta S \approx 3k_{\text{B}}$. With such a concentration, the average spacing between two neighboring defects $\langle Y \rangle$ is greater by a factor of e (e is the base of natural logarithms) than their average size $\langle y \rangle$ [8]:

$$\frac{\langle Y \rangle}{\langle y \rangle} = \frac{1}{\sqrt[3]{X_c}} = e \approx 2.7. \qquad (7)$$

Numerous investigations of the process of accumulation of cracks that are formed in solids (polymers, metals, ionic crystals, glasses, and rocks) under the effect of mechanical stresses [16–18] showed that when the concentration of cracks in the bulk of a solid reaches a value at which relation (7) is valid, the cracks begin to coarsen. The above results show that the criterion for coarsening (7) is valid not only for cracks but also for nanometer-sized defects on the surface of Cu and Mo.

Using this criterion, the phenomenon of oscillations of the concentration of nanodefects formed in the surface layer of molybdenum may be explained as follows. Under the action of a stress, a dislocation emerges onto the surface of a metal. As a result of aggregation of atomic steps, nanodefects of the first rank are formed on the surface. Their concentration grows until it reaches a thermodynamically optimum value ≈0.05. At this level, conditions arise that are favorable for the defect coarsening because of the maximum disorder in the arrangement of nanodefects. Then, part of the nanodefects annihilate, while the others become deeper by a factor of about three and form an ensemble of nanodefects of the second rank. The concentration of the defects of the second rank grows, reaches 5%, and then part of them disappears, whereas the other part is transformed into nanodefects of the third rank, etc. This process is thermodynamically favorable, since the energy of aggregation of new coarse defects is only one-third of the energy of formation of the old, finer defects.

An applied mechanical stress causes the formation of new and new portions of nanodefects of the first rank. Therefore, after the transformation of part of them into nanodefects of the second rank, their concentration again begins growing and the process is repeated cyclically.

The frequency of oscillations of concentration ν, according to the theory of consecutive reactions [19], is related to the rate constant k_1 of the reaction of formation of defects of the first rank as

$$k_1 \approx 12\nu. \tag{8}$$

Under our conditions (room temperature, a stress of 800 MPa), we have $\nu \approx 1.3 \times 10^{-5}$ and $k_1 \approx 1.6 \times 10^{-4}$ s^{-1}. If the nanodefects are produced under the effect of thermal fluctuations, the energy of activation for their generation is

$$U_{01} = k_B T \ln k_0/k_1 = k_B T \ln 10^{13}/k_1 \approx 100 \text{ kJ/mol}.$$

The rate of steady-state creep of the sample is $\dot{\varepsilon} \approx 1 \times 10^{-6}$ s^{-1}, which means that the energy of activation for steady-state creep is greater by 10 kJ/mol:

$$U_0 = k_B T \ln 10^{13}/\dot{\varepsilon} \approx 110 \text{ kJ/mol}.$$

5. MECHANISM OF COARSENING OF NANODEFECTS

In [5, 8, 9], the formation of nanodefects was explained by the emergence of dislocations onto the surface of the sample from closely spaced sources. It follows from the results described above in this paper that the dislocation sources in the surface layer of loaded molybdenum form aggregates which are located in a delocalized manner and also form four statistical ensembles. The distribution of the sources over the number of emitted dislocations in each of the ensembles is described by Eq. (2) (with a replacement of the parameter y by the number of emitted dislocations).

The average size of the nanodefect walls in the ensemble of the first rank is $\langle y_1 \rangle \approx 26$ nm; they are formed as a result of emission of $\langle y_1 \rangle/a \approx 87$ (a is the lattice parameter of molybdenum) dislocations by aggregates of dislocation sources of the first rank. The following ensemble consists of dislocation aggregates of the second rank emitting $3y_1/a \approx 260$ dislocations; the third ensemble consists of aggregates emitting ≈780 dislocations; and the fourth ensemble consists of aggregates emitting ≈2300 dislocations.

The load applied to the sample produces dislocation sources at a rate equal to the creep rate. The aggregates of the first rank are formed from them at a rate that is two orders of magnitude greater; then, aggregates of the second rank arise; then, aggregates of the third rank appear; etc.

6. CONCLUSION

Thus, it was established in this work that nanodefects on the surface of loaded molybdenum form four statistical ensembles. The size distributions of nanodefects in each ensemble is specified by the maximum value of the configurational entropy and is described by the expression for the canonical distribution of energy fluctuations (2). After the application of a tensile stress, the concentration of nanodefects of the first rank that form the first-rank ensemble begins to grow. When it reaches a thermodynamically optimum value of ≈5%, part of them annihilate and the other part are transformed into nanodefects of higher rank. The stress applied to the sample continuously generates nanodefects that form the first-rank ensemble, which leads to periodic oscillations of the concentration of nanodefects in all four ensembles.

ACKNOWLEDGMENTS

This work was supported by the Ministry of Education of Russian Federation, project no. E00-4.0-21.

REFERENCES

1. V. I. Vettegren’, S. Sh. Rakhimov, and V. N. Svetlov, Fiz. Tverd. Tela (St. Petersburg) **38** (2), 590 (1996) [Phys. Solid State **38**, 323 (1996)]; Fiz. Tverd. Tela (St. Petersburg) **38** (4), 1142 (1996) [Phys. Solid State **38**, 632 (1996)]; Fiz. Tverd. Tela (St. Petersburg) **39** (9), 1560 (1997) [Phys. Solid State **39**, 1389 (1997)]; Fiz. Tverd. Tela (St. Petersburg) **40** (12), 2180 (1998) [Phys. Solid State **40**, 1977 (1998)].
2. V. I. Vettegren, S. Sh. Rakhimov, and V. N. Svetlov, Proc. SPIE **3345**, 226 (1997).
3. G. Welzel, J. Plessing, and H. Neuhauser, Phys. Status Solidi A **166** (3), 791 (1998).
4. J. Plessing, Ch. Achmus, H. Neahauser, *et al.*, Z. Metallkd. **88** (8), 630 (1997).
5. V. I. Vettegren’, V. L. Gilyarov, S. Sh. Rakhimov, and V. N. Svetlov, Fiz. Tverd. Tela (St. Petersburg) **40** (4), 668 (1998) [Phys. Solid State **40**, 614 (1998)].
6. V. I. Vettegren’, S. Sh. Rakhimov, and V. N. Svetlov, Neorg. Mater. **35** (6), 756 (1999).
7. M. Kugler, A. Hampel, and H. Neuhauser, Phys. Status Solidi A **175** (2), 513 (1999).
8. Kh. G. Kilian, V. I. Vettegren’, and V. N. Svetlov, Fiz. Tverd. Tela (St. Petersburg) **42** (11), 2024 (2000) [Phys. Solid State **42**, 2083 (2000)]; Fiz. Tverd. Tela (St. Petersburg) **43** (11), 2107 (2001) [Phys. Solid State **43**, 2199 (2001)].
9. G. A. Malygin, Fiz. Tverd. Tela (St. Petersburg) **43** (5), 822 (2001) [Phys. Solid State **43**, 854 (2001)].
10. J. W. Gibbs, *Elementary Principles in Statistical Mechanics* (Yale Univ. Press, New Haven, Conn., 1902; Gostekhizdat, Moscow, 1946).

11. B. L. Lavenda, *Statistical Physics. A Probabilistic Approach* (Wiley, New York, 1997).
12. H. G. Kilian, R. Metzler, and B. Zink, J. Chem. Phys. **107** (12), 8697 (1997).
13. H. G. Kilian, M. Koepf, and V. I. Vettegren, Prog. Colloid Polym. Sci. **117** (1), 172 (2001).
14. N. G. Tomilin, E. E. Damaskinskaya, and V. S. Kuksenko, Fiz. Tverd. Tela (St. Petersburg) **36** (10), 3101 (1994) [Phys. Solid State **36**, 1649 (1994)].
15. V. Kuksenko, N. Tomilin, E. Damaskinskaja, and D. Lockner, Pure Appl. Geophys. **146** (2), 253 (1996).
16. V. S. Kuksenko, V. S. Ryskin, V. I. Betechtin, and A. I. Slutsker, Int. J. Fract. Mech. **11** (4), 829 (1975).
17. V. P. Tamuzh and V. S. Kuksenko, *Fracture Micromechanics of Polymeric Materials* (Zinatne, Riga, 1978).
18. V. A. Petrov, A. Ya. Bashkarev, and V. I. Vettegren', *Physical Principles for Fracture Prediction of Construction Materials* (Politekhnika, St. Petersburg, 1993).
19. N. M. Emanuel' and D. G. Knorre, *Chemical Kinetics; Homogeneous Reactions* (Vysshaya Shkola, Moscow, 1969; Wiley, New York, 1973).

Translated by S. Gorin

Physics of the Solid State, Vol. 44, No. 7, 2002, pp. 1323–1326. Translated from Fizika Tverdogo Tela, Vol. 44, No. 7, 2002, pp. 1266–1268.
Original Russian Text Copyright © 2002 by Marinin, Akimov, Varyukhin, Potapskaya.

Low-Frequency Internal Friction of Polycrystalline ZrO_2–4 mol % Y_2O_3 in the Temperature Range 273–373 K

G. A. Marinin, G. Ya. Akimov, V. N. Varyukhin, and O. N. Potapskaya
Donetsk Physicotechnical Institute, National Academy of Sciences of Ukraine, Donetsk, 83114 Ukraine
e-mail: akimov@host.dipt.donetsk.ua

Received July 16, 2001; in final form, November 25, 2001

Abstract—The specific features in the low-frequency internal friction, structure, and phase composition of polycrystalline ZrO_2–4 mol % Y_2O_3 are investigated in the temperature range 273–373 K. It is demonstrated that the low-frequency internal friction exhibits two peaks upon heating and cooling. The former peak is observed at a temperature of approximately 293 K, and the latter peak is revealed at 313 K. It is assumed that the peak observed in the low-frequency internal friction at a temperature of 293 K is attributed to relaxation dissipation of energy during motion of twin boundaries in the monoclinic phase, whereas the peak at 313 K is associated with relaxation processes due to displacement of the boundaries of tetragonal T' domains. *© 2002 MAIK “Nauka/Interperiodica”.*

1. INTRODUCTION

Investigations into the internal friction of tetragonal polycrystalline ZrO_2–3 mol % Y_2O_3 [1, 2] and stabilized cubic ZrO_2–10 mol % Y_2O_3 [3] (with the use of a torsion pendulum [2, 3]) have revealed no anomalies in the internal friction in the temperature range 273–373 K. However, reliable data on the low-frequency internal friction in ZrO_2–4 mol % Y_2O_3 polycrystals, including those with a high content of the monoclinic phase, are unavailable.

The purpose of this work was to investigate the low-frequency internal friction of polycrystalline ZrO_2–4 mol %Y_2O_3 with an increased content of the monoclinic phase (≈40%).

2. SAMPLE PREPARATION AND EXPERIMENTAL TECHNIQUE

The low-frequency internal friction was investigated using an inverse torsion pendulum [4] with vibration frequencies $f = 10$–24 Hz and strain amplitudes in the range from 10^{-5} to 2.5×10^{-6}. These amplitudes correspond to shear stresses ranging from ≈0.8 to 0.2 MPa. Free damped vibrations were recorded on a photographic film, which made it possible to analyze the amplitude dependence of the low-frequency internal friction. The quantity $Q^{-1} = \Delta/\pi$ was used as a measure of low-frequency internal friction. Here, Δ is the logarithmic decrement, which was determined from the change in the amplitude from A_0 to $0.9A_0$ in all portions of the damping oscillogram. The error in measuring Q^{-1} was no more than ±5%, and the error in measuring the vibration frequency did not exceed ±1%. Repeated measurements were performed on the same sample with a constant inertial system of the pendulum. In this case, the frequency satisfies the relationship $f^2 = G_\omega/KL$, where G_ω is the dynamic shear modulus, K is a constant that depends on the sample diameter and the moment of inertia of the pendulum, and L is the distance between the clamps. Heating and cooling were performed at a rate of 0.05–0.1 K/min. The temperature was measured with copper–constantan differential thermocouples.

The samples used in the experiments were prepared according to the technique described in [5]. The final stage of the preparation of ZrO_2–4 mol % Y_2O_3 ceramics was hot isostatic pressing in an argon atmosphere for 4 h under a pressure of 0.2 GPa at a temperature of 1753 K with subsequent cooling under high pressure. After hot isostatic pressing, we obtained a solid bar of polycrystalline ZrO_2–4 mol % Y_2O_3 with a density of ≈6.0 g/cm^3 (≈100% of the theoretical density). In order to examine the low-frequency internal friction, samples $1 \times 1 \times 60$ mm in size were cut from the solid bar with the use of a diamond disk. The samples thus obtained were not subjected to polishing and heat treatment.

X-ray powder diffraction analysis of the solid bar and samples intended for low-frequency internal friction measurements was performed according to the standard technique [6]. The analysis demonstrated that the process of fabrication of the sample from the solid bar brought about changes in the phase composition of the surface layer of the sample. The amount of the monoclinic (M) phase increased from ≈8% in the solid bar to ≈35–40% in the sample at the expense of a decrease in the transformed tetragonal (T) phase, whereas the amount of the cubic (F) phase remained unchanged

(≈20%). Therefore, the surface layer underwent a conventional mechanically activated martensite transformation $T \longrightarrow M$ [7].

3. RESULTS AND DISCUSSION

Figure 1 shows the micrograph of the fracture surface of the sample under investigation, which was obtained using a scanning electron microscope. Large-sized grains (more than 2 μm) of the cubic F phase can contain tetragonal T' domains formed upon hot isostatic pressing in the course of rapid cooling under pressure due to the martensite transformation $F \longrightarrow T'$ (T' is the tetragonal nontransformed phase). According to the data of x-ray powder diffraction and polarized light microscopy [8], this transformation is not observed in large-sized grains only in the case of slow cooling and at Y_2O_3 contents greater than 6 mol %. Medium-sized grains (up to 1 μm) and small-sized angular grains (up to 0.5 μm) belong to the tetragonal phase, whereas spherical grains are revealed in the monoclinic phase, which is formed as a result of the $T \longrightarrow M$ transformation [9].

The temperature dependences of the low-frequency internal friction Q^{-1} and the shear modulus $G_\omega \sim f^2$ upon cooling and heating of the sample in the temperature range 273–373 K are displayed in Fig. 2. All the experimental points presented in Fig. 2 were averaged over several measurements.

The main feature of the low-frequency internal friction in ZrO_2–4 mol % Y_2O_3 ceramics is as follows: the internal friction exhibits peaks at temperatures of 293 and 313 K, and the shear modulus $G_\omega \sim f^2$ noticeably decreases (increases) in the vicinity of 293 K.

Another important feature is that the anomalies in Q^{-1} and f^2 are observed upon both heating and cooling without a pronounced hysteresis. A decrease in the measurement frequency from 24 to 10 Hz is accompanied by a shift in the temperature of the low-frequency internal friction peak from 293 to 283 K and an increase in the peak height (Fig. 2). This makes it possible to determine the relaxation time τ from the resonance condition $\omega\tau = 1$ (where $\omega = 2\pi f$) and to calculate the activation energy H_1 from the curve $\ln\tau = F(1/T)$. The calculations demonstrate that the activation energy for this peak is estimated to be $H_1 \approx 0.6$ eV.

A weakly pronounced peak of the low-frequency internal friction is observed in the vicinity of 313 K. The frequency dependence of this peak was not analyzed in the present work. The activation energy H_2 for this peak was determined from the frequency and temperature at the maximum of the low-frequency internal

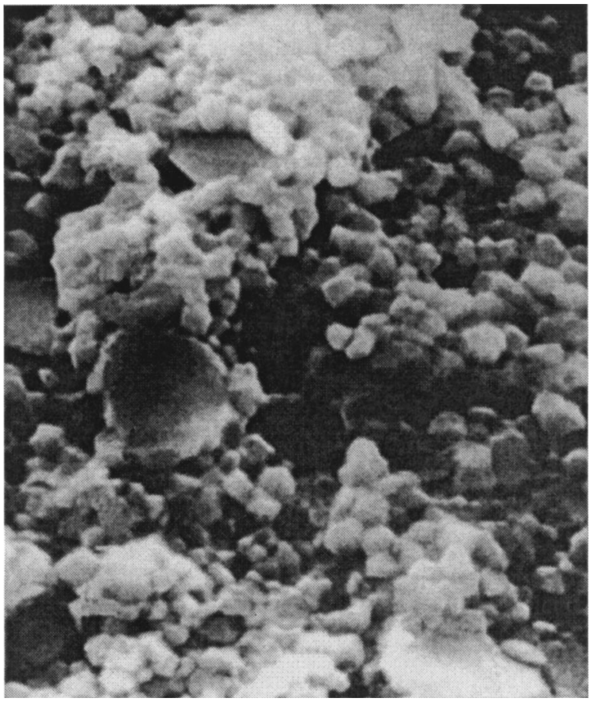

Fig. 1. Scanning electron micrograph of the fracture surface of the sample under investigation.

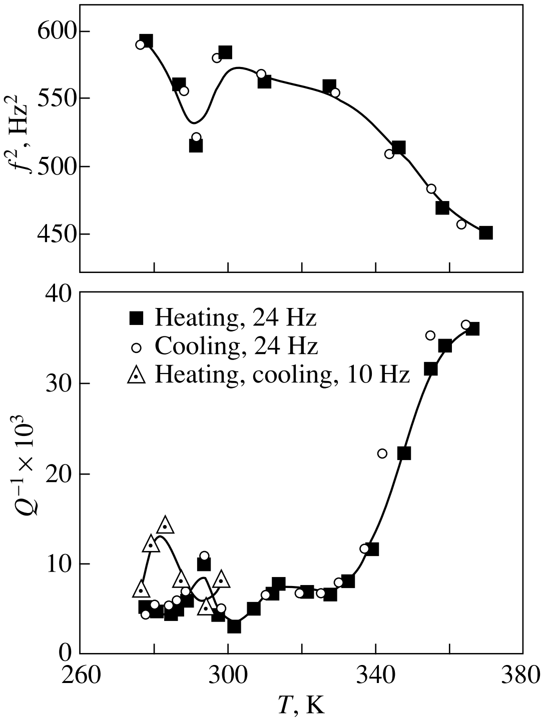

Fig. 2. Temperature dependences of the low-frequency internal friction Q^{-1} and the square of the torsional frequency f^2 upon heating and cooling.

friction with the use of the Werth–Marx formula derived for relaxation phenomena associated with the atomic and molecular rearrangements [10]. According to the estimates, $H_2 \approx 0.7$ eV.

Earlier investigations into the internal friction of tetragonal polycrystalline ZrO_2–3 mol % Y_2O_3 [1, 2] and stabilized single-crystal cubic ZrO_2–10 mol % Y_2O_3 [3] at vibration frequencies $f \approx 1.4$ kHz [1], $f \approx 3$ Hz, and $f \approx 3.06$ kHz in the temperature range 273–600 K revealed a broad maximum of the internal friction in the temperature range 380–480 K. The activation energy for this peak was estimated to be $H_3 \approx 1$ eV [2, 3]. The low-frequency portion of this peak was also observed for polycrystalline ZrO_2–4 mol % Y_2O_3 (Fig. 2).

As was shown above, the distinctive feature of the studied material is that it involves the cubic, tetragonal, and monoclinic phases simultaneously. In order to transform these phases, the changes in stress, temperature, and time should be considerably larger than those used during low-frequency internal friction measurements. The structure of ZrO_2–4 mol % Y_2O_3 after hot isostatic pressing consists of large-sized (≈3 μm) and small-sized (≈0.5 μm) grains (Fig. 1). In the course of the sample preparation for measuring the low-frequency internal friction, mechanical treatment brings about the martensite transformation $T \longrightarrow M$, which is accompanied by twinning [7].

Weller and Shubert [2] discussed the origin of a broad peak in the temperature dependence of the internal friction in the temperature range 380–480 K and proved that this peak could not stem from dissipation of energy during motion of twin boundaries in the monoclinic phase under applied stresses ($\sigma \approx 1$ MPa), as was assumed by Shimada *et al.* [1]. According to the data obtained in [2, 3], the maximum of dielectric loss is observed at the same temperatures. This can be caused only by thermally activated orientation of electric (elastic) dipoles $(V_O^{\bullet\bullet}Y'_{Zr})^{\bullet}$, where the prime denotes the negative charge and the point indicates the positive charge. Electric dipoles of the vacancy–substitutional impurity type are formed upon substitution of Y^{3+} ions for Zr^{4+} ions in the ZrO_2 structure. In this case, there are two Y^{3+} ions for every oxygen vacancy $V_O^{\bullet\bullet}$ instead of the O^{2-} oxygen ion by virtue of the electroneutrality of the crystal [11, 12]. Sukharevskiĭ *et al.* [11] demonstrated that oxygen vacancies substantially stabilize the high-temperature ZrO_2 phases.

A sharp relaxation peak of the low-frequency internal friction can appear at temperatures close to 273 K due to stress relaxation during motion of coherent twin boundaries formed upon martensite transformation from the cubic phase to the tetragonal phase. The nature of this peak was discussed earlier in works devoted to the investigation of manganese–copper alloys [13–15]. The activation energy for this peak was determined from the frequency shift: $H \approx 0.50 \pm 0.05$ eV [15]. This is in good agreement with the energy necessary for the shift of coherent boundaries of polysynthetic twins under shear stresses of ≈0.5 MPa [15]. The specific feature of the aforementioned peak is that it shifts toward low temperatures and increases in height with a decrease in the vibration frequency of the pendulum used in the experiments.

Reasoning from the available data and the experimental results obtained in this work, we can assume that, for the ZrO_2–4 mol %Y_2O_3 sample containing ≈40% *M*, 40% ($T + T'$), and 20% *F*, the first peak observed in the low-frequency internal friction at approximately 293 K is attributed to dissipation of energy during motion of twin boundaries in the monoclinic phase under applied stresses. The second peak revealed in the low-frequency internal friction in the vicinity of 313 K, most likely, can be associated with the relaxation of applied stresses due to displacement of the boundaries of tetragonal T'domains.

In order to verify the above assumptions, the low-frequency internal friction was measured in tetragonal polycrystalline ZrO_2–3 mol % Y_2O_3 which was not subjected to hot isostatic pressing (the grain size was approximately equal to 0.5 μm, and the density was ≈6.05 g/cm^3) but was mechanically treated for low-frequency internal friction measurements in the same manner as the ZrO_2–4 mol % Y_2O_3 sample. After mechanical treatment, the ZrO_2–3 mol % Y_2O_3 sample contained ≈6% *M* phase. However, no noticeable anomalies in the low-frequency internal friction were revealed in the temperature range 273–373 K, except for the low-temperature portion of the peak in the vicinity of 380 K, which is in agreement with the available data [1–3].

ACKNOWLEDGMENTS

We would like to thank V.G. Vereshchak and V.I. Korban’ for their help in preparing the sample used in our investigation.

REFERENCES

1. M. Shimada, K. Matsushita, S. Kuratani, *et al.*, J. Am. Ceram. Soc. **67** (2), C-23 (1984).
2. M. Weller and H. Shubert, J. Am. Ceram. Soc. **69** (7), 573 (1986).
3. M. Weller, Z. Metallkd. **84** (6), 381 (1993).
4. G. A. Marinin, A. V. Leont’eva, I. A. Oberemchenko, and V. A. Strel’tsov, Fiz. Tverd. Tela (Leningrad) **25** (8), 2301 (1983) [Sov. Phys. Solid State **25**, 1321 (1983)].
5. G. Ya. Akimov, V. G. Vereshchak, A. D. Vasil’ev, *et al.*, Ogneupory Tekh. Keram., No. 9, 17 (1998).
6. R. C. Carvie and P. S. Nikolson, J. Am. Ceram. Soc. **55** (6), 303 (1972).

7. M. Rühle and A. G. Evans, Prog. Mater. Sci. **33**, 85 (1989).
8. J. F. Jue and A. V. Vikar, J. Am. Ceram. Soc. **73** (12), 3650 (1990).
9. T. Sato and M. Shimada, J. Am. Ceram. Soc. **67** (10), C-212 (1984).
10. V. S. Postnikov, *Internal Friction in Metals* (Metallurgiya, Moscow, 1974).
11. B. Ya. Sukharevskiĭ, A. N. Gavrish, and B. G. Alapin, *Theoretical and Technical Researches of Refractories*, Ed. by K. G. Romanchenko (Metallurgizdat, Moscow, 1968), Vol. 9 (LVI).
12. A. S. Nowick and B. S. Berry, *Inelastic Relaxation in Crystalline Solids* (Academic, New York, 1972; Atomizdat, Moscow, 1975).
13. F. T. Worrell, J. Appl. Phys. **19** (10), 929 (1948).
14. K. Ziner, in *Elasticity and Inelasticity of Metals: Collected Articles*, Ed. by S. V. Vonsovskiĭ (Inostrannaya Literatura, Moscow, 1954).
15. V. S. Postnikov, I. V. Zolotukhin, and I. S. Pushkin, *Relaxation Phenomena in Solids*, Ed. by V. S. Postnikov (Metallurgiya, Moscow, 1968).

Translated by N. Korovin

Physics of the Solid State, Vol. 44, No. 7, 2002, pp. 1327–1329. Translated from Fizika Tverdogo Tela, Vol. 44, No. 7, 2002, pp. 1269–1271.
Original Russian Text Copyright © 2002 by Épshteĭn.

MAGNETISM AND FERROELECTRICITY

Planar Hall Effect in Ferromagnets

É. M. Épshteĭn

Institute of Radio Engineering and Electronics, Russian Academy of Sciences,
pl. Vvedenskogo 1, Fryazino, Moscow oblast, 141190 Russia

Received July 6, 2001

Abstract—The planar Hall effect in a ferromagnetic conductor is considered within a simple two-liquid hydrodynamic model. It is shown that, even in the simple case of an isotropic Fermi surface in the absence of thermal spread, the magnitude of the Hall effect is comparable to that in semiconductors because of the presence of two groups of conduction electrons with their spins parallel and perpendicular to the quantization axis, respectively. In addition to the planar Hall field, a spin flux parallel to this field arises, with the consequence that the extent of spin polarization of the conduction electrons varies along the Hall field direction (planar spin Hall effect). *© 2002 MAIK "Nauka/Interperiodica".*

The emergence of the novel field of magnetoelectronics called "spintronics" [1] was accompanied by the development of new magnetometry methods, because the conventional methods, such as torque and vibrating-sample magnetometry, are inefficient in the case of small samples [2]. Recently, a method based on the planar Hall effect (PHE) became popular. This effect was first predicted and experimentally investigated in semiconductors in [3–5]. In investigations of ferromagnetic metal films, the PHE has been employed for a fairly long time [6–8], but in recent years, the techniques based on this effect have been further developed [9–11].

In ferromagnets, the PHE, as well as the conventional three-dimensional Hall effect, is determined by the magnetization of the sample rather than by an external magnetic field [7], which means that the anomalous Hall effect is dominant over the ordinary one. The external magnetic field only changes the direction and magnitude of the magnetization vector (in single-domain samples).

Another characteristic feature of the PHE that we analyze in this paper is associated with the origin of this effect in ferromagnets. The PHE is one of the so-called "spread" kinetic effects, which are due to the presence of several groups of carriers that differ in the parameter controlling their interaction with external fields; among such effects are the magnetoresistive effect (magnetoresistance), Ettingshausen effect, Peltier effect, Maggi–Righi–Leduc effect [12], acoustomagnetoelectric effect [13], and some photoinduced effects [14].

In nonmagnetic metals, the spread effects are due to Fermi surface nonsphericity and/or the presence of carriers of several types [12]. In a simple single-band spherical model, these effects are caused by the thermal spread in the Fermi distribution and their magnitude is proportional to the small parameter $(k_BT/E_F)^2$.

In ferromagnets, we have a completely different situation. Even in the simple model mentioned above, due to the *s*–*d* exchange, the conduction band is split into two subbands with electron spins parallel and antiparallel to the quantization axis chosen (spin up and spin down), respectively. The electrons in these subbands have different momenta, $p_{F\uparrow} = \sqrt{2m(E_F + \mu_B B_{\text{ex}})}$ and $p_{F\downarrow} = \sqrt{2m(E_F - \mu_B B_{\text{ex}})}$, respectively, where m is the effective electron mass (independent of spin in the spherical Fermi surface model used here), μ_B is the Bohr magneton, B_{ex} is the exchange field, and E_F is the Fermi energy reckoned from the bottom of the unsplit conduction band. Electrons with different spin orientation have different partial mobility, because the relaxation time of degenerate electrons depends on the Fermi momentum (e.g., in the case of acoustic-phonon scattering, the relaxation time varies in inverse proportion to the Fermi momentum). Therefore, the spread in partial mobilities necessary for the occurrence of the PHE can be much larger than the thermal spread. Asymmetry in the up- and down-spin electron scattering is also introduced by specific magnetic scattering mechanisms, such as scattering by domain walls and magnetic impurities.

It should be noted that the microscopic theory of the PHE in ferromagnetic metals has long since been developed using the density matrix method [15]. However, the general expressions derived within this approach do not clarify the spread nature of the PHE, in particular, the relation of this effect to the exchange splitting of the conduction band. Therefore, it is of interest to treat the PHE within a simple model, which, of course, cannot give a quantitative description of actual ferromagnets but will give insight into the fundamental qualitative features of this effect. Furthermore, such a model predicts the planar spin Hall effect, which shows itself as conduction electron spin polarization varying in magnitude along the PHE field direction and is due to the fact that the electric current of electrons with a certain spin orientation is accompanied by a spin flux (and a magnetic-moment flux).

We will calculate the PHE field in a ferromagnetic conductor within a simple hydrodynamic approximation, starting from the equations for the partial current densities $\mathbf{j}^{(\alpha)}$ for the two electron spin directions:

$$\mathbf{j}^{(\alpha)} = \sigma^{(\alpha)}(\mathbf{E} + 4\pi R^{(\alpha)}[\mathbf{j}^{(\alpha)}\mathbf{M}_s]), \tag{1}$$

where the spin index α takes on two values, $\uparrow$ and $\downarrow$; $\sigma^{(\alpha)}$ and $R^{(\alpha)}$ are the partial conductivities and (anomalous) Hall coefficients, respectively; $\mathbf{E}$ is the electric field; and $\mathbf{M}_s$ is the saturation magnetization. The magnetization vector $\mathbf{M}_s$ lies in the xy plane: $\mathbf{M}_s = \{M_{sx}, M_{sy}, 0\} = \{M_s\cos\varphi, M_s\sin\varphi, 0\}$. The sample is terminated in a power source along the x axis and is open-circuited along the y and z axes; therefore, the total current density $\mathbf{j} = \sum_\alpha \mathbf{j}^{(\alpha)}$ satisfies the boundary conditions $j_y = j_z = 0$.

From the equations

$$\begin{aligned} \sigma_{xx}E_x + \sigma_{xy}E_y + \sigma_{xz}E_z &= j, \\ \sigma_{yx}E_x + \sigma_{yy}E_y + \sigma_{yz}E_z &= 0, \\ \sigma_{zx}E_x + \sigma_{zy}E_y + \sigma_{zz}E_z &= 0 \end{aligned} \tag{2}$$

the PHE field is found to be

$$E_y = \frac{\sigma_{yx}\sigma_{zz} - \sigma_{yz}\sigma_{zx}}{\det|\sigma_{ik}|}j, \tag{3}$$

where $\det|\sigma_{ik}|$ is the determinant of the conductivity tensor.

Solving Eq. (1) for $\mathbf{j}^{(\alpha)}$ and summing over the spin index, we find the components of the conductivity tensor.

For $4\pi R^{(\alpha)}\sigma^{(\alpha)}M_s \ll 1$, in calculating to the lowest order in the magnetization, we obtain

$$E_y = 8\pi^2 M_s^2 \sin 2\varphi \times \frac{\sum_\alpha R^{(\alpha)2}\sigma^{(\alpha)3}\sum_\alpha \sigma^{(\alpha)} - \left(\sum_\alpha R^{(\alpha)}\sigma^{(\alpha)2}\right)^2}{\left(\sum_\alpha \sigma^{(\alpha)}\right)^3}. \tag{4}$$

We introduce the partial mobilities $\mu_\alpha = \sigma^{(\alpha)}/en_\alpha$ (with n_α being the up-spin and down-spin electron concentrations) and assume, intending to make only an order-of-magnitude estimate of the effect, that the partial anomalous Hall coefficients, as well as the ordinary Hall coefficients, are inversely proportional to the corresponding concentrations, $R^{(\alpha)} = r/ecn_\alpha$, with the Hall factor r taking into account the anomalous values of these coefficients (the anomalous Hall effect will be dominant over the ordinary Hall effect if $r \gg 1$). Then, Eq. (4) takes the form

$$E_y = \frac{8\pi^2 r^2 M_s^2 j \sin 2\varphi}{ec^2 n}\frac{\langle\mu^3\rangle\langle\mu\rangle - \langle\mu^2\rangle^2}{\langle\mu\rangle^3}, \tag{5}$$

where

$$\langle\mu^p\rangle \equiv \frac{1}{n}(\mu_\uparrow^p n_\uparrow + \mu_\downarrow^p n_\downarrow), \tag{6}$$

with $n = n_\uparrow + n_\downarrow$ being the electron concentration. From Eqs. (5) and (6), it follows that the PHE field vanishes when $\mu_\uparrow = \mu_\downarrow$, because we have used the isotropic model and neglected the thermal spread in the Fermi distribution.

In the case where the electrons are mainly scattered by acoustic phonons, we have [5]

$$\mu_{\uparrow,\downarrow} = \frac{el}{\hbar k_{\uparrow,\downarrow}}, \tag{7}$$

where $k_{\uparrow,\downarrow} = p_{F\uparrow,\downarrow}/\hbar$ is the Fermi wave vector and l is the mean free path of electrons, which is independent of k_α (for the scattering mechanism chosen). In the spherical Fermi surface approximation, Eq. (5) takes the form

$$E_y = 48\pi^4\frac{r^2 l M_s^2 j}{\hbar c^2}\sin 2\varphi\frac{(k_\uparrow - k_\downarrow)^2}{(k_\uparrow^2 - k_\downarrow^2)^3}. \tag{8}$$

The spin flux density along the PHE field is proportional to the current-density difference of the up-spin and down-spin electrons:

$$J_{sy} = \frac{\hbar}{2e}(j_y^\uparrow - j_y^\downarrow). \tag{9}$$

From Eqs. (1) and (2), to the lowest order in the magnetization, we obtain

$$J_{sy} = \frac{8\pi^2 r^2 M_s^2 \hbar j \sin 2\varphi}{c^2 e n^2}\frac{n_\uparrow n_\downarrow \mu_\uparrow^2\mu_\downarrow^2(\mu_\uparrow - \mu_\downarrow)}{\langle\mu\rangle^3}. \tag{10}$$

Introducing the carrier spin polarization

$$P = \frac{n_\uparrow - n_\downarrow}{n} \tag{11}$$

(which differs from the corresponding expression used in the theory of tunneling magnetoresistance [16], where the densities of states at the Fermi level stand for the corresponding electron concentrations), Eq. (10) can be written as

$$J_{sy} = \frac{16\pi^2 r^2 M_s^2 \hbar j \sin 2\varphi}{c^2 e}\frac{(1 - P^2)\mu_\uparrow^2\mu_\downarrow^2(\mu_\uparrow - \mu_\downarrow)}{[\mu_\uparrow(1 + P) + \mu_\downarrow(1 - P)]^3}. \tag{12}$$

Since the sample is open-circuited along the y axis, the spin flux J_{sy} produced by the electric current along the x axis gives rise to a spin polarization difference ΔP along the y axis. The spin diffusion flux caused by this difference counterbalances the flux J_{sy} in the steady state.

In order to determine the difference ΔP, we find the spin polarization distribution along the y axis, which is described by the time-independent diffusion equation

$$D\frac{d^2P}{dy^2} - \frac{P - P_0}{\tau_s} = 0, \tag{13}$$

where P_0 is the equilibrium polarization, D is the diffusion coefficient of electrons, and τ_s is the spin relaxation time (for the sake of simplicity, D and τ_s are assumed to be the same for both spin orientations).

Solving Eq. (13) and equating the diffusion fluxes at the boundaries $-\hbar DnP'(0)$ and $-\hbar DnP'(L_y)$ to the flux J_{sy}, where L_y is the sample dimension along the y axis, we obtain

$$P(y) = P_0 + \frac{\alpha}{\sinh(L_y/l_s)}\left(\cosh\frac{y}{l_s} - \cosh\frac{L_y - y}{l_s}\right), \tag{14}$$

where $l_s = \sqrt{D\tau_s}$ is the spin relaxation length and $\alpha = \frac{2J_sl_s}{\hbar Dn}$.

The difference in the spin polarization is

$$\Delta P \equiv P(L_y) - P(0) = 2\alpha\tanh\frac{L_y}{2l_s} = 64\pi^2r^2$$
$$\times\frac{j}{env_s}\frac{(1-P^2)\mu_\uparrow^2\mu_\downarrow^2(\mu_\uparrow - \mu_\downarrow)M_s^2\sin2\varphi}{c^2[\mu_\uparrow(1+P)+\mu_\downarrow(1-P)]^3}\tanh\frac{L_y}{2l_s}, \tag{15}$$

where $v_s = \sqrt{D/\tau_s}$ is the spin relaxation velocity. The quantity ΔP is the measure of the planar spin Hall effect.

In the three-dimensional geometry, the spin Hall effect was considered by Hirsch in [17], where possible experimental measurements of the spin polarization difference were also discussed. However, in [17], this effect was considered in paramagnets, where it is due to spin–orbit coupling. As follows from the analysis presented above, the spin Hall effect in ferromagnets is universal and accompanies the ordinary (charge) Hall effect and other galvanomagnetic and thermomagnetic effects.

ACKNOWLEDGMENTS

The author would like to thank Yu.F. Ogrin for his calling the author's attention to this problem and P.E. Zil'berman for helpful discussions.

This study was supported by the Russian Foundation for Basic Research, project no. 00-02-16384.

REFERENCES

1. B. Heinrich, Can. J. Phys. **78** (3), 161 (2000).
2. V. Kubrak, A. Neumann, B. L. Gallagher, *et al.*, J. Appl. Phys. **87** (9), 5986 (2000).
3. F. G. Bass and I. M. Tsidil'kovskiĭ, Zh. Tekh. Fiz. **24**, 1834 (1954).
4. C. Goldberg and R. Davis, Phys. Rev. **94**, 1121 (1954).
5. K. Seeger, *Semiconductor Physics* (Springer, Berlin, 1974; Mir, Moscow, 1977).
6. V. D. Ky and E. F. Kuritsyna, Dokl. Akad. Nauk SSSR **160** (1), 77 (1965) [Sov. Phys. Dokl. **10**, 51 (1965)].
7. V. D. Ky, Izv. Akad. Nauk SSSR, Ser. Fiz. **29** (4), 576 (1965).
8. E. F. Kuritsyna and V. D. Ky, Izv. Akad. Nauk SSSR, Ser. Fiz. **29** (4), 580 (1965).
9. J. C. Wu, C. S. Wu, and T. Wu, J. Appl. Phys. **85** (8), 5795 (1999).
10. G. Li, Z. Lu, C. Chai, *et al.*, Appl. Phys. Lett. **74** (5), 747 (1999).
11. F. Y. Ogrin, S. L. Lee, and Y. F. Ogrin, J. Magn. Magn. Mater. **219**, 331 (2000).
12. F. J. Blatt, *Physics of Electronic Conduction in Solids* (McGraw-Hill, New York, 1968; Mir, Moscow, 1971).
13. É. M. Épshteĭn and Yu. V. Gulyaev, Fiz. Tverd. Tela (Leningrad) **9** (2), 376 (1967) [Sov. Phys. Solid State **9**, 288 (1967)].
14. É. M. Épshteĭn, G. M. Shmelev, and G. I. Tsurkan, *Photostimulated Processes in Semiconductors* (Shtiintsa, Kishinev, 1987).
15. A. A. Abdurakhmanov, *Kinetic Effects in Ferromagnetic Metals* (Rostovskiĭ Univ., Rostov-on-Don, 1978).
16. M. Julliere, Phys. Lett. A **54** (3), 225 (1975).
17. J. E. Hirsch, Phys. Rev. Lett. **83** (9), 1834 (1999).

Translated by Yu. Epifanov

Physics of the Solid State, Vol. 44, No. 7, 2002, pp. 1330–1335. Translated from Fizika Tverdogo Tela, Vol. 44, No. 7, 2002, pp. 1272–1276.
Original Russian Text Copyright © 2002 by Leskovets, Kurkin, Nikolaev, Turov.

MAGNETISM AND FERROELECTRICITY

High-Frequency Properties of $KNiPO_4$ in Alternating Magnetic and Electric Fields

V. V. Leskovets, M. I. Kurkin, V. V. Nikolaev, and E. A. Turov
Institute of Metal Physics, Ural Division, Russian Academy of Sciences,
ul. S. Kovalevskoĭ 18, Yekaterinburg, 620219 Russia
e-mail: leskovez@imp.uran.ru
e-mail: turov@imp.uran.ru

Received October 1, 2001

Abstract—The dependences of the antiferromagnetic resonance frequencies on the constant magnetic field **H** and constant electric field **E** are calculated for a $KNiPO_4$ crystal with spontaneous electric polarization and antiferromagnetic order. It is demonstrated that the $KNiPO_4$ crystal is characterized by an exchange-enhanced effect of the electric field **E** on the antiferromagnetic resonance frequencies. This effect is not revealed in the magnetoelectric materials studied earlier. It is established that oscillations of both magnetization and electric polarization exhibit resonance response at antiferromagnetic resonance frequencies. The expressions for these responses in alternating magnetic and electric fields are presented. © *2002 MAIK "Nauka/Interperiodica".*

1. INTRODUCTION

Our interest in the $KNiPO_4$ compound is dictated by two characteristic properties [1, 2]. First, $KNiPO_4$ belongs to the class of materials without a center of symmetry, which gives rise to spontaneous electric polarization **P**. Second, $KNiPO_4$ contains magnetic atoms of the transition element Ni, which leads to antiferromagnetic ordering (the Néel temperature $T_N \approx 25$ K). The interaction of the polarization **P** and the antiferromagnetic vector **L** with each other and with elastic strains (by virtue of the piezoelectric effect and magnetostriction) suggests a wide variety of magnetic, electrical, and acoustical properties of this compound.

The symmetry of $KNiPO_4$ orthorhombic crystals is represented by the space group $Pna2_1$with a preferred screw axis 2_1 along which the polarization vector **P** is aligned. The unit cell of the crystal contains four Ni^{2+} ions located in the fourfold position 4*a* [3, 4]; consequently, the magnetic structure of this compound is generally described by four magnetic sublattices. A symmetry analysis of the possible exchange magnetic structures was carried out in [3] (see also the monograph [4]). It turned out that the magnetic component of the thermodynamic potential involves approximately 50 different invariants due to the low symmetry of the crystal. In order to decrease the number of invariants, we restrict our consideration to the specific case of only one exchange structure observed in this material as judged from the available experimental data [1, 2]. This structure can be adequately described in the framework of the two-sublattice model with vectors $\mathbf{M}_1$ and $\mathbf{M}_2$. Sublattice *I* is formed by Ni^{2+} ions with indices *1* and *4*, and sublattice *II* is composed of Ni^{2+} ions with indices *2* and *3* (Fig. 1). Instead of vectors $\mathbf{M}_1$ and $\mathbf{M}_2$, it is convenient to use their linear combinations, namely, the antiferromagnetic vector

$$\mathbf{L} = \mathbf{M}_1 - \mathbf{M}_2 \tag{1}$$

and the ferromagnetic vector

$$\mathbf{M} = \mathbf{M}_1 + \mathbf{M}_2. \tag{2}$$

Within this model, the component of the thermodynamic potential of $KNiPO_4$, which depends on the components of vectors **M**, **L**, and **P**, has the following form [3, 4]:

$$\begin{aligned} F = {} & \frac{1}{2}\chi_\perp^{-1}M^2 + \frac{1}{8M_0^2}(\chi_\parallel^{-1} - \chi_\perp^{-1})(\mathbf{ML})^2 + \frac{1}{2}K_{yy}L_y^2 \\ & + \frac{1}{2}K_{zz}L_z^2 - D_{yz}M_yL_z - D_{zy}M_zL_y - (\mathbf{MH}) \\ & - \frac{1}{2M_0}(d_{xxy}P_xM_xL_y + d_{xyx}P_xM_yL_x \\ & + d_{yxx}P_yM_xL_x + d_{yyy}P_yM_yL_y + d_{yzz}P_yM_zL_z \\ & + d_{zyz}P_zM_yL_z + d_{zzy}P_zM_zL_y) - \frac{1}{2M_0}(k_{xxz}P_xL_xL_z \\ & + k_{yyz}P_yL_yL_z + k_{zyy}P_zL_y^2 + k_{zzz}P_zL_z^2) \\ & + \frac{1}{2}\kappa^{-1}(P_x^2 + P_y^2) - (\mathbf{PE}). \end{aligned} \tag{3}$$

Formula (3) is written in the coordinate system in which the axes **X**, **Y**, and **Z** are chosen along three preferred crystallographic axes: $\mathbf{Z} \parallel 2_1$ (2_1 is the twofold screw axis), $\mathbf{X} \perp m_x$, and $\mathbf{Y} \perp m_y$ (m_x and m_y are the two mutually perpendicular mirror planes); $\chi_\perp$ and $\chi_\parallel$ are the magnetic susceptibilities in the magnetic fields $\mathbf{H} \perp \mathbf{L}$ and $\mathbf{H} \parallel \mathbf{L}$, respectively; K_{yy} and K_{zz} are the anisotropy constants; D_{yz} and D_{zy} are the constants of weak ferromagnetism; $d_{\alpha\beta\gamma}$ stands for the constants of the magnetoelectric effect; $k_{\alpha\beta\gamma}$ stands for the antiferroelectric constants; κ is the polarizability of the crystal along equivalent directions **X** and **Y**; and M_0 is the nominal magnetization of each sublattice. It is assumed that the polarization along the **Z** axis remains equal to its spontaneous magnitude.

Compared to the expressions representing the thermodynamic potential F of other two-sublattice antiferromagnets, formula (3) has two specific features. The first feature is that it involves the invariants responsible for the weak ferromagnetism (the terms with D_{yz} and D_{zy}) and for the magnetoelectric effect (the terms with $d_{\alpha\beta\gamma}$). These effects cannot occur simultaneously in crystals with a center of inversion. The second feature of formula (3) is that it involves terms that contain only the components of vectors **P** and **L** (the invariants with $k_{\alpha\beta\gamma}$). They describe the mutual effect of these vectors without participation of vector **M** (the product $k_{\alpha\beta\gamma}P_\alpha = \delta K_{\beta\gamma}$ can be considered a correction to the tensor of the anisotropy constants $K_{\beta\gamma}$ responsible for the orientation of vector **L**, and the product $k_{\alpha\beta\gamma}L_\beta L_\gamma = \delta E_\alpha$ is the correction to the electric field **E** responsible for the change in vector **P**).

The effect of the terms with $d_{\alpha\beta\gamma}$ and $k_{\alpha\beta\gamma}$ [see formula (3)] on the magnetostatics and electrostatics of KNiPO$_4$ was analyzed earlier in [3, 4]. It has been demonstrated that, in the case when $|\mathbf{L}|$ is constant and

$$k_{xxz}^2\kappa > (K_{zz} - D_{yz}^2\chi_\perp), \qquad (4)$$

the vector **L** at an equilibrium state deviates spontaneously ($H = 0$) from the **X** axis through a certain angle $\left(\frac{\pi}{2} - \Theta_L\right)$ (Fig. 2). Such a deviation of vector **L** from the **X** axis gives rise to the weak ferromagnetic moment

$$M_y = \chi_\perp D_{yz} L \sin\Theta_L \qquad (5)$$

and the magnetoelectric polarization

$$P_x = \alpha_{xy}H_y, \quad \alpha_{xy} = \chi_\perp d_{xyx}\cos\Theta_L. \qquad (6)$$

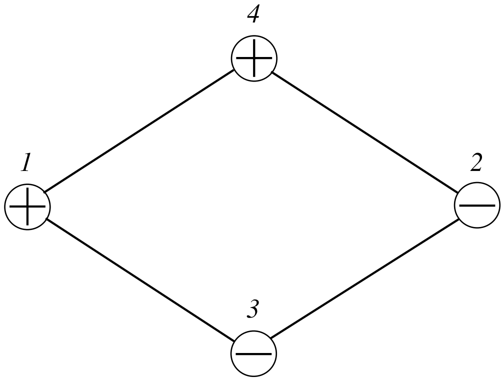

Fig. 1. Exchange magnetic structure of KNiPO$_4$. The “plus” and “minus” signs correspond to different sublattices, $\mathbf{M}_1 \uparrow\downarrow \mathbf{M}_2$.

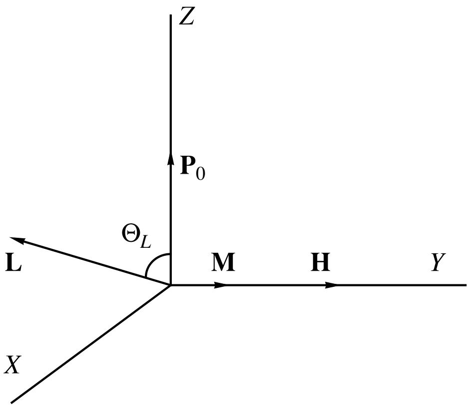

Fig. 2. Rotation of vector **L** in the XZ plane in response to the magnetic field $\mathbf{H} \parallel \mathbf{Y}$.

However, it follows from the experimental data [1, 2] that, instead of inequality (4), the reverse inequality holds for KNiPO$_4$. For this reason, attempts to obtain an exotic state in which the weak ferromagnetism and magnetoelectricity coexist at $\mathbf{H} = 0$ have been unsuccessful. Nonetheless, such an unusual form of the thermodynamic potential F [see formula (3)] should manifest itself in the specific properties of the crystal. One manifestation is revealed in the dependence of the Θ_L angle on the magnetic field $\mathbf{H} \parallel \mathbf{Y}$. This dependence can be described by the following equation [3]:

$$\begin{aligned} 2\kappa k_{xxz}^2\cos^3\Theta_L + (K_{zz} - D_{yz}^2\chi_\perp - \kappa k_{xxz}^2)\cos\Theta_L \\ = D_{yz}\chi_\perp H_y/2M_0. \end{aligned} \qquad (7)$$

The corresponding components of vectors **M** and **P** are determined as follows [3]:

$$\begin{aligned} M_y &= \chi_\perp(H_y + 2M_0D_{yz}\cos\Theta_L), \\ P_x &= \kappa(2M_0k_{xxz}\cos\Theta_L + d_{xyx}M_y)\sin\Theta_L. \end{aligned} \qquad (8)$$

The interrelation of the quantities P_x, M_y, and Θ_L implies that the specific features of the magnetic and electrical properties of KNiPO$_4$ can manifest themselves not only in constant but also in alternating fields $\mathbf{h}(t)$ and $\mathbf{e}(t)$, which can enhance these features in the vicinity of the resonance frequencies of oscillations of **L** and **M**.

In particular, it follows from relationship (7) that the solution $\cos\Theta_L \neq 0$ ($\Theta_L \neq \pi/2$) is actually valid only when inequality (4) holds.

The results of the calculations of the frequency spectrum for linear oscillations of **M** and **L** and the analysis of their possible excitation in alternating fields $\mathbf{h}(t)$ and $\mathbf{e}(t)$ are given below. It is assumed that the eigenmodes of **P** correspond to considerably higher frequencies. This allows one to use the quasi-static approximation

$$P^{\alpha}(t) = \kappa E^{\alpha}_{\mathrm{eff}}(t). \qquad (9)$$

Here, κ is the same electric susceptibility as in formula (3) and

$$E^{\alpha}_{\mathrm{eff}}(t) = -\frac{\partial F}{\partial P^{\alpha}} \qquad (10)$$

is the effective electric field acting on vector **P** in the sample. According to formula (3), this field is determined by the external field **E** and the magnetoelectric interaction parameters $d_{\alpha\beta\gamma}$ and $k_{\alpha\beta\gamma}$; that is,

$$E^{\alpha}_{\mathrm{eff}}(t) = E^{\alpha}(t) + \sum_{\beta\gamma} d_{\alpha\beta\gamma} M_{\beta} L_{\gamma} + \sum_{\beta\gamma} k_{\alpha\beta\gamma} L_{\beta} L_{\gamma}. \qquad (11)$$

The interrelation of the components of vectors **P**, **E**, **M**, and **L**, which is defined by expressions (9) and (11), was used in solving the equations of motion for **M** [formula (1)] and **L** [formula (2)].

2. INITIAL EQUATIONS AND THEIR SOLUTIONS

In general, the motion of vectors **M** and **L**, which corresponds to potential (3), should be described by the equations proposed in [5]. These equations adequately describe the behavior of **M** and **L** within the models with $(\mathbf{ML}) \neq 0$ ($\chi_{\parallel} \neq 0$). In the case when the deviations of **M** and **L** from their equilibrium values $\mathbf{M}_{\mathrm{eq}}$ and $\mathbf{L}_{\mathrm{eq}}$ are small,

$$\mathbf{m} = \mathbf{M} - \mathbf{M}_{\mathrm{eq}}, \quad \mathbf{l} = \mathbf{L} - \mathbf{L}_{\mathrm{eq}}, \qquad (12)$$

these equations have the form

$$\begin{aligned} \dot{\mathbf{m}} &= \gamma_1\left[\mathbf{M}_{\mathrm{eq}}\frac{\partial F}{\partial m}\right] + \gamma_2\left[\mathbf{L}_{\mathrm{eq}}\frac{\partial F}{\partial l}\right], \\ \dot{\mathbf{l}} &= \gamma_2\left[\mathbf{L}_{\mathrm{eq}}\frac{\partial F}{\partial m}\right] + \gamma_3\left[\mathbf{M}_{\mathrm{eq}}\frac{\partial F}{\partial l}\right], \end{aligned} \qquad (13)$$

where γ_i are constants. However, since our calculations are performed in the framework of the equimodulus model in which the magnetization magnitude of the sublattices remains unchanged, we assume that, in the set of equations (13), $\gamma_1 = \gamma_2 = \gamma_3 \equiv \gamma$, which corresponds to the Landau–Lifshitz equations [4, 5] (where γ is the gyromagnetic ratio).

The set of equations (13) yields the most interesting results in the case when the magnetic field **H** is oriented as $\mathbf{H} \parallel \mathbf{Y}$ and the electric field **E** is directed as $\mathbf{E} \parallel \mathbf{X}$ or $\mathbf{E} \parallel \mathbf{Y}$.

2.1. Frequencies and Susceptibilities in the Fields H || Y *and* E || X

In these fields, the oscillation eigenfrequencies have the following form:

$$\begin{aligned} \omega_1^2 &= \gamma^2 4M_0^2(\chi_{\perp}^{-1}K_{zz} - D_{yz}^2)\cos^2\varphi\sin^2\Theta_L + \Delta\omega_1^2(E_x), \\ \omega_2^2 &= \gamma^2 4M_0^2((\chi_{\perp}^{-1}K_{yy} - D_{zy}^2)\cos^2\varphi \\ &\quad + (\chi_{\perp}^{-1}\sin\varphi + D_{32}\cos\varphi\cos\Theta_L)^2) + \Delta\omega_2^2(E_x). \end{aligned} \qquad (14)$$

Here, $\Delta\omega_1^2(E_x)$ and $\Delta\omega_2^2(E_x)$ are the corrections for the electric field,

$$\begin{aligned} \Delta\omega_1^2(E_x) &= \omega_1^2(H, 0) - \omega_1^2(H, E) \\ &= \gamma^2 H_E \kappa k_{xxz} E_x (2 + \cos^2\varphi)\cos^2\varphi\sin 2\Theta_L, \\ \Delta\omega_2^2(E_x) &= \omega_2^2(H, 0) - \omega_2^2(H, E) \\ &= \gamma^2 H_E \kappa k_{xxz} E_x \cos^2\varphi\sin 2\Theta_L, \end{aligned} \qquad (15)$$

$\cos\Theta_L$ is the real root of Eq. (7), and the φ angle is determined from the equation

$$\sin\varphi = (H_y + 2D_{zy}M_0\cos\varphi\cos\Theta_L)/2H_E, \qquad (16)$$

where

$$H_E = \chi_{\perp}^{-1}M_0 \qquad (17)$$

is the exchange field responsible for antiferromagnetic ordering.

Relationships (15) account only for the corrections which contain the factor H_E [defined by expression (17)] and, in this sense, are exchange-enhanced (see, for example, [6]). As a rule, the antiferromagnetic resonance spectrum is characterized by an exchange enhancement of the effects corresponding to the terms involved in expression (3) for the F potential which contain no components of vector **M** [formula (2)]. In particular, no exchange enhancement occurs in the conventional magnetoelectric interaction described by the terms with $d_{\alpha\beta\gamma}$ in expression (3); as a consequence, its contribution to $\Delta\omega_1^2(E_x)$ and $\Delta\omega_2^2(E_x)$ does not enter into formulas (15). The exchange-enhanced contribution of the field **E** to the antiferromagnetic resonance frequency is made by only the antiferroelectric interaction, which is absent in crystals with a center of symmetry. Special attention should be given to an important result following from formula (15): the aforementioned exchange enhancement vanishes when $\cos\Theta_L = 0$ and $\sin\Theta_L = 0$, i.e., at the beginning and the end of the rotation (Fig. 2). The first case corresponds to the magnetic field **H** = 0.

The second feature of the frequency spectrum (14) is related to the magnetic field

$$H_y = H_{\mathrm{cr}} = 2M_0\frac{K_{zz}\chi_\perp^{-1} + \kappa k_{xxz}\chi_\perp^{-1} - D_{23}^2}{D_{23}^2}. \qquad (18)$$

This field satisfies the condition $\cos\Theta_L = 1$ ($\sin\Theta_L = 0$). As was noted above, under this condition ($E_x = 0$), the reorientation of vector **L** from the **X** axis to the **Z** axis (Fig. 2) is completed, which corresponds to the second-order phase transition. The soft mode attributed to this transition is associated with the frequency ω_1^2. However, if we take into account the corrections for the electric field E_x without exchange enhancement, the frequency ω_1^2 at $H_y = H_{\mathrm{cr}}$ will remain finite,

$$\Delta\omega_1^2(E_x, H_{\mathrm{cr}}) = [\gamma\kappa(k_{xxz}\sin\varphi - d_{xyx}\cos\varphi)E_x]^2. \quad (19)$$

In the case when terms of this type are included in expression (7), the value of $\cos\Theta_L = 1$ can be reached only when $H_y \longrightarrow \infty$ (the effect of a smeared phase transition).

The frequencies ω_1 and ω_2 [formulas (14)] correspond to the resonance magnetic $\mathbf{m}(t) = (\mathbf{M}(t) - \mathbf{M}_{\mathrm{eq}})$ and electric $\mathbf{p}(t) = (\mathbf{P}(t) - \mathbf{P}_{\mathrm{eq}})$ responses to high-frequency magnetic $\mathbf{h}(t)$ and electric $\mathbf{e}(t)$ fields; that is,

$$\begin{aligned} m_\alpha(t) &= \sum_\beta(\chi_{\alpha\beta}^m h_\beta^\omega(t) + \alpha_{\alpha\beta}^m e_\beta^\omega(t)), \\ p_\alpha(t) &= \sum_\beta(\alpha_{\alpha\beta}^p h_\beta^\omega(t) + \kappa_{\alpha\beta} e_\beta^\omega(t)). \end{aligned} \qquad (20)$$

In addition, we present the following expressions for the response of vector **L** to the magnetic $\mathbf{h}(t)$ and electric $\mathbf{e}(t)$ fields:

$$l_\alpha(t) = L_\alpha(t) - (L_{\mathrm{eq}})_\alpha = \sum_\beta(\chi_{\alpha\beta}^l h_\beta^\omega(t) + \alpha_{\alpha\beta}^l e_\beta^\omega(t)). \quad (21)$$

It should be noted that χ^l and α^l are not conventional tensors of the magnetic and magnetoelectric susceptibilities; they have a different symmetry and can be transformed as the products $L_\alpha H_\beta$ and $L_\alpha E_\beta$, respectively.

The following components of the tensors χ^m, χ^l, α^m, α^p, α^l, and κ proved to be substantially nonzero:

$$\chi_{yy}^m = \gamma^2 4M_0^2\frac{K_{zz}}{\omega_1^2 - \omega^2}\cos^2\varphi\sin^2\Theta_L,$$

$$\chi_{zz}^m = \gamma^2 4M_0^2\frac{K_{yy}\cos^2\varphi\sin^2\Theta_L + \chi_\perp^{-1}\sin^2\varphi}{\omega_2^2 - \omega^2}, \qquad (22)$$

$$\chi_{xz}^m = (\chi_{zx}^m)^* = -\gamma^2 4M_0^2\frac{\chi_\perp^{-1}K_{yy}\cos^2\varphi\sin 2\Theta_L + \chi_\perp^{-1}(D_{zy}\cos\varphi\sin\Theta_L + i\omega/\gamma 2M_0)\sin\varphi}{\omega_2^2 - \omega^2},$$

$$\chi_{zy}^l = -\gamma^2 4M_0^2\frac{\chi_\perp^{-1}(D_{yz}\cos\varphi\sin\Theta_L + i\omega/\gamma 2M_0)}{\omega_1^2 - \omega^2}\cos\varphi\sin\Theta_L,$$

$$\chi_{yz}^l = -\gamma^2 4M_0^2\frac{\chi_\perp^{-1}(D_{zy}\cos\varphi\sin\Theta_L + \chi_\perp^{-1}\sin\varphi\cos\Theta_L + i\omega/\gamma 2M_0)}{\omega_2^2 - \omega^2}\cos\varphi\sin\Theta_L,$$

$$\alpha_{xy}^m = \alpha_{xy}^p = \kappa(k_{xxz}\chi_{zy}^l(\omega) + d_{xyx}\chi_{yy}^m(\omega))\sin\Theta_L, \qquad (23)$$

$$\alpha_{yz}^m = \alpha_{yz}^p = \kappa(k_{yyz}\chi_{yz}^l(\omega) + d_{yzz}\chi_{zz}^m(\omega))\cos\Theta_L,$$

$$\alpha_{xz}^l = \kappa\left(d_{xyx}\chi_{zy}^l(\omega)\sin\Theta_L + \chi_\perp\frac{\gamma^2 4M_0^2\chi_\perp^{-2}(k_{xxz}\cos 2\Theta_L + d_{xyx}\sin\varphi\cos\Theta_L)\sin\Theta_L}{\omega_1^2 - \omega^2}\right),$$

$$\alpha_{yy}^l = \kappa\left(d_{yzz}\chi_{yz}^l(\omega)\cos\Theta_L + \chi_\perp\frac{\gamma^2 4M_0^2\chi_\perp^{-2}(k_{yyz}\cos\Theta_L + d_{yyy}\sin\varphi)}{\omega_2^2 - \omega^2}\right),$$

$$\kappa_{xx}(\omega) = \kappa(1 + (d_{xyx}\alpha_{xy}^m + k_{xxz}\alpha_{xz}^l)\sin\Theta_L), \qquad (24)$$

$$\kappa_{yy}(\omega) = \kappa(1 + (d_{yzz}\alpha_{yz}^m + k_{yyz}\alpha_{yy}^l)\sin\Theta_L).$$

2.2. Frequencies and Susceptibilities in the Fields **H || Y** *and* **E || Y**

For $\cos\Theta_L \ll 1$, we have

$$\omega_{1,2}^2(H, E) = \frac{1}{2}\left[\omega_1^2(H,0) + \omega_2^2(H,0) \pm \sqrt{(\omega_1^2(H,0) - \omega_2^2(H,0))^2 + (4H_E\kappa k_{yyz}E_y\cos^2\varphi\sin\Theta_L)^2}\right]. \quad (25)$$

Note that, in contrast with the preceding case when **E || X**, the exchange-enhanced contribution of the electric field **E || Y** to the frequencies $\omega_{1,2}^2$ is nonzero even at $\Theta_L = \frac{\pi}{2}$ (i.e., when $H_y = 0$). By contrast, it vanishes when $H_y \longrightarrow H_{\text{cr}}$.

For $\sin\Theta_L \ll 1$, we obtain

$$\begin{aligned} \omega_1^2 &= 2(\kappa k_{yyz}E_y\sin\varphi)^2, \\ \omega_2^2 &= \omega_2^2 - 2(\kappa k_{yyz}E_y\sin\varphi)^2. \end{aligned} \quad (26)$$

In this case, the susceptibilities are virtually identical to the susceptibilities in the fields **H || Y** and **E || X**.

3. RESULTS AND DISCUSSION

When analyzing the high-frequency properties of $KNiPO_4$ in alternating magnetic and electric fields, we tried to answer the following questions.

(i) How much does the constant electric field **E** affect the antiferromagnetic resonance frequencies?

(ii) What is the magnetic response (i.e., the amplitude of oscillations of vector **M**) at antiferromagnetic resonance frequencies upon excitation by alternating magnetic **h**(t) and alternating electric **e**(t) fields?

(iii) What are the factors affecting the amplitude of the resonance oscillations of vector **P** (i.e., the electric response) at antiferromagnetic resonance frequencies in the fields **h**(t) and **e**(t)?

The answer to the first question follows from an analysis of formulas (15) and (25), according to which the exchange can enhance the effect of the electric field **E**. For specific estimates, we can consider, for example, the ratio

$$\frac{\Delta\omega_1^2(E_x)}{\omega_1^2} \approx 3\frac{\Delta\omega_2^2(E_x)}{\omega_2^2} \approx 3\frac{\kappa k_{xxz}E_x}{2M_0K_{zz}}\cot\Theta_L. \quad (27)$$

As follows from formula (3), the combination of parameters $\kappa k_{xxz}E_x$ has the meaning of the anisotropy field being induced by the electric field E_x in the direction of the bisectrix of one of the angles formed by the axes **X** and **Z**. Moreover, in the vicinity of the critical field $H_y \approx H_{\text{cr}}$ at $\sin\Theta_L \ll 1$, the smallness of $\kappa k_{xxz}E_x$ with respect to $2M_0K_{zz}$ is partly compensated for by the large value of $\cot\Theta_L$, which enhances the effect of the field E_x on the antiferromagnetic resonance frequencies ω_1 and ω_2.

It is expedient to investigate experimentally the shift in the antiferromagnetic resonance frequencies in the electric field **E** under the conditions of the spin-reorientation transition. The matter is that, under standard conditions, this shift is insignificant compared to the width of the antiferromagnetic resonance line and its observation is a very difficult task (see, for example, the results of experiments on Cr_2O_3 [7–9]). However, it should be kept in mind that the magnitude of the exchange-enhanced contribution $\Delta\omega(E)$ in the vicinity of H_{cr} decreases with a decrease in the value of $\sin\Theta_L$.

An important inference drawn from the theory is as follows. The existence and manifestation of the exchange-enhanced contribution $\Delta\omega(E)$ to the antiferromagnetic resonance frequency is determined to a large measure by the direction of the electric field.

For example, under the condition **E || X**, the aforementioned contribution appears only in the magnetic field $H_y \neq 0$. As the magnetic field H_y increases, the exchange-enhanced contribution $\Delta\omega(E)$ also increases from zero (at $H_y = 0$), reaches its maximum, and then tends to zero when $H_y \geq H_{\text{cr}}$ (more precisely, when $H_y \longrightarrow \infty$).

At the same time, the exchange-enhanced contribution at **E || Y** satisfies the inequality $\Delta\omega(E) \neq 0$ even in the magnetic field $H_y = 0$ but vanishes again if the non-exchange-enhanced contribution (26) at $H_y \geq H_{\text{cr}}$ is ignored.

Analysis of relationship (22) and (23) provides the answer to the second question. The magnetic response **m**(t) to the alternating magnetic field **h**(t) is described by the components $\chi_{\alpha\beta}^m(\omega)$ involved in relationship (22). They contain no new information as compared to the standard expressions for the high-frequency magnetic susceptibility of two-sublattice antiferromagnets [10].

Relationships (23) describe the magnetic response **m**(t) to the alternating electric field **e**(t) and the electric response **p**(t) to the alternating magnetic field **h**(t). The component α_{xy}^m is of the maximum value and has a singularity only at the antiferromagnetic resonance frequency ω_1:

$$\alpha_{xy}^m = \alpha_{yx}^p \approx \frac{i\gamma\chi_\perp H_E\kappa k_{xxz}}{\omega_1 - \omega} \approx i\chi_{yy}^m(\omega)\kappa k_{xxz}\sqrt{\frac{H_E}{H_A^z}}, \quad (28)$$

where $H_A^\alpha = 2M_0K_{\alpha\alpha}$ is the so-called anisotropy field in the α direction. Compared to the component $\chi^m_{yy}(\omega)$, the component α^m_{xy} contains not only the small parameter k_{xxz} but also the factor $\sqrt{H_E/H_A^z} \gg 1$, which increases the chance of revealing this signal experimentally. It is worth noting that the effect is expected to be maximum in weak fields $H_y \ll H_{\rm cr}$ when $\sin\Theta_L \approx 1$.

Formulas (24) describe the resonance electric response $\mathbf{p}(t)$ to the field $\mathbf{e}(t)$ at the antiferromagnetic resonance frequencies ω_1 and ω_2. For small values of H_y ($H_y \ll H_{\rm cr}$) and $\sin\Theta_L \approx 1$, the maximum component $\kappa_{xx}(\omega)$ with a singularity at the frequency ω_1 can be represented as

$$\kappa_{xx}(\omega) = -\frac{2\gamma\chi_\perp H_E(\kappa k_{xxz})^2}{\omega_1 - \omega}. \tag{29}$$

In the vicinity of the critical value $H_y \approx H_{\rm cr}$, when $\cos\Theta_L \approx 1$, the maximum component

$$\kappa_{yy}(\omega) = \frac{2\gamma\chi_\perp H_E(\kappa k_{yyz})^2}{\omega_2 - \omega} \tag{30}$$

has a resonance singularity at the frequency ω_2.

Compared to the component $\alpha^m_{xy}(\omega)$ [see formula (28)], the component $\kappa_{xx}(\omega)$ [see formula (29)] has an excess degree of the small parameter k_{xxz}. However, this smallness can be partly compensated by the fact that, in the case of $\mathbf{p}(t)$, the dominant electrical component of the electromagnetic response is recorded, rather than the magnetic component as in the case of $\mathbf{m}(t)$ oscillations.

4. CONCLUSIONS

The results presented above allowed us to draw the following conclusions:

(1) It should be expected that, at the antiferromagnetic resonance frequencies ω_1 and ω_2, both the high-frequency magnetic and high-frequency electrical properties of $KNiPO_4$ exhibit resonance features.

(2) Both types of resonance signals (magnetic and electric responses) can be excited by alternating magnetic $\mathbf{h}(t)$ and alternating electric $\mathbf{e}(t)$ fields.

(3) The exchange-enhanced effect of the electric field E_x on the antiferromagnetic resonance frequencies takes place.

(4) The maximum shift in the antiferromagnetic resonance frequencies in the electric field E_x can occur in the vicinity of the critical magnetic field $H_y \approx H_{\rm cr} \approx 10^5$ Oe.

ACKNOWLEDGMENTS

This work was supported by the Russian Foundation for Basic Research, project no. 99-02-16268.

REFERENCES

1. F. Fisher, M. Lujan, F. Kubel, and H. Schmid, Ferroelectrics **162**, 37 (1994).
2. M. Lujan, J.-P. Rivera, S. Kizhaev, *et al.*, Ferroelectrics **161**, 77 (1994).
3. E. A. Turov, Zh. Éksp. Teor. Fiz. **110**, 202 (1996) [JETP **83**, 108 (1996)].
4. E. A. Turov, A. V. Kolchanov, V. V. Men’shenin, I. F. Mirsaev, and V. V. Nikolaev, *Symmetry and Physical Properties of Antiferromagnets* (Fizmatlit, Moscow, 2001).
5. Yu. M. Gufan, Zh. Éksp. Teor. Fiz. **60**, 1537 (1971) [Sov. Phys. JETP **33**, 831 (1971)].
6. E. A. Turov, Usp. Fiz. Nauk **164**, 325 (1994) [Phys. Usp. **37**, 303 (1994)].
7. E. Kita, K. Siratori, and A. Tasaki, J. Phys. Soc. Jpn. **46**, 1033 (1979).
8. E. Kita, A. Tasaki, and K. Siratori, Jpn. J. Appl. Phys. **18**, 1361 (1979).
9. E. Kita, K. Siratori, and A. Tasaki, Jpn. J. Appl. Phys., Part 2 **50**, 7748 (1979).
10. A. I. Akhiezer, V. G. Bar’yakhtar, and S. V. Peletminskii, *Spin Waves* (Nauka, Moscow, 1967; North-Holland, Amsterdam, 1968).

Translated by O. Moskalev

Physics of the Solid State, Vol. 44, No. 7, 2002, pp. 1336–1338. Translated from Fizika Tverdogo Tela, Vol. 44, No. 7, 2002, pp. 1277–1279.
Original Russian Text Copyright © 2002 by Isavnin.

MAGNETISM AND FERROELECTRICITY

Noise Suppression in an Ensemble of Easy-Axis Superparamagnetic Particles Caused by Radio-Frequency-Field Modulation

A. G. Isavnin
Kama Polytechnical Institute, Naberezhnye Chelny, 423810 Russia

Received October 1, 2001

Abstract—Stochastic resonance is investigated theoretically in a thermally activated system of small magnetic particles with easy-axis anisotropy. Calculations are performed within a discrete-orientation model using a quasi-adiabatic approximation. The output power of thermal noise of superparamagnetic particles is calculated and the magnitude of the noise suppression effect in the presence of a radio-frequency field is estimated at different temperatures. Estimates for actual iron samples are made with allowance for a spread in the particle sizes and easy-axis orientations. © *2002 MAIK "Nauka/Interperiodica".*

1. The phenomenon of stochastic resonance, in which the magnitude of the response of a modulated multistable system (having several stable states) passes through a clearly defined peak as the noise uniformly increases, has been well studied theoretically [1] and has found wide practical use. The response to an external weak periodic signal is usually characterized by the signal-to-noise ratio at the output of the system. In [2], the response of a system was characterized by the amplitude of the output periodic signal and the possible amplification of weak periodic signals was investigated. Such a description of stochastic resonance is convenient and allows one to elucidate the physical nature of the phenomenon when considering, for example, the modulation effects in small magnetic particles. In this case, the response of the system to an external weak radio-frequency (RF) field can be determined, e.g., by the components of the dynamic susceptibility of the system. If a system consists of single-domain particles with easy-axis anisotropy (which can be considered to be bistable elements, with two stable states corresponding to the two opposite orientations of their magnetic moments along the easy axis), then stochastic resonance can occur in the system. The smallness of these particles leads to the phenomenon of superparamagnetism; when thermally activated, the magnetic moment of a particle can surmount the potential barrier between the two minima and reverse its direction along the easy axis. The internal noise in this case is caused by these thermal reversals of the magnetic moment, and the noise level is determined by the temperature [3]. The case of quantum fluctuations of magnetization (due to tunneling magnetization reversal) under stochastic-resonance conditions at very low temperatures was considered in [4]. Investigation of this micromagnetic problem is not only of academic interest; it is also a matter of practical importance, because small magnetic particles possess specific properties and determine the characteristics of materials for magnetic recording and storage of information, ferrofluids, cluster structures, pigment dyes, some catalysts, etc.

2. In this paper, a decrease in intensity of thermal magnetization fluctuations is considered as a result of stochastic resonance in an ensemble of magnetic single-domain particles with easy-axis anisotropy placed in an RF field. Calculations are carried out within a discrete-orientation model in which the magnetic moment of a superparamagnetic particle can have only two orientations corresponding to the minima of a double-well potential. The magnetic energy of a particle with uniaxial anisotropy in the problem at hand can be written as

$$E = -Kv\cos^2\Theta - \mu_0 MHv\cos\Theta\cos(\Omega t), \qquad (1)$$

where the first term describes the interaction of the particle's magnetic moment with the anisotropy field (K is the anisotropy constant, v is the particle's volume) and the second term is the interaction energy with an external ac magnetic field (M is the saturation magnetization); H and Ω are the amplitude and frequency of the external ac field, respectively; and Θ is the angle between the magnetization vector and the easy axis. The discrete-orientation model is adequate in the case of a high potential barrier, $Kv \gg kT$, where T is the temperature. Therefore, the magnetic moment of a particle does not diffuse continuously over the sphere but rather undergoes random discontinuous changes from one orientation along the easy axis to the other. Furthermore, calculations in this model are valid only in the quasi-adiabatic limit, where the frequency of the external ac field is lower than the frequency of the superparamagnetic-particle local magnetic-moment relaxation to one of the two directions along the easy axis. The convenience of the discrete-orientation model is that this approximation allows one to pass from the cumbersome Fokker–Planck equation [5] describing the modulated stochastic dynamics of the particle's magnetic moment (which is solved by numerical methods) to a much simpler master equation for the transition rates [1, 3] which can be solved analytically.

When considering stochastic resonance, the modulation by an external field is usually assumed to be weak in comparison with the height of the potential barrier, $\mu_0 MH \ll K$. This case is of interest, because a weak periodic signal does not induce transitions of the system from one state to another in the absence of noise. The time-averaged spectral function of the system, defined for positive frequencies ω, consists of two parts, one of which is a Lorentzian function, corresponding to chaotic thermal changes in the orientation of the magnetization of superparamagnetic particles, and the other is a δ-function peak, describing the periodic motion of the vector $\mathbf{M}$ at the external-signal frequency Ω [3]:

$$\begin{aligned}\langle S(\omega)\rangle_t &= \int \langle\langle x(t)x(t+\tau)\rangle\rangle_t \exp(-i\omega\tau)d\tau \\ &= \left[1-\frac{W_0^2A^2}{2(W_0^2+\Omega^2)}\right]\left[\frac{2M^2W_0}{W_0^2+\Omega^2}\right] \\ &\quad + \frac{\pi M^2W_0^2A^2}{2(W_0^2+\Omega^2)}\delta(\omega-\Omega).\end{aligned} \tag{2}$$

Here, $W_0 = 2\alpha_0\exp(-Kv/kT)$, $A = \mu_0 MHv/kT$, $\alpha_0 = 2\eta\gamma^2 K/\sqrt{2\pi}(1 + \eta^2\gamma^2M^2)$, γ is the gyromagnetic ratio, and η is the Gilbert damping constant [6]. The total output power can be found by integrating Eq. (2) with respect to ω from zero to infinity:

$$\begin{aligned}P &= P_n + P_s \\ &= \left[1-\frac{W_0^2A^2}{2(W_0^2+\Omega^2)}\right]\pi M^2 + \frac{\pi M^2W_0^2A^2}{2(W_0^2+\Omega^2)}.\end{aligned} \tag{3}$$

Here, the first term describes the output noise power and the second term is the output signal power. It is seen that the noise intensity of the system decreases by an amount equal to the signal intensity; that is, the energy of chaotic motion is transformed into the energy of regular motion, which is the stochastic-resonance effect.

3. The ratio of the output noise power of the modulated system to the noise power of the system in the absence of modulation is equal to

$$P_n/P = 1 - W_0^2A^2/2(W_0^2+\Omega^2). \tag{4}$$

Figure 1 shows the temperature dependence of P_n/P for a modulated superparamagnetic iron particle ($K = 4 \times 10^4$ J/m^3, $M = 1.72 \times 10^6$ A/m, $v = 10^{-24}$ m^3, $H = 10^3$ A/m) for different values of the external-field frequency. It is seen that the degree of noise suppression increases with decreasing modulation frequency. Equation (4), derived in the discrete-orientation approximation, allows one to determine the ranges of the internal and external factors (temperature, particle size, modulation frequency) within which the degree of suppression of thermal noise is maximum. In an actual system consisting of a large number of superparamagnetic particles, there is always a spread in particle size, which decreases the above-mentioned effect. Figure 2 shows the temperature dependence of the reduced average

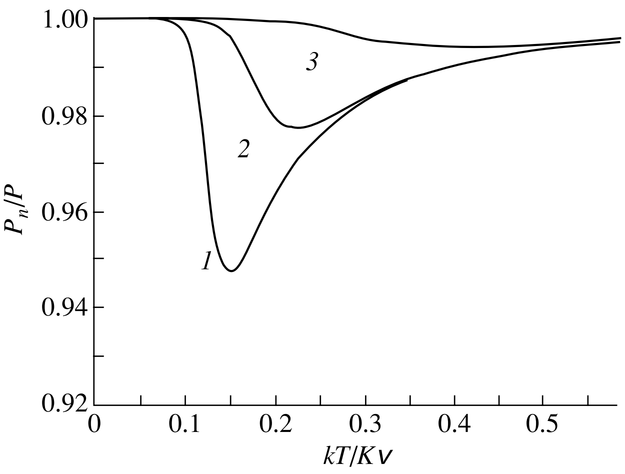

Fig. 1. Temperature dependence of the ratio of the output noise power P_n of an iron superparamagnetic particle placed in an RF field to the noise power P in the absence of an RF field for the external-field frequency Ω equal to (*1*) 10^5, (*2*) 10^6, and (*3*) 10^7 s^{-1}.

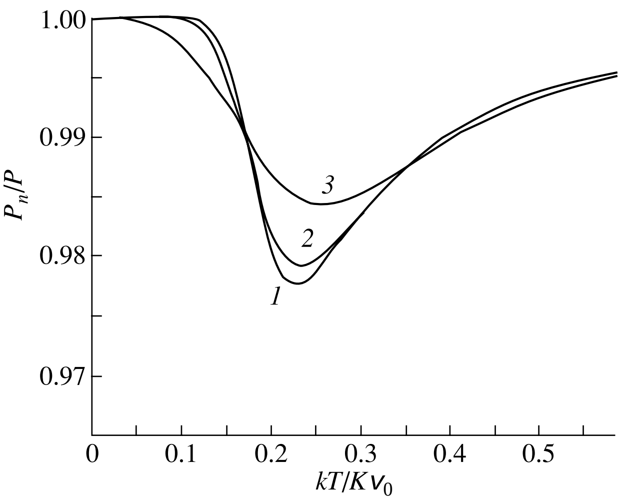

Fig. 2. Temperature dependence of the ratio of the output noise powers P_n/P of an ensemble of iron superparamagnetic particles ($K = 4 \times 10^4$ J/m^3, $M = 1.72 \times 10^6$ A/m, $v_0 = 10^{-24}$ m^3, $H = 10^3$ A/m) averaged over particle sizes in the case of a normal size distribution characterized by parameter D equal to (*1*) 0.01, (*2*) 0.1, and (*3*) 0.3.

output power of a modulated system of iron particles in the case where the particle size (volume) distribution is normal and described by the Gaussian

$$f(v) = \frac{1}{\Delta v\sqrt{2\pi}}\exp\left[-\left(\frac{v-v_0}{\Delta v\sqrt{2}}\right)^2\right], \quad \Delta v = v_0 D. \quad (5)$$

If the easy axes of superparamagnetic particles are oriented at random, this can be taken into account by averaging the scalar product of the vectors **M** and **H** in Eq. (1) over the angle Θ. As a result, the expression for the dimensionless amplitude $A = \mu_0 MHv/kT$ of the external modulating field in Eq. (2) will contain an additional factor,

$$\frac{2}{\pi}\int_0^{\pi/2}\cos\Theta d\Theta = \frac{2}{\pi}. \quad (6)$$

In this case, we can neglect the RF field components perpendicular to the easy axes, because these components do not give rise to stochastic resonance.

The effect of suppression of thermal noise in a certain temperature range and the corresponding increase in the output signal magnitude considered in this paper can be observed in the satellite structure of Mössbauer spectra of superparamagnetic particles placed in an RF field [7].

ACKNOWLEDGMENTS

This study was supported by the International Science Foundation (ISF), grant no. NNT300.

REFERENCES

1. B. McNamara and K. Wiesenfeld, Phys. Rev. A **39** (9), 4854 (1989).
2. P. Jung and P. Hanggi, Phys. Rev. A **44** (12), 8032 (1991).
3. É. K. Sadykov and A. G. Isavnin, Fiz. Tverd. Tela (St. Petersburg) **36** (11), 3473 (1994) [Phys. Solid State **36**, 1843 (1994)].
4. É. K. Sadykov, A. G. Isavnin, and A. B. Boldenkov, Fiz. Tverd. Tela (St. Petersburg) **40** (3), 516 (1998) [Phys. Solid State **40**, 474 (1998)].
5. É. K. Sadykov and A. G. Isavnin, Fiz. Tverd. Tela (St. Petersburg) **38** (7), 2104 (1996) [Phys. Solid State **38**, 1160 (1996)].
6. W. F. Brown, Jr., Phys. Rev. **130** (5), 1677 (1963).
7. É. K. Sadykov, A. I. Skvortsov, Yu. A. Antonov, and A. G. Isavnin, Izv. Ross. Akad. Nauk, Ser. Fiz. **58** (4), 101 (1994).

Translated by Yu. Epifanov

Physics of the Solid State, Vol. 44, No. 7, 2002, pp. 1339–1344. Translated from Fizika Tverdogo Tela, Vol. 44, No. 7, 2002, pp. 1280–1284.

Synthesis of the New Oxocuprate $Cu_5Bi_2B_4O_{14}$ and Investigation of Its Structural, Magnetic, and Resonant Properties

G. A. Petrakovskiĭ*, K. A. Sablina*, A. I. Pankrats*, D. A. Velikanov*, A. D. Balaev*, O. A. Bayukov*, V. I. Tugarinov*, A. M. Vorotynov*, A. D. Vasil'ev*, G. V. Romanenko, and Yu. G. Shvedenkov****

** Kirensky Institute of Physics, Siberian Division, Russian Academy of Sciences,*
Akademgorodok, Krasnoyarsk, 660036 Russia
*** Institute of Inorganic Chemistry, Siberian Division, Russian Academy of Sciences,*
pr. Akademika Lavrent'eva 3, Novosibirsk, 630090 Russia
e-mail: pank@iph.krasn.ru

Received October 30, 2001

Abstract—Single crystals of the new compound $Cu_5Bi_2B_4O_{14}$ are grown and its structural, magnetic, and resonant properties are investigated for the first time. It is found that the $Cu_5Bi_2B_4O_{14}$ crystal synthesized has a triclinic symmetry with space group $P\bar{1}$ and the unit cell parameters $a = 10.132$ Å, $b = 9.385$ Å, $c = 3.458$ Å, $\alpha = 105.443°$, $\beta = 97.405°$, $\gamma = 107.784°$, and $Z = 1$. At a temperature of 24.5 K, the crystal undergoes a magnetic phase transition to the magnetically ordered state. The assumption is made that the ferrimagnetic structure of the $Cu_5Bi_2B_4O_{14}$ crystal consists of two ferromagnetic sublattices coupled through the antiferromagnetic exchange interaction. The unit cell of the crystal contains five copper ions, of which one ion belongs to the first sublattice and the other four ions form the second sublattice. Analysis of the resonant and magnetic static properties demonstrates that the $Cu_5Bi_2B_4O_{14}$ crystal exhibits an easy-axis magnetic anisotropy. The direction of the easy axis coincides with the c axis of the crystal, whereas the a and b axes are the hard magnetic axes with saturation fields approximately equal to 25 and 10 kOe, respectively. *© 2002 MAIK "Nauka/Interperiodica".*

1. INTRODUCTION

The discovery of high-temperature superconductivity gave impetus to active research into oxocuprates. Although oxocuprates possess neither superconductivity nor even metallic conductivity, their crystal structure involves fragments that are similar to those of high-temperature superconductors and determine the magnetic properties of the former compounds in the case of superexchange interactions. In his monograph, Wells [1] noted that bivalent copper should form a larger variety of magnetic structures than is observed for any other chemical element. The great diversity of the magnetic properties of copper oxide compounds can be illustrated using the oxocuprates studied in our earlier works. In particular, $CuGeO_3$ is a chain spin-Peierls magnet with the transition temperature $T_{SP} = 14$ K [2, 3], $LiCu_2O_2$ is a two-dimensional antiferromagnet with a damaged ladder structure and the magnetic phase transition temperature $T_N = 24$ K [4], and Bi_2CuO_4 is a three-dimensional antiferromagnet characterized by the four-spin exchange interaction and the Néel temperature $T_N = 41$ K [5]. For CuB_2O_4 [6–9], the magnetic states at temperatures below 20 K are described by a complex phase diagram, including the transition between the commensurate and incommensurate structures. This paper reports on the first results of investigations into the structural, magnetic, and resonant properties of a new oxocuprate which we found in the ternary $CuO–Bi_2O_3–B_2O_3$ system.

2. GROWTH OF SINGLE CRYSTALS

Earlier, Zargarov *et al.* [10] performed physicochemical investigations into the ternary $CuO–Bi_2O_3–B_2O_3$ system and revealed two copper oxide compounds, namely, $2Bi_2O_3 \cdot CuO \cdot B_2O_3$ and $Bi_2O_3 \cdot 2CuO \cdot B_2O_3$, which crystallize in the orthorhombic crystal system. We also studied the $CuO–Bi_2O_3–B_2O_3$ system and found a new compound with the chemical formula $Cu_5Bi_2B_4O_{14}$.

Single crystals of $Cu_5Bi_2B_4O_{14}$ were grown by spontaneous crystallization from a molten mixture containing 22 mol % Bi_2O_3, 50 mol % CuO, and 28 mol % B_2O_3. Dark green crystals of different shapes were mechanically removed from the crucible. A number of crystals had a perfect faceting typical of bulk skewed prisms, whereas the other crystals had a flatter shape with a less pronounced faceting. Crystals of a particular type could be predominantly grown by varying the ratio of the initial oxides in certain limits. It turned out that crystals of both types exhibited identical x-ray diffraction patterns.

X-ray diffraction analysis was performed both with powders of ground crystals on a DRON-2 diffractometer and with small-sized high-quality single crystals on a CAD4 automated diffractometer (MoK_α radiation). It was found that the crystals synthesized have a triclinic symmetry with space group $P\bar{1}$. The unit cell parameters are as follows: $a = 10.132$ Å, $b = 9.385$ Å, $c = 3.458$ Å, $\alpha = 105.443°$, $\beta = 97.405°$, $\gamma = 107.784°$, and $Z = 1$.

The magnetic susceptibility and the magnetization were measured on a SQUID magnetometer in magnetic fields up to 40 kOe and on a vibrating-coil magnetometer in fields up to 30 kOe in the temperature range 4.2–300 K at different orientations of the magnetic field with respect to the crystallographic axes.

3. EXPERIMENTAL RESULTS

Figure 1 displays the temperature dependences of the magnetic susceptibility and the reciprocal of the magnetic susceptibility for a sample composed of a set of single crystals oriented in a random manner. In the temperature range 170–300 K, the magnetic susceptibility is adequately described by the Curie–Weiss law $\chi = C/(T - \Theta)$ with the following parameters: $C = 2.01 \times 10^{-3}$ K cm^3/g and $\Theta = +17.4$ K. The effective magnetic moment is estimated as $\mu_{\text{eff}} = 0.81\mu_B$. Judging from the positive paramagnetic Curie temperature, this compound predominantly undergoes a ferromagnetic exchange interaction, which is rarely observed in oxocuprates [11, 12].

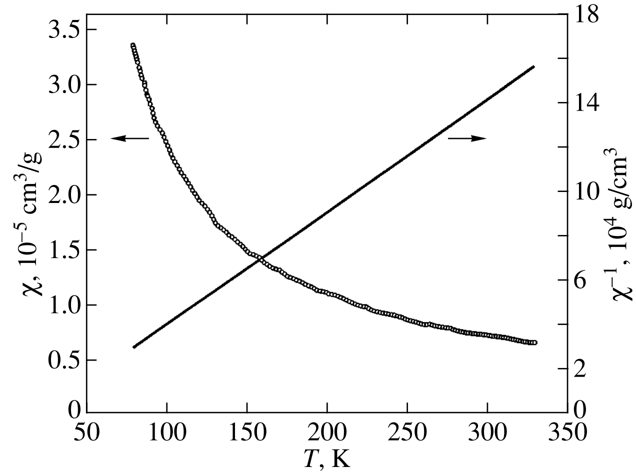

Fig. 1. Temperature dependences of the magnetic susceptibility and the reciprocal of the magnetic susceptibility for the $Cu_5Bi_2B_4O_{14}$ crystal.

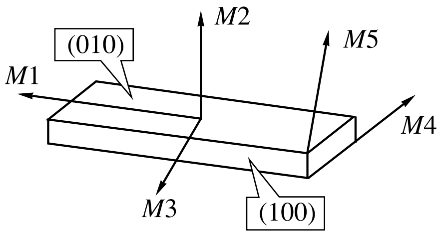

Fig. 2. A geometric shape of the $Cu_5Bi_2B_4O_{14}$ samples and the magnetic field orientations used in the measurements.

The temperature and field dependences of the magnetization of the single crystals under investigation were measured at different magnetic field orientations. Figure 2 shows a geometric shape of the single-crystal samples; in this figure, the magnetic field orientations used in the measurements are designated as $M1$–$M5$. The samples used in these experiments have the form of plates elongated in one direction. The longer edge of the plate is oriented along the c axis of the crystal. The largest and elongated lateral faces lie in the (010) and (100) crystallographic planes, respectively. The magnetic field orientation $M1$ coincides with the c axis of the crystal, the orientation $M2$ is perpendicular to the (010) face, and the field orientation $M3$ is aligned with the (010) plane and is perpendicular to the orientation $M1$. The field orientations $M4$ and $M5$ coincide with the shorter edges of the crystal.

Figure 3 depicts the field dependences of the magnetization measured at $T = 5$ K. For the field orientations $M1$–$M3$, the magnetization linearly increases to saturation and remains virtually constant with a further increase in the magnetic field strength. The saturation magnetizations at the orientations $M1$ and $M2$ coincide with each other and amount to 17.1 emu/g at $T = 5$ K. The saturation magnetization at the orientation $M3$ is equal to 16.6 emu/g. The saturation fields at the orientations $M1$, $M2$, and $M3$ are approximately equal to 350 Oe, 8 kOe, and 23 kOe, respectively. The field dependences of the magnetization at the orientations $M4$ and $M5$ exhibit a nonlinear behavior. Since the magnetization directions $M4$ and $M5$ are close to the directions $M3$ and $M2$, respectively, the field dependences of the magnetization for the directions $M4$ and $M5$ are characterized by the saturation fields which are approximately identical to those for the directions $M3$ and $M2$. The specific feature of the field dependences is that they are anhysteretic to within the experimental error of the magnetization measurement.

The temperature dependences of the susceptibility $\chi = M/H$ (Fig. 4) were measured in magnetic fields corresponding to the initial linear portions of the field dependences of the magnetization. For all the magnetic field orientations used in the measurements, the susceptibility varies only slightly with an increase in the temperature from 4.2 to 24 K and decreases drastically with a further increase in the temperature, which corresponds to a magnetic phase transition.

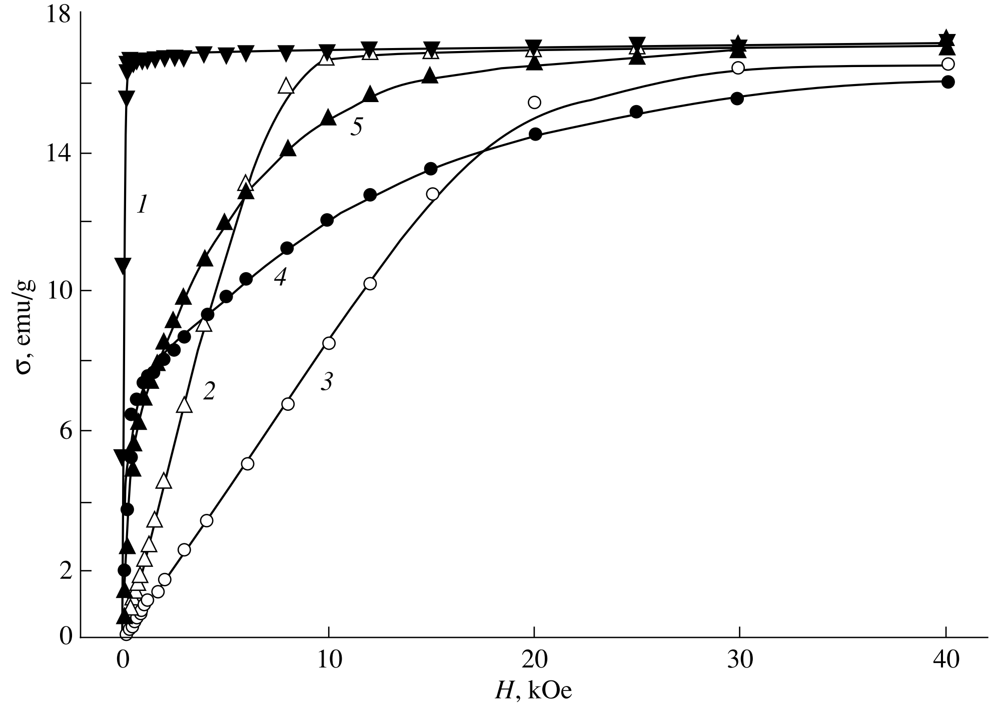

Fig. 3. Field dependences of the magnetization measured at $T = 5$ K. Curves *1*–*5* correspond to the magnetic field orientations *M*1–*M*5, respectively.

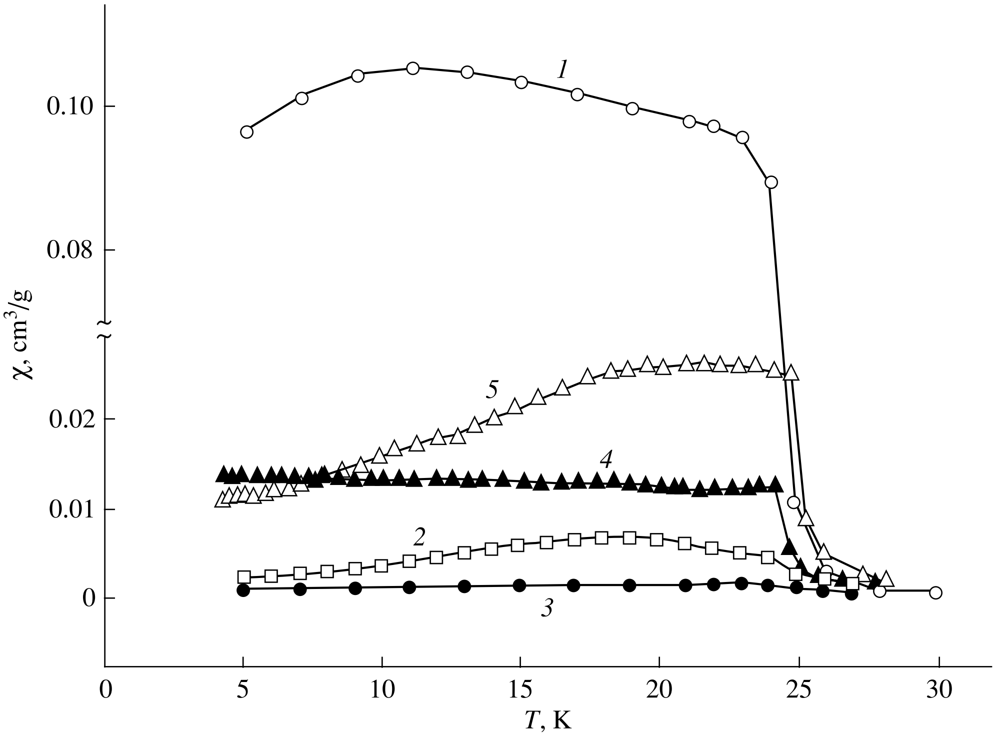

Fig. 4. Temperature dependences of the magnetic susceptibility for the $Cu_5Bi_2B_4O_{14}$ crystal at different orientations and strengths of the measuring field (Oe): (*1*) *M*1, 50; (*2*) *M*2, 500; (*3*) *M*3, 500; (*4*) *M*4, 20; and (*5*) *M*5, 20.

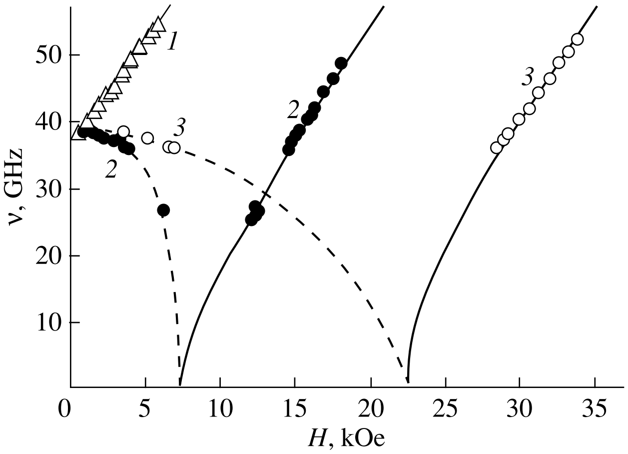

Fig. 5. Frequency–field dependences of the magnetic resonance measured at $T = 4.2$ K for different orientations of the external magnetic field: (*1*) *M*1, (*2*) *M*2, and (*3*) *M*3.

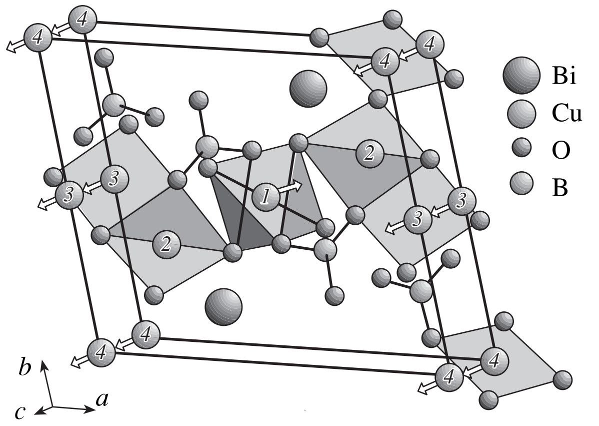

Fig. 6. Crystalline and hypothetical magnetic structures of $Cu_5Bi_2B_4O_{14}$.

The magnetic resonance measurements were performed on a pulsed magnetic spectrometer in the temperature range 4.2–80 K. The frequency–field dependences of the magnetic resonance measured at T = 4.2 K for the magnetic field orientations *M*1, *M*2, and *M*3 are plotted in Fig. 5. The frequency–field dependence at the orientation *M*1 exhibits a linear behavior and is characterized by an energy gap at approximately 36.5 GHz. For the other two orientations of the magnetic field, the frequency–field dependences can be divided into two portions. In weak fields, an increase in the magnetic field strength is accompanied by a decrease in the magnetic resonance frequency from a value determined by approximately the same energy gap as for the orientation *M*1. Then, beginning with a certain magnetic field, an increase in the magnetic field strength leads to an increase in the magnetic resonance frequency. The approximation of both portions in the frequency–field dependence of the magnetic resonance indicates that, for these two orientations of the magnetic field, the softening of the vibrational mode occurs at the same field strengths at which the magnetization reaches saturation.

4. DISCUSSION

The crystal structure of $Cu_5Bi_2B_4O_{14}$ is shown in Fig. 6. The unit cell contains one formula unit. The copper ions occupy four nonequivalent positions, which are designated as Cu(1)–Cu(4) (Fig. 6). The oxygen environment of each copper ion has the form of a distorted, strongly elongated octahedron (also depicted in this figure). The distances from the copper ion to the apical oxygen ions in the octahedron vary from 2.58 to 2.82 Å for different nonequivalent positions. Therefore, in order to evaluate the exchange interactions, it is sufficient to consider only the oxygen environment of the octahedron base in which the Cu–O distances for different positions lie in the range 1.78–2.08 Å. Note that, in this case, the octahedron base is not a regular square and the degree of its distortion differs for different nonequivalent positions.

Let us now consider the exchange interactions in terms of the Anderson–Goodenough–Kanamori theory [13]. It should be noted that all the exchange bonds allowed by the $Cu_5Bi_2B_4O_{14}$ structure occur through one oxygen ion; contrastingly, the exchange bonds in Bi_2CuO_4 [5] and CuB_2O_4 [9] occur through two oxygen ions and bismuth or boron ions. The crystal structure of $Cu_5Bi_2B_4O_{14}$ admits the formation of approximately 90° exchange bonds between the Cu(2) and Cu(3) ions, for which the base squares of the oxygen environment share a common side. There exists also an approximately 90° exchange bond between the Cu(2) and Cu(4) ions, for which the base squares of the oxygen environment share a common site. Moreover, the Cu(1) and Cu(2) ions are coupled by the exchange interaction through the oxygen ion located at a common site of their base squares. However, in the latter case, the bond angle θ is equal to 113.7°.

The estimation of the exchange integrals for these bonds according to the formulas taken from [13] gives

$$\begin{aligned} J_{23} &= 4/3BCJ^{\text{int}} = +5\text{ K}, \\ J_{24} &= BCJ^{\text{int}} = +3\text{ K}, \\ J_{12} &= 2B^2(U - 1/3J^{\text{int}})\cos\theta = -6.2\text{ K}. \end{aligned} \tag{1}$$

Here, B is the parameter of the ligand–cation electron transfer over the σ bonds, C is the parameter of the ligand–cation electron transfer over the π bonds, J^{int} is the intraatomic-exchange integral, and U is the energy of oxygen–copper electron excitation. The above estimates were made using the standard parameters B = 0.02, C = 0.01, U = 2.2 eV, and J^{int} = 1.6 eV for Cu^{2+}

ions [14]. The paramagnetic Curie temperature Θ calculated in the molecular-field approximation using the exchange integrals obtained is equal to +3.6 K. This result is in qualitative agreement with the positive paramagnetic Curie temperature (Θ = +17.4 K), which was determined experimentally.

Reasoning from the results of analyzing the exchange interactions, we can propose the following magnetic structure of the $Cu_5Bi_2B_4O_{14}$ crystal (Fig. 6). The crystal has a ferrimagnetic structure consisting of two magnetic sublattices. In this structure, the Cu(1) ions belong to the first magnetic sublattice and all the other copper ions form the second magnetic sublattice. Judging from the proposed magnetic structure, the saturation magnetization can be estimated from the experimental effective magnetic moment $\mu_{eff} = 0.81\mu_B$, which was determined from the high-temperature portion of the temperature dependence of the magnetic susceptibility. The saturation magnetization thus calculated ($\sigma = 7.6$ emu/g) differs significantly from the experimental saturation magnetization ($\sigma = 17.1$ emu/g) obtained from the field dependences of the magnetization measured at $T = 5$ K (Fig. 3). Under the assumption that the proposed ferrimagnetic structure is incorrect and that the $Cu_5Bi_2B_4O_{14}$ crystal has a ferromagnetic structure, the saturation magnetization σ estimated from the same experimental effective magnetic moment is equal to 12.7 emu/g, which also differs substantially from the experimental value. However, we carried out the calculation for the proposed ferrimagnetic structure with the use of the effective magnetic moment $\mu_{eff} = 1.89\mu_B$, which is characteristic of copper ions. In this case, the effective magnetic moment was estimated from the experimental value $g = 2.18$. As a result, we obtained the saturation magnetization $\sigma = 18.1$ emu/g, which is close to the experimental value. Note that the reason for the considerable difference between the experimental and theoretical effective magnetic moments remains unclear.

The temperature of the magnetic phase transition can be most precisely determined from the experimental temperature dependence of the magnetization in the weak external magnetic field $H = 20$ Oe (Fig. 4). In this case, the true magnetization of the sample in the magnetic field ($m = \sigma + \chi H$) differs only slightly from the spontaneous magnetic moment σ. Therefore, it can be assumed that the drastic increase observed in the true magnetization at $T = 24.5$ K corresponds to a magnetic phase transition.

Thus, we believe that, at temperatures below $T_C = 24.5$ K, the $Cu_5Bi_2B_4O_{14}$ crystal is a collinear ferrimagnet.

Furthermore, the field dependences of the magnetization indicate that the ferrimagnetic structure of the studied crystal exhibits an easy-axis magnetic anisotropy with the easy axis aligned along the *c* axis of the crystal (the orientation *M*1). Since our attempts to determine the crystallographic indices of the small crystal face have been unsuccessful, we cannot argue that the orientations *M*4 and *M*5 coincide with the *a* and *b* axes of the crystal. However, the *a* axis is at least close to the directions *M*3 and *M*4 and the *b* axis is close to the directions *M*2 and *M*5. Hence, reasoning from the triclinic symmetry of the $Cu_5Bi_2B_4O_{14}$ crystal and the field dependences of the magnetization for the orientations *M*2–*M*5, we can assume that the *a* and *b* axes are the hard magnetic axes with saturation fields approximately equal to 25 and 10 kOe, respectively.

The initial linear portion in the field dependence of the magnetization at the orientation *M*1 is most likely associated with the domain structure of the crystal. The formation of a single-domain structure at this orientation is observed in a saturation field of 350 Oe. It can be assumed that the crystal has a predominantly strip domain structure with antiparallel orientations of the magnetic moments along the *c* axis in adjacent domains. Therefore, upon magnetization along the *M*2 and *M*3 directions perpendicular to the *c* axis, the initial portion of a rapid increase in the magnetization due to transformation of the domain structure is absent in the field dependences. For these orientations, an increase in the magnetic field strength immediately leads to rotation of the magnetic moments. Note that the magnetic moments of the adjacent domains rotate to meet each other toward the magnetic field direction and the domain structure is retained until the rotation ceases. For the magnetic field orientations *M*4 and *M*5, the projection of the magnetic field onto the *c* axis is nonzero and a rapid increase in the magnetization in the initial portions of the magnetization curves is caused by the displacement of the domain boundaries.

The above model of magnetic anisotropy in the $Cu_5Bi_2B_4O_{14}$ crystal is confirmed by the results of the magnetic resonance measurements. The magnetic resonance data are in qualitative agreement with the available data on the ferromagnetic resonance in a uniaxial ferromagnet [15]. The theoretical dependences constructed for the easy and hard magnetization directions under the assumption of a uniaxial ferromagnet are depicted by the solid lines in Fig. 5. Upon magnetization along the direction of easy magnetization, the frequency–field dependence exhibits a linear behavior and, in this specific case, can be described by the relationship [15]

$$\omega = \gamma(H_a' + H). \quad (2)$$

Note that the experimental data for the magnetic field orientation *M*1 are well represented by this formula at $H_a' = 11.8$ kOe and the gyromagnetic ratio $\gamma = 3.05$ MHz/Oe (the g factor is equal to 2.18). The parameter H_a' determines the energy gap in the magnetic resonance spectrum and, most likely, is a combination of the anisotropy fields for the *a* and *b* axes.

Upon magnetization along the *M*2 and *M*3 directions close to the hard magnetic axes *b* and *a*, the vibrational frequencies in the initial portions of the frequency–field dependences decrease with an increase in the magnetic field strength. These portions correspond to a state in which the direction of the spontaneous magnetic moment does not coincide with the magnetic field direction and rotates gradually toward the latter direction with an increase in the field strength. The rotation is completed in a magnetic field equal to the anisotropy field in the corresponding direction. With a further increase in the magnetic field strength, the direction of the spontaneous magnetic moment coincides with the magnetic field direction. In this case, the frequency–field dependence can be represented in the following form [15]:

$$\omega = \gamma\{H(H - H_a)\}^{0.5}. \tag{3}$$

For both directions ($M2$ and $M3$), the experimental data in these portions of the frequency–field dependences are adequately described by relationship (3) at anisotropy fields H_{a1} = 7.5 kOe and H_{a2} = 22.5 kOe. These fields are close to the saturation fields determined for the orientations $M2$ and $M3$ from the magnetic measurements.

ACKNOWLEDGMENTS

This work was supported by the Russian Foundation for Basic Research, project no. 01-02-17270-a.

REFERENCES

1. A. Wells, *Structural Inorganic Chemistry* (Clarendon, Oxford, 1984; Mir, Moscow, 1987).
2. G. A. Petrakovskiĭ, K. A. Sablina, A. M. Vorotynov, *et al.*, Zh. Éksp. Teor. Fiz. **98** (4), 1382 (1990) [Sov. Phys. JETP **71**, 772 (1990)].
3. G. A. Petrakovskiĭ, Izv. Vyssh. Uchebn. Zaved., Fiz., No. 1, 91 (1998).
4. A. M. Vorotynov, A. I. Pankrats, G. A. Petrakovskiĭ, *et al.*, Zh. Éksp. Teor. Fiz. **113** (5), 1866 (1998) [JETP **86**, 1020 (1998)].
5. G. Petrakovskii, K. Sablina, A. Pankrats, *et al.*, J. Magn. Magn. Mater. **140–144**, 1991 (1995).
6. G. Petrakovskii, D. Velikanov, A. Vorotinov, *et al.*, J. Magn. Magn. Mater. **205** (1), 105 (1999).
7. A. I. Pankrats, G. A. Petrakovskiĭ, and N. V. Volkov, Fiz. Tverd. Tela (St. Petersburg) **42** (1), 93 (2000) [Phys. Solid State **42**, 96 (2000)].
8. G. A. Petrakovskiĭ, A. D. Balaev, and A. M. Vorotynov, Fiz. Tverd. Tela (St. Petersburg) **42** (2), 313 (2000) [Phys. Solid State **42**, 321 (2000)].
9. B. Roessli, J. Schefer, G. Petrakovskii, *et al.*, Phys. Rev. Lett. **86** (9), 1885 (2001).
10. M. I. Zargarov, N. M. Mustafaev, and N. S. Shuster, Neorg. Mater. **32** (1), 74 (1996).
11. F. Mizuno, H. Masuda, I. Hirobayashi, *et al.*, Nature **345** (7), 788 (1990).
12. M. A. Subramanian, A. P. Ramirez, and W. J. Marshall, Phys. Rev. Lett. **82** (7), 1558 (1999).
13. P. W. Anderson, Phys. Rev. **115** (1), 2 (1959); J. B. Goodenough, *Magnetism and the Chemical Bond* (Interscience, New York, 1963; Metallurgiya, Moscow, 1968).
14. O. A. Bayukov and A. F. Savitskiĭ, Fiz. Tverd. Tela (St. Petersburg) **36** (7), 1923 (1994) [Phys. Solid State **36**, 1049 (1994)].
15. A. G. Gurevich, *Magnetic Resonance in Ferrites and Antiferromagnets* (Nauka, Moscow, 1973).

Translated by O. Borovik-Romanova

Physics of the Solid State, Vol. 44, No. 7, 2002, pp. 1345–1349. Translated from Fizika Tverdogo Tela, Vol. 44, No. 7, 2002, pp. 1285–1289.
Original Russian Text Copyright © 2002 by Bugaev, Gorsky.

MAGNETISM AND FERROELECTRICITY

Nonlinearity of Magnetoacoustic Excitations in Planar Structures

A. S. Bugaev and V. B. Gorsky

Moscow Physicotechnical Institute, Institutskiĭ proezd 9, Dolgoprudnyĭ, Moscow oblast, 141700 Russia

e-mail: dwhome@sbrf.ru

Received November 13, 2001

Abstract—This paper reports on the results of experimental investigations into the threshold power of the onset of nonlinearity of magnetoacoustic vibrations in planar structures (such as a ferrite film–dielectric substrate structure) in the range of phase matching of the higher bulk magnetostatic and acoustic modes. Under the experimental conditions, the wavelength of the higher bulk magnetostatic modes is of the order of 1 μm and shorter. On this basis, the energy of these vibrations with respect to the origin of the magnetostatic wave spectrum is determined by the energy of the inhomogeneous exchange interaction. The standing magnetoacoustic waves are examined in conventional yttrium iron garnet films with free surface spins in which, under standard conditions, only dipole magnetostatic vibrations are excited in planar resonators. Consideration is given to the threshold power of the onset of precession instability of the dipole exchange acoustic modes which, as was shown earlier by the authors, are excited in the range of the phase matching of the exchange and acoustic modes. A comparative analysis is performed for the threshold powers of dipole magnetostatic, exchange acoustic, and dipole exchange acoustic modes. It is demonstrated that the threshold power of the instability of magnetostatic modes decreases significantly when the natural frequencies of the dipole modes coincide with those of the exchange acoustic modes.

1. INTRODUCTION

Longitudinal and transverse excitations of spin waves were examined in the first works concerned with the effect of magnetoacoustic interactions on nonlinear processes in bulk crystals [1, 2]. In particular, Turner [1] revealed that the threshold power of longitudinal excitation increases in the range of phase matching of the secondary spin and elastic waves. This effect was attributed to the increase in the relaxation parameter of the secondary spin waves [1]. In film samples, the magnetoelastic interaction gives rise to a large variety of effects due to the multimode behavior of the magnetoacoustic excitation spectrum. For example, Zil’berman *et al.* [3] experimentally investigated the longitudinal excitation of spin waves with the use of a microstrip transducer and observed the reactive effect of an elastic system on the threshold of spin wave excitation. The coupling between acoustic and spin waves led to a change in the dispersion curves, a decrease in the group velocity at certain frequencies, and an increase in the residence time of spin waves in the excitation range, which resulted in a decrease in the threshold excitation power of the spin waves.

It should be noted that ferrite films are convenient objects for analyzing dipole magnetostatic waves which most frequently serve as a source of excitation in nonlinear processes. The first and second ranges of the parametric excitation of spin waves correspond to the ranges of three-magnon decay and four-magnon scattering of the dipole magnetostatic waves, respectively. The thresholds of the parametric excitation of spin waves coincide with the threshold powers of the magnetostatic wave instability toward three-wave decay or four-wave scattering processes. In planar structures, the coupling of acoustic modes with long-wavelength dipole magnetostatic modes makes it possible to observe the effect of the magnetoelastic interaction not only with the participation of exchange magnetostatic waves but also in the case when the primary magnetostatic wave or wave products of its decay (dipole magnetostatic waves) are coupled with the elastic system. In particular, Zil’berman *et al.* [4] observed a decrease in the threshold of the parametric instability of the dipole magnetostatic mode in the range of the phase matching with a Lamb mode in the film plane. The observed decrease in the instability threshold was explained by the distortion of the dispersion curve, which, in turn, could lead to decay of the dipole magnetostatic mode into secondary magnetostatic modes collinear with respect to the primary magnetostatic mode. It is worth noting that the magnetoelastic coupling of exchange spin waves in the case of their phase matching with acoustic waves is considerably stronger than the magnetoelastic coupling of dipole magnetostatic waves. In this respect, the purpose of the present work was to investigate magnetoelastic effects with the participation of exchange magnetostatic modes.

2. SAMPLES AND EXPERIMENTAL TECHNIQUE

The experiments were carried out with planar structures, namely, yttrium iron garnet films on a gadolinium gallium garnet substrate. The film thickness ranged from 2 to 10 μm. The total thickness of the planar structure was approximately equal to 450 μm. The measurements were performed in the standing-wave mode, i.e., with the use of ferromagnetic resonance. Samples were prepared in the form of disks or squares. The localization of magnetostatic vibrations in the film plane was achieved using an inhomogeneous magnetic field with a "magnetic well" profile. Yttrium iron garnet films with free surface spins were grown according to the standard epitaxial technique. The absence of surface-spin pinning was checked against the spectrum of excited vibrations. In the presence of surface-spin pinning, the exchange excitations should manifest themselves in the spectra of the studied films [5].

In the absence of magnetoelastic effects, the yttrium iron garnet films under investigation exhibited typical dipole spectra of magnetostatic vibrations. The excited vibrations differed from one another in the distribution of ac magnetization over the film plane. In the case of circular-disk resonators or magnetostatic vibrations localized by the cylindrical-magnetic-well method, the spectrum represented as a function of the magnetic field contained a set of nearly equidistant vibrations. In the experiment, the separation between these vibrations in the magnetic field was equal to 8–15 Oe and was determined from the expression $\pi Md(\pi/D)$, where M is the saturation magnetization of the ferrite film, d is the thickness of the ferrite film, and D is the diameter of the localization region of vibrations in the film plane. When the spectrum was represented as a function of the magnetic field, a change in the excitation frequency led to a gradual shift in the spectrum as a whole. For films with free surface spins, the distribution of ac magnetization over the film thickness for higher bulk modes is symmetric with respect to the midplane of the film and the integral of overlap of the ac magnetization distribution with an external exciting electromagnetic field or with a field of dipole magnetostatic modes is equal to zero. As a consequence, these modes were not excited in the absence of the magnetoelastic interaction. The acoustic resonances were eliminated from the spectrum through the destruction of an acoustic resonator formed by the opposite surfaces of the planar structure, for example, through mechanical rough grinding of one surface of the structure.

3. RESULTS AND DISCUSSION

In our recent work [6], we demonstrated that the magnetoacoustic excitation spectrum is strongly distorted in the range of the phase matching of the higher bulk magnetostatic and acoustic modes. The ac magnetization distribution of normal magnetoacoustic modes over the film thickness becomes asymmetric due to

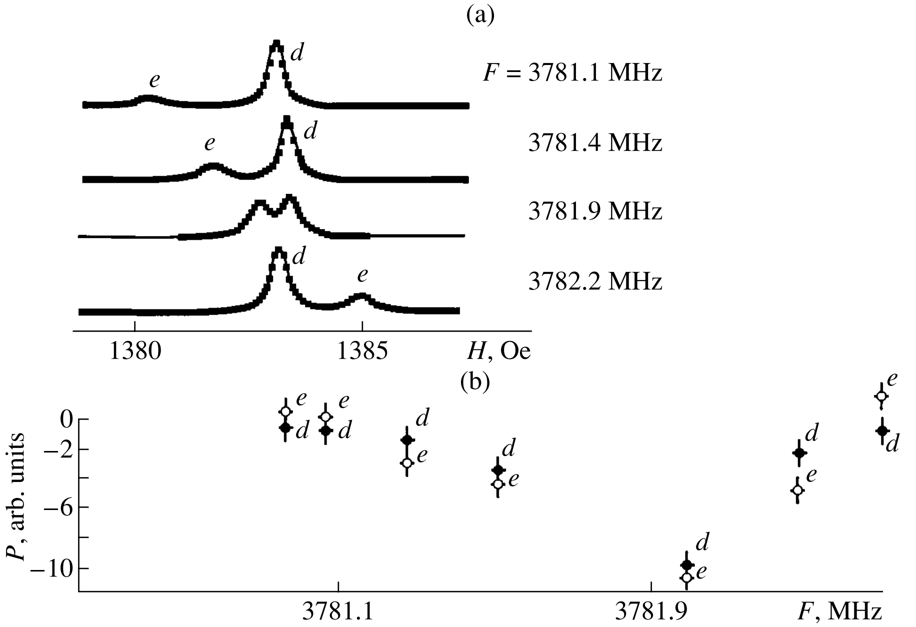

Fig. 1. (a) Spectra of magnetoacoustic vibrations in a circular-disk resonator in the range of magnetic fields corresponding to the phase matching of the higher bulk and transverse acoustic modes at chosen excitation frequencies. The localization length of vibrations is approximately equal to 400 μm. The thickness of the yttrium iron garnet film is about 6 μm. (b) Frequency dependence of the threshold power of the external exciting electromagnetic field at which the vibrations shown in panel (a) become unstable. Designations: d = high-intensity vibration with a dominant dipole energy and e = exchange acoustic vibration.

strong magnetoelastic coupling. As a result, dipole exchange acoustic vibrations with comparable ratios of the dipole, exchange, and acoustic energies are excited in the ranges of frequencies and magnetic fields which correspond to the phase matching of the spin and acoustic waves. In the present work, we investigated the nonlinearity threshold of these vibrations. Analysis was performed in the initial portion of the spectrum in which three-magnon decays were forbidden according to the law of conservation of energy.

Figure 1a displays the experimental vibrational spectra represented as a function of the magnetic field in the range of the magnetoelastic matching of the exchange spin and transverse acoustic waves at four frequencies. The high-intensity vibration corresponds to the second radial lowest bulk dipole mode. In the absence of the magnetoelastic interaction, only this vibration is excited in the given range of magnetic fields. The vibration with a lower intensity is attributed to the exchange acoustic mode. In the spectrum, the location of the exchange acoustic vibration changes at regular intervals with variations in the frequency. For both vibrations (hereafter, they will be referred to as the dipole vibration and the exchange acoustic vibration, respectively), the energies involve all three main components, namely, the dipole, exchange, and acoustic energies. At a frequency of 3781.9 MHz, when the excitation conditions for the dipole and exchange acoustic vibrations coincide, there occurs excitation of two dipole exchange acoustic vibrations.

The threshold powers of the onset of nonlinear processes associated with the vibrations under investigation are presented in Fig. 1b. The threshold power of the onset of nonlinearity was determined by three methods. In the first case, the threshold power P_S (shown in the figures) was taken to be equal to the microwave generator power at which the magnetic susceptibility (determined as the ratio of the absorbed power to the microwave generator power) began to decrease. In the second case, the threshold power P_f was taken as the microwave generator power at which the spectrum of the echo signal exhibited satellites whose frequencies differed from the excitation frequency by approximately 10 MHz. In the third case, the threshold power P_i was taken as the power at which the echo pulsed signal was split. The threshold powers P_f and P_i almost coincide (to within 1 dB), whereas the power P_S is approximately 3 dB less than the powers P_f and P_f. It is clearly seen from the figure that, despite the lower intensity, the exchange acoustic vibration in the vicinity of the dipole vibration possesses a smaller nonlinearity threshold as compared to that of the dipole vibration. The smaller nonlinearity threshold can be explained by the fact that the decay of the exchange acoustic waves is enhanced through the violation of the dispersion law due to magnetoelastic coupling. The distortion of the dispersion curves in the range of the phase matching of the exchange spin and acoustic waves favors the decay into normal modes of the magnetic film resonator. As a result, this leads to a decrease in the effective relaxation parameter of the secondary waves and, hence, to a decrease in the nonlinearity threshold which is proportional to the relaxation parameter. A similar effect was observed by Zil'berman *et al.* [4], who proved that the collinearity in the propagation of the secondary waves and the primary wave brings about a decrease in the secondary-wave energy in the excitation range, which, in turn, leads to a decrease in the effective relaxation parameter of the secondary waves and in the nonlinearity threshold of the primary waves. The minimum nonlinearity threshold was observed at a maximum hybridization of the dipole magnetostatic mode with the exchange acoustic mode in the case of highly efficient excitation of the primary magnetostatic wave when the conditions for decay into secondary waves were readily attained upon distortion of the dispersion curves.

In the preceding case, the interaction between the dipole fields of the dipole magnetostatic and exchange acoustic vibrations is so strong that it leads to a characteristic divergence of the vibrational modes. For the spectra shown in Fig. 2, the relaxation parameters of vibrations and the efficiency of their interaction correspond to the situation when no divergence of the vibrational modes occurs and the location of the modes smoothly varies as if one mode passes through another mode. However, as in the case presented in Fig. 1, the nonlinearity threshold of the dipole exchange acoustic vibration decreases.

Earlier [6], we revealed that both the exchange acoustic and dipole exchange acoustic modes can be excited well away from the range of the phase matching of the exchange spin and acoustic waves. As a consequence, the distortion of the dispersion curves also occurs well away from the point at which the wave numbers of the exchange spin and acoustic modes coincide exactly, even though, in this case, the observed spectral distortions are less pronounced. Let us elucidate how the magnetoelastic interaction affects nonlinear processes. The experimental magnetostatic wave spectra represented as a function of the magnetic field are depicted in Fig. 3. According to our calculation, the range of the phase matching of the exchange spin and acoustic waves is located at a distance of approximately 20 Oe from the origin of the magnetostatic wave spectrum. This calculation is confirmed experimentally: the most efficient excitation of exchange acoustic vibrations is observed in this spectral range. However, these vibrations are excited at a distance of approximately 50 Oe from the magnetic field which corresponds to the matching of the spin wave resonances and acoustic modes. For the situation illustrated in Fig. 3, we analyzed the experimental frequency dependences of the nonlinearity threshold powers of the radial dipole vibrations (6,1,0), (5,1,0), and (4,1,0). In the spectral range under investigation, the excitation of the exchange acoustic modes is very weak and the resonance curve of the dipole magnetostatic vibrations

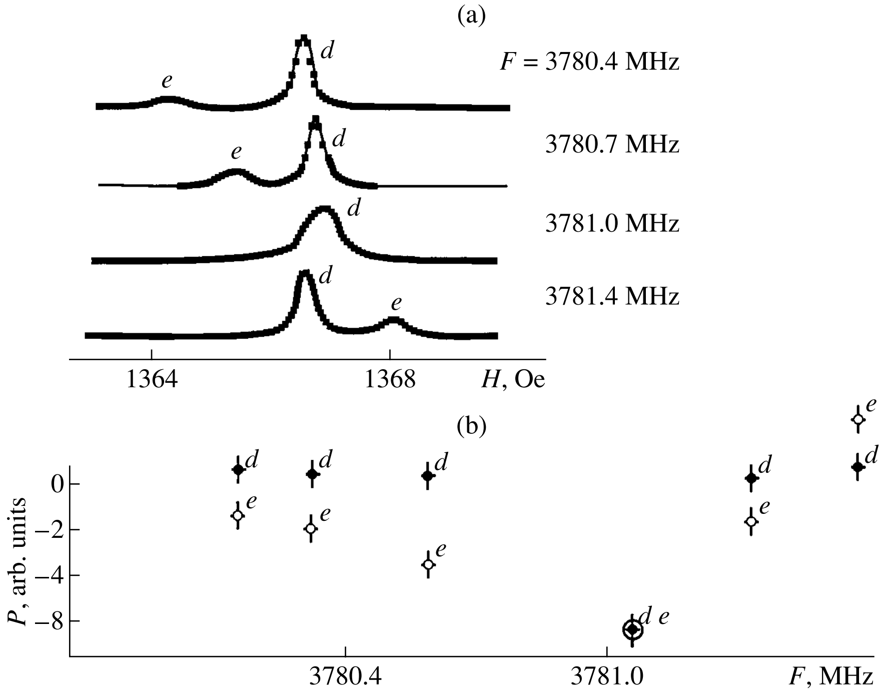

Fig. 2. (a) Spectra of magnetoacoustic vibrations in a circular-disk resonator in the range of magnetic fields corresponding to the phase matching of the higher bulk and transverse acoustic modes at chosen excitation frequencies. The localization length of vibrations is approximately equal to 600 μm. The structure parameters are the same as in Fig. 1. The dipole coupling of vibrations is slightly weaker and their divergence does not exceed the width of the resonance curve as compared to those in Fig. 1. (b) Frequency dependence of the threshold power of the external exciting electromagnetic field at which the vibrations shown in panel a become unstable.

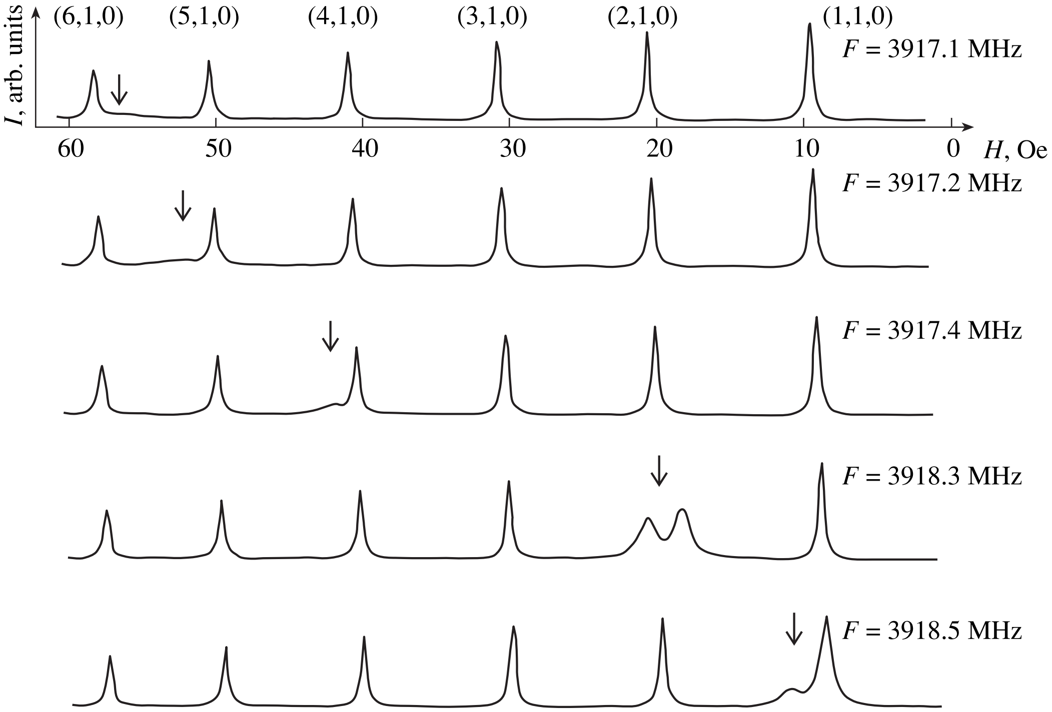

Fig. 3. Spectra of magnetoacoustic vibrations in a circular-disk resonator at different excitation frequencies. The localization length of vibrations is approximately equal to 600 μm. The structure parameters are the same as in Fig. 1. Arrows indicate the excitation of exchange acoustic vibrations.

remains almost unchanged when the resonance magnetic field of the exchange acoustic vibration coincides with the resonance field of one of the aforementioned dipole vibrations. However, it is experimentally found that, when the resonance fields of these vibrations coincide, the nonlinearity threshold decreases by 5–7 dB. Therefore, even a very weak excitation of exchange acoustic vibrations enhances decay processes, which is accompanied by a decrease in the nonlinearity threshold of the dipole modes. As a result, under the condition when the resonance field of these vibrations coincides with the resonance field of the dipole magnetostatic vibration, the resonance curve of the latter vibration remains virtually undistorted; however, the nonlinearity threshold of the dipole magnetostatic vibration decreases by approximately 6 dB.

4. CONCLUSION

Thus, it has been demonstrated that, when the excitation conditions for the dipole magnetostatic and exchange acoustic modes coincide, the nonlinearity threshold of the dipole exchange acoustic vibrations excited in the range of the phase matching of the exchange spin and acoustic waves can decrease by 10–14 dB compared to the nonlinearity threshold of the dipole magnetostatic vibrations, even though the former vibrations are characterized by a lower efficiency of excitation. The observed decrease in the nonlinearity threshold can be explained by the distortion of the dispersion curves for the secondary modes due to their coupling with the acoustic modes. This favors the conservation of energy and momentum in the course of four-magnon scattering attended by excitation of the normal modes of the planar structure. In the case when the excitation conditions for the dipole magnetostatic mode and one of the exchange acoustic modes coincide, the nonlinearity threshold of the dipole magnetostatic vibration decreases well away from the range of the phase matching of the exchange spin and acoustic waves, even though noticeable distortions of the vibrational spectrum are virtually absent. In turn, despite the substantially smaller amplitude of the exchange acoustic magnetostatic vibrations, their nonlinearity threshold can be 5–7 dB less than the nonlinearity threshold of the dipole magnetostatic vibrations.

REFERENCES

1. E. H. Turner, Phys. Rev. Lett. **5** (3), 100 (1960).
2. F. A. Olsen, J. Appl. Phys. **34** (2), 1281 (1963).
3. P. E. Zil'berman, N. S. Golubev, A. G. Temiryazev, and V. M. Dyatlov, Pis'ma Zh. Tekh. Fiz. **14** (7), 585 (1988) [Sov. Tech. Phys. Lett. **14**, 261 (1988)].
4. P. E. Zil'berman, G. T. Kazakov, and V. V. Tikhonov, Pis'ma Zh. Tekh. Fiz. **11** (13), 769 (1985) [Sov. Tech. Phys. Lett. **11**, 319 (1985)].
5. P. E. Zil'berman, V. I. Kozlov, and A. V. Pomyalov, Fiz. Tverd. Tela (Leningrad) **28** (2), 352 (1986) [Sov. Phys. Solid State **28**, 195 (1986)].
6. A. S. Bugaev and V. B. Gorsky, Radiotekh. Élektron. (Moscow) **44** (3), 330 (1999).

Translated by O. Borovik-Romanova

Physics of the Solid State, Vol. 44, No. 7, 2002, pp. 1350–1354. Translated from Fizika Tverdogo Tela, Vol. 44, No. 7, 2002, pp. 1290–1294.
Original Russian Text Copyright © 2002 by Volkov, Petrakovskiĭ, Vasil'ev, Sablina.

MAGNETISM AND FERROELECTRICITY

Two-Phase Paramagnetic–Ferromagnetic State of $La_{0.7}Pb_{0.3}MnO_3$ Single-Crystal Lanthanum Manganite

N. V. Volkov, G. A. Petrakovskiĭ, V. N. Vasil'ev, and K. A. Sablina
Kirensky Institute of Physics, Siberian Division, Russian Academy of Sciences,
Akademgorodok, Krasnoyarsk, 660036 Russia
e-mail: volk@iph.krasn.ru

Received June 26, 2001; in final form, November 13, 2001

Abstract—Two phases, paramagnetic and ferromagnetic, were shown by the magnetic resonance method to coexist below the temperature T_C in $La_{0.7}Pb_{0.3}MnO_3$ single crystals exhibiting colossal magnetoresistance. The magnetic resonance spectra were studied in the frequency range 10–78 GHz. The specific features in the behavior of the spectral parameters were observed to be the strongest at the temperatures corresponding to the maximum magnetoresistance in the crystals. The concentration ratios of the paramagnetic and ferromagnetic phases in the samples were found to be sensitive to variations in temperature and external magnetic field. This behavior suggests realization of the electronic phase separation mechanism in the system under study. *© 2002 MAIK “Nauka/Interperiodica”.*

1. INTRODUCTION

The interest of researchers in impurity-containing perovskite manganites stems primarily from the phenomenon of colossal magnetoresistance (CMR). The CMR phenomenon has application potential. At the same time, numerous experimental studies have revealed structural, magnetic, and electronic properties in manganites which are no less exciting from the physical standpoint. It was found that the materials of this family have a very rich phase diagram [1, 2] which includes regions of the antiferromagnetic, ferromagnetic nonconducting, and ferromagnetic metallic states, as well as regions with orbital and charge ordering. In many cases, these phases are microscopically inhomogeneous. This inhomogeneity has been proved experimentally by scanning tunneling microscopy [3], electron diffraction [4], neutron scattering [5], NMR [6], optical methods [7], etc. We note that the inhomogeneous state manifests itself the strongest in the concentration and temperature ranges where the CMR effect is observed. In addition to the experimental confirmation of the coexistence of phases in materials of this class, considerable progress has been reached in theoretical substantiation of the tendency to phase separation [8]. There is, however, still a long way to go for the pattern of these phenomena to be completely understood; this would require extending the search for materials with phase separation and for experimental methods of their investigation.

Because any of the phase separation scenarios presently discussed [8] assumes the coexisting phases to reside in different magnetic states, magnetic resonance could prove to be of use. It is known that even an insignificant inhomogeneity in magnetic materials noticeably affects the magnetic absorption spectra. While magnetic resonance spectra of manganites have been studied by various groups of authors [9–11], interest was mainly focused therein on the paramagnetic (PM) state. As for the results covering the temperature range near the magnetic phase transition, they exhibit a considerable scatter and are often interpreted from different standpoints.

Our studies of $La_{0.7}Pb_{0.3}MnO_3$ crystals exhibiting the CMR phenomenon revealed an effect of dc and ac transport current on conductivity in the microwave frequency range [12, 13]. The character of the response of this system to an electric current suggests that the mechanisms of the CMR and of the electric-current effect have the same nature and can be qualitatively interpretted in terms of the phase separation model. The existence of the two-phase paramagnetic–ferromagnetic state in single-crystal $La_{0.7}Pb_{0.3}MnO_3$ received supportive evidence from studies of magnetic resonance spectra [14].

We present here the data obtained in an experimental investigation of magnetic resonance in $La_{0.7}Pb_{0.3}MnO_3$ crystals exhibiting CMR.

2. EXPERIMENTAL

All experimental studies were performed on single-crystal $La_{1-x}Pb_xMnO_3$ samples grown by spontaneous crystallization from a solution in melt. A characteristic feature of the technology employed was that PbO and PbF_2 were used as the solvent while simultaneously providing the required amount of Pb in the crystals. The composition of the batch consisting of La_2O_3, MnO_2, and the solvent was chosen so as to obtain a Pb concentration of $x \sim 0.3$. The crystals were grown in a platinum crucible. The technological regime chosen permitted one to grow crystals with an average size of $5 \times 5 \times 5$ mm. X-ray diffraction analysis of the single crystals obtained confirmed that the structure and the lattice parameters correspond to $x \sim 0.3$. The samples prepared for the study were plates measuring $4 \times 2 \times 0.1$ mm whose face coincided with one of the principal symmetry planes of the crystal and whose plate surfaces were polished. The external magnetic field was always applied along the sample plane. The electrical resistivity ρ and the magnetoresistance $\Delta\rho/\rho_0 = (\rho(0) - \rho(H)/\rho(0)) \times 100\%$ of the samples were measured by the standard four-probe method. The magnetic resonance spectra were measured with a 10-GHz spectrometer operating in the traditional arrangement with rf modulation of the magnetic field and with a spectrometer with frequency ν tunable within the range 24–80 GHz and with a pulsed magnetic field.

3. RESULTS AND DISCUSSION

The $La_{0.7}Pb_{0.3}MnO_3$ single crystals grown by us had a ferromagnetic (FM) phase transition temperature $T_C \cong 360$ K. The maximum magnetoresistance in a magnetic field $H = 10$ kOe was 20% at $T \sim 330$ K (Fig. 1a).

The main feature in the magnetic resonance spectra of the crystals under study is the presence of two well-resolved absorption lines within a broad temperature interval below the Curie point T_C. The temperature behavior of the absorption line parameters for the frequency $\nu = 10$ GHz is shown in Figs. 1b and 1c. We believe that the line denoted by F is due to resonance from the crystal regions in the FM state. The F line appears only below the temperature T_C. The decrease in the resonance field H_r with decreasing temperature is associated with anisotropic interactions, namely, with increasing magnetic crystallographic anisotropy and shape anisotropy. As the temperature drops below T_C, line P observed in the PM state of the sample ($T > T_C$) changes its position only insignificantly and its resonance field H_r does not depend on the sample shape and the orientation of the external magnetic field in the crystal. The slight increase in H_r in the temperature range 340–350 K may be associated with a change in the g factor caused by local lattice distortions. Such distortions initiated by strong electron–phonon coupling were observed to exist in a number of impurity-containing perovskite manganites near the transition to the FM state [1]. Figure 2 shows spectra recorded at different microwave-radiation frequencies at $T = 320$ K.

That the P and F lines are due to resonance absorption in the PM and FM regions, respectively, is convincingly argued for by the behavior of their frequency vs. field relations (inset to Fig. 2). Studies performed on spherical samples reveal a comparatively low magnetic crystallographic anisotropy (the effective anisotropy field does not exceed 100 Oe even at $T = 80$ K); therefore, the frequency vs. field dependences for the absorption lines of ferromagnetic resonance should be determined primarily by shape anisotropy. For the geometry of our experiment (with the external magnetic field parallel to the sample plane), one can write

$$\frac{\omega}{\gamma} = [H_r(H_r + 4\pi M_{\text{eff}})]^{1/2}, \tag{1}$$

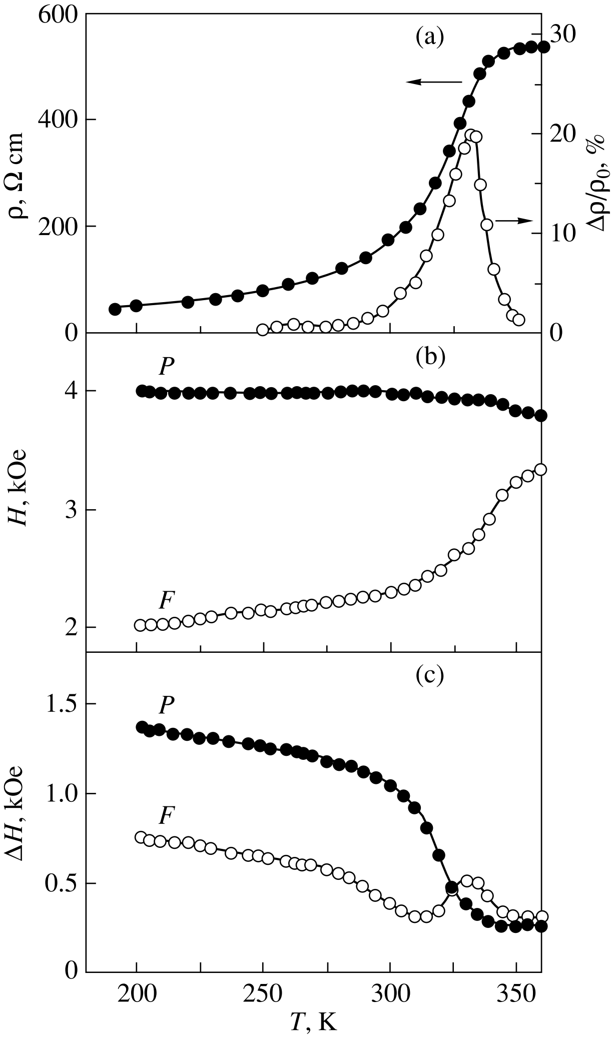

Fig. 1. Temperature dependences (a) of the electrical resistivity ρ and magnetoresistance $\Delta\rho/\rho_0$ in a magnetic field $H = 10$ kOe and of (b) the resonance field and (c) linewidth of the ferromagnetic (F) and paramagnetic (P) absorption lines in the magnetic resonance spectrum ($\nu = 10$ GHz).

where $\omega = 2\pi\nu$ is the circular frequency, $\gamma = (g\mu_B/\hbar)$ is the gyromagnetic ratio, and M_{eff} is the effective magnetization, which, in the general case, is different from the true value M_0 because of the crystallographic anisotropy and possible magnetic inhomogeneity of the crystal. For the PM regions, we have a simple relation,

$$\frac{\omega}{\gamma} = H_r. \tag{2}$$

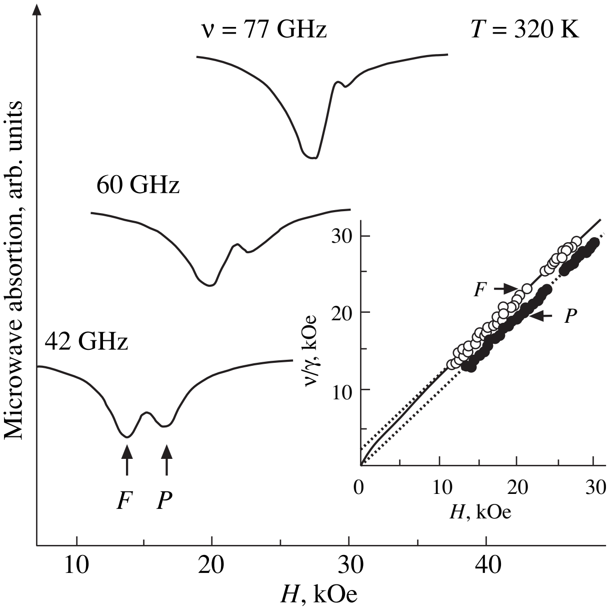

Fig. 2. Magnetic resonance absorption spectra recorded at different microwave frequencies ν at $T = 320$ K. Inset: frequency vs. field plots of the two lines observed in the magnetic resonance spectrum at $T = 320$ K; the solid line is a plot of Eq. (1), and dotted lines are linear extrapolations of the relations.

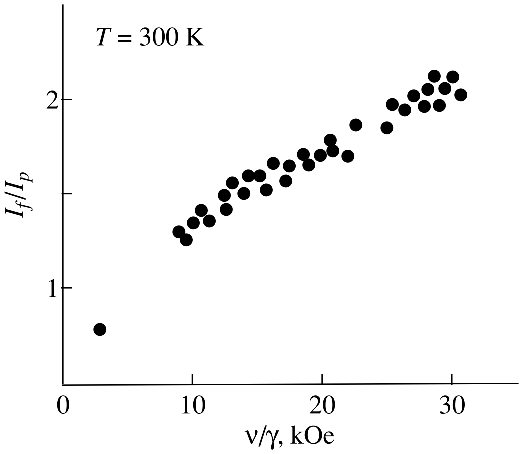

Fig. 3. Ferromagnetic-to-paramagnetic absorption line intensity ratio I_f/I_p in the magnetic resonance spectrum plotted vs. microwave radiation frequency; $T = 300$ K.

Indeed, the frequency vs. field relations for the two observed absorption lines in the spectrum are in full agreement with Eqs. (1) and (2) (inset to Fig. 2). Because the intrinsic magnetic crystallographic anisotropy is small, we succeeded in moving the FM and PM absorption line resonance fields apart by properly choosing the sample shape and geometry of the experiment, thus permitting reliable separate measurement of the lines to be made. The temperature behavior $4\pi M_{\text{eff}}(T)$ derived from the temperature dependences of the resonance field $H_r(T)$ of the ferromagnetic resonance line with due account of Eq. (1) is almost identical to that of the magnetization $4\pi M_0(T)$ found from static measurements.

In addition to the proof of the existence of a two-phase paramagnetic–ferromagnetic state, this study produced another important result; namely, we demonstrated the possibility of controlling the phase volume ratio in a sample by means of an external magnetic field. This is illustrated by Fig. 2, which shows that an increase in the microwave radiation frequency ν and, hence, in the magnitude of the external magnetic field H brings about an increase in the intensity of the FM absorption line and a decrease in that of the PM line. Figure 3 plots the FM-to-PM line intensity ratio I_f/I_p as a function of the microwave radiation frequency at which the magnetic resonance spectra were measured. This situation can be considered to be a control of the phase volume ratio through proper variation of the external magnetic field. An increase in H gives rise to an increase in the FM phase volume and a decrease in the PM phase volume in a sample. One should note, however, that other factors, for instance, variation of the magnetization M_0, can also contribute to the intensity of the ferromagnetic resonance absorption line. However, the frequency vs. field dependence for the FM line is fitted well by Eq. (1) with a constant value $4\pi M_{\text{eff}} \approx 2$ kOe (see inset to Fig. 2); hence, the FM regions were magnetized to saturation in the magnetic fields for which the measurements were carried out. We also analyzed the temperature behavior of the FM and PM absorption line parameters recorded at different microwave radiation frequencies. We focused our attention on the temperature dependence of the resonance line intensities. The intensity was calculated as the area under the absorption curve. Because of a partial overlap of the spectral lines, we assumed the absorption lines to have a Lorentzian shape. Figure 4 shows temperature dependences of the FM-to-PM line intensity ratio obtained when measuring magnetic resonance spectra at 10 and 78 GHz. Note the smooth course of the I_f/I_p temperature dependence, except the region of $T \sim 310$–350 K, where peak-shaped features are observed. The higher the frequency at which the spectra are measured, the stronger these features are. Interestingly, the peak in the I_f/I_p temperature dependences lies in the temperature region where the magnetoresistance $\Delta\rho/\rho_0$ is the largest (Fig. 1a).

The mechanisms responsible for the formation of the heterogeneous state and the role played by this state in the CMR phenomenon are fundamental problems in the study of inhomogeneous states in manganites. It is believed that the complexity of the (x, H, T) phase diagram of these materials results from the spin, charge, and orbital subsystems being strongly coupled. At some specific doping levels, the subsystem interaction energies responsible for the formation of these phases become comparable and the inhomogeneous state with phase separation can be the ground state. The variants that are mainly discussed in the literature are as follows.

(i) Phase separation into regions with different electron densities. The inhomogeneities typically measure a few nanometers in this case, i.e., a few lattice constants [15, 16].

(ii) An alternative mechanism involves phase separation into regions with equal electron concentrations, i.e., into antiferromagnetic (or PM) regions with localized electrons and FM regions with itinerant carriers [17]. It is assumed that this phase separation can be caused by a random distribution of impurity ions in the crystal lattice, which produces a random change in the magnitude of the exchange integral. This makes the ordered (homogeneous) state unstable in the vicinity of the phase transition to the FM state. The clusters forming in this case can reach micron size. In the case of an inhomogeneous impurity distribution, this scenario does not reduce to a trivial chemical separation of a sample into phases having, for instance, different Curie temperatures T_C. At the same time, this variant cannot be disregarded in the more general context of phase separation in manganites.

The magnetic resonance method used by us here to study inhomogeneities in $La_{0.7}Pb_{0.3}MnO_3$ samples is of an integral character, and, therefore, the problem of the size of inhomogeneities and of the topology of the inhomogeneous state remains open. It is believed that the first scenario of electronic phase separation operates at low concentrations x, although estimates [15] do not exclude the possibility of this mechanism being also operative at higher concentrations. Nevertheless, phase separation associated with a random impurity-ion distribution appears to be a more realistic process for $x \sim 0.3$ compositions; this can be supported experimentally.

Our experimental data suggest an inference of fundamental significance, namely, that the heterophase state in $La_{0.7}Pb_{0.3}MnO_3$ is sensitive to the strength of an external magnetic field. This is a persuasive argument in support of the electronic phase separation mechanism, because the effect of external magnetic field cannot be expected to be strong in the case of chemical inhomogeneity. Indeed, in the latter case, the sample would actually be a multiphase system with a different T_C for each phase. Obviously enough, in such a sample, the FM and PM phases should coexist in the vicinity of the transition from the PM to the FM phase (which is also observed experimentally in our case), but the T_C point in each region should not depend on the external magnetic field. Another point of interest is that all the features in the magnetic resonance spectra of the two-phase PM–FM system are observed in the region of the peak in the temperature dependence of magnetoresistance. This suggests a relation between the phase separation and the manifestation of the CMR effect in the materials under study. It is known that the CMR finds a straightforward interpretation in terms of the percolation mechanism [8]. At the same time, the origin of the peaks in the temperature dependences of the FM-to-PM absorption-line intensity ratio I_f/I_p in the magnetic resonance spectrum remains unclear. If our suggestions that the main contribution to I_f/I_p is from the magnetization M_0 of the FM phase and from the volume ratio of the FM and PM phases are correct, one could expect the relations to be smooth. It can be conjectured that in the temperature region where the features are observed, the two-phase state has a complex topology. The energies governing the ground state of the crystal are apparently in a delicate balance; this entails, as a consequence, a high sensitivity to variations in temperature and external magnetic field.

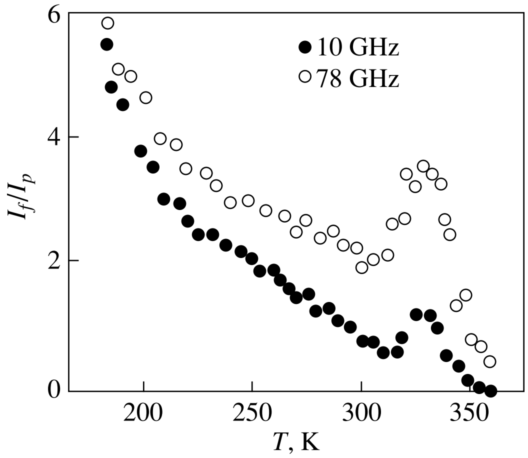

Fig. 4. Ferromagnetic-to-paramagnetic absorption line intensity ratio I_f/I_p in the magnetic resonance spectrum plotted vs. temperature. The relations are presented for the spectra measured at the microwave frequencies ν_1 = 10 GHz and ν_2 = 78 GHz.

4. CONCLUSION

Thus, our experimental study of magnetic resonance spectra in $La_{0.7}Pb_{0.3}MnO_3$ crystals exhibiting CMR revealed the existence of two magnetic phases below T_C. The analysis of the frequency vs. field dependences of absorption spectra permitted their identification as the PM and the FM phase. Studies carried out over a broad frequency range showed the mixed phase state to be sensitive to the magnitude of an external magnetic field. This finding, as well as the specific features in the behavior of the magnetic resonance parameters observed in the CMR region, suggests that the mechanism of electronic phase separation is operative in this system.

REFERENCES

1. A. J. Millis, Nature **392**, 147 (1998).
2. J. P. Renard and A. Ananel, Mater. Sci. Eng. B **B63**, 22 (1999).

3. M. Fath, S. Freisem, A. A. Menovsky, *et al.*, Science **285**, 1540 (1999).
4. M. Uehara, S. Mori, C. H. Chen, and S.-W. Cheong, Nature **399**, 560 (1999).
5. D. Louca, T. Egami, E. L. Brosha, *et al.*, Phys. Rev. B **56**, 8475 (1997).
6. G. Papavassiliou, M. Fardis, M. Belesi, *et al.*, Phys. Rev. Lett. **84**, 761 (2000).
7. N. N. Loshkareva, Yu. P. Sukhorukov, S. V. Naumov, *et al.*, Pis'ma Zh. Éksp. Teor. Fiz. **68**, 89 (1998) [JETP Lett. **68**, 97 (1998)].
8. E. Dagotto, T. Hotta, and A. Moreo, Phys. Rep. **344**, 1 (2001).
9. F. Rivadulla, M. A. Lopez-Quutela, L. E. Hueso, *et al.*, Phys. Rev. B **60**, 11922 (1999).
10. A. Shengelay, Guo-Meng Zhao, H. Ckeller, and K. A. Muller, Phys. Rev. B **61**, 5888 (2000).
11. D. L. Huber, G. Alejandro, A. Caneiro, *et al.*, Phys. Rev. B **60**, 12155 (1999).
12. N. V. Volkov, G. A. Petrakovskiĭ, K. A. Sablina, and S. V. Koval', Fiz. Tverd. Tela (St. Petersburg) **41**, 2007 (1999) [Phys. Solid State **41**, 1842 (1999)].
13. N. V. Volkov, G. A. Petrakovskiĭ, and K. A. Sablina, Fiz. Tverd. Tela (St. Petersburg) **41**, 2187 (1999) [Phys. Solid State **41**, 2008 (1999)].
14. G. A. Petrakovskiĭ, N. V. Volkov, V. N. Vasil'ev, and K. A. Sablina, Pis'ma Zh. Éksp. Teor. Fiz. **71**, 210 (2000) [JETP Lett. **71**, 144 (2000)].
15. L. P. Gor'kov, Usp. Fiz. Nauk **168**, 665 (1998) [Phys. Usp. **41**, 589 (1998)].
16. É. L. Nagaev, Usp. Fiz. Nauk **165**, 529 (1995) [Phys. Usp. **38**, 497 (1995)].
17. A. Moreo, M. Mayr, A. Feiguin, *et al.*, Phys. Rev. Lett. **84**, 5568 (2000).

Translated by G. Skrebtsov

Physics of the Solid State, Vol. 44, No. 7, 2002, pp. 1355–1362. Translated from Fizika Tverdogo Tela, Vol. 44, No. 7, 2002, pp. 1295–1301.
Original Russian Text Copyright © 2002 by Topolov, Turik.

MAGNETISM AND FERROELECTRICITY

An Intermediate Monoclinic Phase and Electromechanical Interactions in $x\mathrm{PbTiO_3}$–$(1 - x)\mathrm{Pb(Zn_{1/3}Nb_{2/3})O_3}$ Crystals

V. Yu. Topolov and A. V. Turik

Rostov State University, ul. Zorge 5, Rostov-on-Don, 344090 Russia
e-mail: topolov@phys.rnd.runnet.ru

Received October 1, 2001

Abstract—The elastic matching of phases in the vicinity of the morphotropic phase boundary in $x\mathrm{PbTiO_3}$–$(1 - x)\mathrm{Pb(Zn_{1/3}Nb_{2/3})O_3}$ crystals is investigated in an external electric field with strength $\mathbf{E} \parallel [001]$. The field dependences of the unit cell parameters of the monoclinic phase are determined experimentally in the range $0 \le E \le 2$ MV/m. The results obtained are used in analyzing specific features in the electromechanical properties of $x\mathrm{PbTiO_3}$–$(1 - x)\mathrm{Pb(Zn_{1/3}Nb_{2/3})O_3}$ crystals ($0.08 \lesssim x \lesssim 0.09$), in which the monoclinic phase is intermediate between the rhombohedral and tetragonal phases and can coexist with these phases. A correlation between the optimum volume concentrations of domains or twins in different two-phases states is revealed and interpreted for the first time. *© 2002 MAIK “Nauka/Interperiodica”.*

1. INTRODUCTION

Ferroelectrics and related materials containing intermediate phases have been extensively investigated over the last decade. It is found that the intermediate ferroelectric phase 3*m*, which is revealed in $\mathrm{PbZrO_3}$ crystals [1, 2] and in $\mathrm{(Pb_{1-x}Sr_x)ZrO_3}$ solid solutions [3], is thermodynamically stable in a narrow range of temperatures T at a molar concentration $x \longrightarrow 0$ and coexists with one of the adjacent phases, namely, the paraelectric phase *m*3*m* or the antiferroelectric phase *mmm*. The intermediate ferroelastic phase 2/*m* can be induced under hydrostatic compression or upon thermocycling [4] in KCN crystals that undergo the *m*3*m*–*mmm* first-order phase transition. In $\mathrm{Cr_3B_7O_{13}Cl}$, the phase $\bar{4}2m$—the sole antiferroelectric phase in crystals with a boracite-type structure [5]—is induced in an electric field or under mechanical stresses in the $\bar{4}2m$–*mm*2 two-phase state. Owing to their unique piezoelectric and dielectric properties and the intermediate phases revealed recently in the vicinity of the morphotropic boundary, considerable attention has been focused on ferroelectric solid solutions with a perovskite-type structure, such as $\mathrm{Pb(Zr_{1-x}Ti_x)O_3}$ (PZT) [6–13], $x\mathrm{PbTiO_3}$–$(1 - x)\mathrm{Pb(Zn_{1/3}Nb_{2/3})O_3}$ (PT–PZN) [7, 8, 14–19], and $x\mathrm{PbTiO_3}$–$(1 - x)\mathrm{Pb(Mg_{1/3}Nb_{2/3})O_3}$ [20, 21]. It is experimentally found that these solid solutions contain intermediate monoclinic ferroelectric phases [10, 11, 17, 20, 21] which can coexist with one of the ferroelectric (tetragonal 4*mm* or rhombohedral 3*m*) phases in certain ranges of temperatures T and molar concentrations x (for example, the 3*m*–*m* and 4*mm*–*m* two-phase states in $\mathrm{Pb(Zr_{1-x}Ti_x)O_3}$ ceramics [12]) or electric field strengths E (in PT–PZN crystals [17, 18]).

In our previous work [13], we theoretically investigated the specific features in the elastic matching of phases in $\mathrm{Pb(Zr_{1-x}Ti_x)O_3}$ solid solutions and established a correlation between the phase boundaries in the refined x–T diagram [12] and the interfaces in crystalline grains. It was demonstrated that the 3*m*–4*mm*, 3*m*–*m*, and 4*mm*–*m* interfaces are oriented along the zero mean strain planes (ZMSP); as a result, the elastic and electrostriction energies of the interacting phases decrease to zero. The zero mean strain line calculated in [13] for the coexisting phases 4*mm* and *m* is nearly parallel to the experimental 4*mm*–*m* phase boundary in the x–T diagram [12]. This manifestation of the elastic interaction between the phases in the $\mathrm{Pb(Zr_{1-x}Ti_x)O_3}$ solid solutions and the experimental data obtained in [17, 18] for PT–PZN crystals stimulated our investigation into the specific features in the heterophase states of these crystals in the vicinity of the morphotropic boundary in an external electric field $\mathbf{E}$. The aim of the present work was to elucidate how the intermediate monoclinic phase affects the elastic matching of the phases and the electromechanical interactions in PT–PZN crystals in the concentration range $0.08 \lesssim x \lesssim 0.09$.

2. POLYDOMAIN (TWINNED) PHASES AND THEIR ELASTIC MATCHING

It is assumed that a mechanically free crystal of PT–PZN undergoes a first-order phase transition in certain ranges of molar concentrations x and electric field strengths E. The axes OX_j of a Cartesian coordinate system $(X_1X_2X_3)$ are oriented parallel to the crystallographic axes of a perovskite cell in the paraelectric phase *Pm*3*m*. In the chosen coordinate system, the orientations of domains (components of the mechanical twins) are specified by the basis vectors ($\mathbf{a}_i$, $\mathbf{b}_i$, $\mathbf{c}_i$) of the unit cells. Four types of 71° (109°) domains in the rhombohedral phase are described by the basis vectors of the unit cells ($\mathbf{a}_{ri}$, $\mathbf{b}_{ri}$, $\mathbf{c}_{ri}$) and the volume concentrations n_{ri} ($i = 1$–4). The basis vectors ($\mathbf{a}_{ri}$, $\mathbf{b}_{ri}$, $\mathbf{c}_{ri}$) are oriented (with due regard for the angles of shear ω_r [12, 22] of the perovskite cell) along the following directions [23]: ([100], [010], [001]) for $i = 1$, ([$\bar{1}00$], [010], [$00\bar{1}$]) for $i = 2$, ([$0\bar{1}0$], [$\bar{1}00$], [$00\bar{1}$]) for $i = 3$, and ([010], [$\bar{1}00$], [$00\bar{1}$]) for $i = 4$. The volume concentrations n_{ri} are expressed in terms of the parameters $0 \le u_r \le 1$ and $0 \le g_r \le 1$ as follows: $n_{r1} = (1 - u_r)(1 - g_r)$, $n_{r2} = (1 - u_r)g_r$, $n_{r3} = u_r(1 - g_r)$, and $n_{r4} = u_r g_r$. The tetragonal phase contains 90° domains of two types. For these domains, the basis vectors ($\mathbf{a}_{tj}$, $\mathbf{b}_{tj}$, $\mathbf{c}_{tj}$) are oriented along the directions ([100], [010], [001]) ($j = 1$) and ([010], [001], [100]) ($j = 2$) and the volume concentrations are equal to n_t and $1 - n_t$, respectively. The monoclinic phase is assumed to be separated into domains of four types [17] with the basis vectors ($\mathbf{a}_{mk}$, $\mathbf{b}_{mk}$, $\mathbf{c}_{mk}$) (Fig. 1) and the volume concentrations n_{mk}, where $\mathbf{c}_{mk} \parallel [001]$ and $k = 1$–4. The volume concentrations $n_{m1} = f_m\nu_m$, $n_{m2} = (1 - f_m)\nu_m$, $n_{m3} = f_m(1 - \nu_m)$, and $n_{m4} = (1 - f_m)(1 - \nu_m)$ are expressed through the parameters (the volume concentrations of the mechanical twins) f_m and ν_m varying in the interval [0, 1].

The distortion matrices of the rhombohedral, tetragonal [13], and monoclinic phases can be written in the following form:

$$\|N_r\| = \begin{pmatrix} \mu_a & \mu(2g_r - 1) & \mu(2u_r - 1)(2g_r - 1) \\ \mu(2g_r - 1) & \mu_a & \mu(2u_r - 1) \\ \mu(2u_r - 1)(2g_r - 1) & \mu(2u_r - 1) & \mu_a \end{pmatrix}, \qquad (1)$$

$$\|N_t\| = n_t\begin{pmatrix} \varepsilon_a & 0 & 0 \\ 0 & \varepsilon_a & 0 \\ 0 & 0 & \varepsilon_c \end{pmatrix} + (1 - n_t)\begin{pmatrix} \cos\varphi_t & 0 & -\sin\varphi_t \\ 0 & 1 & 0 \\ \sin\varphi_t & 0 & \cos\varphi_t \end{pmatrix}\begin{pmatrix} \varepsilon_c & 0 & 0 \\ 0 & \varepsilon_a & 0 \\ 0 & 0 & \varepsilon_a \end{pmatrix}, \qquad (2)$$

$$\|N_m\| = \nu_m\begin{pmatrix} \eta_a & 0 & \eta(2f_m - 1) \\ 0 & \eta_b & 0 \\ 0 & 0 & \eta_c \end{pmatrix} + (1 - \nu_m)\begin{pmatrix} \cos\varphi_{ab} & -\sin\varphi_{ab} & 0 \\ \sin\varphi_{ab} & \cos\varphi_{ab} & 0 \\ 0 & 0 & 1 \end{pmatrix}\begin{pmatrix} \eta_b & 0 & 0 \\ 0 & \eta_a & \eta(2f_m - 1) \\ 0 & 0 & \eta_c \end{pmatrix}. \qquad (3)$$

The distortions of individual domains are expressed in terms of the unit cell parameters a_r and ω_r for the rhombohedral phase; a_t and c_t for the tetragonal phase; a_m, b_m, c_m, and ω_m for the monoclinic phase; and a_0 for the cubic phase as follows: $\mu_a = a_r\cos\omega_r/a_0$, $\mu = a_r\sin\omega_r/a_0$, $\varepsilon_a = a_t/a_0$, $\varepsilon_c = c_t/a_0$, $\eta_a = a_m\cos\omega_m/a_0$, $\eta_b = b_m/a_0$, $\eta_c = c_m/a_0$, and $\eta = a_m\sin\omega_m/a_0$. The angles $\varphi_t = \arccos[2\varepsilon_a\varepsilon_c/(\varepsilon_a^2 + \varepsilon_c^2)]$ and $\varphi_{ab} = \arccos[2\eta_a\eta_b/(\eta_a^2 + \eta_b^2)]$ in formulas (2) and (3) characterize the rotation of the crystallographic axes (see [13, 24]) of contiguous domains in the tetragonal and monoclinic phases for $\varepsilon_a \ne \varepsilon_c$ and $\eta_a \ne \eta_b$, respectively. Further analysis of matrices (1)–(3) will be performed according to the formulas taken from [1, 24] for the purpose of revealing the possible elastic matching of phases along the zero mean strain plane and of determining the optimum volume concentrations of domains (for example, $n_{t,\,\mathrm{opt}}$ and $n'_{t,\,\mathrm{opt}}$ in the tetragonal phase) or twins (for example, $\nu_{m,\,\mathrm{opt}}$ and $\nu'_{m,\,\mathrm{opt}}$ in the monoclinic phase).

3. RESULTS OF CALCULATIONS AND DISCUSSION

3.1. Planes of zero mean strains in two-phase states. The calculated optimum volume concentrations of different-type domains or twins in PT–PZN two-phase crystals in the vicinity of the morphotropic boundary are listed in Table 1. The numerical estimates were obtained from the data on the perovskite unit-cell parameters measured at room temperature in [17] (the rhombohedral and monoclinic phases at $x = 0.08$) and [22] (the tetragonal phase at $x \approx 0.09$). Analysis of the experimental data demonstrates that the unit cell parameters of the tetragonal phase ($a_t = 0.4037$ nm and $c_t = 0.4080$ nm at $E = 0$ [22]) are in good agreement with the perovskite unit-cell parameters estimated by extrapolating the curves $a_m(E)$ and $b_m(E)$ (taken from [17]) to the unit cell parameters $a_m(E') = b_m(E') \ne c_m(E')$ which correspond to the possible transition from the monoclinic phase to the tetragonal phase. Our numerical estimates were made using polynomial extrapolation of the dependences $a_m(E)$ and $b_m(E)$ for PT–PZN crystals with $x = 0.08$ and led to the following results:

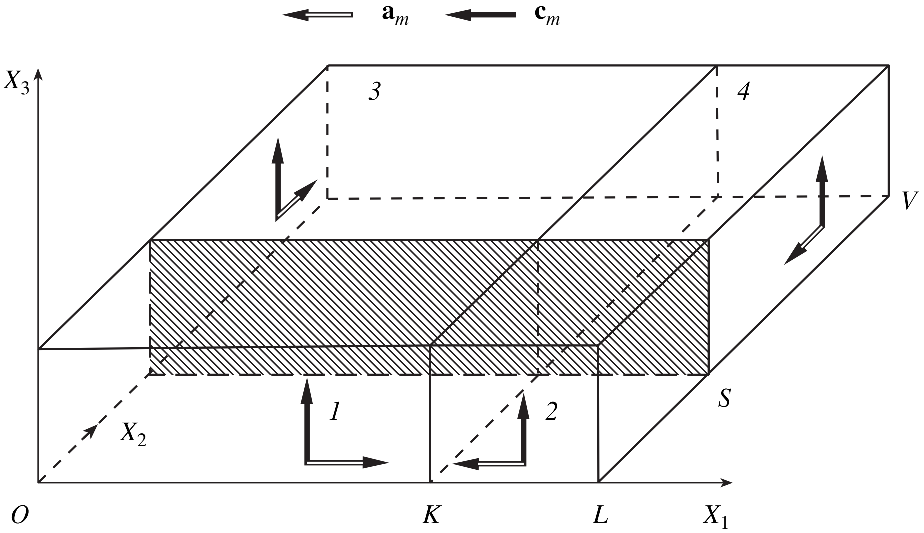

Fig. 1. A schematic drawing of the domain structure induced by the electric field **E** || [001] in the monoclinic phase of xPbTiO$_3$–(1 – x)Pb(Zn$_{1/3}$Nb$_{2/3}$)O$_3$ crystals in the vicinity of the morphotropic phase boundary. $f_m = |OK|/|OL|$ and $v_m = |LS|/|LV|$ are the volume concentrations of twins formed by domains of the (1, 3) and (1, 2) types, respectively. The hatched plane represents the domain wall parallel to the (010) plane of the perovskite cell.

$a_m(E') = b_m(E') \approx 0.4030$ nm, $c_m(E') \approx 0.4090$ nm, and $E' \approx 3.0$–3.5 MV/m. It is worth noting that the estimates for E' closely coincide with the experimental field strengths $E'' \approx 2.5$–4.0 MV/m [14] at which the tetragonal phase is induced.

As follows from the calculations of the optimum volume concentrations of domains or twins, the values of $n_{t,\,\mathrm{opt}}$, $n'_{t,\,\mathrm{opt}}$, $v_{m,\,\mathrm{opt}}$, and $v'_{m,\,\mathrm{opt}}$ change by less than 1% even in the case when the concentration parameters u_r, g_r, and f_m substantially vary in the interval [0, 1]. The virtual constancy of the aforementioned optimum concentrations is due to the fact that the shear distortions of perovskite cells in the rhombohedral and monoclinic phases affect the formation of planar unstrained interfaces insignificantly. This is determined by the off-diagonal elements of the matrices $\|N_r\|$ and $\|N_m\|$, which depend on the parameters u_r, g_r, and f_m [see formulas (1) and (3)] and are small in magnitude as compared to the diagonal elements of these matrices.

It can be seen from Table 1 that the elastic matching of the phases along the zero mean strain plane can occur at two optimum volume concentrations, for example, $n_{t,\,\mathrm{opt}}$ and $n'_{t,\,\mathrm{opt}}$. These concentrations in the interval [0, 1] are determined from the equation [1, 24]

$$\sum_{q=0}^{6} a_q n_t^q = 0, \qquad (4)$$

where a_q are the coefficients expressed through the elements of the distortions matrices (1)–(3). It is assumed that, upon a field-induced transition from the monoclinic phase to the tetragonal phase, an increase in the electric field strength E should be attended by an increase in the volume concentration of domains with $\mathbf{P}_{s1} \uparrow\uparrow \mathbf{E} \parallel OX_3$ (in this case, the bulk density of the electrostatic interaction energy $w_{es,\,1} = -(\mathbf{P}_{s1}\mathbf{E})$ [26] has the lowest value). Hence, it follows from the field dependences represented in Table 1 that the dependence $n_{t,\,\mathrm{opt}}(E)$ has a physical meaning and, in the limiting case, leads to the following result: $n_{t,\,\mathrm{opt}}(E') \longrightarrow 1$. Unlike the dependence $n_{t,\,\mathrm{opt}}(E)$, the calculated dependence $n'_{t,\,\mathrm{opt}}(E)$ gives physically meaningless results $n'_{t,\,\mathrm{opt}}(E') \longrightarrow 0$ and will be ignored in the subsequent discussion.

3.2. The influence of the monoclinic phase on the electromechanical properties of xPbTiO$_3$–(1 – x)Pb(Zn$_{1/3}$Nb$_{2/3}$)O$_3$ crystals.

The results obtained in analyzing the elastic matching of the rhombohedral and monoclinic phases make it possible to interpret the experimentally observed features in the electromechanical characteristics of PT–PZN crystals with $x = 0.08$ in the vicinity of $E = E_0 = 1.5$ MV/m [15, 17, 18, 27]. The calculated optimum concentrations of twins in the monoclinic phase $v_{m,\,\mathrm{opt}} \approx 1$ and $v'_{m,\,\mathrm{opt}} \approx 0$ (Table 1) indicate that the domain structure becomes considerably simpler. As a result, the basis vectors $\mathbf{b}_{mk}$ over the whole crystal are oriented parallel to either of the two axes OX_1 ($k = 3, 4$) or OX_2 ($k = 1, 2$). In an external electric field $E \geq E_0$, the displacements of domain (twin) walls, which are aligned parallel to the (010) plane (Fig. 1) and separate the twins with $\mathbf{b}_{mk} \parallel OX_1$ and $\mathbf{b}_{mk} \parallel OX_2$, are accompanied by strains that arise from the nonequality of the unit cell parameters $a_m \neq b_m$ and can affect the electromechanical properties of the crystals.

Table 1. Elastic matching of phases in $x\text{PbTiO}_3$–$(1 - x)\text{Pb}(\text{Zn}_{1/3}\text{Nb}_{2/3})\text{O}_3$ crystals in the electric field **E** ∥ [001]

Coexisting phases and constant volume concentrations of different-type domains	x	E, MV/m	Optimum volume concentrations of domains or twins for elastic matching of phases along the zero mean strain plane
Rhombohedral ($u_r = g_r = 0$) and tetragonal	0.09	0	$n_{t,\text{ opt}} = 0.620$ or $n'_{t,\text{ opt}} = 0.380$
Rhombohedral ($u_r = g_r = 1/2$) and monoclinic ($f_m = 1/2$)	0.08	0	$v_{m,\text{ opt}} = 0.775$ or $v'_{m,\text{ opt}} = 0.225$
		5	$v_{m,\text{ opt}} = 0.801$ or $v'_{m,\text{ opt}} = 0.199$
		10	$v_{m,\text{ opt}} = 0.873$ or $v'_{m,\text{ opt}} = 0.127$
		15	$v_{m,\text{ opt}} = 0.980$ or $v'_{m,\text{ opt}} = 0.020$
		20	$v_{m,\text{ opt}} > 1$ or $v'_{t,\text{ opt}} < 0$ (ZMSP is absent)
Monoclinic and tetragonal ($v_m = 1$ and $f_m = 1/2$ with an increase in E; $n_t = 1$ and $f_m = 1/2$ with a decrease in E)	0.08–0.09		Phase transition with an increase in E
		0	$n_{t,\text{ opt}} = 0.438$ or $n'_{t,\text{ opt}} = 0.562$
		5	$n_{t,\text{ opt}} = 0.461$ or $n'_{t,\text{ opt}} = 0.539$
		10	$n_{t,\text{ opt}} = 0.519$ or $n'_{t,\text{ opt}} = 0.481$
		15	$n_{t,\text{ opt}} = 0.588$ or $n'_{t,\text{ opt}} = 0.412$
		20	$n_{t,\text{ opt}} = 0.762$ or $n'_{t,\text{ opt}} = 0.238$
		30–35	$n_{t,\text{ opt}} \approx 1$ or $n'_{t,\text{ opt}} \approx 0$
			Phase transition with a decrease in E
		20	$v_{m,\text{ opt}} = 0.429$ or $v'_{m,\text{ opt}} = 0.571$
		15	$v_{m,\text{ opt}} = 0.274$ or $v'_{m,\text{ opt}} = 0.726$
		10	$v_{m,\text{ opt}} = 0.245$ or $v'_{m,\text{ opt}} = 0.755$
		5	$v_{m,\text{ opt}} = 0.224$ or $v'_{m,\text{ opt}} = 0.776$
		0	$v_{m,\text{ opt}} = 0.217$ or $v'_{m,\text{ opt}} = 0.783$

Note: The concentrations $n_{t,\text{ opt}}$ and $n'_{t,\text{ opt}}$ for the rhombohedral–tetragonal phase transition were calculated in [25] before the intermediate monoclinic phase was found in the PT–PZN system. The coexistence of the rhombohedral and tetragonal phases in PT–PZN crystals with $x = 0.08$ in a certain range of electric fields E was observed in the recent work [19]; however, the concentrations $n_{t,\text{ opt}}(E)$ and $n'_{t,\text{ opt}}(E)$ have not been calculated, because reliable data on the experimental dependences $a_r(E)$, $\omega_r(E)$, $a_t(E)$, and $c_t(E)$ are unavailable.

According to the simplest evaluations, which are based on the concepts of elastic displacements of 90° domain walls in crystalline grains of BaTiO_3 ferropiezoelectric ceramics [28], the strains induced at an electric field $E \approx E_0$ are estimated as $\xi^{i}_{jk} \approx (a_m - b_m)/b_m \approx 0.6\%$. This value is comparable to the piezoelectric strain $\xi_{33}(E_0) \approx 0.5\%$ determined experimentally in [27] for the PT–PZN crystal. In our opinion, the displacements of the {100}-type domain walls and subsequent simplification of the domain structure lead to the fact that the characteristic jumps in the field dependences of the piezoelectric coefficient $d_{31}(E)$ and the elastic compliance $s^{E}_{11}(E)$ measured by the resonance method in the crystal [15] occur in the vicinity of $E = E_0$. At the same time, no jumps in the permittivity $\varepsilon^{\sigma}_{33}(E)$ are observed at $E \approx E_0$ [15]. This can also be attributed to the simplification of the domain structure in the monoclinic phase.

The displacements of the interphase boundaries also affect the piezoelectric properties of PT–PZN crystals. According to [16], the strain of a crystal along the OX_3 axis due to displacement of the (001) boundaries along the same axis can be represented as $\xi^{\Delta}_{33,\,rm} = z_m\delta_{rm}$, where z_m is the volume concentration of the induced monoclinic phase and $\delta_{rm} = (c_m - a_r)/a_r$ is the coefficient dependent on the unit cell parameters of the coexisting phases. Note that, in all the domains involved, the basis vectors $\mathbf{c}_{mk}$ are oriented parallel to the OX_3 axis and the basis vectors $\mathbf{c}_{ri}$ are nearly parallel to the OX_3 axis. The contribution of the displacements under consideration to the piezoelectric coefficient d_{33} in the electric field $\mathbf{E} \parallel OX_3$ can be evaluated from the formula

$$\begin{aligned}\Delta d_{33,\,rm} &= d\xi^{\Delta}_{33,\,rm}/dE \\ &= (dz_m/dE)\delta_{rm} + z_m(d\delta_{rm}/dE).\end{aligned} \qquad (5)$$

The calculation with the use of formula (5) involves problems, because experimental data on the kinetics of the induced rhombohedral–monoclinic phase transition and the electromechanical constants for single-domain monoclinic PT–PZN crystals are unavailable. However, we can make the following assumptions: (i) $z_m = 0$ at $E = 0$, (ii) $z_m = 1$ at $E = 2.0$ MV/m (both conditions correlate with the experimental data obtained in [17, 18]), (iii) $z_m(E)$ is a linear function, and (iv) $a_r(E)$ is constant. On this basis, we calculated the field dependence $\Delta d_{33,\,rm}(E)$ (Fig. 2, curve *1*). For comparison, the experimental dependences $d_{33,\,D}(E)$ (curve *2*) and $d_{33,\,P}(E)$ (curve *4*) and the calculated dependence $d_{33,\,rr}(E)$ (curve *3*) are also plotted in Fig. 2. As is seen from this figure, there is a clear correlation between the field dependences $\Delta d_{33,\,rm}(E)$ and $d_{33,\,D}(E)$ and a correlation between the dependences $\Delta d_{33,\,rr}(E)$ and $d_{33,\,P}(E)$. Whatever the phase symmetry and the features in the domain structure, the contributions $\Delta d_{33,\,rm}$ and $\Delta d_{33,\,rr}$ in strong electric fields can amount to as much as 50–90% of the measured piezoelectric coefficients $d_{33,\,D}(E)$ and $d_{33,\,P}(E)$, respectively. The similarity of the curves $d_{33,\,D}(E)$ and $\Delta d_{33,\,rm}(E)$ (Fig. 2, curves *1, 2*) can be associated with the similarity of the curves $\xi_{33}(E)$ [27] and $c_m(E)$ [17] or $\delta_{rm}(E)$. The peaks observed in the curves $d_{33,\,D}(E)$ and $\Delta d_{33,\,rm}(E)$ in the vicinity of $E = E_0$ stem from the maximum slope of the curves $\xi_{33}(E)$ and $c_m(E)$, respectively. Noheda *et al.* [17] also emphasized the similarity of the field dependences $\xi_{33}(E)$ and $c_m(E)$; however, no consideration was given to the piezoelectric and other properties of PT–PZN crystals.

The dependence $\Delta d_{33,\,rm}(E)$ calculated from formula (5) becomes incorrect at $E > E_0$ due to neglect of the aforementioned simplification of the domain structure in the monoclinic phase, the nonlinear dependence $z_m(E)$, and the jump in the dependence $c_m(E)$. The simplification of the domain structure affects the elastic, piezoelectric, and dielectric properties of the monoclinic phase and, consequently, brings about variations in the internal mechanical and electric fields and in the conditions of displacement of the interphase boundary. The jump in the unit cell parameter c_m at $E \approx E_0$ leads to a change in the matrix element $N_{m,\,33}$ [see formula (3)] and to redistribution of the internal fields, which also affects the displacement of the interphase boundary.

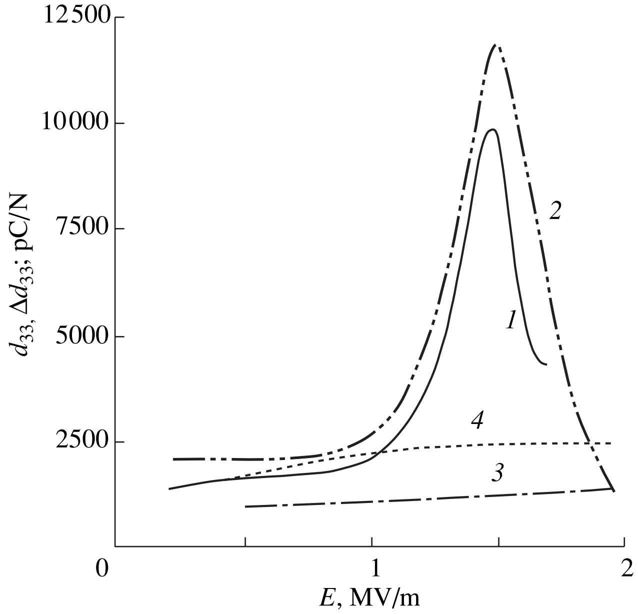

Fig. 2. (*1, 3*) Calculated and (*2, 4*) experimental field dependences of the piezoelectric coefficient $d_{33}(E)$ and the contribution $\Delta d_{33}(E)$ of the displacement of the interphase boundaries to the piezoelectric coefficient of the 0.08PbTiO$_3$–0.92Pb(Zn$_{1/3}$Nb$_{2/3}$)O$_3$ crystal: (*1*) $\Delta d_{33,\,rm}(E)$, (*2*) $d_{33,\,D}(E)$ (upon induced rhombohedral–monoclinic phase transition), (*3*) $\Delta d_{33,\,rr}(E)$, and (*4*) $d_{33,\,P}(E)$ (in the rhombohedral phase). The dependence $\Delta d_{33,\,rm}(E)$ (curve *1*) is calculated from formula (5). The dependences $d_{33,\,D}(E)$ and $d_{33,\,P}(E)$ (curves *2, 4*) are constructed according to the data (taken from [27] and [14]) on the strain $\xi_{33}(E)$ measured in an increasing electric field. The dependence $\Delta d_{33,\,rr}(E)$ (curve *3*) is calculated in terms of the model concepts [16] regarding the displacement of (001) domain walls in the rhombohedral phase in which individual domains are characterized by the molar concentration $x_d \neq 0.08$ [25] due to composition fluctuations and other factors.

Durbin *et al.* [18] made the assumption that the monoclinic and tetragonal phases can coexist in the absence of the electric field **E**, which is confirmed by the results of our calculations (Table 1). Moreover, the interphase boundaries can be oriented along the zero mean strain plane upon both the direct and reverse phase transitions over a wide range of electric field strengths E. Upon the field-induced transition to the tetragonal phase, the formation a single-domain state (i.e., $n_{t,\,\mathrm{opt}} \longrightarrow 1$) in the vicinity of $E = 3.0$ MV/m can also affect the field dependences $d_{33}(E)$ and other electromechanical characteristics of PT–PZN crystals.

3.3. Comparison with the available data for Pb(Zr$_{1-x}$Ti$_x$)O$_3$ solid solutions. A comparison of the results of calculations for the zero mean strain planes in PT–PZN crystals (Table 1) with those obtained in our previous work [13] for Pb(Zr$_{1-x}$Ti$_x$)O$_3$ solid solutions indicates that the concentrations $n_{t,\,\mathrm{opt}}$ (or $n'_{t,\,\mathrm{opt}}$) for the rhombohedral–tetragonal phase transition at $E = 0$ dif-

Table 2. Relation between the optimum volume concentrations of domains (twins) and the mutual orientation of the spontaneous polarization vectors of domains in the coexisting phases

Condition for optimum volume concentrations	Condition for angles formed by the spontaneous polarization vectors of domains	Constraints imposed on the Miller indices of the zero mean strain plane	Range of applicability of conditions (6)–(9)
(6)	$\alpha \approx (\mathbf{P}_{Mc,\,a}, \wedge\, \mathbf{P}_{Mc,\,b})$	$h_a \lesssim 1$; $h_b \ll 1$	For conditions (6) and (7): $300 \le T \le 550$ K, $0.45 \le x \le 0.46$ (according to numerical estimates obtained in [13]), $E = 0$
(7)	$\pi/2 - \alpha \approx (\mathbf{P}_{Mc,\,a}, \wedge\, \mathbf{P}_{Mc,\,c})$	$h_a \lesssim 1$; $h_c \approx 1/4$	
(8)	$\alpha \approx (\mathbf{P}_{Mc,\,d}, \wedge\, \mathbf{P}_{Mc,\,e})$	$k_d \lesssim 1$; $h_e \ll 1$	For conditions (8) and (9): $T \approx 300$ K, $0.08 \le x \le 0.09$, $0 \le E \le 1.0$ MV/m
(9)	$\pi/2 - \alpha \approx (\mathbf{P}_{Mc,\,d}, \wedge\, \mathbf{P}_{Mc,\,f})$	$k_d \approx h_f \lesssim 1/4$	

Note: The spontaneous polarization vectors of individual domains in the rhombohedral and tetragonal phases are specified, according to [7], in the perovskite axes as $\mathbf{P}_{Rh} \parallel [111]$ and $\mathbf{P}_{Tg} \parallel [001]$, respectively. In the monoclinic phase of $\mathrm{Pb(Zr_{1-x}Ti_x)O_3}$, the spontaneous polarization vector $\mathbf{P}_{Mc,\,i} \parallel [h_i h_i 1]$ (where $0 < h_i < 1$) rotates from [111] to [001]. In the monoclinic phase of PT–PZN, the rotation of the spontaneous polarization vector is characterized by the following sequence of vector orientations: $\mathbf{P}_{Mc,\,d} \parallel [1k_d1] \longrightarrow \mathbf{P}_{Mc,\,g} \parallel [1k_g1] \longrightarrow \mathbf{P}_{Mc,\,f} \parallel [h_f01] \longrightarrow \mathbf{P}_{Mc,\,e} \parallel [h_e01]$, where $k_d \gg k_g$ and $h_f \gg h_e$.

fer only slightly (by less than 10%). This can be explained both in terms of the approximate equality of the spontaneous strain ratios $\xi^s_{11,\,t}/\xi^s_{33,\,t} = (\varepsilon_a - 1)/(\varepsilon_c - 1)$ for the perovskite cells in the tetragonal phases of PT–PZN crystals and $\mathrm{Pb(Zr_{1-x}Ti_x)O_3}$ solid solutions in the vicinity of the morphotropic boundary and by the weak effect of shear spontaneous strains ($\xi^s_{ik,\,t} = \mu$) in the unit cells of the rhombohedral phases on the internal mechanical fields. The electric field $\mathbf{E}$ affects the unit cell parameters a_m and c_m of PT–PZN crystals [17] and, hence, changes the anisotropy of the spontaneous strains $\xi^s_{11,\,m} = \eta_a - 1$, $\xi^s_{22,\,m} = \eta_b - 1$, and $\xi^s_{33,\,m} = \eta_c - 1$. Eventually, this results in noticeable changes in the concentrations $v_{m,\,\mathrm{opt}}$ and $n_{t,\,\mathrm{opt}}$ or $v'_{m,\,\mathrm{opt}}$ and $n'_{t,\,\mathrm{opt}}$ (Table 1). As regards the interphase boundaries, which are the zero mean strain planes in $\mathrm{Pb(Zr_{1-x}Ti_x)O_3}$ crystalline grains [13] and PT–PZN crystals, their orientations calculated according to the formulas taken from [24] are close to those of the $\{0kl\}$ planes in the perovskite cell. The specific features in the temperature, concentration [10, 12], and field [17] dependences of the unit cell parameters and the domain structures of the monoclinic phases [12, 13, 17] are governed by the different ratios of the Miller indices k/l.

The optimum volume concentrations of domains or twins that correspond to the zero mean strain plane in the vicinity of the triple points satisfy the conditions

$$n_{t,\,\mathrm{opt}}(Rh - Tg) \approx n_{m,\,\mathrm{opt}}(Rh - Mc)\,n_{m,\,\mathrm{opt}}(Tg - Mc), \quad (6)$$

$$n'_{t,\,\mathrm{opt}}(Rh - Tg) \approx n'_{m,\,\mathrm{opt}}(Rh - Mc)\,n_{t,\,\mathrm{opt}}(Mc - Tg) \quad (7)$$

for $\mathrm{Pb(Zr_{1-x}Ti_x)O_3}$ crystalline grains and

$$n_{t,\,\mathrm{opt}}(Rh - Tg) \approx v_{m,\,\mathrm{opt}}(Rh - Mc)\,v'_{m,\,\mathrm{opt}}(Tg - Mc), \quad (8)$$

$$n'_{t,\,\mathrm{opt}}(Rh - Tg) \approx v_{m,\,\mathrm{opt}}(Rh - Mc)\,n_{t,\,\mathrm{opt}}(Mc - Tg) \quad (9)$$

for PT–PZN crystals.[1] Let us associate the optimum concentration $n_{t,\,\mathrm{opt}}(Rh - Tg)$ with the angle $\alpha = (\mathbf{P}_{Rh}, \wedge\, \mathbf{P}_{Tg})$ between the spontaneous polarization vectors of individual domains in the rhombohedral and tetragonal phases and place the right-hand sides of relationships (6) and (8) in correspondence with the angles between the spontaneous polarization vectors $\mathbf{P}_{Mc,\,a}$, $\mathbf{P}_{Mc,\,b}$, … of domains in the monoclinic phase. As a result, we observe a correlation between the optimum concentrations and the mutual orientations of the aforementioned vectors (Table 2). A similar correlation can be observed in the case when the concentrations $n_{t,\,\mathrm{opt}}(Rh - Tg)$ are replaced by the concentrations $n'_{t,\,\mathrm{opt}}(Rh - Tg)$ from relationships (7) and (9) and the angle α is replaced by $\pi/2 - \alpha$. It should be noted that the equality of the angles presented in Table 2 is achieved despite the different trajectories [111] $\longrightarrow$ [001] described by the tips of vectors $\mathbf{P}_{Mc,\,a}$ [7] in $\mathrm{Pb(Zr_{1-x}Ti_x)O_3}$ and PT–PZN. In this case, there is a certain correspondence between the thermodynamic parameters T, x, and E and the Miller indices h_a, h_b, …, h_f, and k_d: all the above quantities vary in sufficiently narrow ranges. In general, the revealed correlation considerably extends the notion of the monoclinic phase as a bridge between the tetragonal and rhombohedral phases [10]. However, this correlation has defied comprehensive analysis, because experimental data on the electrostriction coefficients and the spontaneous polarization of the single-domain phases in the studied solid solutions at different T, x, and E are unavailable.

The largest (peak) piezoelectric coefficient $d_{33,\,\mathrm{sup}} \approx 3000$ pC/N was observed upon induced rhombohedral–

---

[1] Relationships (6)–(9) are represented in the form $A \approx BC$. The two-phase states are given in parentheses ($I - II$), where I and II are the coexisting single-domain and polydomain phases, respectively. The optimum concentrations are calculated for a particular type of domains or twins of phase II (see Table 1 and [13]). For brevity, the coexisting phases are designated as follows: Mc is the monoclinic phase, Rh is the rhombohedral phase, and Tg is the tetragonal phase.

monoclinic phase transition in $Pb(Zr_{0.53}Ti_{0.47})O_3$ disordered crystals [9]. This is approximately 15 times larger than the experimental value of $d^*_{33,\,PZT}$ obtained for ferropiezoelectric ceramics [6] and is almost eight times larger than the theoretical value of $d_{33,\,PZT}$ obtained for a single-domain crystal of the same composition in the absence of an electric field [29]. However, the piezoelectric coefficient $d_{33,\,sup}$ is approximately four times smaller than the maximum piezoelectric coefficient $d_{33,\,max}$ for the PT–PZN crystal with $x = 0.08$ (Fig. 2, curve *2*). The differences in the moduli $d_{33,\,sup}$, $d^*_{33,\,PZT}$, and $d_{33,\,PZT}$ can be attributed to both the presence of the monoclinic phase in the samples studied in [9] and the effects associated with the motion of interphase and domain (twin) boundaries in the electric field $\mathbf{E} \parallel OX_3$. It is quite possible that one of the reasons for the difference between the moduli $d_{33,\,sup}$ and $d_{33,\,max}$ lies in the difference between the elastic compliances s^E_{33} of these crystals in the vicinity of the morphotropic boundary. In actual fact, the compliance s^E_{33} of the PT–PZN crystal even in a weak field **E** [14] is approximately four times larger than the compliance s^E_{33} estimated in [30] for the $Pb(Zr_{0.5}Ti_{0.5})O_3$ single-domain crystal. The decrease in s^E_{33} and other components of the elastic compliance tensor suggests an increase in the rigidity of the crystal, affects the displacement of interphase boundaries in the electric field **E** [16], and leads to a decrease in the contribution of these displacements to the piezoelectric coefficients d_{ij} and other electromechanical constants. Another reason for the difference in the piezoelectric properties of the induced monoclinic phases lies in the different ways of reorienting the spontaneous polarization vector $\mathbf{P}_{Mc}$ of domains in $Pb(Zr_{1-x}Ti_x)O_3$ and PT–PZN solid solutions [7, 17] and manifests itself in different shapes of the curves $d_{33}(E)$ [9] and $d_{33,\,D}(E)$ (Fig. 2, curve *2*). At present, for lack of experimental data on the monoclinic phases, it is difficult to establish the main reason for the above differences. Experimental investigations of this problem and the problem concerning the influence of different physical factors on the electromechanical properties of PT–PZN and $Pb(Zr_{1-x}Ti_x)O_3$ heterophase solid solutions are of special interest.

4. CONCLUSIONS

Thus, the results obtained in the present work can be summarized as follows.

(1) For PT–PZN crystals, the field dependences of the unit cell parameters of the monoclinic phase predetermine the formation of rhombohedral–monoclinic and monoclinic–tetragonal interphase boundaries oriented along the zero mean strain plane over a wide range of electric field strengths **E**. The domain structures of the coexisting phases are characterized by the optimum volume concentrations of domains or mechanical twins of particular types, which provide complete relaxation of internal mechanical stresses.

(2) The specific features observed earlier experimentally in the behavior of the piezoelectric coefficient $d_{31}(E)$, the elastic compliance $s^E_{11}(E)$, and the unit cell parameter $c_m(E)$ of the monoclinic phase in the vicinity of $E = 1.5$ MV/m are associated with the simplification of the domain structure of PT–PZN crystals upon an induced rhombohedral–monoclinic phase transition. In this case, the displacements of the interphase boundaries in the electric field $\mathbf{E} \parallel [001]$ can make a considerable contribution Δd_{33} to the piezoelectric coefficient d_{33} of these crystals and the similarity of the calculated dependence $\Delta d_{33,\,rm}(E)$ and the experimental dependence $d_{33,\,D}(E)$ is closely allied to the similarity of the field dependences of the strain $\xi_{33}(E)$ and the unit cell parameter $c_m(E)$ over a wide range of electric fields E.

(3) Although the domain structures in the monoclinic phases of PT–PZN and $Pb(Zr_{1-x}Ti_x)O_3$ solid solutions differ in symmetry and the spontaneous polarization vectors of the domains in these phases rotate in different directions, both systems are characterized by similar correlations between the optimum volume concentrations of different-type domains (twins) and the mutual orientation of the spontaneous polarization vectors of individual domains in the rhombohedral, tetragonal, and monoclinic phases.

REFERENCES

1. V. Yu. Topolov, L. E. Balyunis, A. V. Turik, *et al.*, Izv. Akad. Nauk, Ser. Fiz. **56** (10), 127 (1992).
2. L. E. Balyunis, V. Yu. Topolov, I. S. Bah, and A. V. Turik, J. Phys.: Condens. Matter **5** (9), 1419 (1993).
3. A. S. Tarek, V. G. Smotrakov, A. T. Kozakov, *et al.*, Izv. Akad. Nauk, Ser. Fiz. **57** (3), 135 (1993).
4. F. Schmidt, L. Gruber, and K. Knorr, Z. Phys. B **87** (1), 127 (1992).
5. Z.-G. Ye, J.-P. Rivera, and H. Schmid, Ferroelectrics **116** (1–4), 251 (1991).
6. A. V. Gorish, V. P. Dudkevich, M. F. Kupriyanov, A. E. Panich, and A. V. Turik, *Piezoelectric Instrument Making*, Vol. 1: *Physics of Ferroelectric Ceramics* (IPRZh “Radiotekhnika,” Moscow, 1999).
7. H. Fu and R. E. Cohen, Nature (London) **403** (6767), 281 (2000).
8. D. Vanderbilt and M. H. Cohen, Phys. Rev. B **63** (9), 094108 (2001).
9. L. Bellaiche, A. Garcia, and D. Vanderbilt, Phys. Rev. B **64** (6), 060103 (2001).
10. B. Noheda, J. A. Gonzalo, L. E. Cross, *et al.*, Phys. Rev. B **61** (13), 8687 (2000).
11. R. Guo, L. E. Cross, S.-E. Park, *et al.*, Phys. Rev. Lett. **84** (23), 5423 (2000).
12. B. Noheda, D. E. Cox, G. Shirane, *et al.*, Phys. Rev. B **63** (1), 014103 (2001).

13. V. Yu. Topolov and A. V. Turik, Fiz. Tverd. Tela (St. Petersburg) **43** (8), 1525 (2001) [Phys. Solid State **43**, 1585 (2001)].
14. S.-E. Park and T. R. Shrout, J. Appl. Phys. **82** (4), 1804 (1997).
15. D.-S. Paik, S.-E. Park, S. Wada, *et al.*, J. Appl. Phys. **85** (2), 1080 (1999).
16. V. Yu. Topolov and A. V. Turik, Fiz. Tverd. Tela (St. Petersburg) **43** (6), 1080 (2001) [Phys. Solid State **43**, 1117 (2001)].
17. B. Noheda, D. E. Cox, G. Shirane, *et al.*, Phys. Rev. Lett. **86** (17), 3891 (2001).
18. M. K. Durbin, J. C. Hicks, S.-E. Park, and T. R. Shrout, J. Appl. Phys. **87** (11), 8159 (2000).
19. S. Kim, S.-I. Yang, J.-K. Lee, and K. Sun, Phys. Rev. B **64** (9), 094105 (2001).
20. G. Xu, H. Luo, H. Xu, and Z. Yu, Phys. Rev. B **64** (2), 020102 (2001).
21. Z.-G. Ye, B. Noheda, M. Dong, *et al.*, Phys. Rev. B **64**, 184114 (2001).
22. J. Kuwata, K. Uchino, and S. Nomura, Ferroelectrics **37** (1–4), 579 (1981).
23. S. Wada, S.-E. Park, L. E. Cross, and T. R. Shrout, Ferroelectrics **221** (1–4), 71 (2001).
24. G. Metrat, Ferroelectrics **26** (1–4), 801 (1980).
25. V. Yu. Topolov and Z.-G. Ye, Ferroelectrics **253** (1–4), 71 (2001).
26. M. E. Lines and A. M. Glass, *Principles and Applications of Ferroelectrics and Related Materials* (Oxford Univ. Press, Oxford, 1977; Mir, Moscow, 1981).
27. M. K. Durbin, E. W. Jacobs, J. C. Hicks, and S.-E. Park, Appl. Phys. Lett. **74** (19), 2848 (1999).
28. E. I. Bondarenko, V. Yu. Topolov, and A. V. Turik, Ferroelectrics **110**, 53 (1990).
29. M. J. Haun, E. Furman, S. J. Jang, and L. E. Cross, Ferroelectrics **99** (1–4), 63 (1989).
30. V. Yu. Topolov, D. Bolten, U. Böttger, and R. Waser, J. Phys. D **34** (5), 711 (2001).

Translated by O. Borovik-Romanova

Physics of the Solid State, Vol. 44, No. 7, 2002, pp. 1363–1369. Translated from Fizika Tverdogo Tela, Vol. 44, No. 7, 2002, pp. 1302–1308.
Original Russian Text Copyright © 2002 by Grishachev.

MAGNETISM AND FERROELECTRICITY

Magnetic-Field-Induced Changes in the Photorefractive Sensitivity of Lithium Niobate

V. V. Grishachev
Moscow State University, Vorob'evy gory, Moscow, 119899 Russia
e-mail: grishachev@genphys.phys.msu.su

Received May 15, 2001; in final form, October 16, 2001

Abstract—The effect of a magnetic field on the average photorefractive sensitivity of an undoped $LiNbO_3$ crystal is studied by phase-mismatched second-harmonic generation. The experimental data obtained show the photorefractive sensitivity to reverse sign as the external magnetic field exceeds $B_1 = -0.38 \pm 0.04$ T. The magnetic field is oriented perpendicular to the crystal optical axis and to the plane of laser radiation polarization. The variation of the photorefractive sensitivity is associated with paramagnetic iron centers, whose photoionization probability depends on the direction of their magnetic moment relative to the optical axis. *© 2002 MAIK "Nauka/Interperiodica".*

1. INTRODUCTION

The variation of the refractive index of a crystal induced by laser radiation is associated with photovoltaic currents, the photorefractive effect, thermal effects, and other phenomena [1–5]. The photorefractive properties of crystals are used in holographic storage devices and for solving wave conjugation problems. On the other hand, the same properties place a constraint on the application of crystals in nonlinear-optics devices, whose operation requires stability of the optical parameters. The photorefractive parameters of crystals can be controlled by doping them with specially chosen ions, by properly varying the operating temperature, and by the application of an external electric field. One more possibility is based on varying the photorefractive properties in a magnetic field [6–10]. The main mechanism underlying the influence of the magnetic field is associated with the Hall effect, which is connected closely with the diffusion, drift, and photovoltaic currents. Other mechanisms have also been proposed [9, 10].

The photorefractive properties of crystals are studied primarily by the holographic and interference methods. One can also employ nonlinear-optics techniques for this purpose. Second harmonic generation (SHG) is most frequently used; it has been applied to advantage in studying optical homogeneity [11] and temperature-induced phase mismatch in lithium niobate crystals [12]. This communication reports on an experimental investigation of the effect of a magnetic field on the SHG kinetics in an undoped lithium niobate crystal (see also [10]).

2. EXPERIMENT

Assuming constant pumping, the SHG intensity in a crystal can be written as [13]

$$I_{2\omega} = A(I_\omega)^2 \left\{ \frac{\sin(\pi(L/\lambda_\omega)\Delta n)}{\Delta n} \right\}^2, \qquad (1)$$

where I_ω and $I_{2\omega}$ are the pump and SHG intensities, respectively; A is a constant parameter determined by the properties of the crystal; L is the crystal length; λ_ω is the pump radiation wavelength; $\Delta n = |n_\omega - n_{2\omega}|$; and n_ω and $n_{2\omega}$ are the refractive indices at the pump and second harmonic (SH) frequencies, respectively. As is evident from Eq. (1), if the geometry of wave interaction (the propagation direction and polarization of the radiation) remains unchanged, the SHG intensity $I_{2\omega}$ depends only on the difference between the refractive indices Δn.

Let us assume that, at the initial moment of generation, we have $\Delta n = \Delta n_0$ and $\pi(L/\lambda\omega)\Delta n_0 = (2m+1)\pi/2$ (here, m is an integer), which corresponds to a local maximum in SHG intensity; then afterwards, $\Delta n = \Delta n_0 + \delta n$. The photoinduced changes in the refractive index will be due to several mechanisms: $\delta n = \delta n_{pr} + \delta n_{pv} + \delta n_{tr} + \ldots$, where δn_{pr} are the changes associated with the photorefractive effect, δn_{pv} originates from the photovoltaic currents, and δn_{tr} reflects the thermally induced changes. Thus, the kinetics of the SHG intensity $I_{2\omega}$ is determined by the variation δn.

Let us introduce a parameter of SH conversion $\eta = I_{2\omega}/(I_\omega)^2$ and let $\eta_1 = \eta(\Delta n = \Delta n_0)$; then, for $\Delta n_0 \gg \delta n$ or $m \gg 1$, we obtain

$$\frac{\eta}{\eta_1} = \left\{ \cos\left(\pi \frac{L}{\lambda_\omega}\right)\delta n \right\}^2. \qquad (2)$$

The condition $\Delta n_0 \gg \delta n$ is satisfied in most cases, except in the phase-matching region, where $m = 0$. Hence, using phase-mismatched SHG in an experiment will make relations (1) and (2) more accurate because $I_\omega \gg I_{2\omega}$. Furthermore, the crystal used in the experiment is undoped lithium niobate whose region of maximum photorefractive sensitivity lies in the blue-green

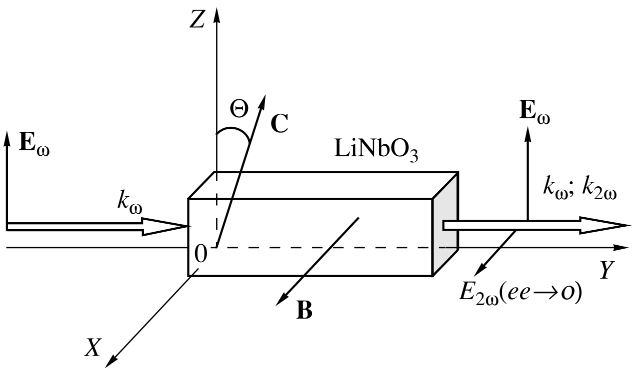

Fig. 1. Mutual orientation of the crystal under study ($LiNbO_3$) and external electric and magnetic fields. **C** is the direction of the optical axis; $\Theta = 6°$; $\mathbf{E}_\omega$ and $\mathbf{E}_{2\omega}$ are the electric-field vectors for the laser beam and SH wave, respectively; and **B** is the external magnetic-field induction vector.

spectral region and at shorter wavelengths. While the SH falls into this region of maximum sensitivity, the laser radiation does not. If the phase-matching conditions are met, the SHG intensity reaches the level of the order of the pump intensity, which gives rise to substantial optical distortions and, in the cases of prolonged illumination, may bring about crystal coloring accompanied by an appreciable drop in transmission and by saturation of the $I_{2\omega}(I_\omega)$ relation. To avoid such distortions, we used phase-mismatched SH, whose intensity cannot reach critical levels and for which Eqs. (1) and (2) are valid under prolonged crystal illumination.

We note that δn in Eq. (2) is determined by the difference between the refractive indices at different wavelengths. The change in the refractive index at one wavelength can be isolated using a special experimental geometry. In crystals such as $LiNbO_3$ [1, 2], refractive-index changes for the extraordinary ray (e) are several times larger than those for the ordinary ray (o); therefore, if collinear interaction $ee \longrightarrow o$ or $oo \longrightarrow e$ is studied, the change in the refractive index of the ordinary wave can be neglected.

The experimental investigation of the $I_{2\omega}$ kinetics was done in the optical arrangement used to measure the SH conversion coefficient in the case where the pump wave crossing the $LiNbO_3$ crystal is transformed through the $ee \longrightarrow o$ interaction. The geometry of the experiment is shown in Fig. 1. We made use of a YAG : Nd^{3+} solid-state pulsed Q-switched laser operating at the wavelength $\lambda_\omega = 1.06$ μm with the pulse length $\tau_p \approx 10$ ns, average pulse energy $W_0 = 2$ mJ, beam diameter $2R = 0.8$ mm, and pulse repetition frequency $f = 25$ Hz. One pump mode was isolated in the radiation. The SH was discriminated with absorbing color filters and a monochromator. The pump intensity was measured with a photodiode; the SH intensity, with a gated PM tube in each laser pulse. The lithium niobate crystal was 5.93×5.93 mm in cross section and $L = 15.87$ mm long. The crystal was of high optical quality and was employed for frequency conversion of the radiation of this laser. The field of the electromagnet was perpendicular to the polarization plane and to the crystal optical axis, and its induction did not exceed 1.5 T.

3. RESULTS

The database of each measurement consisted of 300000–400000 values of the $I_\omega(N)$ and $I_{2\omega}(N)$ intensities and magnetic field induction $B(N)$ in relative units (here, N is the laser pulse number). This database was used to calculate the conversion parameter $\eta(N)$ and the energy of the laser radiation transmitted through the crystal $W(N) = W_0\sum_{i=1}^{N} I_\omega(i)/I_\omega^0$, where $I_\omega^0 = W_0/\tau_p$ was determined in the experiment. The $\eta(N)$ and $W(N)$ data were employed to construct the $\eta(W)$ relation, which was subsequently smoothed. The smoothed relation made it possible to find the maximum (η_{max}) and minimum (η_{min}) values. After this, the final relation $(\eta/\eta_1) = (\eta - \eta_{min})/(\eta_{max} - \eta_{min})$ was derived. This method of data processing results in the appearance of negative experimental values for the quadratic $\eta(W)/\eta_1$ dependence given by Eq. (2) and permits one to do without two additional parameters in the fitting procedure. The magnetic field was maintained constant during the experiment. To reduce the effect of laser instability, the values of $\eta(N)$ were averaged over 100 adjacent points. The results of the experiment are presented in Fig. 2 for various magnetic field strengths.

The measurements were performed without thermostatting of the sample; the influence of thermal effects (thermally induced variation of the refractive index, thermal expansion of the crystal, etc.) was reduced by preliminarily illuminating the sample by laser pulses for 30–60 min. This time interval was excluded from the subsequent consideration. This gives us grounds to maintain that the crystal temperature remained constant to within ±0.1°C during the measurements. The temperature variations associated with random thermal sources were excluded by smoothing the experimental relation (the form of the functional relation was known, which improved the accuracy of approximation). After the experiment, the induced changes in the refractive index persisted for a long time (a few days) and the optical parameters of the crystal were recovered, albeit incompletely, by illuminating the crystal with white light from an incandescent lamp for several hours. This permitted us to resume the experiments in one to two days, but the crystal did not recover to the initial state; therefore, the initial phase of the experimental relations in Fig. 2 is not the same. After a series of experiments, optical distortions formed in the transverse plane of the sample, which were seen in daylight as a transparent ring 2–3 cm in diameter around the beam.

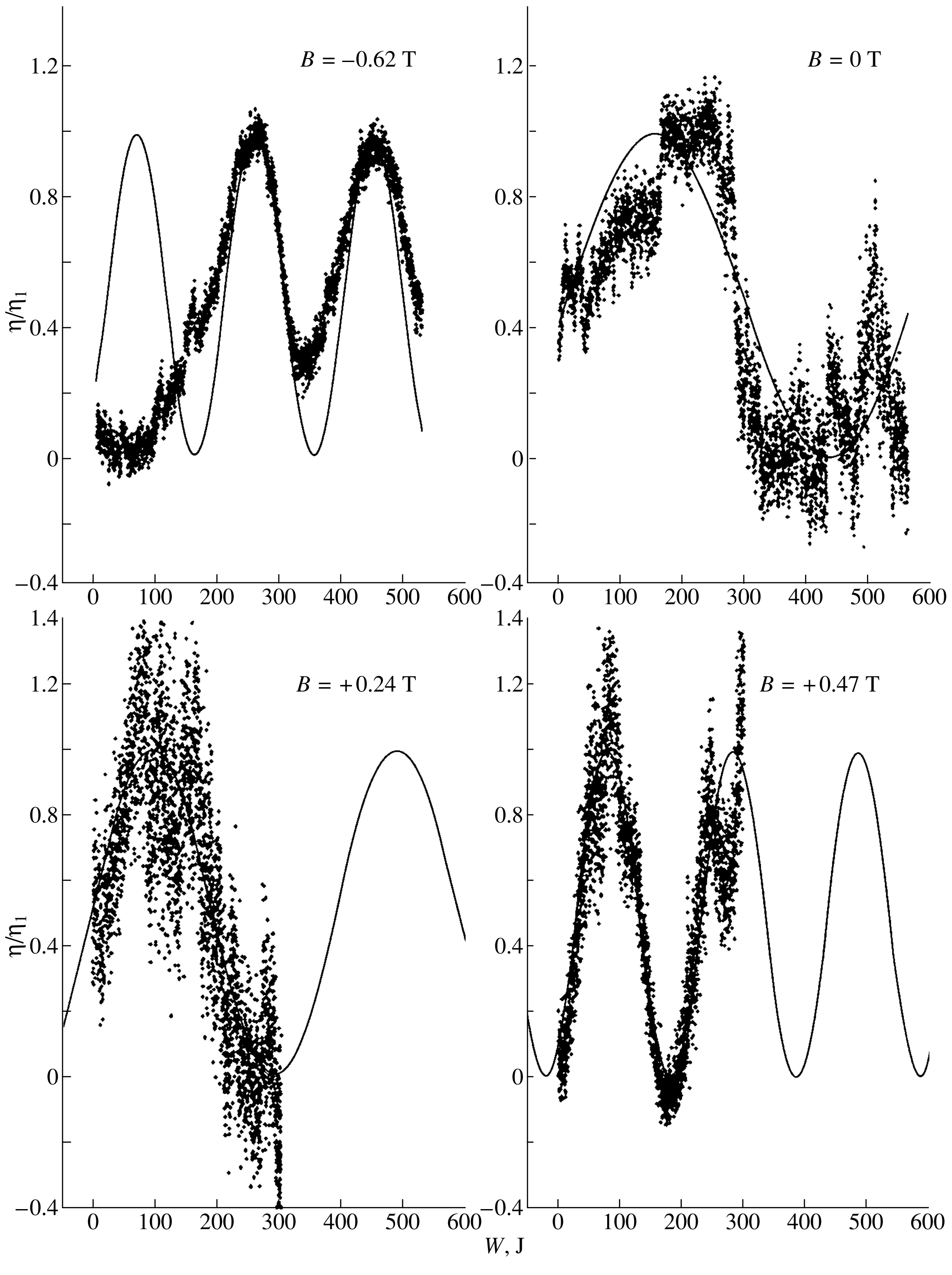

Fig. 2. Dependence of coefficient η normalized against its maximum value η_1 on laser radiation energy W passed through the crystal plotted for various values of the dc magnetic field B. Points are experiment, and the line is fitting by the $\{\cos[\pi(W - W_s)/W_p]\}^2$ function.

The experimental values of (η/η_1) can be approximated by the relation $\{\cos(\pi(W - W_s)/W_p)\}^2$, where W_s and W_p are fitting constants. By comparing the approximating function with Eq. (2), one can derive the average photorefractive sensitivity of the crystal in the linear approximation in the absorbed energy density [2, 3]:

$$S_p = \frac{\pi R^2}{\alpha W_p}\left(\frac{\lambda_\omega}{L}\right). \qquad (3)$$

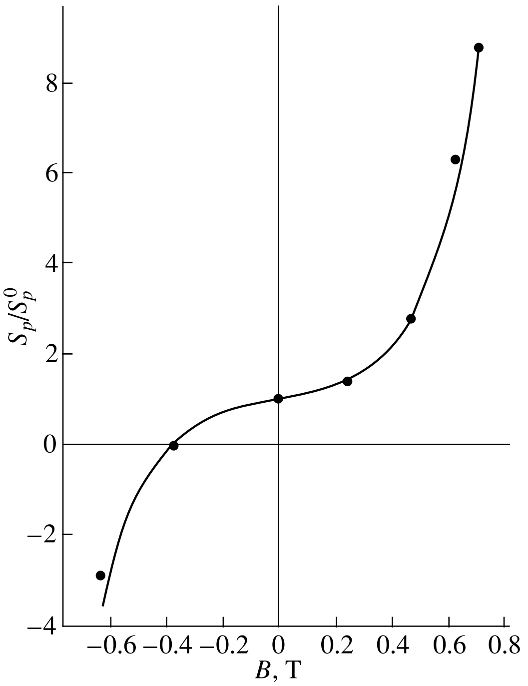

Fig. 3. Dependence of photorefractive sensitivity S_p normalized against photorefractive sensitivity S_p^0 in a zero magnetic field on a dc magnetic field B. Points are experiment, and the line is fitting by the $\{\sinh(B_1/B_0) + \sinh(B/B_0)\}$ function.

Here, α is the absorption coefficient of the pump radiation and ($\alpha W_p/\pi R^2$) is the absorbed energy density required to change the refractive index difference by $0.5\delta n_0 = (\lambda_\omega/L)$. The quantity $\delta n_0 = 3.35 \times 10^{-5}$ corresponds to the change in η in a full period and can be used to estimate photorefraction in the crystal for each experiment. The data presented in Fig. 2 is used to calculate the $S_p(B)$ relation, which is normalized to the average photorefractive sensitivity S_p^0 with no magnetic field present (Fig. 3). Attempts at approximating the $S_p(B)$ relation by various functions show that the best fit to the experiment is obtained with the function

$$S_p(B) = S\left\{\sinh\left(\frac{B_1}{B_0}\right) + \sinh\left(\frac{B}{B_0}\right)\right\}, \qquad (4)$$

where $S = S_p^0 \sinh^{-1}(B_1/B_0) = (3.8 \pm 0.6) \times 10^{-10}$ cm^3 J^{-1}, $B_1 = 0.38 \pm 0.04$ T, and $B_0 = 0.16 \pm 0.02$ T are the fitting parameters. The value $\sinh^{-1}(B_1/B_0) = 0.19$ characterizes the magnetic contribution to $S_p(B)$. The average photorefractive sensitivity S_p^0 of the crystal with no external magnetic field applied is of the order of 2×10^{-9} cm^3 J^{-1}; this value fits the measurements of the holographic sensitivity in the visible spectral region and the data on photorefraction obtained by interference and holographic methods in undoped lithium niobate covered in review papers [1–3]. Reversing the sign of the magnetic field entails reversal of the sign of the average photorefractive sensitivity; as a result, at $B = -B_1$, the optical distortions present with no magnetic field applied become cancelled. We note that the magnetic field induction $B = -B_1$ at which the photorefraction is compensated was calculated from other experimental data and confirmed in subsequent experiments (Fig. 4).

4. DISCUSSION OF RESULTS

The experimental relations (Figs. 2, 4) reveal random oscillations of the conversion parameter about the values given by Eq. (2). This behavior can be assigned to the random heat sources which surround the sample and are likewise of a random nature. In addition to such random events, one observes regular variations corresponding to the reverse course of the parameter kinetics (Fig. 2, $B = 0.47$ T) or variations repeating after the same pulse numbers (Fig. 2, $B = 0$ and -0.62 T). Such a behavior can be related to photoinduced scattering of the coherent laser radiation from optical inhomogeneities in the crystal, including thermal ones [3].

The crystal under study has a low dark conductivity; therefore, the effect of magnetic field on the photovoltaic current, diffusion, and drift of carriers may be neglected. This finds explanation in the ratios of the characteristic times corresponding to the experiment and to the crystal properties; namely, $\tau_p \ll (f)^{-1} \ll t \ll \tau_M$, where $\tau_p = 10^{-8}$ s is the laser pulse duration, $(f)^{-1} = 0.04$ s is the pulse spacing, $t = 1.6 \times 10^4$ s is the duration of the experiment, and $\tau_M = 10^{10}$ s is the dielectric relaxation time. The short laser pulse duration results in a short total illumination time $\tau_p t f = 4 \times 10^{-3}$ s; under these conditions, the photoconductivity plays a significant role. Hence, when describing the effect of a magnetic field on optical distortions, the photoconductivity can be neglected. The intrinsic conductivity does not affect the processes occurring during an experiment ($t \ll \tau_M$). In earlier studies [6–9], the effect of a magnetic field on the photorefractive sensitivity was investigated by holographic techniques in heavily doped crystals, which possess a high photorefractive sensitivity in the spectral region of interest. As a result, the main contributions to the formation of the holographic grating are made by the photovoltaic effect and the associated transport phenomena. In our experiment, the currents are low; therefore, the effect of a magnetic field is assigned to the magnetic-field-induced change in the asymmetry of the impurity ion photoionization rather than to the Hall effect. However, the contribution to the total variation in the refractive index from the effects associated with charge transfer is long lasting. This manifests itself in the formation, after a series of

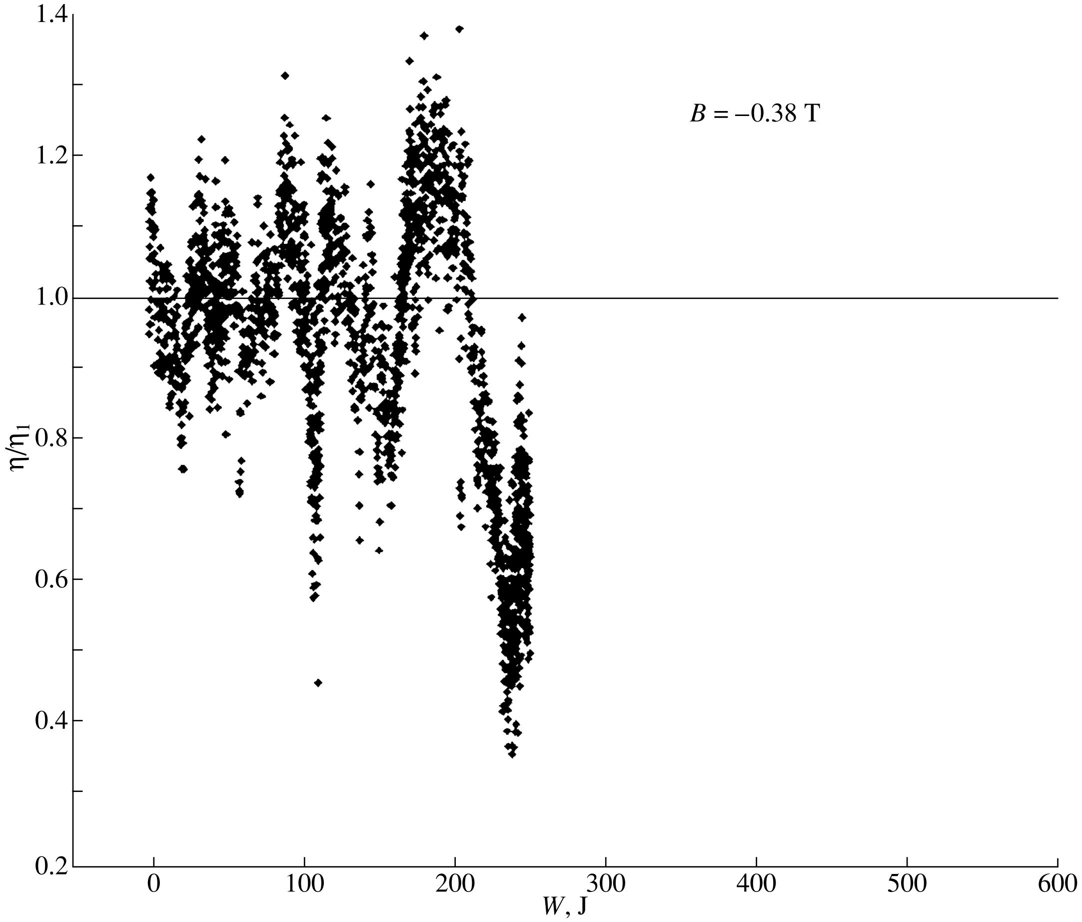

Fig. 4. SHG kinetics in an external magnetic field with induction $B = -0.38$ T cancelling the intrinsic photorefraction. Points are experiment, and the line is fitting by a linear function.

experiments, of transparent rings of optical inhomogeneity, which persists for a long time. The main contribution is due to the mechanism of local ion charge exchange first considered in [14].

The photorefractive properties of lithium niobate are determined by impurities, which are present even in a pure crystal. The paramagnetic ions revealed by EPR in an undoped crystal [15] are primarily Fe^{2+} ($\sim 3 \times 10^{16}$ cm^{-3}), as well as Mn^{2+}, Cr^{3+}, and Ti^{3+} ($<10^{15}$ cm^{-3}). The photoinduced variation of the refractive index in lithium niobate is assigned to charge exchange of the photorefractive centers $Fe^{2+} \rightleftarrows Fe^{3+} + e^-$. The charge system thus formed acts on the optical properties of the crystal through the electrooptical effect. The Fe^{2+} photoionization energies are typically $E_g = 3.1$–3.2 eV [1, 2], and the magnetic moments are $\mu(Fe^{2+}) = 5.4\mu_B$ and $\mu(Fe^{3+}) = 5.9\mu_B$ [16], where μ_B is the Bohr magneton. The laser photon energy at the fundamental frequency is $\hbar\omega = 1.165$ eV. The $E_g/\hbar\omega$ ratio coincides in order of magnitude with the experimental ratio B_1/B_0 which determines the influence of atomic characteristics on the asymmetry of the photoionization process.

Photorefractive properties are related to asymmetry in the photoionization process, whose probability depends on the relative orientation of the laser radiation polarization, optical crystal anisotropy, and external dc fields [3]. In steady-state conditions, the probability of this process depends on the direction of the photoelectron momentum and can be written in the form $\Psi(\theta) = \Psi_0\{1 + f(\vartheta)\}$, where Ψ_0 is the symmetric part of the photoionization probability and $f(\vartheta)$ is a function of direction of the photoelectron momentum relative to the optical axis ϑ characterizing the asymmetry of the process. For optically uniaxial crystals, this function should meet the following requirements: $|f(\vartheta)| \ll 1$ and $f(0) = -f(\pi)$. If the process is one-dimensional, it will suffice to introduce two photoionization probabilities, more specifically, along (Ψ_+) and counter to the optical axis (Ψ_-), which are defined by the equations

$$\Psi_{\pm} = \Psi_0\{1 \pm \xi_A\}, \tag{5}$$

where ξ_A is the asymmetry parameter which characterizes the asymmetry in the photoionization probability and is defined as the ratio of the nonsymmetric to symmetric part of the probability. The photorefractive sensitivity is proportional to the asymmetry parameter, $S_p(B) \sim \xi_A$. Recalling the approximation (4) of the experimental relation $S_p(B)$, we obtain

$$\xi_A(B) = \xi_A^0\left\{1 + \sinh\left(\frac{E_g}{\hbar\omega}\frac{B}{B_1}\right)\sinh^{-1}\left(\frac{E_g}{\hbar\omega}\right)\right\}, \qquad (6)$$

where ξ_A^0 is the asymmetry parameter with no magnetic field applied.

The magnetic field B_1 corresponds to the effective local internal field responsible for the asymmetry in the iron ion potential. This follows from the shape of the magnetic-field dependence of photorefractive sensitivity, Eq. (4), because $S_p(B = -B_1) = 0$. The energy corresponding to field B_1 is $\mu(\mathrm{Fe}^{2+})B_1 = 1.2 \times 10^{-4}$ eV and characterizes the asymmetry of the ion potential in the local crystal lattice field. This energy is much smaller in magnitude than the thermal vibration energy at room temperature $kT = 2.6 \times 10^{-2}$ eV, which becomes manifest in the independence of the processes involved and in the additivity of the photoionization probabilities.

The B_1 field is of an electrical origin, but it acts as an effective magnetic field in the presence of an external magnetic field. An external magnetic field can change the condition of ionization of the photorefractive centers. This field gives rise to an elastic orientational distortion of electronic shells without an attendant electric-charge displacement, which induces an additional asymmetry of the potential. When properly oriented, an external magnetic field cancels the potential asymmetry caused by the internal field.

The experiment reveals an apparent contradiction in the measured data and the experimental geometry having different symmetries. For instance, the experimental dependence of photorefractive sensitivity on magnetic field given by Eq. (4) includes only an odd function, which is the hyperbolic sine, while the experimental geometry has a mirror symmetry with respect to the plane in which the optical axis and the pump wave vector lie (Fig. 1). This contradiction finds ready explanation in the fact that the magnetophotorefractive effect depends not only on the orientation of the iron ion magnetic moment relative to the optical axis but also on the orientation of the laser beam polarization plane and wave vector with respect to the optical axis and magnetic moment, which appears only natural. In the absence of an external magnetic field, the photorefractive sensitivity is nonzero; hence, there is an asymmetry in secondary photoionization of the impurity ions which depends on both the orientation of the optical axis and the directions of the photon momentum and polarization. An external magnetic field introduces an additional asymmetry into the already asymmetric process of photoionization, which is due to the magnetic moments being oriented primarily along the external magnetic field. Thus, the symmetry of the photoionization process is determined by the directions of four vectors, more specifically, those of the optical axis, external magnetic field, and laser radiation wave vector and polarization.

It should be pointed out that the results of a study of the magnetophotorefractive effect performed in the same conditions and on the same sample as in this work can be found in [10]. The only difference is in the crystal orientation relative to the external magnetic field and the pump radiation polarization. The optical axis and the magnetic-induction vector were perpendicular to the pump polarization plane (the case of phase-matched SHG, $oo \longrightarrow e$). The magnetic field amplified the photorefractive effect. The study was carried out only for one value of the field because of the inherent complexity of interpretation of the results obtained. In the case of the $oo \longrightarrow e$ interaction, the SH intensity is comparable with that of the pump radiation and the two intensities vary along the length of the crystal; therefore, in this study, the crystal was rotated through 90° about the laser beam axis. As a result, the SH intensity decreased to a level barely discernible to the eye, which permitted us to neglect its influence and assume the pump radiation to be constant over the crystal length.

Thus, the technique of measuring photorefractive parameters proposed here is based on the kinetics of the phase-mismatched SHG intensity and permits one to determine photorefractive sensitivity in high-quality crystals. To improve the sensitivity of the technique, crystals of large length are needed. Crystals with a high photorefractive sensitivity may be much shorter. The main requirement for the crystals to be studied is that they be of high quality and homogeneity.

The experimental results presented in this communication reveal that a magnetic field noticeably affects the photorefractive processes of undoped lithium niobate. This effect is assigned to the enhancement of asymmetry in the photoionization of the magnetic impurity, namely, of the iron ions present in small amounts in the crystal. The magnetic-field-induced changes in photorefractive sensitivity in crystals with a high content of magnetic impurities (Fe^{2+}) can reach quite high levels, which suggests the possibility of controlling hologram recording parameters and stabilization through proper variation of the magnetic field. This effect can also be used to stabilize the operation of nonlinear-optics devices, in which the effect of photorefractive parameters places a constraint on the application of such crystals.

REFERENCES

1. M. P. Petrov, S. I. Stepanov, and A. V. Khomenko, *Photorefractive Crystals in Coherent Optics* (Nauka, St. Petersburg, 1992).
2. Yu. S. Kuz'minov, *Electrooptical and Nonlinear-Optical Lithium Niobate Crystals* (Nauka, Moscow, 1987).
3. B. I. Sturman and V. M. Fridkin, *Photovoltaic Effect in Media without Center of Symmetry and Related Phenomena* (Nauka, Moscow, 1992).

4. K. Buse, Appl. Phys. B **64**, 273 (1997).
5. K. Buse, Appl. Phys. B **64**, 391 (1997).
6. A. R. Pogosyan, B. N. Popov, and E. M. Uyukin, Fiz. Tverd. Tela (Leningrad) **24**, 2551 (1982) [Sov. Phys. Solid State **24**, 1448 (1982)].
7. I. F. Kanaev, V. K. Malinovskiĭ, and A. M. Pugachev, Fiz. Tverd. Tela (Leningrad) **29**, 692 (1987) [Sov. Phys. Solid State **29**, 396 (1987)].
8. C. Dam-Hansen, P. M. Johansen, P. M. Petersen, and V. M. Fridkin, Phys. Rev. B **52**, 13098 (1995).
9. M. P. Petrov, V. M. Petrov, and P. M. Karavaev, Fiz. Tverd. Tela (St. Petersburg) **39**, 2168 (1997) [Phys. Solid State **39**, 1938 (1997)].
10. V. V. Grishachev, in *Proceedings of the XVII International School–Workshop "Novel Magnetic Materials for Microelectronics"* (Izd. "URSS", Moscow, 2000), p. 264.
11. Chr. A. D. Horst, K.-U. Kasemir, and K. J. Betzler, J. Appl. Phys. **84**, 5158 (1998).
12. K.-U. Kasemir and K. J. Betzler, Appl. Phys. B **68**, 763 (1999).
13. N. I. Koroteev and I. L. Shumaĭ, *Physics of Power Laser Emission* (Nauka, Moscow, 1991).
14. A. P. Levanyuk and V. V. Osipov, Izv. Akad. Nauk SSSR, Ser. Fiz. **39** (4), 686 (1975).
15. I. Sh. Akhmadullin, V. A. Golenishchev-Kutuzov, and S. A. Migachev, Fiz. Tverd. Tela (St. Petersburg) **40**, 1109 (1998) [Phys. Solid State **40**, 1012 (1998)].
16. K. P. Belov, *Electron Processes in Ferrites* (Mosk. Gos. Univ., Moscow, 1996).

Translated by G. Skrebtsov

Physics of the Solid State, Vol. 44, No. 7, 2002, pp. 1370–1379. Translated from Fizika Tverdogo Tela, Vol. 44, No. 7, 2002, pp. 1309–1317.
Original Russian Text Copyright © 2002 by Zarochentsev, Troitskaya.

The Forbidden Gap and Insulator–Metal Transition under Pressure

E. V. Zarochentsev and E. P. Troitskaya
Donetsk Institute of Physics and Technology, National Academy of Sciences of Ukraine, Donetsk, 83114 Ukraine
e-mail: zero@host.dipt.donetsk.ua

Received April 18, 2001

Abstract—The behavior of the energy bands and the band gap width of a compressed insulator crystal is studied. The conduction band energy at the center of a face of the Brillouin zone first increases and then abruptly decreases upon an increase in compression, resulting in a collapse of the forbidden gap and in an insulator–metal (IM) transition. A model proposed for the mechanism of this transition interprets it to be a phase transition of order two and a half. The compression ratio and pressure at which an IM transition occurs in neon under pressure are predicted on the basis of nonempirical calculations of the valence and conduction bands. A simplified model suitable for calculating the metallization effect in more complex crystals is proposed. *© 2002 MAIK “Nauka/Interperiodica”.*

1. INTRODUCTION

In the past 15–20 years, considerable progress has been made in studying the properties of crystals subjected to ultrahigh pressures. This is due to the fact that the experimental investigations of substances under high pressures were carried out on setups containing diamond-anvil cells (DAC) [1]. In this way, pressures of the order of megabars can be attained without a loss in the precision of measurements.

For a number of substances, a sequence of structural phase transitions and the nature of magnetic transformations have been established and electronic-structure transformations of the insulator–metal type (metallization) have been detected. Investigations have been carried out on a wide class of materials including ionic crystals, oxides, silicate glasses, metals, and (in recent years) crystalline structures formed by rare-gas atoms. Of special interest are studies of metallization in compressed rare-gas crystals (RGC), since these crystals are pressure-transmitting media in experimental setups and remain transparent in the optical range under megabar pressures. The change in the type of chemical bonds in the pressure range $p < 0.1$ Mbar was thoroughly traced for the first time for cesium [2].

The progress made in DAC technology necessitated considerable correction to the values of metallization pressure. For example, the metallization pressure in Xe varied from 0.33 Mbar [3] to 1.32 Mbar [4] and 1.5 Mbar [5]. Simultaneous calculations of the band structure predicted the metallization pressure for Xe to be in a wide range from 0.82 to 2.0 Mbar [4]. As a rule, the authors themselves indicated the reason for this discrepancy (the muffin-tin approximation to the APW potential, local exchange, basis, etc.). Similar calculations for Ne predict the metallization pressure to be in the interval from 10 to 1300–1500 Mbar [6–8]. The two-orders-of-magnitude difference cannot be attributed to the approximations used; this difference rather indicates the inapplicability of the methods used. Such approaches are based on a statistical approximation (similar to the Thomas–Fermi approximation) for the exchange-correlation potential, which is well substantiated only for crystals with a large number of electrons in the atom. In recent years, substances containing elements with a small atomic number Z were classed into a special class of low-Z materials. These include solid neon, hydrogen, helium, their solid solutions, etc. [1]. Low-Z materials are employed in investigations in the high-pressure range, since they possess a high compressibility (ensuring a large change in atomic spacing) and a simple electronic structure.

What is the phase-transition mechanism? At what points does the energy band gap vanish? What are the degrees of compression and pressures at which the insulator–metal (IM) transition occurs? These questions must be answered in principle in the course of theoretical investigations. For this purpose, exact band calculations appropriate for high degrees of static compression are required.

This imposes the following requirements on the computational methods used in analyzing the band structure and the equation of state [9] (and, ultimately, the metallization effect): these methods (1) must be free of fitting parameters, (2) must not involve approximations to the crystal field potential which are difficult to control upon varying pressure, (3) must use basis functions suitable for any degree of compression up to the metallization pressure, and (4) should not assume that the overlap integrals of localized basis orbitals are small.

It is expedient to use as a basic approach the Hartree–Fock method, which is clearly formulated, sufficiently accurate, and is not so complicated as to prevent its realization on modern computers.

Band calculations are usually made for $T \neq 0$ disregarding the electron–phonon interaction. Anharmonic effects (at $T \neq 0$) and electron–phonon interaction are generally beyond the framework of the adiabatic approximation and are due to nonadiabatic interactions between quasiparticles. In this paper, we will not consider the many-particle effects in the band structure.

We will discuss the results of analysis of the band structure of neon under pressure. The theory for calculating conduction and valence bands is presented in [10–12] and [13], respectively. Here, we will study the applicability of the Hartree–Fock method modified by us in [12] and the method of hole bands modified in [14] for high pressures. In the framework of the one-electron theory, metallization can be interpreted as an electron topological transition [15].

The present work aims at finding answers to the following three important questions. (1) What is the role of the second- and higher order corrections in overlap integrals to the energy bands? (2) Is it necessary to exactly calculate the energy of filled bands in order to find the crystal potential? (3) What is the microscopic mechanism of the IM transition in terms of the band structure?

We analyzed the behavior of the energy bands and the forbidden gap using different models, including those that are simple in comparison to the comprehensive cluster approach [10, 16]. Using simplified models is dictated by the exact cluster calculations being cumbersome. This article contains the following. In Section 2, the results of calculations of the band structure of solid neon are presented. The behavior of the band gaps upon an increase in compression is considered in Section 3. The mechanism leading to metallization is proposed in Section 4. The obtained results are discussed in Section 5.

2. THE BAND STRUCTURE

In the Hartree–Fock method, the exact (one-particle) Hamiltonian of the crystal is used. This is especially important for calculating the band structure under pressure, since a model for the crystal potential that is valid for normal pressure may become inapplicable under high pressures. The only approximation made in the Hartree–Fock method is the choice of a trial function in the form of one or several determinants constructed from one-electron functions. For a crystal composed of atoms with filled electron shells, we can confine our analysis to the one-determinant approximation without any loss of generality [17]. In analogy with the Hartree–Fock method, hole bands are defined as the energy difference of systems of $2L - 1$ and $2L$ electrons.

The theory of band structure used by us here is described in detail in [10–13]. We will write only the equations and expressions for the potentials of hole bands and conduction bands. The nonlinear set of the Hartree–Fock equations has the form

$$\sum_{s'}^{M}[\delta_{ss'}(\varepsilon_s - E_{\mathbf{k}\nu}) + V_{ss'}(\mathbf{k};\{c\})]c_{s'\nu} = 0, \qquad (1)$$

where ε_s is the energy of an electron of an isolated atom, $E_{\mathbf{k}\nu}$ is the band energy to be determined, $c_{s\nu}(\mathbf{k})$ are variational parameters, and

$$V_{ss'}(\mathbf{k};\{c\}) = N^{-1}\sum_{\mathbf{ln}}\exp[i\mathbf{k}(\mathbf{l}-\mathbf{n})]V_{ss'}^{\mathbf{ln}} \qquad (2)$$

is the one-particle crystal potential, in which

$$\begin{aligned} V_{ss'}^{\mathbf{ln}} &= S_{ss'}^{\mathbf{ln}}\varepsilon_s + [V_{ss'}^{\mathbf{ln}}]_{\mathrm{LCAO}} \\ &+ [\Delta V^{(1)}[\mathcal{R}]]_{ss'}^{\mathbf{ln}} + [\Delta V^{(2)}[\mathcal{R};\{c\}]]_{ss'}^{\mathbf{ln}}. \end{aligned} \qquad (3)$$

Here, $S_{ss'}^{\mathbf{ln}}$ is the overlap integral for orbitals s and s' of atoms $\mathbf{l}$ and $\mathbf{n}$; the second term in Eq. (3) is the potential in the LCAO method taking into account the exchange of electrons from different atoms. Corrections $\Delta V^{(1)}$ and $\Delta V^{(2)}$ depend on the overlapping of orbitals through the matrix

$$\mathcal{R} = I - (I + S)^{-1/2}, \qquad (4)$$

where I is the unit matrix and S is the matrix of overlap integrals with elements $S_{ss'}^{\mathbf{ln}}$. The crystal potential of the cluster-expansion hole band (CEHB) method[1] contains the same terms as does the potential given by Eq. (3) in the Hartree–Fock method, except the last term $\Delta V^{(2)}$.

The conduction band (or the excess electron energy) is calculated using the equation

$$\sum_{\mathbf{g}'}[E_{\mathbf{k}c}\delta_{\mathbf{gg}'} - H_{\mathbf{gg}'}]a_{\mathbf{g}'}(\mathbf{k}) = 0, \qquad (5)$$

where $\mathbf{g}'$ is a reciprocal-lattice vector and $a_{\mathbf{g}'}(\mathbf{k})$ is a parameter to be found. The crystal potential in the OPW method has the form

$$\begin{aligned} H_{\mathbf{gg}'} &= \frac{\hbar^2}{2m^*}(\mathbf{k}+\mathbf{g})^2\delta_{\mathbf{gg}'} + V_{\mathrm{C}}(|\mathbf{g}-\mathbf{g}'|) \\ &+ V_{\mathrm{ex}}(\mathbf{k}+\mathbf{g}, \mathbf{k}+\mathbf{g}') + V_{\mathrm{PK}}(\mathbf{k}+\mathbf{g}, \mathbf{k}+\mathbf{g}'), \end{aligned} \qquad (6)$$

$$V_{\mathrm{C}}(\mathbf{q}) = \frac{4\pi e^2}{\mathbf{q}^2\Omega_0(\rho(\mathbf{q}) - Z)}, \qquad (7)$$

---

[1] The methods for calculating conduction bands (OPW) and hole bands using the cluster expansion [17] are denoted as CEOPW [10] and CEHB [13].

where V_C is the form factor of the Coulomb interaction potential between an excess electron and the remaining electrons of the crystal, m^* is the mass of a band electron, Ω_0 is the unit-cell volume, ρ is the Fourier component of the electron density in the crystal,

$$V_{\text{ex}}(\mathbf{q}, \mathbf{q}') = -\frac{e^2}{2\pi^2}\sum_s \int k^{-2} d\mathbf{k} \Big\{ I_s^*(\mathbf{q}-\mathbf{k}) I_s(\mathbf{q}'-\mathbf{k})$$

$$-\Big[I_s^*(\mathbf{q}-\mathbf{k}) \sum_{s'} I_{s'}(\mathbf{q}'-\mathbf{k}) \mathcal{R}^*_{s's}(\mathbf{q}'-\mathbf{k}) + \text{H.c.} \Big] \quad (8)$$

$$+ \sum_{s's''} I^*_{s'}(\mathbf{q}-\mathbf{k}) I_{s''}(\mathbf{q}'-\mathbf{k}) \mathcal{R}_{s's}(\mathbf{q}-\mathbf{k}) \mathcal{R}^*_{s''s}(\mathbf{q}'-\mathbf{k}) \Big\},$$

V_{ex} is the form factor of the exchange interaction potential, V_{PK} is the form factor of the Phillips–Kleinman potential given by

$$V_{\text{PK}}(\mathbf{q}, \mathbf{q}') = \sum_{ss'} \sum_{\nu} c_{s\nu}(E_{\mathbf{k}c} - E_{\mathbf{k}\nu}) \Big\{ I_s^*(\mathbf{q}) I_{s'}(\mathbf{q}')$$

$$-\Big[I_s^*(\mathbf{q}) \sum_t I_t(\mathbf{q}') \mathcal{R}_{ts'}(\mathbf{q}') + \text{H.c.} \Big] \quad (9)$$

$$+ \sum_{tt'} I_t^*(\mathbf{q}) I_{t'}(\mathbf{q}') \mathcal{R}_{ts}(\mathbf{q}) \mathcal{R}^*_{t's'}(\mathbf{q}') \Big\},$$

and $I_s(\mathbf{q})$ and $\mathcal{R}_{ts}(\mathbf{q})$ are the Fourier transforms of the atomic orbitals $\varphi_{\mathbf{l}s} = |\mathbf{l}s\rangle$ and of the elements of matrix $\mathcal{R}$, respectively:

$$I_s(\mathbf{q}) = \int \varphi_s^*(\mathbf{r}) \exp(-i\mathbf{q}\mathbf{l}) d\mathbf{r},$$

$$\mathcal{R}_{ts}(\mathbf{q}) = \sum_{\mathbf{l} \neq 0} \exp(i\mathbf{q}\mathbf{l}) \mathcal{R}^{l0}_{ls} + \mathcal{R}^{00}_{ls}, \quad \mathcal{R}_{ts}(\mathbf{q}) = \mathcal{R}^*_{sl}(\mathbf{q}).$$

The Phillips–Kleinman potential in the CEOPW method given by Eq. (9) contains the coefficients of wave functions $c_{s\nu}(\mathbf{k})$ and energies $E_{\mathbf{k}\nu}$ of the filled bands of the crystal. In the standard OPW method, $c_{s\nu} = \delta_{s\nu}$, $E_{\mathbf{k}\nu} = \varepsilon_s$ (ε_s is the energy of an isolated atom), and $\mathcal{R} = 0$ ($S = 0$); i.e., only the first term is retained. Solving the secular equations for systems with a one-electron potential in the approximation of two-particle, three-particle, etc. clusters [17], we can obtain the band energy of an electron (CEOPW [10]) and a hole (CEHB [13]) with the accuracy required in each method.

Figure 1 shows the filled bands (with negative energy) and the conduction band (positive energy) of neon in symmetric directions of the Brillouin zone (BZ) for different degrees of compression (from zero to a compression close to metallization).

The analysis was carried out on the basis of several models using different sets of control parameters (overlap integrals S): (1) the standard LCAO (for filled bands) and OPW (for conduction bands) methods without orthogonalization of atomic functions ($S = 0$) (model *1*); (2) the CEHB [13] and CEOPW methods with orthogonalization of atomic functions to the first order in S (model *2*); and (3) the CEHB and CEOPW methods with orthogonalization of atomic functions in two-particle cluster (TPC) approximation [10], which implies a partial summation of the entire series in S (model *3*).

In all three models, the wave functions and energies involved in the Phillips–Kleinman potential were calculated using the corresponding modification of the CEHB method (models *1–3*) or were taken to be equal to their atomic analogs (models *1a–3a*).

The band structure of an uncompressed crystal is that typical of an insulator (Fig. 1a). The lowest two filled (nondegenerate) bands are mainly formed by the 1*s* and 2*s* electronic states and, for $\mathbf{k} = 0$, have the symmetry of the *s* states of an isolated atom (Fig. 1 shows the 2*s* band). Under a compression $u = \Delta V/V_0 \leq 0.9$, the 1*s* band virtually does not differ in energy from the 1*s* energy level of the neon atom (–891.18 eV). The upper filled band originates mainly from the 2*p* levels.

The forbidden gap (which is referred to as the fundamental gap at point Γ, $\mathbf{k} = 0$) separates the filled bands from the conduction bands: a 3*s*-like lower band (having a single branch) and a 3*p*-like band (having two branches, one of which is doubly degenerate and the other is nondegenerate). For low degrees of compression, the lowest conduction band is almost parabolic in shape with $m^* = 0.82m_e$ (m_e is the electron mass). The conduction bands exhibit strong dispersion even in the uncompressed crystal and overlap considerably on the energy scale.

The experimental value of the fundamental gap $E_g(\Gamma)$ in neon under atmospheric pressure is 21.4 eV [18], while the value calculated in model *3* is 25.32 eV. The difference is due to the application of the one-electron approximation, which leads to exaggerated values of the forbidden gap. In [19], the energy of the crystal polarization caused by a hole was estimated to be E = 0.75 eV in calculating the band structure of uncompressed neon; taking into account this polarization, we have $E_g(\Gamma)$ = 24.57 eV.

In Figs. 1b and 1c, the symbols indicate the calculated conduction bands at symmetry points of the Brillouin zone in models *1a–3a* in which the electron energies in an isolated atom are used in the Phillips–Kleinman potential. The largest spread in energies obtained in different models is observed at point X. For all degrees of compression, the following regularity can be seen: the orthogonalization to the first order in S

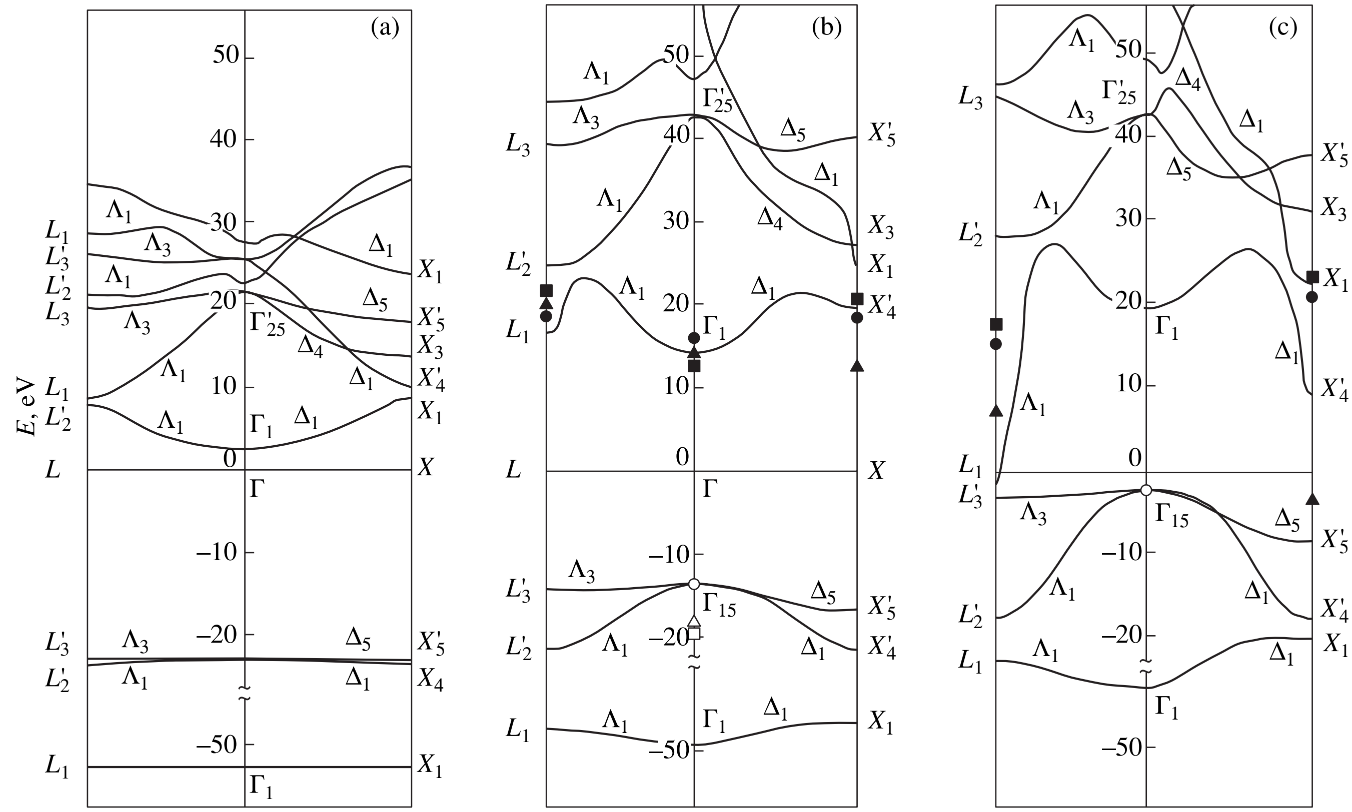

Fig. 1. Band structure of neon for the compression ratio $\Delta V/V_0$ equal to (a) 0, (b) 0.7, and (c) 0.77. Solid curves correspond to energies calculated in model *3*. Dark symbols correspond to the conduction band energy in models *1a* (squares), *2a* (triangles), and *3a* (circles). Light symbols correspond to the valence band energy in models *1* (squares), *2* (triangles), and *3* (circles).

decreases $E(X_4')$ by 25% as compared to its value given by the standard OPW method for $u = 0.7$ and by 130% for $u = 0.77$. However, the inclusion of cluster expansion increases $E(X_4')$.

Let us analyze the effect of the energies of filled bands on the conduction bands in the OPW method. The substitution of the energies of filled bands into the Phillips–Kleinman potential (in model *3*) decreases $E(X_4')$ by more than 50% for $u = 0.77$ (as compared to the result obtained in model *3a*). In contrast to model *3*, the employment of the Bloch functions and energies of the filled bands in the Phillips–Kleinman potential in models *1* and *2* increases the energies of the conduction bands (as compared to the results obtained in models *1a* and *2a*).

It can be seen from Fig. 1 that a difference in the computational models is manifested for large compressions (in the vicinity of the metallization point of the crystal). This allows us to investigate the role of the pointlike-core approximation and of the cluster expansion in the formation of the band structure, as well as the effect of the energies of filled bands on the behavior of the conduction bands under pressure. According to the results of calculations, the contribution of the cluster expansion is the largest among the above-mentioned effects.

Figure 2 shows the results of calculations of the lower conduction bands of neon at all symmetry points and symmetry directions of the Brillouin zone. These bands are calculated using the cluster expansion (taking into account all orders in *S*) in model *3a*. It can be seen from Fig. 2 that the forbidden-gap collapse can occur only at points *L* and *X* (the centers of BZ faces), at which the energy decreases upon an increase in compression. At the remaining points (Γ, *K*, *W*, *U*), the energy (and, hence, the band gap) increases with compression. These results confirm the estimates obtained earlier [19].

3. THE BEHAVIOR OF BAND GAPS IN THE VICINITY OF METALLIZATION

Since the insulator–metal (IM) transition is interpreted as the collapse of the forbidden gap, we will analyze in detail the behavior of the relevant bands and the variation of the gap between the valence bands and empty bands.

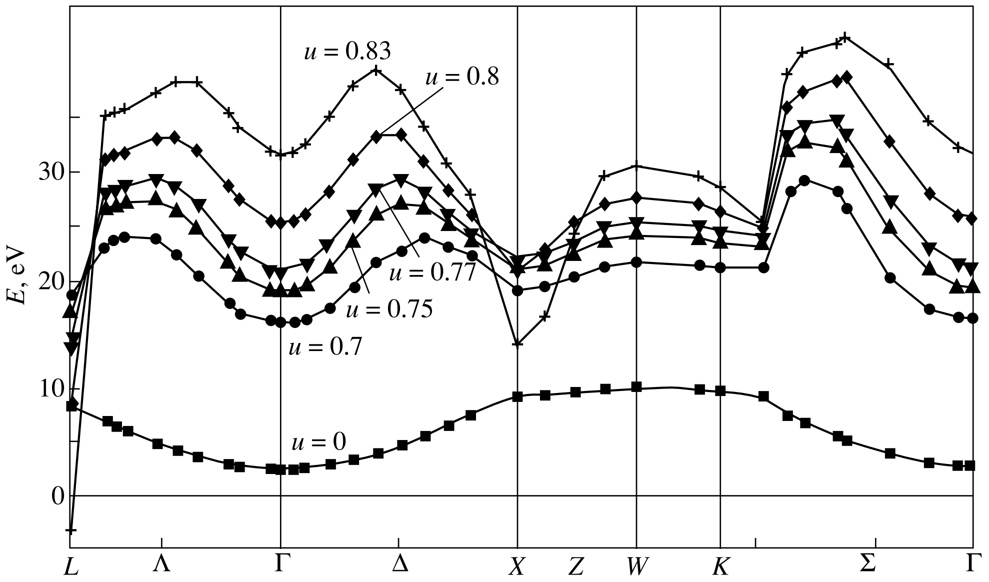

Fig. 2. Theoretical dispersion curves of neon for different values of the compression ratio $u = \Delta V/V_0$.

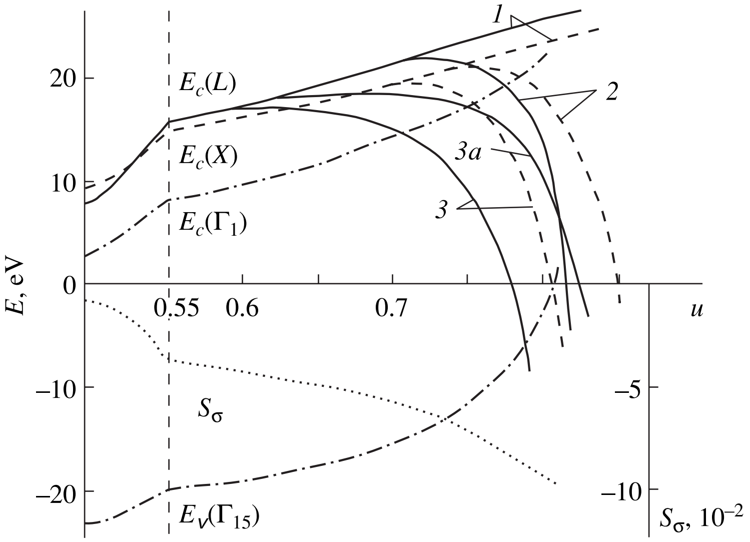

Fig. 3. Energies of the lower conduction bands and the upper filled band of neon as functions of the compression ratio. Solid curves denote energies $E_c(L)$ in models *1–3* and *3a*, dashed curves correspond to $E_c(X)$ in models *1–3*, dot-and-dash curves correspond to $E_v(\Gamma_{15})$ (CEHB method) and $E_c(\Gamma_1)$ (the results obtained in all models coincide to within the graphic error), and the dotted curve corresponds to the largest overlap integral S_σ (see the right-hand scale).

Figure 3 shows the energies of upper valence bands $E_v(\Gamma)$ at point Γ and of the lower conduction band E_c at points Γ, *X*, and *L* (the energies of the conduction band are calculated in different models, see Section 2). The energies $E_v(\Gamma)$ and $E_c(\Gamma)$ increase with the compression ratio $u = \Delta V/V_0$, while the energies $E_c(X)$ and $E_c(L)$ decrease abruptly, starting from $u \sim 0.6$ in models *2* and *3* (but not in model *1*). It can be seen from Fig. 3 that there is no IM transition at all in model *1*, while the metallization compression ratio u_m (corresponding to the IM transition) in model *3* is minimum; this model apparently describes the metallization effect most correctly. The same conclusion is confirmed even more visually in Fig. 4. As before, the smallest value of u_m is obtained in model *3*. The compression ratio corresponding to the IM transition in model *3* is $u_m = 0.78 \pm$

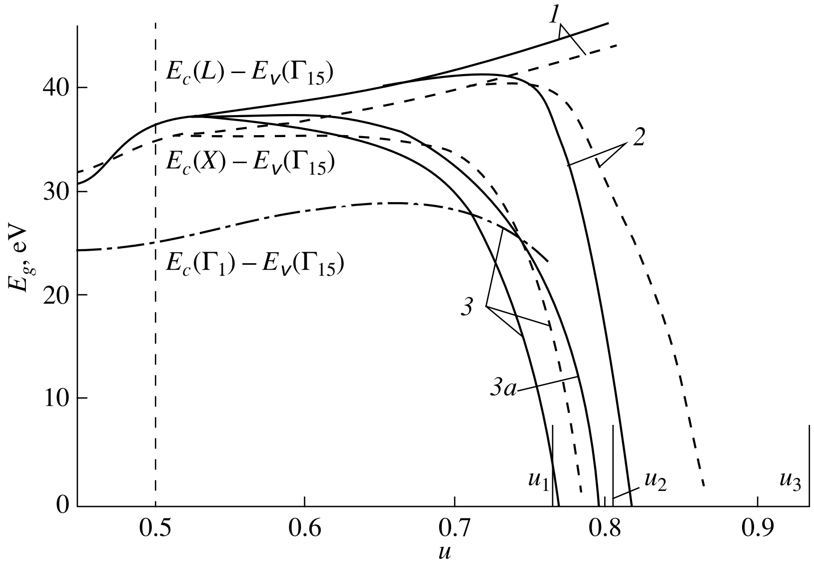

Fig. 4. Band gaps of neon between points *L*, *X*, and Γ of the Brillouin zone as functions of the compression ratio. Solid curves correspond to indirect gaps $E_c(L) - E_v(\Gamma_{15})$ in models *1–3* and *3a*; dashed curves correspond to $E_c(X) - E_v(\Gamma_{15})$ in models *1–3*; and the dot-and-dash curve corresponds to the direct gap $E_c(\Gamma_1) - E_v(\Gamma_{15})$ in model *3*. Vertical lines correspond to theoretical metallization compression ratios u_1 [19], u_2 [6], and u_3 [8].

0.01, which is very close to the estimate obtained in [19]: $u_m = 0.77 \pm 0.02$ (denoted by u_1 in Fig. 4). Other calculations of the metallization compression (u_2 [6], u_3 [8]) give higher values for this quantity. The metallization compression ratio u_m for neon calculated by us in different models falls in the interval 0.80 ± 0.03. This rules out the contingency in determining the metallization point and confirms the reliability and accuracy of our results.

Thus, the metallization compression can be calculated quite accurately in the band theory (the spread in the values of this quantity amounts to 1–3%). However, in view of the fast (almost exponential) increase in pressure with the compression ratio, the determination of the pressure p becomes complicated. This hampers the determination of the equation of state of a crystal for high pressures [9].

A typical feature is a sharp decrease in the energy of lower conduction bands upon an increase in compression (see Figs. 3, 4). The reason for this energy decrease for an excess electron is the repulsion of the lower branches of the conduction band (branches Λ_1, Δ_1; see Figs. 1b, 1c). As a result, the energy of these branches at points *L* and *X* decreases abruptly, while the energy at the remaining symmetry points of the Brillouin zone (Γ, *W*, *K*, *U*) increases with the compression ratio as before. The steep ascent of the upper valence band to point Γ (see Fig. 3) also facilitates the collapse of the indirect gap $E(L, X) - E(\Gamma)$. The descent of the conduction bands at points *L* and *X* does not depend on the model used for band calculations, but the value of the metallization compression is sensitive to the choice of the model. For example, in the model taking into account only $S_\sigma \neq 0$ to the first order, the IM transition occurs at point *X* (and not at *L*), while for $S \equiv 0$, metallization is absent altogether (see Figs. 3, 4).

4. THE MECHANISM OF THE INSULATOR–METAL TRANSITION IN NEON

The structure of the form factor of the potential in the secular equation in the first order in the overlap integral *S* and in the exact cluster theory (cf. the potentials in [10] and [19]) leads to the conclusion that the role of the terms containing the overlap matrix $\mathscr{R}$ in the exact theory increases as the wave vector **k** approaches the BZ boundary. The strong difference between the results of calculations in the vicinity of the BZ boundary with $S \equiv 0$ and to the first order in *S* does not necessitate the inclusion of higher order terms in *S* (matrices $\mathscr{R}$ and *P* differ from *S* insignificantly). This difference is due to the mixing of two lower conduction bands and the form factor *V*, which increases significantly with pressure (Fig. 5). This effect is manifested most strongly at the BZ boundary. Let us illustrate this statement using an fcc lattice as an example.

The calculated $E_{\mathbf{k}c}$ dispersion curves show that a distinguishing feature in the behavior of energy bands under strong compression is the emergence of a minimum in the symmetric directions at points *L* and *X* of the BZ boundary for an fcc lattice. As the compression ratio $\Delta V/V_0$ increases, the $E_{\mathbf{k}c}$ curves ascend at different rates. The lower conduction band at the BZ boundary relatively decreases, and a part of this band (near points *L* and *X*) ultimately overlaps on the energy scale with a part of the valence band near point Γ, indicating the

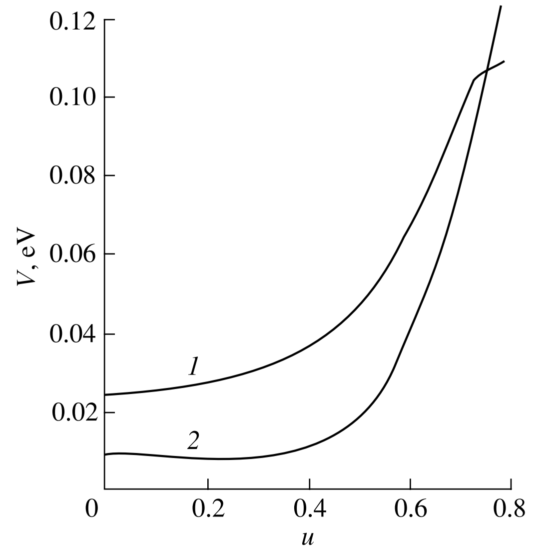

Fig. 5. Dependence of the form factor of potentials on the compression ratio $u = \Delta V/V_0$: $V_L = V(\mathbf{k} + (-1, -1, -1); \mathbf{k})$ for $\mathbf{k} = (0.5, 0.5, 0.5)$ (curve *1*) and $V_X = V(\mathbf{k} + (-2, 0, 0); \mathbf{k})$ for $\mathbf{k} = (1, 0, 0)$ (curve *2*).

onset of an insulator–metal transition. Such a situation may emerge under two different circumstances. First, the lowest and the next-to-lowest conduction bands may be separated by a gap and a minimum at point L (or X) emerges in the lowest band irrespective of the behavior of the next band. Second, the lowest two conduction bands have the same symmetry and ascend at different rates under compression; the lower band “catches up” with the next band, and the minimum of the lower band is a part of the next band, which ascends more slowly.

Let us consider the second possibility in greater detail. We will show (using a simple two-band model) that this situation is of general nature and can be realized not only for neon (in the fcc phase) but in all cases where there are energy bands moving at different velocities.

Calculations show [2] that repulsion of bands takes place in compressed metallic cesium. In this case, band repulsion occurs at points X and L of the Brillouin zone of a bcc lattice and also leads to a phase transition of order two and a half. In contrast to neon, however, this transition is not an insulator–metal transition [15].

For the sake of definiteness, we consider point L. The set of equations for conduction bands under pressure (see, for example, [20]) can be reduced to a set of two equations; i.e., we can effectively take into account only two waves, one with $\mathbf{g} = 0$ and one with $\mathbf{g} = \frac{\pi}{2}(111)$. The reduced excess potential due to compression that mixes these bands can be written as

$$V = V(u) - V(0). \tag{10}$$

Then, the set of equations has the form (in atomic units)

$$\begin{aligned} \left(\frac{1}{2}\mathbf{k}^2 - E\right)a_{\mathbf{k}} + Va_{\mathbf{k}+\mathbf{g}} &= 0, \\ V^*a_{\mathbf{k}} + (1/2(\mathbf{k}+\mathbf{g})^2 - E)a_{\mathbf{k}+\mathbf{g}} &= 0. \end{aligned} \tag{11}$$

Solving the secular equation of this set, we find that, in the case of large compressions $V \geq E_s$ (E_s is the gap between the first and second conduction bands), the lowest conduction band in the vicinity of metallization has the energy

$$E_{c1} = E_0 - V - ax^4 + bx^2, \tag{12}$$

where E_0 is the effective energy of the lowest conduction band at point L and $x = |\mathbf{k} - \mathbf{k}_L|$ is the wave number along the [111] direction. The coefficients a and b can be easily determined (a is always positive).

Expression (12) leads to the following two conclusions: (1) in the vicinity of the metallization point, we have $b \approx a(p_0 - p)$, where p_0 is a certain pressure of the order of the pressure corresponding to the IM transition, and (2) the free term $E_0 - V$ in Eq. (12) is a function of pressure p (or compression), which decreases upon an increase in pressure (since potential V increases, see Fig. 5) and can become negative. The function $E_c(x)$ of Eq. (12) describes the evolution of the lowest conduction band upon an increase in p from a curve with a single peak at point L (for small $p < p_0$) to a curve with two peaks positioned in direction Λ at points $\mathbf{k}_M = \mathbf{k}_L \pm \sqrt{b/2a}$ and a minimum at point L. The phase-transition mechanism is not associated with the inclusion of S and is universal in nature, although the inclusion of S considerably affects the magnitude of compression (or pressure) corresponding to metallization.

We note that, in this model, the density of states in the conduction band at point L has a singularity $|p_0 - p|^{1/4}$ [21] which differs from the van Hove singularity $|p_0 - p|^{1/2}$. This circumstance can serve as an experimental confirmation of a certain model of the conduction bands.

5. DISCUSSION

Let us consider quantitative manifestations of the inclusion of the Abarenkov–Antonova cluster expansion (CE) for the orthogonalizing matrix for compressed neon. First, we will analyze the effect of the CE on the localized basis functions.

In the two-particle cluster approximation [17], the orthogonalized atomic orbitals χ_{1s} are constructed from nonorthogonal atomic orbitals $\varphi_{\mathbf{l}s}$:

$$\begin{aligned}\chi_{\mathbf{l}s} &\equiv \varphi_{\mathbf{l}s} - \sum_{\mathbf{l}\neq\mathbf{l}'}\sum_{s'}\varphi_{\mathbf{l}'s'}\mathcal{R}[\mathbf{l}\mathbf{l}']^{\mathbf{l}'\mathbf{l}}_{s's} - \sum_{\mathbf{l}\neq\mathbf{l}'}\sum_{s'}\varphi_{\mathbf{l}s'}\mathcal{R}[\mathbf{l}\mathbf{l}']^{\mathbf{l}\mathbf{l}'}_{s's} \\ &= \varphi_{\mathbf{l}s} - \frac{1}{2}\sum_{\mathbf{l}\neq\mathbf{l}'}\sum_{s'}\varphi_{\mathbf{l}'s'}S^{\mathbf{l}'\mathbf{l}}_{s's} + \frac{3}{8}\sum_{s'}\varphi_{\mathbf{l}s'}(S^2)^{\mathbf{l}\mathbf{l}}_{s's} + O(S^3),\end{aligned} \tag{13}$$

where $\mathcal{R} = I - (I + S)^{-1/2}$, $\mathbf{l}$ and $\mathbf{l}'$ are the vectors of the direct lattice, and index s labels the orbitals of an isolated atom. Orthogonalization that takes into account the CE [first row in Eq. (13)] differs from orthogonalization to the first order in S [the term proportional to S in the second row in Eq. (13)] by (a) the substitution $\mathcal{R}$ in the off-diagonal block of matrix $\mathcal{R}^{\mathbf{l}\mathbf{l}'} \longrightarrow \frac{1}{2}S^{\mathbf{l}\mathbf{l}'}$ (i.e., for $\mathbf{l} \neq \mathbf{l}'$) and (b) the presence of diagonal blocks $\mathcal{R}^{\mathbf{l}\mathbf{l}} \sim S^2 + O(S^4)$, which are disregarded in orthogonalization to the first order in $\mathbf{S}$.

In the case of neon, the contribution from the cluster expansion to the elements of the off-diagonal block $\mathcal{R}^{\mathbf{l}\mathbf{l}'}$ is small (1–2% for $u = 0$–0.8). This is due to the smallness of the overlap integrals for neon as compared to other RGCs [12]. The relation between the diagonal and off-diagonal blocks is approximately the same (the values of $\mathcal{R}^{\mathbf{l}\mathbf{l}}_{ss'}$ constitute 25–30% of $\mathcal{R}^{\mathbf{l}\mathbf{l}'}_{ss'}$ for $u \sim 0.7$–0.8) for all RGCs. In some cases (e.g., while calculating the exciton states), the excited states of electrons in the atom must be included in the basis. In this case, the overlap integrals are large even for neon ($S_{3s2p} = -0.0503$, $S_{3s3s} = 0.527$) for $u = 0$ [22] and the necessity of the cluster expansion becomes obvious.

Although the value of $\mathcal{R}^{\mathbf{l}\mathbf{l}}$ is an order of magnitude smaller than $\mathcal{R}^{\mathbf{l}\mathbf{l}'}$ for small compressions ($u < 0.5$), the diagonal block constitutes approximately 25% of the off-diagonal block even for $u \sim 0.75$. Furthermore, the larger quantities $\mathcal{R}^{\mathbf{l}'\mathbf{l}}$ in Eq. (13) are multiplied by small "tails" of the functions centered at neighbor sites, while the smaller quantities $\mathcal{R}^{\mathbf{l}\mathbf{l}}$ are multiplied by the function $\varphi_{\mathbf{l}s}$ centered at the same site. For this reason, both blocks make comparable contributions to function χ. This effect also occurs in the density matrix of a solid.

Let us estimate the effect of the CE on the conduction band. In this case, dispersion curves depend on the CE through the elements of matrix $\mathcal{R}_{ss'}(\mathbf{k})$ appearing in the crystal potential in Eq. (6). These curves are displaced relative to those obtained in the lowest order approximation in S by a quantity which is independent of the wave vector $\mathbf{k}$ and increases with compression. This quantity is given by

$$\delta_{ss'} = \mathcal{R}_{ss'}(\mathbf{k}) - S_{ss'}(\mathbf{k}) \approx \sum_{\mathbf{h}}\mathcal{R}[\mathbf{h}0]^{00}_{ss'}, \tag{14}$$

where $\mathbf{h}$ is a vector of the direct lattice. However, in the equations of the OPW method, $\mathcal{R}_{ss'}$ is multiplied by functions of the wave vector; therefore, the CE contribution to the band energies depends on the point of the Brillouin zone. The largest contribution comes from the cluster expansion at points X and L of the Brillouin zone for compressions higher than $u \sim 0.7$ (Fig. 1).

The refining of Eq. (5) of the OPW method with the help of orthogonalization of atomic orbitals and cluster expansion (CEOPW method) reveals the problem associated with the linear dependence of the OPW basis functions, leading to the emergence of parasitic roots. The measure of the linear dependence of the OPW basis functions is the magnitude of Gram's determinant, which is the determinant of the matrix constructed from the overlap integrals for different OPWs [23]. The application of the cluster expansion reduces the value of Gram's determinant by one or two orders of magnitude for $u = 0.7$–0.8 (in the vicinity of the metallization point), facilitating the emergence of parasitic roots. This can be avoided by using rougher models (e.g., with $S = 0$), but these models do not guarantee correct values of the metallization compression. Consequently, knowing the features of parasitic roots [24], one must separate them from solutions having a physical meaning.

The inclusion of the cluster expansion in calculations of only conduction bands leads to an increase in the band energies and band gaps. The inclusion of the CE in the calculations of filled bands leads to a decrease in the band gaps. In addition, the substitution of the filled-band energies calculated with the CE in the Phillips–Kleinman potential (model *3*) reduces the conduction band energies, this effect being the strongest at the center of a BZ face (Fig. 1). The balance of the abovementioned three tendencies gives the metallization compression $u = 0.78 \pm 0.01$ in model *3*.

Let us consider possible simplified models suitable for calculation of the properties of complex crystals, namely, models with the following simplifications: (1) orthogonalization of wave functions to the first order in S and (2) substitution of the energy of electrons of isolated atoms for the electron energies in filled bands in the Phillips–Kleinman potential.

The dependence on the variable atomic spacing through the overlap integrals is present explicitly in matrices $\mathcal{R}$ and P and implicitly in the variational parameters c_α and in the hole band energy $E_{\mathbf{k}}$, which are calculated separately for each value of pressure. The table illustrates the effect of varying S on the band energy at the center of the BZ (point Γ) and at its boundaries (points X, L, K, W). For the compression ratio $\Delta V/V_0 = 0.6$, a change in S_σ by a few percent introduces a change in energy of the same order of magnitude at high-symmetry points X and L on the BZ boundary and an order-of-magnitude smaller energy change at the BZ center and at less symmetric points K and W. For $\Delta V/V_0 = 0.75$, the change in energy amounts to tens of percent (40% at point X and 68% at point L), remain-

Effect of variation of S_σ on energy bands at symmetry points of the Brillouin zone for different compression ratios

$\Delta V/V_0$	0.6	0.7	0.75
$\lvert S_\sigma \rvert$	0.043	0.064	0.079
$\lvert \Delta S_\sigma \rvert$	0.002	0.003	0.004
ζ	4.6	4.7	5
η_Γ	0.20	0.26	0.29
η_X	4.12	11.90	39.54
η_L	4.69	18.29	67.93
η_K	0.44	2.38	4.42
η_W	0.59	0.98	1.19
dE_Γ/dS	0.35	0.467	0.55
dE_X/dS	–10.55	–16.45	–7.425
dE_L/dS	–10.30	–11.13	–7.45
dE_K/dS	1.60	–7.17	–9.58
dE_W/dS	2.20	3.13	–3.25

Note: E_Z is the conduction band energy at point Z, $\eta_Z = \frac{\lvert E_Z(S + \Delta S) - E_Z(S) \rvert}{E_Z(S)} \times 100\%$, and $\zeta = \frac{\Delta S_\sigma}{S_\sigma} \times 100\%$.

Energy values are in electronvolts, η and ζ in percent, and S_σ are dimensionless.

ing insignificant at points Γ, *K*, *W*, and *U*. The last five rows of the table show that as we approach the metallization point, the values of the derivatives dE/dS decrease, remaining negative at points *X* and *L*.

The increase in the role of wave function overlapping at the BZ boundary casts a shadow of doubt over the confinement of the theory to the lowest order in *S*. However, considering that the structure of the form factor of the potential as a function of overlapping is completely the same in the lowest order in *S* and in the exact cluster theory (cf. the potentials in [19] and in [10–12]), we have no grounds to complicate the theory by introducing higher order terms in *S* for describing the insulator–metal transition in neon and more complicated crystals. As in the simplified model in [19], the calculations based on a more exact model *3a* confirmed that the energy bands at points Γ, *K*, *W*, and *U* are not affected by a change in the overlap integrals. As regards the replacement of the energies of valence bands in the Phillips–Kleinman potential by atomic levels, calculations (based on models with letter "a" and without it in their labels) show that the magnitude of the metallization compression changes insignificantly.

6. CONCLUSIONS

Thus, the calculations show unambiguously that the metallization compression ratio is not sensitive to the details of the model used; however, the pressure corresponding to the insulator–metal transition is extremely sensitive to the model used even for neon in view of the exponential form of the equation of state and can amount to 3 to 10 Mbar for neon according to our calculations [9].

The calculations based on a more exact model, *3a*, for symmetry directions in the Brillouin zone allow one to draw a further conclusion. These calculations indicate the upper boundary for the metallization compression in the Hartree–Fock method used by us. The metallization compression ratio $u_m = \Delta V/V_0 = 0.83$ obtained in this model still differs significantly from the metallization compression ratio $u_m > 0.94$ [7, 8].

In [7, 8], the band structure and metallization of Ne under pressure were investigated. In [7], the Kohn–Sham equations with the exchange-correlation correction for a homogeneous electron gas and with a correction for the electron self-action were solved. The 1*s* electrons of atoms were included in the rigid core. The potential created by these electrons was taken into account in the muffin-tin (MT) approximation. The energies and wave functions of 1*s* electrons were assumed to be equal to their atomic counterparts. The direct gap (19.5 eV) calculated in [7] for normal pressure turned out to be close to the experimental value 21.4 eV [18]. However, the metallization pressure was found to be anomalously high (p_m = 1580 Mbar, $u_m = \Delta V/V_0 = 0.98$). Hama [7] explained such a high metallization pressure (a) as a consequence of the MT approximation used, (b) the inadequacy of the rigid-core approximation, and (c) the possible structural pressure-induced phase transitions disregarded in [7].

The first two explanations were refuted by Boettger [8], who did not use the MT approximation and did not divide electrons into core electrons and valence electrons. Boettger employed the Kohn–Gaspar–Sham local-density approximation to the exchange potential and the method of linear combination of Gaussian-type orbitals developed by him earlier. The obtained value of metallization pressure p_m = 1340 Mbar was not regarded as anomalous for Ne in [8] and was explained (a) by the collapse of more distant energy bands as regards the principal quantum numbers (each band was assumed to be formed by a single electron shell of the atom) and (b) by strong repulsion between 1*s* electrons upon a decrease in the distance between the atoms, which makes the Ne crystal rigid.

A common feature of publications [7] and [8] is the application of a local-density approximation for the exchange potential, which cannot be controlled under high pressures. In our opinion, the anomalously high values of p_m obtained in [7, 8] and the closeness of the results of calculations in those papers are associated precisely with this circumstance.

Our calculations based on a nonlocal exchange potential do not lead to an anomalously high value of metallization pressure for neon but do match the result that was obtained in [6] (10 Mbar) and corresponds to the Herzfeld criterion [25] predicting $u_m \sim 0.8$ for the entire series of RGCs; this was confirmed experimentally for Xe. Consequently, methods based on the statistical approximation may be inapplicable to crystals with a small atomic number Z (low-Z materials), including light cryocrystals.

ACKNOWLEDGMENTS

The authors are grateful to V.G. Bar'yakhtar for his interest in this research and for valuable discussions of the results and to their colleagues for their help in calculations.

This work was supported by the International Science Foundation, grant no. QSU 082067.

REFERENCES

1. R. J. Hemley and H. K. Mao, in *Encyclopedia of Applied Physics* (Wiley-VCH, Weinheim, 1997), Vol. 18, p. 555.
2. S. G. Louie and M. L. Cohen, Phys. Rev. B **10** (8), 3237 (1974).
3. D. A. Nelson and A. L. Ruoff, Phys. Rev. Lett. **42** (6), 383 (1979).
4. K. A. Goettel, J. H. Eggert, J. F. Silvera, and W. C. Moss, Phys. Rev. Lett. **62** (6), 665 (1989).
5. R. Reichlin, K. I. Brister, A. K. McMahan, *et al.*, Phys. Rev. Lett. **62** (6), 669 (1989).
6. N. H. March, in *Advances in High Pressure Research*, Ed. by R. S. Bradley (Academic, New York, 1969), Vol. 3, p. 241.
7. J. Hama, Phys. Lett. A **105** (6), 303 (1984).
8. J. C. Boettger, Phys. Rev. B **33** (8), 6788 (1986).
9. E. V. Zarochentsev and E. P. Troitskaya, Fiz. Tverd. Tela (St. Petersburg) **43** (7), 1292 (2001) [Phys. Solid State **43**, 1345 (2001)].
10. Yu. V. Eremeĭchenkova, E. V. Zarochentsev, and E. P. Troitskaya, Teor. Mat. Fiz. **106** (3), 498 (1996).
11. E. Troitskaya, Yu. Eremeichenkova, and E. Zarochentsev, Condens. Matter Phys. **8**, 157 (1996).
12. V. G. Bar'yakhtar, E. V. Zarochentsev, E. P. Troitskaya, and Yu. V. Eremeĭchenkova, Fiz. Tverd. Tela (St. Petersburg) **40** (8), 1464 (1998) [Phys. Solid State **40**, 1330 (1998)].
13. E. V. Zarochentsev, E. P. Troitskaya, and Yu. V. Eremeĭchenkova, Metallofiz. Noveĭshie Tekhnol. **21** (5), 3 (1999).
14. V. K. Sribnaya and K. B. Tolpygo, Fiz. Nizk. Temp. **6** (3), 366 (1980) [Sov. J. Low Temp. Phys. **6**, 175 (1980)].
15. E. V. Zarochentsev and E. P. Troitskaya, Fiz. Tverd. Tela (Leningrad) **30** (8), 2367 (1988) [Sov. Phys. Solid State **30**, 1365 (1988)].
16. I. V. Abarenkov and I. M. Antonova, Fiz. Tverd. Tela (Leningrad) **20** (2), 565 (1978) [Sov. Phys. Solid State **20**, 326 (1978)].
17. I. V. Abarenkov, I. M. Antonova, V. G. Bar'yakhtar, V. L. Bulatov, and E. V. Zarochentsev, *Methods of Computational Physics in the Theory of Solid State: Electronic Structure of Perfect and Imperfect Crystals* (Naukova Dumka, Kiev, 1991).
18. U. Rossler, in *Rare Gas Solids*, Ed. by M. L. Klein and J. Venables (Academic, New York, 1975).
19. E. V. Zarochentsev and E. P. Troitskaya, Fiz. Tverd. Tela (Leningrad) **27** (11), 2474 (1985) [Sov. Phys. Solid State **27**, 1480 (1985)].
20. V. G. Bar'akhtar, E. V. Zarochentsev, and E. P. Troitskaya, *Theory of Adiabatic Potential and Atomic Properties of Simple Metals* (Gordon & Breach, London, 1999).
21. *Problems of Physical Kinetics and Physics of Solid State: Collection of Scientific Works*, Ed. by A. G. Sitenko (Naukova Dumka, Kiev, 1990), p. 176.
22. V. K. Sribnaya, K. B. Tolpygo, and E. P. Troitskaya, Fiz. Tverd. Tela (Leningrad) **20** (6), 1688 (1978) [Sov. Phys. Solid State **20**, 977 (1978)].
23. V. V. Dyakin, B. I. Reser, and V. P. Shirokovskii, Phys. Status Solidi B **50**, 459 (1972).
24. B. I. Reser and V. V. Dyakin, Phys. Status Solidi B **87**, 41 (1978).
25. K. F. Herzfeld, Phys. Rev. **29**, 701 (1927).

Translated by N. Wadhwa

Physics of the Solid State, Vol. 44, No. 7, 2002, pp. 1380–1387. Translated from Fizika Tverdogo Tela, Vol. 44, No. 7, 2002, pp. 1318–1325.

Phase Transformations in CuO Caused by Bombardment by He^+ Ions and by the Action of Spherical Shock Waves

**B. A. Gizhevskiĭ*, V. R. Galakhov*, D. A. Zatsepin*, L. V. Elokhina*,
T. A. Belykh**, E. A. Kozlov***, S. V. Naumov*, V. L. Arbuzov*,
K. V. Shal'nov*, and M. Neumann******

** Institute of Metal Physics, Ural Division, Russian Academy of Sciences,
ul. S. Kovalevskoĭ 18, Yekaterinburg, 620219 Russia*

e-mail: gizhevskii@imp.uran.ru

*** Ural State Technical University, ul. Mira 19, Yekaterinburg, 620002 Russia*

**** All-Russia Research Institute of Technical Physics, Russian Federal Nuclear Center,
Snezhinsk, Chelyabinsk oblast, 454070 Russia*

***** Osnabrück University, Osnabrück, D-49069 Germany*

Received July 10, 2001

Abstract—The valence state of copper ions and the phase composition of copper monoxide CuO subjected to bombardment by He^+ ions and explosive shock waves are studied by the methods of x-ray photoelectron spectroscopy (XPS) and x-ray emission spectroscopy (XES). Measurements of photoelectron Cu 2*p* and emission O K_α spectra revealed a decrease in the concentration of Cu^{2+} ions and partial reduction of CuO to Cu_2O as a result of both ion bombardment and shock-wave loading. The concentration of the Cu_2O phase attained values of 10–15%. The Cu_2O phase is revealed by the XPS and XES methods even at concentrations lower than its threshold concentration for detection by x-ray diffraction measurements. This points to the effectiveness of XPS and XES techniques in studying nanocrystalline materials and defect structures containing finely dispersed inclusions. A model for the emergence of Cu_2O due to the formation of charged clusters under the action of stress waves is proposed. *© 2002 MAIK "Nauka/Interperiodica".*

1. INTRODUCTION

High-intensity external effects, such as bombardment by high-energy ions, the action of shock waves, and considerable plastic strains, may change the charge (valence) states of ions in compounds of transition metals and cause phase transformations associated with such changes. Complex compounds may experience a deviation from the local stoichiometric composition, decomposition, and segregation of impurities. These effects are responsible for changes in the physical and chemical properties of the initial compound and the formation of new phases. Information on such processes is important for creating new materials, as well as for explaining the behavior of a material under extreme conditions.

Under the action of external agents, oxides can experience partial reduction or oxidation accompanied by a change in the valence of the cation. Copper monoxide CuO can serve as an example of such a system. This compound has become an object of intense investigations in connection with high-temperature superconductivity, since CuO forms the chemical basis of HTSC cuprates and possesses properties similar to those of the semiconductor phases of HTSC compounds [1]. In addition, CuO is of interest for practical application as a photosensitive material, a catalyst, and a gas sensor [2–4]. The effect of ion bombardment on the properties and phase composition of CuO has been investigated by a few authors [5–7]. There are practically no publications devoted to the effect of shock waves on the electron structure and properties of CuO. For this reason, study of the effects of ion bombardment and shock-wave loading of CuO is of considerable interest.

Analysis of systems subjected to intense external effects is complicated by a lack of clarity as to the type of transformation involved, as well as by a small amount or high dispersity of newly formed phases. The application of standard methods of x-ray phase analysis (XPA) based on x-ray diffraction measurements is hampered in view of diffraction line broadening due to finely dispersed inclusions and high lattice stresses. Effective methods for studying such complicated defect systems are x-ray photoelectron spectroscopy (XPS) and x-ray emission spectroscopy (XES). These methods make it possible to determine the charge (valence) state of ions and the type of variation of the chemical bonds and to detect new phases [8]. In the present work, the XPS and XES methods were used for studying changes in the valence state of Cu ions and phase transformations in copper monoxide (CuO) irradiated by helium ions or subjected to the action of spherical isentropic shock waves [9–11].

Copper monoxide is a comparatively stable oxide with a decomposition temperature exceeding 1000°C under atmospheric pressure. It was proved by us earlier [5–7] that CuO is reduced to Cu_2O as a result of bombardment by high-energy ions or electrons, as well as under intense plastic strains (pressure-induced shear). According to x-ray diffraction measurements, new phases are formed in CuO for fluences $F \geq 3 \times 10^{17}$ cm^{-2} of He^+ ions ($E = 4.65$ MeV). However, changes in the electrical and optical properties, as well as in the lattice parameters, are observed for lower fluences (~10^{17} cm^{-2}). In the present work, we concentrate our attention on CuO samples subjected to bombardment with ions and to shock-wave loading in which the formation of new phases cannot be detected by the standard x-ray diffraction methods.

2. SAMPLES AND EXPERIMENTAL TECHNIQUES

Polycrystalline samples of CuO were obtained from CuO powder of 99.8% purity by annealing in air at 1220 K for 50 h. The sample of $Cu_{0.99}Li_{0.01}O$ used was prepared using the method of solid-phase reactions, carried out at 970 K for 24 h (using an appropriate mixture of CuO and Li_2CuO_3) followed by annealing at 1220 K. The CuO single crystal was grown from a solution in melt. According to x-ray diffraction measurements, the obtained samples had a single phase, a monoclinic lattice, and unit-cell parameters typical of CuO: $a = 0.4689$ nm, $b = 0.3423$ nm, $c = 0.5128$ nm, and $\beta = 99.58°$. The parameters of the $Cu_{0.99}Li_{0.01}O$ sample were $a = 0.4686$ nm, $b = 0.3416$ nm, $c = 0.5124$ nm, and $\beta = 99.60°$.

Bombardment by He^+ ions was carried out on a U-120 cyclotron at the Ural State Technical University. The energy of He^+ ions was 4.65 MeV, the beam flux density was 1.2×10^{12} cm^{-2} s^{-1}, the fluence F was varied from 10^{17} to 3×10^{17} cm^{-2}, and the temperature at which the bombardment was carried out did not exceed 370 K. In the case of a single-crystal sample, the natural face (110) was exposed to radiation. The thickness of the irradiated samples was 1–2 mm.

The loading of CuO by converging spherical isentropic shock waves was carried out at the All-Russia Research Institute of Technical Physics, Russian Federal Nuclear Center, by detonation of a hexogen-containing explosive layer with an RDX-based composition, having a thickness $h = 8$ mm, placed on the surface of a hermetic steel casing containing a CuO sphere of diameter 49 mm with an initial density constituting ~70% of the theoretical value. The spherical billet (prior to its explosive compression) was prepared by static compression of CuO powder followed by fritting [10, 11]. During explosive loading, the pressure on the outer surface of the CuO sphere was ~20 GPa for a load pulse duration of 1.5 μs. The pressure at the front of a converging spherical shock wave in the central part (of radius ≤1 mm) of the sphere exceeded 200 GPa. The experimental setup for explosive loading by converging spherical shock waves is described in [9, 10]; the results of investigation of a material subjected to bulk compression are presented in [10, 11].

Samples for spectral investigations were cut from different spherical layers of a loaded sphere characterized by the relative radius r/r^* (r is the radius of the layer under investigation, and r^* is the radius of the CuO sphere after loading). As a converging spherical shock wave propagates to the center of a sphere, the radial and tangential components of stresses at the front of the converging shock wave increase considerably. The temperature and the plastic strain also increase. These factors can lead to decomposition of the material under investigation, stimulate redox reactions for certain values of the layer radius, and facilitate the formation of new phases [12, 13]. It was shown in [14] that a nanocrystalline microstructure with a crystallite size of 10–100 nm formed in spherical layers with $r/r^* > 0.5$ as a result of explosive loading of CuO carried out according to [9, 10]. In deeper layers, the crystallites had a larger size due to the annealing being performed at an elevated temperature after loading. The crystallite size was estimated using scanning tunneling microscopy. The obtaining of nanocrystalline CuO (by using loading with spherical isentropic shock waves) and its microscopic structure are considered in greater detail in [14].

The x-ray Cu 2p photoelectron spectra were obtained on a Perkin Elmer PHI 5600 ci Multitechnique System x-ray photoelectron spectrometer with excitation by monochromatized Al K_α radiation (energy of exciting photons of 1486.6 eV). The samples (single crystals or pressed pellets) were crushed in a high vacuum (preparation chamber) before recording. The fracture of samples in vacuum ensured a clean surface free of external impurities that were not present in the prepared sample. The resolution of the spectrometer was 0.3–0.4 eV.

The x-ray O K_α emission spectra were obtained by the primary technique on a JCXA-733 x-ray microanalyzer. The instrumental broadening was ~0.5 eV.

3. RESULTS AND DISCUSSION

3.1. X-ray Diffraction Measurements

The x-ray diffraction measurements of the irradiated samples indicate a certain broadening of diffraction lines. A slight increase in parameter b is observed for polycrystals. The Cu_2O phase could not be seen on the diffraction patterns of irradiated samples for $F < 3 \times 10^{17}$ cm^{-2}. The nanocrystalline samples obtained from explosive loading display a considerable broadening of diffraction lines and a certain change in the lattice parameters [14]. No new phases were observed on the diffraction patterns of shock-wave loaded samples for $0.6 < r/r^* \leq 1$.

3.2. X-ray Cu 2p Photoelectron Spectra

X-ray photoelectron spectroscopy is a powerful tool for investigating the state of oxidation of metal atoms. The valence state of ions determines the binding energy of electrons in inner shells and the form of the spectrum.

Figure 1 shows the x-ray Cu 2*p* photoelectron spectra of a CuO single crystal and a $Cu_{0.99}Li_{0.01}O$ polycrystal bombarded by He ions ($F = 1 \times 10^{17}$ cm^{-2}), as well as of a CuO sample subjected to the action of spherical isentropic shock waves ($r/r^* = 0.75$). The spectra of standard CuO and Cu_2O samples are also shown for comparison. In addition, the spectrum of standard CuO in the form of solid lines is superimposed, for the sake of visualization, on the spectra of all samples subjected to the shock-wave action or irradiation. The Cu 2*p* photoelectron spectrum of a $Cu_{0.99}Li_{0.01}O$ sample before irradiation coincided with the spectrum of undoped CuO. The photoelectron spectra of irradiated samples were recorded from the fracture surface perpendicular to the irradiated surface. We did not strive to trace the variation of the spectrum over the depth of the sample, since the measuring-beam diameter (~0.1 mm) was much larger than the projective mean free path of He^+ ion, amounting to 10.4 μm according to estimates obtained using the "Transport of Ions in Matter" (TRIM) program. The choice of position of the beam on the fracture surface was determined by the conditions of the most intense signal and the minimum distance from the irradiated surface.

The Cu_2O spectrum has a spin-doublet form; i.e., it contains Cu $2p_{3/2}$ and Cu $2p_{1/2}$ lines with a binding energy of 932.5 and 952.3 eV, respectively. The CuO spectrum is characterized by peaks at higher values of binding energy (M_1 and M_2 peaks) and satellites S_1 and S_2. According to the concept of charge transfer from oxygen ions to a metal [15], the fundamental lines M_1 and M_2 are due to electron configurations $2p^53d^{10}\underline{L}$ of the final state of the electron system, while the satellite structure S_1 and S_2 is associated with the multiplet

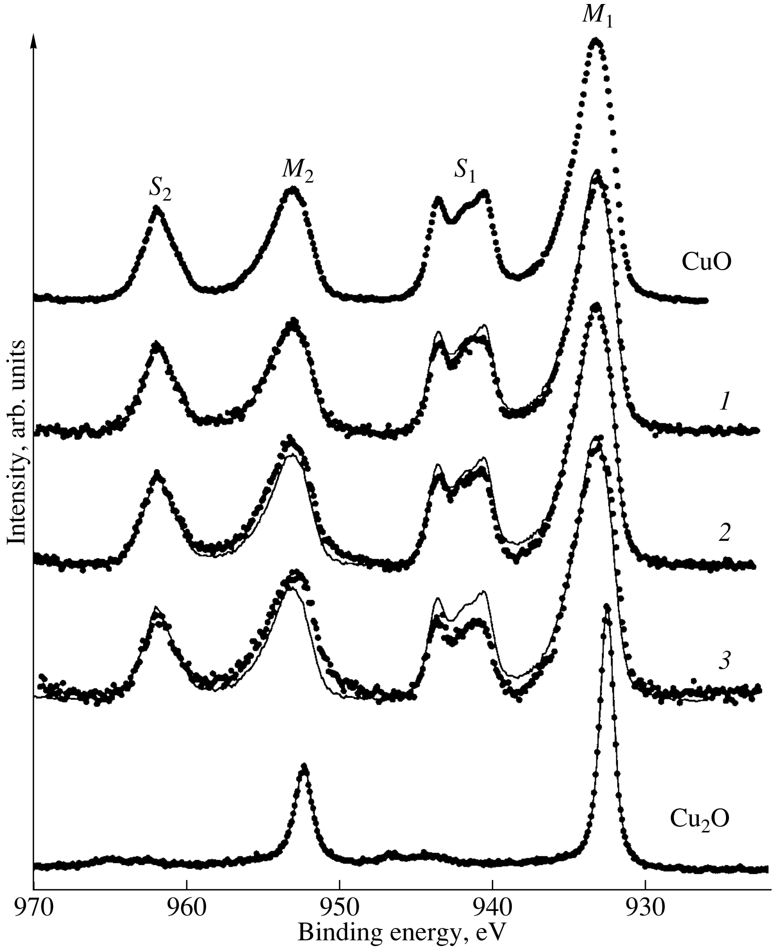

Fig. 1. X-ray Cu 2*p* photoelectron spectra of (*1*) a CuO single crystal, (*2*) a $Cu_{0.99}Li_{0.01}O$ polycrystal irradiated with He^+ ions, and (*3*) a CuO sample subjected to the action of spherical isentropic shock waves. The solid curve shows the spectrum of the initial sample. The spectra of standard samples of monocrystalline CuO and polycrystalline Cu_2O are also shown.

nature of electron states in the Cu^{2+} ion and corresponds to the $2p^5 3d^9$ configuration. Here, $\underline{L}$ denotes a hole in the $2p$ shell of oxygen ions appearing as a result of charge transfer to the $3d$ shell of copper ions.

After the effect of shock waves or bombardment by He ions, the spectra experience certain changes; the intensity of the satellite structure decreases, and peaks M_1 and M_2 are slightly displaced towards lower energies. The decrease in the intensity of the satellites in samples subjected to external effects indicates a decrease in the concentration of Cu^{2+} ions as compared to the initial state; i.e., it indicates a reduction process. It can be seen from Fig. 1 that the decrease in the intensity of the satellites is observed in all samples subjected to irradiation or the action of shock waves, indicating a partial reduction of the samples. After the bombardment by ions, reduction is observed both for single crystals and for polycrystals. It should be noted that doping with Li does not hamper the reduction process, in spite of the fact that this doping formally leads to the formation of Cu^{3+}.

If the Cu_2O phase is formed as a result of external action on CuO, the x-ray Cu $2p$ photoelectron spectrum of an irradiated sample or of a sample subjected to explosive loading can be represented as the sum of the spectra of the initial components (CuO and Cu_2O). The normalization of the spectra can be carried out assuming that the satellites of the charge-transfer transition have the same intensity, i.e., by normalizing to the amount of the CuO phase. In this case, the difference spectrum must reflect the Cu_2O phase. In Fig. 2a, such a procedure is carried out for a CuO sample irradiated by He^+ (spectrum *1* in Fig. 1), while Fig. 2b shows the spectrum of a CuO sample subjected to the action of shock waves (spectrum *3* in Fig. 1). The difference spectrum coincides with the spectrum of Cu_2O in the position of the peak. Hence, it follows that we have indeed singled out the contributions from monovalent copper ions in the Cu_2O phase and that the changes in the Cu $2p$ photoelectron spectra of the samples after the external action are mainly associated with the formation of Cu_2O. The contribution from monovalent copper is estimated from the relative intensity of the normalized spectra of CuO subjected to external effects and of the standard CuO sample. The concentration of monovalent copper for the irradiated sample amounts to ~6%. In the case of the shock-wave loaded sample ($r/r^* = 0.75$), the concentration of Cu^+ ions is approximately 7% of the total amount of copper.

3.3. X-ray O K_α Emission Spectra

Measurements of x-ray emission oxygen K_α spectra of CuO subjected to intense external effects confirm and supplement the results of photoelectron investigations. The O K_α emission spectra emerge as a result of the electron transition O $2p \longrightarrow$ O $1s$ and reflect the distribution of the O $2p$ partial states of oxygen in the valence band. These spectra are different for CuO and Cu_2O oxides [8]. It can be seen from Fig. 3 that the O K_α spectrum of the bivalent-copper oxide CuO has a more intense peak *A* at 526 eV as compared to peak *B* at 524.5 eV. Partial reduction of CuO, i.e., the transition from CuO to Cu_2O, reduces the relative intensity of peak *A*. This makes it possible to use the O K_α spectra to identify the oxides of monovalent and bivalent copper.

Indeed, for CuO samples irradiated by He^+ ions with a fluence of 3×10^{17} cm^{-2}, for which the Cu_2O phase can be clearly seen on the diffraction patterns, the O K_α spectra exhibit a considerable suppression of peak *A* and an increase in the height of peak *B* (Fig. 3). An approximation of such a spectrum under the assumption that CuO and Cu_2O spectra make additive contributions leads to an estimate of the concentration of the Cu_2O phase at approximately 20%. The method of detection of the Cu_2O phase through the measurement of O K_α spectra is found to be more sensitive than the measurement of x-ray diffraction patterns. This can be seen for CuO bombarded by electrons with an energy at 5 MeV and a fluence of 3×10^{18} cm^{-2} (Fig. 3). Diffraction measurements do not reveal the presence of the Cu_2O phase in this sample. However, the O K_α spectra show that the sample contains approximately 3% Cu_2O.

The measurements of x-ray emission O K_α spectra were also used in studying phase transformations in CuO subjected to loading by spherical isentropic shock waves. Figure 4 shows the emission O K_α spectra for five CuO samples cut from spherical layers of a compressed sphere lying at different depths (having different relative radii). Samples *1–5* correspond to the relative radii $r/r^* = 0.5$, 0.6, 0.7, 0.9, and 0.95, respectively. It can be seen from Fig. 4 that with decreasing sample number, i.e., with decreasing distance from the center of the sphere, peak *A* decreases and peak *B* increases, indicating an increase in the amount of Cu_2O. The description of the experimental spectra by the additive sum of the spectra for CuO and Cu_2O makes it possible to estimate the concentration of the Cu_2O phase. In the extreme outer sample *5*, the Cu_2O phase was not detected. As we approach the center of the sphere, the Cu_2O concentration increases and amounts to 7, 9, 12, and 17% for samples *4*, *3*, *2*, and *1*, respectively. For these samples, thorough x-ray diffraction measurements were made in order to reveal a second phase. The measurements were made on a STADY-P diffractometer in the transmission mode with a large statistics of counts. Cu_2O traces were revealed only for samples *1* and *2*. The diffraction patterns for the remaining samples contained only the lines of the monoclinic CuO lattice with slightly increased parameters [14]. Thus, the phase analysis of the nanocrystalline system Cu–O carried out on the basis of the x-ray O K_α emission spectra

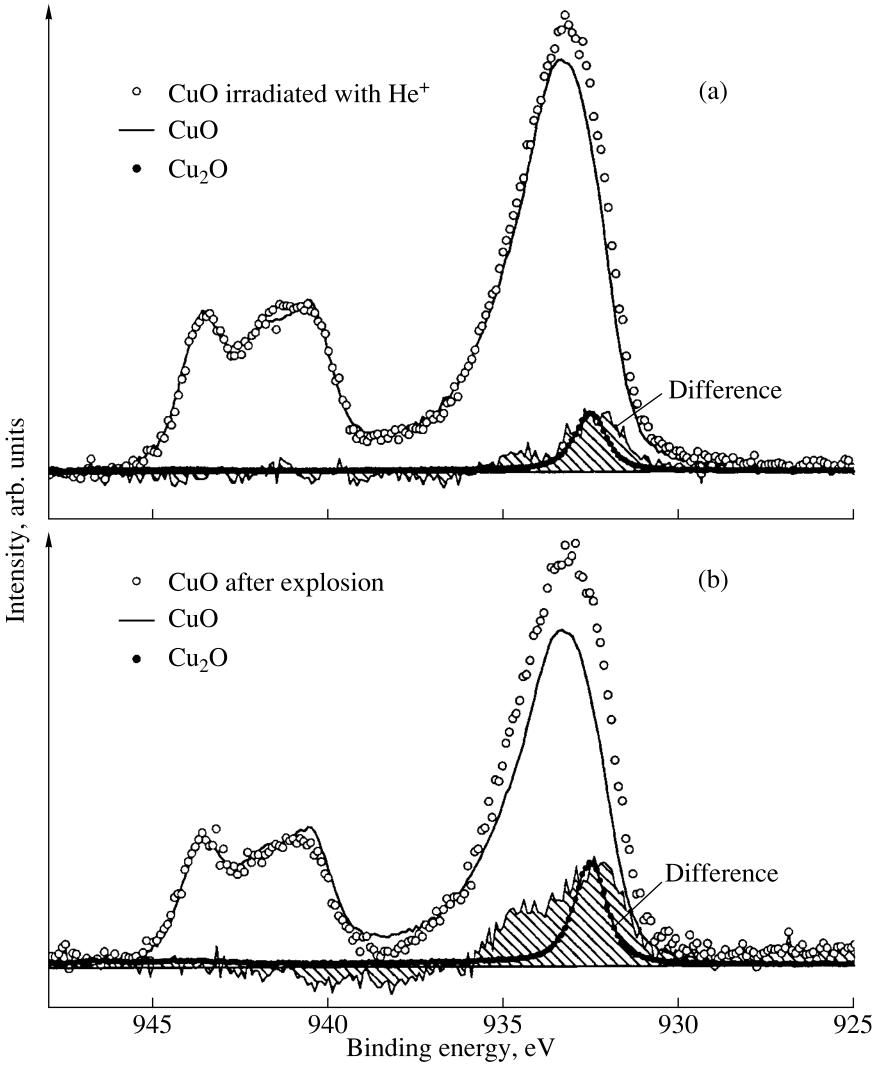

Fig. 2. (a) X-ray Cu $2p_{3/2}$ photoelectron spectra of a CuO sample irradiated by He^+ ions and of a standard CuO sample and the "difference" spectrum compared with the Cu $2p_{3/2}$ spectrum of Cu_2O. The intensities of the first two spectra are leveled out according to the satellite structure. (b) The same for a CuO sample subjected to the action of shock waves.

proves to be more effective than the x-ray diffraction methods.

The results presented in Fig. 4 were obtained three months after the explosive loading of the sphere and opening of the hermetic casing. Approximately 1.5 years later, measurements of the O K_α spectra were repeated. After 1.5-year holding, the spectra of all the samples were found to be virtually the same as the spectrum of pure CuO. This means that the finely dispersed phase of Cu_2O embedded into the nanocrystalline phase of CuO is not stable under conventional holding conditions. The return to the CuO composition (oxidation of Cu_2O) occurs not only on the surface but also in the bulk of the sample. This follows from the O K_α spectra obtained from the fracture of the samples. The instability of nanocrystalline powders, which are nonequilibrium systems with a high reactivity, is well known [16]. In the present case, this effect is apparently also associated with the metastable nature of nanocrystalline material even if the sample is in the compacted high-density state as in our experiments. It should be noted that a certain amount of excess oxygen could be diluted in the CuO lattice after the shock-wave loading and decomposition of some part of CuO in deeply lying layers of the sphere. The possibility of obtaining a solid solution of oxygen in CuO under an elevated pressure is reported in [17].

It was mentioned above that the changes in the Cu 2*p* photoelectron spectra of CuO may be associated with a decrease in the Cu^{2+} concentration, changes in the chemical bond, and the formation of new phases containing copper ions with a different valence. In our opinion, a possible reason for a distortion of photoelectron spectra could be the formation of clusters and com-

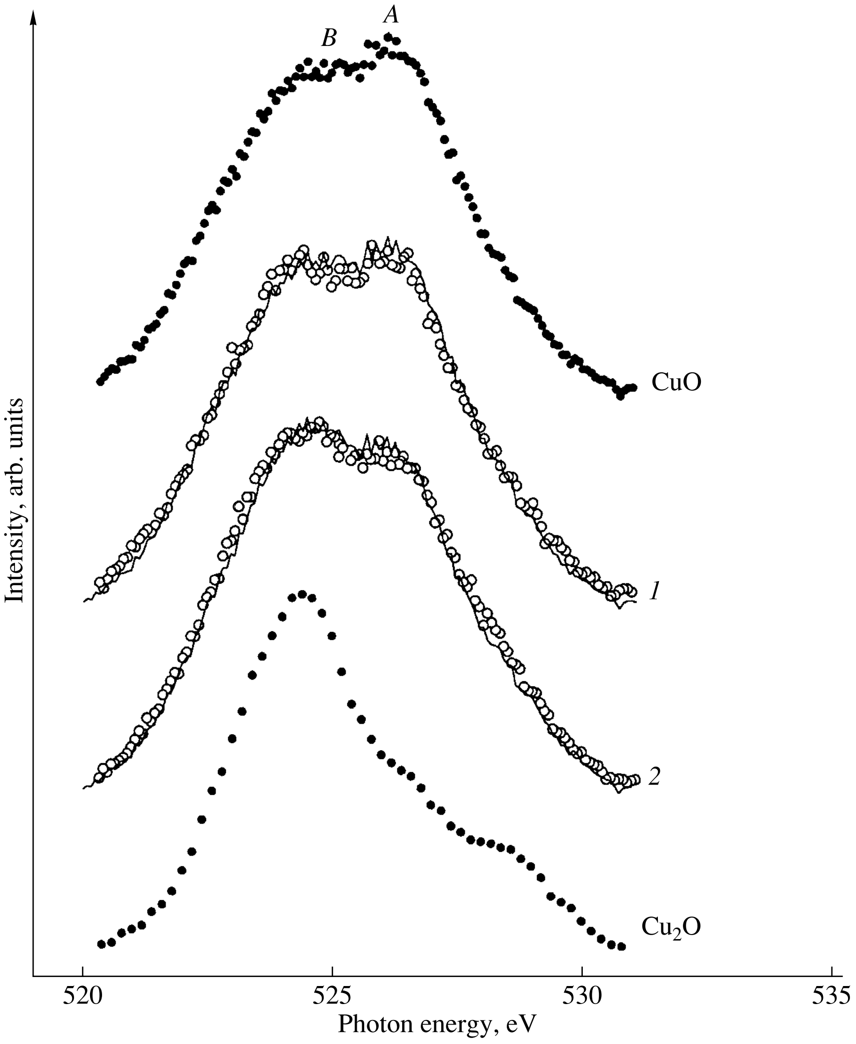

Fig. 3. X-ray O K_α emission spectra of CuO samples bombarded with (*1*) electrons and (*2*) ions. Experimental spectra are shown by light circles, and calculated spectra are shown by solid curves. Dark circles correspond to the spectra of the standard CuO and Cu_2O samples.

plexes containing copper ions with an intermediate valence. The possibility of the formation of such clusters in CuO was demonstrated in [1]. According to that publication, random factors or external effects (including irradiation by charged particles and plastic deformations) lead to the formation of electron $(CuO_4)^{7-}$ and hole $(CuO_4)^{5-}$ clusters in CuO. The existence of such clusters was established experimentally [1, 5] from the emergence of absorption bands in the IR spectra of CuO. Such bands were also observed by us in CuO subjected to shock-wave loading. The electron and hole clusters have an extra electron or hole as compared to the unperturbed cluster $(CuO_4)^{6-}$, which determines the electron structure of CuO and is a structural element of CuO and HTSC cuprates. The excess charge is smeared over the entire cluster. In the case of an electronic cluster, the effective valence of the cation decreases. If the concentration of electronic clusters is high enough, they can serve as the centers of formation of the reduced phase Cu_2O. Thus, the emergence of electronic clusters, which are electronic defects, and the subsequent formation of the reduced phase on their basis can serve as the microscopic mechanism of formation of Cu_2 in CuO upon irradiation by charged particles or loading by shock waves and under intense static plastic deformations.

In addition to the reduction of CuO to Cu_2O under high-intensity external effects, the formation of solid solutions and intermediate phases, such as Cu_4O_3, is also possible. This compound is known to be a very rare mineral (paramelaconite) that cannot be synthesized in pure form [18]. The existence of Cu_4O_3 and a number of other copper oxides was substantiated by the thermodynamic analysis carried out in [19]. An analysis of the

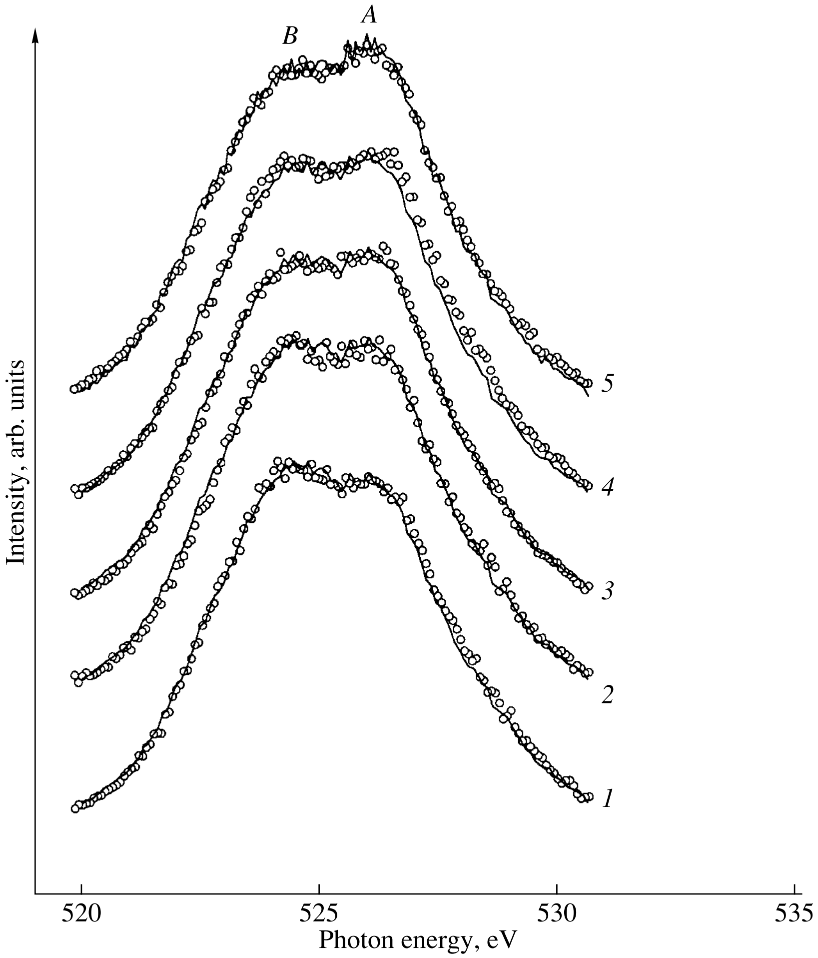

Fig. 4. X-ray O K_α emission spectra of CuO samples subjected to the action of shock waves for r/r^* equal to (*1*) 0.5, (*2*) 0.6, (*3*) 0.7, (*4*) 0.9, and (*5*) 0.95. Experimental spectra are shown by circles, and calculated spectra are shown by solid curves.

emission spectra of CuO subjected to the action of shock waves revealed that the O K_α spectrum for one of the samples could not be described by the additive sum of the spectra of Cu_2O and CuO; however, that spectrum turned out to be unstable and, after some time, reverted to a form similar to the spectra of other samples in Fig. 4. It cannot be ruled out that immediately after cutting of the compressed sphere, this sample contained a certain amount of unstable Cu_4O_3.

A comparison of the results of investigations for CuO samples irradiated by charged particles and subjected to shock-wave loading shows that the reduction process takes place in both cases. The reduction in this case is not a conventional temperature-controlled process, since in both cases the temperature is not high. Under the conditions of shock-wave loading, this statement is true for the outer layers of the sphere with $r/r^* > 0.5$ [10, 11]. During the bombardment with ions, the substrate with samples was cooled with water and the temperature was monitored by a thermocouple. The cause of phase transformations in this case could be stress waves leading to “loosening” of the crystal lattice, the emergence of charged defects, and the displacement of oxygen atoms (which are more mobile in CuO [20]). Stress waves are noticeably intensified near the center of the sphere upon its loading by converging spherical shock waves. Similar waves are also formed at the end of collision cascades in the case of bombardment with ions [21]. Direct experiments on the reduction of CuO at room temperature by shear under pressure confirm our assumption [5, 6]. The microscopic mechanism of the redox processes generated by stress waves in the Cu–O system may be associated with the formation of electron and hole clusters.

4. CONCLUSIONS

Thus, we have demonstrated the effectiveness of the methods of x-ray photoelectron and x-ray emission spectroscopy in the study of the charge state of cations and phase transformations in CuO as a result of intense external effects such as irradiation with high-energy ions and explosive shock-wave loading. The application of XPS and XES opens new opportunities in the study of nanocrystalline materials and defect structures containing finely dispersed inclusions for which the application of classic x-ray diffraction methods is insufficient. The XPS and XES methods mutually control and supplement each other, ensuring quantitative estimates of the concentration of copper ions of various valences and the concentration of various phases in the Cu–O system.

We have demonstrated the possibility of the reduction processes in CuO proceeding as a result of ion bombardment and shock-wave loading for much lower fluences and amplitudes of pressure (plastic strains) in the shock wave front than those at which new phases can be detected using the standard XPA methods. The main factor acting on these processes is the high-intensity stress waves. The common microscopic mechanism of the reduction of CuO as a result of irradiation with ions and shock-wave loading may be the formation of electronic clusters with a formally lowered valence of the cation, which serve as nuclei for the formation of reduced phases.

It is found that the Cu_2O phase formed in nanocrystalline CuO after shock-wave loading is unstable. At the same time, finely dispersed inclusions of Cu_2O emerging in CuO single crystals and polycrystals after their bombardment with ions remain relatively stable for several years.

It should be noted that the developed methods of analysis of the Cu–O system with the help of x-ray photoelectron and x-ray emission spectroscopy are applicable not only to copper oxides but also to compounds of other transition metals.

ACKNOWLEDGMENTS

This work was supported by the Russian Foundation for Basic Research (project nos. 01-02-96403, 99-03-32503, 00-15-96575) and by the “X-ray Spectroscopy of Oxides of *d* Metals Subjected to High-Intensity Actions” grant awarded to the winners of the Competition of Young Scientists (Russian Academy of Sciences) on Fundamental and Applied Studies.

REFERENCES

1. A. S. Moskvin, N. N. Loshkareva, Yu. P. Sukhorukov, *et al.*, Zh. Éksp. Teor. Fiz. **105** (4), 967 (1994) [JETP **78**, 518 (1994)].
2. P. J. Sebastion, Mater. Manuf. Processes **11** (2), 215 (1996).
3. A. S. Ahmad, G. A. Elshobaky, A. N. Alnoaini, and H. G. Elshobaky, Mater. Lett. **26** (1–2), 107 (1996).
4. D. J. Yoo and S. J. Park, J. Electrochem. Soc. **143** (4), L89 (1996).
5. B. A. Gizhevskiĭ, T. A. Belykh, S. V. Naumov, *et al.*, Fiz. Khim. Obrab. Mater., No. 1, 9 (1998).
6. D. A. Zatsepin, V. R. Galakhov, B. A. Gizhevskii, *et al.*, Phys. Rev. B **59** (1), 211 (1999).
7. N. N. Loshkareva, Yu. P. Sukhorukov, S. V. Naumov, *et al.*, Fiz. Tverd. Tela (St. Petersburg) **41** (9), 1564 (1999) [Phys. Solid State **41**, 1433 (1999)].
8. D. A. Zatsepin, V. R. Galakhov, M. A. Korotin, *et al.*, Phys. Rev. B **57** (8), 4377 (1998).
9. E. A. Kozlov, E. V. Abakshin, and V. I. Tarzhanov, RF Patent No. 2124716 (1997).
10. E. A. Kozlov and B. A. Gizhevskiĭ, Preprint No. 137, VNIITF RFYaTs (All-Russia Research Institute of Technical Physics, Russian Federal Nuclear Center, Snezhinsk, 1998).
11. B. A. Gizhevskiĭ, E. A. Kozlov, M. V. Degtyarev, *et al.*, Fiz. Khim. Obrab. Mater., No. 3, 52 (1999).
12. E. A. Kozlov, Yu. N. Zhugin, B. V. Litvinov, *et al.*, Dokl. Akad. Nauk **353** (2), 183 (1997) [Phys. Dokl. **42**, 128 (1997)].
13. S. S. Batsanov, Usp. Khim. **40** (4), 579 (1986).
14. B. A. Gizhevskiĭ, E. A. Kozlov, A. E. Ermakov, *et al.*, Fiz. Met. Metalloved. **92** (2), 41 (2001).
15. J. Zaanen, C. Westra, and G. A. Sawatzky, Phys. Rev. B **33** (12), 8060 (1986).
16. A. I. Gusev, Usp. Fiz. Nauk **168** (1), 55 (1998) [Phys. Usp. **41**, 49 (1998)].
17. G. A. Slack, G. Demazeau, T. Plante, and L. Rabardel, Phys. Rev. B **47** (18), 12018 (1993).
18. P. E. D. Morgan, D. E. Partin, B. L. Chamberland, and M. O’Keeffe, J. Solid State Chem. **121**, 33 (1996).
19. G. K. Moiseev and N. A. Vatolin, Zh. Fiz. Khim. **72** (10), 1751 (1998).
20. N. J. Calos, J. S. Forrester, and G. B. Schaffer, J. Solid State Chem. **122** (2), 273 (1996).
21. D. I. Tetel’baum, V. P. Sorvina, and M. G. Belyanina, Vysokochist. Veshchestva **2**, 47 (1995).

Translated by N. Wadhwa

Physics of the Solid State, Vol. 44, No. 7, 2002, pp. 1388–1393. Translated from Fizika Tverdogo Tela, Vol. 44, No. 7, 2002, pp. 1326–1331.
Original Russian Text Copyright © 2002 by Akopyan, Labzovskaya, Novikov, Golubok, Rozanov, Denisov, Pavlova, Fedorov.

LOW-DIMENSIONAL SYSTEMS
AND SURFACE PHYSICS

Formation of the HgI_2 Crystalline Phase in the Bulk and on the Surface of Nanocrystalline Matrices

I. Kh. Akopyan*, M. É. Labzovskaya*, B. V. Novikov*, A. O. Golubok, V. V. Rozanov**, E. P. Denisov***, T. A. Pavlova***, and D. L. Fedorov*****

** Research Institute of Physics, St. Petersburg State University,*
Ul’yanovskaya ul. 1, Petrodvorets, St. Petersburg, 198904 Russia
*** Institute of Analytical Instrument Making, Russian Academy of Sciences,*
Rizhskiĭ pr. 26, St. Petersburg, 198103 Russia
**** Baltic State Technical University, St. Petersburg, 198005 Russia*

Received August 2, 2001; in final form, October 22, 2001

Abstract—This paper reports on the results of investigations into the phase composition of HgI_2 microcrystals formed in the bulk and on the surface of different nanocrystalline matrices: pressed, finely dispersed (with a specific surface of more than 210 m^2/g) aluminum oxide powders; porous borosilicate glasses with pore radii ranging from 2 to 20 nm; and Al_2O_3–HgI_2 and SiO_2–HgI_2 nanocrystalline composites. The results of spectroscopic analysis (diffuse reflection, absorption, and luminescence spectroscopy) are complemented by the data of atomic-force microscopy (AFM) and x-ray diffraction. The experimental results indicate that nonequilibrium modifications, namely, the high-temperature yellow phase and the orange phase metastable in bulk crystals at all temperatures, can be stabilized in HgI_2 nanoparticles at room temperature. *© 2002 MAIK “Nauka/Interperiodica”.*

1. INTRODUCTION

In recent years, considerable interest has been expressed by researchers in manifestations of quantum-well effects in optical spectra of semiconductors [1]. A large amount of experimental data has been accumulated to date. However, these data should be analyzed with due regard for the fact that a decrease in the size of particles can be accompanied by a change in their crystal structure. In particular, this is indicated by the tendency of small-sized particles to crystallize in the cubic modification for CdS and CdSe [2] and in the hexagonal modification for CuBr [3]. Earlier [4], we demonstrated the possibility of stabilizing nonequilibrium phases in HgI_2 and PbI_2 nanocrystals. In the present work, we continued these investigations and examined the growth kinetics of HgI_2 crystal nuclei on the surface of nanocrystalline matrices. Moreover, we analyzed the possibility of forming metastable modifications of small-sized HgI_2 crystals. According to Bube [5], HgI_2 crystals can occur in the red tetragonal α modification, which is stable at temperatures below 134°C, and in the high-temperature yellow orthorhombic β modification. It is also known that HgI_2 crystals can exist in the orange modification, which is metastable over the entire temperature range covered (15–134°C) [6].

2. SAMPLE PREPARATION

The experiments were performed with the following samples.

(1) Composites $x\mathrm{HgI}_2$–$(1 - x)\mathrm{Al}_2\mathrm{O}_3$ were prepared by mechanical mixing of chemically pure HgI_2 with a finely dispersed Al_2O_3 powder (with a specific surface of more than 210 m^2/g) under standard conditions. This powder was predominantly composed of nanoparticles. Pores between nanoparticles could serve as a matrix for mercuric iodide whose mole fraction x varied from 1 to 0.05. Silicon dioxide was also used as a nanocrystalline adsorbent. Since the adsorbent surface readily absorbed water, powders of Al_2O_3 and SiO_2 prior to mixing were heat treated for a few hours at $T = 200°C$ in order to remove water from the pores. A number of prepared mixtures were also heat treated at $T = 100°C$.

(2) Composites $x\mathrm{HgI}_2$–$(1 - x)\mathrm{Al}_2\mathrm{O}_3$ and $x\mathrm{HgI}_2$–$(1 - x)\mathrm{SiO}_2$ were prepared by the mixing of components preliminarily dried under vacuum.

(3) Microcrystals of HgI_2 were formed in the bulk and on the surface of different matrices: (i) pellets of nanocrystalline Al_2O_3 were pressed under a pressure of 0.2–0.7 MPa and filled with mercuric iodide through diffusion in the course of direct contact between the pellets and HgI_2, and (ii) porous borosilicate glasses with pore radii ranging from 2 to 20 nm either were filled with mercuric iodide through diffusion or were saturated using a HgI_2 solution in acetone [4].

The formation of HgI_2 crystal nuclei on the surface was investigated as mercuric iodide escaped from the bulk of the HgI_2-filled matrices.

3. RESULTS AND DISCUSSION

3.1. The composites prepared in an air atmosphere (both subjected and not subjected to preliminary heat treatment) have a pink color whose intensity depends on the mole fraction of HgI_2. It is found that, as the concentration x in these composites decreases, the temperature of the structural phase transition from the red modification to the yellow modification of mercuric iodide increases ($T_0 = 134°C$ is the temperature of the $\alpha \longrightarrow \beta$ transition for pure bulk crystals) and reaches $T = 154°C$ for mixtures with $x = 0.1$ (see table).

According to Newkirk [7], the phase transition temperature can increase to 154°C for HgI_2 particles when their radius becomes less than 20 μm. Newkirk [7] attributed the considerable shift of the interphase boundary to size-dependent superheating processes and assumed that the surface nucleation spontaneously occurs in more homogeneous small-sized particles. Maskasky [8] also observed an increase in the temperature of the structural phase transition in small-sized AgI crystals (from 147°C in bulk crystals to 168°C in microcrystals with a decrease in their size to 260 nm).

Taking into consideration the results obtained in [7], it can be assumed that, as the concentration x in the aforementioned mixtures decreases, the relative number of particles with small sizes increases and the mean size of crystallites in the mixtures with $x = 0.1$ does not exceed at least 20 μm.

3.2. Upon the mixing of powders preliminarily dried in a cell evacuated to a pressure of $\sim 10^{-3}$ mm Hg, the color of $xHgI_2$–$(1 - x)Al_2O_3$ and $xHgI_2$–$(1 - x)SiO_2$ composites depends on the HgI_2 concentration: at room temperature, the composites with a mole fraction $x < 0.2$ are yellow, whereas the composites with $x > 0.2$ have a pink color. The samples prepared in an air atmosphere do not change color with a decrease in the HgI_2 concentration and remain pink at $x < 0.2$. Analysis of the low-temperature ($T = 77$ K) luminescence spectra demonstrated that the spectra of the pink mixtures always involve a luminescence band in the range of 533 nm, which, as is known [9], is associated with the exciton emission in α-HgI_2. This band is absent in the luminescence spectra of the yellow mixtures. The yellow color of the mixtures with $x < 0.2$ is retained as long as they remain under vacuum. In an air atmosphere, the color gradually changes and, within hours, the composites become pink and a band in the range of 533 nm appears in their low-temperature luminescence spectra. This process is substantially accelerated upon grinding of the samples.

Temperatures (°C) of the $\alpha \longrightarrow \beta$ phase transition in mercuric iodide in the composition of $xHgI_2$–$(1 - x)Al_2O_3$ mixtures

Mole fraction x of HgI_2 in the mixture	Al_2O_3			
	finely dispersed (specific surface is more than 210 m^2/g)			coarse-grained
	without heat treatment	with preliminary heat treatment	with preliminary grinding	
1	134	134	134	134
0.5	140	140	144	137
0.25	144	144	149	139
0.1	154	–	–	139

It can be assumed that grinding of the samples with high concentrations x and the filling of pores of the nanocrystalline powder with HgI_2 lead to the formation of composites containing HgI_2 particles of different sizes. Some part of HgI_2 is incorporated into the smallest sized pores not filled with water. Apparently, in order to prepare composites with a large fraction of small-sized pores filled with HgI_2, the mixing should be performed under vacuum and at low HgI_2 concentrations. As was noted above, it is these composites that are yellow in color. Upon contact of these composites with air, when HgI_2 particles are displaced from the smallest sized filled pores, the composites change color to red. We believe that the yellow color of the composites stems from the fact that mercuric iodide in the smallest sized pores occurs in the form of the yellow β phase. In this case, the change in color in air implies that an increase in the particle size is attended by the transformation from the β modification to the α modification. It is reasonable that the transformation to the stable phase should be accelerated under deformation, which is actually observed upon grinding of the mixtures.

An increase in the HgI_2 concentration in the mixtures results in an increase in the fraction of filled large-sized pores, which are filled with excess mercuric iodide that has remained after saturation of the small-sized pores. This circumstance is responsible for the pink color of the composites with $x > 0.2$. The low-temperature luminescence spectra of the pink mixtures contain a band associated with the exciton emission in α-HgI_2, whereas the yellow mixtures do not exhibit luminescence. This does not contradict the proposed interpretation, because the edge luminescence, as is known, is absent in β-HgI_2.

3.3. The yellow HgI_2 phase also formed on the surface of the nanocrystalline Al_2O_3 powder pressed into pellets 11 mm in diameter and 0.5 mm thick. One surface of the pellet was brought into contact with a polycrystalline powder of the red modification of HgI_2. The growth of HgI_2 crystal nuclei was observed on the opposite surface. The contact was accomplished in small-sized closed vessels at temperatures of 30, 55, and 100°C.

After contact with the red modification of HgI_2 for two weeks at $T = 30°C$, the pellet remains colorless. However, in an air atmosphere, the pellet slowly

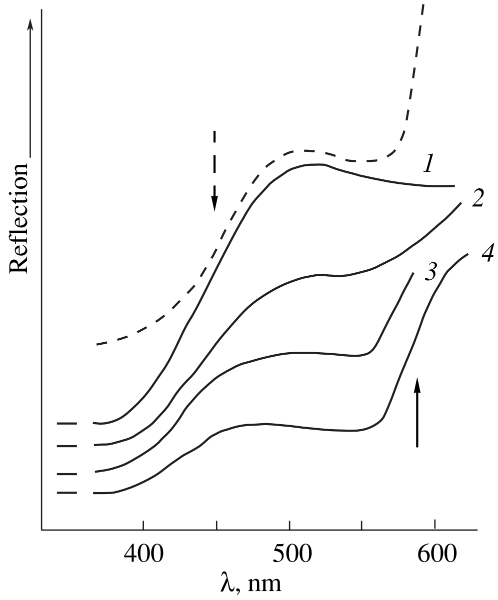

Fig. 1. Diffuse reflection spectra of the surface of an Al_2O_3 pellet at room temperature after contact with α-HgI_2 (for three weeks at T_{cont} = 55°C) at different times of storage in air: (*1*) two hours, (*2*) two days, (*3*) two weeks, and (*4*) five months. The dashed line represents the diffuse reflection spectrum of yellow β-HgI_2 at T = 17°C (according to the data taken from [5]). The solid arrow indicates the location of the absorption edge for α-HgI_2 at room temperature, and the dashed arrow shows the location of the absorption edge for β-HgI_2 at T = –69°C [5].

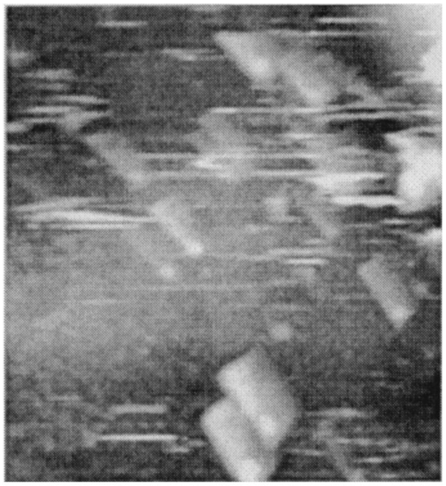

Fig. 2. AFM image of the surface of the HgI_2-filled Al_2O_3 matrix within one month after contact. The scanned area is 7000 × 7000 nm^2.

changes color. There arise yellow island formations which progressively cover the pellet surface. Examination of the fractures revealed that the pellet in the bulk remains white and a yellow color appears in the fractures only after the time needed for mercuric iodide to escape from the pores. This effect is observed within four or five days for pellets held at a temperature of 55°C and within a few hours for pellets held at 100°C. In these cases, too, the pellet, as a rule, remains colorless before exposure to air. The rates of saturation of pellets with HgI_2 and the subsequent formation of yellow particles on the surface increase with an increase in the pressure of pellet pressing.

Let us now consider the evolution of particles on the surface of pellets placed in air. Within a few hours (for pellets pressed at P = 7 MPa and filled with HgI_2 at T = 55°C), larger sized red particles are formed among yellow formations. These are crystals of the red HgI_2 modification whose number and size increase with time. Note that this process on the contact surface proceeds at a higher rate and is substantially retarded in a closed vessel in HgI_2 vapors.

In order to identify the crystal structure of the particles formed as mercuric iodide escapes from the bulk to the surface, we analyzed the diffuse reflection spectra of the surface of the studied pellets.

Figure 1 shows the diffuse reflection spectra of the layer formed on the surface of a pressed Al_2O_3 pellet after contact with the red HgI_2 modification at different stages of the layer evolution. It can be seen that, at the first stage (when the surface is almost completely covered with yellow particles), the diffuse reflection spectrum (curve *1*) is characterized by the absorption edge of the yellow β-HgI_2 modification. At the stage when the red crystals are formed on the surface, the diffuse reflection spectra (curves *2*, *3*) exhibit two features associated with the absorption edges of both HgI_2 modifications. In the case when the yellow particles are virtually absent in the surface layer, the diffuse reflection spectrum (curve *4*) shows a feature corresponding to the absorption edge of the red α-HgI_2 modification. It should be noted that the last spectrum almost coincides with the diffuse reflection spectrum of the frozen β phase (dashed curve in Fig. 1) [5].

The new formations on the structurally inhomogeneous surface of the pellet containing yellow particles and larger sized red crystals were investigated by scanning probe microscopy with the use of an atomic-force microscope (AFM) (Fig. 2). The sizes of yellow particles are estimated at 40–150 nm. The large-sized particles elongated in shape with a size of ~1.5 μm are also clearly seen in Fig. 2.

It should be emphasized that, after contact with mercuric iodide, the HgI_2-filled Al_2O_3 matrix, like porous glasses with a pore size of 2–10 nm, remains colorless prior to the escape of HgI_2 from the bulk to the surface. We can propose two possible variants of filling of the matrix in the bulk: (i) the matrix is filled with colorless ions Hg^{2+} and I^-, and (ii) the matrix is filled with HgI_2 nanoparticles whose absorption edge, owing to the quantum-well effect, is considerably shifted toward the high-energy range as compared to that for bulk crystals. The latter assumption is confirmed by the experimental data on size effects in the optical spectra of HgI_2 in porous glasses [4].

The formation of yellow HgI_2 particles on the surface and their transformation into the red α modification with an increase in size is also observed in borosilicate glasses (with a pore size of 2–10 nm) preliminarily filled with HgI_2 in the same manner (through diffusion in the course of direct contact between porous glasses and HgI_2).

3.4. The microstructure of the pressed Al_2O_3 pellets prior to and after diffusion of HgI_2 was investigated on a Rigaku D/max x-ray diffractometer (CuK_α radiation, $\lambda = 0.15418$ nm). Upon normal incidence of x-rays, the maximum depth of the studied layer was equal to 120 μm for Al_2O_3 and 2.4 μm for HgI_2. In the case of small angles, the maximum depth was smaller by a factor of 100. The scattering intensity was recorded in the ranges of small (0.03°–4°) and large (up to 140°) angles.

According to x-ray diffraction analysis, the pure (unfilled) matrix involves 95% amorphous material and 5% θ-Al_2O_3 crystals 5.6–7.2 nm in size. The maxima in the size distribution of pores are observed at 6, 18, 38, 84, 134, and 230 nm. As can be seen from Fig. 3, an increase in the pressure leads to a twofold or threefold increase in the fraction of small-sized pores (especially, with sizes of 38 and 84 nm). The pore shape is far from spherical. More likely, the pores resemble elongated holes or channels.

The filling of pores with HgI_2 results in an increase in the intensity of all the scattering peaks (Fig. 4). For 30- to 90-nm pores, the intensity increases by a factor of approximately two for the samples pressed at a maximum pressure and by a factor of four to eight for the samples prepared at a minimum pressure. This corresponds to the filling of 0.5% of the pores in the matrix prepared at a pressure of 7 MPa and 1–2% of the pores in the matrix with a looser structure. The observed shift of the scattering peaks toward the large-angle range implies a decrease in the distance between scattering centers by 6–30%. This shift either can indicate that small-sized pores are filled initially or can characterize the mean size of crystalline grains or amorphous HgI_2 nuclei in large-sized pores.

It is found that the volume of the crystalline phase consisting predominantly of the tetragonal α-HgI_2 modification (Hg_2I_2 is also present) accounts for only 0.001% of the sample volume or 1.2% of the total HgI_2 content in the matrix. Consequently, most mercuric iodide in the pores is in the amorphous or finely crystalline (with a grain size of less than 5 nm) state.

The absence of reflections attributed to the orthorhombic modification (the size of yellow formations is as large as 150 nm) suggests that the β-HgI_2 modification formed on the matrix surface also predominantly occurs in the amorphous state or has a texture with directions of the crystallographic planes that give no reflections.

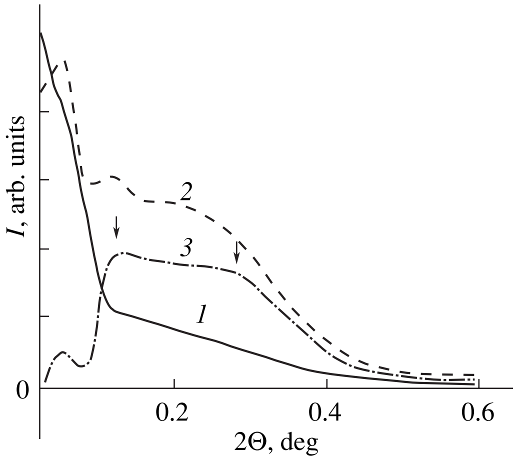

Fig. 3. Comparison of the scattering profiles for the unfilled Al_2O_3 matrices pressed at P = (*1*) 0.2 and (*2*) 7 MPa. Curve *3* is the difference between curves *1* and *2*.

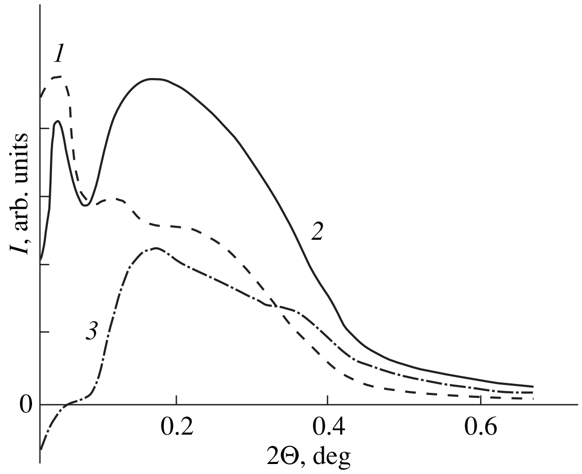

Fig. 4. Comparison of the scattering profiles for (*1*) unfilled Al_2O_3 matrix and (*2*) HgI_2-filled Al_2O_3 matrix pressed at P = 7 MPa. Curve *3* is the difference between curves *1* and *2*.

3.5. In order to refine the parameters of microstructural elements forming the surface relief of the pressed Al_2O_3 matrices, we obtained a number of AFM images of the initial surface of the matrix (Fig. 5) and the surface of the HgI_2-filled matrix (Figs. 6, 7).

The initial matrix has a porous surface whose relief changes in a random manner with the height difference Δ ~ 4 nm (Fig. 5b). Examination of the AFM images and their cross sections at different points on the matrix surface revealed the presence of a large number of oval pores with a characteristic lateral mean size of ~40 nm.

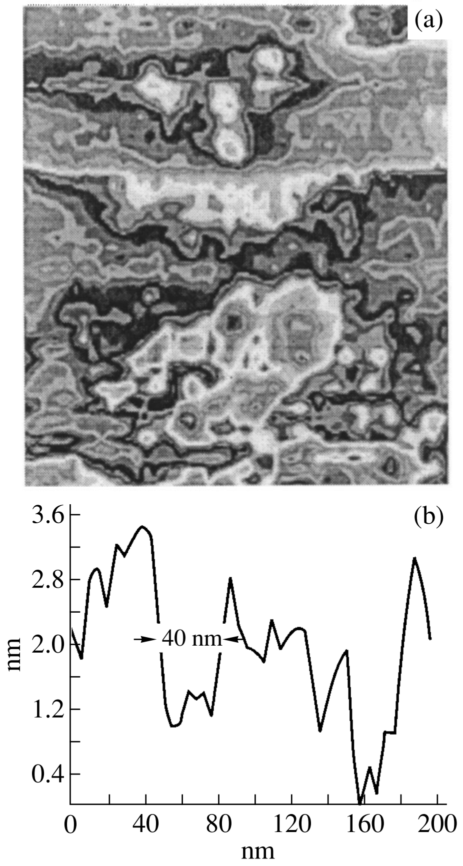

Fig. 5. AFM image of the surface of the initial Al_2O_3 matrix. The scanned area is 220 × 220 nm^2. (a) Constant-height map and (b) characteristic cross section with the height difference $\Delta \sim 3.6$ nm.

The characteristic lateral size of the smallest sized pores is approximately equal to 15–20 nm. These results are for the most part in agreement with the x-ray diffraction data obtained for the Al_2O_3 matrix. Moreover, elongated holes (channels) with a width of more than 50 nm are observed on the matrix surface; however, their number is substantially less than that in the matrix bulk.

The surface relief of the HgI_2-filled matrix differs significantly (Figs. 2, 6, 7). The structure of the surface predominantly covered with yellow formations consists of uniformly arranged oval particles (Fig. 6a) with a characteristic size of 40–150 nm. As was noted above, spatially oriented elongated particles (columns) with a characteristic size of ~1.5 μm and a mean length-to-width ratio of 1.25 are also observed on the surface of the HgI_2/Al_2O_3 samples (Fig. 2). The AFM image of the surface of the HgI_2/Al_2O_3 pellet composed predominantly of red crystals after holding in air for several months is displayed in Fig. 7. Nanometer-sized steps are clearly seen on the surface of the formed crystals. It can be assumed that these steps have a deformation origin and arise from dislocations generated under the action of stresses [10].

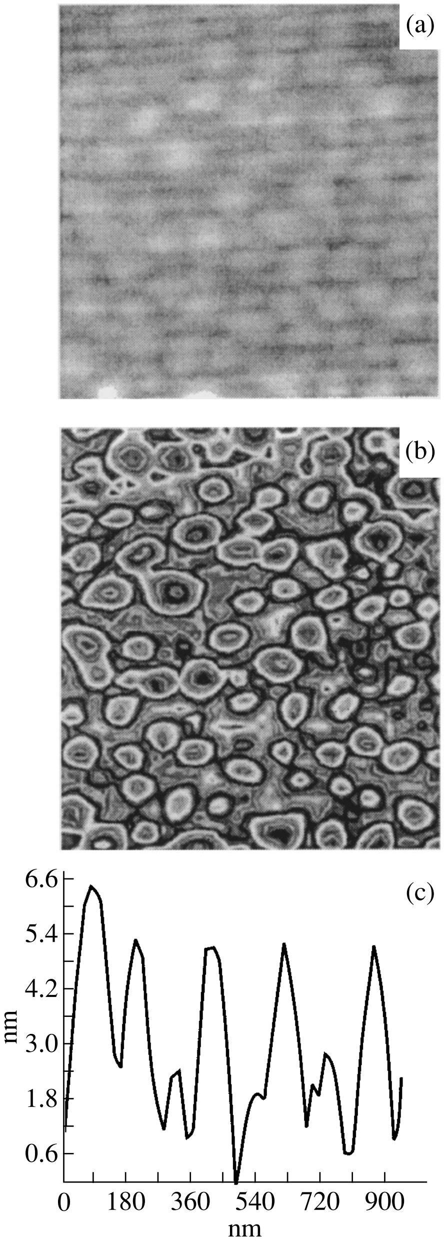

Fig. 6. AFM image of the surface of the HgI_2-filled Al_2O_3 matrix. The scanned area is 940 × 940 nm^2. (a) Half-tone image, (b) constant-height map, and (c) characteristic cross section with the height difference $\Delta \sim 6.6$ nm.

Thus, the experimental data on the kinetics of formation of the crystalline HgI_2 phase on the surface of pressed Al_2O_3 matrices and the analysis of the phase composition of HgI_2–Al_2O_3 and HgI_2–SiO_2 composites demonstrate that mercuric iodide in small-sized particles can occur in the form of the high-temperature yellow β phase at temperatures substantially less than the temperature of the $\alpha \longrightarrow \beta$ phase transition. This phase

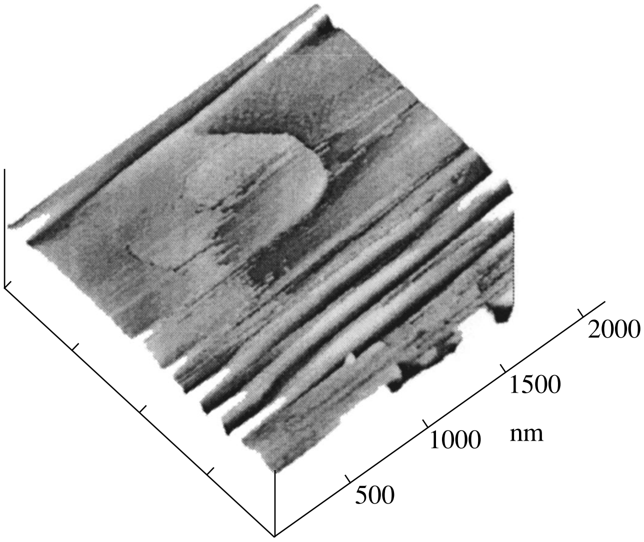

Fig. 7. AFM image of the surface of the HgI_2-filled Al_2O_3 matrix. The scanned area is 2000×2000 nm^2.

remains stable in 150- to 200-nm particles. At larger sizes, the β modification transforms into the red α modification that is stable at these temperatures.

In our earlier work [4], we revealed that the metastable orange HgI_2 modification is formed on the surface of HgI_2-filled porous glasses as mercuric iodide escapes from the pores. The same result was obtained by Agekyan *et al.* [11] for HgI_2 in a polymeric matrix. It seems likely that, depending on the nucleation conditions, mercuric iodide can nucleate in different metastable modifications. The formation of the yellow modification on the surface of different matrices and, in particular, on the surface of porous glasses, i.e., matrices identical to those studied in [4], indicates that the substrates, their structure, and geometry do not play a decisive role. It is quite possible that the formation of a particular metastable modification depends on the method of filling the matrix bulk with HgI_2 and, as a consequence, on the rates of formation and growth of nuclei, the content of defects in nuclei, and the degree of deviation from stoichiometry.

It can be assumed that, in all the cases under consideration, the stable crystalline phase HgI_2 grows through the sequential formation of two nonequilibrium modifications: the yellow phase at the first stage and then the orange phase. Note that, in order to reveal the presence of HgI_2 on the matrix surface and to identify the orange modification, the authors of [4, 11] used luminescence spectroscopy; however, as was noted above, the yellow β phase of mercuric iodide does not exhibit luminescence.

4. CONCLUSION

Thus, the experimental results obtained in the present work demonstrate that the crystal structure of small-sized HgI_2 particles is dependent on size. The estimates were made for the maximum sizes of particles occurring in the metastable β modification.

ACKNOWLEDGMENTS

This work was supported by the Russian Foundation for Basic Research, project no. 00-02-16891.

REFERENCES

1. S. V. Gaponenko, Fiz. Tekh. Poluprovodn. (St. Petersburg) **30** (4), 577 (1996) [Semiconductors **30**, 315 (1996)].
2. R. Rossetti, S. Nakamura, and L. E. Brus, J. Chem. Phys. **79** (2), 1086 (1983); H. Weller, H. M. Schmidt, U. Koch, *et al.*, Chem. Phys. Lett. **124** (6), 557 (1986).
3. A. I. Ekimov, I. A. Kudryavtsev, and O. G. Lyublinskaya, Fiz. Tverd. Tela (St. Petersburg) **39** (9), 1657 (1997) [Phys. Solid State **39**, 1479 (1997)].
4. I. Kh. Akopyan, O. N. Volkova, B. V. Novikov, and B. I. Venzel', Fiz. Tverd. Tela (St. Petersburg) **39** (3), 468 (1997) [Phys. Solid State **39**, 407 (1997)].
5. R. H. Bube, Phys. Rev. **106** (4), 703 (1957).
6. V. S. Gorskiĭ, Zh. Éksp. Teor. Fiz. **5** (2), 155 (1935).
7. J. B. Newkirk, Acta Metall. **4** (3), 316 (1956).
8. J. E. Maskasky, Phys. Rev. B **43** (7B), 5769 (1991).
9. I. Kh. Akopyan, B. V. Bondarenko, B. A. Kazennov, and B. V. Novikov, Fiz. Tverd. Tela (Leningrad) **29** (2), 419 (1987) [Sov. Phys. Solid State **29**, 238 (1987)].
10. G. A. Malygin, Fiz. Tverd. Tela (St. Petersburg) **43** (2), 248 (2001) [Phys. Solid State **43**, 257 (2001)].
11. V. F. Agekyan, A. Yu. Serov, and Yu. A. Stepanov, Fiz. Tverd. Tela (St. Petersburg) **42** (10), 1786 (2000) [Phys. Solid State **42**, 1832 (2000)].

Translated by O. Borovik-Romanova

Physics of the Solid State, Vol. 44, No. 7, 2002, pp. 1394–1398. Translated from Fizika Tverdogo Tela, Vol. 44, No. 7, 2002, pp. 1332–1336.
Original Russian Text Copyright © 2002 by Gall, Rut'kov, Tontegode.

LOW-DIMENSIONAL SYSTEMS AND SURFACE PHYSICS

Interaction of Aluminum with the Rhenium Surface: Adsorption, Desorption, and Growth of Surface Compounds

N. R. Gall, E. V. Rut'kov, and A. Ya. Tontegode
Ioffe Physicotechnical Institute, Russian Academy of Sciences,
Politekhnicheskaya ul. 26, St. Petersburg, 194021 Russia
e-mail: gall@ms.ioffe.rssi.ru

Received September 20, 2001

Abstract—The interaction of aluminum with the $(10\bar{1}0)$ rhenium surface was studied experimentally within a broad temperature range, 300–2000 K. Surface aluminide (SA) ReAl with a concentration of adsorbed Al atoms $N_{\mathrm{Al}} = 1.6 \times 10^{15}$ cm^{-2} was found to form. It was shown that aluminum escapes from the surface by thermal desorption at temperatures from 1300 to 1600 K, with the desorption activation energy changing abruptly from ~3.6 to ~4.2 eV when passing through the concentration corresponding to the SA. *© 2002 MAIK "Nauka/Interperiodica".*

1. INTRODUCTION

Elements which behave as classical metals in the condensed state exhibit essentially nonmetallic properties when in the form of individual atoms or molecules. For instance, intermetallides and high-melting compounds formed by transition metals with beryllium and aluminum turn out to be close in terms of their properties to silicides, sulfides, and borides [1, 2] while differing strongly from classical metal alloys.

This does not come as a surprise, because the interaction of an impurity atom, say, Si, P, or Al, with a high-melting metal is dominated by the dimensions of the atom, which determine its capacity of incorporation into the lattice; by its electronegativity, as a generalized characteristic describing electron transfer from or to the impurity; and, finally, by the structure of the outer terms, i.e., the number of electrons and empty orbitals suitable for chemical bonding [3]. The atoms of Si, Al, and S are very close in size [2] and have similar diffusion parameters in transition-metal lattices [2], and the silicides, aluminides, and sulfides they form are frequently isostructural [2, 4, 5].

It appears unquestionable that this similarity should also become reflected in the behavior of Al layers adsorbed on the surface of high-melting compounds. In particular, one should expect the formation of surface chemical compounds whose properties would be similar to those of the surface silicides, carbides, and sulfides.

2. EXPERIMENTAL

The studies were carried out in the ultrahigh vacuum ($P \sim 10^{-10}$ Torr) high-resolution Auger spectrometer described in [6]. The sample was an ac-heated polycrystalline rhenium ribbon measuring 1 × 0.02 × 40 mm. The ribbon was cleaned by alternately heating in an ultrahigh vacuum at 2500 K and in an oxygen environment ($P_{\mathrm{O}_2} \sim 10^{-6}$ Torr); after the cleaning, the ribbon produced only rhenium Auger electron peaks. The cleaning was accompanied by texturing, with the $(10\bar{1}0)$ face emerging onto the surface with a work function $e\varphi = 5.15$ eV (the figure typical of this face [7]). X-ray diffraction measurements showed the degree of the face orientation relative to the surface to be 99.9%, and STM images revealed the average grain size to be ~20–30 μm. The ribbon temperature was measured with a micropyrometer and, in the region where pyrometry could not be used, by linear extrapolation of the dependence of the temperature on the heater current.

The aluminum was deposited on all of the ribbon surface simultaneously from a custom-designed large-area source, whose operation was based on preliminary dissolution of aluminum in the bulk of a high-melting metal followed by aluminum desorption. After proper aging, no Auger electron peaks besides the ones due to aluminum were found in the spectra of the deposited layers. We used the Al Auger electron peak with E = 68 eV and the Auger electron triplet of rhenium with E = 162–177 eV, and the peak-to-peak amplitude was taken for the Auger signal intensity. The Auger peak of metallic aluminum did not overlap with any substrate Auger electron peak. To study desorption, an auxiliary Re ribbon was mounted beside and parallel to the operating Re ribbon, as was done in [8].

3. RESULTS AND DISCUSSION

3.1. *Deposition of Aluminum on Rhenium at Various Temperatures*

Figure 1 presents the variation in Auger signals of the adsorbate and substrate obtained during Al deposition on $(10\bar{1}0)$Re at a constant flux at two different temperatures, 300 and 1300 K. Deposition at room temperature results in a gradual decrease in the substrate Auger signal down to zero, which indicates the formation of a continuous multilayer adsorbate film. In the initial deposition stages, up to 80 s, the aluminum Auger signal grows linearly, after which the rate of this growth slows down. The height of the Auger peak of rhenium decreases by a factor of ~1.5; that of aluminum, by ~60 units. The linear growth of the Auger peak in the initial stage apparently reflects the accumulation of all aluminum atoms falling on the surface in the first adsorbed layer, and the inflection corresponds to the beginning of growth of the second layer on the surface.

Deposition of Al on rhenium at elevated temperatures occurs in a radically different way. As seen from Fig. 1, deposition at 1300 K results initially in the same growth of the aluminum Auger signal in the case of deposition at room temperature, which means that each aluminum atom striking the surface remains on it in the first adsorbed layer. However, the situation changes after a characteristic concentration N_{Al}^{*} has been reached; now, the surface coverage remains constant despite the continuing arrival of Al atoms. These curves resemble very much, in character, those produced by the surface silicides forming in the deposition of silicon on W and Re [9, 10]. By analogy, we call the adsorption state with N_{Al}^{*} the surface aluminide (SA). The SA can also be obtained by heating an aluminum film two or three layers thick at 1250–1300 K for one to two minutes.

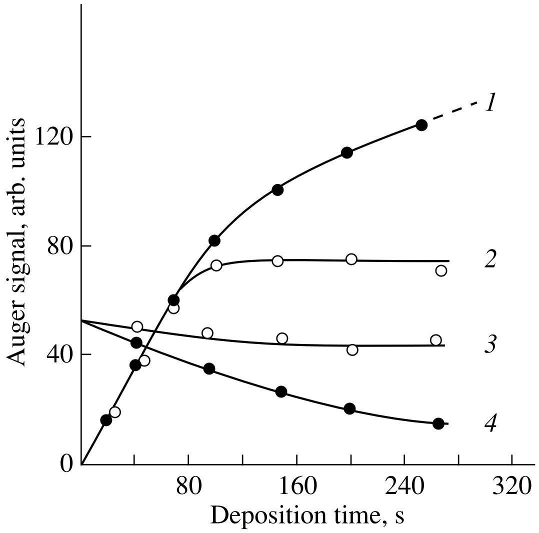

Fig. 1. Auger peak intensity of (*1*, *2*) aluminum and (*3*, *4*) rhenium plotted vs. time of aluminum adsorption at a constant flux and for temperature equal to (*1*, *4*) 300 and (*2*, *3*) 1300 K; $\nu_{\mathrm{Al}} = 1.6 \times 10^{13}$ cm^{-2} s^{-1}.

3.2. *Annealing of Aluminum Films of Various Thicknesses on Rhenium*

Curves *1* and *2* in Fig. 2 illustrate the effect of annealing of a multilayer aluminum film deposited on rhenium at room temperature. The surface concentration of aluminum in the film is ~$(8–10) \times 10^{15}$ cm^{-2} (the rhenium Auger peak is ~15 times smaller than that of aluminium). The film was annealed in steps 30 s long at each temperature.

Up to 900 K, the film remains stable, after which the Auger peak of rhenium starts to grow monotonically; that of aluminum, to decrease. No aluminum is left on the surface at 1500 K.

For comparison, Fig. 2 also presents the variation of the adsorbate and substrate Auger signals when a submonolayer aluminum film, whose thickness is approximately one-half the SA thickness (with rhenium screened 1.2 times), is annealed. The film remains stable up to 1300 K, after which the decrease in height of the aluminum Auger peak follows the same curve as in the case of a thicker film. This similarity shows that the mode of escape of aluminum from the rhenium surface is the same for substantially different surface concentrations.

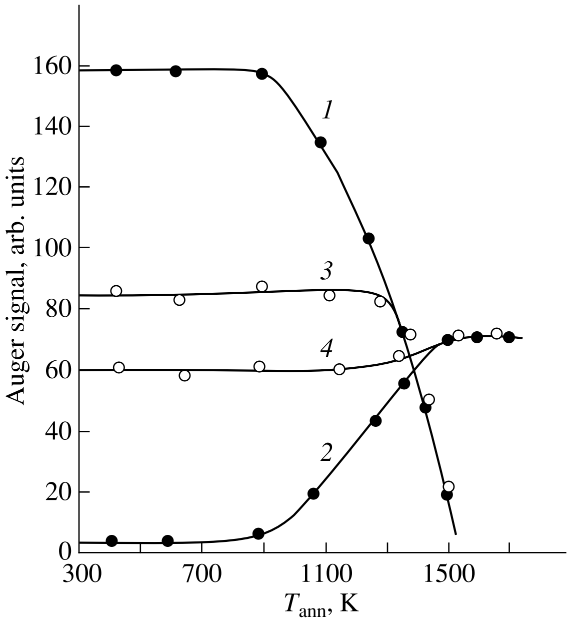

Fig. 2. Auger peak intensity of (*1*, *3*) aluminum and (*2*, *4*) rhenium plotted vs. temperature for stepped (100 K) annealing of Al films with surface concentration N_{Al} equal to (*1*, *2*) $(8–10) \times 10^{15}$ and (*3*, *4*) 0.7×10^{15} cm^{-2}; time at each temperature is 30 s.

3.3. The Absolute Concentration of Aluminum Atoms in the Surface Aluminide

In view of the absence of a reliable reference for the surface coverage of metals by aluminum, we calculated the absolute concentration of Al atoms in the SA using the data on the surface concentration of silicon in the silicide on $(10\bar{1}0)$Re [10]. We first had to determine the coefficient of elemental sensitivity of aluminum with respect to silicon. We could not use reference data, for instance, from [11], because the Auger electron spectrum presented there features not only the peaks of aluminum but also those of oxygen; this could lead to considerable errors caused by the differences in the coefficients of elemental sensitivity for metallic and oxidized aluminum. Our data are listed in the table.

We use the following relations for the intensity of Auger signals from thick films:

$$I = n\lambda kT, \tag{1}$$

where n is the atomic concentration in the film, λ is the mean free path, k is the elemental sensitivity coefficient, and T is the spectrometer transmission, which remains constant during the experiments.

Next, we apply Eq. (1) to thick silicon and aluminum films and divide one of the two relations obtained by the other:

$$k_{Si}/k_{Al} = (I_{Si}/I_{Al})(n_{Al}/n_{Si})(\lambda_{Al}/\lambda_{Si}). \tag{2}$$

Assuming the mean free paths for the Auger electrons of both elements to be equal, we obtain

$$k_{Si}/k_{Al} = (282/260)\times(6/5)\times 1 \approx 1.3 \pm 0.4. \tag{3}$$

The 30% scatter originates first of all from the errors reported in the reference data on the mean free paths.

Now, we calculate the surface concentration of aluminum in the SA. For surface compounds, we can use the relation [12]

$$I = kNT, \tag{4}$$

where N is the surface concentration of the adsorbate. Applying Eq. (4) to Auger signals for the SA and the surface silicide recorded on the same scale and dividing one relation by the other yields

$$N_{Al} = N_{Si}(I_{Al}/I_{Si})(k_{Si}/k_{Al}). \tag{5}$$

Substituting the values from the table and from Eq. (3), we obtain

$$N_{Al} = N_{Si}(1.2 \pm 0.4).$$

Thus, the atomic concentrations of silicon and aluminum in the SA and the surface silicide on rhenium are similar and, hence, $N^*_{Al} = (1.6 \pm 0.5) \times 10^{15}$ cm^{-2} [10].

3.4. Desorption of Aluminum from the Rhenium Surface

To construct a consistent physical scenario of the interaction of aluminum with the rhenium surface, one has first to isolate the dissolution of aluminum in the bulk of the metal from its thermal desorption. This was achieved in the following experiment. We used an auxiliary Re ribbon identical to the operating one, mounted at an angle of 45° to the sample surface at a distance of ~15 mm from it. One could produce the same adsorption states on it as on the operating ribbon, and the ribbons were arranged geometrically so that their operating surfaces intercepted the same aluminum fluxes from the source. The experimental setup is shown schematically in Fig. 3a. A multilayer aluminum film was deposited on the auxiliary ribbon. Then, the operating ribbon was cleaned by heating to $T = 2200$ K and maintained afterwards at $T = 300$ K, whereas the auxiliary ribbon was heated in steps. In desorbing from the latter film, the Al atoms accumulated on the clean surface of the operating ribbon, where they were analyzed by Auger electron spectroscopy (AES). The ribbon arrangement used in the experiment permitted about 1/30 of all the adsorbate atoms desorbing from the auxiliary ribbon to be collected on the surface of the operating ribbon.

Figure 3b presents the results of this experiment. No aluminum desorption is observed to occur from the surface for $T < 1200$ K. At higher temperatures, the amount of desorbing adsorbate increases, and, at $T > 1500$ K, no new adsorbate atoms impinge on the surface of the operating ribbon, which attests to the completion of desorption. The amount of adsorbate atoms transferred from the auxiliary onto the operating ribbon, as calculated from geometrical considerations, coincides to within good accuracy with the measured values presented in Fig. 3b.

Let us compare the data in Figs. 2 and 3b. Aluminum is seen to start desorbing only at $T > 1200$ K; hence, the decrease in its surface concentration at lower temperatures can only result from its dissolution. Because the SA is thermally stable up to 1300–1350 K, it decomposes apparently only through thermal desorption. Moreover, it appears reasonable to suggest that it is the thermal desorption of the newly arriving aluminum

Auger signal intensities of the substrate, silicon, and aluminum for various adsorption states on the rhenium surface (all data are on the same scale)

$I_{Re\ (pure)}$	$I_{Al\ (SA)}$	$I_{Si\ (SS)}$	$I_{Re\ (with\ SA)}$	$I_{Si\ (multilayer)}$	$I_{Al\ (multilayer)}$
40	118	125	26	282	260

Note: SA is surface aluminide, and SS is surface silicide.

atoms that accounts for the constancy of the surface concentration corresponding to the SA when Al is deposited on Re at 1300 K. This essentially distinguishes the system under study from the Si/W(100) and Si/Re($10\bar{1}0$) adsorption systems, where the stability of the surface silicides is due to dissolution of excess silicon atoms in the bulk of the metal substrate [9, 10].

3.5. Kinetics of Aluminum Escape from Rhenium at Various Temperatures

Let us consider in more detail how aluminum escapes from the rhenium surface. Figure 4 illustrates the effect of annealing of a deposited aluminum film with $N_{\mathrm{Al}} = 3 \times 10^{15}$ cm^{-2} (i.e., approximately twice the SA concentration) performed at 1300 K. We readily see that the aluminum Auger signal fairly rapidly (in ~100 s) reaches the level corresponding to the SA and that in the subsequent 300 s, the coverage decreases further by ~15–20%. A comparison with the data in Fig. 3b suggests thermal desorption to be the most probable mechanism of adsorbate removal.

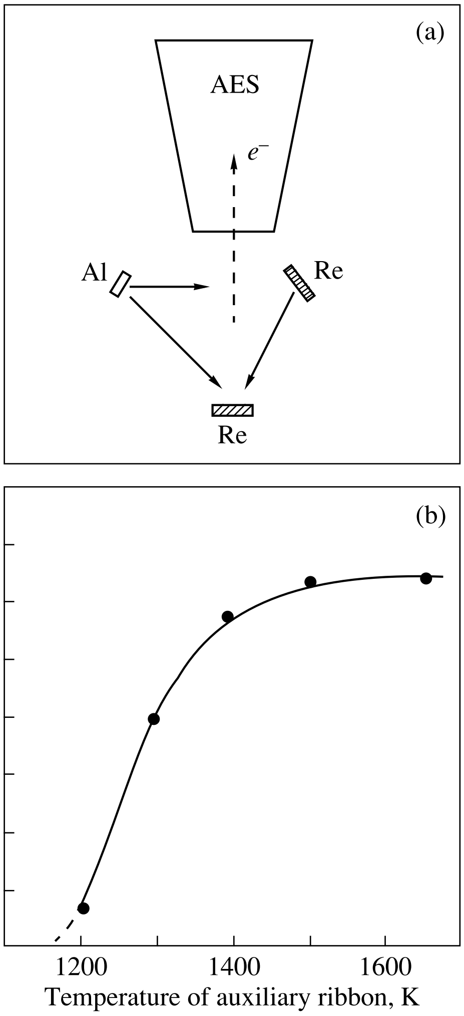

Fig. 3. (a) Experimental setup for the study of desorption and (b) increase in the aluminum Auger signal on the surface of the operating ribbon under stepped (in 100-K steps) annealing of an auxiliary ribbon coated by an aluminum multilayer film with $N_{\mathrm{Al}} = (8\text{–}10) \times 10^{15}$ cm^{-2}; time at each temperature is 30 s.

Using the Arrhenius relation for the lifetime of an adsorbed aluminum atom, we can estimate the activation energy for desorption of Al when its surface concentration is in excess of that in the SA. This energy is $E_{\mathrm{des}} \sim 3.6$ eV. Interestingly, this value is considerably higher than the aluminum sublimation energy from its melt ($E_{\mathrm{sub}} = 2.9$ eV [13]); this suggests that even at concentrations in excess of that in the SA the aluminum atoms are strongly attracted by the substrate on which they are adsorbed.

Figure 5 presents data on the destruction of the SA at 1500 K (apparently, through desorption). The aluminum Auger signal drops by more than ten times in 25 s. Based on the desorption time, one can estimate the desorption energy from the Arrhenius relation ($E_{\mathrm{des}} = 4.2$ eV). The narrow temperature interval of desorption comes as a surprise: the SA remains stable at 1300 K for hundreds of seconds but decomposes rapidly at 1500 K. This essentially discriminates the surface compound of aluminum from the similar compounds of silicon or sulfur with a rhenium surface, whose temperature interval of desorption is quite broad, ~500 K.

We note that when the SA forms, the activation energy for its removal from the substrate (in our case, through thermal desorption) jumps by ~0.6 eV. Similar jumps were also observed to occur in the formation of

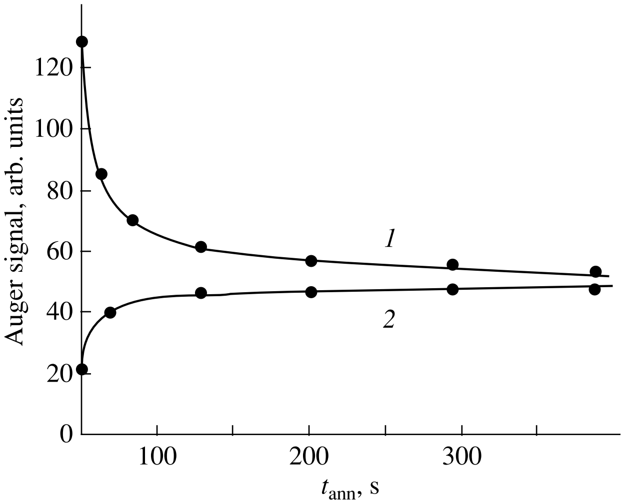

Fig. 4. Auger peak intensity of (*1*) aluminum and (*2*) substrate plotted vs. time of isothermal annealing at 1300 K of an aluminum film with $N_{\mathrm{Al}} \sim 3 \times 10^{15}$ cm^{-2} (about twice the SA concentration).

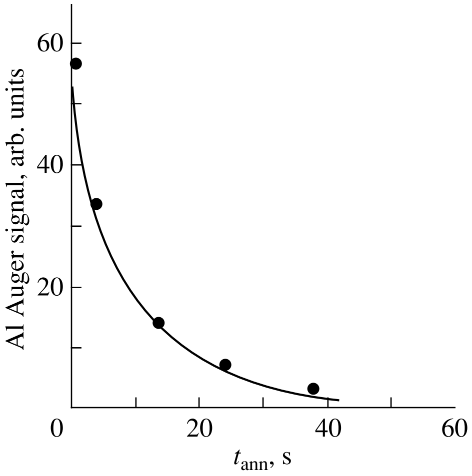

Fig. 5. Auger peak intensity of aluminum plotted vs. time of isothermal annealing at 1500 K of an aluminum film with the concentration $N_{\text{Al}} = 1.6 \times 10^{15}$ cm^{-2} corresponding to the SA.

other surface compounds, for instance, of the surface silicides of W and Re [9, 10] or of the surface carbides on W and Ta [14, 15].

It is of interest to compare our results with the data from [16], wherein aluminum adsorption on $(10\bar{1}0)$Re was also studied and the coverages were calibrated by LEED. The coverage estimated in [16] as a monolayer produced a double-humped peak in the temperature dependence of the desorption rate with maxima at ~1400 and 1550 K, while the half-monolayer coverage corresponded to a single-humped peak in the range 1350–1450 K. The desorption activation energies derived by us from the above data correlate well with the figures obtained in our experiments, which permits one to identify the half-monolayer in [16] with the SA. It turns out that the aluminum monolayer dealt with in [16] does not have a clear-cut physical meaning, which stresses once more the hazard associated with extrapolating LEED data to high-temperature processes.

Thus, high-temperature adsorption of aluminum or annealing of an aluminum film at T = 1250–1300 K results in the formation of an SA with an aluminum concentration $N_{\text{Al}} = 1.6 \times 10^{15}$ cm^{-2}, which is close to the ReAl stoichiometry with respect to the surface rhenium atoms. After the SA formation, all the aluminum atoms striking the surface apparently desorb from it. The SA can be decomposed by thermal desorption at $T >$ 1400 K, the desorption activation energy jumping from ~3.6 to ~4.2 eV when one crosses the concentration corresponding to the SA.

ACKNOWLEDGMENTS

This study was supported by the State Program of the Ministry of Science of the RF “Surface Atomic Structures,” project no. 4.6.99.

REFERENCES

1. H. J. Goldschmidt, *Interstitial Alloys* (Butterworths, London, 1967; Mir, Moscow, 1971), Vol. 2.
2. V. G. Samsonov and I. M. Vinitskiĭ, *Refractory Compounds: Handbook* (Metallurgiya, Moscow, 1976), pp. 232–240.
3. C. Kittel, *Introduction to Solid State Physics* (Wiley, New York, 1976; Nauka, Moscow, 1978).
4. E. M. Savitskiĭ, Zh. Neorg. Khim. **6**, 1003 (1961).
5. T. T. Tsong, Surf. Sci. Rep. **8** (3/4), 127 (1988).
6. N. R. Gall, S. N. Mikhailov, E. V. Rut’kov, and A. Ya. Tontegode, Surf. Sci. **191**, 185 (1987).
7. V. S. Fomenko, *Emission Properties of Materials: Handbook* (Naukova Dumka, Kiev, 1981).
8. N. R. Gall, E. V. Rut’kov, and A. Ya. Tontegode, Pis’ma Zh. Tekh. Fiz. **25** (14), 57 (1999) [Tech. Phys. Lett. **25**, 573 (1999)].
9. V. N. Ageev, E. Yu. Afanas’eva, N. R. Gall, *et al.*, Poverkhnost, No. 5, 7 (1987).
10. N. R. Gall, E. V. Rut’kov, and A. Ya. Tontegode, Zh. Tekh. Fiz. **60** (4), 125 (1990) [Sov. Phys. Tech. Phys. **35**, 475 (1990)].
11. L. E. Davis, N. C. McDonald, P. W. Palmberg, G. E. Rich, and R. E. Weber, *Handbook of Auger Electron Spectroscopy* (Physical Electronics Industries, Eden Prairie, 1976).
12. N. R. Gall, E. V. Rut’kov, A. Ya. Tontegode, and M. M. Usufov, Phys. Low Dimens. Struct. **9/10**, 17 (1998).
13. An. N. Nesmeyanov, *Vapor Pressure of Chemical Elements* (Akad. Nauk SSSR, Moscow, 1961).
14. N. R. Gall, E. V. Rut’kov, and A. Ya. Tontegode, Izv. Akad. Nauk, Ser. Fiz. **62** (10), 1980 (1998).
15. N. R. Gall, E. V. Rut’kov, and A. Ya. Tontegode, Surf. Sci. **472**, 187 (2001).
16. M. Parschan and K. Cristmann, Surf. Sci. **347**, 63 (1996).

Translated by G. Skrebtsov

Physics of the Solid State, Vol. 44, No. 7, 2002, pp. 1399–1405. Translated from Fizika Tverdogo Tela, Vol. 44, No. 7, 2002, pp. 1337–1343.

LOW-DIMENSIONAL SYSTEMS AND SURFACE PHYSICS

Mechanism and Kinetics of Early Growth Stages of a GaN Film

S. A. Kukushkin*, V. N. Bessolov, A. V. Osipov*, and A. V. Luk'yanov*****

** Institute for Problems of Mechanical Engineering, Russian Academy of Sciences,*
Bol'shoĭ pr. 61, Vasil'evskiĭ ostrov, St. Petersburg, 199178 Russia
*** Ioffe Physicotechnical Institute, Russian Academy of Sciences,*
Politekhnicheskaya ul. 26, St. Petersburg, 194021 Russia
**** Foundation for Support of Science and Education, St. Petersburg, 192007 Russia*
e-mail: ksa@math.ipme.ru

Received May 28, 2001; in final form, October 25, 2001

Abstract—The growth of GaN islands on the substrate surface covered with an AlN buffer layer is theoretically investigated at the stages of nucleation and Ostwald ripening in the temperature range 480–1000°C. The following inferences are made from analyzing the results obtained. (1) At temperatures $T > 650°\text{C}$, the growth of islands is controlled by the chemical reaction of formation of GaN molecules around the periphery of the island surface. Islands nucleated at these temperatures are characterized by a large spread in their sizes. (2) At temperatures $T < 600°\text{C}$, the island growth is governed by the surface diffusion of nitrogen atoms. Islands nucleated at these temperatures are virtually identical in size. (3) In the temperature range 600–650°C, the mechanism of island growth gradually changes over from the mechanism associated with the surface diffusion of nitrogen atoms with a large mean free path to the mechanism determined by the diffusion of gallium atoms with a smaller mean free path. The supersaturation, flux, and size distribution functions of GaN nuclei are calculated at different substrate temperatures. The phase diagrams describing the evolution in the phase composition of GaN islands with variations in temperature are constructed. *© 2002 MAIK "Nauka/Interperiodica".*

1. INTRODUCTION

In recent years, serious effort has been made in GaN-based electronics, first, to prepare high-quality epitaxial layers on foreign substrates (SiC, Al_2O_3, and GaAs) [1] and, second, to grow GaN nanocrystals on polycrystalline substrates (SiO_2 and metals) [2]. In this respect, detailed knowledge of the nucleation and growth of GaN island films is necessary for solving both problems. In our previous work [3], we analyzed the early stages of nucleation of GaN films formed on the surface of AlN buffer layers at substrate temperatures ranging from 480 to 1000°C. At the initial stage, the number of islands is so small that the supersaturation ξ and, correspondingly, the critical radius R_{cr} of islands remain unchanged in the course of growth. As the number of nuclei on the substrate surface increases, they begin to absorb the material arriving at the substrate; as a consequence, the supersaturation decreases and the critical radius R_{cr} of nuclei increases. The rate of change in the supersaturation ξ is determined by the growth mechanism of individual islands. At the nucleation stage, the distribution of islands depends on the mechanism of their growth [4, 5]. After the nucleation stage, under certain growth conditions, islands can undergo an Ostwald ripening, during which they interact with each other through a generalized diffusion field of adatoms on the surface [4, 5]. This stage is characterized by a universal island size distribution that depends on the growth mechanism and the flux of atoms arriving at the substrate. With knowledge of the growth mechanism of islands, it is possible to control efficiently the size distribution and the composition of islands [5]. Over the last decade, experimental investigations into the early stages of heteroepitaxial growth of GaN films have attracted the particular attention of many researchers [6]. However, possible growth mechanisms of GaN films have not been analyzed theoretically.

In this respect, the aim of the present work was to investigate theoretically the nucleation and growth of GaN islands at the stages of nucleation and Ostwald ripening.

2. THE POSSIBLE MECHANISM AND KINETICS OF NUCLEATION OF GaN ISLANDS

For a theoretical consideration of GaN nucleation, it is necessary to construct a system of equations describing the evolution of islands of stoichiometric composition [4]. A theoretical treatment for multicomponent stoichiometric compounds has only been accomplished for the stage of Ostwald ripening [5]. Later, the nucleation theory was developed for single-component compounds and compounds forming a continuous series of solid solutions [4]. In [4], the authors generalized the system of equations describing the nucleation of single-component compounds to the case of nucleation of a multicomponent stoichiometric compound. By omitting intermediate mathematical manipulations, the final form of this system can be represented as

$$\frac{\partial g(i,t)}{\partial t}+\frac{\partial}{\partial i}[g(i,t)V_i] = 0, \tag{1}$$

$$\xi(t) = \xi(0) + (\tau^{\mathrm{GaN}})^{-1}\int_0^t[\xi_0-\xi(t')]dt' - N_{sa}^{-1}\int_0^\infty ig(i,t)dt. \tag{2}$$

Here, $\xi(t)$ is the supersaturation at the instant of time t; $\xi(0)$ is the supersaturation at the instant of the onset of multiple nucleation; $\tau^{\mathrm{GaN}} = (\tau_{\mathrm{Ga}}\tau_{\mathrm{N}})/(\tau_{\mathrm{Ga}}+\tau_{\mathrm{N}})$; τ_{Ga} and τ_{N} are the lifetimes of gallium and nitrogen atoms on a substrate, respectively; $N_{sa} = C_{0\mathrm{Ga}}C_{0\mathrm{N}}N_0$; $C_{0\mathrm{Ga}}$ and $C_{0\mathrm{N}}$ are the equilibrium concentrations of gallium and nitrogen, respectively; N_0 is the equilibrium number of GaN molecules on the substrate; $g(i, t)$ is the island size distribution function; and V_i is the growth rate of an island consisting of i atoms (molecules). It can be seen that, for a multicomponent compound, unlike a single-component compound, a number of parameters are determined by the properties of nitrogen and gallium. Methods of solving this system are outlined in [4]. Here, we give the final result obtained at short lifetimes τ and steady fluxes of deposited atoms. For a multicomponent compound, the solution has the following form:

$$\xi(t) = \frac{\xi_0}{1+\frac{1}{\Gamma}T^k(t)\varphi_k(T(t))}, \tag{3}$$

$$I(t) = \frac{I(\xi_0)\exp[-T^k(t)\varphi_k(T(t))]}{1+\frac{1}{\Gamma}T^k(t)\varphi_k(T(t))}, \tag{4}$$

$$N(t) = I(\xi_0)t_k\varphi_k(T(t)), \tag{5}$$

$$g(\rho,t) = \left\{\frac{I(\xi_0)t_0}{\xi_0}\exp\left[-\left(T(t)-\frac{t_0\rho}{t_k\xi_0}\right)^k\varphi_k\left(T(t)-\frac{t_0\rho}{t_k\xi_0}\right)\right]\right\}, \tag{6}$$

$$\rho \le \xi_0\frac{t_k}{t_0}T(t),$$

$$g(\rho,t) = 0, \quad \rho > \xi_0\frac{t_k}{t_0}T(t),$$

$$T = \frac{t}{t_k}-\frac{1}{\Gamma}\int_0^T x^k\varphi_k(x)dx, \tag{7}$$

$$t_k = \frac{t_0}{\xi_0}\left[\frac{\xi_0 N_{sa}}{(k+1)\Gamma I(\xi_0)\tau^{\mathrm{GaN}}}\right]^{1/(k+1)}. \tag{8}$$

Here,

$$\rho = i^{1/(k+1)}, \quad \xi_0 = \frac{J_{\mathrm{Ga}}J_{\mathrm{N}}\tau_{\mathrm{Ga}}\tau_{\mathrm{N}}}{N_{sa}}-1,$$

H is the work of formation of an island, φ_k is the auxiliary function for all possible values of the coefficient k, $\Gamma \sim i_c$, i_c is the number of atoms in a critical nucleus, $I(t)$ is the flux of new-phase islands formed by the instant of time t, $N(t)$ is the number density of islands nucleated by the instant t, and $\xi(t)$ is the supersaturation at the instant t. The appropriate relationships for H and Γ are available in [4]. It is seen that the physical meaning of a number of parameters entering into these equations for multicomponent compounds differs from that for single-component compounds. In order to determine the quantities involved in relationships (3)–(8), it is necessary to establish the coefficient k which depends on the growth mechanism of islands. This mechanism determines the coefficient k and, hence, the behavior of $I(t)$, $N(t)$, and $\xi(t)$ and the distribution functions $g(\rho, t)$. According to the results obtained in [4, 5], at $k = 0$, the growth of islands occurs through the surface diffusion of atoms (molecules) in the case when the mean free path of the atoms (molecules) over the surface satisfies the condition $\lambda_s \gg R$, where R is the mean radius of the island base. At $k = 1/2$, the growth of islands can proceed through either the surface diffusion ($\lambda_s \ll R$) or the incorporation of atoms (molecules) into islands, i.e., when the island growth is limited by the chemical reaction over the surface around the periphery of the island. The situation when $k = 1$ will not be considered in the present work, because, according to [5], this corresponds to the growth of nuclei in convectively stirred systems. At $k = 2$, the islands can grow either through the evaporation–condensation mechanism or (if the diffusion occurs in the gas phase) due to the chemical reaction during which atoms add throughout the lateral surface of the island. Let us now predict the possible mechanisms of the growth of islands at different substrate temperatures. The height h of disk-shaped islands at which the mechanism of mass transfer changes over from the diffusion-controlled mechanism in the gas phase to the mechanism associated with the surface diffusion was determined in [5]. The relationship for this height, as applied to GaN, takes the form

$$\bar{h} \approx \frac{B\sqrt{k_{\mathrm{B}}T}\tau_{\mathrm{N},s}}{\omega_{\mathrm{N}}\sqrt{2m_{\mathrm{N}}\pi}N_0} \times\left[1+\frac{\beta_{\mathrm{N}}C_{0\mathrm{N}}\sqrt{m_{\mathrm{N}}}\omega_{\mathrm{N}}\tau_{\mathrm{Ga},s}}{\beta_{\mathrm{Ga}}C_{0\mathrm{Ga}}\sqrt{m_{\mathrm{Ga}}}\omega_{\mathrm{Ga}}\tau_{\mathrm{N},s}}\right]\left[1+\frac{\beta_{\mathrm{N}}C_{0\mathrm{N}}}{\beta_{\mathrm{Ga}}C_{0\mathrm{Ga}}}\right]^{-1}. \tag{9}$$

Here, β_{Ga} and β_{N} are the specific boundary fluxes of gallium and nitrogen atoms, which determine the rates of attachment of the atoms to a nucleus; ω_i is the atomic volume of the ith component; $\beta_i = N_{si}\gamma_i\exp(-E_{ai}/k_{\mathrm{B}}T)$; γ_i is the frequency of normal vibrations of atoms of the

ith sort on the surface of GaN islands; E_{ai} is the adsorption energy for atoms of the ith sort on the GaN surface; N_{si} is the number density of atoms of the ith sort on the GaN surface; m_N is the atomic mass of nitrogen; m_{Ga} is the atomic mass of gallium; and k_B is the Boltzmann constant. If the mean height of islands on the substrate satisfies the inequality $h_e > h$, the island growth occurs by the evaporation–condensation mechanism. Otherwise, the islands grow through surface diffusion. Our estimates demonstrate that, at $T > 480°C$, the growth of GaN islands occurs through the surface-diffusion mechanism, because, in this case, $h_e \ll h$. The growth of GaN islands is limited by the mean radius of islands R [4, 5] at which there occurs a crossover of the mechanism of island growth. The mean radius R is defined by the expression

$$R = \frac{D_s^0 N_0}{\beta_s^0}, \tag{10}$$

where $N_0 \sim 1/B^2$ is the number of adsorption sites on the substrate surface (B is the lattice parameter of the substrate) and

$$D_s^0 = \left[\sum_{i=1}^{n^s} \frac{p_i^2 \ln(\lambda_{si}/R)}{D_{ai} C_{0i}}\right]^{-1}. \tag{11}$$

Here, D_s^0 is the generalized diffusion coefficient (for GaN, this coefficient characterizes the velocity of motion of the island boundary); C_{0i} is the equilibrium concentration of adatoms of the island material on the substrate; p_i are the reduced stoichiometric coefficients (for GaN, $p_i = 1/2$); D_{ai} is the diffusion coefficient of the ith component; λ_{si} is the mean free path of atoms over the surface; and β_s^0 is the generalized specific boundary flux, which is represented in the form

$$\beta_s^0 = \left[\sum_{i=1}^{n^s} \frac{p_i^2}{\beta_{si} C_{0i}}\right]^{-1}. \tag{12}$$

Here, p_i stands for the reduced stoichiometric coefficients (taken from [4]) and β_{si} are the specific boundary fluxes of gallium and nitrogen atoms, which were determined in our earlier work [3]. Note that formula (10) can be used for the estimates only in the case when $\lambda_N \gg R$ and $\lambda_{Ga} \gg R$. Otherwise, if $\lambda_N \ll R$ and $\lambda_{Ga} \ll R$, according to [5], the coefficient β_s^0 should be compared directly with the generalized diffusion coefficient D_s^0. For GaN, the diffusion coefficient D_s^0 is determined by the expression

$$D_s^0 = \frac{D_{aGa} D_{aN} C_{0Ga} C_{0N}}{4(D_{aGa} C_{0Ga} \lambda_{0N} + D_{aN} C_{0N} \lambda_{0Ga})}. \tag{13}$$

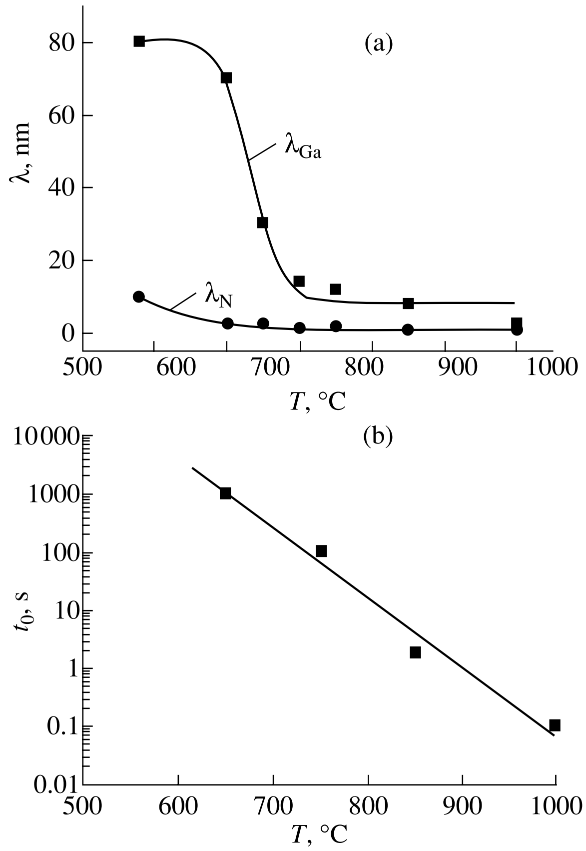

Fig. 1. Dependences of (a) the diffusion length of gallium (λ_{Ga}) and nitrogen (λ_N) atoms and (b) the characteristic time t_0 of attachment of an atom to the surface on the growth temperature.

If the mean radius of islands in the experiments meets the condition $R_e \gg R$, the growth is limited by the diffusion of atoms over the surface. For $R_e \ll R$, the growth is controlled by the rate of attachment of gallium and nitrogen atoms to the surface of islands along their periphery. With the aim of estimating the radii R, we calculate the mean free paths of nitrogen atoms λ_N and gallium atoms λ_{Ga} according to the formula $\lambda = (D_{ai}\tau_i)^{1/2}$. It turns out that, as the substrate temperature increases, the values of λ_N and λ_{Ga} approach each other and become comparable at $T > 700°C$ (Fig. 1a). Widmann *et al.* [6] demonstrated that the diameter of islands nucleated during the molecular-beam epitaxial growth of GaN on the AlN surface is equal to 15–20 nm. It can be seen from Fig. 1a that the diffusion length of nitrogen atoms on the GaN surface is smaller than the experimentally found size of GaN islands over the entire temperature range, whereas the diffusion length of gallium atoms becomes smaller than the experimental size only at temperatures above 700°C. This should manifest itself in a crossover of the mechanism of the GaN growth, which, at $T > 750°C$, is associated with the incorporation of gallium and nitrogen atoms into the crystal structure of islands. King *et al.*

[7] experimentally observed the change-over from the Stranski–Krastanov mechanism of island growth to the Frank–van der Merve mechanism in the course of molecular-beam heteroepitaxy of GaN at temperatures above ~800°C.

In the case when the growth is controlled by the rate of attachment of gallium and nitrogen atoms to the surface of islands along their periphery, the growth rate of islands in the form of a flat disk can be represented in the form [5]

$$\frac{dR}{dt} + \frac{R}{2}\left(\frac{d\ln h}{dt}\right) = \frac{\beta_s^0 \nu_s^2 \sigma}{k_B T R h}\left(\frac{R}{R_{cr}} - 1\right), \tag{14}$$

where h is the height of the island, R is the radius of the island, R_{cr} is the critical radius of the island, σ is the nucleus–natural vapor interfacial tension, and ν_s is the molecular volume of the chemical compound.

It should be noted that, in the general case, the island height at the multiple nucleation stage and the subsequent stage of Ostwald ripening ceases to be constant and equal to the height of a monoatomic step [5]. In [5], it was proved that, at the stage of Ostwald ripening, the height and the radius of disk-shaped islands vary with time in a similar manner.

Let us assume that, at the nucleation stage, the height and the radius of islands also vary in a similar manner and that the derivative $d\ln h/dt$ changes rather slowly [8]. Hence, it follows that the equation

$$\frac{dR}{dt} \sim \frac{\beta_s^0 \nu_s^2 \sigma}{k_B T R h}\left(\frac{R}{R_{cr}} - 1\right) \tag{15}$$

represents the nucleation process with sufficient accuracy.

By rewriting this equation for the number i of particles involved in nuclei and taking into account that $h \sim R$, we obtain the relationship

$$V_i = 3\pi^{2/3}\nu_s^{1/3}\beta_s^0(\bar{C}_N\bar{C}_{Ga} - C_{0N}C_{0Ga})i^{1/3}, \tag{16}$$

where $\bar{C}_N$ and $\bar{C}_{Ga}$ are the mean concentrations of nitrogen and gallium on the substrate, respectively. Relationship (17) is derived by ignoring the effect of the surface tension and under the condition $R \gg R_{cr}$, which is satisfied at the multiple nucleation stage [4].

Next, we rewrite Eq. (16) in the following form:

$$V_i = 3\frac{\xi_{GaN}}{t_0}i^{1/3}, \tag{17}$$

$$t_0 = \frac{1}{\pi^{2/3}\nu_s^{1/3}\beta_s^0}, \tag{18}$$

where ξ_{GaN} is the GaN supersaturation. For a multicomponent system, the supersaturation ξ_{GaN} can be represented as

$$\xi_{GaN} = \frac{\prod_{i=1}^{n^s}\overline{C_i^{\nu_s}} - K_\infty^s}{K_\infty^s}, \tag{19}$$

where

$$K_\infty^s = \prod_{i=1}^{n^s}\overline{C_{i0}^{\nu_i}}$$

is the equilibrium constant for the chemical reaction of formation of an island of the compound with composition s (introduced in our recent work [3]), $\bar{C}_i$ is the mean concentration of the ith component in the multicomponent system on the substrate surface, and t_0 is the characteristic time of the growth of an island of the multicomponent compound.

The calculations of the island growth at the substrate temperature $T = 600°\text{C}$ demonstrate that the growth rate of nuclei is controlled by the surface diffusion when $\lambda_i \gg R_i$. In this case, we have

$$V_i = \frac{\xi_{GaN}}{t_0}, \tag{20}$$

where

$$t_0 = \frac{1}{D_s^0 \pi N_0}. \tag{21}$$

According to the estimates, the characteristic time t_0 is approximately equal to 10^5 s. At the substrate temperature $T = 650°\text{C}$, the growth rate can be determined from expression (18) at the time t_0 defined by the relationship

$$t_0 = \frac{1}{D_s^0 \pi^{2/3}\nu_s^{1/3}N_0}, \tag{22}$$

where D_s^0 is the diffusion coefficient determined from formula (13). At this temperature, the characteristic time t_0 is estimated at ~10^6 s.

It follows from expressions (17) and (20) that, at large supersaturations ξ, the growth rates of nuclei are quite reasonable (of the order of one or two monolayers in a second). At small supersaturations, no growth of nuclei occurs and the growth mechanism of nuclei can change only after the formation of a transition layer. In this situation, the nuclei will grow because the characteristic time of their growth becomes shorter. The characteristic time t_0 was estimated from formulas (18), (21), and (22) at different growth temperatures. It was found that the time t_0 considerably decreases with an increase in the growth temperature (Fig. 1b).

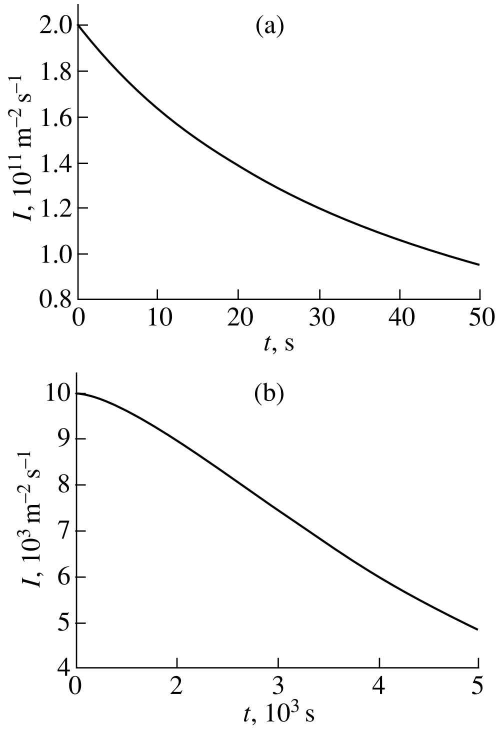

Fig. 2. Time dependences of flux I of GaN nuclei at two temperatures: (a) 600 and (b) 750°C.

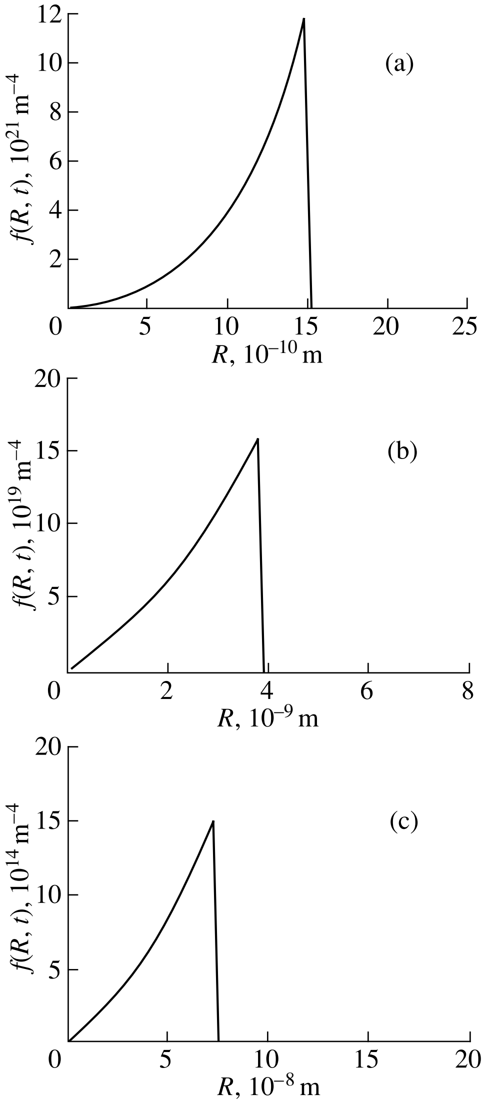

Fig. 3. Size distribution functions $f(R, t)$ of GaN nuclei at the nucleation stage. Temperature, °C: (a) 600, (b) 650, and (c) 700.

Now, we construct the time dependences of the flux $I(t)$ of GaN nuclei (Fig. 2), the size distribution functions $f(R, t)$ of GaN nuclei (Fig. 3), and the time dependences of the number density $N(t)$ of GaN islands (Fig. 4) at different substrate temperatures.

The supersaturation calculated from expression (19) at temperatures of 600–750°C is relatively large and corresponds to reasonable fluxes of nuclei. On the other hand, the number i_{GaN} of GaN molecules in a critical nucleus at the same supersaturation is very small according to the calculation from the relationship [4]

$$i_{\text{GaN}} = a/\ln^2(\xi+1). \qquad (23)$$

Here,

$$a = (\sigma_s/k_{\text{B}}T)^2\nu_s\pi/h, \quad \sigma_{\text{st}} \sim h\sigma,$$

and σ_{st} is the surface tension per unit length of a cylindrical island. For a smaller supersaturation, we obtain reasonable numbers of molecules in a critical nucleus but the fluxes of nuclei become close to zero over the entire range of temperatures. It should be noted that the physical meaning of the supersaturation in multicomponent systems (in which the crystal nuclei are stoichiometric in composition) differs from that in single-component systems. For single-component systems, the supersaturation is defined as the difference between the mean concentration and the equilibrium concentration in vapors of the same composition. For multicomponent systems, the supersaturation is defined as the difference between the product of the concentrations of material vapors, whose composition differs from the island composition, and the equilibrium constant for formation of nuclei. During the formation of new-phase nuclei in single-component systems, the supersaturation, as a rule, is less than unity (i.e., $\xi < 1$). At larger ξ, the system appears to be in the metastable region, which results in spinodal decomposition [4]. The high value of ξ in the course of the formation of GaN nuclei can be explained by introducing the notion of a Ga–N transition layer between the GaN solid nucleus and the gas phase. The chemical reaction proceeding between gallium and nitrogen on the nucleus surface results in the formation of a Ga–N transition layer whose properties differ from those of the GaN solid phase. In the general case, the transition layer can be formed on the substrate surface where the nuclei grow. The interfacial tension between the GaN solid phase and the Ga–N transition layer should be less than the standard surface tension of GaN [9]. It is these properties of the Ga–N transition layer that determine the growth rate of a nucleus. Upon formation of the transition layer, the supersaturation ξ becomes less than unity and the GaN critical nucleus has a reasonable size. Therefore, in the general case, the parameters available in the literature must be corrected for the formation of a Ga–N transition layer. Our estimates demonstrate that, for nucleation of GaN ($T < 700$°C), the high value of ξ is actually underestimated by virtue of the formation of the Ga–N transition layer, which, in turn, leads to correct results for the fluxes of nuclei.

The time dependences of the flux $I(t)$ and the number density $N(t)$ of nuclei and the nucleus size distribution functions $f(R, t)$ at different temperatures are displayed in Figs. 2–4. It should be noted that nuclei whose size varies over a wide range are formed at $T >$ 700°C (Fig. 3c), whereas islands with a particular size (10–15 nm) predominantly nucleate at $T <$ 600°C (Fig. 3a). An increase in the temperature from 600 to 700°C brings about a substantial decrease in the flux I (Figs. 2a, 2b) and the number density $N(t)$ of nuclei on the substrate (Figs. 4a, 4b).

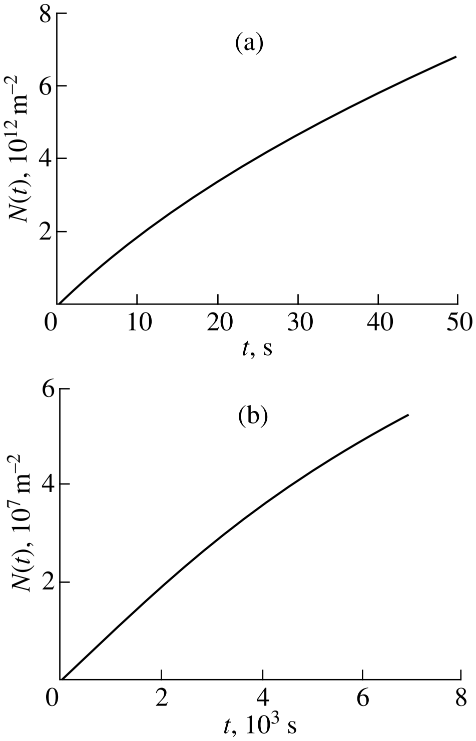

Fig. 4. Time dependences of the number density $N(t)$ of GaN islands at two temperatures: (a) 600 and (b) 700°C.

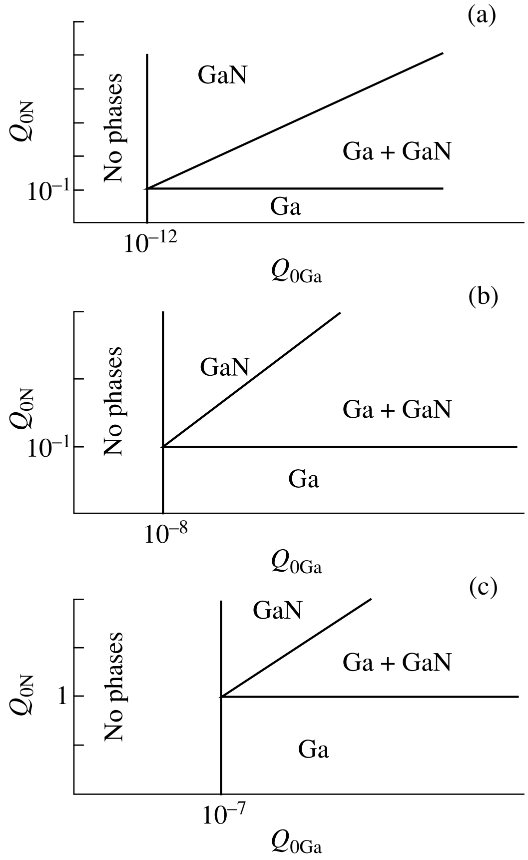

Fig. 5. Phase diagrams of GaN island films at different temperatures: (a) 480, (b) 850, and (c) 1000°C.

3. OSTWALD RIPENING IN AN ENSEMBLE OF GaN ISLANDS

The Ostwald ripening is the late stage of the first-order phase transition. For the growth mechanism with $k = 1/2$ and steady flux of the atoms arriving at the substrate, the stage of Ostwald ripening is absent. The Ostwald ripening can occur only provided the power of the external source of nitrogen and gallium atoms varies with time according to the relationship $g_i(t) = g_{0i}\,nt^{n-1}$, where g_{0i} is the power of the source of nitrogen and gallium atoms at the initial instant of time and n is the exponent of the decrease in the source power. The necessary conditions for Ostwald ripening to proceed are considered in detail in [4, 5]. Since we established that $k = 1/2$, the changes in the mean critical radius $\bar{R}$ and the mean height $\bar{h}$ of islands with time can be described by the following formulas [4, 5]:

$$\bar{R}^3(t) = \bar{R}_0^3 + A_3 t, \tag{24}$$

$$\bar{h}^3(t) = \bar{h}_0^3 + A_3 t. \tag{25}$$

Here, $\bar{R}_0$ and $\bar{h}_0$ are the mean radius and the mean height of islands in an ensemble by the time of onset of Ostwald ripening, respectively, and the constant A_3 is given by

$$A_3 = \frac{\beta_s^0 \sigma \nu_s}{2k_B T}, \tag{26}$$

where β_s^0 is the generalized specific boundary flux, which is defined by expression (12).

Earlier [3], we demonstrated that, in addition to GaN islands, liquid gallium islands can also occur on the substrate surface. As a consequence, the equilibrium concentrations C_0 in the expression for β_s^0 differ from those determined from the data on the evaporation of the compounds not interacting with each other. According to [5], these concentrations can be found from the solution of the following system of equations:

$$\begin{gathered} Q_{0\mathrm{Ga}} = C_{0\mathrm{Ga}} + J^{\mathrm{Ga}} + J^{\mathrm{GaN}}, \\ Q_{0\mathrm{N}} = C_{0\mathrm{N}} + J^{\mathrm{GaN}}, \\ \left(1 - \frac{1}{Q_{0\mathrm{N}}} J^{\mathrm{GaN}}\right)\left(1 - \frac{1}{Q_{0\mathrm{Ga}}} J^{\mathrm{GaN}} - \frac{1}{Q_{0\mathrm{Ga}}} J^{\mathrm{Ga}}\right) = \frac{K_\infty^s}{Q_{0\mathrm{N}} Q_{0\mathrm{Ga}}}, \\ C_{0\mathrm{Ga}} = k^{\mathrm{Ga}}, \end{gathered} \tag{27}$$

where $Q_{0\mathrm{N}}$ and $Q_{0\mathrm{Ga}}$ are the total initial relative amounts of nitrogen and gallium on the substrate and in new-phase nuclei by the time of onset of the Ostwald ripening stage, J^{Ga} and J^{GaN} are the amounts of the material in liquid gallium and GaN nuclei by the time of completion of the Ostwald ripening stage, K_∞^s is the dissociation constant for GaN on the substrate surface, and k^{Ga} formally replaces the rate constant of the chemical reaction for single-component compounds.

By analogy with the calculations described in [5], we solve the system of equations (27) for J^{Ga} taken equal to zero and obtain a line dividing the plane of the $Q_{0\mathrm{N}}$–$Q_{0\mathrm{Ga}}$ phase diagram into two parts. Above this line, the islands are present, whereas below it, the islands are absent. In order to determine the region of existence of GaN, the quantity J^{GaN} should be taken equal to zero and the system of equations (27) should be solved by expressing J^{GaN} in terms of $Q_{0\mathrm{N}}$ and $Q_{0\mathrm{Ga}}$. Then, taking into account the physically reasonable roots for J^{GaN}, we obtain

$$J^{\mathrm{GaN}} = \frac{Q_{0\mathrm{N}} + Q_{0\mathrm{Ga}}}{2} - \frac{1}{2}\sqrt{(Q_{0\mathrm{N}} - Q_{0\mathrm{Ga}})^2 + 4K_\infty^s}. \tag{28}$$

Analysis of the phase diagrams for GaN island films formed at the stage of Ostwald ripening (Fig. 5) shows that an increase in the temperature leads to changes in the regions of existence of the phases involved. It should be noted that the phase diagram reflects only a thermodynamic tendency of the process. Moreover, liquid islands consisting of pure gallium do not necessarily occur in the coexistence region of Ga and GaN and, quite probably, Ga can contain GaN impurities.

For $Q_{0\mathrm{N}} = Q_{0\mathrm{Ga}}$, the specific boundary flux β_s^0 can be represented in the form

$$\beta_s^0 = \frac{\beta_{s\mathrm{N}}\beta_{s\mathrm{Ga}}K_{s\infty}^{1/2}}{4(\beta_{s\mathrm{N}} + \beta_{0\mathrm{Ga}})}. \tag{29}$$

Finally, we estimate the constant A_3 for GaN. In the case when $Q_{0\mathrm{Ga}} = Q_{0\mathrm{N}}$, we obtain $A_3 \sim 10^{-33}$ m^3 s^{-1} at $T = 650°\mathrm{C}$, $A_3 \sim 10^{-29}$ m^3 s^{-1} at $T = 850°\mathrm{C}$, and $A_3 \sim 10^{-28}$ m^3 s^{-1} at $T = 1000°\mathrm{C}$. Hence, it follows that the growth rate of GaN islands substantially depends on the temperature.

4. CONCLUSIONS

Thus, the results obtained in the present work allowed us to draw the following conclusions. (1) At high temperatures ($T > 700°\mathrm{C}$), the growth of islands is controlled by the chemical reaction of formation of gallium nitride. The nuclei formed in this case are characterized by a large spread in their sizes. (2) At lower temperatures ($T < 600°\mathrm{C}$), the island growth is limited by the surface diffusion of nitrogen atoms. The islands nucleated at these temperatures are virtually identical in size. (3) In the temperature range 600–700°C, the growth of islands occurs through a combined mechanism.

ACKNOWLEDGMENTS

This work was supported by the St. Petersburg Research Center of the Russian Academy of Sciences, the Foundation for Support of Science and Education (St. Petersburg), and the Russian Foundation for Basic Research (project nos. 02-0217216 and 02-0332471). V. N. Bessolov acknowledges the support of the "Surface Atomic Structures" Program, project no. 5-4-99.

REFERENCES

1. S. C. Jain, M. Willander, J. Narayan, and R. van Overstraeten, J. Appl. Phys. **87**, 965 (2000).
2. M. Hiroki, H. Asahi, H. Tampo, *et al.*, J. Cryst. Growth **209**, 387 (2000).
3. S. A. Kukushkin, V. N. Bessolov, A. V. Osipov, and A. V. Luk'yanov, Fiz. Tverd. Tela (St. Petersburg) **43**, 2135 (2001) [Phys. Solid State **43**, 2229 (2001)].
4. S. A. Kukushkin and A. V. Osipov, Usp. Fiz. Nauk **168**, 1083 (1998) [Phys. Usp. **41**, 983 (1998)].
5. S. A. Kukushkin and V. V. Slezov, *Disperse Systems on Solid Surfaces* (Nauka, St. Petersburg, 1996).
6. F. Widmann, B. Daudin, G. Feuillet, *et al.*, J. Appl. Phys. **83**, 7618 (1998).
7. S. W. King, E. P. Carlson, R. J. Therrien, *et al.*, J. Appl. Phys. **86**, 5584 (1999).
8. R. S. Q. Fareed, J. W. Yang, J. Zhang, *et al.*, Appl. Phys. Lett. **77**, 2343 (2000).
9. J. Neugebauer, T. Zywietz, M. Scheffer, and J. Northrup, Appl. Surf. Sci. **159–160**, 355 (2000).

Translated by O. Borovik-Romanova